

Research Conference Proceedings

International Ground Source Heat Pump Association
Annual Conference, December 6-8, 2022, Las Vegas, Nevada, USA

Editors: Jeff Spitler, José Acuña, Michel Bernier, Massimo Cimmino,
Zhaohong Fang, Signhild Gehlin, Saqib Javed, Xiaobing Liu,
Simon Rees, Andrew Stumpf



The Groundwork for Sustainability: Geothermal

International Ground Source Heat Pump Association
Research Conference Proceedings

Las Vegas, Nevada, USA

December 6-8, 2022

Editors: Jeffrey Spitler, José Acuña, Michel Bernier, Massimo Cimmino,
Zhaohong Fang, Signhild Gehlin, Saqib Javed, Xiaobing Liu,
Simon Rees, Andrew Stumpf

DOI: <https://doi.org/10.22488/okstate.22.000010>

Table of Contents

Foreword.....	8
Committee Membership.....	9
Session 1: General	8:00 AM - 10:00 AM Tuesday 12/6
<i>Session Chair: Philippe Pasquier</i>	
Impact Analysis of Heating Electrification in US Buildings with Geothermal Heat Pumps. Liu, X., M. Malhotra, Y. Li, J. Lian, X. Wang, J. Ho.....	11
Long-term GSHP system performance measurement in the USA and Europe. Spitler, J.D., S. Gehlin ..	19
Climate change effects on the energy performance of a residential groundsource heat pump system. Sabbagh, G., M. Bernier	27
Potential Mapping of Ground Source Heat Pump Systems Considering Groundwater Pumping. Fujii, H., K. Yamashita, S. Tsuya, H. Kosukegawa	37
Session 2: GHE modeling and design	10:15 AM - 12:15 PM Tuesday 12/6
<i>Session Chair: Michel Bernier</i>	
pygfunction 2.2 : New Features and Improvements in Accuracy and Computational Efficiency. Cimmino, M., J. Cook	45
Ground Heat Exchanger Design Tool with RowWise Placement of Boreholes. Spitler, J. D., T.N. West, X. Liu	53
Development of a Topology Optimization Method for the Design of Ground Heat Exchangers. Noël A., M. Cimmino	61
Influence of buildings on geothermal boreholes – a comparison between two models. Fasci, M.	69
Session 3: TRT	1:15 PM - 3:15 PM Tuesday 12/6
<i>Session Chair: Xiaobing Liu</i>	
Stationary and non-stationary deconvolution to recover long-term transfer functions. Dion, G., P. Pasquier, D. Marcotte, G. Beaudry	78
Accuracy of analytical approaches to thermal response test interpretation. Oh, H.-R., S. Kim, B. Park, J. Baek, K. Lee	86
Uncertainty assessment of the hydraulics properties surrounding a standing column well with a thermal response test. Jacques, L., P. Pasquier	95
Field tests and numerical simulation of a novel thermal response test equipment for water wells . Tanaka, S., H. Fujii, H. Kosukegawa, S. Tsuya	104

Table of Contents

Session 4: Groundwater 8:00 AM - 10:00 AM Wednesday 12/7

Session Chair: Jeffrey Spitler

Column Experiments to Anticipate Clogging of Standing Column Wells. Cerclet, L., B. Courcelles, P. Pasquier	112
Forecasting Hydraulic Head Changes in Injection Wells Using LSTM Network. Rose, C., P. Pasquier, A. Nguyen, G. Beaudry	121
A Case Study on High-Resolution Monitoring Network of Groundwater Heat Pump System. Baek, J.-Y., H.-R. Oh, S.-W. Ha, S.-S. Lee, K.-K. Lee	131
Modeling and performance evaluation of fractured thermal energy storage (FTES). Hesselbrandt, M., J. Acuña	139

Session 5: Systems and case studies 1:30 PM - 3:30 PM Wednesday 12/7

Session Chair: Massimo Cimmino

Economic Optimization and Parametric Analysis of Large Hybrid Ground Source Heat Pump Systems: A Case Study. Nguyen, A., P. Eslami-Nejad, J. Tamasauskas, M. Kegel	147
Ground heat exchangers with large diameter pipes: What are the benefits?. Raymond, J., J. Gosselin, J. Lavoie	156
Ground heat exchanger performance with variable speed ground-source heat pumps. Viviescas, G., M. Bernier	164
Impacts of Prospective LEED Building's Energy Loads on a Borehole Heat Exchanger: A Case Study in Central Illinois. Zhao, Z., A. Stumpf, Y.-F. Lin, X. Wang	173

Session 6: GHE modeling & simulation 4:00 PM - 5:00 PM Wednesday 12/7

Session Chair: Maria Letizia Fasci

Transient heat transfer in ground heat exchangers under groundwater flow. Prieto, C., M. Cimmino ...	182
Dynamic simulation of ground source heat pump systems with nonstationary convolutions. Beaudry, G., P. Pasquier	190

Table of Contents

Session 7: Systems and case studies 8:00 AM - 10:00 AM Thursday 12/8

Session Chair: Matt Mitchell

A technical and economic evaluation of a ground source heat pump with thermal and battery energy storage systems for residential dwellings in Quebec. Eslami-Nejad, P. , S. Kimiaei, S. Kazemi-Ranjbar 199

Investigation of Design and Control Strategies for Combining Photovoltaic Thermal (PVT) Solar Modules with Ground-Source Heat Pump Systems: Case Example for Net Zero Building in a Moderately Cold Climate. Almoatham, S., A. Chiasson, R. Mulford, M. Moreno-Pena, C. Yavuzturk, R. Revankar, S. Hamstra, M. Zender, S. Melink 208

The Characterization of Helical Steel Pile Performance Under Varying Soil Conditions. Henry-Mathieu, K., S. Antoun, S. Dworkin 216

Experimental Performance Analysis of a Dual Source Heat Pump Integrated with Thermal Energy Storage. Liu, X., L. Wang, B. Shen, X. Liu, A. Gehl, L. Shi, M. Qu 228

Session 8: Controls & Analytics 10:15 AM - 12:15 PM Thursday 12/8

Session Chair: Jasmin Raymond

Long-term sustainable operation of hybrid geothermal systems through optimal control. Cupeiro Figueroa, I., L. Helsen 236

A control strategy evaluation framework for Ground Source Heat Pumps using Standing Column Wells. Tonellato, G., M. Kummert, J. Candanedo, G. Beaudry, P. Pasquier 246

Machine-learning-based models for predicting the performance of Ground-source heat pumps using experimental data from a residential Smart Home in California.. Najib, A., A. Hussain, S. Krishnamoorthy 256

An open library of g-functions for 34,321 configurations. Spitler J., T. West, X. Liu, I. Borshon 264

Session 9: Design tools 1:15 PM - 2:15 PM Thursday 12/8

Session Chair: Parham Eslami-Nejad

Novel tool and guidelines for ground source heat pumps in densely populated areas: a Swedish project. Fasci, M. L., L. Eriksson 272

Development of a Web-based Screening Tool for Ground Source Heat Pump Applications. Liu X., J. Degraw, M. Malhotra, W. Forman, M. Adams, G. Accawi, B. Brass, N. Kunwar, J. New, J. Guo 280

Foreword

This conference on the success of the first “research track” at the 30th annual IGSHPA conference held in Denver in March 2017 and a standalone research conference held at the Royal Institute of Technology in Stockholm Sweden during September of 2018. There has been a lengthy hiatus due to some reorganization of IGSHPA, and the global pandemic.

The organization started with formation of an expanded Executive Scientific Committee and an International Scientific Committee, both listed on the following pages. (The Executive Scientific Committee agreed on the following list of topics in the call for papers:

- Advanced design of GHEs
- Measured performance of GSHP systems and alternative GHE designs
- Modeling and simulation of GSHPs and GSHP systems
- New system configurations and supporting models
- Environmental aspects of GSHP systems
- Design and performance of GSHPs and GSHP components
- Modeling and simulation of GHE and validation of GHE and GSHP models
- Coupled groundwater and borehole heat transfer models
- Community- or district-scale GSHP systems
- Thermal response tests for measurement of ground thermal properties
- Optimal control, operation and fault detection of GSHP systems
- Advances in materials and working fluids used in GHE
- Energy storage integrated with GSHP systems
- Developments in the regulation and permitting of GSHP systems
- Application of GSHP systems in the urban environment
- Application of GSHP systems for agriculture
- Energy geostructures (geo-piles, energy shafts, geo-tunnels, geo-walls)
- Open loop GSHP systems (e.g., standing column wells)
- Integration of alternative thermal energy sources (surface water, wastewater, etc.) with GSHP systems
- Other GSHP-related phenomena (e.g., moisture transport, groundwater flow, freezing/thawing).
- History of GSHPs and GSHP technology

A total of 44 abstracts were submitted, leading to 32 papers scheduled to be presented here in Las Vegas. The review process for each paper was managed by one of the Executive Scientific Committee members and each paper was reviewed by at least two peer reviewers drawn from the International Scientific Committee and other experts. Most of the papers went through two rounds of reviews before being accepted. **A big thank you goes out to all the authors, committee members and reviewers!**

To help ensure that the papers remain widely available, they will be available from both the IGSHPA website and SHAREOK, which is the joint institutional repository for the University of Oklahoma Libraries and Oklahoma State University Libraries. All papers have received digital object identifiers (DOI); these appear on each paper and give a persistent and permanent link to the paper.

I wish everyone a fruitful and productive conference!

Jeffrey D. Spitler

Chair, Executive Scientific Committee

EXECUTIVE SCIENTIFIC COMMITTEE

- Jeffrey D. Spitler, Oklahoma State University, USA
- José Acuña, KTH, Sweden
- Michel Bernier, Polytechnique Montréal, Canada
- Massimo Cimmino, Polytechnique Montréal, Canada
- Zhaohong Fang, Shandong Jianzhu University, China
- Signhild Gehlin, Swedish GeoEnergy Center, Sweden
- Saqib Javed, Lund University, Sweden
- Xiaobing Liu, Oak Ridge National Laboratory, USA
- Simon Rees, University of Leeds, UK
- Andrew Stumpf, University of Illinois at Urbana-Champaign, USA

INTERNATIONAL SCIENTIFIC COMMITTEE

- P. Bayer, MLU, Germany
- R. Beier, Oklahoma State University, USA
- Chiasson, University of Dayton, USA
- P. Eslami-Nejad, CANMET Energy, Canada
- M. Fossa, University of Genoa, Italy
- G. Hellström, NeoEnergy, Sweden
- L. Helsen, KU Leuven, Belgium
- Lazzarotto, KTH, Sweden
- M. Mitchell, NREL, USA
- H.Ö. Paksoy, Cukurova University, Turkey
- Palm, KTH, Sweden
- P. Pasquier, Polytechnique Montréal, Canada
- J. Raymond, INRS, Canada
- R. Curtis, GeoScience, UK
- H. Yang, HKPU, China
- G. Zhang, Hunan University, China
- K. Zhu, Shandong Architectural University, China



Impact Analysis of Heating Electrification in US Buildings with Geothermal Heat Pumps

Xiaobing Liu
Xiaofei Wang

Mini Malhotra
Jonathan Ho

Yanfei Li

Jamie Lian

ABSTRACT

Few studies have investigated the impacts of large-scale deployment of geothermal heat pumps (GHPs, also called ground source heat pumps) on the electric grid. GHPs utilize the ground as a heat source to warm buildings more efficiently than other space-heating systems. The coupling with the ground offers seasonal thermal storage so that GHPs can also cool buildings in summer more efficiently than other space-cooling systems. This study simulated the performance of GHP systems for various commercial and residential buildings in 15 climate zones in the United States. Combined with the latest End-Use Load Profiles of the US building stock and grid modeling, this study aims to assess the impacts of a national deployment of GHP systems on the US electric grid in terms of energy consumption, emissions, and operational resilience. The preliminary results show that the GHP deployment can save 429 billion kWh of electricity (a 19% reduction from baseline) and reduce carbon emissions by 496 million tons per year (a 31% reduction from baseline). A geographical view of the results indicates that retrofitting existing HVAC systems with new GHP systems can lead to further reductions in annual electricity consumption and peak electricity demand in the southern regions of the United States than in other parts of the country. On the other hand, GHP retrofits result in higher percentages of site energy savings and carbon emission reduction in the north (cold climates) than in the south (warm climates).

INTRODUCTION

In the United States, the building sector (including residential and commercial buildings) consumes 40% of primary energy and accounts for 75% of electricity use, which contributes to 35% of carbon emissions in the United States (EIA 2020). The US administration has set a target to reduce greenhouse gas emissions by 50% by 2030 and to become a carbon-neutral economy by 2050 (Kerry 2022). The administration also set a goal to achieve 100% clean electricity by 2035. Using heat pumps to replace fossil-fuel furnaces has become a trend in the building sector to achieve decarbonization. Mai et al. (2018), Tarroja et al. (2018), and White and Rhodes (2019) indicate that using air-source heat pumps to replace gas-fired furnaces in the residential sector would result in higher annual electricity consumption and a shift in electric peak demand from summer to winter, and this shift would be a substantial change in how the grid operates and would require substantial new investments in electric power infrastructure.

Xiaobing Liu (liux2@ornl.gov) and Mini Malhotra are R&D Staff at Oak Ridge National Laboratory (ORNL). Yanfei Li is an associate R&D staff at ORNL. Jamie Lian is the group leader at ORNL. Xiaofei Wang is a PhD student from the University of Tennessee, Knoxville. Jonathan Ho is an energy analyst at the National Renewable Energy Laboratory.

This manuscript has been authored by UT-Battelle, LLC, under contract DE-AC05-00OR22725 with the US Department of Energy (DOE). The US government retains and the publisher, by accepting the article for publication, acknowledges that the US government retains a nonexclusive, paid-up, irrevocable, worldwide license to publish or reproduce the published form of this manuscript, or allow others to do so, for US government purposes. DOE will provide public access to these results of federally sponsored research in accordance with the DOE Public Access Plan (<http://energy.gov/downloads/doe-public-access-plan>).

Previous studies (e.g., Bayer et al. 2012, Yuan et al. 2012, You et al. 2021) have reported that geothermal heat pumps (GHPs, also called ground source heat pumps) are more energy-efficient than conventional heating and cooling systems. GHPs achieve this efficiency by utilizing the ground, which has a stable temperature year-round, as a heat source for heating operation and a heat sink for cooling operation. When driven with renewable power, GHPs do not result in any emissions. Liu et al. (2015) reported that by 2012 the cumulative capacity of GHPs installed in the United States had reached 3.9 million refrigeration tons. The US Department of Energy’s (DOE’s) GeoVision study (2019) predicted that the “equivalent of more than 28 million households [would be] using geothermal heat pumps by 2050.” Previous studies (Trumpy et al. 2016 and Liu et al. 2019) estimated the potential energy savings and emission reductions of retrofitting US buildings with GHPs, but few studies have investigated the impacts of large-scale deployment of GHPs on the electric grid.

The contiguous US electric power system can be divided into 134 balance areas (BAs) for modeling purposes, as shown in Figure 1. Each BA represents the topology of the contiguous US electric power system. These regions are delineated by counties and represent the spatial resolution at which generation, load, and transmission are balanced in the grid model. The boundaries of the balancing areas align with the boundaries of the county groups.

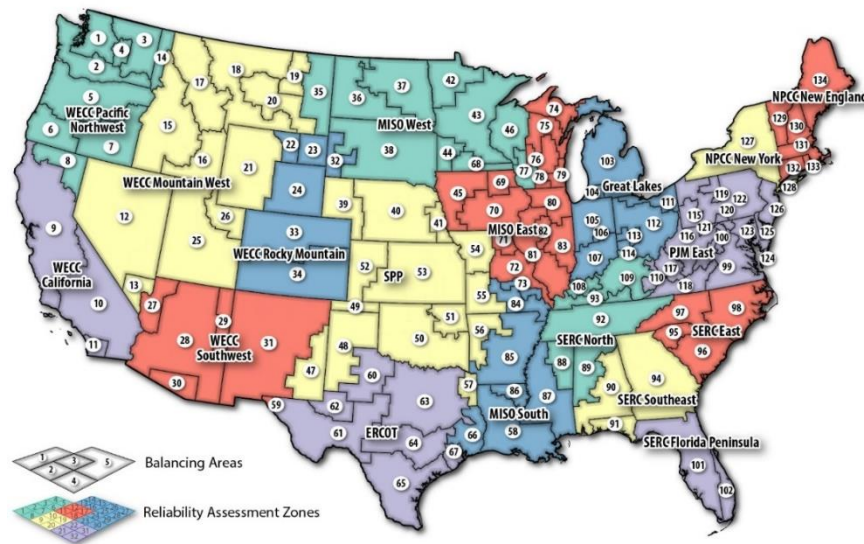


Figure 1 BAs of the contiguous US electric power system considered in this study.

This paper introduces the methodology and data sources used to evaluate the impacts on energy consumption and carbon emissions that would result from a mass deployment of GHP in the United States. The results of this analysis are presented for each BA of the contiguous US electric power system. Additionally, a geospatial representation of energy savings and emission reductions across the United States is presented.

METHODOLOGY

The procedure for analyzing the impacts of mass GHP deployment on the US grids includes two steps. In the first step, the impacts of GHP retrofits on the energy consumption and electricity demand of residential and commercial building stocks were quantified for each BA and aggregated across the contiguous United States (i.e., excluding Alaska and Hawaii). In the second step, the difference in hourly electricity use that resulted from the GHP retrofits is used as an input in the grid modeling. The grid modeling is ongoing as of this writing, and the results will be reported in a future

paper. Existing buildings have diverse characteristics and operation schedules that must be considered when calculating the end-use load profile (EULP) of existing building stocks. This study uses the EULP dataset published by the National Renewable Energy Laboratory (2021) for US building stock as the baseline for assessing the impacts of GHP retrofits. New EULPs that result from retrofitting all applicable buildings in the United States with new GHP systems were calculated with the following procedure (as shown in Figure 2):

1. Replace existing HVAC systems in the prototype models with new distributed GHP systems.

These prototype models include 16 commercial building types (e.g., office, school, retail, restaurant, hotel, hospital, warehouse) and 4 single-family house types, each with different space-heating systems (gas/oil furnace, electric resistance, or air-source heat pump). These prototype models represent typical US buildings (US DOE 2022) in 15 climate zones in the United States (ASHRAE 2013).

Distributed GHP systems are commonly used in the United States, and they provide independent climate control in each thermal zone of the building without using supplemental heating or cooling. The GHP unit's rated coefficients of performance (COP) are 4.0 for heating and 6.5 for cooling. A vertical bore ground heat exchanger (VBGHE)¹ is sized to maintain the leaving fluid temperature of the VBGHE between 1°C and 35°C year-round. Outdoor air is provided with a dedicated ventilation system in parallel with the distributed GHP system.

2. Predict energy consumption of the retrofitted building by using an integrated GHP simulation program developed at DOE's Oak Ridge National Laboratory (ORNL) (Liu et al. 2022).

The program accounts for energy savings from the GHP system's higher operational efficiency; from avoiding simultaneous heating and cooling, which is common in the conventional variable air volume systems; and from the reduced fan power use owing to a dedicated outdoor air ventilation system and improved fan control and efficiency.

3. Calculate hourly relative differences (fraction factors) in the HVAC-related site energy consumption between the existing HVAC system and a new GHP system for each prototype building in the 15 climate zones.

4. Identify valid candidates for GHP retrofits by using the metadata summary of the characteristics of the residential and commercial building stock in the latest EULP database.

This process excludes buildings that use district heating/cooling (i.e., no energy consumption for heating/cooling at the building), mobile homes, buildings without heating/cooling, and buildings that already use GHPs.

5. Apply the fraction factors to the EULPs of existing buildings (i.e., baseline) that are valid candidates for GHP retrofits to determine the new EULPs that result from the GHP retrofit.²

6. Aggregate the baseline and new EULPs by county and by BA to calculate changes in hourly electricity consumption, the annual peak electricity demand, and fossil fuel use in each BA.

7. Calculate the resulting carbon-emission reduction in each BA by using the 2021 Cambium data for Long-run Marginal Emission Rates for Electricity (Gagnon, Hale, and Cole 2022) and ASHRAE Standard 105-2021 for carbon emission factors of various fossil fuels (ASHRAE 2022).

¹ Boreholes are laid out in a square of a near-square field with 6.1 m (20 ft) bore spacing.

² This may result in some misalignment between the thermal demands and the fraction factors for some buildings in shoulder seasons.

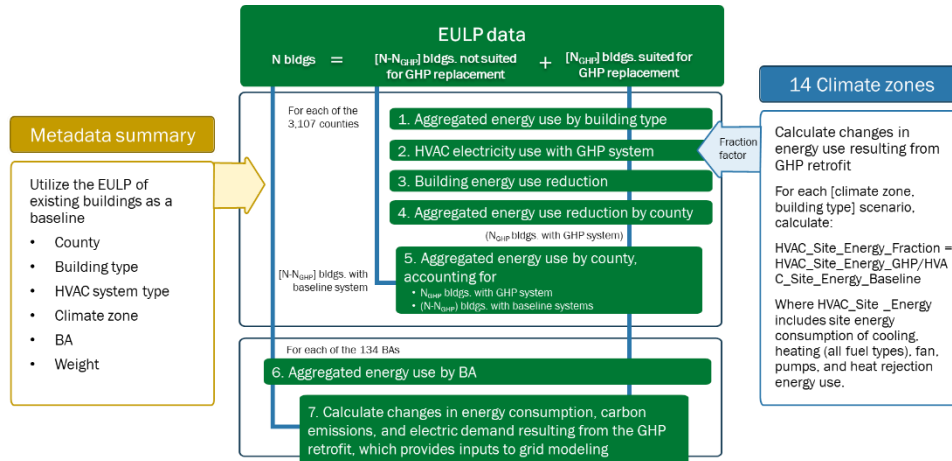


Figure 2 Flowchart of impact analysis for energy consumption and carbon emissions.

RESULTS AND ANALYSIS

Results from the study indicate that retrofitting all applicable buildings in the United States with GHPs can reduce electricity usage by 429 billion kWh (a 19% reduction from the baseline EULP) each year. It will also eliminate 4,920 billion MJ of annual fossil fuel (e.g., natural gas, heating oil, propane) consumption. As a combined result of the reduced electricity and fossil fuel consumption, 496 million MT of carbon emissions will be avoided (a 36% reduction from baseline) each year. The impacts on energy consumption in each BA and the geospatial characterization of the energy savings and emission reduction are presented below.

GHP Impacts at Each BA

Table 1 lists the minimum, maximum, and average values of the changes in electricity and fossil fuel consumption as well as the carbon emissions that result from the GHP retrofits in the 134 BAs. The percentages of these changes are also shown. Positive values indicate savings or reduction compared with the baseline and reflect the benefits of GHP retrofits. Negative values indicate an increase in energy use or carbon emission. Most BAs show savings in electricity, and fossil fuel consumption and carbon emissions are reduced in all BAs. The GHP retrofits lead to increased electricity consumption in a few BAs in the northeastern United States because most space heating in these BAs is provided by furnaces or boilers that consume fossil fuels. Replacing these furnaces and boilers with GHPs will consume more electricity but will eliminate fossil fuel consumption for space heating. Propane and heating oil are not used in all BAs. In BAs without propane or heating oil consumption, the change in propane or heating oil consumption is zero. The large negative value in the percentage of peak electricity demand reduction is in a BA for which cooling demand is low, but heating demand is high, and the existing heating systems are gas furnaces. Therefore, GHP retrofits result in a peak electric demand in winter that is higher than the previous peak electric demand, which occurred in summer.

Table 1. Changes in Energy Consumption from GHP Retrofits in all BAs

Energy Consumption Items	Min	Max	Mean
Electricity Savings [TWh = 10 ⁹ kWh]	-0.2	28.0	3.2
Percentage of Electricity Savings [%]	-2.1	65.9	20.2
Peak Electricity Demand Reduction [GW = 10 ⁶ kW]	-0.1	11.9	1.5
Percentage of Peak Electricity Demand Reduction [%]	-68.4	75.2	32.9
Natural Gas Savings [PJ = 10 ¹⁵ J]	0.0	405.0	29.9

Percentage of Natural Gas Savings [%]	1.4	82.3	62.4
Heating Oil Savings [PJ = 10 ¹⁵ J]	0.0	103.9	4.4
Percentage of Heating Oil Savings [%]	0.0	100.0	57.2
Propane Savings [PJ = 10 ¹⁵ J]	0.0	25.7	2.5
Percentage of Propane Savings [%]	0.0	90.1	61.5
Carbon Reduction [Million MT = 10 ⁹ kg]	0.003	3.8	0.37
Percentage of Carbon Reductions [%]	18.7	82.6	50.7

Figure 3 shows the changes in annual electricity consumption and peak electricity demand in each of the 134 BAs. The red bars represent the absolute values of the changes, and the blue dots indicate the percentages of the changes compared with baseline EULP. Electricity savings (positive values) are predicted for most BAs. More than 10 TWh of electricity can be saved each year in 15 BAs, which include populated areas. The annual peak electricity demand is also reduced significantly (around 30%) in these BAs. Figure 4 shows the annual savings in natural gas, heating oil, and propane in each BA, including the magnitude of savings and percentage of savings. In 9 BAs, more than 100 PJ of natural gas consumption can be avoided by performing GHP retrofits. Across all the BAs, the average natural gas savings is about 63%. Heating oil is used only in a small number of BAs in the northeastern United States, and the magnitude of savings is only about 25% of the natural gas savings. The magnitude of savings for propane is lower than that of natural gas and heating oil. However, propane is more widely used in various BAs than heating oil, and 8 BAs would have more than 8 PJ of propane savings each year. Figure 5 shows the magnitude and percentages of carbon emission reduction in each BA. More than 1.15 million MT of carbon emissions can be reduced in each of the 13 BAs that have more significant emission reduction than other BAs by replacing existing HVAC systems with GHPs. On average, carbon emissions would be reduced by 50.7% in all BAs.

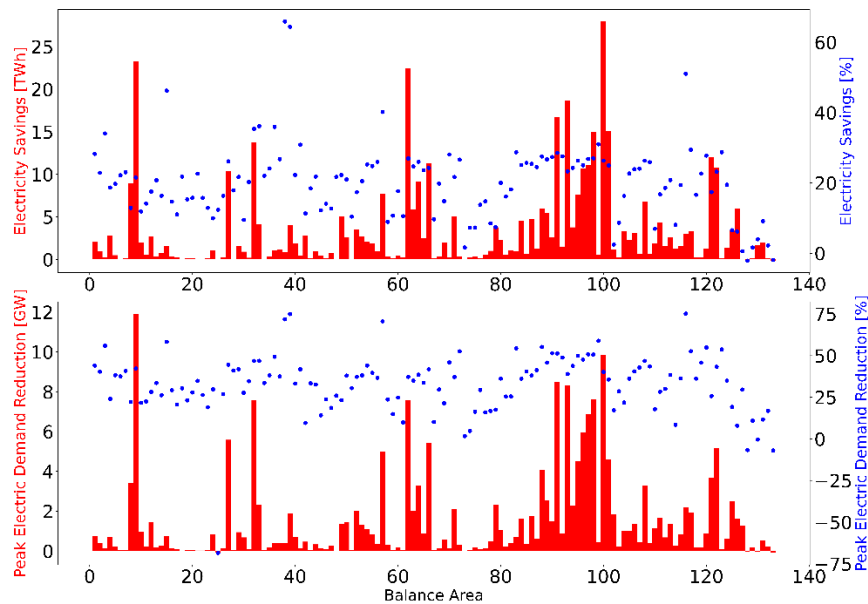


Figure 3 Annual electricity savings and peak electric demand reduction in each of the 134 BAs after GHP retrofits.

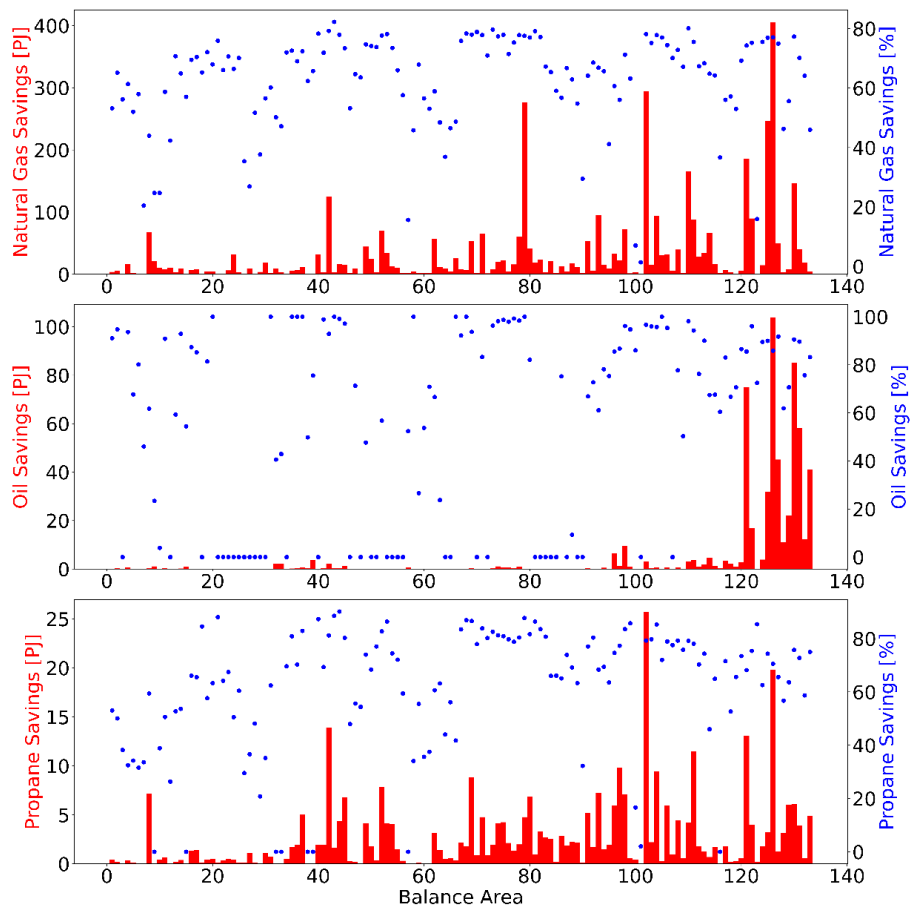


Figure 4 Annual savings in fuel consumption in each of the 134 BAs after GHP retrofits.

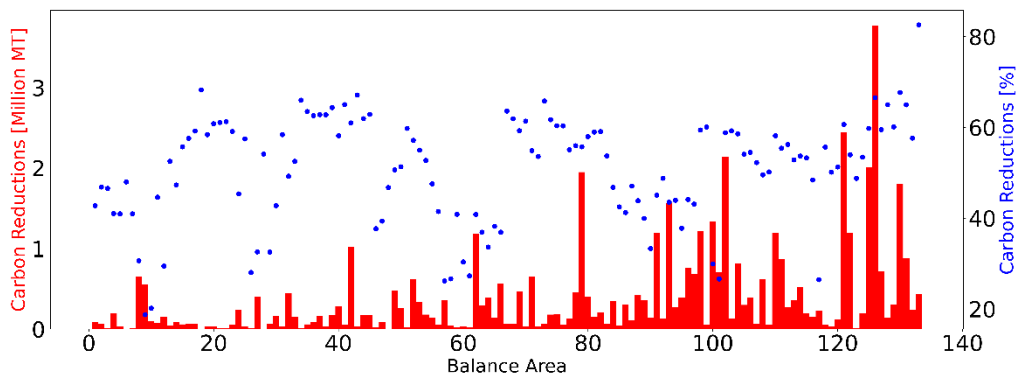


Figure 5 Annual carbon emission reduction in each of the 134 BAs after GHP retrofits.

Geospatial Characterization of the Impacts

Figure 6 provides a geospatial representation of the changes in annual electricity consumption, annual peak electric demand, site energy consumption, and carbon emissions that result from the mass deployment of GHPs in each BA. Figures 6(a) and 6(b) show that retrofitting the existing HVAC systems with new GHPs will reduce electricity consumption in most parts of the United States, except in a few BAs in the northeastern region. More significant

reductions in annual electricity consumption and peak electric demand will be achieved in southern BAs. On the other hand, Figures 6(c) and 6(d) show that GHP retrofits result in higher percentages of site energy savings and carbon emission reduction in the northern BAs (colder climates) than in the southern BAs.

These regional differences are due to different heating and cooling demands in each BA and the energy sources used for providing space heating in the existing HVAC systems. According to EIA (2021), more than 99% of existing HVAC systems consume electricity to provide space cooling. GHPs will reduce electricity consumption for space cooling because they are more efficient than existing space cooling systems. Existing space heating systems use electricity or fossil fuels. If a GHP replaces an electric heating system (e.g., electric resistance or air-source heat pump), then it will further reduce electricity consumption. But if it replaces fuel-burning heating equipment, then it will eliminate fuel consumption while consuming some electricity. Therefore, in the southern BAs, where the cooling demand is higher and more than 40% of space heating is provided with electricity, the GHP retrofits will result in significant savings in electricity. In a contrast, because most space heating in the northern BAs is provided by fossil fuels, the GHP retrofits will result in increased electricity consumption in the heating season that will offset a part of the electricity savings obtained during the cooling season; in some situations, this may even increase annual electricity consumption. Therefore, electricity savings gained from GHP retrofits in the northern BAs are not as significant as in the southern BAs. Furthermore, the difference in energy efficiency between GHPs and conventional HVAC for cooling (e.g., a GHP with 6.5 cooling COP vs. a chiller with 5 cooling COP), which is determined based on the site energy consumption, is smaller than that for heating (e.g., a GHP with 4.0 heating COP vs. a natural gas furnace with 0.8 burner efficiency). Therefore, the site energy reduction would be higher in the northern BAs, where buildings have larger heating demands.

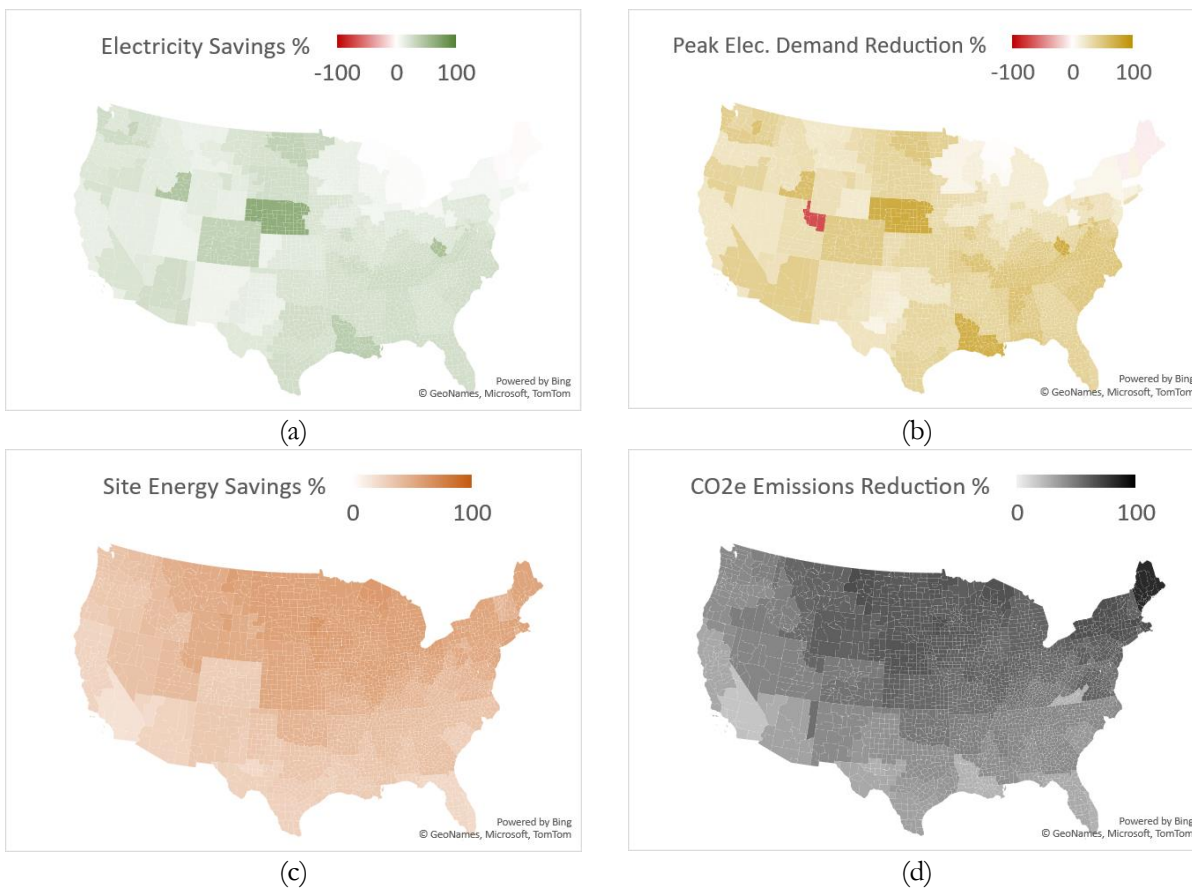


Figure 6 Geospatial representation of the changes in (a) annual electricity consumption, (b) annual peak electric demand, (c) site energy consumption, and (d) carbon emissions that would result from the mass deployment of GHPs in each BA.

CONCLUSIONS

This study assessed the impacts of the national deployment of GHP systems on the US electric grid in terms of energy consumption, peak demand, and carbon emissions. To accomplish this task, the EULP of residential and commercial buildings before and after the GHP retrofits were calculated and aggregated by BAs to represent the topology of the contiguous US electric grid. Carbon emission reductions associated with the GHP retrofits were also evaluated based on the latest information on the grid mix and emission factors of various fossil fuels.

The preliminary results of this study indicate that the national deployment of GHPs can save 429 billion kWh of electricity (a 19% reduction from baseline) annually and reduce 496 million tons of carbon emissions (a 31% reduction from baseline) each year. The GHPs in cold climates are more effective for reducing site energy consumption and carbon emissions. Higher electricity savings can be achieved in the southern BAs than in other parts of the United States, and peak electric demand reduction is highest in densely populated areas in the southern United States.

ACKNOWLEDGMENTS

This material is based upon work funded by the DOE's Geothermal Technologies Office (GTO). This research used resources from ORNL's Building Technologies Research and Integration Center. This manuscript has been authored by UT-Battelle LLC under contract DEAC05-00OR22725 with DOE. The US government retains and the publisher, by accepting the article for publication, acknowledges that the US government retains a nonexclusive, paid-up, irrevocable, worldwide license to publish or reproduce the published form of this manuscript or allow others to do so, for the US government purposes.

REFERENCES

- ASHRAE. 2022. "ANSI/ASHRAE 105-2021 - Standard Methods of Determining, Expressing, and Comparing Building Energy Performance and Greenhouse Gas Emissions."
- ASHRAE, ANSI. 2013. "Standard 169-2013, Climatic Data for Building Design Standards." *ASHRAE, Atlanta*.
- Bayer, Peter, Dominik Saner, Stephan Bolay, Ladislaus Rybach, and Philipp Blum. 2012. "Greenhouse Gas Emission Savings of Ground Source Heat Pump Systems in Europe: A Review." *Renewable and Sustainable Energy Reviews* 16(2):1256–67.
- EIA. 2020. "U.S. Energy-Related Carbon Dioxide Emissions 2020." Retrieved January 14, 2022 (<https://www.eia.gov/environment/emissions/carbon/>).
- Gagnon, Pieter, Elaine Hale, and Wesley Cole. 2022. "Long-Run Marginal Emission Rates for Electricity - Workbooks for 2021 Cambium Data." 4 files.
- Kerry, John. 2022. "The Long-Term Strategy of the United States, Pathways to Net-Zero Greenhouse Gas Emissions by 2050."
- Liu, Xiaobing, Jason DeGraw, M. Malhotra, N. Kunwar, W. Forman, M. Adams, G. Accawi, B. Brass, and Joshua New. 2022. "Development of a Web-Based GSHP Screening Tool." Las Vegas, NV.
- Liu, Xiaobing, Shilei Lu, Patrick Hughes, and Zhe Cai. 2015. "A Comparative Study of the Status of GSHP Applications in the United States and China." *Renewable and Sustainable Energy Reviews* 48:558–70. doi: 10.1016/j.rser.2015.04.035.
- Luo, Jin, Joachim Rohn, Wei Xiang, David Bertermann, and Philipp Blum. 2016. "A Review of Ground Investigations for Ground Source Heat Pump (GSHP) Systems." *Energy and Buildings* 117:160–75.
- Mai, Trieu T., Paige Jadun, Jeffrey S. Logan, Colin A. McMillan, Matteo Muratori, Daniel C. Steinberg, Laura J. Vimmerstedt, Benjamin Haley, Ryan Jones, and Brent Nelson. 2018. *Electrification Futures Study: Scenarios of Electric Technology Adoption and Power Consumption for the United States*. National Renewable Energy Lab. (NREL), Golden, CO (United States).
- Tarroja, Brian, Felicia Chiang, Amir AghaKouchak, Scott Samuelson, Shuba V. Raghavan, Max Wei, Kaiyu Sun, and Tianzhen Hong. 2018. "Translating Climate Change and Heating System Electrification Impacts on Building Energy Use to Future Greenhouse Gas Emissions and Electric Grid Capacity Requirements in California." *Applied Energy* 225:522–34.
- White, Philip M., and Joshua D. Rhodes. 2019. "Electrification of Heating in the Texas Residential Sector." *Technical Report IdeaSmiths, LL C*.
- You, Tian, Wei Wu, Hongxing Yang, Jiankun Liu, and Xianting Li. 2021. "Hybrid Photovoltaic/Thermal and Ground Source Heat Pump: Review and Perspective." *Renewable and Sustainable Energy Reviews* 151:111569.
- Yuan, Yanping, Xiaoling Cao, Liangliang Sun, Bo Lei, and Nanyang Yu. 2012. "Ground Source Heat Pump System: A Review of Simulation in China." *Renewable and Sustainable Energy Reviews* 16(9):6814–22.



Long-term GSHP system performance measurement in the USA and Europe

Jeffrey D. Spitler

Signhild E.A. Gehlin

ABSTRACT

This paper presents an overview of the International Energy Agency (IEA) technology collaboration program Heat Pumping Technologies (HPT) Annex 52, “Long term performance measurement of ground source heat pump (GSHP) systems serving commercial, institutional and multi-family buildings.” This project, which ran from 2018 through 2021, focused on measuring the performance of larger GSHP systems, going beyond energy use intensities which commingle the performance of the building envelope, occupancy effects and the system performance. Instead, performance factors were calculated, similar to coefficients of performance, but measured over various time intervals and system boundaries. The primary objectives of the Annex were refining and extending methodologies to better characterize system performance in larger buildings, creating a library of quality long-term measurements in the form of case studies, and providing guidelines for instrumentation, uncertainty analysis, key performance indicators, data management and quality assurance.

This paper summarizes the Annex outcome and illustrates use of the Annex boundary levels with a comparison between typical European and US GSHP systems. It is anticipated that this experience and the guidelines produced as a result of this experience will lower the cost and improve consistency and quality for future performance measurements.

INTRODUCTION

The energy consumption of building heating and cooling systems often exceeds design expectations. This difference is often referred to as the “building energy performance gap.” (de Wilde 2014, Scofield 2009, Spitler 2020). Reasons for the gap include errors in design and installation, as well as non-optimal operating and control settings. Problems that don’t lead to occupant discomfort may neither be detected nor mitigated for months or years unless performance measurements are made. Despite the need for such measurements, published results from long-term performance monitoring of building energy systems are scarce. Instead of long-term measurements, energy use intensity (EUI) is a widely used indicator of building energy consumption, usually given as annual energy consumption per square meter or square foot of building floor area. As a minimum, EUI calculation requires only building utility bills and floor area. However, analyses of EUI have limitations in the difficulty to differentiate between the effects of the building envelope loads and occupants and the performance of the HVAC system. A high energy use in a building may be caused by e.g., a poor building envelope, high internal heat gains or other occupant effects, or by poor HVAC system performance. The EUI does not identify the cause(s) for the high energy use. For that we need more detailed performance measurements.

Also, in buildings that utilize ground-source heat pump (GSHP) systems the actual performance may vary widely. Gleeson and Lowe (2013) reviewed field measurements of heat pump systems for residential buildings, mainly single-family buildings, comprising 600 heat pump systems in six European countries. For larger non-residential ground-source heat pump (GSHP) systems. Spitler and Gehlin (2019) give an overview of published long-term (>1 year) measured

Jeffrey Spitler (spitler@okstate.edu) is a professor of mechanical engineering at Oklahoma State University. Signhild Gehlin (signhild.gehlin@geoenergicentrum.se) is CEO of the Swedish Geoenergy Center.

seasonal performance factor (SPF) and coefficient of performance (COP) values reported in the literature for 55 systems worldwide. Such systems are necessarily more complex than GSHP systems for small residential buildings, and often include both heating and cooling as well as supplementary heating and cooling sources and heat recovery. For larger GSHP systems in particular, owners have made significant investments with expectations of high performance, hence it is important that high performance be achieved. The literature review showed that there is little or no consistency in how to measure the performance and report the results. Cost-effective measurement programs are hindered by this lack of consistency and a lack of guidance regarding measurement system design. This was the starting point of a new international collaboration project – Annex 52.

IEA HPT Annex 52

IEA HPT Annex 52 - *Long-term performance monitoring of GSHP systems for commercial, institutional and multi-family buildings* was carried out during 2018-2021 by seven participating countries: Sweden, the USA, the UK, the Netherlands, Germany, Norway and Finland. The aims of Annex 52 were to (1) survey and create a library of quality long-term measurements of GSHP system performance for commercial, institutional, and multi-family buildings, (2) refine and extend current methodology to better characterize performance of such systems with the full range of features shown on the market, and (3) provide a set of benchmarks for comparisons of GSHP systems in the participating countries.

The main publications from Annex 52 are summarized in Table 1. These publications comprise more than 1000 pages in total and are available on the Annex 52 webpage¹. In addition, three sets of open-source measurement data from two GSHP systems have been made available. These outcomes from Annex 52 help building owners, designers and technicians evaluate, compare, and optimize GSHP systems, and provides useful guidance to manufacturers of instrumentation and GSHP system components, as well as to developers of tools for monitoring, controlling and fault detection/diagnosis. In the long run, this will lead to energy and cost savings.

Table 1. Overview of Annex 52 Guidelines and Reports

Report	Main content	Reference
Instrumentation Guideline	Overview of instrumentation that is typically required to measure the long-term performance of GSHP systems. Information about the use of heat meters and distributed temperature sensing in GSHP studies. Discusses challenges of data management and some methods to address these challenges.	Davis et al, 2021
Uncertainty Calculation Guideline	Practical introduction to calculation of uncertainties in measured performance factors for GSHP systems with the goal of helping practitioners estimate the uncertainty in performance factors.	Spitler et al, 2021a
Key Performance Indicator Guideline	Lists and defines recommended key performance indicators for larger GSHP systems. Defines and explains a new system boundary schema suitable for describing larger GSHP systems.	Gehlin et al, 2022
Annotated Bibliography	82 publications reporting at least one full season of measured data performance values (SPF, COP) for larger GSHP systems	Gehlin and Spitler, 2022a
Case Study Summary Report	2-page summaries of 29 GSHP system case studies	Gehlin and Spitler, 2022b
Annex 52 Final Report	Umbrella report summarizing the main work and results	Gehlin and Spitler, 2022c
Individual case study reports	27 individual case study reports for 29 larger GSHP systems in multiple countries.	

¹ <https://heatpumpingtechnologies.org/annex52/>

SYSTEM BOUNDARY SCHEMA AND KEY PERFORMANCE INDICATORS

A main contribution from Annex 52 is the development of a system boundary schema that, unlike most of the previously published system boundary schemas, is detailed and flexible enough to handle the complexity of larger GSHP systems. The starting point was the SEPEMO system boundary schema (Nordman et al. 2012), developed mainly for small heat pump systems in single family buildings, and which is widely used within the EU. The four boundaries allow analysis of the performance of different parts of the system – (1) heat pump, (2 & 4) circulating pumps on both sides of heat pump, and (3) auxiliary heating. Spitler and Gehlin (2019) evaluated six similar schemas, including the SEPEMO schema. These schemas have limitations when accounting for the complexity of larger GSHP systems, which led to the development of a new boundary schema. The Annex 52 boundary schema (Gehlin and Spitler 2021a) includes six boundaries and an indicator for use of supplemental heating or cooling (Figure 1). Every SEPEMO boundary matches one of the Annex 52 boundaries, but there is also a system boundary for the ground heat exchanger circuit (boundary 0), and one boundary that helps identifying the effect on the performance by buffer tanks (boundary 3). For boundary 1 (heat pump unit only and the electricity used for the compressor), none of the Annex 52 monitoring projects found it practical to exclude parasitic losses within the heat pump from the electricity measurement. An asterisk in the boundary level (e.g. HC5*) denotes an approximation was made – in this case including parasitic losses in the measured performance factor.

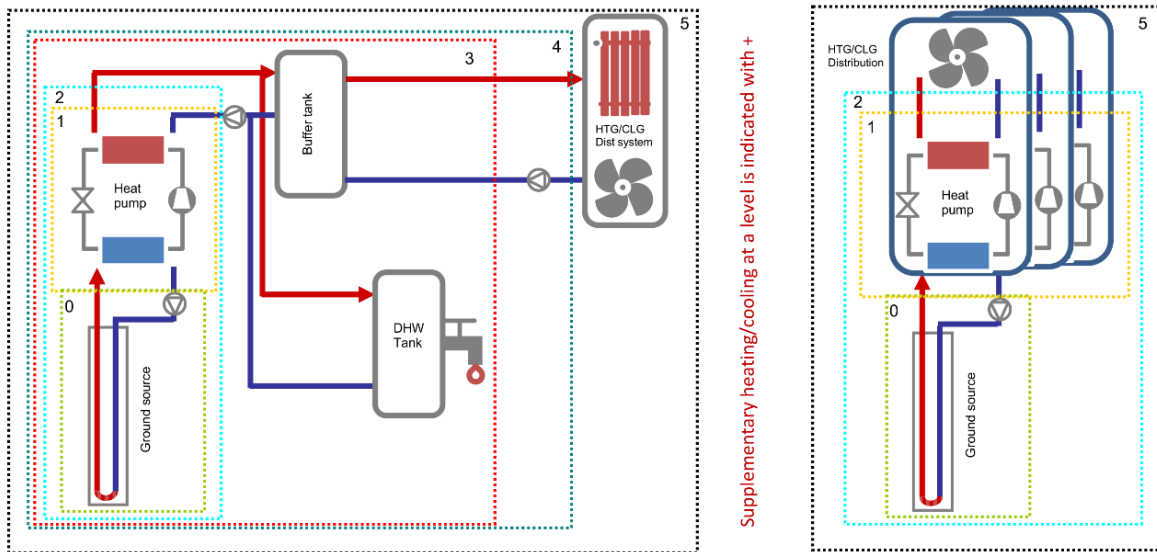


Figure 1 The Annex 52 system boundary schema applied for a centralized (left) and a distributed (right) GSHP system. Supplementary heating/cooling at a boundary level is indicated with +. (Gehlin and Spitler 2021)

A consistent and well-defined system boundary schema is paramount when analyzing the performance of a GSHP system. The performance differs depending on how the boundaries are defined. However, in the literature there has unfortunately been little consistency in the use of system boundaries. In fact, system boundaries are often not clearly defined at all, which makes it difficult to compare and evaluate the reported performance.

The Annex 52 key performance indicator guidelines (Gehlin et al. 2022) list and define a number of key performance indicators (KPIs) suitable to characterize performance of GSHP systems at various system boundaries. These include KPIs for the ground source, for the system components, and for the overall GSHP system level, as well as some KPIs for the overall building level to give an understanding for the loads on the GSHP system. While the Annex 52 scope didn't include financial indicators, several of the KPI could be extended to give financial indicators. Among other performance indicators, the guideline explains the terms COP, SCOP², EER and SEER, commonly used by the heat

² SCOP = Seasonal coefficient of performance; EER = Energy efficiency ratio; SEER = Seasonal energy efficiency ratio

pump industry to refer to KPI based on laboratory testing of a heat pump unit under one or more conditions. These KPI often have implications for codes and regulations. To distinguish between laboratory measurements and field measurements, Annex 52 promotes using the term “performance factor” when referring to field measurements, such as in the Annex 52 case study reports. The performance factor (PF) should be used with an indicator of the time period (Seasonal, Monthly, Weekly, Daily, or Binned – SPF, MPF, WPF, DPF, BPF), and with subscripts that correspond to the defined boundary conditions, e.g. H1 for heating at boundary level 1, C2 for cooling at boundary level 2 and HC4 for combined heating and cooling at boundary level 4.

All six system boundaries in the Annex 52 system boundary schema do not necessarily appear in every GSHP system. If, for example, there is no buffer tank installed in the system, the boundary level 3 does not exist, and for ground source systems with direct heating and/or cooling and no heat pump, boundary 1 does not exist and system boundary 0 and 2 become the same. For a distributed heat pump system, where there is no central heat pump, but multiple heat pump units are installed in the building, system boundaries 3 and 4 do not exist.

IEA HPT Annex 52 case studies

Annex 52 resulted in long-term measurement programs for more than 30 larger GSHP systems in seven countries (Figure 2). These GSHP systems cover a range of different building types and system applications and features. All but one of the GSHP projects have central heat pumps, as is common in Europe. The GSHP system located in the USA has distributed heat pumps in the building. As for ground sources, most of the monitored buildings use boreholes as the source for heating and cooling; four use energy piles, of which one combines energy piles with boreholes; and five use groundwater.

29 of these GSHP systems are described in individual detailed case study reports, available for download on the Annex 52 website³.

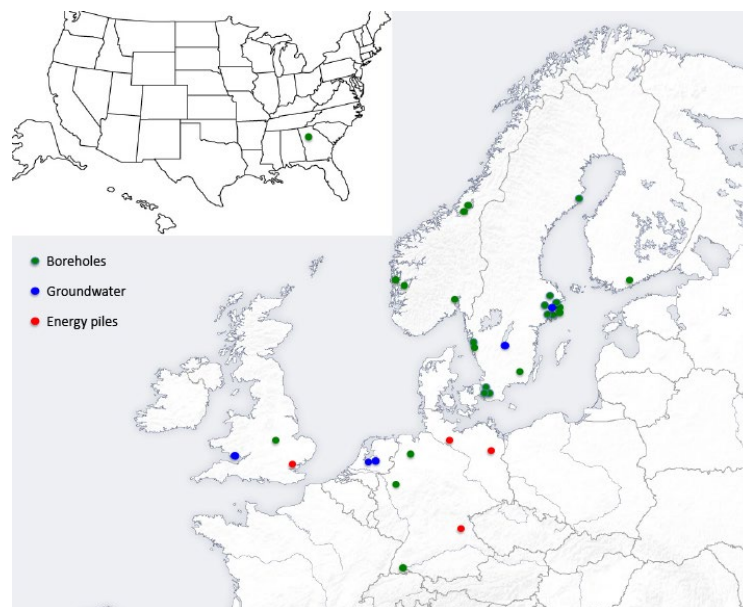


Figure 2 Monitored GSHP systems in the IEA HPT Annex 52 international collaboration project 2018-2021.

³ <https://heatpumpingtechnologies.org/annex52/documents/>

A TALE OF TWO BUILDINGS

To illustrate the use of the boundary levels developed in Annex 52, we consider two of the GSHP systems – a central system and a distributed system.

The Studenthuset building

Studenthuset (“The Student Building”) is a 6300 m² general purpose building used for student activities at the University of Stockholm (left in Figure 3). It was completed in 2013. The four-story building contains offices, small meeting rooms, study-booths for students and a café. Space heating and domestic hot water (DHW) are provided by a ground source heat pump (GSHP) system consisting of five water-to-water ground-source heat pumps, of nominal heating capacity 40 kW each when providing 40°C hot water for building heating. For DHW, the heat pump provides 55°C hot water, and its temperature is further increased by a Legionella protection system consisting of an electric resistance heater that raises the hot water temperature from 55°C to 60°C and a continuously-operating hot water recirculation pump. “Free cooling” is provided by circulating fluid from the ground loop to fan coil units in the building.

The bore field consists of 20 groundwater-filled boreholes in hard rock, drilled to a depth of 200 m, and fitted with single U-tubes filled with an ethanol/water mixture. The bore field is located below a landscaped courtyard, and the boreholes are drilled at an angle so that they reach under the surrounding building. Further details of the building, GSHP system and system performance are given in Spitler and Gehlin (2019, 2021b).



Figure 3 Studenthuset (left) and ASHRAE Headquarters building (right)



Figure 4 Studenthuset Heating SPF

Year-by-year seasonal performance factors at four boundary levels are shown in Figure 4. Although there is some year-to-year variation, the largest difference occurs as the boundary level is changed. The change in performance from boundary H1* to boundary H2 reflects the energy usage of the source-side circulating pump (SSCP). The Legionella protection system (LPS) causes the decrease from boundary level H2 to H3+. Finally, the load side circulating pumps (LSCP) consume a considerable amount of energy and significantly reduce the performance between boundary levels H3+ and H5+. Taking the year 2020 as an example, the SPF decreases from 4.1 to 3.6 to 2.7 to 1.6 underlines the importance of distribution energy in overall system performance.

Likewise, for cooling, the SPF is quite high when only considering the source-side circulating pump for the “free” cooling. However, accounting for the internal distribution energy lowers the SPF from about 35 to 3. Another ramification related to the distribution energy is that system performance can be quite good when the load is high but suffers under low load conditions. This is discussed below in the Comparison section.

The ASHRAE Headquarters building

The former ASHRAE headquarters building (right in Figure 3) was renovated in 2007-2008, and part of the renovation included installation of a GSHP system serving the 2nd floor of the building. Further details of the renovation and system performance are given by Spitler, et al. (2021b); see also references cited there. The GSHP system is configured as a distributed system with 14 water-to-air heat pumps with a total nominal capacity of 111 kW (31 ½ tons).

The closed-loop vertical borehole heat exchanger field lies under the parking lot and consists of twelve 122-m deep vertical boreholes containing single U-tube 1 ¼” nominal diameter HDPE pipes, grouted with thermally-enhanced grout. Water is circulated from the field to the 14 heat pumps with a central variable-speed pump, controlled to maintain the loop differential pressure set point. Individual heat pumps have solenoid valves that shut off the loop flow to the heat pump when it is off. Combined with the pump speed control, this has the effect of keeping flow rate to each heat pump approximately constant when the heat pump is on. SPFs for the entire system are shown in Figure 5 for a two-year period where data were available. The increase in SPF from the 1st year to the 2nd year is largely due to changing the differential pressure set point, which was found to be too high in April of 2012.

Comparison

Comparison of central and distributed ground source heat pump systems in two climates with different load profiles and different ground temperatures is difficult at best. Figure 6 is an attempt at making such a comparison. The daily overall (heating+cooling) performance factors (Boundary level 5) for the two systems are plotted against daily heating and cooling loads normalized by the maximum daily heating and cooling loads for each system. For Studenthuset, since free cooling is used, it is helpful to distinguish whether heating or cooling dominates; the days have been color-coded accordingly. This is not done for the ASHRAE HQ building since heat pumps are used for both heating and cooling.

For both systems, the performance increases as the load increases. For the Studenthuset building, this is true for all three modes, with the highest performance factors for cooling-dominated days. Even though the ground temperature is considerably cooler in Stockholm than in Atlanta, and the Stockholm system uses “free cooling” while the Atlanta system uses a compressor for both heating and cooling, the performance factors at boundary level 5 are higher for the distributed GSHP system in Atlanta than the central GSHP system in Stockholm. While this finding can’t be generalized, it is a reminder that the distribution energy is quite important to the overall system performance.

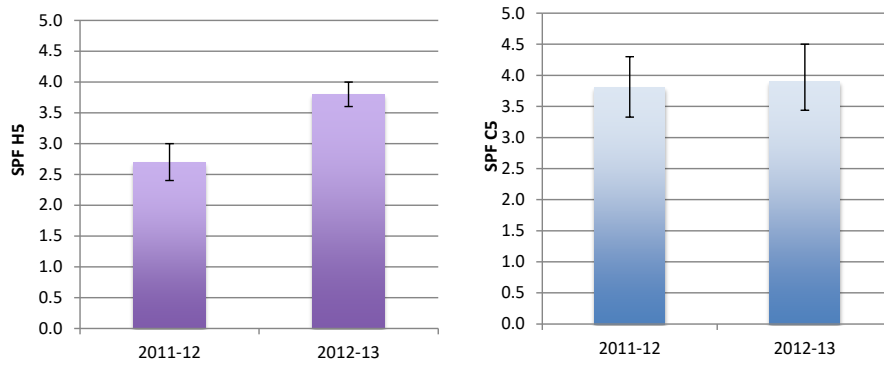


Figure 5 ASHRAE Headquarters Heating and Cooling SPF



Figure 6 Daily heating and cooling performance factor for system boundary 5 (DPFHC5+) against daily heating and cooling loads normalized by the maximum daily heating and cooling loads for each system.

CONCLUSIONS

Annex 52 has provided useful methodologies and guidelines to support performance measurements of GSHP systems, availability of which should lower the cost of measurement programs, as it allows more informed selection of instrumentation and reduced analysis effort later. Annex 52 has provided benchmarking data for 29 GSHP systems, but the real value will increase as performance measurement becomes ubiquitous. As performance data for more systems and more system types over a wider geographical distribution become available, the usefulness for benchmarking will increase. The availability of widespread high-quality performance measurement will facilitate better design and operation of GSHP systems.

Systems serving two buildings – a central GSHP system with water-to-water heat pumps and a distributed GSHP system with water-to-air heat pumps, typical of Scandinavian and North American practice, respectively - were compared. Although the results from two buildings can't be generalized, they certainly provide incentive for further investigation. The central GSHP system used significantly more energy for distribution, lowering the overall SPF considerably. We hope that these results spur increased attention to the role of distribution systems in GSHP system performance. Though this study has focused on GSHP systems, distribution energy also plays a significant role in the performance

of other HVAC systems. System performance measurement using well-defined boundary levels and KPI is a useful tool in all HVAC systems.

ACKNOWLEDGMENTS

The support from the authors' employers, the Swedish Energy Agency (TERMO Grant 45979-1), GEO, and the OG&E Energy Technology Chair is gratefully acknowledged. This work is part of the IEA HPT Annex 52, Long-term performance measurement of GSHP systems serving commercial, institutional and multi-family buildings.

REFERENCES

- Davis J.M., Martinkauppi I, Witte H, Berglöf K, Vallin S. 2021. *Guidelines for Instrumentation and Data*. IEA HPT Annex 52 - Long-term performance monitoring of GSHP systems for commercial, institutional, and multifamily buildings. DOI: <https://doi.org/10.23697/tgr4-qn89>.
- de Wilde P. 2014. *The gap between predicted and measured energy performance of buildings: a framework for investigation*. Automation in Construction. 2014;41:40-9.
- Gehlin, S., Spitler, J.D. 2021a. *Half-term Results from IEA HPT Annex 52 – Long-term Performance Monitoring of Large GSHP Systems*. Proceedings of the 13th IEA Heat Pump Conference. April 26-29, Jeju, Korea.
- Gehlin, S., Spitler, J.D. 2021b. *Case study report for Studenthuset, Stockholm, Sweden. Long-term performance analysis of the GSHP system for a student union building*. IEA HPT Annex 52 – Long-term performance monitoring of GSHP systems serving commercial, institutional and multi-family buildings. <https://doi.org/10.23697/pmr0-0778>
- Gehlin, S., Spitler, J.D. 2022a. *Subtask 1 Report – Annotated Bibliography – Final Document*. IEA HPT Annex 52 – Long-term performance monitoring of GSHP systems serving commercial, institutional and multi-family buildings. <https://doi.org/10.23697/dzpy-yp81>
- Gehlin, S., Spitler, J.D. 2022b. *Case Study Summary Report*. IEA HPT Annex 52 – Long-term performance monitoring of GSHP systems serving commercial, institutional and multi-family buildings. <https://doi.org/10.23697/qfnt-rb80>
- Gehlin, S., Spitler, J.D. 2022c. *Final report*. IEA HPT Annex 52 – Long-term performance monitoring of GSHP systems serving commercial, institutional and multi-family buildings. <https://doi.org/10.23697/xsbr-xn83>
- Gehlin, S., Spitler, J.D. Witte, H., Andersson, O., Berglöf, K., Davis, M., Javed, S., Bockelmann, F., Turner, J., Clauss, J. 2022. *Subtask 3 Report – Guide for analysis and reporting of GSHP system performance – system boundaries and key performance indicators (KPI) – Final Document*. IEA HPT Annex 52 – Long-term performance monitoring of GSHP systems serving commercial, institutional and multi-family buildings. <https://doi.org/10.23697/xa7z-vd92>
- Gleeson C.P., Lowe R. 2013. *Meta-analysis of European heat pump field trial efficiencies*. Energy Build. 2013;66(0):637-47.
- IEA HPT. 2019. *Annex 52 - Long term performance measurement of GSHP Systems serving commercial, institutional and multi-family buildings*. <https://heatpumpingtechnologies.org/annex52/>
- Nordman, R.; Kleefkens, O.; Riviere, P.; Nowak, T.; Zottl, A.; Arzano-Daurelle, C.; Lehmann, A.; Polyzou, O.; Karytas, K.; Riederer, P. 2012. *SEPEMO—Seasonal Performance Factor and Monitoring for Heat Pump Systems in the Building Sector*, SP Technical Research Institute of Sweden: Borås, Sweden.
- Scofield J.H. 2009. *Do LEED-certified buildings save energy? Not really*. Energy Build. 2009;41(12):1386-90.
- Spitler J.D. 2020. *Addressing the building energy performance gap with measurements*. Science and Technology for the Built Environment. 2020;26(3):283-4. <https://doi.org/10.1080/23744731.2020.1718871>
- Spitler J.D, Berglöf K, Mazzotti Pallard W, Witte H. 2021a. *Guidelines for Calculation of Uncertainties* IEA HPT Annex 52 - Long-term performance monitoring of GSHP systems for commercial, institutional and multi-family buildings.. DOI: <https://doi.org/10.23697/m2em-xq83>.
- Spitler, J.D. and S.E.A. Gehlin. 2019. *Measured performance of a mixed-use commercial-building ground source heat pump system in Sweden*. Energies (2019), 12; <https://doi.org/10.3390/en12102020>
- Spitler, J.D., Southard, L., Liu, X. 2021b. *Case study report for ASHRAE Headquarters Building, USA. Performance of a distributed water-to-air ground source heat pump system*. IEA HPT Annex 52 – Long-term performance monitoring of GSHP systems serving commercial, institutional and multi-family buildings. <https://doi.org/10.23697/j89c-en10>

Climate change effects on the energy performance of a residential ground-source heat pump system

Gabriel Sabbagh

Michel Bernier

ABSTRACT

The objective of this paper is to examine the impact of climate change on the energy performance of a typical residential ground-source heat pump (GSHP) system equipped with a horizontal ground heat exchanger (GHE) and located in a heating dominated climate (Montréal, Canada). Simulations results under future weather conditions (Relative Concentration Pathway – RCP8.5) show a drop in heating and a rise in cooling energy loads over 30 years. The outlet temperature from the GHE increases consistently from year to year and shows a high degree of variability in-line with the general trend of future ambient temperature fluctuations. In terms of electricity consumption, the main conclusion is that the use of current TMY weather files is inadequate to predict the yearly electricity consumption fluctuations.

INTRODUCTION

As most future climate predictions suggest, global warming will involve changes in annual weather patterns. Projected ambient temperature increases for 2081-2100 relative to 1986-2005 are between 2.6°C and 4.8°C for the Relative Concentration Pathway RCP8.5 (Collins, et al., 2013). As shown by Robert and Kummert (2012) and Deroubaix et al. (2021), buildings located in cold climates will experience a decrease in annual heating needs and an increase in annual cooling needs. The performance of heating/cooling systems will also be influenced by ambient temperature changes. In the case of ground-source heat pumps (GSHP), the ground heat exchanger (GHE) will be affected by ground temperature variations associated with ambient temperature variations. The changing ratio of the annual heating and cooling needs will also affect the amount of heat being rejected/collected in the ground on an annual basis.

Kharseh et al. (2009) showed that the effect of a 4.5°C linear increase in the ambient temperature over 130 years reduced the required length of a GHE by 50% for a specific case. In another study, Kharseh et al. (2011) measured the impact of global warming on the performance of GSHP systems in buildings for linear increases of 1.5°C and 4.5°C of the ambient temperature over 100 years. It is shown that a linear increase of 4.5°C in the ambient temperature over 100 years reduces the electricity consumption of GSHP systems by 37% in cold climates while it increases by 55% in hot climates compared to the consumption with no ambient temperature increase. These studies were performed with a simple building model based on the degree-day method and a simple linear ambient temperature increase over time.

Shen and Lukes (2015) simulated buildings located in different US climate zones for different climate change scenarios between 2040 and 2069. In regions currently categorised as heating dominated such as Chicago and Philadelphia, global warming will transform these regions into cooling dominated regions and reduce the benefits of a higher COP for the

Gabriel Sabbagh (gabriel.sabbagh@polymtl.ca) is a graduate student and Michel Bernier (michel.bernier@polymtl.ca) is a professor of mechanical engineering at Polytechnique Montréal.

heat pump in heating. Pertzborn et al. (2011) investigated the impact of year-to-year weather variability on the optimal design of hybrid GSHP systems for office buildings. In a heating dominated climate (Madison, Wisconsin) it is shown that the yearly variations in weather conditions has a minimal impact on the required size of the GHE but that the auxiliary boiler is larger to accommodate colder years. It is unclear, however, how ground temperature changes resulting from ambient temperature variations are accounted for in their simulations.

Analytical and numerical models have been developed to predict the ground temperature evolution through time. One such model is the numerical model developed by Xing (2014) who used a full surface heat balance coupled with weather files to numerically calculate the ground temperature. Although the numerical model provides ground temperature estimates with good accuracy, it is computationally demanding. The one-harmonic analytical model (Thomson, 1862) can be sufficiently accurate to approximate the ground temperature variation. If high precipitation volumes, snow fall and soil freezing/melting occur, a two-order analytical harmonic model can be used. Results from the numerical model and the two analytical models compared favorably well with soil temperatures measured across the US (Xing & Spitler, 2017).

Luo and Asproudi (2015) aggregated soil temperature measurements at Cockley Park in the UK for over a century spanning from 1907 to 2011. Increases of 0.15°C and 0.17°C per decade were measured at 30 and 100 centimeters, respectively. Seong-Kyun and Youngmin (2020) simulated ground temperature profiles around a GHE in the region of Daejeon in South Korea between 2019 and 2050 while taking into consideration different Representative Concentration Pathway (RCP) scenarios. The temperature difference at 50 meters between the best and worst climate scenario in 2050 was 0.17°C .

In summary, this review of the literature indicates that there are apparently no studies which isolate the impact of climate change on the performance of GHEs from the impact climate change has on the building heating and cooling loads. The present analysis attempts to alleviate this deficiency for the case of a residential building located in a cold climate with the aim of presenting a general methodology that could be used for other building types and locations. It also examines the potential inaccuracies in the evaluation of future GSHP electricity consumption that would occur if GSHP were designed with current weather conditions. The paper is divided into four major parts. First, the weather files used in this study are presented. Then, the impact of climate change on the evolution of ground temperature is examined. This is followed by a presentation of the simulation methodology including the incorporation of past and future weather files. Finally, results are presented followed by a conclusion.

WEATHER FILES

In this article, four weather data sets for Montréal (Canada) are used: Two Typical Meteorological Years (TMY) and two series of weather files for successive years. The first set is a Typical Meteorological Year based on actual meteorological weather files from 1998-2017. It was obtained from Environment Canada (2022) and it will be referred to as Current TMY, i.e. the one that would currently be used to design and simulate GSHP systems. The second data set contains future weather files from the years 2020 to 2049 under a RCP 8.5 climate scenario. These files were developed by Hosseini et al. (2021) using a machine learning approach. The dataset will be referred to as the RCP85-20-49 dataset. The third data set is a TMY created using these 30 future years. This dataset will be referred to as the Future TMY. The fourth set, called AMY1998-2017, are actual CWEEDS (Canadian Weather Energy and Engineering Datasets) weather files for this 20-year period and are available from Environment Canada (2022).

GROUND TEMPERATURE MODEL

In this study, a simple one-dimensional finite volume ground model is developed to predict the time evolution of the undisturbed ground temperature. The model assumes that ground properties remain constant through time and that they are not affected by snow cover, freezing/thawing or ground water movement. Heat is transferred from the air to

the ground and is diffused solely by conduction. The governing one-dimensional transient heat conduction equation is:

$$\rho C_p \frac{\partial T}{\partial t} = k \frac{\partial^2 T}{\partial x^2} \quad (1)$$

where T is the ground temperature in °C and x is the depth in meters. Other parameters have their usual meaning and are defined in the nomenclature. Equation (1) is solved numerically using Patankar's finite volume method (Patankar, 1980). The result is a series of algebraic equations to determine the node temperatures at each axial grid location. The initial ground temperature profile is evaluated using the analytical approach presented by Lunardini (1981):

$$T(x) = T_m + gx - (T_{max} - T_m)e^{-x\sqrt{\frac{\omega}{2\alpha}}} \cos\left(\omega\Phi + x\sqrt{\frac{\omega}{2\alpha}}\right) \quad (2)$$

The values used for the various parameters in Equation 2 are specified in Table 1. They correspond to data specific to Montréal (Canada). The ground is meshed exponentially with finer grids near the surface. A grid independence check was performed where the number of nodes was varied from 10 to 100 and the time step from 0.1 to 120 hours. The different configurations yielded results within 0.02 °C of each other. Furthermore, the ground temperatures from the numerical model and the ones predicted by Kharseh et al. (2011) were within 0.01 °C of each other over a depth of 300 meters for a period of 100 years with a 1-hour time step.

The ground temperature model was used to examine the impact of climate change on the ground temperature with the RCP85-20-49 dataset and the ground properties specified in Table 1. Results are shown in Figure 1 where annual average temperatures on the surface and over two depths are plotted. It can be seen in Figure 1 that the average ground temperature over the first 3 meters can experience large variations from year to year. For example, there is a 2°C difference in the yearly average ground temperature between the years 2029 and 2030. The temperature swings are less severe if the average temperature over the first 30 meters is considered. Looking at the trends (dotted lines in Figure 1), the average yearly surface temperature is increasing at a rate of 0.52°C/decade and the average ground temperature of the first 3 meters follows this trend closely with an increase of 0.51°C/decade. The average ground temperature of the first 30 meters is less affected by the surface temperature increase with an increase of 0.24°C/decade. This implies that horizontal GHE located near the surface will be affected more by climate change than vertical GHE.

Table 1. Ground and weather parameters

Parameter	Value	Units
ρC_p	2.2×10^6	J/m ³ K
k	2.5	W/m K
T_m	7.77	°C
T_{max}	22.97	°C
g	0.02	°C/m
ω	1.99×10^{-7}	rad/s
α	1.14×10^{-6}	m ² /s
Φ	1794240	s

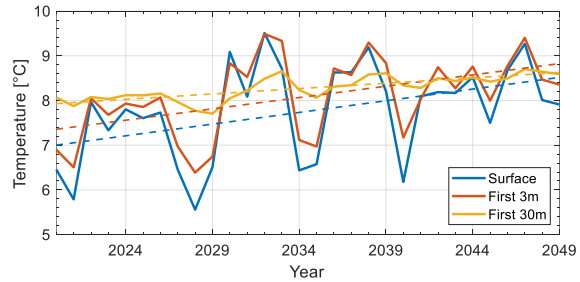


Figure 1 Average yearly ground temperature at the surface, for the first 3 meters and the first 30 meters from 2020 to 2049 using the RCP85-20-49 future weather dataset. The dotted lines represent the result of linear regressions.

SYSTEM SIMULATION

The impact of climate change on the performance of a residential GSHP system equipped with a horizontal GHE is examined here using multi-year TRNSYS simulations. The important components of the system are shown in Figure 2. Standard TRNSYS components are used except for the horizontal GHE model which required modifications as

presented below. The residential building is a modified version of the example building contained in the TEES Library of TRNSYS 18 (Klein, et al., 2017). It consists of a two-story building with a basement and an attached garage as well as a sunroom. Each story has a 139 m² area. It is modeled in TRNSYS using Type 56. The building is subdivided into six thermal zones: basement, ground floor, first floor, garage, sunroom and attic. Only the first three are heated and cooled. The original insulation levels have been upgraded to meet the National Energy Code of Canada for Buildings or NCEB (2022). Internal heat gains from people and appliances at a 15-minute time interval were read from an external file. These data are based on studies performed at the Canadian Center for Housing Technologies (Swinton et al., 2001). Exposed to the Current TMY weather conditions, the peak heating and cooling loads are 13.1 and 6.3 kW, respectively.

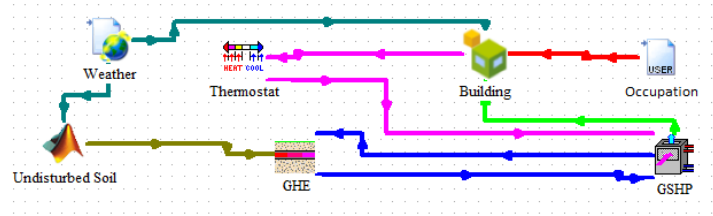


Figure 2 Main TRNSYS components and connections.

The energy performance of the water-to-air GSHP is based on a commercially available 3-ton (10.5 kW) single-speed machine (Water Furnace, 2022). Manufacturer data were processed to obtain normalized heating and cooling performance maps to be used in TRNSYS with Type 919. Figure 3 shows the resulting normalised heating and cooling capacities as well as the COP in heating and cooling as a function of the entering water temperature. The heating and cooling capacities are 9.38 and 10.73 kW at 10 and 21.1 °C, respectively (marked as a red cross in Figure 3). Using a normalised performance map is useful as the nominal heating or cooling capacity can be adjusted for values other than 3-ton but keeping the same performance trends. A GSHP with a nominal heating capacity of 11.6 kW for an EWT of 10°C was selected. With this capacity, the GSHP is able to meet 70% of the peak heating load with an entering water temperature of 0°C in accordance with canadian practice (CSA Group, 2021). A 10 kW electric auxiliary heater provides backup heating in peak periods.

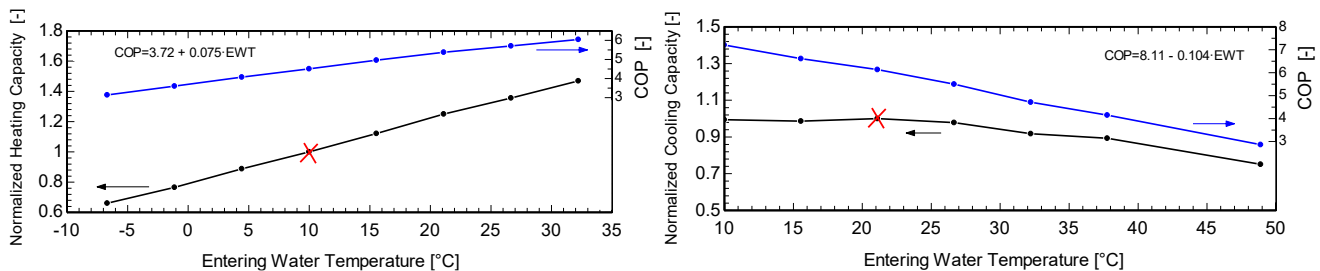


Figure 3 Normalized capacity and COP in heating and cooling as a function of the entering water temperature (EWT). The red cross indicates the rated heating and cooling conditions.

The result of a linear curve fit on the COP is indicated on both figures. It shows that the COP variation as a function of the entering water temperature is relatively small. In fact, the COP in heating increases by 1.66% for a 1 °C change of the EWT at 10 °C and in cooling it decreases by 1.7 % for a 1 °C change of the EWT at 21.1 °C.

The horizontal GHE was modeled using a modified version of Type 952 to take into account the changing ground temperature profile due to the changing climate conditions. The original version uses an analytical equation, internal to Type 952, analogous to equation 2 to calculate the far-field ground temperature at the different depths around the GHE

to perform the required heat transfer calculations. It can be seen that equation 2 is solely dependant on the initial parameters and can not account for ambient temperature changes. In the modified version of Type 952 the far-field ground temperatures are calculated externally for the different required depth (using a Matlab subroutine of a unidimensionnal finite volume model of the ground as described earlier) using the ambient temperature as the ground surface temperature and inputed into Type 952 at each simulation timestep as indicated in Figure 2. All the far-field temperatures calculated as well as the soil temperatures are updated at each timestep. The horizontal GHE was designed based on a 30 year simulation of the complete system performed with the Current TMY weather file. Based on these simulations, a GHE with a length of 300 m at a depth of 3 m was selected. With these conditions, the minimum inlet fluid temperatures to the heat pump was -3.7°C .

RESULTS

To establish a baseline energy consumption for the residence, a one-year simulation is undertaken using both Current and Future TMY files. Figure 4 shows the resulting monthly cooling and heating loads. The heating and cooling load variations are not uniformly distributed throughout the months of the year. In fact, Figure 4 shows that future weather conditions induce increased heating loads in certain months when compared to the current weather conditions. As for the cooling loads, future weather conditions lead to increases in monthly cooling loads for almost every month.

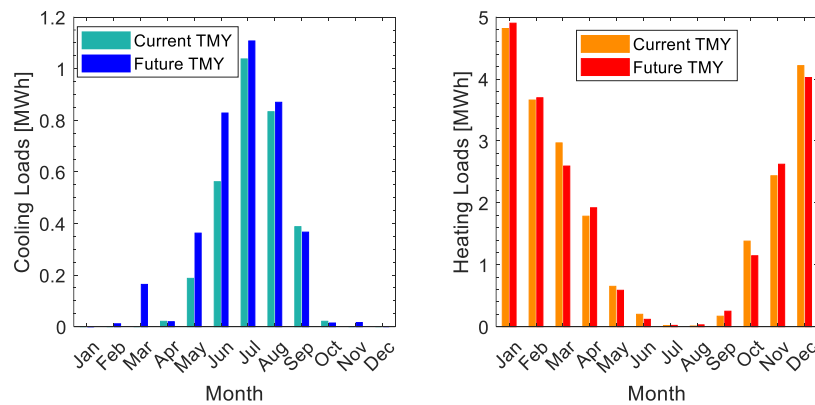


Figure 4 Monthly cooling (left) and heating (right) loads of the residence under Current and Future TMY.

Figure 5 illustrates the yearly building load variations for three weather data sets. As shown in Table 2, loads increase from 3.1 to 3.8 MWh in cooling and decrease from 22.3 to 21.9 MWh in heating when results obtained with Current and Future TMY files are compared. When the RCP85-20-49 weather conditions are used, the heating loads decrease by 3.5% (761 kWh) per decade (tendency line on Figure 5) while the cooling loads increase by 7% (268 kWh) per decade. Table 2 shows the highest (H), lowest (L), and average (A) annual loads of the residence under both the RCP85-20-49 and AMY1998-2017 conditions. Notable details include a higher maximum heating load under the RCP85-20-49 conditions compared to the AMY1998-2017 conditions (25.60 vs 24.43 MWh). However, the annual heating loads calculated with the Current and Future TMYs, and the average heating loads calculated using the AMY1998-2017 and RCP85-20-49 data sets are very similar (22.30, 21.90, 22.31, 21.84 MWh). As for the cooling loads, RCP85-20-49 conditions lead to a high yearly cooling load reaching a value 55% above predictions with the Current TMY (4.81 vs 3.1 MWh). This is much greater than the highest value experienced with the AMY1998-2017 weather file (3.80 MWh).

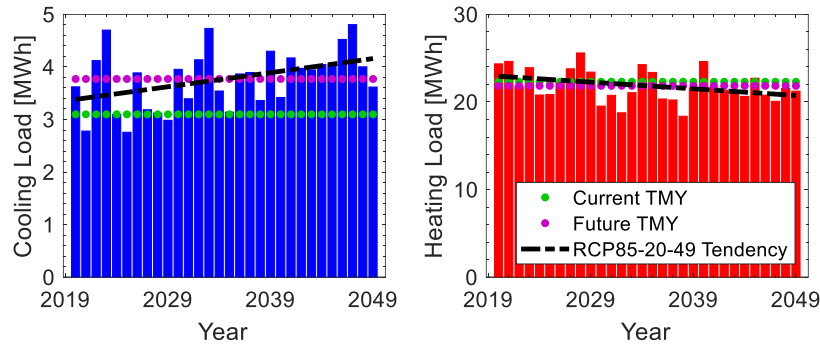


Figure 5 Yearly cooling and heating loads of the residence under the RCP85-20-49 and the Current and Future TMY weather conditions.

Table 2. Annual loads and electricity consumption under four weather datasets (H, A, and L stand for Highest, Average, and Lowest) as well as the heating SPF and the average cooling COP.

Annual Building Heating and Cooling Loads [MWh]					Annual GSHP System Electricity Consumption [MWh]						
	Heating	Relative	Cooling	Relative		Heating	Relative	SPF	Cooling	Relative	COP
C TMY	22.30	100%	3.10	100%	C TMY	7.27	100%	3.07	0.76	100%	4.08
F TMY	21.90	98%	3.80	123%	F TMY	7.51	103%	2.92	0.92	120%	4.13
AMY 98-17	H 24.43	110%	3.81	123%	AMY 98-17	H 8.93	123%	2.74	0.93	122%	4.10
	A 22.31	100%	3.10	100%		A 7.36	101%	3.03	0.75	99%	4.13
	L 19.77	89%	2.03	66%		L 5.85	81%	3.38	0.49	64%	4.14
RCP8.5 20-49	H 25.60	115%	4.81	155%	RCP8.5 20-49	H 10.18	140%	2.51	1.24	162%	3.88
	A 21.84	98%	3.77	122%		A 7.51	103%	2.91	0.93	123%	4.05
	L 18.37	82%	2.76	89%		L 5.22	72%	3.52	0.65	85%	4.25

Before moving to the analysis of the annual electricity consumption, the evolution of the inlet temperatures to the GSHP (i.e. the outlet temperature from the horizontal GHE) will be examined in Figure 6 for the Current TMY and RCP85-20-49 weather conditions. In the case of the Current TMY, the same file is used over the 30 year period much like what would be done if such a system were designed today.

As expected, the minimum and maximum GSHP inlet temperatures decrease over time (0.09°C/decade) when the Current TMY is used in the 30 year simulation. This reduction is due to the heating dominated nature of the loads and therefore an overall energy extraction from the ground occurs which in turn reduces the average ground temperature around the GHE. The minimum and maximum yearly GSHP inlet temperatures experience several important fluctuations caused by climate variability and the inlet temperatures to the GSHP dips well under the -3.7 °C minimum attained under the Current TMY weather conditions even reaching a value of -5.2 °C for harsh winters occurring in the first half of the 30 year period. It can be shown that this minimum temperature can be reached under the Current TMY weather conditions with a 240 m GHE (20% shorter). The minimum inlet temperature increases at an average rate of 0.38°C/decade under the RCP85-20-49 weather conditions while, as shown earlier, the ground temperature increase over the first 3 m is of the order 0.51°C/decade with no GHE. This difference is partly accounted for, as the building loads are still heating dominated, by the natural decrease of the ground temperature around the GHE (in the order of 0.09°C/decade as shown earlier) due to the overall energy extraction during a full heating/cooling season cycle as mentioned above.

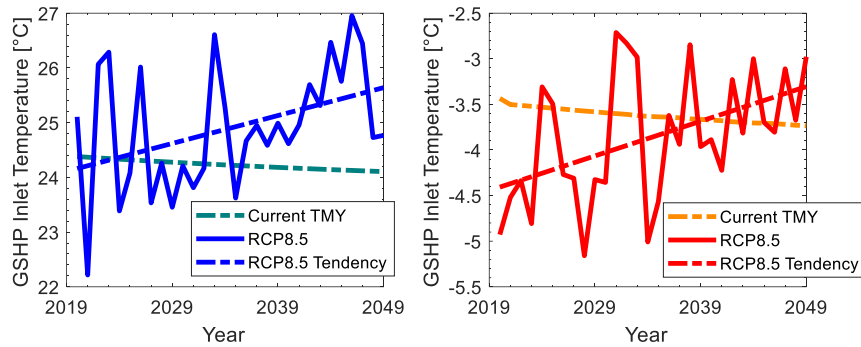


Figure 6 GSHP maximum (left) and minimum (right) yearly inlet temperature.

A similar picture is painted by the maximum yearly inlet temperature in Figure 6 with an average yearly increase of $0.51^{\circ}\text{C}/\text{decade}$ under the RCP85-20-49 weather conditions. One would have expected an average increase similar to the minimum yearly inlet temperature but this difference is due to a secondary effect (shown in Figure 7) related to the fact that the electricity consumption of the GSHP system in cooling mode increases by 8% per decade (+7.4 kWh/year), implying an overall increase in the GSHP operation time from year to year in cooling mode and therefore, a higher heat injection in the GHE during the summer.

It can be concluded that for heating dominated climates, where a GHE is sized for the heating load, more extreme winters will induce strains on the GHE and the GSHP as the minimum inlet temperature will dip considerably below the design temperature predicted with the Current TMY weather file. For example, in the year 2028, the minimal EWT dips down to -5.2°C , 1.5°C below the -3.7°C design temperature. For regions where the cooling load is much larger than the heating load, it is expected that the surplus heat injected during a full heating/cooling season cycle will add to the already rising ground temperature due to global warming and the maximum inlet temperature will increase from year to year, a point to be taken into consideration while dimensioning the GHE.

The trends in yearly electricity consumption of the GSHP system in heating and cooling over the 30-year period for three weather data sets (Current TMY, Future TMY, and RCP85-20-49) are shown in Figure 7. The electricity consumption includes the consumption of the GSHP, the ventilators, the controllers as well as the auxiliary heater in heating. Table 2 summarises these results and shows the highest (H), lowest (L), and average (A) annual electricity consumption as well as the heating SPF and the average cooling COP for the RCP85-20-49 and AMY1998-2017 weather data sets. Figure 7 shows a decrease of 8%/decade (-60 kWh/year) in the total electricity consumption of the GSHP system in heating mode under the RCP85-20-49 weather conditions. This is due to the combined effect of a 23%/decade (-43 kWh/year) decrease in the auxiliary heating electricity consumption and a 3%/decade (-17 kWh/year) decrease in the GSHP system electricity consumption (excluding the auxiliary heating) over the 30 years. Consequently, the GSHP system becomes less reliant on the inefficient (compared to the GSHP) auxiliary heater.

Future cooling electricity consumption is, on average, underestimated by 20% when compared to Current TMY conditions (0.76 vs 0.92 MWh). However, the heating electricity consumption predicted using Future TMY conditions is 3% higher (7.27 vs 7.51 MWh) than what is predicted using Current TMY conditions. Even though the building's heating load is on average lower with Future TMY conditions, harsher winters, affecting the EWT and building loads, reduce the COP of the GSHP and causes a higher usage of the auxiliary heater that is less efficient causing the increase in the overall electricity consumption ($7.27+0.76$ vs $7.51+0.92$) as well as a decrease in the heating SPF (3.07 vs 2.92). Therefore, the heating system will operate less in the future but when operating it will run under harsher conditions reducing its overall efficiency.

Table 2 shows the highest (H), lowest (L), and average (A) loads of the residence under both the RCP85-20-49 and

AMY1998-2017 conditions. It is interesting to note that the highest yearly heating loads under the RCP85-20-49 conditions is higher than the one calculated with the AMY1998-2017 data set (25.60 MWh vs 24.43 MWh). The highest yearly cooling electricity consumption under the RCP85-20-49 conditions is 62% higher the predicted annual cooling electricity consumption using the Current TMY conditions. The heating electricity consumption under the RCP85-20-49 weather conditions ranges (L to H) from 72% to 140 % of the prediction obtained with the Current TMY. The corresponding values are 81% and 123% for the AMY1998-2017 weather conditions. This indicates a higher variability in electricity consumption in the future due to strong variability in the predicted climate. The average cooling COP of the GSHP system exhibits a 0.04 variation (4.14-4.10) during the AMY1998-2017 years in contrast to a 0.37 variation (4.25-3.88) during the RCP85-20-49 years implying higher cooling performance variations from year to year.

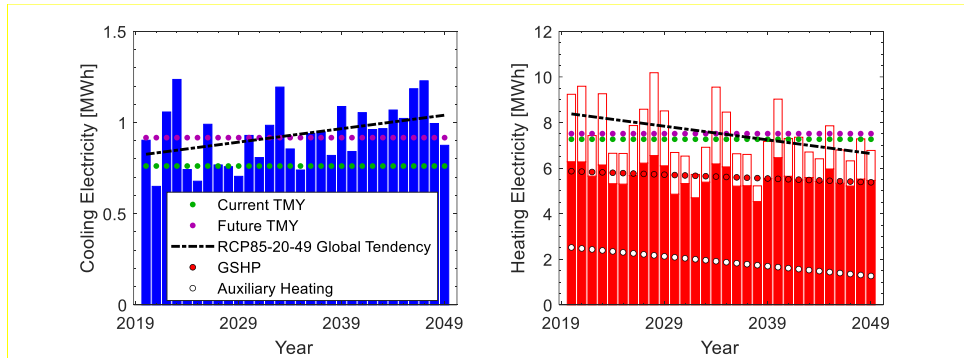


Figure 7 GSHP system electricity consumption in cooling and heating mode with its global variation tendency over the 2020-2049 period as well as the mean consumption under Current and Future TMY.

CONCLUSION

The effect of climate change on a residential building equipped with a GSHP system coupled with a horizontal GHE located in a cold climate (Montréal, Canada) is examined using multi-year TRNSYS simulations. Four different weather data sets are used: 20 years of actual weather (AMY1998-2017); 30 years of future weather (RCP85-20-49) and two TMY (called Current and Future) based on these two sets of data.

In the first part of the paper, a simple one-dimensional numerical ground model is presented. When used with the RCP85-20-49 weather files, it is shown (Figure 1) that the yearly average ground temperature over the first three meters increases by $0.51^{\circ}\text{C}/\text{decade}$ which closely corresponds to the surface temperature change ($0.52^{\circ}\text{C}/\text{decade}$). The ground model is incorporated in a modified version of the horizontal GHE model in TRNSYS to better predict ground temperatures changes as a function of ambient temperature changes.

If the GSHP system is designed with the Current TMY (same weather file used for 30 years), the minimum heat pump inlet temperature is expected to reach -3.7°C after 30 years. However, when the RCP85-20-49 weather is used, large yearly fluctuations are observed and the minimum inlet temperature to the heat pump reaches -5.2°C in a harsh winter. This can induce a 20% difference in the GHE design length.

Yearly electricity consumption are compared using the four different weather data sets and the main results are shown in Figure 7 and Table 2. The average yearly electricity consumption for cooling obtained with Current TMY is 20% below the value obtained with the Future TMY. However, the heating electricity consumption predicted using Future TMY conditions is 3% higher than what is predicted using Current TMY conditions. Even though the building's heating load is on average lower with Future TMY conditions, harsher winters, affecting the inlet temperature to the heat pump and the building loads, reduce the COP of the GSHP and causes a higher usage of the auxiliary heater causing the increase in the overall electricity consumption and a reduction of the heating SPF. The maximum cooling electricity consumption under the RCP85-20-49 conditions is 62% above the predicted consumption using the Current TMY

conditions. The heating electricity consumption range under the RCP85-20-49 conditions is 68% (140%-72%) compared to 42% (123%-81%) under the AMY1998-2017 conditions indicating a higher future electricity consumption variability.

These results show that designing a GSHP system with Current TMY files as weather conditions for multi-year simulations might be inadequate. It is preferable to use future weather files which show the range of expected electricity consumption and variability in the outlet temperature from the GHE which are essential in its sizing. This study has only looked at climate change effects on a residential building heated and cooled by a GSHP equipped a horizontal GHE and located in a cold climate. More work is needed on different building types, locations, and climate change scenarios. Hopefully, the approach used here could be employed under other conditions to further broaden the understanding of the influence of climate change on the dimensioning and operation of GSHP systems.

ACKNOWLEDGEMENTS

The authors would like to acknowledge the assistance of Dru Crawley and Linda Laurie from climate.onebuilding.org for the creation of the Future TMY file used in this study.

NOMENCLATURE

α	=	Ground thermal diffusivity [m ² /s]	ω	=	Climatic period [rad/s]
t	=	Elapsed time [s]	H	=	Highest
ρ	=	Density [kg/m ³]	A	=	Average
C_p	=	Ground specific heat [J/kg K]	L	=	Lowest
k	=	Ground thermal conductivity [W/m K]	C	=	Current
T	=	Temperature [°C]	F	=	Future
g	=	Geothermal gradient [°C/m]	SPF	=	Seasonal Performance Factor
m	=	mean	COP	=	Coefficient Of Performance
max	=	Maximum	TMY	=	Typical Meteorological Year
Φ	=	Initial phase shift [s]	GSHP	=	Ground Source Heat Pump

REFERENCES

- Collins, M. et al., 2013. *Long-term Climate Change: Projections, Commitments and Irreversibility*. Climate Change 2013: The Physical Science Basis. Contribution of Working Group I to the Fifth Assessment Report of the Intergovernmental Panel on Climate Change.
- CSA Group, 2021. *Design and installation of ground source heat pump systems for commercial and residential buildings*. ANSI/CSA/IGSHPA C448 Series-16 (R2021).
- Deroubaix, A. et al., 2021. *Large uncertainties in trends of energy demand for heating and cooling under climate change*. Nature Communications, 12: 5197.
- Environment Canada, 2022. Engineering Climate Datasets. [Online] Available at: https://climate.weather.gc.ca/prods_servs/engineering_e.html [Accessed 3 June 2022].
- Hosseini, M., A. Bigtashi and B. Lee. 2021. *Generating future weather files under climate change scenarios to support building energy simulation – A machine learning approach*. Energy & Buildings, 230: 110543.
- Kharseh, M., L. Altorkmany and B. Nordell. 2009. *The effect of global warming on BTES systems*. Stockholm, Energi- och Miljötekniska Föreningen / EMTF Förlag.
- Kharseh, M., L. Altorkmany and B. Nordell. 2011. *Global warming's impact on the performance of GSHP*. Renewable Energy, 36: 1485-1491.
- Klein, S. et al., 2017. *TRNSYS 18: A Transient System Simulation Program in... \Tess Models\Examples\Ground Coupling Library\Type 56 Basement Example*, University of Wisconsin: Solar Energy Laboratory.
- Lunardini, V. J., 1981. *Heat Transfer in Cold Climates*. Van Nostrand Reinhold Company.
- Luo, Z. and C. Asproudi. 2015. *Subsurface urban heat island and its effects on horizontal ground-source heat pump potential under climate change*. Applied Thermal Engineering 90: 530-537.

- National Research Council of Canada, 2022. *National Energy Code of Canada for Buildings: 2020*. Canadian Commission On Building And Fire Codes.
- Patankar, S., 1980. *Numerical Heat Transfer and Fluid Flow*. Hemisphere Publishing Corporation.
- Pertzborn, A., G. Nellis and S. Klein. 2011. *Impact of weather variation on ground-source heat pump design*. HVAC&R Research, 17(2): 174-185.
- Robert, A. and M. Kummert. 2012. *Designing net-zero energy buildings for the future climate, not for the past*. Building and Environment, 55: 150-158.
- Seong-Kyun, K. and L. Youngmin. 2020. *Evaluation of Ground Temperature Changes by the Operation of the Geothermal Heat Pump System and Climate Change in Korea*. Water 12(10):2931.
- Shen, P. and J. R. Lukes. 2015. *Impact of global warming on performance of ground source heat pumps in US climate zones*. Energy Conversion and Management 101: 632-643.
- Swinton, M., H. Moussa and R. Marchand. 2001. *Commissioning twin houses for assessing the performance of energy conserving technologies*. Proceedings for Performance of Exterior Envelopes of Whole Buildings VIII: Integration of Building Envelopes, Clearwater Beach, Florida, 1-10
- Thomson, W., 1862. 3. *On the Reduction of Observations of Underground Temperature, with applications to Professor Forbes' Edinburgh Observations and the Continued Calton Hill Series*. Proceedings of the Royal Society of Edinburgh 4: 342-346.
- Water Furnace, 2022. *Model NS036 - Single Speed PSC (1250 CFM)*. [Online] Available at: <https://www.waterfurnace.com/literature/5series/sc2500an.pdf> [Accessed 12 February 2022].
- Xing, L., 2014. *Estimations of undisturbed ground temperatures using numerical and analytical modeling*. PhD thesis, Oklahoma State University, Stillwater, Oklahoma.
- Xing, L. and J. D. Spitler. 2017. *Prediction of undisturbed ground temperature using analytical and numerical modeling, Part I: Model development and experimental validation*. Science and Technology for the Built Environment, 23(5): 787-808.



Potential Mapping of Ground Source Heat Pump Systems Considering Groundwater Pumping

Hikari Fujii Kanako Yamashita Shunsuke Tsuya Hiroyuki Kosukegawa

ABSTRACT

The pumping of groundwater near GHEs improves the performance of GSHP systems due to the advection of the induced groundwater flow when the hydraulic conductivity of the formation is favorable. To quantify the effect, we first carried out performance analysis of a GSHP heating system under the influence of groundwater pumping. The heating operation data clearly showed the improved COP of the heat pump when the groundwater is pumped. To evaluate the effect of groundwater pumping, we then collected the water pumping data from the groundwater snow-melting system in Akita City, Japan and input those data to the existing field-scale numerical groundwater flow and heat transport model of the area. The model was run to calculate the groundwater velocity and temperature in the area under the influence of groundwater pumping. Then, the output from the model was used for developing another numerical model, small-scale GHE model, which can estimate the minimum necessary GHE length for a Japanese standard detached house at several locations in the area. The GHE length data were mapped using GIS software to generate the GSHP potential map under the influence of groundwater pumping. The comparison between the potential maps with and without groundwater pumping clearly indicated the contribution of water pumping in reducing the GHE length and the initial cost of GSHP systems.

INTRODUCTION

The potential maps of ground source heat pump (GSHP) systems show the necessary number and length of ground heat exchangers (GHEs) required for the heating and cooling of a standard house or buildings. These maps are being developed in many residential areas of Japan for promoting the use of GSHP systems. The necessary length of the GHEs is conventionally determined based on the output of large-scale simulation models constructed based on the local geological and groundwater information. Since these models generally assume a steady state groundwater flow, the groundwater flow velocity is constant throughout the year. In the northern part of Japan, the cumulative snow fall can reach several meters in one winter and the snow-melting on roads or pavements is commonly performed by groundwater circulation or using the water as the heat source of heat pumps. Some snow-melting systems pump a large amount of groundwater and these pumping operation arises a fast groundwater flow in the vicinity of pumping wells. As is well known in past researches (e.g., Choi et al., 2013, Luo et al., 2018), the existence of groundwater flow enhances the heat exchange capacity of GHEs due to its advection effect. This research focuses on the evaluation of the water pumping effects on the GHE performance using real operation data and the development of potential maps of GSHP systems considering groundwater pumping.

To confirm the improvement of GHE performance using real operation data, we first carry out a long term heating test using two GHEs in Akita City, northern Japan. The GHEs are located in a permeable deposit near groundwater pumping wells and the influence of groundwater pumping is analyzed based on the results of heating tests. After evaluating the effect of groundwater pumping, we collect the water pumping data in Akita City used for snow melting. The information is input to the existing large-scale numerical groundwater flow and heat transport model which covers

Hikari Fujii (fujii@mine.akita-u.ac.jp) is a professor, Kanako Yamashita is a MS student, Hiroyuki Kosukegawa is a chief technical staff at Akita University. Shunsuke Tsuya is an engineer at Zeneral Heatpump Industry Co., Ltd.

the entire area of Akita City. The model then calculates the groundwater velocity and temperature in the area under the influence of groundwater pumping. The output from the model is used to develop small-scale GHE models, which estimate the minimum necessary GHE length for a Japanese standard detached house of 120 m² at several locations in the area based on the local weather data. The GHE length data are compiled using GIS software to generate the GSHP potential map under the influence of groundwater pumping. The generated map is compared with the potential map developed without consideration to groundwater pumping to evaluate the benefit of groundwater pumping in reducing the GHE length of GSHP systems.

PERFORMANCE OF GSHP SYSTEM NEAR GROUNDWATER PUMPING WELLS

In the first stage of the research, we carried out a long-term heating test using a GSHP heating system in Akita City, northern Japan, to confirm the improvement of GHE performance using the actual operation data of GSHP system. The configuration of the GSHP system and the conditions and results of the heating test are described below.

System configuration

The long-term heating test was performed from 2019 to 2020 in a GSHP cooling and heating system constructed in the campus of Akita University, Akita City, Japan in 2018. The GSHP system consists of two GHEs, GHE1 and GHE2, on the primary side, three fan coil units on the secondary side, and a heat pump of 10 kW heating and cooling capacity, respectively. The heating and cooling area of the air-conditioning test room is 90 m², and the working fluids in the primary and secondary side are 10.6 wt% ethylene glycol and 23.0 wt% propylene glycol, respectively. Figure 1 shows the completion of the GHEs and the geological column at the GHE location. The GHEs are 60 m deep and completed with steel casings of 150 mm ID without grouting. The heat exchangers are double U-tubes composed of HDPE (ID/OD: 27 mm/34 mm). The steel casings are slotted for the aquifer of sand and gravel layers (40-50 m depth) to allow the groundwater flow through the GHE and enhance the performance of the GHE. The groundwater level was measured as GL-5.6 m. A water-level sensor was installed 15 m below the ground surface in the GHE.

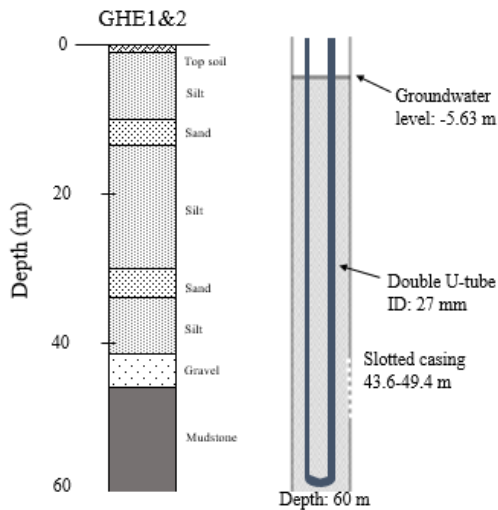


Figure 1 Geology and completion of GHEs

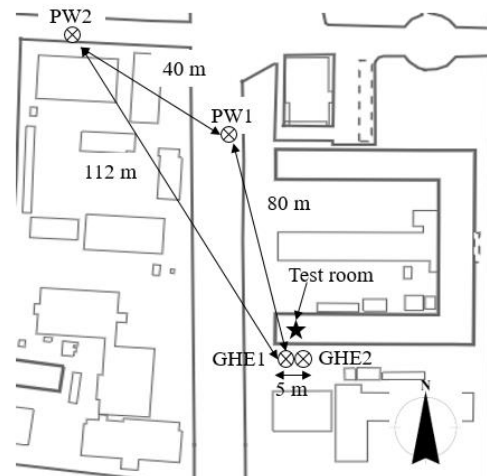


Figure 2 Locations of wells.

Figure 2 shows the locations of the GHEs and pumping wells. Two pumping wells, named as PW1 and PW2, are located 80-112 m apart from GHE1. The elevation difference between the four wells is negligibly small. Groundwater is pumped from these wells and circulated below the road or pavement for snow melting when ambient temperature is below 1 °C.

Both pumping wells have slotted casings at a depth of 40–50 m to pump from an aquifer, which is mainly composed of gravel. When the pumps are working, 430 and 700 L/min of groundwater are pumped from PW1 and PW2, respectively. Water level sensors are installed at 35 m below the ground surface, and groundwater levels were measured every minute in both pumping wells. The geology of the GHEs and pumping wells partly differ, although the main geological distribution trends are similar.

System performance

The heating test using the GSHP system was carried out from December, 2019 to April, 2020. The operating conditions of the GSHP system were as follows: circulation rate of the GHE was 35.0 L/min, circulation rate of the fan coil unit was 22.5 L/min, and water supply temperature on the secondary side was 40 °C. Figure 3 shows the GHE inlet and outlet temperatures and circulation rate during the heating test. The heat pump was continuously operated from Jan. to Mar., 2020, while the operation was intermittent in Dec., 2019. The results showed that the average heat exchange rate (sum of GHE1 and GHE2) remained at approximately 5.0 kW throughout the heating test period, except in the late Dec., 2019, when the data gathering system had a malfunction.

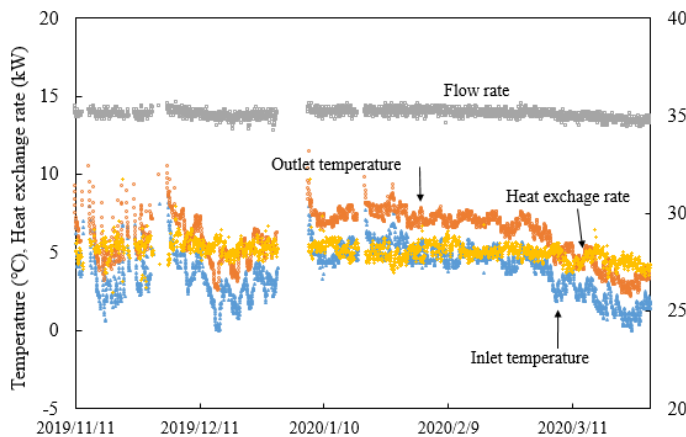


Figure 3 Measured heat medium temperatures and heat exchange rates during heating test.

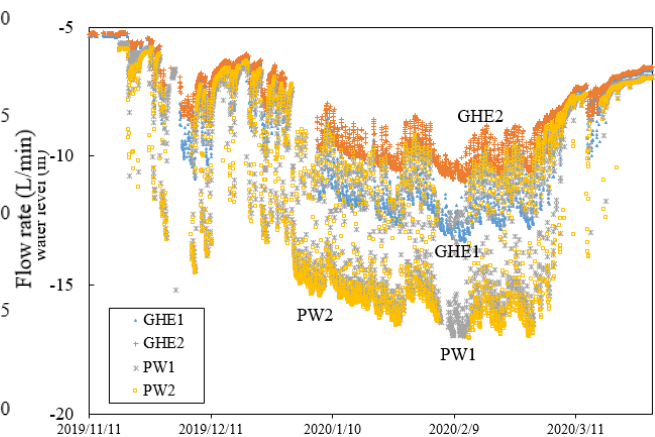


Figure 4 Measured groundwater levels of GHEs & pumping wells during heating test.

Figure 4 shows the groundwater level changes in GHE1, GHE2, PW1, and PW2. The groundwater level dropped sharply from the beginning of December when snow fall started until January, 2020 and remained deep in February. Then, the groundwater level recovered when pumping was stopped and recovered to the natural groundwater level. The heat medium temperature decreased rapidly from the beginning until December 15, 2019, after which the GHE outlet temperature recovered because the artificial groundwater flow caused by pumping recovered the ground temperature and improved the heat exchange capacity of the GHE. The outlet temperature was stable at approximately 7.5 °C from January to February with the nearly continuous water pumping. The GHE outlet temperature declined significantly in March due to the reduced frequency of the pumping operation in spring. It should be noted that the drop of groundwater level seems a negative factor for the ability of ungrouted GHEs because the effective U-tube length, the tube length in groundwater, reduces when the level drops. However, the heat medium temperatures are maintained from January to February, when the groundwater levels are low, because the benefit of the advection of groundwater flow is more important than the reduction of effective U-tube length. Figure 5 compares the groundwater level at GHE1

and the COP of the heat pump calculated based on the temperatures and flow rates of the heat medium and power consumption of the heat pump. As mentioned above, the COP increased with the decline in groundwater levels, except for in February 2020. This can be explained by the intermittent pumping operation in late February, which reduced the advection effect of groundwater flow. The above results of the heating tests indicate that installation of a GSHP system near a pumping well could reduce the required length of GHEs and initial investment costs.

The above field tests were carried out using ungrouted GHEs filled with groundwater. In Japan, GHEs are commonly grouted to avoid the collapse of the well wall and to protect U-tubes since the GSHP systems are usually located in unconsolidated deposits. The benefit of groundwater pumping, however, will not change significantly since most of the GHE are grouted using permeable materials and groundwater flow occurs through the GHE.

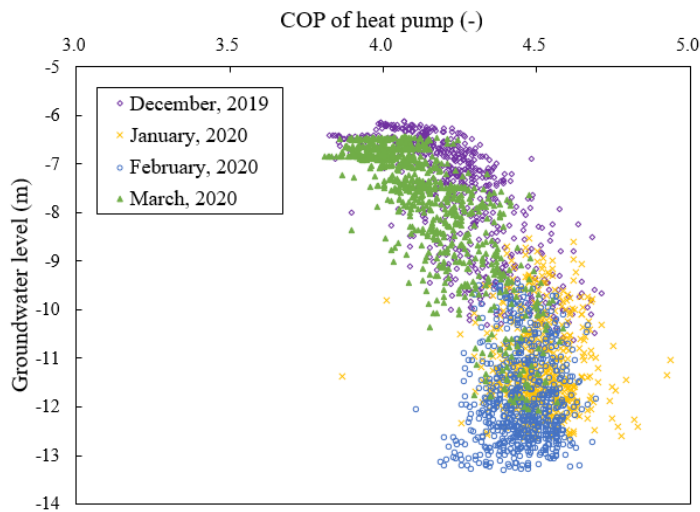


Figure 5 Correlation between groundwater level at GHE1 and COP of heat pump.

POTENTIAL MAPPING OF GSHP SYSTEMS CONSIDERING GROUNDWATER PUMPING

Since the positive effects of water pumping near GHEs have been confirmed in the field test, the findings are extended to field-scale. We first collected the water pumping data in Akita City used for snow melting, which is then input to the existing large-scale numerical groundwater flow and heat transport model for the entire area of Akita City and its surrounding mountains. The model calculates the groundwater velocity and temperature in the area under the influence of groundwater pumping, which are used as the input of small-scale GHE model. The GHE model estimates the minimum necessary GHE length for a Japanese standard detached house of 120 m² based on the weather data of Akita City at several locations in the area. The GHE length data are compiled using GIS software to generate the GSHP potential map under the influence of groundwater pumping.

Model description

The large scale numerical model covers Akita Plain including the city and the surrounding mountains as shown in Figure 6. Akita Plain is an alluvial deposit of the Quaternary System with a dimension about 16 km from north to south. The alluvial deposits are transported mainly by Omono River and its tributaries flowing in the plain. The deposit consists of sand, gravel, and silt. The thickness of the deposit varies from 0 m in the surrounding mountains to around 100 m in the north-western lowlands. The basement underlying the Quaternary System consists of mudstones and siltstones in the Tertiary System. The climate zone of Akita Plain is a humid subarctic climate and falls in the cold weather region of Japan. It receives heavy snowfall as it is located close to the Sea of Japan. In summer, it has hot and humid weather.

Atmospheric temperature varies from below freezing point in winter to above 30 °C in summer.

The large scale groundwater flow and heat transport model was constructed using FEFLOW ver.7.0 (Diersch, 2014). The model area is shown with bold lines in Figure 6. The model consists of 16 layers as shown in Figure 7; Layers 1-5 for the Quaternary System, Layers 6-16 for the Tertiary System. For groundwater flow analysis, model top was set with groundwater table calculated as a function of surface elevation. The model bottom was set as impermeable. At lateral sides, no groundwater flow was considered. Rivers were fixed with 10-year average elevation of the river surface. For heat transport analysis, the model top was fixed with temperature values estimated from the yearly average atmospheric temperature measured at Akita City of 10.9 °C and its decrement rate with elevation of 6.5×10^{-3} °C/m. The model bottom was fixed with values estimated by using geothermal gradient of 0.057 °C/m. The hydraulic and thermal conductivity and porosity values in Quaternary and Tertiary Systems are set as shown in Table 1 after the history matching on groundwater levels and ground temperature profiles measured at over 20 observation wells. Details and verification of the numerical model are discussed in Shrestha, et al. (2020).

Table 1 Parameters in the large scale simulation model.

	Quaternary System (1–5 Layers)	Tertiary System (6–16 Layers)
Hydraulic conductivity (m/s)	1×10^{-6}	1×10^{-8}
Porosity (-)	0.15	0.05
Thermal conductivity (W/m/K)	1.77	1.01

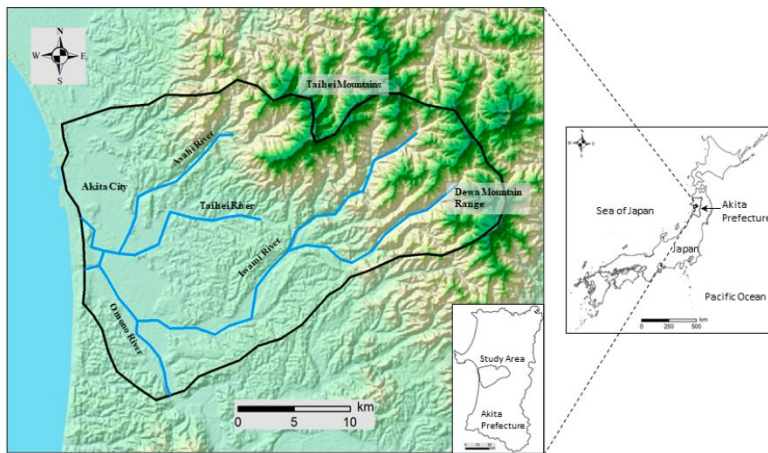


Figure 6 Location of Akita Plain and boundaries of large-scale model.

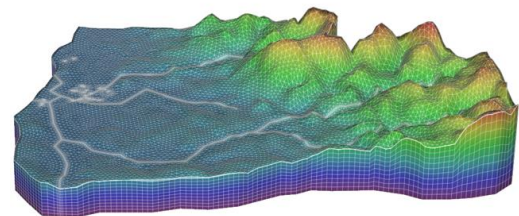


Figure 7 3D view of large scale numerical model of Akita Plain

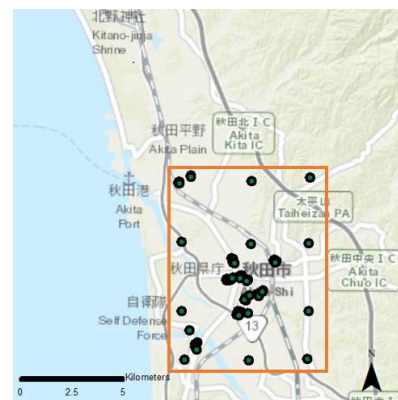


Figure 8 Map of Akita City and location of pumping wells (circle). The area in square is the mapping area in Figures 10 and 11.

In this work, we collected the water pumping data in Akita City used for snow melting for the input of the large scale numerical model. According to the provided information from Akita local government, a total of 30 pumping wells, whose locations are shown in Figure 8, are in use when snow fall is detected. The pumping rates ranged from 240-1150 L/min depending on the water productivity of the pumping wells. The large scale simulation model was run to calculate the velocity and temperature of groundwater for the entire area of Akita Plain. The calculated groundwater velocity and temperature were input to small-scale GHE model, which calculates the necessary length of GHEs.

In the GHE model (Figure 9), the material properties are set same as the large-scale model as shown in Table 1. The groundwater flow is defined by setting the hydraulic head at the upstream and downstream of the model, which yields the groundwater velocity at the GHE calculated by the large-scale model. The other sides, top and bottom of the GHE model are set as no flow boundary. As the boundary condition for heat transport, the top and bottom boundaries are set as fixed temperature which are obtained from the large-scale model. The peripheral boundaries are set as adiabatic. The thickness of the GHE model is refined as 2 m below -50 m to accurately determine the GHE length.

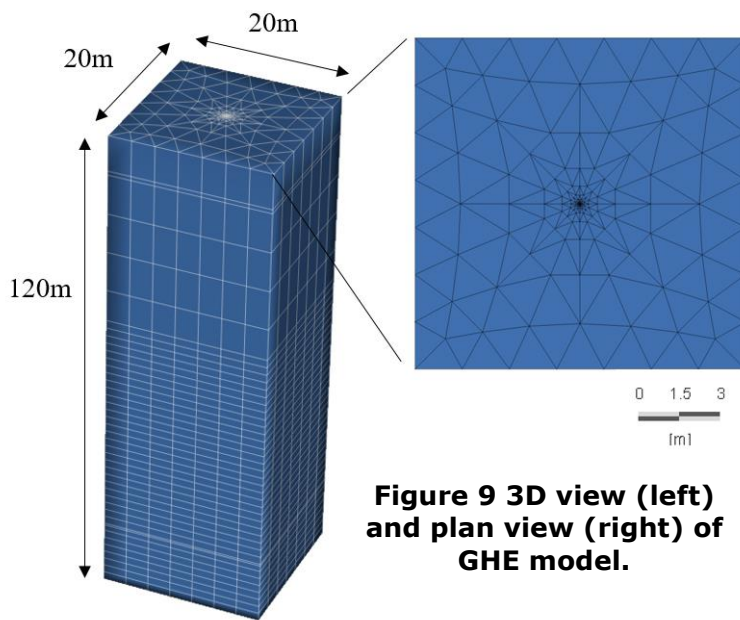


Figure 9 3D view (left) and plan view (right) of GHE model.

The Heating and cooling loads required to heat and cool a typical standard Japanese detached residence were calculated using the standardized plan of building load conditions which is based on the 2013 Energy Conservation Standard supervised by National Institute for Land and Infrastructure Management and Building Research Institute of Japan (Shrestha, et al., 2020). GHE was affixed at the center with a 150 mm diameter of borehole. Double U-tube of external diameter 32 mm and thickness 2.9 mm was considered, which was grouted in the borehole with silica sand. For Akita Plain, which has cold weather in winter, propylene glycol 15%, an antifreeze, was used as a heat-transfer medium. The particular GHE depth was determined with trial and error until the minimum of the average of inlet and outlet temperatures of GHE becomes between -1.9 °C and -2 °C.

Results of mapping

According to the above procedures, the required depth of the GHE for a standard Japanese detached house was calculated by conducting a long term simulation using the GHE model. The simulation locations, shown with green symbols, are mainly positioned around the pumping wells, where the influence of water pumping is expected. Based on the calculated GHE length, a potential map showing the distribution of required GHE length was constructed using GIS software at the central part of Akita City. Figures 10a and 10b show the same potential map with and without water pumping, respectively. Red symbols show the location of pumping wells. The benefit of water pumping is clearly seen in the neighborhood of pumping wells. Figure 11 shows the reduction rate of GHE length obtained based on the GHE length in the cases without and with water pumping. The central area of the city where many pumping wells are located due to the heavy traffic, large reduction rates exceeding 30% are observed, which results in the significant reduction of initial cost of GSHP systems. On the other hand, the effect of water pumping was negligible in areas 3 km apart from pumping wells.

To generalize the above results, the improvement by the water pumping could be less in a fractured rocky aquifer due

to a smaller porosity and water content. This should be investigated as future works using the GSHP operation data from other geological conditions.

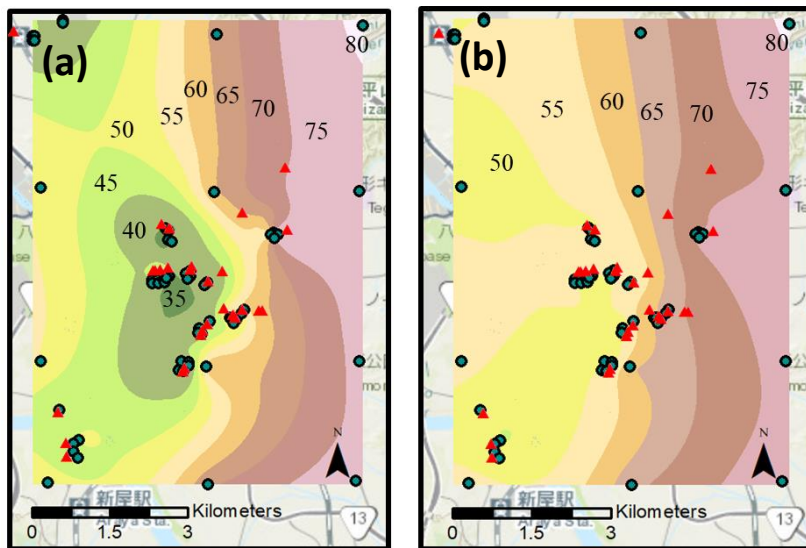


Figure 10 Map of necessary GHE length in meters (a) with groundwater pumping and (b) without pumping in the central part of Akita City.

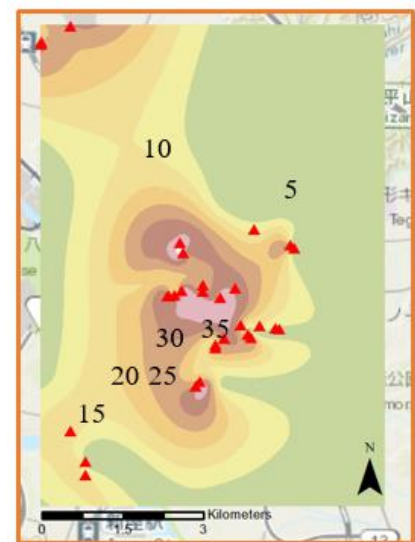


Figure 11 Distribution of GHE length reduction rate in % by water pumping.

CONCLUSIONS

In this work, we carried out performance analysis of a GSHP heating system in Akita City, Japan, under the influence of groundwater pumping from a permeable deposit. The heating operation data clearly showed the improved COP of the heat pump when the groundwater is pumped. Next, we collected the water pumping data in Akita City and input them to the existing field-scale numerical groundwater flow and heat transport model of the area. The minimum necessary length of GHE for a standard Japanese detached house were estimated using small-scale GHE models at several locations in the city. The GHE length data were then mapped using GIS software to generate the GSHP potential map under the influence of groundwater pumping. The comparison between the potential maps with and without groundwater pumping clearly indicated the contribution of water pumping in reducing the GHE length and initial cost of GSHP systems.

ACKNOWLEDGMENTS

This work was partly supported by Grants-in-Aid for Scientific Research (B) (19H02655) from JSPS.

REFERENCES

- Choi, J. C., Park, J., Lee, S. R. 2013. *Numerical evaluation of the effects of groundwater flow on borehole heat exchanger arrays*. *Renew Energy* 52: 230–40.
- Diersch, H.J.G. 2014. *FEFLOW Finite Element Modeling of Flow, Mass and Heat Transport in Porous and Fractured Media*. Springer, 996 p.
- Fujii, H., Itoi, R., Fujii, J. and Uchida, Y. 2005 *Optimizing the design of large-scale ground-coupled heat pump systems using groundwater and heat transport modeling*, *Geothermics* 34: 347-364.
- Fujii, H., Inatomi, T., Itoi, R. and Uchida, Y. 2007. *Development of suitability maps for ground-coupled heat pump systems using groundwater and heat transport modeling*, *Geothermics* 36: 459-472.

- Japan Meteorological Agency. Past Weather Data Search. Available online: www.data.jma.go.jp/obd/stats/etrn/index.php.
(In Japanese)
- Luo, J., Tuo, J., Huang, W., Zhu, Y. Q., Jiao, Y. Y., Xiang, W. 2018. *Influence of groundwater levels on effective thermal conductivity of the ground and heat transfer rate of borehole heat exchangers*. Applied Thermal Engineering 128: 508–516.
- Shrestha, G., Uchida, Y., Yoshioka, M., Fujii, H., Ioka, S. 2015. *Assessment of development potential of ground-coupled heat pump system in Tsugaru Plain, Japan*, Renewable Energy 76: 249-257.
- Shrestha, G., Yoshioka, M., Fujii, H., Uchida, Y. 2020. *Evaluation of Suitable Areas to Introduce a Closed-Loop Ground Source Heat Pump System in the Case of a Standard Japanese Detached Residence*. Energies 13, 4294; doi:10.3390/en13174294.

pygfunction 2.2 : New Features and Improvements in Accuracy and Computational Efficiency

Massimo Cimmino

Jonathan C. Cook

ABSTRACT

Recent improvements to pygfunction, an open-source tool for the calculation of g -functions, are presented. The latest version 2.2 enables the calculation of g -functions for fields containing inclined boreholes. Various changes introduced in versions 2.0, 2.1 and 2.2 have led to significant decreases in calculation time and memory usage while increasing the accuracy of calculations. This allows the calculation of g -functions of fields comprised of thousands of boreholes. A development roadmap towards a version 3.0 is presented. This future release will increase the scope of the tool to consider additional physical processes.

INTRODUCTION

Thermal response factors, or g -functions, are dimensionless step-response functions that give the effective temperature variation at the borehole walls in a bore field due to constant heat extraction from the bore field. g -Functions are utilized in ground heat exchanger (GHE) simulations by superposition of building heating and cooling loads to predict variations of borehole wall temperatures throughout time. During the design process, GHE simulations are iteratively performed to determine a suitable design for installation. Therefore, quick and accurate evaluation of g -functions enables the development of optimal designs and is critical to the efficient operation of a ground source heat pump (GSHP) system.

Eskilson (1987) introduced the concept of g -functions and developed a numerical finite difference model to evaluate them. g -Functions are defined by the relation:

$$T_b^*(\tau) = T_g - \frac{\bar{Q}'}{2\pi k_s} \cdot g\left(\tau, \frac{r_b}{H}, \frac{B}{H}, \frac{D}{H}\right) \quad (1)$$

where T_b^* is the effective borehole wall temperature, τ is the dimensionless time, T_g is the undisturbed ground temperature, \bar{Q}' is the constant average heat extraction rate per unit borehole length, k_s is the soil thermal conductivity, g is the g -function, r_b is the borehole radius, B is the borehole spacing, D is the borehole buried depth, and H is the borehole length. Figure 1 presents the g -functions of a field of 8 inclined boreholes, where t/t_s is the dimensionless time with $t_s = H^2/9\alpha_s$ the borefield characteristic time and α_s the ground thermal diffusivity.

Massimo Cimmino (massimo.cimmino@polymtl.ca) is a professor of mechanical engineering at Polytechnique Montréal and Jonathan C. Cook (jack-c-cook@proton.me) is a software engineer and a private researcher.

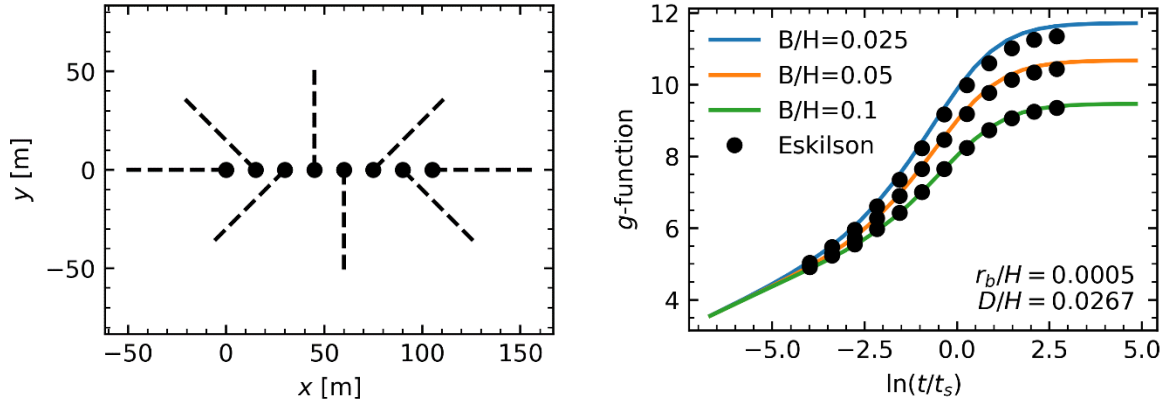


Figure 1 Top view of the bore field (left), and comparison between pygfunction and Eskilson's g -functions (right)

Following the reintroduction of the analytical finite line source solution (FLS) by Zeng et al. (2002), spatial superposition of the FLS was proposed to evaluate g -functions (Lamarche and Beauchamp, 2007; Claesson and Javed, 2011). g -Functions evaluated in this manner were shown to overestimate Eskilson's g -functions due to differences in the boundary condition at the borehole walls (Fossa, 2011). Cimmino and Bernier (2014) proposed to axially discretize each borehole into segments and superimpose the FLS solution in both space and time to reproduce Eskilson's uniform borehole wall temperature boundary condition. Their method was later extended to inclined boreholes (Lazzarotto, 2016), and to more detailed boundary conditions accounting for the heat transfer between the fluid and the borehole wall (Cimmino, 2015, 2019). Although not presented here, there is ongoing research on the development of analytical solutions and g -functions for fields of boreholes with groundwater advection and depth-dependent ground properties.

A series of simplifications and algorithmic improvements have been proposed to speed-up the evaluation of g -functions (Cimmino, 2018a; Dusseault et al., 2018; Nguyen and Pasquier, 2021; Prieto and Cimmino, 2021). While these newer methods successfully lower computational requirements for the evaluation of g -functions, they are often more complex than their predecessors, thereby hindering their adoption and extension by other researchers and practitioners. The reproducibility of results poses additional issues when considering computational efficiency, as it depends not only on the method but also on the specifications of the machine it runs on, the programming language and environment (including the version), and the often-overlooked quality of the implementation.

The open-source pygfunction package (Cimmino, 2018b) enables the evaluation of g -functions of fields of arbitrarily positioned boreholes with different boundary conditions and solvers. The package has seen active development since its introduction. It now supports the calculation of g -functions of fields of thousands of boreholes with orders of magnitude reduction in calculation time and memory usage, along with several new features. These improvements are in part due to the implementation of new methods and optimization of the codebase but also from updates to other open-source projects pygfunction depends on; namely NumPy (Harris et al., 2020) for array programming, SciPy (Virtanen et al., 2020) for scientific computing, Matplotlib (Hunter, 2007) for visualization, and CoolProp (Bell et al., 2014) for physical properties of fluids. The open-source nature of the package makes it possible for anyone to evaluate g -functions using state-of-the-art methods or for researchers to modify or extend the package for their own use. pygfunction has already been used within other open-source projects aimed at the design of borefields: GHEtool (Peere et al., 2021) and the Ground Heat Exchanger Design Toolbox (GHEDT) (Cook, 2021).

This paper details the new features and improvements to pygfunction from its initial version 1.0 to the current version 2.2. An overview of changes affecting its computational efficiency and accuracy is first presented. Then, the

implementation of support for inclined boreholes is described. Results present the evolution of computational efficiency and accuracy across versions. Finally, a development roadmap leading to a version 3.0 release is presented.

NEW FEATURES AND CHANGES TO EXISTING MODULES

pygfunction is structured into modules: *boreholes*, *gfunction*, *heat_transfer*, *load_aggregation*, *media*, *networks*, *pipes*, and *utilities*. The modules were presented in an earlier publication (Cimmino, 2018b), except for the *networks* and *media* modules introduced in versions 1.1.1 and 2.0, respectively. The *networks* module enables the configuration of piping connections between boreholes and the evaluation of *g*-functions for mixed parallel and series connections between boreholes (Cimmino, 2019), including fields of coaxial boreholes since version 2.1. The *media* module gives access to fluid properties using CoolProp (Bell et al., 2014). The *gfunction* module was refactored to replace the dedicated functions for different boundary conditions by a single class that can handle all calculation options. pygfunction supports 3 boundary conditions: uniform and equal heat extraction rates (Claesson and Javed, 2011), uniform and equal borehole wall temperatures (Cimmino and Bernier, 2014), and mixed inlet fluid temperatures (Cimmino, 2019). When computing *g*-functions, a user might use a combination of the *boreholes*, *pipes*, *networks* and *media* modules to define the borefield, depending on the chosen boundary condition, and use the *gfunction* module to evaluate the *g*-functions.

Since version 2.0, pygfunction is exclusively developed in Python 3, and pygfunction has seen continuous improvements in computational efficiency between each release. Part of these improvements is due to the implementation of a new solver (i.e. the *equivalent* solver) based on the equivalent borehole method of Prieto and Cimmino (2021) in version 2.1, and to the implementation of an approximation of the FLS (Cimmino, 2021) in version 2.2. The *equivalent* solver identifies groups of boreholes (usually 3 to 5) within the borefield that are expected to share similar borehole wall temperatures and heat extraction rates. Each group is represented by a single “equivalent” borehole (i.e. all boreholes of the same group share the same borehole wall temperature and heat extraction rate profiles). This massively reduces the size of the system of equations and the number of required FLS evaluations.

Significant performance improvements have been achieved by extensive use of NumPy array computations. NumPy and SciPy operations performed on NumPy arrays are executed in optimized low-level (C or Fortran) compiled code. All modules have been refactored to make better use of NumPy array computations. pygfunction v1.0 computed segment-to-segment responses in pure Python syntax with multi-threading. Cook and Spitler (2021) computed FLS responses 8.6 times faster in C++ with multi-threading. Since v2.0, pygfunction now has vectorized the FLS evaluation via the *quad_vec* function recently introduced in SciPy v1.4. This allows pygfunction to evaluate the FLS for multiple pairs of boreholes at the same time without the need for the *multiprocessing* package. The computational efficiency of *quad_vec* dwarfs multi-threaded C++ code as implemented by Cook (2021, p. 57).

An important driver for improvements has been feedback from users and researchers. Cook and Spitler (2021) highlighted issues with memory usage in pygfunction. Their results also showed that the *similarities* solver (Cimmino, 2018a) did not scale well with the number of boreholes. This motivated the refactoring of the *similarities* solver and the *gfunction* module. Several new features have been introduced following user involvement on the GitHub repository of pygfunction. This is the case for coaxial boreholes, the *media* module, and the development of an unequal discretization scheme along boreholes (described in the next section), all proposed by the second author.

Non-uniform segment discretization along boreholes

The calculation of *g*-functions using the FLS solutions was previously done using a uniform discretization of boreholes (i.e. segments of equal lengths). Cimmino and Bernier (2014) suggested the use of $n_s = 12$ equal segments along the length of the boreholes after observing a 4.7 % maximum error on the steady-state value of the *g*-functions of fields up to 100 boreholes. Equal segments were chosen to simplify the evaluation of the FLS, since similarities can reduce the number of required evaluations in this case (Cimmino, 2018a). The purpose of the discretization is to capture the

variation of heat extraction along the borehole length. The heat extraction rate varies the most at the top and bottom of the borehole (Cimmino and Bernier, 2014). Thus, a uniform segment length is sub-optimal. Eskilson (1987) proposed an expanding discretization towards the middle of the boreholes, with a factor $\gamma = \sqrt{2}$ between the length of 2 consecutive segments. The maximum number of segments considered was 12.

A non-uniform segment discretization scheme was implemented into pygfunction. The implemented scheme specifies the end-length-ratio (i.e. the ratio x_1 of the total length H represented by each of the first and last segments along the borehole), rather than the expansion factor. The expansion factor can be evaluated from the roots of the polynomial:

$$\begin{cases} 0 = (1 - 2x_1) - x_1 \cdot \gamma + 2x_1 \cdot \gamma^{n_s/2} & \text{if } n_s \text{ is even} \\ 0 = (1 - 2x_1) - x_1 \cdot \gamma + x_1 \cdot \gamma^{(n_s-1)/2} + 2x_1 \cdot \gamma^{(n_s-1)/2+1} & \text{if } n_s \text{ is odd} \end{cases} \quad (2)$$

where x_1 is the end-length-ratio, γ is the expansion factor, and n_s is the number of segments.

Values of $x_1 = 0.02$ and $n_s = 8$ provide accurate results, as will be shown in the results section. For this combination of parameters, the expansion factor is $\gamma = 2.485$. This is in line with the findings of Lamarche (2017) who used a piecewise-linear discretization of heat extraction rates along boreholes, which allowed them to represent sharp variations of heat extraction rates at the ends of the boreholes and lowered the number of segments to 8. Figure 2 compares a uniform discretization of 12 segments and a non-uniform discretization of 8 segments. It is shown that the non-uniform discretization has a finer discretization at the ends of the borehole.

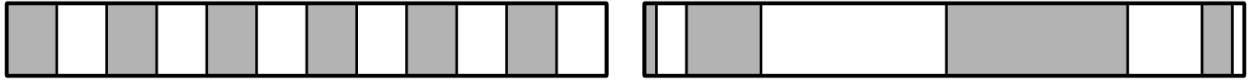


Figure 2 Uniform discretization of 12 segments (left), and non-uniform discretization of 8 segments (right)

Inclined boreholes

Calculation of g -functions for fields with inclined boreholes using discretized boreholes with uniform borehole wall temperature has so far been limited to the work of Lazzarotto (2016) and Lazzarotto and Björk (2016). Inclined boreholes were implemented into pygfunction version 2.2. The FLS is solved following the method of Lazzarotto (2016), with the remaining two integrals solved using a Gauss-Legendre quadrature over the segment lengths and an adaptative quadrature over the time variable (using the *quad_vec* function). Inclined boreholes are fully integrated with the different solvers and features of pygfunction, including the *similarities* solver to accelerate the evaluation of g -functions and an approximation of the FLS based on the method of Cimmino (2021).

Figure 1 presents the g -functions of a field of 8 boreholes with an inclination of 20° , calculated with a non-uniform discretization of 8 segments using the *similarities* solver. Eskilson's g -functions are a reproduction of the curves presented in the thesis (Eskilson, 1987). The maximum error is 2.5 % and is observed for $B/H = 0.025$ and $\ln(t/t_s) = 2.70$. Possible causes for this error are a mismatch of the buried depth D used in the calculation (this information was not provided by Eskilson) and unconverged values of the g -functions due to the coarse grids used by Eskilson. Each g -function was evaluated in an average of 2.36 seconds for 30 time steps.

RESULTS

The evolution of the accuracy and computational efficiency of pygfunction since version 1.0 is presented by evaluating the g -functions of fields of up to 400 boreholes with a uniform borehole wall temperature boundary condition. All L-shaped, U-shaped, box-shaped and rectangular array configurations of 1×2 to 20×20 boreholes are tested, as well as

random configurations of up to 400 boreholes in increments of 10 boreholes generated from Poisson disk sampling using Bridson’s algorithm (Bridson, 2007). This totals 1635 borefields. Boreholes have a length $H = 150$ m, a burial depth $D = 4$ m and a radius $r_b = 0.075$ m. The nominal spacing in the borefields is $B = 7.5$ m ($B/H = 0.05$). The ground has a thermal diffusivity $\alpha_s = 10^{-6}$ m²/s. g -Functions are evaluated from $t_1 = 100$ h to $t_{30} = 3\,000$ yr at 30 geometrically expanding time steps, with $t_n = t_1 \cdot (1 - \gamma^n)/(1 - \gamma)$ and $\gamma = 1.479$.

All g -functions are computed on a computer with an Intel Core i9-11900K 3.5 GHz 8-core processor. The computer runs on Kubuntu 20.04.4 LTS (operating system), Python 3.7.13, NumPy 1.21.6, SciPy 1.7.3, Coolprop 6.4.1 and Matplotlib 3.5.1. Reference results to quantify the accuracy are generated with pygfunction version 2.2 using the *detailed* solver and 32 unequal segments along the boreholes. The reference vertical grid is generated by splitting segments of the 8 unequal segment discretization into 4 segments each. The *detailed* solver is used as a reference since it does not consider any simplifications for the evaluation of the FLS. Other combinations of versions and solver options are chosen to highlight the progression of pygfunction: (1) version 1.0 using the *similarities* solver and 12 uniform segments, (2) version 2.0 using the *similarities* solver and 12 uniform segments, (3) version 2.1 using the *similarities* solver and 8 non-uniform segments, (4) version 2.1 using the *equivalent* solver and 8 non-uniform segments, and (5) version 2.2 using the *equivalent* solver, 8 non-uniform segments and the approximation of the FLS.

Accuracy

Figure 3 compares the maximum relative error, $(g - g_{ref})/g_{ref}$, for the different versions of pygfunction. Versions 1.0 and 2.0 show similar errors. The decreased error from version 2.0 to 2.1 is due to the non-uniform segment discretization. The *equivalent* solver is not as accurate as the *similarities* solver since it introduces additional simplifications in the thermal model, but version 2.1 *equivalent* with 8 unequal segments is still more accurate than version 2.0 *similarities* with a uniform discretization of 12 segments. Version 2.2 shows a negligible increase in the error due to the use of the approximation of the FLS. Overall, it is shown that pygfunction has gained accuracy compared to version 1.0.

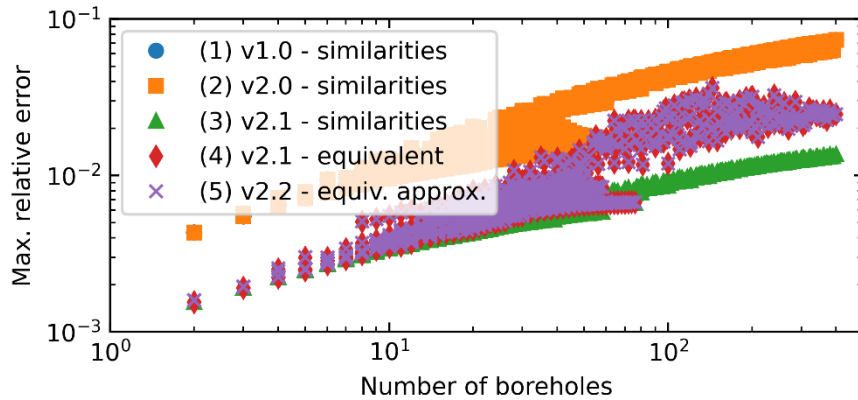


Figure 3 Maximum relative error on the g -functions

Computational efficiency

Figure 4 compares the calculation time and memory usage for the different versions of pygfunction. The decreased calculation time from version 1.0 to 2.0 is mainly due to a refactoring of the *similarities* solver to make better use of NumPy capabilities and to the use of the newly introduced *quad_vec* function of SciPy. The decreased calculation time

from version 2.0 to 2.1 is due to the decrease in the number of segments enabled by an unequal segment discretization. The *equivalent* solver is significantly faster than the *similarities* solver due to the reduced number of evaluations of the FLS. The efficiency gain increases with the number of boreholes: the calculation times for a field of 400 randomly positioned boreholes are 26.1 and 0.775 seconds for the *similarities* and *equivalent* solvers, respectively. The decreased calculation time from version 2.1 to 2.2 is due to the approximation of the FLS and further optimization of the code, lowering the calculation time to 0.245 seconds for the same field. The efficiency gains introduced by the *equivalent* solver removes the requirement of a g -function database for use in pygfunction integrated design tools (Cook, 2021). In terms of memory usage, the decrease from version 1.0 to 2.0 are due to code refactoring following the observations of Cook and Spitler (2021). The memory usage for the *similarities* method is mainly a function of the total number of segments, which explains the decrease from version 2.0 to 2.1. The *equivalent* solver in versions 2.1 and 2.2 significantly decreases the memory usage when compared to the *similarities* solver, due to the reduced number of considered equivalent boreholes in the calculations. The reduction is such that memory usage ceases to be an issue: the required memory for a field of 400 randomly positioned boreholes is 5.26 Gb and 43.7 Mb for the *similarities* and *equivalent* solvers, respectively. The memory usage of the *equivalent* solver shows plateaus at approximately 0.8 Mb and 10 Mb for versions 2.1 and 2.2, respectively. The cause of these plateaus is unknown.

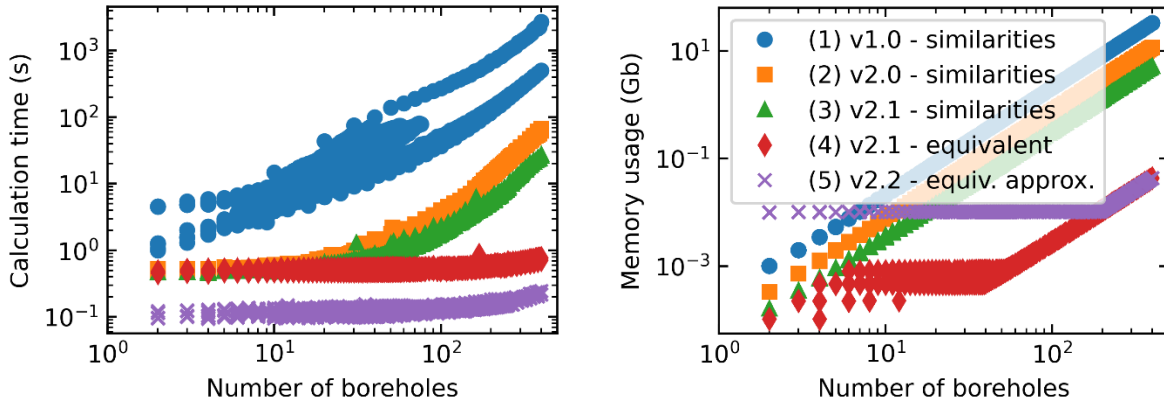


Figure 4 Calculation time (left), and peak memory usage (right)

The reductions in calculation time and memory usage make the calculation of g -functions of very large fields possible. The largest borefield known to the authors is located at Daxing International Airport (China) and is reported to be comprised of 10 497 boreholes. g -Functions of such large borefields have never been reported due to the previously enormous requirements in calculation time and memory usage (Cook and Spitler, 2021). Figure 5 presents the g -functions of a field of 110×100 borehole in a rectangular configuration. The calculation time was 78.0 seconds on average, with 68.0 seconds devoted to the identification of equivalent boreholes and 8.18 seconds devoted to the calculation of the g -function over 30 time steps. Note that the identification of equivalent boreholes is independent of the number of time steps.

DEVELOPMENT ROADMAP

While pygfunction version 1.0 contributed the first open-source tool for the calculation of g -functions, versions 2.0, 2.1 and 2.2 focused on increasing its computational efficiency. pygfunction is now able to evaluate g -functions for fields containing vertical or inclined boreholes with relative ease. Going forward, efforts will be put into increasing its capabilities and its ease of use. Two major changes are planned for an eventual version 3.0: (1) a restructuring of the

documentation, including the introduction of a “Getting started” tutorial, and (2) a simulation module to enable the simulation of complete ground-source heat pump systems, including the borefield and the heat pump. For subsequent releases, the scope of g -function calculations will be increased to consider additional physical processes, e.g. groundwater advection, layered ground conditions, and short-term effects. This poses significant challenges: while there are known analytical solutions that can be used for the calculation of g -functions, they require extensive changes to the *similarities* and *equivalent* solvers to enable efficient calculations.

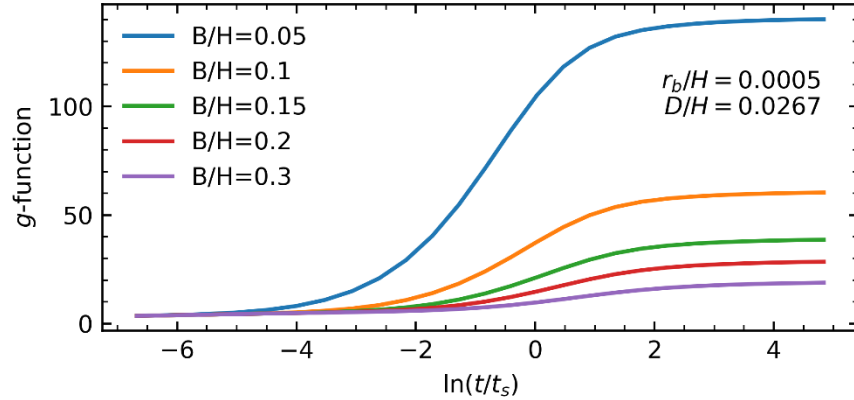


Figure 5 g -Functions of a field of 11 000 boreholes in a 110×100 configuration

CONCLUSION

The recent improvements to pygfunction were presented. New features since its original release include the implementation of inclined boreholes, the *media* and *network* modules, and the *equivalent* solver. Factoring in optimizations to the codebase and updates to other open-source projects, pygfunction version 2.2 achieves higher accuracy than version 1.0 at a fraction of the cost in calculation time and memory usage. Future development will increase the scope of pygfunction to include additional physical processes such as groundwater advection, layered ground conditions, and short-term effects.

ACKNOWLEDGMENTS

Contributions to open-source projects like pygfunction are not limited to code development. Various indirect contributions in the form of questions, bug reports and comments on efficiency made on the GitHub platform have led to improvements in the computational efficiency of pygfunction, in the clarity of its documentation and its ease of use. We acknowledge all who initiated or participated on “issues”. The second author would like to acknowledge the DOE and Dr. Jeffrey D. Spitler for indirectly aiding contributions to pygfunction.

NOMENCLATURE

α_s = Ground thermal diffusivity (m^2/s)	k_s = Ground thermal conductivity ($\text{W}/\text{m}\cdot\text{K}$)
γ = Segment discretization expansion factor (-)	D = Borehole buried depth (m)
B = Borehole spacing (m)	n_s = Number of segments (-)
D = Borehole buried depth (m)	\bar{Q}' = Average heat extraction rate per unit borehole length (W/m)
g = g -function (-)	r_b = Borehole radius (m)
H = Borehole length (m)	

T_b^*	=	Effective borehole wall temperature (°C)	t_s	=	Borefield characteristic time (s)
T_g	=	Undisturbed ground temperature (°C)	x_1	=	End-length-ratio (-)
t	=	Time (s)			

REFERENCES

- Bell, I. H., J. Wronski, S. Quoilin and V. Lemort. 2014. *Pure and pseudo-pure fluid thermophysical property evaluation and the open-source thermophysical property library CoolProp*. Industrial & Engineering Chemistry Research 53(6): 2498-2508.
- Bridson, R. 2007. *Fast Poisson disk sampling in arbitrary dimensions*. SIGGRAPH sketches 10(1): 1.
- Cimmino, M. and M. Bernier. 2014. *A semi-analytical method to generate g-functions for geothermal bore fields*. International Journal of Heat and Mass Transfer 70: 641-650.
- Cimmino, M., 2015. *The effects of borehole thermal resistances and fluid flow rate on the g-functions of geothermal bore fields*. International Journal of Heat and Mass Transfer 91: 1119-1127.
- Cimmino, M. 2018a. *Fast calculation of the g-functions of geothermal borehole fields using similarities in the evaluation of the finite line source solution*. Journal of Building Performance Simulation 11(6): 655-668.
- Cimmino, M. 2018b. *pygfunction: an open-source toolbox for the evaluation of thermal response factors for geothermal borehole fields*. eSim 2018 – the 10th conference of IBPSA-Canada, Montréal, Canada: 492-501.
- Cimmino, M., 2019. *Semi-Analytical Method for g-Function Calculation of bore fields with series-and parallel-connected boreholes*. Science and Technology for the Built Environment 25(8): 1007-1022.
- Cimmino, M. 2021. *An approximation of the finite line source solution to model thermal interactions between geothermal boreholes*. International Communications in Heat and Mass Transfer 127: 105496.
- Claesson, J. and S. Javed. 2011. *An analytical method to calculate borehole fluid temperatures for time-scales from minutes to decades*. In ASHRAE Transactions 117(2): 279-288.
- Cook, J. C. 2021. *Development of computer programs for fast computation of g-functions and automated ground heat exchanger design*. M.Sc. Thesis. Oklahoma State University, Stillwater, OK, USA.
- Cook, J. C. and J. D. Spitler. 2021. *Faster computation of g-functions used for modeling of ground heat exchangers with reduced memory consumption*. International Building Simulation Conference 2021. Bruges, Belgium.
- Dusseault, B., P. Pasquier and D. Marcotte. 2018. *A block matrix formulation for efficient g-function construction*. Renewable Energy 121: 249-260.
- Eskilson, P. 1987. *Thermal analysis of heat extraction boreholes*. Ph.D. Thesis. Lund university, Lund, Sweden.
- Fossa, M. 2011. *The temperature penalty approach to the design of borehole heat exchangers for heat pump applications*. Energy and Buildings 43(6): 1473-1479.
- Harris, C. R., K. J. Millman, S. J. van der Walt et al. 2020. *Array programming with NumPy*. Nature 585(7825): 357-362.
- Hunter, J. D. 2007. *Matplotlib: A 2D Graphics Environment*. Computing in Science & Engineering 9(3): 90-95.
- Lamarche, L. and B. Beauchamp. 2007. *A new contribution to the finite line-source model for geothermal boreholes*. Energy and Buildings 39(2): 188-198.
- Lamarche, L. 2017. *G-function generation using a piecewise-linear profile applied to ground heat exchangers*. International Journal of Heat and Mass Transfer 115: 354-360.
- Lazzarotto, A. 2016. *A methodology for the calculation of response functions for geothermal fields with arbitrarily oriented boreholes – Part 1*. Renewable Energy 86: 1380-1393.
- Lazzarotto, A. and F. Björk. 2016. *A methodology for the calculation of response functions for geothermal fields with arbitrarily oriented boreholes – Part 2*. Renewable energy 86: 1353-1361.
- Nguyen, A. and P. Pasquier. 2021. *A successive flux estimation method for rapid g-function construction of small to large-scale ground heat exchanger*. Renewable Energy 165: 359-368.
- Peere, W., D. Picard, I. Cupeiro Figueroa, W. Boydens and L. Helsen. 2021. *Validated combined first and last year borefield sizing methodology*. International Building Simulation Conference 2021. Bruges, Belgium.
- Prieto, C. and M. Cimmino. 2021. *Thermal interactions in large irregular fields of geothermal boreholes: the method of equivalent boreholes*. Journal of Building Performance Simulation 14(4): 446-460.
- Virtanen, P., R. Gommers, T. E. Oliphant et al. 2020. *SciPy 1.0: Fundamental algorithms for scientific computing in Python*. Nature Methods 17(3): 261-272.
- Zeng, H. Y., N. R. Diao and Z. H. Fang. 2002. *A finite line-source model for boreholes in geothermal heat exchangers*. Heat Transfer – Asian Research 31(7): 558-567.



Ground Heat Exchanger Design Tool with RowWise Placement of Boreholes

Jeffrey D. Spitler

Timothy West

Xiaobing Liu

ABSTRACT

Simulation-based design tools have been used since the late 1980s for designing ground heat exchangers (GHE) used with ground source heat pump (GSHP) systems. The ground heat exchanger simulations used in these tools rely on thermal response functions known as g-functions. Because of the significant computational burden in computing g-functions for even a single configuration, the design tools have relied on libraries of pre-computed g-functions. These g-functions were available for standard configuration shapes, such as lines, rectangles, open rectangles, L-shapes, and U-shapes. Standard shapes are often sub-optimal. For any building on a site, the available land may preclude use of a standard shape. For large GSHP systems with significantly imbalanced annual heat rejection and extraction loads, large rectangular fields may experience significant heat build-up (or heat draw-down) in the interior of the field. This paper describes a new ground heat exchanger design tool capable of automatically selecting and sizing both standard and irregular configurations. The focus of this paper is a method for creating, selecting and sizing irregular configurations where the available land area and “no-go” zones are described as irregular polygons.

INTRODUCTION

Development of thermal response functions, known as g-functions, by Prof. Claesson of Lund University and his graduate students (Claesson and Eskilson 1985, 1988) allowed simulation of ground heat exchangers with multiple vertical boreholes, accounting for borehole-to-borehole thermal interference. The effects of thermal interference are particularly important for larger ground heat exchangers used with GSHP systems serving commercial and institutional buildings. Simulation-based design tools such as GLHEPRO (Spitler 2000) and EED (BLOCON 2015) use pre-calculated libraries of g-functions for standard shapes (lines, rectangles, etc.) because, up until recently, computation of g-functions was too time-consuming to be done “on the fly”.

However, in situations where the annual heat rejection and extraction are significantly imbalanced, long-term temperature build-up or draw-down can drive the total drilling requirements to infeasibly high levels. Spitler, et al. (2020) compared designs based on a library rectangular g-function to a custom configuration where the boreholes were wrapped around the building. For this specific case, wrap-around configurations could achieve drilling savings of 34-43% depending on the depth constraint. The design of the wrap-around configuration took many engineer-hours to locate the boreholes, iteratively adjusting the number of boreholes and borehole positions, and calculating g-

Jeffrey D. Spitler (spitler@okstate.edu) is a professor, Timothy West is a research assistant, at Oklahoma State University. Xiaobing Liu is senior research staff at Oak Ridge National Laboratory.

functions (taking many computer hours) for each configuration. Methods for automatically placing boreholes in an optimal¹ or near-optimal manner are of significant interest.

Bayer, et al. (2014) described a method for designing GHE starting with a pre-defined configuration and systematically removing boreholes based on their effectiveness. Robert and Gosselin (2014) described a GSHP system optimization that selected uniformly spaced rectangular borehole fields. This paper describes a recently developed design tool, GHEDesigner², which can automatically select and size borehole configurations (that is, place the boreholes and determine the depth that meets the design temperature constraints.) The focus of this paper is the addition of a new algorithm for creating and selecting borehole configurations – the RowWise algorithm.

GHEDESIGNER

GHEDesigner (Ground Heat Exchanger Designer) is a recently developed simulation-based design tool for ground heat exchangers. An earlier version, GHEDT (Ground Heat Exchanger Design Tool) was described by Cook (2021). It serves a similar purpose to other simulation-based design tools such as GLHEPRO (Spitler 2000) and EED (BLOCON 2017) but has new features. The most significant feature being the capability to both select and size a ground heat exchanger configuration. It has several search routines for selecting configurations, including:

- The unconstrained square/near-square search will search a domain of square ($n \times n$) and near-square ($(n-1) \times n$) boreholes, with uniform spacing between the boreholes.
- Uniform and bi-uniform constrained rectangular searches will search domains of rectangular configurations that have either uniform spacing or “bi-uniform” spacing – that is, uniform in the x direction and uniform in the y direction, but the two spacings may be different.
- The bi-uniform constrained zoned rectangular search allows for rectangular configurations with different interior and perimeter spacings.
- The bi-uniform polygonal constrained rectangular search (BUPCRS) can search configurations with an outer perimeter and no-go zones described as irregular polygons. This is still referred to as a rectangular search because it is still based on a rectangular grid, from which boreholes that are outside the perimeter or inside a no-go zone are removed.

By comparison, GLHEPRO sizes a user-specified configuration. EED has features to automatically search constrained rectangular borehole fields and allow conversion of a user-specified irregularly shaped field to an equivalent rectangular field. It does not allow automated placement of irregularly shaped borehole fields.

GHEDesigner relies on an integer bisection search to select the configuration. Each configuration is simulated for the design period, giving a ground heat exchanger exiting fluid temperature (GHE ExFT) for each time step. The search parameter, the excess temperature, is the maximum temperature difference by which the design temperature constraints are exceeded. The bisection search looks for the root but returns the configuration with the smallest magnitude but negative excess fluid temperature as the design. The different search domains above have been chosen to be unimodal; here this means that the excess fluid temperature always decreases as the number of boreholes are increased. This means that there is only one root.

GHEDesigner uses pygfunction (Cimmino 2018) to compute the long time step (LTS) g-functions on the fly. By

¹ Finding a true global optimum for large fields is not currently feasible – global large scale optimization methods that could actually optimize placement of hundreds of boreholes are a current area of research and, in the authors’ opinions, seem likely to be reduced to practice for GHE design in the near future

² The authors plan to release an open-source version of the design tool, named GHEDesigner, with the RowWise algorithm in 2022. See: <https://github.com/BETSRG/GHEDesigner>

default, the equivalent borehole model (Prieto and Cimmino 2021) with eight non-uniform finite line sources per borehole (Cook 2021) is used to allow rapid computation for any borefield geometry. A single g-function can be computed on a standard desktop PC in a few seconds. For sizing purposes, five g-functions are computed for different depths and interpolated between. Borehole thermal resistance and short time step (STS) g-functions can be computed for single U-tube, double U-tube, and co-axial configurations.

GHEDesigner uses an improved hybrid time-step scheme as recommended by Cullin and Spitler (2011). The duration and length of monthly peak loads as well as average monthly loads are automatically determined from hourly loads. GHEDesigner can also size based on an hourly simulation, but this becomes rather slow. Unlike GLHEPRO, but like EED, the user currently has to specify the ground heat rejection/extraction loads rather than loads on the heat pump(s). Heat pump models will be added in the future.

ILLUSTRATIVE EXAMPLE

To better illustrate the process that the RowWise and search algorithms use, a specific example is used in this paper, based on (1) an actual medical office building in Stillwater, Oklahoma, from which the building footprint and property boundaries are taken, and (2) a medical outpatient building from the DoE commercial buildings library (USDOE 2022), simulated in Stillwater, Oklahoma, from which the load profile is taken. The library medical outpatient building has a floor area of 3804 m² (40,946 sq. ft.) and annual heat rejection that is 11.6 times the annual heat extraction; the annual loads are significantly imbalanced. For purposes of creating several examples, the simulated hourly loads were scaled as described in the results section. The property boundary (orange line) is irregularly shaped, and the building footprint and a no-go zone (gray lines) for utility easements are shown in Figure 1. The property boundary and no-go zones are represented as counterclockwise lists of points.

ROWWISE METHODOLOGY

The RowWise method systematically distributes boreholes across a property, if needed, or can reduce the footprint of the borehole field, if desirable. The goal of this method is to place boreholes in a way that both retains the row structure that borefields often have as well as efficiently utilizing space available on the property. Retaining the row structure should simplify locating the boreholes during drilling and reduce the complexity of the header piping system. The RowWise algorithm has two parts. For a specified target spacing, the RowWise placement algorithm generates many fields with different rotations, returning the field with the maximum number of boreholes. The RowWise search algorithm searches target spacings, calling the RowWise placement algorithm, and evaluating the borefields' exiting fluid temperature and total drilling to find a good design.

To utilize the space available on a property, the user specifies two minimum spacings, an inter-row minimum spacing and intra-row minimum spacing. Together, these determine the maximum number of boreholes that can be placed on the available property. The design intra-row spacing will often be higher than the minimum intra-row spacing, as borehole positions are adjusted in the algorithm to take full use of the available space along each row. Figure 1 shows sample results with the blue lines representing each row and the blue dots representing the boreholes. The right-hand figure uses independent perimeter borehole target spacing.

A further option in the RowWise algorithm is a separate input minimum spacing for the perimeter boreholes, which allows reduced perimeter spacing. This is often advantageous. In addition to the minimum spacing and property inputs³, other inputs control the row rotations, setting the range of rotation and rotation step size.

³ Property boundaries and no-go zones are input as polygons with points specified in counterclockwise order.

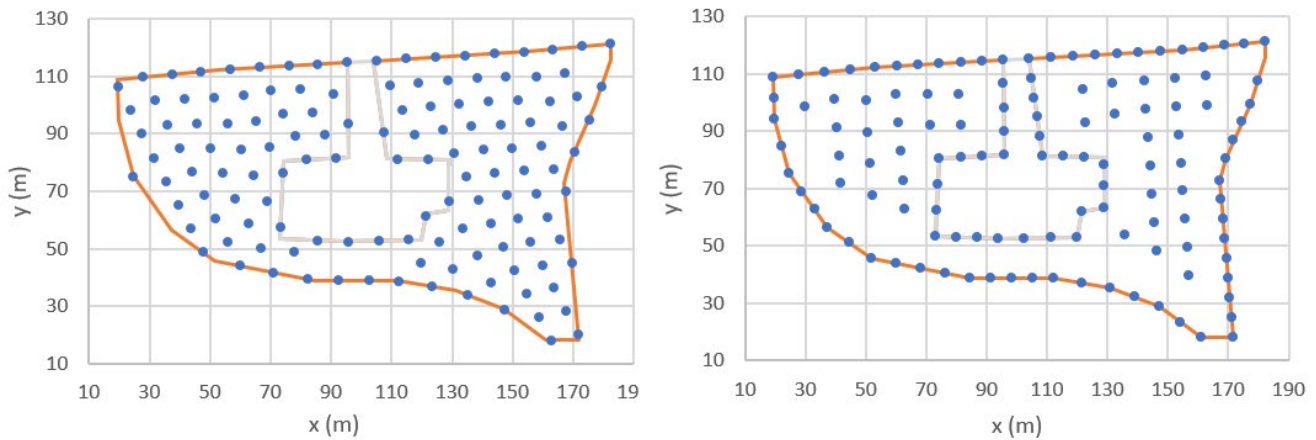


Figure 1 Sample RowWise fields. The left field uses the standard RowWise algorithm, (90° clockwise row rotation) but the right field uses independent perimeter spacing (86° clockwise row rotation).

RowWise Placement Algorithm

The RowWise placement algorithm has an outer loop that controls the row rotation (angle of each row from horizontal). The user can specify the range and rotation step size. We have commonly used 0° - 90° for the range of rotation and 0.1° for the rotation step size. For any particular rotation, the algorithm starts by determining the direction normal to the rows and finds the lowest and highest point on the property boundary relative to that direction. The algorithm then determines the maximum number of rows that can fit on the property while maintaining at least the minimum inter-row spacing. The row spacing is then adjusted upwards to fully use the property, with rows going through the highest and lowest points on the property boundary.

The next major step is the borehole placement in each row. For each row, the algorithm finds the intersections between the row and the property boundary as well as any no-go zones. These intersections are used to subdivide the current row into smaller colinear row segments (avoiding the no-go zones). Boreholes are distributed along each row segment based on the minimum intra-row spacing, adjusted upwards to make full use of each row segment. If the row segment is smaller than the minimum intra-row spacing, a single borehole is placed in the middle of the row segment. An exception would be the case where the distance across a no-go zone or irregular property boundary is less than the minimum intra-row spacing. In that case, the row segment on which boreholes can be placed is shortened to maintain the minimum intra-row spacing.

An option is to separately treat the perimeter, in which case the interior boreholes are distributed as described above; boreholes are then placed uniformly along each perimeter segment at or above the specified perimeter spacing.

The borehole distribution across a property boundary varies unpredictably with the row rotation. Therefore, boreholes are placed for each row rotation step, and the rotation that gives the maximum number of boreholes is selected⁴. This is significant because the possible number of boreholes varies widely with rotation, and, in turn, the total drilling⁵ required varies widely with rotation, as shown in Figure 2 for cases with and without separate treatment of the perimeter. For both cases, minimum inter-row and intra-row spacings of 5m were used. For the case with separate treatment of the perimeter, a perimeter spacing of 4m was used.

⁴ We note that choosing the rotation with the maximum number of boreholes reflects an unproven assumption – that maximizing the number of boreholes for a given minimum spacing is desirable. It should, at the least, give the maximum capacity.

⁵ Total drilling is the number of boreholes multiplied by the final design depth.

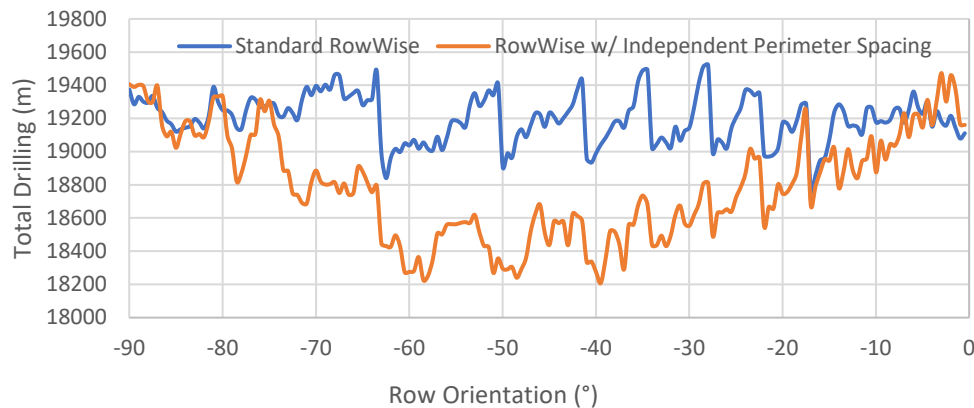


Figure 2 Sensitivity of total drilling to row orientation

RowWise Search Algorithm

In order to automatically select and size RowWise configurations, a search algorithm that finds a minimal cost design that will meet the design temperature constraints is needed. This section presents the current search algorithm, which is organized as a one-dimensional search by keeping the minimum inter-row and intra-row spacings to be the same and keeping the minimum perimeter spacing at a fixed ratio to the other spacing. In addition to the inputs for the RowWise placement algorithm described above, the search algorithm requires several additional user inputs: maximum target spacing, maximum borehole depth, and parameters related to the optional use of an exhaustive search at the end: the number of fields evaluated and a spacing increment for exhaustive searches. As described below, the search algorithm makes an initial determination of the domain, then follows one of two search procedures, optionally followed by an exhaustive search near the solution given by the first search procedure.

Initial Domain Determination

The solution may lie in one of three domains, which might be described as follows: (1) no feasible solution – load is larger than can be supported by available property using the maximum number of boreholes corresponding to the minimum target spacing; (2) the available property is adequate and will be fully utilized using spacing somewhere between the minimum and maximum target spacing; (3) the available property is more than adequate and using the maximum target spacing would still result in more boreholes than needed. The domain is determined by generating a RowWise configuration for both the minimum and maximum target spacings. If the excess temperature is positive for both cases, there is no feasible solution – domain (1) - and an error message is returned. If the excess temperature is positive for the maximum target spacing and negative for the minimum target spacing, the solution lies in domain (2) and the spacing search with optional exhaustive search will be performed. If the excess temperature is negative for the maximum target spacing and negative for the minimum target spacing, the solution lies in domain (3) and the borehole removal search will be initiated. These searches are described in the following two sections.

Spacing search with optional exhaustive search

If this search is used, the design solution will fall somewhere between the minimum spacing field and the maximum spacing field. So, a bisection search is performed on the target spacing domain. During each iteration of the search, excess temperature is evaluated based on maximum borehole height and a target spacing halfway between the current maximum and minimum spacing. Based on this outcome, half the domain will be eliminated at each step. If the maximum number of iterations is reached (10 by default) or the maximum and minimum fields produce the same

excess temperature (within a tolerance), the field corresponding to the minimum target spacing is returned since it is guaranteed to have a negative excess temperature.

Because the domain is not perfectly unimodal, e.g., a slight increase in target spacing can sometimes return a field with more boreholes and more or less total drilling required, it may be worthwhile to search for a better solution near the design solution. This is done with a one-dimensional exhaustive search in the target spacing. (At the time of this writing, we have not yet found a better solution using the exhaustive search, but it seems likely that there will be cases where a better solution might be found.) The search procedure is illustrated in Figure 3, where the number of boreholes and excess temperature are plotted versus the search step. The first two search points correspond to the minimum and maximum target spacings. The blue circles represent the bisection search, with the solution represented by step 11, which has a target spacing of 8.57 m, an excess temperature of -0.15°C , and 139 boreholes. The orange triangles represent the exhaustive search, which evaluates target spacings between 8.07 m and 9.07 m, at intervals of 0.1 m. The final result corresponds to step 11; that is, the exhaustive search didn't provide a better solution. After the configuration is selected, a final sizing step would adjust the borehole depth downwards to give an excess temperature of 0°C .

Borehole removal search

For situations where the available land area exceeds what is needed, it is desirable to give a working design with fewer boreholes and less trenching than would be achieved with the maximum target spacing, using all the land area. The search algorithm we have developed starts with the maximum target spacing configuration determined in the domain search, then has two steps: (1) sorting the boreholes in some order of desirability, e.g. distance from a point on the building where the piping will enter the mechanical room, and (2) using a bisection search to systematically reduce the number of boreholes in such a way that the least desirable locations are preferentially removed. An alternative is to leave the boreholes sorted in rows, such that the boreholes will be removed row-by-row. This search proceeds in a similar way to the target spacing search and continues until the maximum number of iterations has been reached or when the maximum and minimum fields are within 1 borehole of being the same size. This search is not followed by an exhaustive search, but the final depth is again calculated to give 0°C excess temperature.

EXAMPLES

The BUPCRS (Cook 2021) has a similar goal to the RowWise search – it distributes the boreholes around the available land area and therefore we use it to verify that the RowWise algorithm is working and giving reasonable results. For this example, the hourly loads were scaled by 5X to test the sizing for domain (2). For both algorithms, minimum and maximum spacing were set to 5m and 12m respectively. The RowWise algorithm investigated row orientations between -90° and 0° at increments of 0.5° . Figure 4 illustrates the RowWise search algorithm iterations. Figure 3 shows the resulting borefields from the two methods. In addition, a case where the RowWise algorithm was tested with perimeter minimum spacing was scaled to be 70% of the minimum interior spacing. Figure 5 compares the results for final borehole depth, number of boreholes, total drilling length, and calculation time. For this case, the standard RowWise search takes about 3 times as long as the BUPCRS but gives a 12% savings in total drilling. With scaled perimeter spacing, the RowWise method gives an 18% savings in total drilling. The RowWise placement algorithm needs further refinement to improve its computational speed.

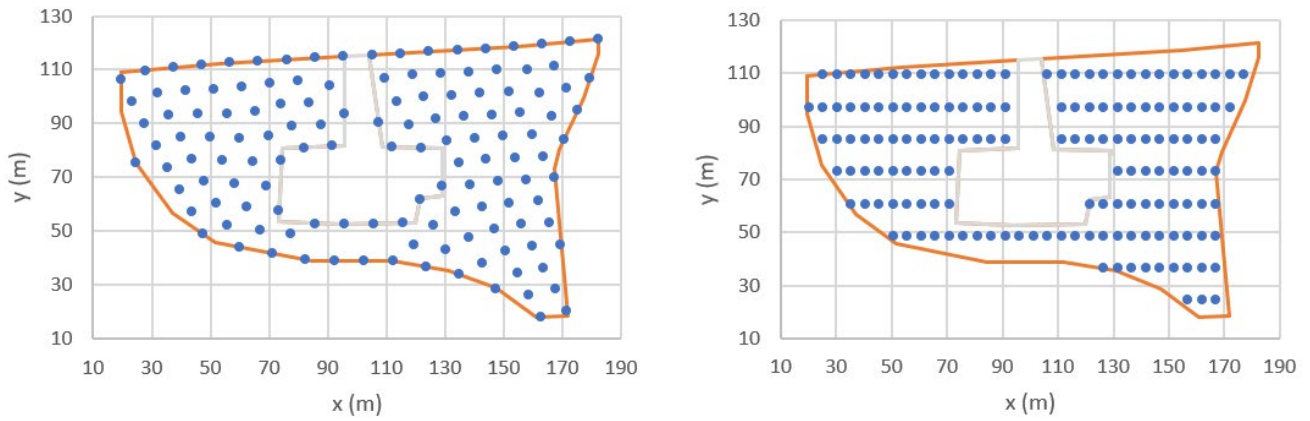


Figure 3 Design solutions for the RowWise without independent perimeter spacing (left) and BUPCRS (right) algorithms

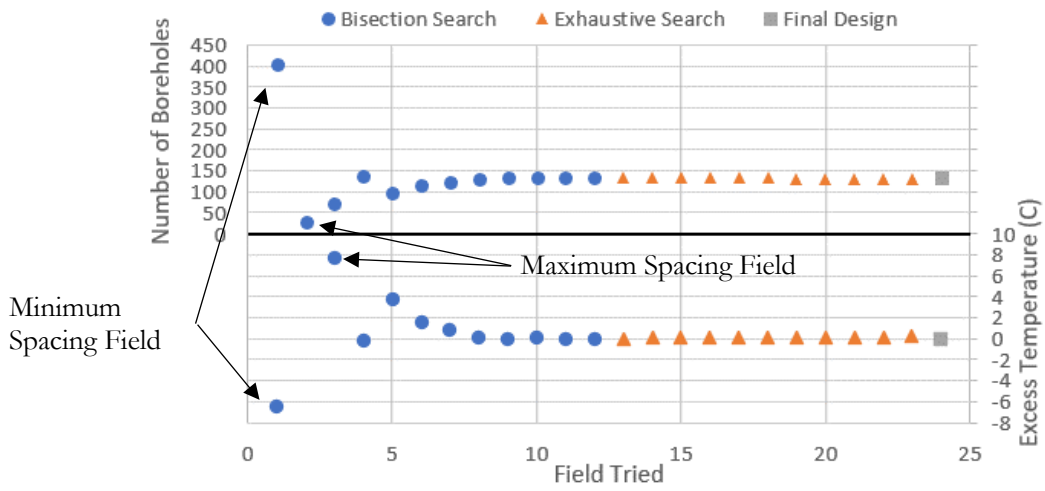


Figure 4 Search points used to find best design

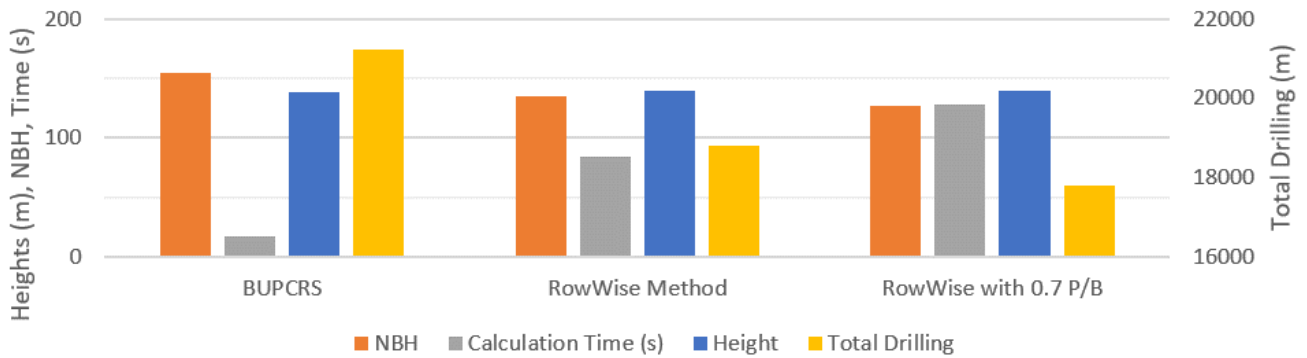


Figure 5 Comparison of BUPCRS and RowWise search algorithms

CONCLUSIONS AND RECOMMENDATIONS

This paper describes a borehole placement and configuration search algorithm that we refer to as RowWise. It can take advantage of irregularly shaped properties and allows automated designs that were not previously possible. Compared to another newly developed algorithm that uses a rectangular grid and removes boreholes in no-go zones, the RowWise algorithm shows considerable progress with one example giving an 18% decrease in total drilling required.

Space precluded presentation of more examples, and a more comprehensive investigation of different geometries is needed. Furthermore, the optimization used for the design has been organized as a one-dimensional search with the minimum intra-row and inter-row spacing set equal, and the perimeter spacing, where “independent” was actually set to be a fixed ratio to the interior spacings. Further development of multi-dimensional optimization is needed. At present, this optimization will still have to be parameterized. Finally, the design does not currently consider the cost of drilling and trenching, but rather uses total drilling length as the metric to minimize, while making use of a user-specified maximum spacing to limit excessive spacing between the boreholes. Development of a cost model and additional research into drilling and trenching costs are needed to support minimizing first costs or life cycle costs rather than drilling lengths.

ACKNOWLEDGMENTS

Development of the GHE design tool was funded through Department of Energy contract DE-AC05-00OR22725 via a subcontract from Oak Ridge National Laboratory. Most of the original development was done by OSU research assistant, Mr. Jack Cook and is reported in his MS thesis. The RowWise algorithm was developed by Timothy West, who was supported by the Center for Integrated Building Systems under project 21-19.

REFERENCES

- Bayer, P., M. de Paly, M. Beck. 2014. *Strategic optimization of borehole heat exchanger field for seasonal geothermal heating and cooling*. Applied Energy. 136:445-453.
- BLOCON. 2015. “Earth Energy Designer (EED) Version 3.2 Manual.” <https://buildingphysics.com/eed-2/>
- Cimmino, M. 2018. *pygfunction: an open-source toolbox for the evaluation of thermal response factors for geothermal borehole fields*. eSim 2018 – the 10th conference of IBPSA-Canada, Montréal, Canada: 492-501.
- Claesson, J. and P. Eskilson. 1985. *Thermal analysis of heat extraction boreholes*. Proceedings of 3rd International Conference on Energy Storage for Building Heating and Cooling ENERSTOCK 85, Toronto (Canada), 222–227. September 22-26.
- Claesson, J., and Eskilson P. 1988. *Conductive Heat Extraction to a Deep Borehole: Thermal Analyses and Dimensioning Rules*. Energy 13(6): 509-527.
- Cook, J. C. 2021. *Development of Computer Programs for Fast Computation of G-functions and Automated Ground Heat Exchanger Design*. M.S. Thesis, Oklahoma State University.
- Prieto, C. and M. Cimmino. 2021. *Thermal interactions in large irregular fields of geothermal boreholes: the method of equivalent boreholes*. Journal of Building Performance Simulation 14(4): 446-460.
- Robert, F. and L. Gosselin. 2014. *New methodology to design ground coupled heat pump systems based on total cost minimization*. Applied Thermal Engineering. 62:481-491
- Spitler, J.D. 2000. *GLHEPRO -- A Design Tool For Commercial Building Ground Loop Heat Exchangers*. Proceedings of the Fourth International Heat Pumps in Cold Climates Conference, Aylmer, Québec. August 17-18, 2000.
- Spitler, J. D., J. C. Cook and X. Liu 2020. *A Preliminary Investigation on the Cost Reduction Potential of Optimizing Bore Fields for Commercial Ground Source Heat Pump Systems*. Proceedings, 45th Workshop on Geothermal Reservoir Engineering, Stanford, California, Stanford University.

Development of a Topology Optimization Method for the Design of Ground Heat Exchangers

Alexandre Noël

Massimo Cimmino

ABSTRACT

A new method for sizing vertical ground heat exchangers is proposed using topology optimization to reduce the number of boreholes required to fulfill the cooling and heating demand. The ASHRAE sizing equation is adapted to formulate a topology optimization problem to minimize the number of boreholes required in a bore field. The results show that topology optimization can help reduce the number of boreholes required when compared to a sizing performed on a regular grid using conventional sizing methods. These optimized configurations show smaller spacings between the boreholes located on the perimeter and larger spacings between the boreholes located in the center of the bore field.

INTRODUCTION

The design phase is a crucial part of the installation of a ground heat exchanger (GHE). Many aspects must be considered such as the heating and cooling loads of the building, the properties of the ground and the operating conditions. The operating conditions are usually a constraint that is imposed on the temperature of the fluid when entering or leaving the borehole. Multiple boreholes are often required to satisfy all the design parameters. However, boreholes interfere with each other, which may lead to a decrease in the performance of the GHE and an increase in the required borehole length. A higher drilling length in the GHE tends to increase the initial investment cost, which is one of the biggest obstacles for a wider use of GHEs. Working on ways to reduce these expenses by minimizing the total drilling length is a task that could be beneficial for the adoption of the technology on a larger scale.

Existing design methods usually evaluate the minimal required total drilling length given a regular and already planned GHE configuration. An example is ASHRAE's sizing method, as modified by Ahmadfard & Bernier (2018):

$$L_{tot} = \frac{q_a R_{ga,g} + q_m R_{gm,g} + q_h R_{gh,g} + q_h R_{gh,g}}{(T_m - T_g)_{ref}} \quad (1)$$

where L_{tot} is the total drilling length, q_a , q_m and q_h are respectively the mean annual ground load, the mean monthly ground load for the design month, and the hourly peak ground load for the design month, $R_{ga,g}$, $R_{gm,g}$, and $R_{gh,g}$ are the respective thermal resistances for each load which are evaluated using g -functions, T_m is the mean fluid temperature inside the borehole, and T_g is the undisturbed ground temperature. Both T_m and T_g are imposed in that method, thus the notation “ $()_{ref}$ ” in equation 1.

Alexandre Noël (alexandre.noel@polymtl.ca) is a master's student and Massimo Cimmino (massimo.cimmino@polymtl.ca) is a professor of mechanical engineering at Polytechnique Montréal

Previous research has identified different design strategies to optimize bore field configurations. Cimmino & Bernier (2014) studied the effect of adding or removing boreholes by modifying the spacing between the boreholes in a regular configuration. Guo et al. (2017) studied the impact of the ground temperature variation when displacing boreholes from the center of the bore field to its perimeter. Spitler et al. (2020) analyzed strategies such as irregular spacings and configurations that wrap around the buildings. These previous investigations on the optimization of GHE configurations result in similar conclusions: increasing the spacing with longer boreholes and a density of boreholes that is higher on the perimeter and lower in the center leads to savings in total drilling length and to more effective bore fields. Most of the research made on the subject proposed design strategies that compare advantageously with a base case, usually a regular configuration. The question remains as to how close these strategies are to the optimal layout.

Automated methods to optimize GHEs have been developed over the years. Beck et al. (2013) proposed to optimize both the positioning of the boreholes and their heat extraction rates using linear programming and evolutionary computation. They found that optimizing a combination of both parameters produced minimal differences in the results. Bayer et al. (2014) developed a method to balance the workloads of each borehole in a bore field by removing the least effective ones. More recently, Edigi et al. (2021) proposed a method for evaluating bore field configurations for a fixed number of boreholes that relied on minimizing the sum of squares of the temperature difference in the ground due to the long-term operation of the bore field using the steepest descent method. Even though the objective function of that problem is not a condition that is usually used when designing GHEs, it led to results similar to previous studies. Cook (2021) developed the GHEDT program. The tool searches through pre-defined configurations via various design routines to find a combination of configurations that will optimize the bore field. These methods all converged to configurations where the perimeter is denser in boreholes than the center.

As mentioned by Sigmund & Maute (2013), topology optimization originated for mechanical design applications but has since been used in many other fields of study. The idea behind topology optimization is to find the placement of material that will give the best structural performance. Most topology optimization approaches are density based and are performed on a prescribed domain. This domain is usually divided in elements and a design variable (ρ) that can take either the value of 0 (void) or 1 (solid) is introduced. The optimization process evaluates which elements will contain material to meet the constraints. However, this is a discrete problem, and it is difficult to solve it directly (Sigmund & Maute, 2013). The problem is usually reformulated into a continuous one which allows to use more efficient gradient-based methods. The continuous problem takes the following form:

$$\begin{cases} \text{Minimize: } f_0(\boldsymbol{\rho}) \\ \text{Subject to: } f_i(\boldsymbol{\rho}) \leq 0 \text{ for } i = 1, \dots, m \\ 0 \leq \rho_j \leq 1 \text{ for } j = 1, \dots, n \end{cases} \quad (2)$$

where f_0 is the cost-function (i.e. the function to minimize), f_i are the constraints, m is the number of constraints, n is the number of elements in the domain, and $\boldsymbol{\rho}$ is the vector of design variable.

Even though the solving process is more efficient with the continuous formulation, the problem does not always converge to values of 0 or 1, which may create non-feasible solutions. A method to facilitate the convergence to values of 0 or 1 is the Simplified Isotropic Material with Penalization (SIMP) (Bendsoe, 1989), where a penalization term (p) is introduced in the problem formulation. For $p = 1$, the solution is the same as if no penalization was introduced. For $p > 1$, intermediate values of ρ are penalized. As pointed out by Rozvany (2001) and Sigmund & Maute (2013), the optimization problem is solved repeatedly by slowly increasing the values of p which leads to better results.

The placement of the boreholes that compose a GHE has proven to be a parameter that influences the design process because of the thermal interactions between the boreholes. Strategically placing them can lead to significant savings in drilling length, which should usually help reduce the cost of investment of GHEs. This paper proposes a topology optimization method for the design of ground heat exchangers to minimize the number of boreholes in a GHE by strategically placing them inside the available area, adapting the modified ASHRAE sizing method.

METHODOLOGY

Problem Formulation

A problem of the form of equation 2 must be formulated to apply topology optimization for the design of GHEs. The objective of the proposed method is to minimize the number of boreholes of a given length inside a prescribed domain. The problem is constrained by the maximum temperature difference between the undisturbed ground and the fluid circulating in the boreholes, as in the modified ASHRAE sizing equation (equation 1). Contrary to many topology optimization problems, the domain is discretized in points instead of elements as only the coordinates of the boreholes are needed. The optimization determines which combination of boreholes of length L minimizes its number, where L is a fixed parameter. This procedure is explained in details in the next section. With respect to equation 2, the proposed optimization problem can be written as follows:

$$\begin{cases} \text{Minimize: } f_0(\boldsymbol{\rho}) = \sum_{i=1}^n \rho_i \\ \text{Subject to: } f_1(\boldsymbol{\rho}) = (T_m - T_g) - (T_m - T_g)_{ref} \leq 0 \\ 0 \leq \rho_i \leq 1 \text{ for } i = 1, \dots, n \end{cases} \quad (3)$$

where ρ_i represents the fraction of a borehole of length L on every point inside the domain (which would ideally only take the value of 0 or 1), and $(T_m - T_g)_{ref}$ the imposed temperature constraint. As previously mentioned, gradient-based optimization methods are efficient, but require a continuous problem formulation, which is why ρ_i is continuous in equation 3.

The modified ASHRAE sizing equation has to be modified to evaluate $(T_m - T_g)$ while taking into account the design variable. The temperature is evaluated as follows:

$$T_m - T_g = \frac{q_a R_{ga,g} + q_m R_{gm,g} + q_h R_{gh,g} + q_b R_b}{\sum_{i=1}^n \rho_i \cdot L} \quad (4)$$

with:

$$R_{ga,g} = \frac{g(t_f) - g(t_f - t_1)}{2\pi k_s} \quad (5)$$

$$R_{gm,g} = \frac{g(t_f - t_1) - g(t_f - t_2)}{2\pi k_s} \quad (6)$$

$$R_{gh,g} = \frac{g(t_f - t_2)}{2\pi k_s} \quad (7)$$

where k_s is the ground thermal conductivity, L the individual length for a borehole, and g the g -functions evaluated at timesteps t_f , $t_f - t_1$ and $t_f - t_2$, with $t_1 = 10$ years, $t_2 = t_1 + 1$ month and $t_f = t_2 + 6$ hours. The g -functions are evaluated by superposition of the finite line source (FLS) solution:

$$g(t) = \frac{\boldsymbol{\rho}^T [b_{ij} \cdot h_{ij}] \boldsymbol{\rho}}{\sum_{i=1}^n \rho_i^p} \quad (8)$$

with:

$$h_{ij} = \frac{1}{2L} \int_{1/\sqrt{4\alpha t}}^{\infty} \frac{1}{s^2} \exp(-d_{ij}^2 s^2) I_{ls}(Ls, Ds) ds \quad (9)$$

$$I_{ls}(Ls, Ds) = 2 \cdot \text{ierf}(Ls) + 2 \cdot \text{ierf}(Ls + 2Ds) - \text{ierf}(2Ls + 2Ds) - \text{ierf}(2Ds) \quad (10)$$

where $[b_{ij} \cdot h_{ij}]$ is the array of thermal response factors for a borehole positioned on the j -th node on a borehole positioned on the i -th node, multiplied by a constant. The h_{ij} factors are evaluated using the FLS model as proposed by Claesson & Javed (2011), with d_{ij} representing the radial distance between the i -th and the j -th borehole (with $d_{ii} =$

r_b), D the buried depth of the boreholes, and α the ground thermal diffusivity. The b_{ij} factor is added to ensure a minimal spacing between the boreholes in the solution. It acts as a soft constraint that takes either the value of 5 if $d_{ij} < B_{min}$ or 1 if $d_{ij} \geq B_{min}$, where B_{min} is the imposed minimal spacing. The value of 5 has shown sufficient to fulfill the imposed minimal spacing constraint for the different cases tested. It has however been chosen arbitrarily and is subject to further research. The penalization is added in equation 8. Having the penalization at this specific position was found to be the most efficient way of obtaining discrete values of the design variable.

Optimization Procedure

The available domain is first discretized using the pygmsh 7.1.17 Python module (Schlömer, 2022) with the default Frontal-Delaunay algorithm and is then reloaded with the trimesh 3.11.2 Python module (Dawson-Haggerty et al., 2022) with processing for future manipulations of the grid. The positions are determined with more precision with a finer discretization, at the cost of increasing calculation time. The array of thermal response factors is evaluated for every point in the domain using pygfunction 2.1.0 and the method of similarities (Cimmino, 2018a, 2018b). At this point, it is assumed that there is a borehole on every point of the discretization. The initial value of ρ is generated randomly to avoid the convergence of the solution to a local minimum.

The method of moving asymptotes (MMA) (Svanberg, 1987, 2002) as implemented in the NLOpt 2.7.0 Python module (Johnson, 2020) is used to perform the optimization. The MMA requires the evaluation of the derivatives of the cost-function and the constraints functions with respect to the design variable on every point in the domain. The derivatives of the cost function in equation 3 are given by:

$$\frac{\partial(f_0)}{\partial\rho} = [1, \dots, 1]^T \quad (11)$$

and the derivatives of the constraint function in equation 4 are given by:

$$\frac{\partial(f_1)}{\partial\rho} = \frac{\partial(T_m - T_g)}{\partial\rho} = \frac{q_a \frac{\partial R_{ga,g}}{\partial\rho} + q_m \frac{\partial R_{gm,g}}{\partial\rho} + q_h \frac{\partial R_{gh,g}}{\partial\rho}}{L \sum_{i=1}^n \rho_i} - \frac{q_a R_{ga,g} + q_m R_{gm,g} + q_h R_{gh,g} + q_h R_b}{L (\sum_{i=1}^n \rho_i)^2} \quad (12)$$

The ground thermal resistance requires the evaluation of the derivatives of the g -function, given by:

$$\frac{\partial g}{\partial\rho} = \frac{1}{\sum_{i=1}^n \rho_i^p} (-p\rho^{p-1}g + (\mathbf{b} \circ \mathbf{h})\rho + \rho^T(\mathbf{b} \circ \mathbf{h})) \quad (13)$$

The process is repeated for values of p ranging from 1 to 3 by increments of 0.05. The limit of 3 was found to provide configurations that contain almost exclusively values of 0 or 1 for the design variable. Gradual refinement of the grid is also proposed to reduce the calculation time. The grid is refined using trimesh around the points where $\rho \geq 0.001$ in the previous solution. The penalization process is repeated starting from $p = 1$ to $p = 3$ using the new refined grid.

CASE STUDY

The medium office from the commercial building library of the U.S. Department of Energy located in the city of International Falls, MN, is chosen for the case study (DOE & PNNL, 2020). The heating and cooling loads are evaluated, and it is assumed that this demand is met by a ground source heat pump system with a COP of 3 in both modes. The three ground loads are then evaluated and multiplied by a factor of 4, requiring a larger bore field. A large imbalance in cooling was found for the ground loads, therefore the sizing is only performed in cooling mode. An additional constraint could be added to equation 3 to also cover the heating mode.

The study is performed on an L-shaped area of 6800 m². A first sizing is done with the modified ASHRAE sizing method using a regular configuration and serves as the base case (case 1). A target length of around 125 m was aimed and multiple combinations of spacings were tested to find the minimum total drilling length. These combinations were

tested manually, which means that it is possible that a better configuration could have been achieved. A spacing of 10 m in the x direction and 5 m in the y direction was finally chosen. Another sizing is performed using the topology optimization method, with boreholes of the same length as the ones evaluated with the first method (case 2). It is then proposed to size the bore field using topology optimization by increasing the individual length of the boreholes (cases 3 and 4). The purpose of these last two cases is to analyze the behavior of the topology optimization method when increasing the individual length, and how it compares to previous studies that analyzed this parameter. A minimal spacing of 2.5 m is imposed for all three sizings done using topology optimization, and the initial grid is refined two times starting from a grid where the longest distance between two consecutive points is 5 m. The parameters used for the sizing are presented in Table 1. The value of $T_{m,ref}$ used in constraint f_1 from equation 3 is evaluated at 37.5°C. This results in a value of 23.5°C for the $(T_m - T_g)_{ref}$ constraint.

Table 1. Parameters Used in the Simulation

Bore field parameters		
Borehole buried depth (D)	4	m
Borehole radius (r_b)	0.075	m
Borehole thermal resistance (R_b)	0.2	m-K/W
Ground properties		
Thermal diffusivity (α)	1.0×10^{-6}	m ² /s
Thermal conductivity (k_s)	2.0	W/m-K
Undisturbed ground temperature (T_g)	14	°C
Annual ground load (q_a)	108.60	kW
Monthly ground load (q_m)	255.72	kW
Hourly ground load (q_h)	773.36	kW
Fluid properties (propylene-glycol 20% concentration)		
Flow rate (\dot{V}_f)	0.05	L/s per kW of peak load
Density (ρ_f)	1008	kg/m ³
Specific heat capacity ($c_{p,f}$)	4014	J/kg-K
Entering fluid temperature ($T_{o,f}$)	40	°C

RESULTS AND DISCUSSION

Figure 1 presents the comparison for sizings done using the methods described in the previous section. These are filtered results, meaning that only the locations where $\rho_i \geq 0.01$ are shown. Figure 2 presents the results for the sizing of case 1. The complete grid after refinement is shown, and the shaded points represent locations where the value of ρ_i is approximately 0. A summary of the four cases is presented in Table 2.

The optimized configurations using topology optimization are in accordance with previous studies and present a combination of the design strategies identified in the literature. The configurations are usually denser on the perimeter and have spacings that increase in the middle of the bore field. The method can achieve significant savings as case 2 presents savings of 9.8% compared to case 1. As previous studies showed, increasing the maximum length of the individual boreholes (cases 3 and 4) usually tends to higher savings in the total drilling length. The perimeter is still filled with boreholes, and the density of boreholes at the center is reduced. The spacing between boreholes is also increased, both on the perimeter and in the center.

The penalization introduced in equation 8 is not sufficient to ensure that ρ converges to values of 0 and 1. The total drilling length in Table 2 for cases 2, 3 and 4 is not equal to the product of the number of boreholes and the individual borehole length. This causes errors in the calculation of the total drilling length since boreholes that are only partially present are accounted for in the cost function which can lead to two phenomena. The first one is when the value of ρ on a given point is significant depending on the case but not equal to 1. For example, case 2 has a point with a value of

$\rho \approx 0.76$. The other case is when multiple values of ρ are small but not equal to 0. These additional lengths are small for a single point in the domain but become significant when summed for the entire domain.

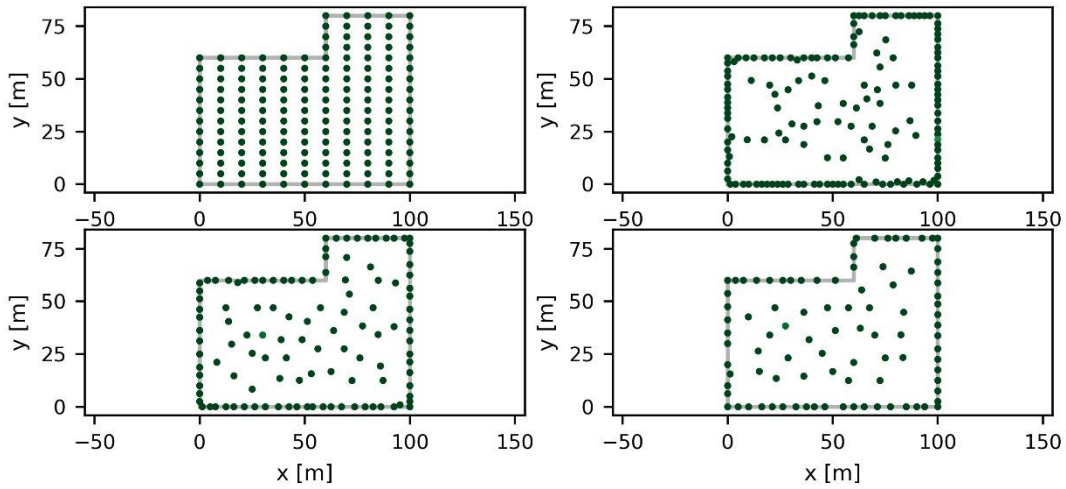


Figure 1 Bore field sizing filtered results case 1 (top left), case 2 (top right), case 3 (bottom left), case 4 (bottom right)

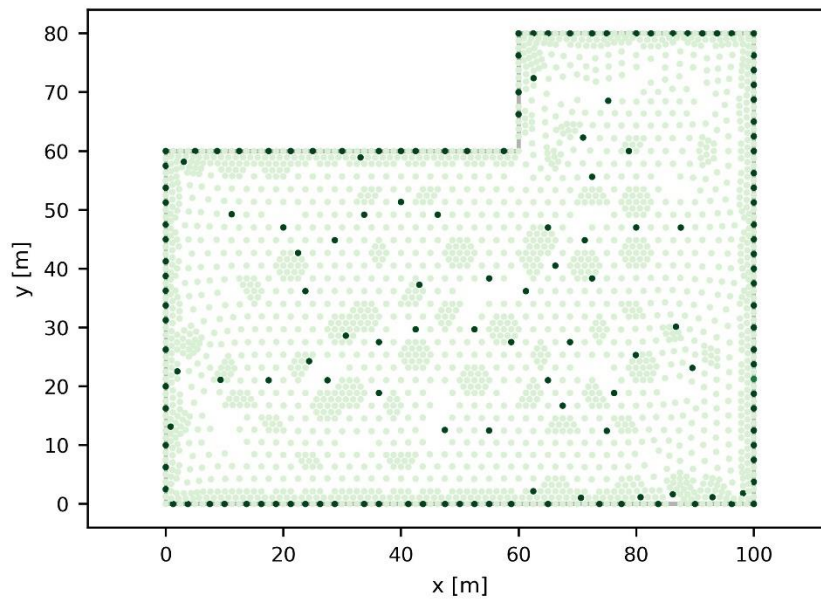


Figure 2 Detailed sizing results with topology optimization for case 2

The optimized configurations are complex and impractical for real applications. The boreholes in the middle are scattered in what seems a random configuration. Since the optimization procedure relies on g -functions, it is the borehole density (e.g. in boreholes per square meter) across the domain that affects the temperature difference and thus

affects the presence or absence of boreholes in a given region of the domain. There might be multiple configurations that will satisfy the design criteria with similar total drilling lengths. A “feasibility” constraint could be considered in future work, but this necessitates a quantitative criterion compatible with the problem formulation of equation 2.

Table 2. Sizing Results

Case	Method	Number of boreholes	Individual borehole length (m)	Total drilling length (m)	Savings (%)
1	Modified ASHRAE sizing method	163	127.3	20 750	0.0
2	Topology optimization	150	127.3	18 714	9.8
3	Topology optimization	117	150.0	17 528	15.5
4	Topology optimization	94	175.0	16 426	20.8

The time consumption of the method also represents one of its limits. The method may take a couple of hours for large bore fields that are finely discretized. The optimization method however does not require supervision. Once all the design parameters are entered, the method produces the result automatically. On the other hand, ASHRAE’s sizing method takes a couple of seconds, and the same can be said for some of the more recent sizing tools, such as GHEDT.

CONCLUSION

Borehole placement is an important aspect to consider when designing a GHE. Previous research has shown the effect of placement on the total drilling length, and many strategies have been explored to optimize bore field configurations. This paper has proposed a new method to optimize GHEs based on topology optimization.

A case study has been presented, which compared this new optimization method with one that is used frequently when designing bore fields. It has been shown that this method can reduce the total drilling length using efficient and robust optimization algorithms. The configurations obtained are in accordance with the more recent research made on the optimization of bore fields: boreholes should be more densely placed on the perimeter and more coarsely in the center. The current state of the method shows that directly applying topology optimization can lead to savings in total drilling length, but that the resulting configurations are complex. It should however help uncover new design strategies that have not been explored yet. The results can also serve to produce reference lower bounds on the total drilling length to compare other design methods. It is finally worth noting that this paper proposes only one formulation for the design problem. As long as the objective function and the constraints are in respect with the problem formulation in equation 2, different types of optimizations, e.g. techno-economic optimization, could be performed.

ACKNOWLEDGMENTS

This work was supported by the Natural Sciences and Engineering Research Council of Canada [grant number RGPIN-2018-04471].

NOMENCLATURE

α	=	Ground thermal diffusivity (m ² /s)	$c_{p,f}$	=	Fluid specific heat capacity (J/kg-K)
ρ	=	Design variable (-)	d_{ij}	=	Radial distance between the i -th and the j -th borehole (m)
ρ_f	=	Fluid density (kg/m ³)	D	=	Borehole buried depth (m)
b_{ij}	=	Distance multiplying factor	f_0	=	Cost-function
B_{min}	=	Imposed minimal spacing (m)	f_1	=	Constraint function

$g(t)$	= g -function evaluated at time t (-)	r_b	= Borehole radius (m)
\mathbf{h}	= Array of ground thermal response factors (-)	$R_{g_i,g}$	= Ground thermal resistance evaluated using g -functions (m-K/W)
$ierf$	= Error function integral (-)	T_m	= Mean fluid temperature ($^{\circ}$ C)
k_s	= Ground thermal conductivity (W/m-K)	T_g	= Undisturbed ground temperature ($^{\circ}$ C)
L_{tot}	= Total bore field drilling length (m)	ΔT	= Temperature variation constraint ($^{\circ}$ C)
L	= Individual borehole length (m)	$T_{o,f}$	= Entering fluid temperature ($^{\circ}$ C)
p	= Penalization value (-)	\dot{V}_f	= Fluid flow rate (L/s per kW of peak load)
q_i	= Ground loads (W)		
R_b	= Borehole thermal resistance (m-K/W)		

REFERENCES

- Ahmadfard, M. and M. Bernier. 2018. *Modifications to ASHRAE's sizing method for vertical ground heat exchangers*. Science and Technology for the Built Environment 24(7): 803-817.
- Bayer, P., M. de Paly and M. Beck. 2014. *Strategic optimization of borehole heat exchanger field for seasonal geothermal heating and cooling*. Applied Energy 136: 445-453.
- Beck, M., P. Bayer, M. de Paly, J. Hecht-Mendez and A. Zell. 2013. *Geometric arrangement and operation mode adjustment in low-enthalpy geothermal borehole fields for heating*. Energy 49: 434-443.
- Bendsoe, M.P. 1989. *Optimal shape design as a material distribution problem*. Structural Optimization 1: 193-202.
- Cimmino, M. and M. Bernier. 2014. *Effects of unequal borehole spacing on the required borehole length*. ASHRAE Transactions 120(2): 158-173.
- Cimmino, M. 2018a. *Fast calculation of the g-functions of geothermal borehole fields using similarities in the evaluation of the finite line source solution*. Journal of Building Performance Simulation 11(6): 655-668.
- Cimmino, M. 2018b. *pygfunction: an opensource toolbox for the evaluation of thermal response factors for geothermal borehole fields*. Proceedings of eSim 2018, the 10th conference of IBPSA-Canada. IBPSA Canada. 492-501.
- Claesson, J. and S. Javed. 2011. *An analytical method to calculate borehole fluid temperatures for time-scales from minutes to decades*. ASHRAE Transactions. 117(2). 279-288.
- Cook, J.C. 2021. *Development of Computer Programs for Fast Computation of g-functions and Automated Ground Heat Exchanger Design*. Master's thesis. Oklahoma State University, Stillwater, Oklahoma, United States.
- DOE and PNNL. 2020. *Commercial Prototype Building Models*, Richland, WA, Pacific Northwest National Laboratory. Available at https://www.energycodes.gov/development/commercial/prototype_models
- Dawson-Haggerty, M. et al. 2022. *trimsh*. Version 3.11.2. <https://trimsh.org/>.
- Egidi, N., G. Josephin and P. Maponi. 2021. *Inverse heat conduction to model and optimise a geothermal field*. arXiv preprint. arXiv:2111.08618.
- Guo, M., N. Diao, K. Zhu, Z. Fang. 2017. *Optimization of Ground Heat Exchangers in Area with Imbalanced Heating and Cooling Load*. Procedia Engineering. 205: 3727-3734.
- Johnson, S.G. 2020. *The NLOpt nonlinear-optimization package*. Version 2.7.0. <http://github.com/stevengi/nlopt>
- Rozvany, G.I.N. 2001. *Aims, scope, methods, history and unified terminology of computer-aided topology optimization in structural mechanics*. Struct Multidisc Optim 21: 90-108.
- Schlömer, N. 2022. *pygmsb: A Python frontend for Gmsb*. Version 7.1.17. <https://doi.org/10.5281/zenodo.1173105>
- Sigmund, O. and K. Maute. 2013. *Topology optimization approaches*. Structural and Multidisciplinary Optimization 48(6): 1031-1055.
- Spitler, J. D., J.C. Cook and X. Liu. 2020. *A Preliminary Investigation on the Cost Reduction Potential of Optimizing Bore Fields for Commercial Ground Source Heat Pump Systems*. 45th Workshop on Geothermal Reservoir Engineering Stanford University, Stanford, California: 1-12.
- Svanberg, K. 1987. *The method of moving asymptotes-a new method for structural optimization*. International Journal for Numerical Methods in Engineering. 24(2). 359-373.
- Svanberg, K. 2002. *A class of globally convergent optimization methods based on conservative convex separable approximations*. SIAM journal on optimization 12(2): 555-573.

Influence of buildings on geothermal boreholes – a comparison between two models.

Maria Letizia Fasci

ABSTRACT

The spread of ground source heat pumps has led to the development of several models to estimate the thermal interference between independent geothermal boreholes in densely populated areas. Some of these models take into account the changes in the ground surface temperature, thus allowing to account for the heat flux from the buildings, potentially high in densely populated areas. In this study, we investigated two models accounting for the ground surface temperature change; both models are based on the Stacked Finite Line Source (SFLS) model. The first model treats the ground surface as a set of rectangles, each with its own temperature; the second model treats the ground as an infinite surface with imposed temperature. The first model is more accurate, as it allows to consider different temperatures for different surfaces. However, the second model requires less computational time and is easier to implement. Therefore, we investigated whether the latter model can provide a good approximation of the former. Our results suggest that the second model can often provide a good approximation with significantly less computational time, especially for larger built areas; however, it could be unacceptably inaccurate for smaller neighbourhoods. We also investigated a strategy to improve its accuracy without compromising its computational speed; the strategy seems promising but requires more investigation.

INTRODUCTION

The increasing spread of Ground Source Heat Pumps (GSHPs), and thus the increasing number of areas characterized by a high density of these systems, has led to the development of several models and tools to calculate the thermal interference between neighbouring independent energy boreholes (Rivera et al. 2015; Fasci et al. 2021; Stockholms stad 2022; Witte 2018). Areas characterized by a high density of GSHPs are typically also characterized by a high density of buildings, responsible for the underground heat island effect, i.e., increased temperatures in the underground (Gunawardhana et al. 2011). Therefore, taking into account the heat island effect is potentially paramount for the accurate estimation of the operation of GSHPs, as this can increase the geothermal potential of areas with dominating heating demand and decrease the geothermal potential of areas with dominating cooling demand (Rivera et al. 2017).

Models to simulate the operation of energy boreholes accounting for the underground heat island effect have been proposed. They model the effect that temperature changes in the ground surface have on the underground assuming either a homogenous or a spatially variable change of the ground surface temperature (Rivera et al. 2015, Rivera et al. 2016, Fasci et al. 2022).

Maria Letizia Fasci (mlfasci@kth.se) is a PhD student at KTH - Royal Institute of Technology, Department of Energy Technology, Stockholm (Sweden).

Since the ground surface is subject to different uses, e.g., buildings, asphalt, gardens, etc., and is thus characterized by local temperature changes, models that can account for a spatially variable ground surface temperature are more accurate. However, models that consider the ground surface as homogeneous, thus not considering the spatial variability of the ground usage, are easier to implement and computationally less demanding.

Therefore, in this paper, we investigate the accuracy of approximating the ground surface as a surface at uniform temperature rather than accounting for its spatial variability. We calculate the borehole wall temperatures in densely populated areas accounting for the effect of the boreholes operation and ground surface temperature. We compare the results obtained using two different models: a model that considers the spatial variability of the ground surface temperature and a model that considers the ground surface temperature as homogeneous. We evaluate the accuracy of the approximation for several synthetic scenarios and investigate a strategy to improve its accuracy.

METHODOLOGY

We have considered 18 scenarios (see section *Case studies*) and calculated the borehole wall temperature evolution during 50 years with the two models under research using a 1-year time resolution. We can use such a coarse time resolution compared to the 1-hour resolution often used for the study of GSHPs since we are comparing two models that differ in how they handle the effect of heat conduction from the ground surface to the borehole wall. This is a relatively slow phenomenon for which a 1-year resolution is sufficient, as shown for a comparable problem (Fasci et al, 2018). For all the scenarios, we have compared the two models by calculating the absolute and relative differences between the borehole wall temperature changes given by the models for each borehole and at each time step, i.e., the values:

$$\overline{\Delta T}_i^{\text{absolute}}(t) = |\overline{\Delta T}_i^{\text{FLS IV}_{\text{GST}}=} (t) - \overline{\Delta T}_i^{\text{FLS IV}_{\text{GST}}\sim} (t)| \quad (1)$$

and

$$\overline{\Delta T}_i^{\text{relative}}(t) = \frac{|\overline{\Delta T}_i^{\text{FLS IV}_{\text{GST}}=} (t) - \overline{\Delta T}_i^{\text{FLS IV}_{\text{GST}}\sim} (t)|}{\overline{\Delta T}_i^{\text{FLS IV}_{\text{GST}}=} (t)} \quad (2)$$

where $\overline{\Delta T}_i^{\text{FLS IV}_{\text{GST}}=} (t)$ and $\overline{\Delta T}_i^{\text{FLS IV}_{\text{GST}}\sim} (t)$ are the wall temperature change of the borehole i at time t calculated with the models $\text{FLS IV}_{\text{GST}}=$ and $\text{FLS IV}_{\text{GST}}\sim$ respectively (details about the models are given in the section *Models*).

Then, we have investigated a strategy to decrease the difference between the models. This strategy is described in the subsection $\text{FLS IV}_{\text{GST}}\sim$.

Models

The models we have compared are based on the strategy described by Fasci et al. (2022). Each borehole is modelled as a set of 12 stacked segments on top of each other, so that it is possible to impose a uniform borehole wall temperature along the boreholes (Cimmino, 2014). The depth-averaged temperature $\overline{T}_{i,j}(t)$ on each borehole segment i,j at time t is calculated as the sum of :

- the initial depth-averaged undisturbed ground temperature $\overline{T}_{i,j}^{\text{IC}}$;
- the depth-averaged ground temperature change induced on the borehole segment by the heat extraction/rejection of all the boreholes in the area $\overline{\Delta T}_{i,j}^{\text{BHES}}(t)$
- the depth-averaged temperature change induced on the borehole segment by changes in the ground surface temperature compared to the initial condition $\overline{\Delta T}_{i,j}^{\text{TBC}}(t)$:

$$\overline{T}_{i,j}(t) = \overline{T}_{i,j}^{\text{IC}} + \overline{\Delta T}_{i,j}^{\text{BHES}}(t) + \overline{\Delta T}_{i,j}^{\text{TBC}}(t) \quad (3)$$

In this study we have assumed the undisturbed temperature uniform throughout the ground, i.e.:

$$\bar{T}_{ij}^{IC} = \bar{T}^{IC} \quad \forall \text{ borehole segment } i, j \quad (4)$$

The term $\overline{\Delta T}_{ij}^{BHEs}(t)$ is calculated using the Finite Line Source (FLS) model (Spitler and Bernier, 2016). The term $\overline{\Delta T}_{ij}^{TBC}(t)$ is calculated in two different ways depending on the model adopted: whether the model accounts for the spatial variability of the ground surface temperature or not. We will refer to the two models as the “accurate model” and “approximated model” respectively. We will also refer to them with the acronyms FLS IV_{GST}⁼ and FLS IV_{GST}[~] respectively. Details on the calculation of $\overline{\Delta T}_{ij}^{TBC}(t)$ are given in the following subsections.

Writing equation 3 for each borehole segment we can calculate all the borehole wall temperatures in an area. For more details on the complete model we refer to Fasci et al. (2022).

FLS IV_{GST}⁼. Our formula to calculate $\overline{\Delta T}_{ij}^{TBC}$ with the accurate model is an extension of the formula given by Rivera et al. (2017). $\overline{\Delta T}_{ij}^{TBC}$ is calculated as:

$$\overline{\Delta T}_{ij}^{TBC}(t) = \frac{1}{8 H_{ij} \sqrt{\pi}} [(H_{ij} + D_{ij}) \cdot f(H_{ij} + D_{ij}, t) - D_{ij} \cdot f(D_{ij}, t)] \quad (5)$$

where H_{ij} and D_{ij} are respectively the length and buried depth of the borehole segment ij ; the function f is calculated as:

$$f(z, t) = \sum_{k=1}^{n_{\text{surf}}} \Delta T_{GST}^k \int_{z^2}^{\infty} \frac{1-e^{-u}}{u^{3/2}} \left[\operatorname{erf}\left(\frac{y_i - y_b^k}{z} \sqrt{u}\right) - \operatorname{erf}\left(\frac{y_i - y_a^k}{z} \sqrt{u}\right) \right] \left[\operatorname{erf}\left(\frac{x_i - x_b^k}{z} \sqrt{u}\right) - \operatorname{erf}\left(\frac{x_i - x_a^k}{z} \sqrt{u}\right) \right] du \quad (6)$$

where n_{surf} is the number of ground surfaces on which the temperature changes compared to the initial condition, e.g., the number of buildings; ΔT_{GST}^k is the ground surface temperature change of the k^{th} surface; α is the ground thermal diffusivity; x_i and y_i are the coordinates of the i^{th} borehole; $x_a^k, x_b^k, y_a^k, y_b^k$ are the coordinates delimiting the k^{th} surface; erf is the error function (Andrews, L.C. 1998). One may notice that in equation 6 the term ΔT_{GST}^k is treated as a constant and appears outside of the integral, while in the original formulation by Rivera et al. (2017) ΔT_{GST}^k is expressed as a function of time and therefore appears inside the integral. We could have left this term inside the integral for the sake of generalizability, however, since our methodology is tailored to the built environments, where we assume the ground surface temperature below the buildings to be constant, we have moved the term outside of the integral. We will also refer to the term ΔT_{GST}^k as the ground temperature change below the k^{th} building.

FLS IV_{GST}[~]. The approximated model calculates $\overline{\Delta T}_{ij}^{TBC}$ as in Fasci et al. (2022):

$$\overline{\Delta T}_{ij}^{TBC}(t) = \frac{\Delta T_{GST}}{H_{ij}} [(H_{ij} + D_{ij}) \cdot g(H_{ij} + D_{ij}, t) - D_{ij} \cdot g(D_{ij}, t)] \quad (7)$$

with:

$$g(z, t) = \left\{ \operatorname{erf}\left(-\frac{z}{\sqrt{4\alpha t}}\right) + \sqrt{\frac{4\alpha t}{\pi z^2}} \left(1 - e^{-\frac{z^2}{4\alpha t}}\right) + 1 \right\} \quad (8)$$

where ΔT_{GST} is the ground surface temperature change, considered uniform along the infinite ground surface. When calculating the borehole wall temperatures by using FLS IV_{GST}[~], we have considered:

$$\Delta T_{GST} = \frac{A^0 \cdot \Delta T_{GST}^0 + \sum_{k=1}^{n_{\text{surf}}} \Delta T_{GST}^k \cdot A^k}{A^0 + \sum_{k=1}^{n_{\text{surf}}} A^k} \quad (9)$$

i.e., the ground surface temperature change on the uniform infinite surface is equal to the weighted average between the ground surface temperature change below the buildings - ΔT_{GST}^k - and the ground surface temperature change in the area delimited by the buildings - ΔT_{GST}^0 - (Figure 1). Since we assume that $\Delta T_{GST}^0 = 0$ K we have cancelled the term $A^0 \cdot \Delta T_{GST}^0$

in equation 9. We will refer to this model as the “basic FLS IV_{GST}”.

We have then evaluated the possibility to minimize the difference between the models by an optimal choice of ΔT_{GST} :

$$\Delta T_{GST} = \frac{\sum_{k=1}^{n_{surf}} \Delta T_{GST}^k \cdot A^k}{c (A^0 + \sum_{k=1}^{n_{surf}} A^k)} \quad (10)$$

where c is a multiplication factor we calculated for each scenario by minimizing the Root Mean Square Error (RMSE) between FLS IV_{GST}= and FLS IV_{GST}~, i.e., where c is such that:

$$\sqrt{\frac{1}{50 \cdot n_{boreholes}} \sum_{t=1}^{50 \text{ years}} \sum_{i=1}^{n_{boreholes}} (\overline{\Delta T}_i^{FLS IV_{GST}=} (t) - \overline{\Delta T}_i^{FLS IV_{GST}~} (t, c))^2} \quad (11)$$

is minimum. We will refer to this model as to the “optimized FLS IV_{GST}”.

Scenarios

We have studied areas with boreholes positioned in square grids. We have considered the number of boreholes per side equal to $N = 2, 3 \dots 10$; the total number of boreholes in an area is equal to $n_{boreholes} = N^2$. Each borehole is centred on a house of area $10 \times 10 \text{ m}^2$. We have assumed that the ground surface temperature change below the houses is 7 K, otherwise 0 K. We have considered grids characterized by borehole distances $B_1 = 15 \text{ m}$ and $B_2 = 20 \text{ m}$. The scenario with $N=2$ and $B = 20 \text{ m}$ is shown as an example (Figure 1).

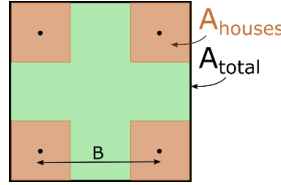


Figure 1 Map of the case study with $N = 2, B = 20 \text{ m}$. The ground properties used for the simulations are shown in Table 1. The borehole properties are shown in Table 2.

Table 1. Ground Properties

Undisturbed temperature T_o [°C]	Thermal conductivity k [W/mK]	Thermal diffusivity α [m ² /s]
8.0	3.1	$1.55 \cdot 10^{-6}$

Table 2. Boreholes Properties

Radius [m]	Buried depth [m]	Length [m]	Constant linear heat load [W/m]
0.0575	6	200	-15 (extraction)

RESULTS AND DISCUSSION

We show the results for the central and corner boreholes of our scenarios. The central boreholes correspond to the one borehole at the centre of the area when N is odd, and to the four boreholes at the center of the area when N is even; the corner boreholes are always four. The cases for $N = 3$ and $N = 4$ are shown in Figure 2 as an example.

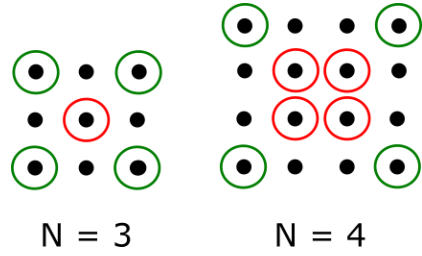


Figure 2 Central (red circles) and corner (green circles) boreholes in the scenarios with $N = 3$ and $N = 4$.

The temperature evolutions calculated with FLS $IV_{GST}^=$ and the basic FLS IV_{GST}^{\sim} for the central and corner boreholes of the scenarios with $B = 15$ m are shown in Figure 3 for the cases $N = 2$ and $N = 10$. Details about the differences between the two models are given in Table 3 and Table 4 for all values of N considered.

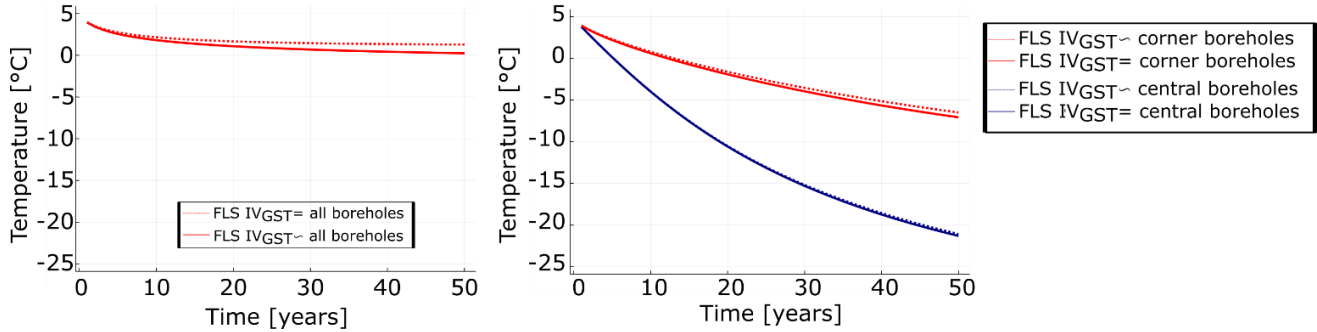


Figure 3 Temperature evolutions of the corner and central boreholes for the scenarios with $B = 15$ m and $N = 2$ (left), $N = 10$ (right).

Table 3. Difference Between FLS $IV_{GST}^=$ and FLS IV_{GST}^{\sim} @ $t = 10$ Years for $B = 15$ m

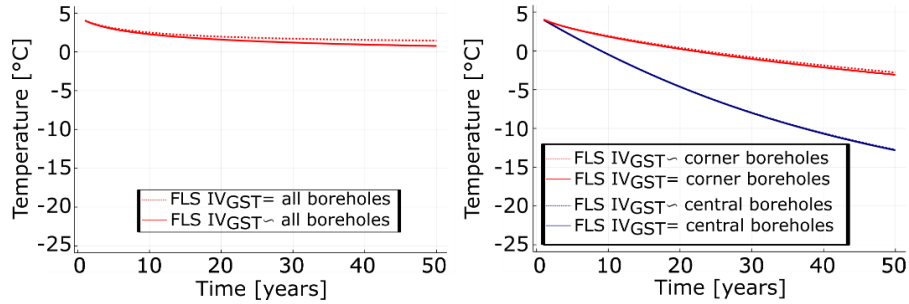
		$N = 2$	$N = 3$	$N = 4$	$N = 5$	$N = 6$	$N = 7$	$N = 8$	$N = 9$	$N = 10$
Central BHE	Absolute [K]	0,35	0,22	0,15	0,10	0,07	0,05	0,036	0,026	0,021
	Relative [%]	5,6	2,6	1,6	0,92	0,65	0,41	0,30	0,22	0,17
Corner BHE	Absolute [K]	0,35	0,26	0,23	0,21	0,20	0,19	0,19	0,18	0,18
	Relative [%]	5,6	3,8	3,2	2,9	2,7	2,6	2,6	2,5	2,5

The results show that the difference between the models is higher for smaller neighbourhoods and increases with time both in absolute and relative terms. For example, after 10 years of operation, the results between the models differ by 5,6% for the boreholes of the smallest neighbourhood ($N = 2$) and by 2,5% for the corner boreholes of the biggest neighbourhood ($N = 10$). The differences increase to 14% and 3,9% respectively after 50 years. It can also be noticed that the difference between the models is smaller for the central boreholes than the corner boreholes. For example, after 50 years, the difference for the central boreholes of the biggest neighbourhood is 0,78%, the difference for the corner boreholes of the same neighbourhood is 3,9%.

Table 4. Difference Between FLS IV_{GST}= and FLS IV_{GST}~ @ t = 50 Years for B = 15 m

		N = 2	N = 3	N = 4	N = 5	N = 6	N = 7	N = 8	N = 9	N = 10
Central BHE	Absolute [K]	1,1	0,82	0,69	0,57	0,48	0,40	0,33	0,27	0,23
	Relative [%]	14	7,0	4,7	3,1	2,3	1,7	1,3	0,97	0,78
Corner BHE	Absolute [K]	1,1	0,87	0,77	0,71	0,66	0,63	0,61	0,60	0,59
	Relative [%]	14	8,7	6,6	5,4	4,8	4,4	4,2	4,0	3,9

The temperature evolutions calculated with FLS IV_{GST}= and the basic FLS IV_{GST}~ for the central and corner boreholes of the scenarios with B = 20 m are shown in Figure 4 for the cases N = 2 and N = 10. Details about the differences between the two models are given in Table 5 and Table 6 for all values of N considered.

**Figure 4** Temperature evolutions of the corner and central boreholes for the scenarios with B = 20 m and N = 2 (left), N = 10 (right).**Table 5. Difference Between FLS IV_{GST}= and FLS IV_{GST}~ @ t = 10 Years for B = 20 m**

		N = 2	N = 3	N = 4	N = 5	N = 6	N = 7	N = 8	N = 9	N = 10
Central BHE	Absolute [K]	0,22	0,11	0,07	0,038	0,025	0,015	0,009	0,0053	0,0025
	Relative [%]	3,84	1,54	0,90	0,46	0,30	0,17	0,11	0,062	0,0297
Corner BHE	Absolute [K]	0,22	0,15	0,12	0,10	0,096	0,09	0,086	0,083	0,080
	Relative [%]	3,84	2,41	1,9	1,7	1,55	1,46	1,39	1,34	1,30

Table 6. Difference Between FLS IV_{GST}= and FLS IV_{GST}~ @ t = 50 Years for B = 20 m

		N = 2	N = 3	N = 4	N = 5	N = 6	N = 7	N = 8	N = 9	N = 10
Central BHE	Absolute [K]	0,70	0,47	0,36	0,27	0,21	0,16	0,12	0,090	0,069
	Relative [%]	9,67	4,56	2,90	1,81	1,29	0,87	0,65	0,45	0,33
Corner BHE	Absolute [K]	0,70	0,51	0,43	0,38	0,35	0,33	0,32	0,31	0,298
	Relative [%]	9,67	5,83	4,36	3,6	3,2	3,0	2,86	2,76	2,69

The results for the scenarios with B = 20 m confirm the trends observed for the scenarios with B = 15 m. Moreover, these results show that the difference between the models is lower for higher values of B. For example, the difference between the models for the smallest neighbourhood after 50 years is 14% when B = 15 m and 9,7% when B = 20 m; for the corner boreholes in the biggest neighbourhood, the difference after 50 years is 3,9% when B = 15 m and 2,7% when B = 20. However, we believe that the difference between the models has a non-monotone trend with B since for $B \rightarrow \infty$ the value ΔT_{GST} used by the approximated model tends to 0, neglecting the presence of the houses. More investigation is needed to confirm the trend of the difference with B.

Overall, our simulations show that the difference between the two models can often be considered acceptable, being lower than 3% and 6% after respectively 10 and 50 years for all the boreholes in 14 out of the 18 scenarios studied. However, the difference between the models could be considered unacceptable for smaller neighbourhoods for which we have calculated differences of up to 14%.

From the results, we notice that despite the heat losses from the buildings, the borehole wall temperature decreases monotonously. This result is specifically related to the case studies analysed, where the heat losses from the buildings do not compensate the heat extraction from the boreholes. The borehole wall temperature trend could be different for different scenarios. Another observation is that in some cases the borehole wall temperature decreases below $-12\text{ }^{\circ}\text{C}$. While this is possible in our simulations where we imposed a constant heat extraction from the ground for 50 years, in reality, heat pumps typically turn off when the inlet brine temperature decreases below $-7^{\circ}\text{C}/-12\text{ }^{\circ}\text{C}$, limiting the ground temperature decrease.

Figure 5 shows the computational time for our scenarios. We want to point out that we did not perform a proper benchmarking and the results might be slightly affected by the use of the computer for other purposes. Moreover, although our scenarios present symmetries, these are not exploited so that comparable results can be expected for real scenarios, typically not presenting many symmetries. The results were obtained with a computer equipped with a Intel(R) Core(TM) i7-7600U processor (2.8 GHz) and 32 Gb of RAM.

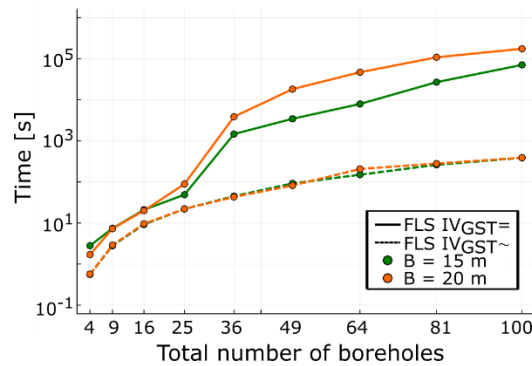


Figure 5 Computational time of our scenarios.

Figure 5 shows that the computational time of the accurate model is relatively low for the smaller neighbourhoods – for which the approximated model is less accurate –, and significantly higher for the bigger neighbourhoods – for which the approximated model is more accurate. Therefore, we suggest the use of the accurate model for the smaller neighbourhoods and of the approximated model for the bigger neighbourhoods. As a rule of thumb, we suggest to use the accurate model for neighbourhoods with less than 25 buildings, given the sharp increase in computational time for bigger neighbourhoods. We believe that the sharp increase in computational time for bigger neighbourhoods may be due to the influence of many buildings being negligible for many boreholes when the neighbourhood is bigger; therefore, the result of the integral in equation 6 being close to 0 for many computations. In fact, we had noticed in the past that the numerical computation of integrals close to 0 can be more expensive (Fasci et al, 2019). However, we have not analysed this further.

The multiplication factors obtained for the optimized FLS IV_{GST}~ and the RMSE of the optimized FLS IV_{GST}~ are shown in Figure 6.

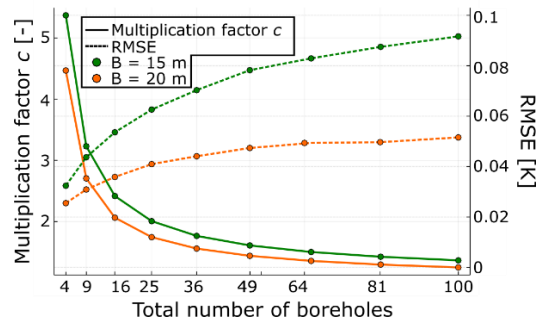


Figure 6 Multiplication factors c and root mean square errors of the optimized FLS IV_{GST}[~]

The multiplication factor decreases as the size of the neighbourhood increases. This is consistent with the previous results showing that the basic FLS IV_{GST}⁼ is more accurate for bigger neighbourhoods. It is also higher for the scenarios with $B = 15$ m than for $B = 20$ m. This is also consistent with the previously discussed results. The optimized FLS IV_{GST}[~] is significantly more accurate than its basic version. In fact, the maximum RMSE calculated with the optimized FLS IV_{GST}[~] is lower than 0.1 K in opposition to the maximum RMSE of the basic FLS IV_{GST}⁼ - 0.5 K-. One may also notice that while the basic FLS IV_{GST}⁼ is most accurate with bigger neighbourhoods, the optimized FLS IV_{GST}[~] is most accurate with smaller neighbourhoods.

Although optimizing FLS IV_{GST}[~] increases significantly the accuracy of the model, the calculation of the multiplication factors c requires the use of FLS IV_{GST}⁼, making the model pointless. More investigation is needed to understand if a correlation between the multiplication factors and other characteristics of the neighbourhood or precalculated multiplication factors can be found and to extend the results to areas characterized by an irregular distribution of boreholes and houses.

CONCLUSION

We have compared two models to calculate the borehole wall temperature evolutions in densely populated areas taking into account the thermal impact of the buildings on the underground. One of the models - FLS IV_{GST}⁼ - is more accurate but computationally more demanding, while the other - FLS IV_{GST}[~] - is an approximation of the first and computationally cheaper. We have showed that FLS IV_{GST}[~] tends to be a good approximation of FLS IV_{GST}⁼ for bigger neighbourhoods, but is less accurate for smaller neighbourhoods. We have also initiated the investigation of a strategy to improve the accuracy of FLS IV_{GST}[~] without reducing its speed. The resulting “optimized” FLS IV_{GST}[~] is a good approximation of FLS IV_{GST}⁼ even for smaller neighbourhoods.

This study analysed several case studies, however, we believe that more should be analysed to draw generalised conclusions and understand the effect of several parameters not analysed in this article, like the boreholes length and the relative position between boreholes and houses.

ACKNOWLEDGMENTS

This project is supported by the Swedish Energy Agency under grant P43647-3. The project is carried on in partnership with Bengt Dahlgren Geoenergi, Borrforetagen i Sverige, Neoenergy Sweden, Nibe, Nowab, Stockholms stad, Svenskt Geoenergicentrum, Thermia and Täby kommun.

REFERENCES

- Andrews, L. C. 1998. *Special functions of mathematics for engineers*. SPIE Press.
- Cimmino, M., and M. Bernier. 2014. *A semi-analytical method to generate g-functions for geothermal bore fields*. *International Journal of Heat and Mass Transfer* 70: 641-650.
- Fascì, M. L., A. Lazzarotto, J. Acuna, and J. Claesson. 2018. *Thermal influence of neighbouring GSHP installations: Relevance of heat load temporal resolution*. Proceedings of the IGSHPA Research Track 2018
- Fascì, M. L., A. Lazzarotto, J. Acuña, and J. Claesson. 2019. *Analysis of the thermal interference between ground source heat pump systems in dense neighbourhoods*. *Science and Technology for the Built Environment* 25: 1069-1080.
- Fascì, M. L., A. Lazzarotto, J. Acuña, and J. Claesson. 2021. *Simulation of thermal influence between independent geothermal boreholes in densely populated areas*. *Applied Thermal Engineering*, 196, 117241.
- Fascì, M. L., W. Mazzotti, A. Lazzarotto, and J. Claesson. 2022. *Temperature of Energy Boreholes Accounting for Climate Change and the Built Environment - a New Model for its Estimation*. SSRN preprint 4113861.
- Gunawardhana, L. N., S. Kazama, and S. Kawagoe. 2011. *Impact of urbanization and climate change on aquifer thermal regimes*. *Water resources management* 25.13: 3247-3276.
- Rivera, J. A., P. Blum, and P. Bayer. 2015. *Analytical simulation of groundwater flow and land surface effects on thermal plume of borehole heat exchangers*. *Applied Energy* 146: 421-433.
- Rivera, J. A., P. Blum, and P. Bayer. 2016. *Influence of spatially variable ground heat flux on closed-loop geothermal systems: Line source model with nonhomogeneous Cauchy-type boundary conditions*. *Applied Energy* 180: 572-585.
- Rivera, J. A., P. Blum, and P. Bayer, 2017. *Increased ground temperatures in urban areas: estimation of the technical geothermal potential*. *Renewable Energy* 103: 388-400.
- Spitler, J. D., and M. Bernier. 2016. *Vertical borehole ground heat exchanger design methods*. In *Advances in Ground-Source Heat Pump Systems*. S.J. Rees, ed. London: Woodhead Publishing.
- Stockholm stad. 2022/06/09. *Beräkningsprogram för dimensionering av energibrunnar*. Retrieved from <https://boende.stockholm/siteassets/mitt-boende/blanketter/miljoforvaltningen/varmepumpar/om-berakningsprogram-for-dimensionering-av-energibrunnar.pdf>
- Witte, H. J. 2018. *A novel tool for assessing negative temperature interactions between neighbouring borehole heat exchanger systems*. 14th International Conference on Energy Storage - EnerSTOCK 2018.

Stationary and non-stationary deconvolution to recover long-term transfer functions

Gabriel Dion

**Philippe Pasquier
Gabrielle Beaudry**

Denis Marcotte

ABSTRACT

To design a ground heat exchanger, simulations are frequently used. One way to perform simulations is to use the well-known g -functions to obtain the ground temperature. These functions are usually obtained by analytical or numerical models, which limits the precision or takes long simulation time. Recent advances show that the short-term g -functions can also be retrieved by a deconvolution algorithm. However, the known deconvolution algorithm is only validated for a set of operating parameters and duration of less than 10 days. A first objective of this article is to demonstrate that longer g -functions can be retrieved with such an algorithm. Then, a second objective is to extend the application of the deconvolution to consider time varying operating parameters throughout a ground heat exchanger's operation. To achieve those objectives, the deconvolution will be first applied to various numerical year-long simulations of a ground source heat pump system with stationary conditions. Then, an extended multi-signal deconvolution will be applied to a non-stationary thermal response test of 30 days. Both tests show adequate temperature reconstruction with RMSE of less than 0.05 °C and 0.2 °C for the first and second scenarios respectively.

INTRODUCTION

Employing a geothermal heat pump connected to a ground heat exchanger (GHE) can significantly reduce a building's heating and cooling energy consumption, affecting positively the building sector's carbon emission (Omer, 2008; Sarbu & Sebarchievici, 2014). To design a GHE, simulations employing g -functions are commonly performed to compute the ground temperature (Eskilson, 1987). These functions describe the time evolution of the ground temperature along the borehole length to a unit impulse signal, and are generally used to find the borehole temperatures under a varying heating load (Zanchini & Lazzari, 2014). Various methods were developed to compute these functions. They rely on analytical (Cimmino & Bernier, 2013; Marcotte & Pasquier, 2014; Nguyen & Pasquier, 2021; Wei et al., 2016), polynomial (Zanchini & Lazzari, 2014), numerical (Robert & Gosselin, 2014) or block matrix (Dusseault et al., 2018) methodology. All these methods have limitations in some ways, either by assumption on analytical model or high computation cost to retrieve the site-specific g -function.

Recent advances have made it possible to use a deconvolution algorithm to obtain the short-term g -function (STgF) from the experimental data of a thermal response test (TRT) (Beier, 2020; Dion et al., 2022). Such an algorithm does not require a direct analytical or numerical model and directly uses the experimental data to obtain the STgF. Another advantage is that defining the STgF at the borehole outlet, as done by Dion et al. (2022), incorporates the thermal conductivity and capacity of the ground and of the GHE (e.g., casing, grout, pipe, and fluid). Such deconvolution

Gabriel Dion (gabriel.dion@polymtl.ca) is a Ph.D. candidate at Polytechnique Montréal, Canada.

Philippe Pasquier (philippe.pasquier@polymtl.ca) is professor of geological engineering at Polytechnique Montréal, Canada.

Denis Marcotte (denis.marcotte@polymtl.ca) is professor of geological engineering at Polytechnique Montréal, Canada.

Gabrielle Beaudry (gabrielle.beaudry@polymtl.ca) is a research associate at Polytechnique Montréal, Canada.

algorithm performs an inversion on a set of nodes, so that the convolved temperatures are closest to their experimental counterparts. At publishing time, the deconvolution algorithm has not been used to obtain g -functions longer than periods or time representative of TRTs (e.g., 3 to 10 days).

Often, the heating power and the flow rate will vary to accommodate a heating demand, creating a system that is non-stationary through time. Recent advances in convolution algorithms allow to consider such non-stationary conditions and hands high quality results with both flow rate and heating power variations (Beaudry et al., 2021). To resolve such situations, several transfer functions are used (one for each state encountered) and convolved under the assumption of non-stationarity. Using such an approach, Beaudry et al., (2022) observed that including non-stationarity can ensure adequate ground temperatures and reduce peak demand to the electricity network.

On currently operating systems, temperatures at the inlet and outlet of a GHE are often available. However, matching these temperatures with a model is usually difficult because the input parameters used to design the GHE are often inaccurate, obtained with erroneous assumptions or do not consider heterogeneity. Therefore, using a calibrated model to evaluate the future response of a GHE under various operating parameters, analyze the performance and durability of a GHE or understanding a GHE's interaction with a nearby system is still a challenge. An alternative could be to use the experimental long-term g -function of a GHE and use it for simulations. Obtaining such experimental long-term g -function has never been done before.

The goals of this article are twofold: first to apply the single-deconvolution algorithm of Dion et al., (2022) to long GSHP system operation to obtain long-term g -function. Second, to provide an extension to the deconvolution algorithm of Dion et al. (2022) to recover a set of transfer functions corresponding to the different operating parameters in a GHE, occurring during the operation of a GSHP system.

METHODOLOGY

A deconvolution algorithm is simply the inverse of a convolution. Both convolution and deconvolution are usually only applied to stationary systems (e.g., a GHE with constant flow and bleed rates). It is, however, possible to consider non-stationarity, for which the specific case is stationarity. This section first presents the non-stationary convolution used for GSHP system and then, the deconvolution algorithm.

Non-Stationary Convolution (forward problem)

The forward model is based on the convolution equation, which is described with the equation:

$$T_{out}(t) - T_0 = (f * g)(t) = \sum_{j=1}^i f(t_j) \cdot g(t_{i-j+1}) \quad (1)$$

In this equation, f is the excitation function and corresponds to the heating power change $f = Q(t_i) - Q(t_{i-1})$. T_0 is the initial ground temperature and T_{out} is the GHE borehole outlet temperature. The variable g is a transfer function, which corresponds to the variation of a system to a unit impulse. In the case of a GSHP system, it is the GHE response to an impulse of 1W throughout the length of the operation period. Hence, by normalizing f by 1W, the units of g are °C, which differs from the dimensionless g -function of Eskilson (1987). Hereinafter, the expression transfer function will be used to avoid misunderstanding but the underlying concept is the same.

Eq. (1) is valid for a steady circulation flow or bleed rate, which describes the state of the GHE operation. To account for state changes, during operation, Beaudry et al. (2021) incorporated a time dependence to the transfer function of Eq. (1), $g(t_{i-j+1}, t)$. In that way, the convolved borehole outlet temperature becomes a combination of the excitation function convolved by the corresponding transfer function. In that form, the combination results in discontinuous signal at the state changes. To correct the signal, a correction function is added to the convolution so that, for each state

transition, a corresponding state variation is applied. To the interested reader, the non-stationary convolution is described in greater details in Beaudry et al. (2021).

It is worth mentioning that the accuracy of the non-stationary convolution is within a mean-absolute-error of less than 0.06 °C on the operating temperature of a GSHP system. Hence, the method has a high accuracy, but is not an exact solution, as would be a stationary convolution.

Stationary or Non-Stationary Signal Deconvolution (inverse problem)

The deconvolution algorithm is akin to an optimization problem, in which the parameter to be optimized is the transfer function in Eq. (1). This section presents an extension to the algorithm of Dion et al., (2022) to deconvolve a set of transfer functions for the non-stationary case instead of a single one in a stationary scenario. The algorithm is closely related to the original one and can also be used for single-signal deconvolution.

Using a non-stationary convolution, multiple transfer functions can be obtained. To achieve that, a set of nodes τ_j (between 20 and 40 per function), spaced logarithmically on each transfer function, are selected as the optimization parameters. To reconcile the nodes τ_j and the time array t of the GSHP system operation, a piecewise cubic Hermite interpolation polynomial (PCHIP) is performed on each transfer function before the non-stationary convolution. The goal of the inversion is then to optimize the nodes values of each transfer function, so that the non-stationary convolution is close to the experimental operation temperatures $T = T_{out} - T_0$. The goal to attain is:

$$\hat{g}_{Set}(t) = arg \min_{\hat{g}(\tau_j)} \left(\|\hat{T} - T_{Exp}\|_2 \Big|_{C_1, C_2} \right) \quad (2)$$

In the previous equation, \hat{g}_{Set} is the estimated transfer functions obtained by deconvolution, τ_j are the nodes selected on each transfer function, t is the time vector, \hat{T} is the estimated temperature obtained by non-stationary convolution, T_{Exp} is the experimental temperature. Finally, $\|\cdot\|_2$ is the l_2 norm.

In Eq. 2, the parameters C are positive derivative and negative second derivative constraints applied to each node of each transfer function. The first constraint is to impose the fact that the transfer function must be increasing with time. The second constraint reflects the general observation that the temperature is slowly reaching a steady state under a constant heating power. This is enforced by constraining the slope of the transfer function's first derivative to be strictly negative after a certain point. The two following equations describe the constraints, which are implemented in the optimization as linear inequality equations on the nodes.

$$C_1 \quad 0 < \hat{g}(\tau_j) < \hat{g}(\tau_{j+1}) \quad \forall j \in [0, n - 1] \quad (3)$$

$$C_2 \quad \hat{g}'(\tau_{j+1}) < \hat{g}'(\tau_j) \quad \forall j \in [z, n - 1] \quad (4)$$

where z is the node τ_j from which the first derivative has a negative slope.

To ensure faster convergence, a first approximation of the optimization problem is required. Here, an initial guess of the transfer function set used by the main optimization algorithm is obtained with the use of 2 subsequent inversion problems. The first one assumes a stationary state and fits a single transfer function based on an exponential integral equation, of the form $\tilde{g}_0(x_1, x_2, t) = x_1 \int_{x_2} \frac{e^{-t}}{t} dt$ with x_1 and x_2 being the optimization parameters, to the experimental temperature: $\hat{g}_0(t_i) = \min_{x_1, x_2} \|(f(t) * \tilde{g}_0(x_1, x_2, t)) - T_{Exp}(t)\|_2$. The temperatures with this method are not well reproduced in a non-stationary scenario, since only one set of circulating flow and bleed rates (i.e., state) is considered. To enhance the fit, one transfer function per state \hat{g}_s can be obtained by scaling the initial function \hat{g}_0 by coefficients a_s , i.e., $\hat{g}_s(t) = a_s \cdot \hat{g}_0(t)$. The coefficients a_s are obtained through the minimization with non-stationary convolution:

$a_s = \min_{a_s} \|(f * (a(s) \cdot \hat{g}_0))(t) - T_{Exp}(t)\|_2$. The main optimization will then use the set of $\hat{g}_s(\tau_j)$ evaluated at nodes τ_j for each state s as the initial solution.

VALIDATION SCENARIOS

To assess the performance of the proposed deconvolution algorithm and to fulfill the objective of the paper, two test cases are used. The first one is a set of four year-long numerical simulations with different sets of constant operating parameters of a GSHP system using a SCW. This case will be used to obtain long-term transfer functions with the stationary deconvolution. The second case is a field TRT of 30 days with time-varying circulating flow and bleed rates. This case will employ the deconvolution to retrieve an experimental set of transfer functions with the non-stationary deconvolution.

The stationary case is made using the numerical model based on the work of Beaudry et al., (2022) on a system with 5 SCWs. The recordings have time steps of one hour, over a year of operation. Four simulations were generated, each using different constant sets of operating circulating flow and bleed rates, as described in Table 1. Each state is described by its respective numerically generated transfer function. Then, temperatures T_{out} are generated by applying a superposition principle (or convolution) to the known ground heating power profile and the numerical transfer functions. These signals are then used in a stationary deconvolution to obtain the long-term transfer function.

The non-stationary case has samplings at every minute and is performed on the SCW site described by Beaudry et al. (2018, 2019), which was built in Varennes, Quebec. The SCW is 215 m deep and an injection well of 150m was dug at about 10 m from the main well to receive the bled flow rate. The TRT was performed in July 2019 and varies the heating power, the circulating and bleed rates to stimulate the well under non-stationary operating conditions. In total, 4 successive states occur during the TRT and are described in Table 1. Two different circulating flow rates are used, and a bleed flow rate of approximately 10% is activated in the middle of each sequence. To minimize the impact of high frequency noise on the data, a moving average filter with a window of 10 points was used on both the temperature and heating power of the field TRT. For both test cases, the physical parameters are reported in Table 2.

Table 1. Circulating flow and bleed rates for the four different states used for the stationary and non-stationary cases.

Test case	Flow rate	g_1	g_2	g_3	g_4
Stationary	Circulating (L/min)	326	408	489	568
	Bleed (L/min)	65	82	98	170
Non-stationary	Circulating (L/min)	71	71	145	145
	Bleed (L/min)	0	7	0	15

Table 2. Thermal properties of the numerical model used for the stationary (left) and non-stationary (right) cases.

Parameter	Symbol	Unit	Ground	Pipe	Water
Volumetric Heat Capacity	ρC_p	$\text{kJ m}^{-3} \text{K}^{-1}$	2160 2070	2000 2174	4187 4176
Porosity	n	-	0.01 0.02	0 1e-05	1 1
Thermal Conductivity	k	$\text{W m}^{-1} \text{K}^{-1}$	3.99 2.78	0.45 0.42	0.57 0.59
Hydraulic Conductivity	K	m s^{-1}	6.5e-5 5.7e-7	1e-9 1e-09	1000 1000
Specific storage	S_s	m^{-1}	1e-4 6.4e-4	4e-6 4e-10	4e-6 4e-10

RESULTS

Stationary case – Simulated temperatures

In Figure 1, the results of the stationary deconvolution applied to four different simulations are presented. It can be noted that both the transfer functions and the temperature are reproduced with great accuracy. The RMSE of the various transfer functions are all less than $0.001 \text{ }^\circ\text{C}/\text{W}$ and the RMSE of the 4 temperature fits are of less than $0.044 \text{ }^\circ\text{C}$. In all cases, the constraints C_1 and C_2 are always respected. Indeed, each case shows strictly growing transfer functions and strictly downward first derivative slope from the beginning of the transfer functions, showing that the value z in the constraint C_2 can be taken as the first hour of operation. The larger deviations on the curves are at the end of the functions and mostly visible on the derivatives. All the stationary deconvolution converged in under 30 seconds.

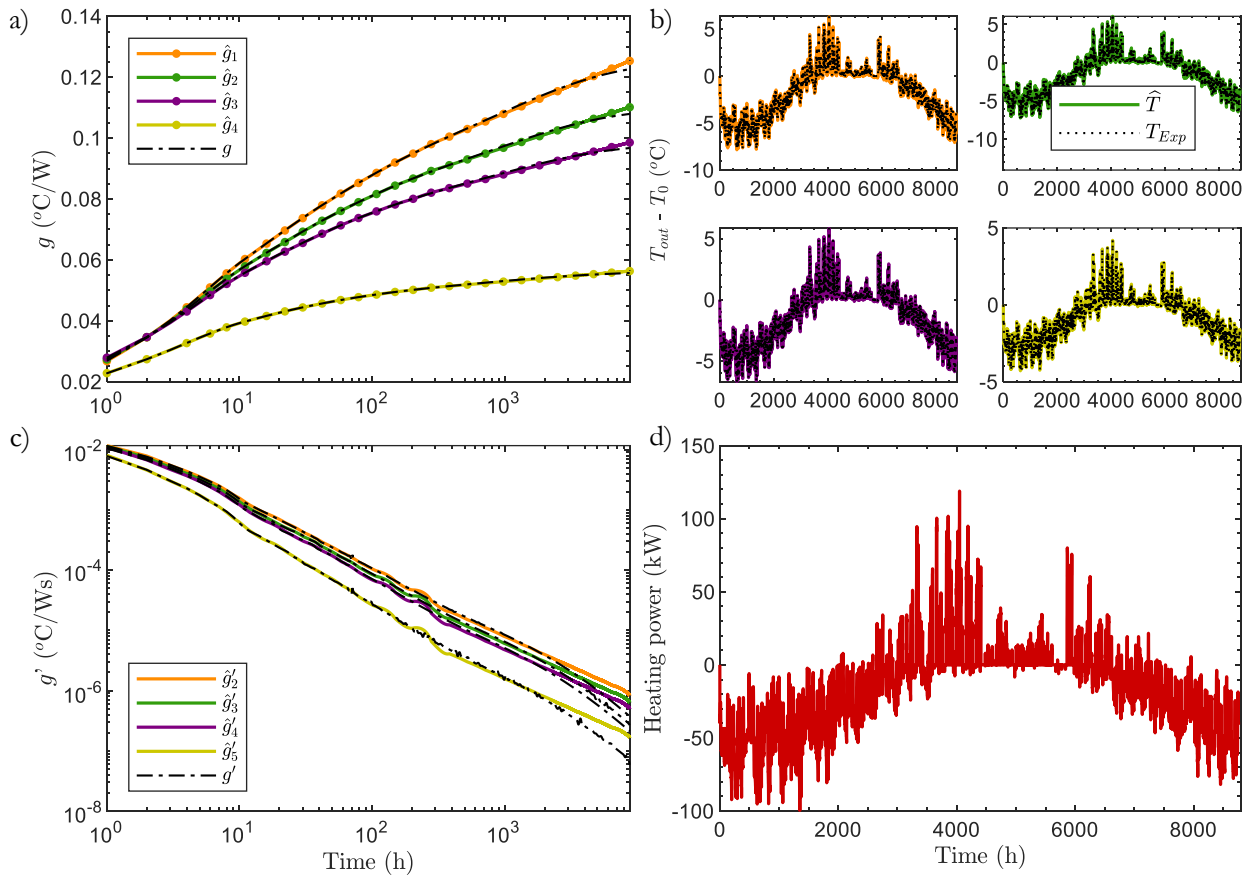


Figure 1. Stationary deconvolution results on 4 numerical test cases using the same heating power profile. a) and c) Deconvolved and numerical transfer functions and their derivatives respectively. b) Convolved and simulated temperatures. d) Heating power profile used in each deconvolution. The dots in a) show the nodes τ_j . The RMSE for the 4 cases are respectively: 0.04, 0.04, 0.03 and 0.01 $^\circ\text{C}$.

Non-Stationary Case – Experimental Temperatures

In Figure 2, the results of the non-stationary deconvolution applied to the TRT experimental data are shown, with the associated temperature RMSE being of 0.19 °C. One can notice that the transfer functions are not all the same length. Instead, they are only illustrated on their respective activation time. This means that, for example, the function corresponding to the first state (i.e., flow rate of 71 L/min and bleed rate of 0 L/min) is only used for the first 8 days of the TRT. The second function, corresponding to the second state (i.e., flow rate of 71 L/min and bleed rate of 7 L/min), is used on the first 16 days since the first 8 days impact the temperature between 8 and 16 days. The vertical lines on Figure 2 shows the ending moment of each transfer function.

The algorithm converged in only 57 iterations and 35 minutes but had difficulty to enforce the C_2 constraint, as can be seen in Figure 2 c). This could be explained by the difficulty of the algorithm to find a global minimum due to the large number of nodes to optimize. Indeed, each function has 22 nodes, which amount to 88 parameters to estimate on a test composed of 43200 data points.

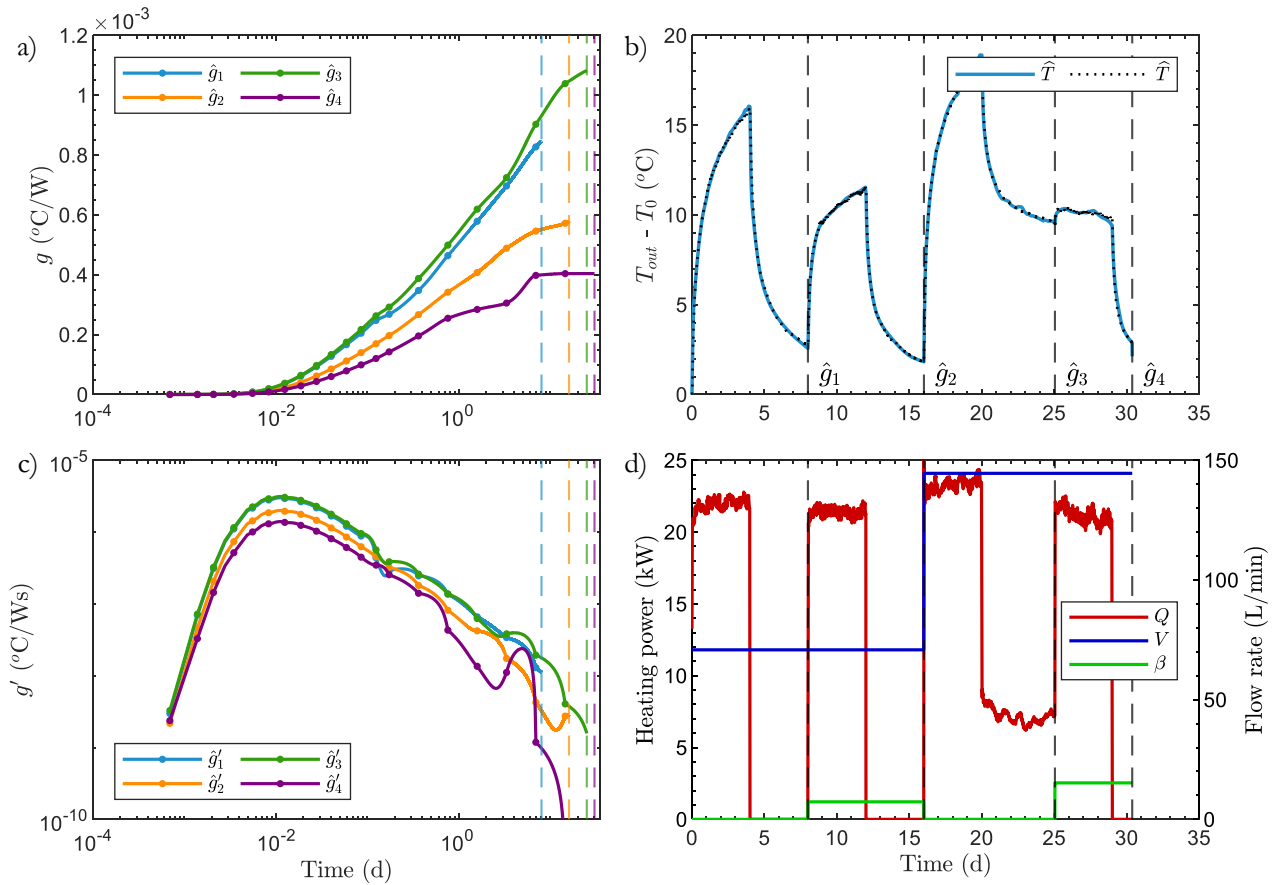


Figure 2. Non-stationary deconvolution result on an experimental TRT with 4 successive states. a) and c) Length dependent deconvolved transfer functions and their derivatives respectively. b) Convolved and experimental temperatures. d) Heating power (Q) profile, circulating flow (V) and bleed (β) rates used in each deconvolution. The dots on the curves in a) show the location of the nodes τ_j . The temperature RMSE is 0.19 °C.

DISCUSSION

The results show that both the stationary and non-stationary deconvolution algorithms are quite good at reproducing the temperature of either the year-long simulation or the long field TRT. This stems from the use of the temperature as the sole factor in the objective function of Eq. 2. In the stationary deconvolution algorithm, the transfer functions show a great fit with the numerical ones. Although the experimental ones are not available for the TRT, the transfer functions are not as smooth as expected. This could stem from the way the optimization problem is set to optimize only the temperature fit. Note, however, that the fluctuations of the first derivative appear visually exaggerated using a log-log scale. One way to smooth the transfer function could be to add regularization terms to the objective function.

Also, it is noticeable that the constraint C_2 described at Eq. 4 is not always respected during the non-stationary deconvolution. This is apparent by the slope of the transfer function first derivatives that are not always negative after around 3 hours of test. This last value was taken arbitrarily, to ensure that the TRT was in a relative steady state. In that section of the transfer function, the first derivative's slope should be strictly downward, as can be seen in the stationary deconvolution in Figure 1. In Figure 2, some functions show positive first derivative at long times, even if the nodes show a downward trend for these times. Indeed, PCHIP interpolation ensures that g is increasing but not that its derivative behaves as desired. This shows the complexity of the inversion problem, and that further work is needed to obtain in non-stationary case transfer functions with all the desired properties.

It is worth noting that for both stationary and non-stationary deconvolution, the measurement errors of the flow and bleeding flow rates are simplified to continuous or step signals. The flow rates shown in Figure 2 are segmented averages of their measured signals. However, these signals are affected by natural variation and measurement errors. This simplification is used to ensure that a limited number of transfer functions are deconvolved. Otherwise, there could be as much transfer functions as data point in the flow rates signals. The impacts of such a simplification are hard to estimate but are to be considered when analyzing deconvolution results.

Finally, an aspect limiting the fit in the non-stationary case is the precision of the forward model. In Beaudry et al. (2021), it is mentioned that the non-stationary convolution method has higher residuals within the fluid residence time due to slight imprecision in the correction function. Also, vertical temperature profiles are not considered in the current application of the forward model. This could represent an additional error since it was demonstrated that it has a significant influence on the groundwater temperature along the borehole wall in SCW operations (Beaudry et al., 2019).

CONCLUSION

In this article, a deconvolution algorithm was used both in stationary and non-stationary conditions to recover transfer functions related to the operating parameters occurring in the GHE. The stationary deconvolution showed that long-term transfer functions can be obtained, and the application of non-stationary deconvolution was demonstrated on an experimental test case. It has been shown that the experimental temperature can be recovered with temperature fits with accuracies of less than 0.05 °C with stationary deconvolution and 0.2 °C with non-stationary deconvolution.

This algorithm has the potential to help GHE response simulation by providing a way to obtain experimental transfer functions on both stationary and non-stationary scenarios. The extension of the deconvolution toward non-stationary situations makes the algorithm more flexible and applicable to a larger set of situations that can be encountered in field application, such as GSHP systems that have been operating for several years or with time-varying flow rates. In this case, the deconvolution can be applied to validate the performance of the system.

ACKNOWLEDGMENTS

The authors wish to acknowledge the support and funding provided by the Natural Sciences and Engineering Research Council of Canada (grant number RDCPJ 530945), the Trottier Energy Institute, Hydro-Québec, FTE drilling, Marmott Energies, Richelieu Hydrogeology and Versaprofiles.

NOMENCLATURE

a	=	Scalar weights to roughly adjust $\hat{g}_{0,Set}$ (-)
β	=	Bleed flow rate (L/min)
C	=	Constraint applied on the nodes in the optimization problem (-)
E	=	Objective function to evaluate (-)
f	=	Incremental heating power function (W)
g	=	Transfer function (°C/W)
τ	=	Nodes used as optimization parameters (-)

Q	=	Heating power (W)
T	=	Temperature (°C)
V	=	Circulating flow rate (L/min)

Subscripts

Exp	=	Experimental
0	=	Initial
out	=	Borehole outlet
s	=	State identifier
Set	=	Group of transfer functions

REFERENCES

- Beaudry, G., Pasquier, P., & Marcotte, D. (2018). Hydrogeothermal characterization and modelling of a standing column well experimental installation. *Proceedings of the IGSHPA Research Track 2018*, 1–10. <https://doi.org/10.22488/okstate.18.000009>
- Beaudry, G., Pasquier, P., & Marcotte, D. (2019). The impact of rock fracturing and pump intake location on the thermal recovery of a standing column well: Model development, experimental validation, and numerical analysis. *Science and Technology for the Built Environment*, 25(8), 1052–1068. <https://doi.org/10.1080/23744731.2019.1648133>
- Beaudry, G., Pasquier, P., & Marcotte, D. (2021). A fast convolution-based method to simulate time-varying flow rates in closed-loop and standing column well ground heat exchangers. *Renewable Energy*. <https://doi.org/10.1016/j.renene.2021.04.045>
- Beaudry, G., Pasquier, P., Marcotte, D., & Zarrella, A. (2022). Flow rate control in standing column wells: A flexible solution for reducing the energy use and peak power demand of the built environment. *Applied Energy*, 313, 118774. <https://doi.org/10.1016/j.apenergy.2022.118774>
- Beier, R. A. (2020). Deconvolution and convolution methods for thermal response tests on borehole heat exchangers. *Geothermics*, 86, 101786. <https://doi.org/10.1016/j.geothermics.2019.101786>
- Cimmino, M., & Bernier, M. (2013). Preprocessor for the generation of g-functions used in the simulation of geothermal systems. *BS2013*, 8.
- Dion, G., Pasquier, P., & Marcotte, D. (2022). Deconvolution of experimental thermal response test data to recover short-term g-function. *Geothermics*, 100, 102302. <https://doi.org/10.1016/j.geothermics.2021.102302>
- Dusseault, B., Pasquier, P., & Marcotte, D. (2018). A block matrix formulation for efficient g-function construction. *Renewable Energy*, 121, 249–260. <https://doi.org/10.1016/j.renene.2017.12.092>
- Eskilson, P. (1987). *Thermal Analysis of Heat Extraction Boreholes*. 222.
- Marcotte, D., & Pasquier, P. (2014). Unit-response function for ground heat exchanger with parallel, series or mixed borehole arrangement. *Renewable Energy*, 68, 14–24. <https://doi.org/10.1016/j.renene.2014.01.023>
- Nguyen, A., & Pasquier, P. (2021). A successive flux estimation method for rapid g-function construction of small to large-scale ground heat exchanger. *Renewable Energy*, 165, 359–368. <https://doi.org/10.1016/j.renene.2020.10.074>
- Robert, F., & Gosselin, L. (2014). New methodology to design ground coupled heat pump systems based on total cost minimization. *Applied Thermal Engineering*, 62(2), 481–491. <https://doi.org/10.1016/j.applthermaleng.2013.08.003>
- Wei, J., Wang, L., Jia, L., & Cai, W. (2016). A new method for calculation of short time-step g-functions of vertical ground heat exchangers. *Applied Thermal Engineering*, 99, 776–783. <https://doi.org/10.1016/j.applthermaleng.2016.01.105>
- Zanchini, E., & Lazzari, S. (2014). New g-functions for the hourly simulation of double U-tube borehole heat exchanger fields. *Energy*, 70, 444–455. <https://doi.org/10.1016/j.energy.2014.04.022>

Accuracy of analytical approaches to thermal response test interpretation

Hae-Rim Oh Seong-Kyun Kim Byeong-Hak Park Ji-Young Baek Kang-Kun Lee

ABSTRACT

Thermal conductivity obtained via thermal response test (TRT) is one of the essential parameters for the design of shallow geothermal systems, especially a borehole heat exchanger (BHE). During TRT analysis, several factors (e.g., start time of analysis and test duration) could influence the estimated thermal conductivity. In addition, the influence of the factors may be different depending on the characteristics of the borehole and ground. This study investigated the effects of the start time and test duration through numerically generated TRT data under a diversity of environment and BHE information such as the thermal conductivity of grouting and ground. The generated numerical data were analyzed with three analytical approaches having different assumptions about the heat source to interpret the sensitivity of factors in the TRT analysis. By conducting the analytical sensitivity analysis, the importance of determining the appropriate start time and test duration could be emphasized when designing the test.

INTRODUCTION

Thermal conductivity is one of the essential parameters when designing the shallow geothermal system (Marcotte and Pasquier, 2008). A thermal response test (TRT), first presented by Mogensen (1989), has been used to determine the in-situ thermal conductivity, called an effective thermal conductivity. When estimating the effective thermal conductivity using analytical models, it is important to consider a start time and a test duration. Since the response signal is initially influenced by the BHE properties, the start time is intended to ignore the data at the beginning of the test (Stauffer et al., 2013). Gehlin (2002) suggested that the dimensionless time related to the borehole radius, thermal diffusivity, and start time should be greater than 5 for the maximum error to be within 10%. On the other hand, the test duration could affect the cost and accuracy of the test (Raymond et al., 2011). To suggest the appropriate test duration, Beier and Smith (2003) developed a quick method to determine the minimum testing time, and Signorelli et al. (2007) used a numerical simulation to see the effect of test duration according to the ground thermal conductivity. There have been many studies to investigate the influence of the start time and test duration on the effective thermal conductivity. However, although their influences may be different depending on the properties of BHE and ground, few studies have investigated the relationship between the two factors and the experimental environment.

The purpose of this study is to investigate the effect of the start time and the test duration on effective thermal conductivity under various BHE and ground characteristics. First, numerical simulations were performed and the numerically generated data were analyzed using two analytical models having different boundary conditions. Then, the effective thermal conductivity was estimated with varying the start time and test duration. Through the comparison with the thermal conductivity used for the numerical simulation, we investigated how the effective thermal conductivity changed depending on the start time and test duration.

Hae-Rim Oh (ohr0721@snu.ac.kr) is a PhD student at Seoul National University, Seong-Kyun Kim (kskinc@kigam.re.kr) is a researcher at Korea Institute of Geoscience and Mineral Resources, Byeong-Hak Park (bh-park@kaeri.re.kr) is a researcher at Korea Atomic Energy Research Institute, Ji-Young Baek (bjy14114@snu.ac.kr) is a PhD student at Seoul National University, and Kang-Kun Lee (kklee@snu.ac.kr, corresponding author) is a professor of school of earth and environmental sciences at Seoul National University.

METHODOLOGY

Numerical simulation

Numerical simulations were performed using TOUGH3 (Lawrence Berkeley National Laboratory, Berkeley, CA, USA), which was developed for multi-dimensional fluid and heat flows of multiphase, multicomponent fluid mixtures in porous and fractured media (Jung et al., 2018). The general form of the basic energy balance equations in a porous medium used in TOUGH3 is expressed as follows (Pruess et al., 1999):

$$\frac{d}{dt} \int_{V_n} M dV_n = \int_{\Gamma_n} F \cdot nd\Gamma_n + \int_{V_n} q dV_n \quad (1)$$

The heat accumulation term M , defined as the energy per unit volume, can be rewritten as follows:

$$M = \rho_R c_R T \quad (2)$$

The conductive heat flux (F) is estimated as follows:

$$F = -\lambda \nabla T \quad (3)$$

Figure 1 shows 2D top view of the model domain. The entire 3D model had a size of 20 m × 20 m × 80 m (length × width × depth) in consideration of the BHE length. The mesh to discretize the model domain was generated using an adaptive gridding technique called a centroidal Voronoi tessellation (CVT) developed by Kim et al. (2015). The mesh generated by the CVT always satisfies the orthogonal shape grid of TOUGH3. The fluid flow was not considered in the simulations. An annual average groundwater temperature of the study site corresponding to 13.0 °C was set as the boundary condition for the entire domain. The basal heat flow of 59.62 mW/m² was estimated from the ground thermal conductivity of 2.00 W/m/K and the thermal gradient. Table 1 shows the parameters for the numerical simulation such as the physical properties of BHE and the ground and the experimental conditions. The parameters in Table 1, except for water using the reference value, were derived from actual experimental information. This experiment was conducted according to the guideline (MOTIE, 2019), and the simulation was performed based on this experimental data. We conducted numerical simulations with a time step of 5 minutes.

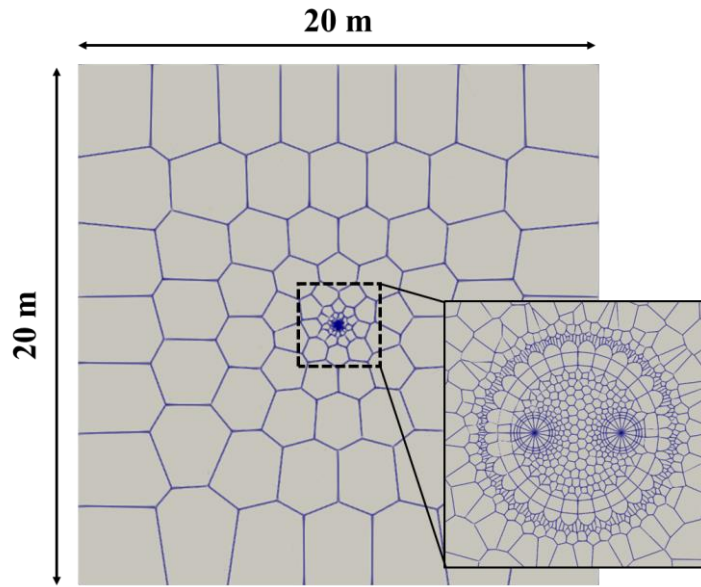


Figure 1 2D top view of the model domain. The domain size is 20 m × 20 m × 80 m (length × width × depth). There are 8,755 elements and 32,814 connections.

Table 1. Model input parameters

Parameters (unit)		Value
Borehole heat exchanger		
	Borehole depth (m)	76
	Borehole diameter (m)	0.152
U-tube: Polyethylene		
	Outer diameter (m)	0.040
	Inner diameter (m)	0.036
Grout		
	Thermal conductivity (W/m/K)	0.79
	Specific heat (kJ/kg/K)	2.00
Heat carrier fluid: Water		
	Thermal conductivity (W/m/K)	0.58
	Specific heat (kJ/kg/K)	4.20
Ground		
	Thermal conductivity (W/m/K)	2.00
	Volumetric heat capacity (MJ/m ³ /K)	3.55
Experimental conditions		
	Heat flow rate per unit length of borehole (W/m)	62.66
	Average flow rate of the fluid (L/min)	17.05
	Initial temperature (°C)	13.45
	Average temperature difference (°C)	4.01

In order to consider the influence of λ_{ground} and λ_{grout} , we generated several numerical data under various conditions (Table 2). λ_{grout} values were additionally assigned as 1.35 (used in Brettmann et al. (2011)), 1.73, and 2.10 W/m/K (used in Choi et al. (2011)), respectively. Considering that the thermal conductivity may vary depending on the ground, λ_{ground} values were set to 1, 2, 3, and 4 W/m/K. Figure 2 shows the mean fluid temperature between the inlet and outlet of BHE in the simulation results.

Table 2. Conditions for data generation under various thermal conductivity of ground and grouting material

Factor	Thermal conductivity of ground (W/m/K)	Thermal conductivity of grouting material (W/m/K)
Ground thermal conductivity	1.00	0.79
	2.00	
	3.00	
	4.00	
Grout thermal conductivity	2.00	0.79
		1.35 (used in Brettmann et al. (2011))
		1.73
		2.10 (used in Choi et al. (2011))

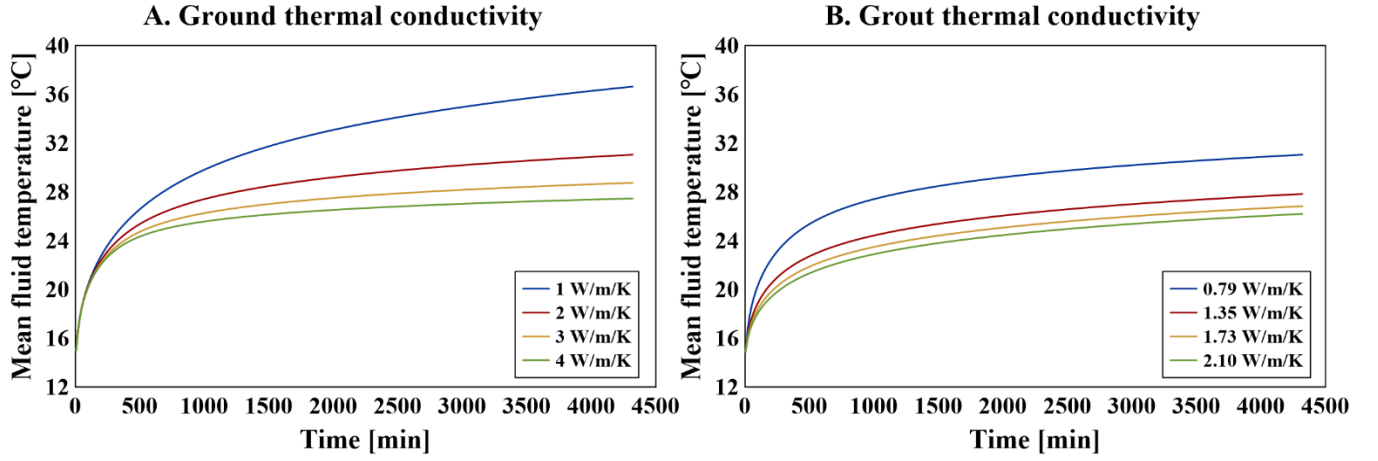


Figure 2 Simulated mean fluid temperature for (a) Ground thermal conductivity and (b) Grout thermal conductivity.

Analytical models

In this study, two analytical models with different assumptions of the heat source were used to estimate the thermal conductivity. Numerically generated data were analyzed by an infinite line source (ILS) model expressed in Equation 4 (Carslaw and Jaeger, 1959).

$$T_f(t) = \frac{q_{tb}}{4\pi\lambda_{eff}} \ln(t) + q_{tb} \left[R_b + \frac{1}{4\pi\lambda_{eff}} \left(\ln \left(\frac{4\alpha t}{r_b^2} \right) - \gamma \right) \right] + T_0 \quad (4)$$

The logarithmic approximation of the ILS model can be expressed as a linear regression function as follows (Eklöf and Gehlin, 1996):

$$\frac{dT_f}{d(\ln(t))} = \frac{q_{tb}}{4\pi\lambda_{eff}} \quad (5)$$

λ_{eff} can be determined using Equation 5, and the obtained λ_{eff} is referred to as $\lambda_{ILS-lin}$ in this study.

$$\lambda_{ILS-lin} = \frac{q_{tb}}{4\pi} \left(\frac{dT_f}{d(\ln(t))} \right)^{-1} \quad (6)$$

An infinite cylindrical source (ICS) model that extends a line source to a cylindrical source with radius r was also used to analyze the numerically generated data. The ICS model can be expressed in Equation 7 (Ingersoll et al., 1954).

$$T_f(t) = T_0 + \frac{q_{tb}}{\pi^2\lambda_{eff}} \int_0^\infty \frac{e^{-\beta^2 Fo} - 1}{j_1^2(\beta) + Y_1^2(\beta)} \times [J_0(R\beta)Y_1(\beta) - J_1(\beta)Y_0(R\beta)] \frac{d\beta}{\beta^2} + q_{tb}R_b \quad (7)$$

Parameter estimation approach. When using the ILS model, the measured temperature data can be fitted by a linear regression method in Equations 5 and 6 or a parameter estimation method (Stauffer et al., 2013). The parameter estimation method was used not only in ILS but also in ICS, which cannot be represented by the linear regression. To estimate thermal parameters, two variables (thermal conductivity and borehole thermal resistance) were obtained when the root mean squared error (RMSE) was the minimum. RMSE was calculated by changing the variables within the established reference range. Thermal parameters having the minimum RMSE were determined at each step. The RMSE between the observed and modeled values was given by the following formula:

$$RMSE = \sqrt{\frac{\sum_{i=1}^N (T_{f,model}(t_i) - T_{f,meas}(t_i))^2}{N}} \quad (8)$$

$T_{f,model}$ can be obtained by using ILS and ICS (Equations 4 and 7). $\lambda_{ILS-par}$ and λ_{ICS} were used as λ_{eff} estimated by each model.

RESULTS

Analytical sensitivity analysis

We set a comparison criterion to quantitatively compare the effect of factors. Kavanaugh (2000) stated that 10% change in thermal conductivity could lead to 4.5–5.8% error of the borehole length, which could lead to a 1% change in cooling capacity and 0.7% change in heating capacity. Based on the results in Kavanaugh (2000), an acceptable change was defined as within 10% in this study.

Effect of start time. To conduct the analytical sensitivity analysis of the start time for the thermal conductivity estimation, the start time was ranged from 0 to 1,000 minutes in 100 minutes' increments. The test duration was fixed at 4,320 minutes. Figure 3 shows the change of the estimated thermal conductivity with the start time. Figure 3a shows the change in λ_{eff} with the start time in the case of λ_{ground} . When comparing λ_{eff} with λ_{num} , the largest differences were shown in the order of λ_{ICS} (-37.50%), $\lambda_{ILS-par}$ (-34.50%), and $\lambda_{ILS-lin}$ (-30.49%). These results were obtained when λ_{ground} was the highest at the minimum start time within the analysis range. As the start time increased, the difference between λ_{eff} and λ_{num} decreased. The start time for the difference to reach within 10% increased with increasing λ_{ground} . In these results, the start time had to be at least 600 minutes to have an acceptable difference within 10%.

In the case of λ_{grout} (Figure 3b), the largest differences were also shown in the order of λ_{ICS} (-24.00%), $\lambda_{ILS-par}$ (-19.00%), and $\lambda_{ILS-lin}$ (-17.48%). As with the results of λ_{ground} , the difference between λ_{eff} and λ_{num} decreased with increasing the start time. The difference between $\lambda_{ILS-lin}$ and λ_{num} was the largest when λ_{grout} was 2.10 W/m/K. On the other hand, the differences of $\lambda_{ILS-par}$ and λ_{ICS} were more than 10% as the maximum when λ_{grout} was 0.79 W/m/K. Considering λ_{grout} of 0.79 W/m/K with the largest change according to the start time, the start time showed a difference within 10% after 300 minutes.

Comparing the results of λ_{ground} (Figure 3a) and λ_{grout} (Figure 3b), λ_{eff} was estimated significantly different from λ_{num} in the early part of the two analysis results. λ_{ground} had a greater effect on the results of start time than λ_{grout} . In our results, the change of λ_{eff} within the analysis range was the greatest having the highest λ_{ground} and the lowest λ_{grout} .

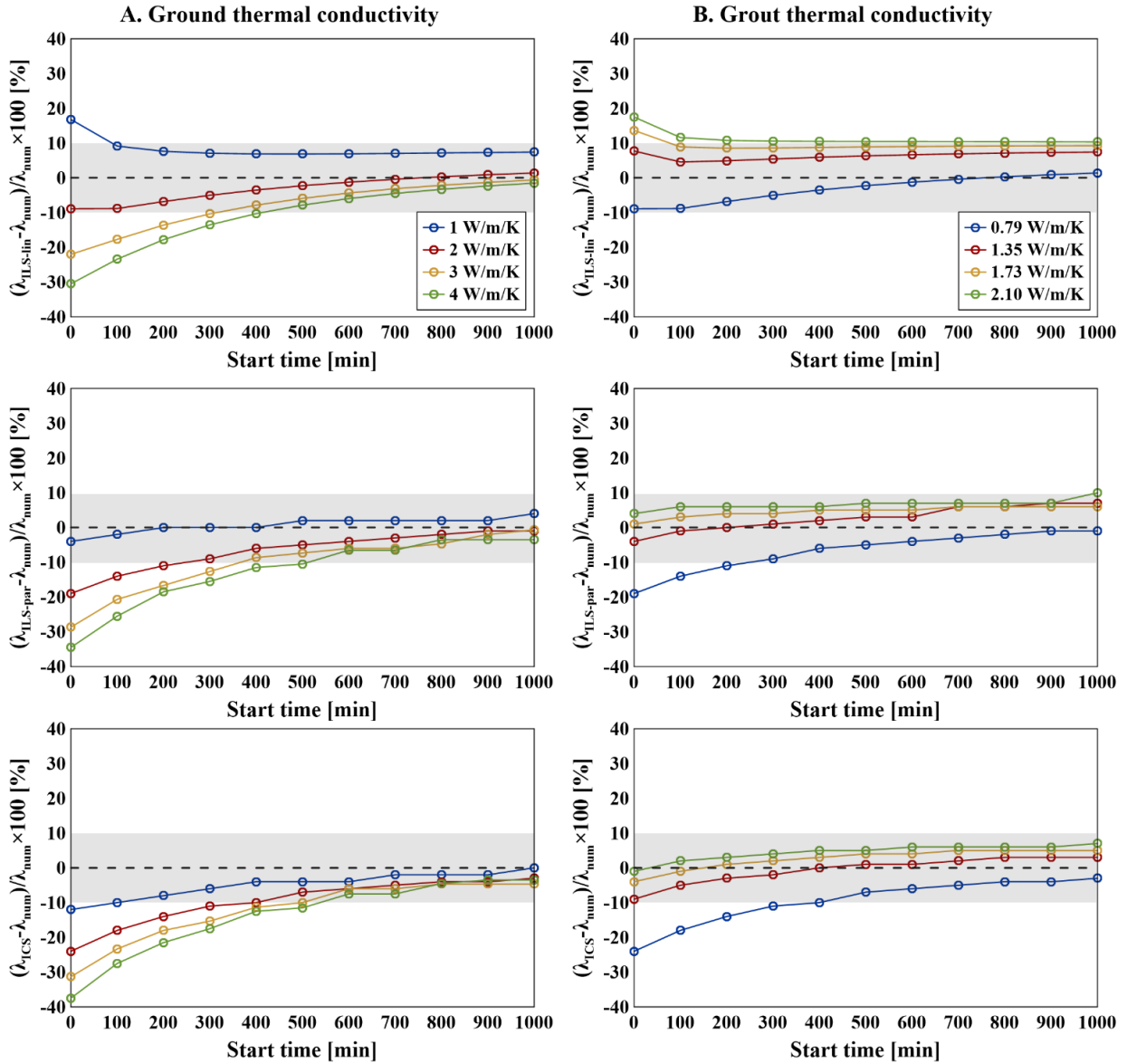


Figure 3 The change in estimated thermal conductivity when the start time is changed from 0 to 1,000 minutes in cases of (a) Ground thermal conductivity and (b) Grout thermal conductivity. The gray area means the section within the acceptable difference of 10%.

Effect of test duration. In the process of the sensitivity analysis, the test duration was changed from 2,880 to 4,320 minutes in 60 minutes' increments. During this analysis, the start time was set at 720 minutes according to MOTIE (2019), and other factors were not changed. Figure 4 shows the change in estimated thermal conductivities according to the test duration.

In case of λ_{ground} (Figure 4a), the maximum difference between $\lambda_{\text{ILS-lin}}$ and λ_{num} was shown in the order of λ_{ICS} (-10.50%), $\lambda_{\text{ILS-par}}$ (-10.00%), and $\lambda_{\text{ILS-lin}}$ (8.13%). The largest differences of λ_{ICS} and $\lambda_{\text{ILS-par}}$ were greater than 10% when λ_{ground} was 3 or 4 W/m/K. At the case of λ_{ground} of 3 W/m/K, the largest difference was calculated in the initial part of the analysis

range, and it was determined in the middle part when λ_{ground} was 4 W/m/K. With a few exceptions, the estimates were generally within the acceptable range. Figure 4b shows the change of λ_{eff} according to the test duration in the case of λ_{ground} . Except for $\lambda_{\text{ILS-in}}$ (10.55%), the largest differences of $\lambda_{\text{ILS-par}}$ and λ_{ICS} were smaller than the comparison criterion of 10%. Considering the specific test duration that exceeded 10%, it was confirmed that the longer the test duration, the better.

As shown in Figure 4, the estimated thermal conductivities are relatively constant compared to the results of start time (Figure 3). That is, even if the test duration was increased, the difference from λ_{num} did not change significantly. Therefore, it seems difficult to mention that there was a noticeable change in the estimated thermal conductivity according to the test duration within the analysis range in this study.

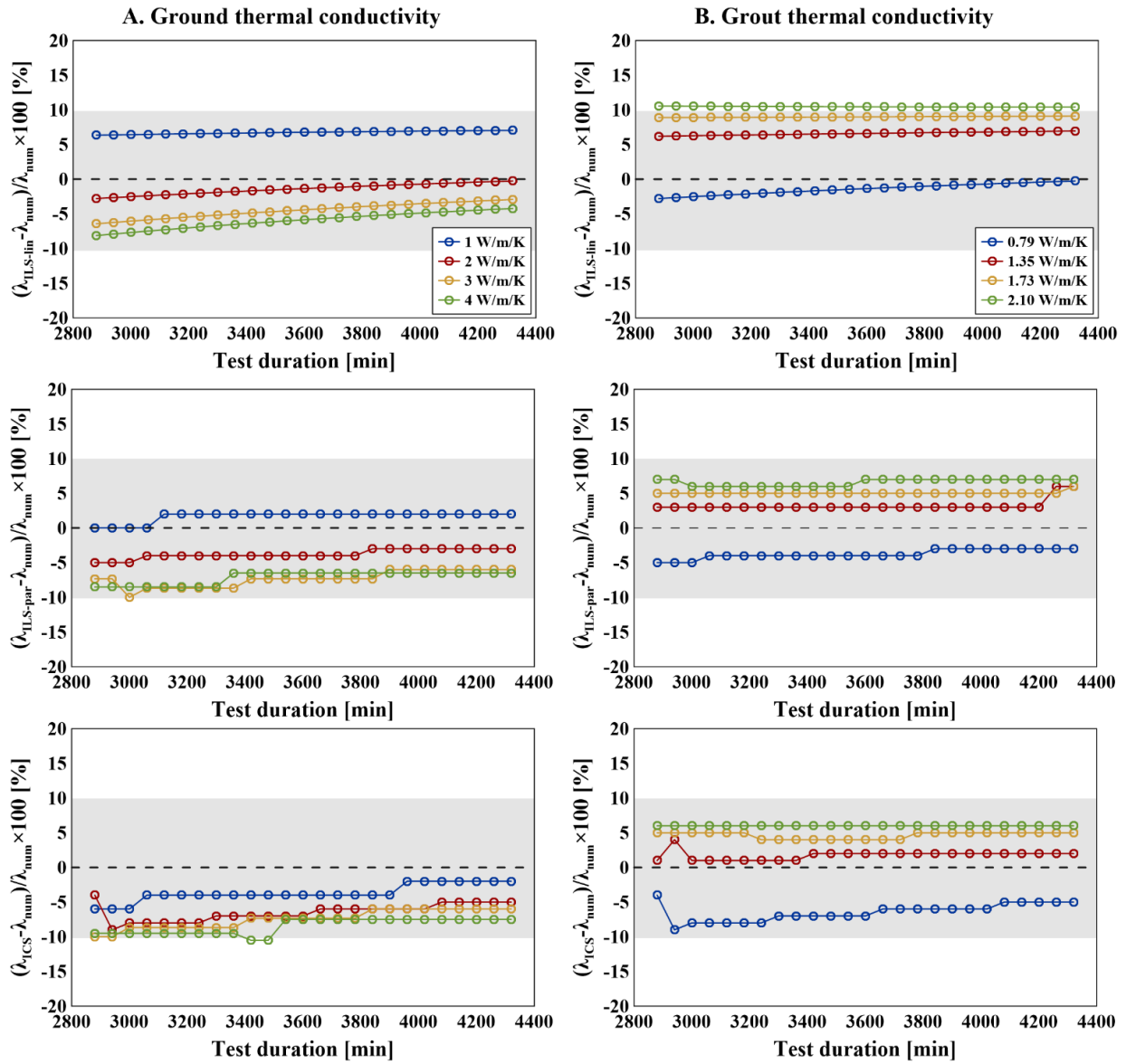


Figure 4 The change in estimated thermal conductivity when the test duration is ranged from 2,880 to 4,320 minutes in cases of (a) Ground thermal conductivity and (b) Grout thermal conductivity. The gray area means the section within the acceptable difference of 10%.

CONCLUSION

This study conducted the analytical analysis to investigate the effect of start time and test duration on TRT interpretation when the thermal properties of BHE and ground were different. First, several numerical simulations were conducted to generate experimental data with different thermal conductivity of the grouting material and ground. Then, three commonly used analytical methods were used to estimate the thermal conductivity, and the influence of start time and test duration on the methods used was compared. The results showed that the start time could have more influence on the effective thermal conductivity more than the test duration. In particular, the ground thermal conductivity had a greater impact on the start time. In these results, the effective thermal conductivity could be appropriately estimated when the start time was greater than 600 minutes and the test duration was greater than 3,540 minutes (with the start time of 720 minutes). However, it is difficult to generalize these results because there are a lot of factors related to the characteristics of the ground and BHE. Other factors should be considered to suggest the appropriate start time and test duration. These results suggest that it is important to consider BHE and ground characteristics for accurate TRT analysis. This analysis is expected to help design the BHE more efficiently.

ACKNOWLEDGMENTS

This work was supported by the National Research Foundation of Korea (NRF) grant funded by the Korea government (MSIP) (No. 2022R1A2C1006696). This work was also supported by the Institute for Korea Spent Nuclear Fuel (iKSNF) and National Research Foundation of Korea (NRF) grant funded by the Korean government (Ministry of Science and ICT, MSIT) (Grant number: 2021M2E1A1085200).

NOMENCLATURE

V_n	=	Arbitrary subdomain bounded by the closed surface Γ_n (m^3)
n	=	Normal vector on the surface element $d\Gamma_n$ pointing inward into V_n (-)
F	=	Heat flux (mW/m^2)
q	=	Heat sources or sinks (J/s)
M	=	Heat accumulation term (J/m^3)
ρ	=	Density (kg/m^3)
c	=	Specific heat ($J/kg/K$)
λ	=	Thermal conductivity ($W/m/K$)
T	=	Temperature ($^{\circ}C$)
q_{tb}	=	Heat flow rate per unit length of the borehole (W/m)
r	=	Radial distance (m)
α	=	Thermal diffusivity (m^2/s)
T_o	=	Undisturbed ground temperature ($^{\circ}C$)
t	=	Time (s)
γ	=	Euler's constant ($=0.5722$) (-)
R_b	=	Effective borehole resistance (mK/W)
R	=	Dimensional cylindrical radius ($=r/r_0$) (-)

J_n = Bessel function of the first kind of order n
 Y_n = Bessel function of the second kind of order n

Subscripts

eff = Effective
 f = Fluid
 b = Borehole wall
 $model$ = Modeled
 $meas$ = Measured
 ILS = Infinite line source (ILS) model
 ICS = Infinite cylindrical source (ICS) model
 lin = Linear regression method
 par = Parameter estimation method
 $grout$ = Grouting material
 $ground$ = Ground
 num = Numerical model

REFERENCES

- Beier, R.A. and Smith, M.D. 2003. *Minimum duration of in-situ tests on vertical boreholes*. ASHRAE Transactions, 109, 475.
- Brettmann, T. and Amis, T. 2011. *Thermal conductivity evaluation of a pile group using geothermal energy piles*. In Geo-Frontiers 2011: Advances in Geotechnical Engineering (pp. 499-508).
- Carslaw, H. S. and Jaeger, J. C. 1959. *Conduction of heat in solids*. Oxford, UK: Oxford University Press.
- Choi, J. M., Lee, C., Park, M., Kang, S. H. and Choi, H. 2011. *Numerical simulation for thermal response test performance in closed-loop vertical ground heat exchanger*. Science China Technological Sciences, 54(7), 1668-1673.
- Eklöf, C. and Gehlin, S. 1996. *TED: a mobile equipment for thermal response test*. Master's Thesis, 1996: 198E, Luleå University of Technology, Sweden.
- Gehlin, S. 2002. *Thermal response test: method development and evaluation*. PhD Thesis, Luleå University of Technology, Sweden.
- Ingersoll, L. R., Zabel, O. J. and Ingersoll, A. C. 1954. *Heat conduction with engineering, geological, and other applications*. New York, USA: McGraw-Hil.
- Jung, Y., Pau, G. S. H., Finsterle, S. and Doughty, C. 2018. *TOUGH3 user's guide*. University of California, Berkeley.
- Kavanaugh, S. P. 2000. *Field tests for ground thermal properties--methods and impact on ground-source heat pump design*. Univ. of Alabama, Tuscaloosa, AL (US).
- Kim, S. K., Bae, G. O. and Lee, K. K. 2015. *Improving accuracy and flexibility of numerical simulation of geothermal heat pump systems using Voronoi grid refinement approach*. Geosciences Journal, 19(3), 527-535.
- Marcotte, D. and Pasquier, P. 2008. *On the estimation of thermal resistance in borehole thermal conductivity test*. Renewable energy, 33(11), 2407-2415.
- Mogensen, P. 1983. *Fluid to duct wall heat transfer in duct system heat storages*. Document-Swedish Council for Building Research, (16), 652-657.
- MOTIE. 2019. *Standards of Support, Installation, and Management of New and Renewable Energy system*. South Korea.
- Pruess, K., Oldenburg, C. M. and Moridis, G. J. 1999. *TOUGH2 user's guide version 2* (No. LBNL-43134). Lawrence Berkeley National Lab.(LBNL), Berkeley, CA (United States).
- Raymond, J., Therrien, R., Gosselin, L. and Lefebvre, R. 2011. *A review of thermal response test analysis using pumping test concepts*. Groundwater, 49(6), 932-945.
- Signorelli, S., Bassetti, S., Pahud, D. and Kohl, T. 2007. *Numerical evaluation of thermal response tests*. Geothermics, 36, 141-166.
- Stauffer, F., Bayer, P., Blum, P., Giraldo, N. M. and Kinzelbach, W. 2013. *Thermal use of shallow groundwater*. CRC Press.

Uncertainty assessment of the hydraulics properties surrounding a standing column well with a thermal response test

Louis Jacques

Philippe Pasquier

ABSTRACT

The standing column well (SCW) is known for being a highly efficient ground heat exchanger as it relies on both conduction and advection heat transfer processes. Therefore, the interpretation of a thermal response test (TRT) is strongly influenced both by the hydraulic and thermal properties surrounding the SCW. In this study, it is shown that a TRT can allow identifying the thermal and hydraulic properties around a SCW. The analysis is conducted in a Bayesian framework allowing an accurate and robust identification of the hydraulic properties and their uncertainties. A closed-form expression of the likelihood is used to consider the autocorrelation of the residuals between observed and simulated temperatures. A coupled numerical model is used to generate a training database for an artificial neural network. Then, the latter serves as an emulator of the SCW's short-term g-function given various input parameters. A case study is presented based on a 100-hour TRT performed on a SCW built at a demonstration site located in the city of Mirabel, Canada. For the specific site studied, hydraulic properties were identified with an uncertainty of less than 30 % at a two-sigma level. Such important results lead to more appropriate and efficient design of SCWs.

INTRODUCTION

A ground source heat pump system using SCWs can provide significant energy savings and low peak power usage for buildings (Beaudry *et al.*, 2022). Such ground heat exchangers are also particularly suitable for dense urban areas (Pasquier *et al.*, 2016; Laroche *et al.*, 2022). In a SCW, advective and conductive heat transfer processes are active within the borehole and the geological material surrounding it. Therefore, the design of SCWs requires identifying both thermal and hydraulic properties (Pasquier *et al.*, 2016). To identify hydraulic conductivities, common practice includes hydrogeological investigations, drilling of a test well and pumping tests (Snijders & Drijver, 2016; Beaudry *et al.*, 2018). For the estimation of thermal properties, a TRT can be conducted. For SCWs, estimating the thermal properties with purely conductive models can lead to unrealistic values when hydraulic conductivity is high (Jeon *et al.*, 2016; Robert *et al.*, 2022). However, the interpretation of such a TRT can be done with coupled hydraulic and thermal numerical models (Beaudry *et al.*, 2018; Robert *et al.*, 2022).

Indeed, Robert *et al.* (2022) recently interpreted a TRT in the presence of high hydraulic conductivity ($>5 \times 10^{-5}$ m/s) and obtained a mean absolute error of 0.04 °C between the modelled and measured temperatures. To construct their numerical model, the values of the layered hydraulic conductivity were chosen based on the groundwater cumulative flow observed during drilling and matched with the mean hydraulic conductivity estimated with a pumping test. In this model, the hydrostratigraphic properties are essential to accurately reproduce the measured temperatures (Beaudry *et al.*,

Louis Jacques (louis.jacques@polymtl.ca) is a PhD candidate at Polytechnique Montréal and Philippe Pasquier is a professor of Geological Engineering at Polytechnique Montréal.

2019). For closed-loop ground-heat exchangers, the identification of hydraulic flux with a thermal response test has been demonstrated in presence of advection. Indeed, interpretation methods have proposed to use the Peclet number to deduce groundwater velocities (Lehr & Sass, 2014; Rouleau *et al.*, 2016) and average hydraulic conductivity (Wagner *et al.*, 2014). Moreover, Lehr & Sass (2014) made use of the groundwater cumulative flow observed during drilling to correlate Peclet number to the thermal conductivity along the profile. Altogether, no TRT interpretation method has yet offered a robust identification of the hydraulic properties around SCWs.

Robustness implies that the methodology employed leads to accurate results, while also dealing with any error it faces. For TRT, errors come from three sources according to Witte (2013). These are measurement errors (instrument precision and resolution), parameter errors (fixed parameters such as borehole length or radius) and model errors (accuracy of the conceptual model itself). For a simple analytical model, an analytical expression of the uncertainty can be used to describe the confidence interval of the variables (Witte, 2013). For more complex mathematical models, Pallard & Lazzarotto (2021) developed a methodology in a stochastic framework taking into account the measurement error and allowing for bias estimation. With a similar goal in mind, Choi *et al.* (2018a) used Bayesian inference to obtain the statistical distributions of unknown thermal properties. Yet, their approach neglected the temporal correlation of the residuals, which is present in temporal series. To solve this problem and accelerate inference, Pasquier & Marcotte (2020) proposed a closed-form equation for the likelihood and an artificial neural network for direct simulations.

In a similar way, this article proposes to use Bayesian inference to assess both the hydraulic and thermal properties surrounding a SCW with TRT data. The methodology used provides the marginal and joint distributions of the properties and, thus, an uncertainty quantification. Since the approach requires millions of simulations, an efficient direct model in the form of a neural network is trained to reproduce the temperatures measured at an experimental SCW. The following sections describe the methodology, an overview of the experimental setup and the main results obtained.

METHODOLOGY

Bayesian Inference

The Bayesian inference framework leads to the marginal and joint distributions of variables Θ by drawing from the posterior distribution $P(\Theta|x)$ given observations x . In the case of a TRT, these observations are the residuals between the simulated and observed temperatures. The posterior is sampled using a Markov Chain Monte Carlo (MCMC) algorithm which makes use of the simplified Bayes Theorem (Equation 1).

$$P(\Theta|x) \propto P(\Theta) \cdot P(x|\Theta) \quad (1)$$

Prior distributions $P(\Theta)$. Firstly, the prior is defined before observations are available. Indeed, a prior reflects an expert judgment of a random variable behaviour. Previously, both Choi *et al.* (2018a) and Pasquier & Marcotte (2020) opted for non-informative uniform priors for all variables. The inference results for these studies showed Gaussian marginal distributions for the thermal properties. Considering these past results, Choi *et al.* (2018b) used triangular prior for the effective thermal conductivity. Again, they obtained marginal distributions following a Gaussian model. On this basis, the present study is using Gaussian distribution as prior, but large standard deviations (σ) are used for each variable. A similar approach was used for hydraulic conductivity as this assumption allows the mean hydraulic conductivity to stay closer to the one deduced from the pumping test.

Likelihood function $P(x|\Theta)$. The second step is to evaluate the likelihood function which expresses the probability of making observations conditional to some input properties. The likelihood of the residuals is described by a zero-mean multi-Gaussian distribution which considers temporal correlation, as expressed by Equation (2).

$$P(x|\Theta) = (2\pi)^{-\frac{n}{2}} |\Sigma|^{-\frac{1}{2}} e^{-\frac{1}{2}x'\Sigma^{-1}x} \quad (2)$$

For large covariance matrix (Σ), evaluation of Equation 2 is costly and this work used the exact closed-form solution

proposed by Pasquier & Marcotte (2020) to ease its evaluation. The solution requires modeling the variogram of the residuals and estimation of the variance and correlation range.

Posterior sampling $P(\Theta|\mathbf{x})$. To sample the posterior distribution an ensemble slice sampler based on the work of Karamanis & Beutler (2021) and allowing for a parallel and efficient inference was used. The sampler was employed with 50 parallel chains and 100 000 samples per chain. Since the acceptance rate was around 15%, the direct model was called more than 33 million times. A fast and efficient direct model is therefore required to complete the inference in a realistic time frame.

Direct Model and Training Database

A coupled numerical model was constructed within the Comsol Multiphysics environment (Comsol, 2022) to simulate groundwater flow and heat transfer. This model was used to assemble a training database that was used later to train an artificial neural network (ANN) designed to construct the short-term g-function of the SCW. The numerical modelling strategy is the same as the one described by Beaudry *et al.* (2019). An axisymmetric model is used to represent the SCW with the center of the well located on the symmetry axis. Table 1 presents the main components of the numerical model as reported by Robert *et al.* (2022) for the study site. The thermal conductivities of the subsurface materials ($k_{s,i}$) and the hydraulic conductivities of the hydrostratigraphic layers ($K_{h,i}$) are variable in the inference. The thermal boundary conditions are composed of a null heat flux at the bottom of the model and a constant temperature at the surface and at the far field. These boundary conditions are based on the quasi-constant temperature observed in the wells during three different thermal profile logging. Regarding the hydraulic boundary conditions, flow was restricted at the bottom and top of the model and a constant hydraulic head was applied at the far-field limit to represent the fact that groundwater was 2.5 m deep. Finally, the groundwater flow was simulated under a steady state since a long continuous circulation phase is conducted in the TRT before heat injection.

Table 1. Numerical model main components for the SCW and subsurface materials

Parameter	Units	Water/Well	HDPE	Till	Sandy dolomite	Quartz arenite
Thickness (b)	m	133.20	0.00549	10.05	89.01	34.14
Diameter	m	0.152	0.0493 /0.0603	150*	150*	150*
Porosity	%	-	0.001	20	2.2	5.9
Volumetric heat capacity (C)	MJ/(m ³ K)	4.18	2.28	2.30	2.31	2.18
Thermal conductivity (k)	W/(m K)	0.56	0.42	Θ	Θ	Θ

*This diameter represents the extension of the axisymmetric numerical model.

Artificial Neural Network and Simulation Approach

The numerical model exploits an optimized mesh and efficient solver. However, computation of the g-functions is still long for the current purpose of this study. Indeed, every call of the numerical model requires more than a minute and the inference process would converge after multiple years of computation. To accelerate the inference, an ANN inspired from Pasquier *et al.* (2018) and Pasquier & Marcotte (2020) was used as a surrogate model. The ANN architecture includes 10 hidden layers with 50 neurons each and an output layer of 95 neurons. The input layer is composed of seven parameters (Θ) and nine enriched parameters (ψ), chosen to accelerate network training. Here, these parameters are the thermal diffusivity ($\alpha=k/C$), hydraulic transmissivity ($K \cdot b$) and the weighted average of k and K (\bar{k} and \bar{K}). Table 2 summarizes these parameters. Before training the ANN, a transformation is applied to the short-term g-function as it also helps the training process. Moreover, a normalization between -1 and +1 is applied to all input and output.

Table 2. Training parameters (θ) and enriched parameters (ψ)

Parameter	Till	Sandy dolomite	Quartz arenite	Hydrostratigraphic layers			
θ	$k_{s,1}$	$k_{s,2}$	$k_{s,3}$	$K_{h,2}$	$K_{h,3}$	$K_{h,4}$	$K_{h,5}$
ψ	$\alpha_{s,1}$	$\alpha_{s,2}$	$\alpha_{s,3}$	$K_{h,2} \cdot b_{h,2}$	$K_{h,3} \cdot b_{h,3}$	$K_{h,4} \cdot b_{h,4}$	$K_{h,5} \cdot b_{h,5}$
		\bar{k} (weighted average)		\bar{K} (weighted average)			

The ANN directly provides the g-function corresponding to the entering water temperature (EWT) at the TRT unit (Figure 1 a)). Then, the leaving water temperature (LWT) signal is obtained efficiently using fast Fourier transforms (see Marcotte & Pasquier, 2008, Pasquier et al. 2018) through:

$$LWT(t) = T_{i=0} + (f * g)(t) + \Delta T(t) \quad (3)$$

where g is the short-term g-function and f is the excitation function specified by Equation (4).

$$f(t) = \Delta T(t_i) - \Delta T(t_{i-1}) = \frac{\dot{Q}(t_i) - \dot{Q}(t_{i-1})}{\dot{V}c} \quad (4)$$

Experimental Case Study

A TRT was conducted at an experimental site located in the city of Mirabel, Québec. The study site is described in detail by Robert *et al.* (2022). Figure 1 a) presents the TRT unit connected to the SCW. The TRT unit includes monitoring of the entering and leaving water temperature (EWT and LWT). For their base case, Robert *et al.* (2022) demonstrated an optimal fit of temperatures with specific values of thermal and hydraulic conductivities. Figure 1b) shows these base case values for the thermal conductivity varying according to the three subsurface materials. Figure 1c) shows the

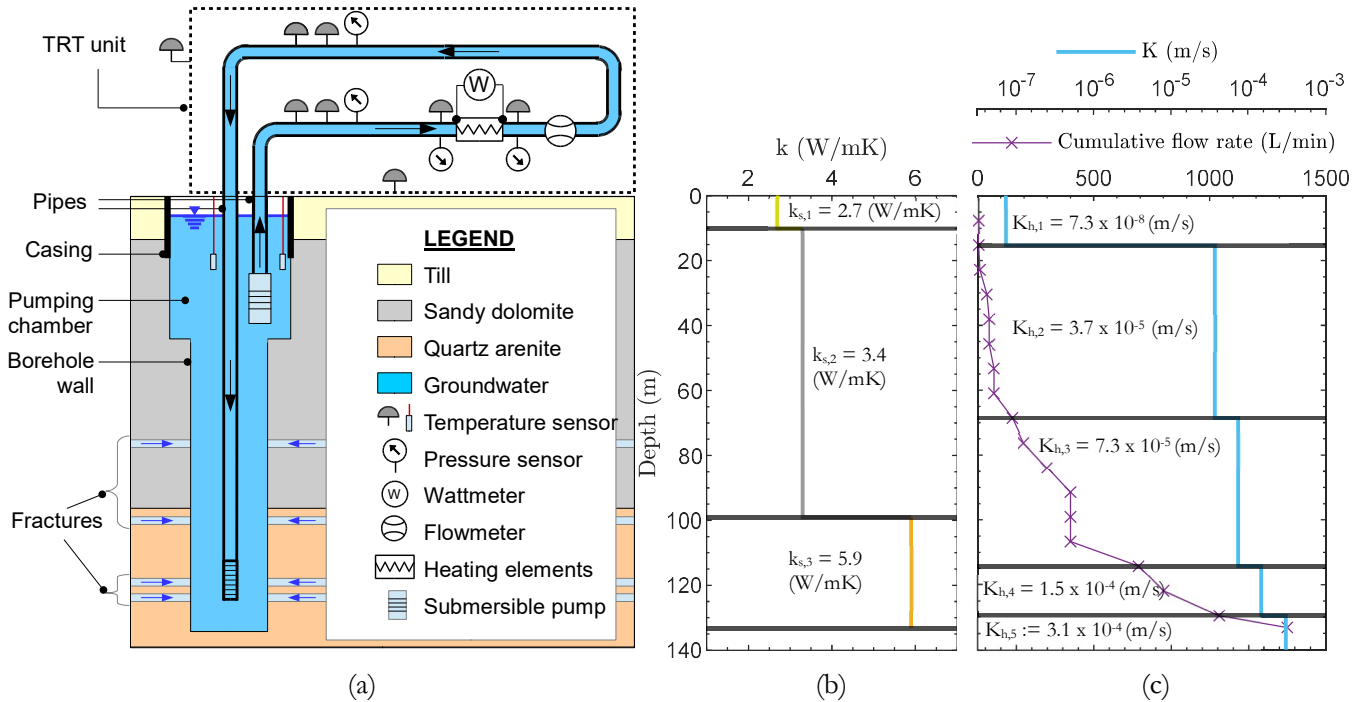


Figure 1 a) Stratigraphy, experimental SWC and TRT unit. b). Stratigraphy and base case values of thermal conductivity ($k_{s,i}$ for $i=1, 2$ and 3) for each subsurface materials. c) Hydrostratigraphy, groundwater flow rates observed during drilling and base case values of hydraulic conductivity ($K_{h,j}$ for $j=1,2,3,4$ and 5) for each hydrostratigraphic layers is shown in pale blue.

hydraulic conductivity following the five different hydrostratigraphic units (light blue). These hydrostratigraphic units are based on the variation of groundwater flow regime in the materials and their delimitation is independent of the nature of these materials. This hydraulic conductivity profile matches the groundwater cumulative flow observed while drilling and the mean value of 6.5×10^{-5} m/s obtained by the pumping test (Robert et al., 2022). Also, Figure 1c) illustrates groundwater cumulative flow rates observed while drilling.

Figure 2 (upper left) presents the observed LWT during the TRT and the simulated temperatures. The temperature variation ΔT is used to evaluate the excitation function $f(t)$ shown on the right axis. This TRT is separated in two phases. The first one is a continuous circulation phase that lasted for approximately 18 hours. Afterwards, the heating phase was started and lasted 83 hours. During this phase, the heating elements were powered at around 21 kW. Figure 2 (lower left) presents the residuals between simulated and observed temperatures during the heating phase. Note that the first 4.67 hours were discarded. Indeed, the circulation pump was interrupted for 103 minutes prior to the heating phase and fitting the model to the data was more difficult at the onset of the TRT. Finally, Figure 2 (right) shows the variogram corresponding to the optimal residuals as obtained by a single multidimensional optimization. The variogram has a

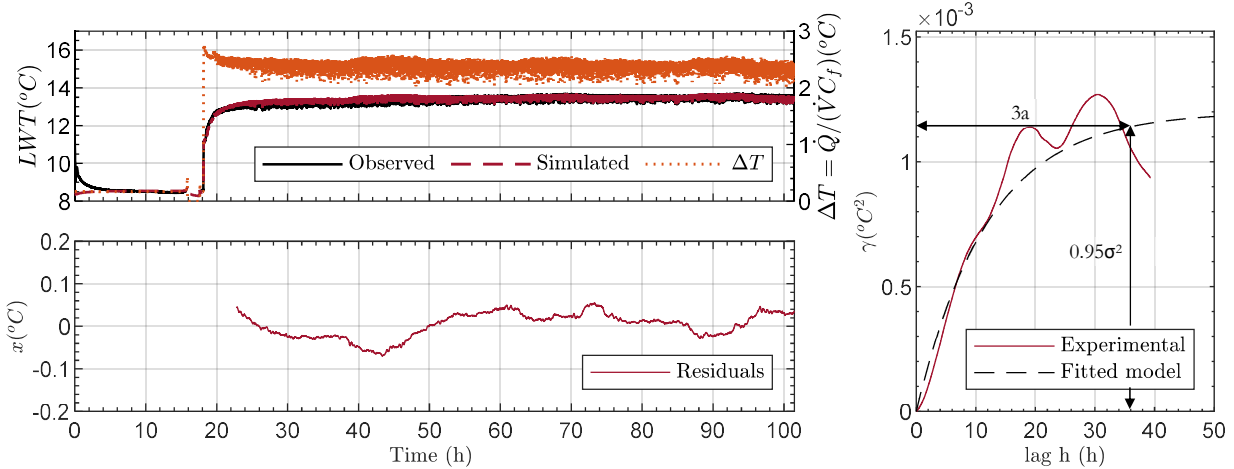


Figure 2 Upper left: Observed and optimal simulated leaving water temperatures used to compute residuals x and temperature variation ΔT used to compute excitation function f . Bottom left: temperature residuals used to compute experimental variogram. Right: experimental variogram (γ) and fitted covariance model.

variance of $\sigma^2 = 1.2 \times 10^{-3}$ °C² and a correlation range of $a = 12$ h.

RESULTS AND DISCUSSION

A Bayesian inference was conducted using the parameters of the experimental variogram to evaluate the likelihood. Gaussian priors were set for the three subsurface thermal conductivities ($k_{s,i}$ for $i=1, 2$ and 3) and for the four deepest hydraulic conductivities ($K_{h,j}$ for $j=2$ to 5). Indeed, the first hydrostratigraphic layer is not inferred as this layer is sealed with a casing for most of its depth. Hence, we observed that this layer's hydraulic conductivity has no significant influence on the evolution of EWT.

The Bayesian inference is completed with a posterior distribution of 100 000 samples for each of the 50 chains, for a total of 5 million samples. The acceptance rate reached 14.4 %, resulting in a total of 34.7 million simulations and a computation time of approximately 116 hours. A burn-in period of 50 000 samples per chain was used to analyze the marginal and joint distributions. Accordingly, Figure 3 presents these distributions, along with a scatter plot showing the correlation between each pair of variables. On the diagonal, the marginal samples are plotted in orange, while the green line corresponds to the prior distributions. As an indication of the success of the inference, the mean absolute

error of the corresponding residuals stands between $0.02\text{ }^{\circ}\text{C}$ and $0.04\text{ }^{\circ}\text{C}$ (at a two-sigma level). These results correspond to the mean absolute error (MAE) of $0.04\text{ }^{\circ}\text{C}$ obtained by Robert *et al.* (2022) for their base case and which correspond to the vertical black lines in Figure 3.

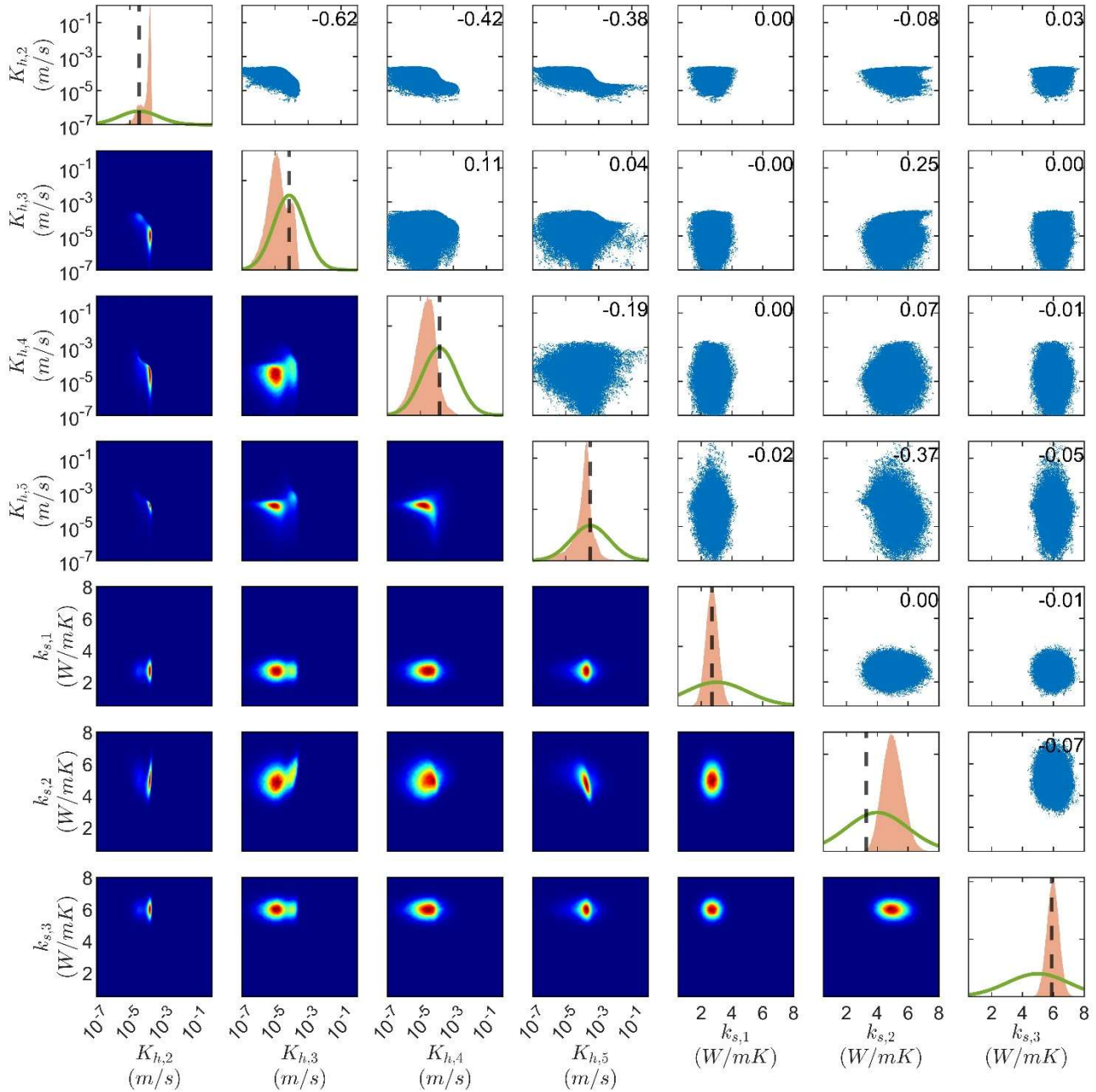


Figure 3 - Marginal (diagonal) and joint (lower triangle) distributions of the hydraulic conductivity of the four deepest hydrostratigraphic layers ($K_{h,j}$ for $j=2, 3, 4$ and 5) and thermal conductivity of the different subsurface materials ($k_{s,i}$ for $i=1, 2$ and 3). Scatter plots and correlation (upper triangle). On the diagonal, the Gaussian prior are drawn in green and the dashed black lines represents the base case values from Robert *et al.* (2022).

The most striking result is the fact that inferred distributions are all well defined Gaussian-like distributions and all significantly differ from their priors. Even more interesting is the fact that the mean hydraulic conductivity obtained in this work is almost the same as the one obtained by a pumping test. Indeed, Figure 4 a) presents the weighted average for all samples of K using the unit's thickness b as weight. The mean value inferred is 7.5×10^{-5} m/s while a value of 6.5×10^{-5} m/s was obtained with a pumping test, leading to a difference of +1.5 % of their logarithmic value. Therefore, inferring hydraulic properties with a TRT is feasible and can be done with great accuracy.

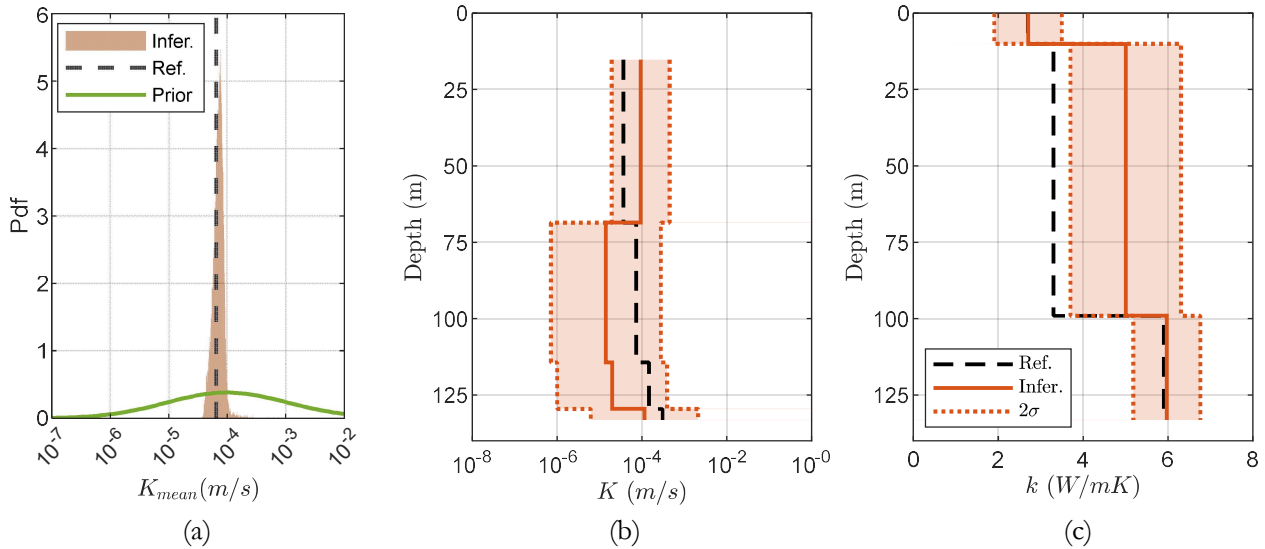


Figure 4 - a) Weighted average of the hydraulic conductivities. Values obtained by inference (orange), by a pumping test (black) or given by the prior (green). b) Mean hydraulic conductivities for each hydrostratigraphic unit and c) and thermal conductivity of subsurface materials and their uncertainties at a two-sigma level.

Figure 4b) presents a comparison with the reference case from Robert *et al.* (2022) for the inferred hydraulic conductivities. The mean values of the marginal distributions for the three deepest units are all inferior (orange dashed line) to the reference case, while the value of the second layer is higher. Thus, the inferred mean values observed on Figure 4b) contradict the pattern of the reference case that was based on the cumulative groundwater flow observed during drilling (see Figure 1). In fact, these drilling observations are prone to increasing error as the cumulative flow rise. This is somehow illustrated by the fact that confidence interval for the hydraulic conductivities increases with depth with values of 6 %, 18 %, 19 % and 22 %. Even so, all hydraulic conductivities from the reference case are within the uncertainty of the inferred hydraulic conductivities.

For the thermal conductivities, Figure 4c) indicates that the values of the first and last subsurface materials are unchanged in comparison with the reference case. However, the value inferred for the sandy dolomite ($k_{s,2}$) reached 5.0 W/(mK) in contrast with expected value of 3.4 W/(mK), leading to a difference of 47 %. It should be noted, however, that the value of 3.4 W/(mK) comes from a laboratory test performed on a rock sample gathered a few kilometers from the study site. To finish, we mention that as reported by Jeon *et al.* (2016), it is difficult to obtain accurate thermal conductivity in a context of high hydraulic conductivity ($>5 \times 10^{-5}$ m/s).

CONCLUSION

In this paper, a methodology is proposed to infer hydraulic conductivities and their uncertainties with a thermal response test (TRT) conducted on a standing column well (SCW). In a Bayesian framework, the computation of likelihood is completed considering residuals between measured and simulated temperatures. To ease the evaluation of the likelihood, an exact closed-form solution of the likelihood is employed. The temperature is simulated with an artificial neural network mimicking a numerical model that couples heat transfer and groundwater flow. A case study presents a TRT conducted on a SCW. High cumulative groundwater flows were observed during drilling. Thus, advective heat transfer plays an important role for this case study. Using Bayesian inference, it was shown that identification of hydraulic properties is possible with a thermal test. The average hydraulic conductivity inferred has a difference of 1.5 % in comparison with the results of a pumping test conducted on the same SCW. Moreover, the highest confidence interval reached 22 % for the hydraulic properties.

ACKNOWLEDGMENTS

The authors acknowledge the support from partners of the Geothermal Research Chair on the Integration of SCWs in Institutional Buildings, namely Hydro-Québec, the Ministry of higher education of Québec, CSSMI, CSSDM, CSSS, Versa Profiles, Marmott Energy, CanmetEnergy and NSERC. Additionally, we thank the anonymous reviewers and colleagues (A. Courchesne and M. Arbi Ben Aoun) that provided constructive comments. This work was financed by the Natural Sciences and Engineering Research Council of Canada through grant number ALLRP 544477-19.

NOMENCLATURE

α	= thermal diffusivity (m ² /s)	P	= probability
b	= thickness (m)	\dot{Q}	= heating power (W)
C	= volumetric heat capacity (J/(m ³ K))	σ	= standard deviation
f	= excitation function (°C)	T	= temperature (°C)
g	= short term g-function (-)	Θ	= parameters
γ	= variogram function (units ²)	Ψ	= enriched parameters
φ	= diameter (m)	x	= temperature residuals (°C)
k	= thermal conductivity (W/(mK))	\dot{V}	= circulation flow rate (m ³ /s)
K	= hydraulic conductivity (m/s)		
n	= number of residuals (-)		

Subscripts

h	= hydrostratigraphic layer	s	= subsurface layer
-----	----------------------------	-----	--------------------

REFERENCES

- Beaudry, G., Pasquier, P., and D. Marcotte. 2018. *Hydrogeothermal characterization and modelling of a standing column well experimental installation*. Proceedings of the IGSHPA Research Track 2018, 1–10.
- Beaudry, G., Pasquier, P., and D. Marcotte. 2019. *The impact of rock fracturing and pump intake location on the thermal recovery of a standing column well: Model development, experimental validation, and numerical analysis*. Science and Technology for the Built Environment, 25(8)
- Beaudry, G., Pasquier, P., Marcotte, D., and A. Zarrella. 2022. *Flow rate control in standing column wells: A flexible solution for reducing the energy use and peak power demand of the built environment*. Applied Energy, 313, 118774.
- Choi, W., Kikumoto, H., Choudhary, R., and R. Ooka. 2018. *Bayesian inference for thermal response test parameter estimation and uncertainty assessment*. Applied Energy, 209, 306–321.

- Choi, W., Menberg, K., Kikumoto, H., Heo, Y., Choudhary, R., and R. Ooka. 2018. *Bayesian inference of structural error in inverse models of thermal response tests*. *Applied Energy*, 228, 1473–1485.
- Comsol A.B. 2022. *COMSOL Multiphysics v. 6.0.*, Stockhol; Sweden.
- Jeon, J.-S., Lee, S.-R., and W.-J. Kim. 2016. *Applicability of thermal response tests in designing standing column well system: A numerical study*. *Energy*, 109, 679–693.
- Karamanis, M., and F. Beutler. 2021. *Ensemble Slice Sampling: Parallel, black-box and gradient-free inference for correlated & multimodal distributions*. ArXiv:2002.06212 [Astro-Ph, Stat].
- Laroche, V., Pasquier, P., and B. Courcelles. 2022. *Integration of standing column wells in urban context: A numerical investigation-case in the City of Montreal*. *Sustainable Cities and Society*, 78, 103513.
- Lehr, C., and I. Sass. 2014. *Thermo-optical parameter acquisition and characterization of geologic properties: A 400-m deep BHE in a karstic alpine marble aquifer*. *Environ Earth Sci*, 17.
- Marcotte, D., and P. Pasquier. 2008. *Fast fluid and ground temperature computation for geothermal ground-loop heat exchanger systems*. *Geothermics*, 37(6), 651–665.
- Pallard, W. M., and A. Lazzarotto. 2021. *Thermal response tests: A biased parameter estimation procedure?* *Geothermics*, 97, 102221.
- Pasquier, P., and D. Marcotte. 2020. *Robust identification of volumetric heat capacity and analysis of thermal response tests by Bayesian inference with correlated residuals*. *Applied Energy*, 261, 114394; 1–18.
- Pasquier, P., Nguyen, A., Eppner, F., Marcotte, D., and P. Baudron. 2016. *10—Standing column wells*. In S. J. Rees (Ed.), *Advances in Ground-Source Heat Pump Systems* (pp. 269–294). Woodhead Publishing.
- Pasquier, P., Zarrella, A., and R. Labib. 2018. *Application of artificial neural networks to near-instant construction of short-term g-functions*. *Applied Thermal Engineering*, 143, 910–921.
- Robert, S., Pasquier, P., and A. Nguyen. 2022. *Impact of layered heterogeneity on thermal response test interpretation performed on a standing column well operated without bleed*. *Geothermics*, 101, 102353.
- Rouleau, J., Gosselin, L., and J. Raymond. 2016. *New concept of combined hydro-thermal response tests (H/TRTS) for ground heat exchangers*. *Geothermics*, 62, 103–114.
- Snijders, A. L., and B. C. Drijver. 2016. *9—Open-loop heat pump and thermal energy storage systems*. In S. J. Rees (Ed.), *Advances in Ground-Source Heat Pump Systems* (pp. 247–268). Woodhead Publishing.
- Wagner, V., Bayer, P., Bisch, G., Kübert, M., and P. Blum. 2014. *Hydraulic characterization of aquifers by thermal response testing: Validation by large-scale tank and field experiments*. *Water Resources Research*, 50(1), 71–85.
- Witte, H. J. L. 2013. *Error analysis of thermal response tests*. *Applied Energy*, 109, 302–311.



Field tests and numerical simulation of a novel thermal response test equipment for water wells

Satoshi Tanaka
Shunsuke Tsuya

Hikari Fujii

Hiroyuki Kosukegawa

ABSTRACT

The objective of this study is to develop a novel thermal response test (TRT) equipment that can be applied to existing water wells instead of borehole heat exchangers (BHEs). Accordingly, field tests were conducted using new and conventional equipment to estimate the vertical distribution of ground thermal conductivity. The result showed that the estimated thermal conductivity profile was higher than the reference profile obtained using conventional equipment. The temperature behavior in the well was considered to be unstable due to natural convection because the heating time was 4 hours, which is not long enough. Next, a numerical model of the water well including the novel equipment was developed, and the model was validated through history matching by using the temperature change in each depth. Finally, the TRT was simulated for two days using the model, and the simulated thermal conductivity profile was similar to the reference profile except near the end of the heated section. This result indicates that a more accurate thermal conductivity profile can be obtained by increasing the heating time until approximately 1.5 days.

INTRODUCTION

The installation of a ground source heat pump (GSHP) system requires drilling a borehole heat exchanger (BHE) to extract and inject heat from and to the ground. However, drilling costs associated with a BHE are higher in Japan than those in other countries because of complex geological structures. The high drilling cost is one of the factors hindering the widespread use of GSHP systems. Therefore, optimizing the length and number of BHEs is important for minimizing the drilling costs. A thermal response test (TRT) is necessary for estimating the thermal properties of the ground and the heat exchange capacity of the BHEs. However, the conventional TRT is conducted using a BHE, which requires drilling of BHEs in the preliminary investigation phase, thus resulting in high costs and operation times.

The objective of this research is to develop a novel TRT equipment that can be applied to existing water wells instead of BHEs for estimating the vertical distribution of thermal conductivities. TRTs using existing water wells can be implemented at lower costs and in a shorter time than the conventional TRT using BHE, as no new wells need to be drilled. If the validity of the proposed equipment can be demonstrated, it can be used to implement TRTs in several wells in Japan, such as pumping wells, re-injection wells, snowmelt wells, and observation wells. In addition, the potential map of the GSHP system is expected to become more sophisticated owing to a significant increase in the number of wells capable of performing TRTs.

Satoshi Tanaka (m6022220@s.akita-u.ac.jp) is a master course student, Hikari Fujii is a professor, Kosukegawa Hiroyuki is a chief engineer, and all at the graduate school of international resource sciences at Akita University. Shunsuke Tsuya is an assistant section chief, Development Department General Heatpump Industry Co., Ltd.

We reviewed research about TRTs for estimating the distribution of thermal conductivities. Fujii et al. (2006) conducted TRTs using optical fiber thermometers in two types of BHEs and estimated the distribution of thermal conductivities of the ground using a nonlinear regression method. Moreover, Fujii et al. (2009) estimated the distribution of thermal conductivities using the optical fiber sensors inserted into the U-tubes and indicated the reliability of the optical fiber and interpretation method by consistent estimated distribution with the measured one. Raymond et al. (2015) installed ten short heating cables in the pipe of the heat exchanger to inject heat and estimate the distribution of subsurface thermal conductivity. Isabel et al. (2018) conducted distributed thermal response tests (DTRT) using a heating cable and a fiber optic temperature sensor and attempted to obtain the thermal conductivity distribution. Zhang et al. (2020) conducted an actively heated fiber optics based TRT (ATRT) and obtained a reliable thermal conductivity distribution through comparison with the results of a conventional TRT. A type of copper mesh heated optical cable was used in the ATRT as a heating source along with a temperature sensing cable. Hakara et al. (2022) presented an enhanced thermal response test (ETRT) using a hybrid cable containing copper wires and fiber optics and determined the vertical distributions of thermal conductivities along the drill hole. Advanced TRTs for estimating the distribution of thermal conductivities were summarized by Wilke et al. (2020). However, TRTs using existing water wells by fixing the heating cable and optical fiber on the casing have not been mentioned so far.

Next, we present a study about TRT using ungrouted BHEs. Fujii et al. (2016) conducted an experimental study to confirm the applicability of a TRT to ungrouted wells. They compared the results of a TRT conducted using an ungrouted BHE saturated with groundwater to those of a TRT conducted using a BHE filled with silica sand. They found good agreement between the interpretation results for both the average and depth-specific thermal conductivities. The results indicate that TRTs using ungrouted BHE with casing inner diameters of up to 100 mm are feasible for estimating the thermal conductivity of the ground. Therefore, TRT can be implemented in small-diameter water wells by inserting a U-tube. However, thus far, no TRT equipment using an optical fiber thermometer has been developed that can be directly applied to a water well of large diameters.

TRT using an ungrouted BHE

First, a TRT was conducted using an ungrouted BHE to obtain the vertical distribution of the ground thermal conductivity as reference data. The test field was located on the Akita University campus in Akita City, northern Japan (Fig. 1(a)). The BHE was 60 m long and had a hole diameter of 230 mm. The BHE is cased with the 150 mm/160 mm ID/OD steel casing. The well screen ranged between 42 to 47.5 m, and the BHE was filled with groundwater below the groundwater level of -5.5 m (Fig. 1(b)). The outer and inner diameters of the U-tubes were 34 mm and 27 mm, respectively. The heating medium in the U-tube was 9% ethylene glycol. The inlet and outlet temperatures of the heating medium were measured using the Pt100.

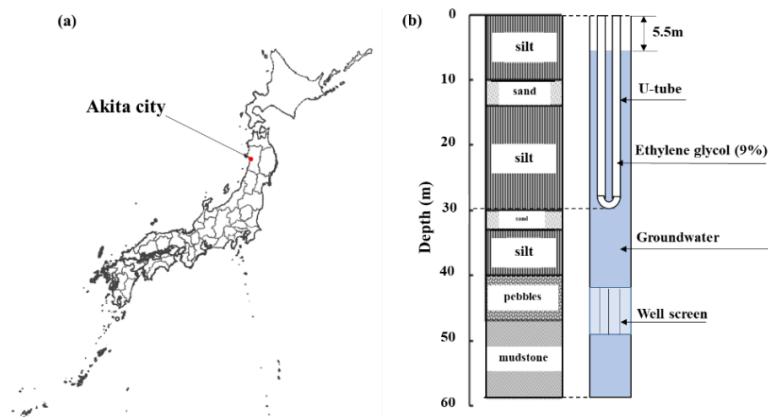


Figure 1 (a) Location of the test field in Japan. (b) Geological columnar section at the test field and overview of the BHE.

The TRT was conducted for 48 h with a circulation rate of 15 L/min and a heating load of 1.5 kW. A fiber-optic thermometer was installed in the U-tube return tube, and the temperature profiles were measured every minute at 0.5 m intervals from the start of the TRT to 72 h after it was completed.

The TRT results are shown in Fig. 2(a). The temperature behavior was temporarily disturbed owing to the reduced heater output during the TRT; however, the heat medium temperature was stable during the entire test period. Figure 2(b) shows the average inlet and outlet temperatures of the heat medium plotted on a semi-logarithmic graph. The apparent thermal conductivity of the ground around the BHE was estimated to be 1.58 W/m/K using the slope method. Additionally, the temperature after the stabilized heater output was used to estimate thermal conductivity. The temperature profiles measured by the optical fiber at each time point are shown in Fig. 3(a). The temperature profiles shown in the figure are at the end of the TRT; 12, 24, 48, and 72 h after the end of the TRT; and before the start of the TRT. Next, we estimated the thermal conductivity profile of the ground using the analysis method proposed by Fujii et al. (2009). This analysis method is based on a nonlinear regression method, and the thermal conductivity profile is estimated by minimizing the evaluation function F defined in equation (1).

$$F = \alpha \sum_{nstep} (T_{o(obs)} - T_{o(cal)})^2 + (1 - \alpha) \sum_{ntest} \left(\sum_{nlayer} (T_{ro(obs)} - T_{ro(cal)})^2 \right) \quad (1)$$

The parameters used for the calculation in Equation (1) are listed in Table 1. Considering the groundwater level, the number of layers was set to 25 (each layer was 1 m thick) because the effective length of the BHE is 25 m. The length and number of time steps were set to 12 min and 240, respectively, corresponding to the period of the TRT. The thermal conductivity profile of the ground around the BHE was estimated using the above-mentioned analysis method (Fig. 3(b)). The average thermal conductivity of the entire ground was 1.51 W/m/K, which was similar to the apparent thermal conductivity of 1.58 W/m/K (Fig. 2(b)). Therefore, the thermal conductivity profile estimated using the analysis method was considered as the reference data.

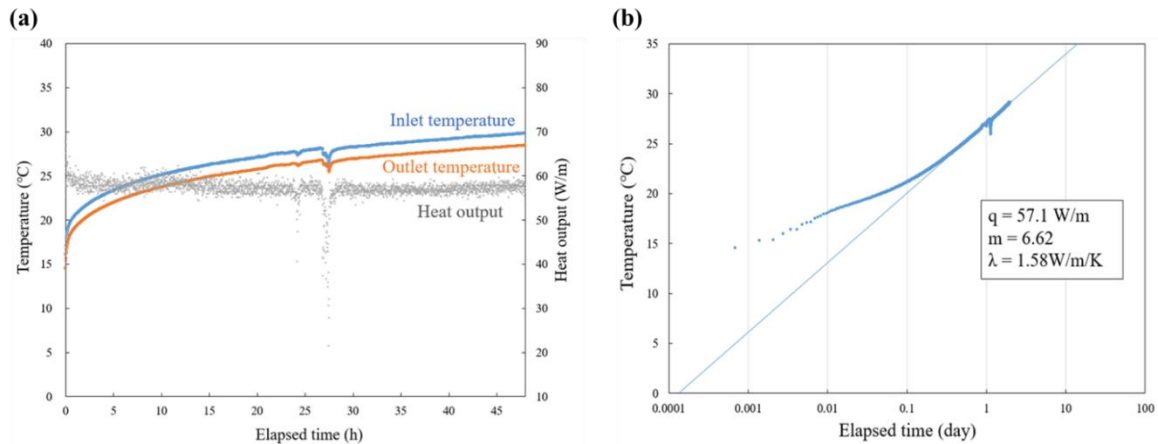


Figure 2 (a) Inlet and outlet temperatures and heat output during the TRT. (b) Change in the average inlet and outlet temperatures of the heat medium.

Table 1. Parameters used in equation (1) to determine the evaluation function

Number of Layers	nlayer	25
Number of calculations	nstep	240
Number of temperature comparisons	nstep	3
Weighting constant	α	0.05

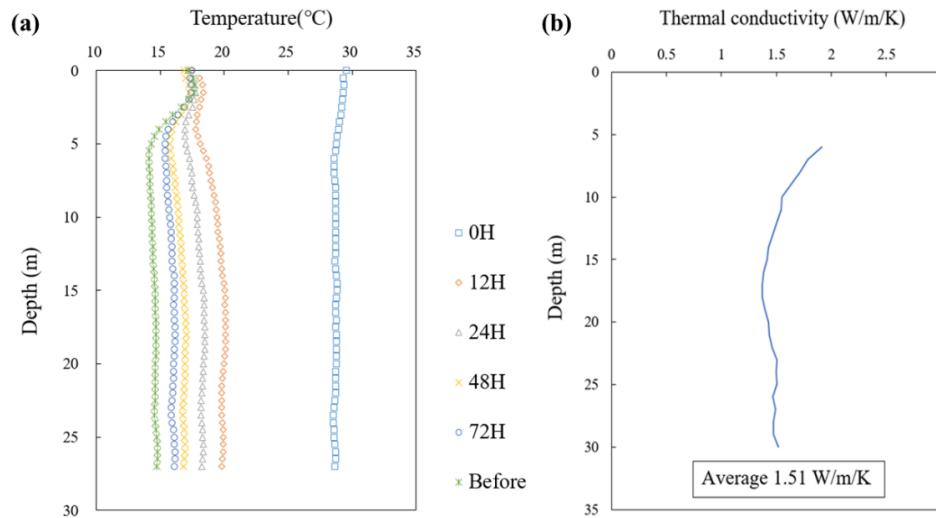


Figure 3 (a) Temperature profiles measured using the optical fiber at each time step. (b) Thermal conductivity profile of the ground around the BHE.

A TRT using the novel TRT equipment

Figure 4(a) shows a photograph of the novel TRT equipment, and Fig. 4(b) shows a schematic of the equipment installation. The equipment was composed of a ground control unit and a measurement cable installed in the water wells. The measurement cable comprised three parts: a waterproof ribbon heater, a fiber optic thermometer, and electromagnet units. Each electromagnet unit is equipped with an electromagnet and integrated on the measurement cable at 2.2 m intervals. The electromagnet in electromagnet unit adheres to the casing by passing an electric current by the control unit. Then, the electromagnet unit draws the heater and optical fiber to the casing. Figure 5(a) shows the main monitor of the control unit, and Fig. 5(b) shows a photograph of the test equipment installed at the field test site. This new equipment was designed to be used in the existing water wells instead of BHEs, and the measurement cable was fixed on the inner wall of the steel casing in the water well via adsorption of the electromagnet units. During the TRT, the ground around the water well was heated using a ribbon heater. Water temperature was measured at 0.5 m intervals using a fiber optic thermometer to estimate the thermal conductivity at each depth using the slope method.

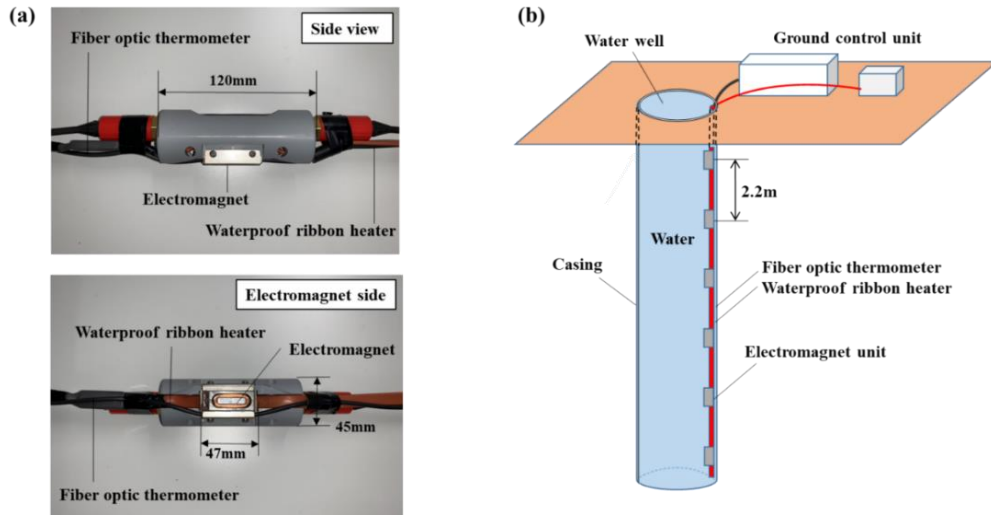


Figure 4 (a) Electromagnet unit of the novel TRT equipment. (b) Schematic of the installation of the novel TRT equipment.

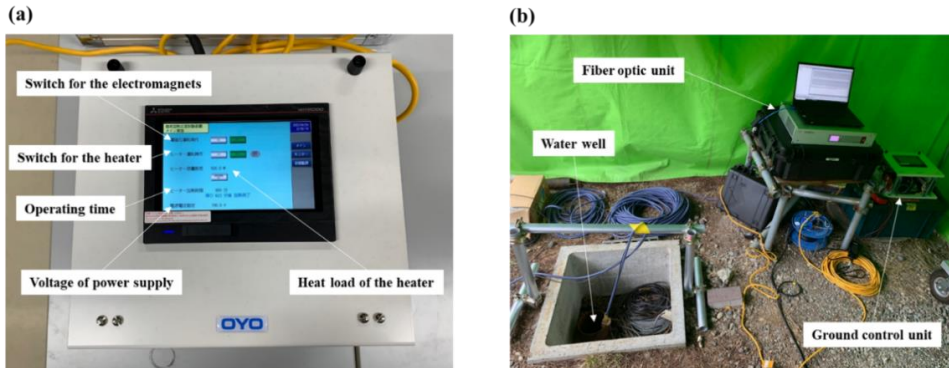


Figure 5 (a) Main monitor of the ground control unit. (b) Installed equipment for conducting the TRT.

A TRT was performed using the new equipment with a test duration of 4 h and a heating load of 50 W/m. The water well used in this TRT was a BHE without a U-tube. The measurement cable was installed in the section located between the 10 m and 20 m depths of the water well. L-shaped supports were used to ensure that each electromagnetic unit faces the inner wall of the casing after the measurement cable was installed. Using an underwater camera, we confirmed that the measurement cable was installed along the inner wall of the casing.

Figure 6(a) shows the measured temperature at each depth during the TRT. To smooth the fluctuation of fiber optic thermometer measurements, the measured temperatures were output as a 5-minute moving average. The results indicated that the temperature increase at both ends of the measurement cable was smaller than that around the central part of the measurement cable. This result is considered to be due to the presence of unheated sections at the top and bottom of the measurement cable, which suppressed the temperature rise. Figure 6(b) compares the thermal conductivity profile estimated using the new TRT equipment and the reference profile shown in Fig. 3(b). The comparison results showed that the estimated thermal conductivity at -16 m (near the center of the heated section) was

the lowest among all depths. In addition, the thermal conductivity increased from a depth of 16 m toward both ends of the measurement cable. Moreover, the thermal conductivities estimated using the TRT equipment were higher than those of the reference profile at all depths. This is considered that the water well was not sufficiently heated because the test time was only 4 h, and the temperature behavior was unstable owing to natural convection. Therefore, to obtain a more accurate thermal conductivity profile, a longer testing time is necessary.

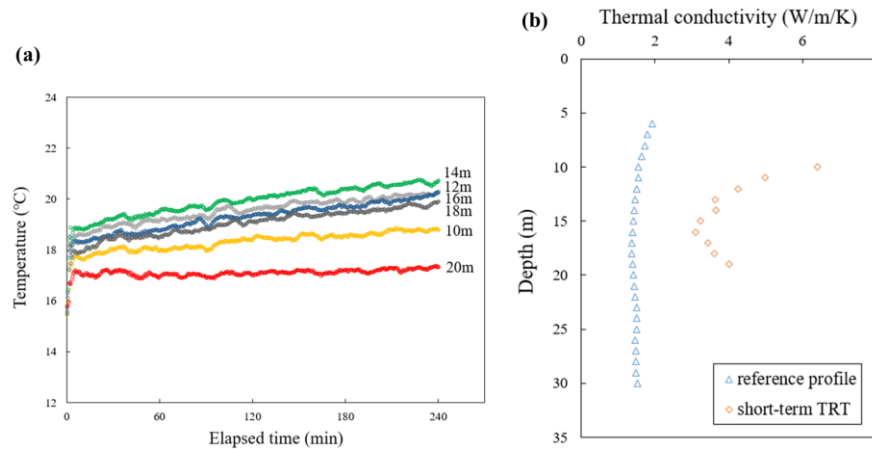


Figure 6 (a) Temperature change at each depth during the TRT. (b) Thermal conductivity profile estimated via the TRT.

Numerical modeling of the TRT using the new equipment

A numerical model including the new TRT equipment, ground, and water well was developed using the finite element subsurface FLOW (FEFLOW) software ver. 7.1 to reproduce the TRT. The developed numerical model is shown in Fig. 7. The radius and height of the model were 3 m and 40 m, respectively. The inner diameter and casing thickness of the water well were set to 0.15 m and 0.005 m, respectively. The number of layers with a thickness of 0.5 m is 60 from the top to -30 m, while two layers with a thickness of 5 m are located between 30 m and 40 m. The thermal conductivity of the ground was input for each layer based on the reference thermal conductivity profile. The thermal conductivity deeper than 30 m and permeability of ground at each layer were determined by referring to the geological column shown in Fig. 1(b). The heat flux of the heater on the casing wall was fixed from -10 to -20 m. The external boundary of the model was adiabatic, and the initial temperature of the model was set at 16.37°C based on the TRT result.

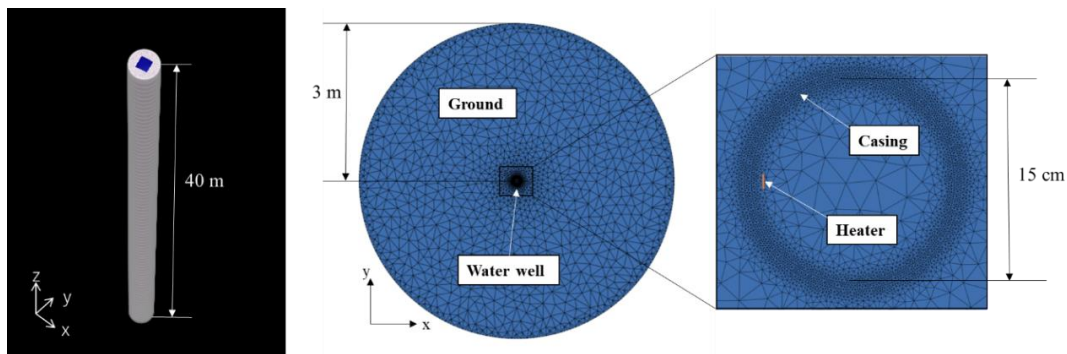


Figure 7 Structure of the numerical model.

To confirm the validity of the numerical model, history matching was performed by using the measured temperature changes at each depth. Figure 8 shows the results of history matching at depths of 14, 15, and 16 m. From the results, the calculated and measured values showed generally good agreement. Therefore, the model is considered valid.

Next, a 2 days TRT simulation was performed using the developed model, and the thermal conductivity profile was estimated from the calculated temperature changes at each depth. Figure 9(a) shows the simulated temperature change at each depth during the simulated TRT. Figure 9(b) shows a comparison between the thermal conductivity profiles estimated using the simulated TRT and reference profiles. To estimate the thermal conductivity, the simulated temperatures from 1 to 1.5 days were used. The results indicated that the thermal conductivity profiles estimated by using the TRT simulation generally agreed with the reference profiles, except near the end of the heated section. Therefore, the TRT equipment developed in this study was considered capable of estimating generally accurate thermal conductivity profiles with a test time of approximately 1.5 days. In the next step of this research, we will perform longer TRTs, while modifying the TRT equipment to estimate a more accurate thermal conductivity profile.

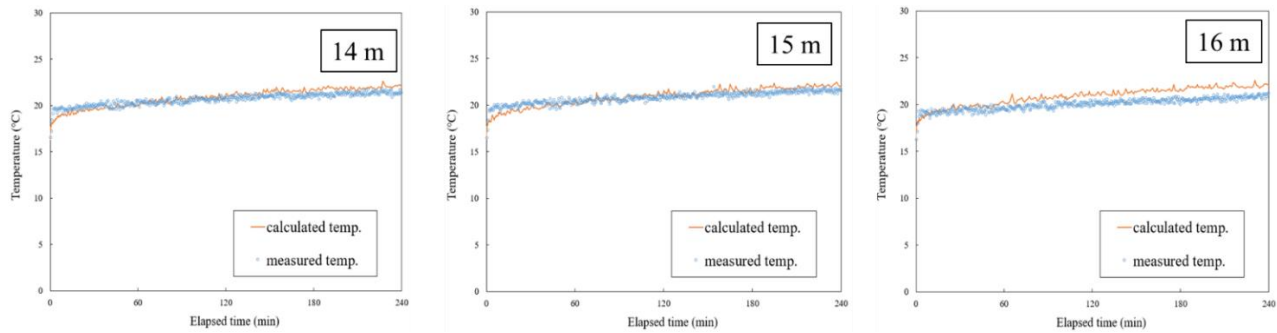


Figure 8 History matchings of water temperature at depths of 14, 15, and 16 m.

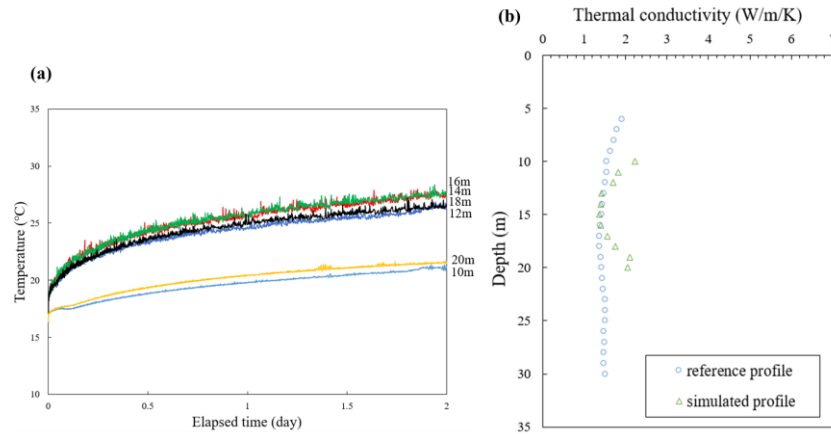


Figure 9 (a) Calculated temperature changes at each depth during the 2 days TRT. (b) Thermal conductivity profile estimated using the result of the TRT simulation.

CONCLUSION

A TRT was conducted using the novel equipment to estimate the thermal conductivity profile. Consequently, the

temperature increase at the end of the heated section was small; however, it augmented toward the center of the heated section. The thermal conductivities estimated using the measured temperatures were greater than those of the reference profile at all depths of the measured section. This is because the test was only conducted for 4 h, during which the temperature behavior in the water well was not stable due to natural convection.

A numerical model including the new TRT equipment was developed using FEFLOW ver. 7.1. To confirm the validity of the numerical model, a numerical simulation reproducing the field test was conducted, and history matching was performed using the TRT result. The measured and calculated temperature changes at each depth showed generally good agreement, and the validity of the model was confirmed. Next, a TRT simulation was performed for two days, and the thermal conductivity profile was estimated using the calculated temperature changes at each depth. The estimated thermal conductivity profile was in good agreement with the reference profiles except near the end of the heated section. Therefore, a sufficient TRT period (approximately 1.5 d) is estimated to stabilize the temperature behavior in the water and realizes accurate thermal conductivity profiles.

ACKNOWLEDGMENTS

This paper is based on results obtained from a project, JPNP19006, subsidized by the New Energy and Industrial Technology Development Organization (NEDO).

NOMENCLATURE

- F = Evaluation function (K²)
- α = Wighting constant (-)
- T = Temperature (°C)

Subscripts

- o* = outlet of U-tube
- ro* = outer wall of a ground heat exchanger
- obs* = observation
- cal* = calculation

REFERENCES

- Fujii, H., H, Okubo and R, Ito. 2006. *Thermal response tests using optical fiber thermometers*. Geothermal Resources Council 30: 545-551.
- Fujii, H., H, Okubo., K, Nishi., R, Itoi., K, Ohyama and K, Shibata. 2009. *An improved thermal response test for U-tube ground heat exchanger based on optical fiber thermometers*. Geothermics 38: 399-406.
- Fujii, H., H, Kosukegawa., H, Farabi and S, J, Nasrabad. 2016. *Experimental study on the applicability of ungrouted ground heat exchangers on thermal response tests*. J.Geotherm. Res. Soc. Japan 28(2): 43-51.
- Hakala, P., S, Vallin., T, Arola and I, Martinkauppi. 2022. *Novel use of the enhanced thermal response test in crystalline bedrock*. Renewable Energy 182: 467-482.
- Isabel, M., V, Márquez., J, Raymond., D, Blessent., M, Philippe., N, Simon., O, Bour and L, Lamarche. 2018. *Distributed Thermal Response Tests Using a Heating Cable and Fiber Optic Temperature Sensing*. Energies 11: 3059.
- Raymond, J., L, Lamarche and M, Malo. 2015. *Field demonstration of a first thermal response test with a low power source*. Applied Energy 147: 30-39.
- Wilke, S., K, Menberg., H, Steger and P, Blum. 2020. *Advanced thermal response tests: A review*. Renewable and Sustainable Energy Reviews 119: 109575.
- Zhang, B., K, Gu., B, Shi., C, Liu., P, Bayer., G, Wei., X, Gong and L, Yang. 2020. *Actively heated fiber optics based thermal response test: A field demonstration*. Renewable and Sustainable Energy Reviews 134: 110336.



Column Experiments to Anticipate Clogging of Standing Column Wells

Léo Cercllet

Benoît Courcelles

Philippe Pasquier

ABSTRACT

Standing column wells are a promising solution to reduce the environmental footprint of building energy consumption. Nevertheless, as in other open-loop wells, they can be affected by clogging processes if detrimental hydrogeological conditions are present locally. This problem is relatively rare and still difficult to anticipate, even though some specific factors have been reported, such as substratum mineralogy and groundwater quality. This study proposes the use of a column experiments and coupon cell to anticipate clogging at two different sites near Montréal, Canada. The experiments were performed for duration of 50 and 52 d using thermoregulated columns at four temperatures. The results identified a difference in the chemistry of each site without any significant clogging risk. Site A showed a decrease in carbonates, magnesium, and calcium ions, and scanning electron microscopy showed a minor tendency to form carbonate deposits. Sulfate and calcium dissolution of the bedrock material were observed at Site B. Scanning electron microscopy of the coupons revealed organic matter with high carbon and sulfate concentrations. The same type of deposits was observed at Site B after three years of operation. In conclusion, these tests helped identify various potential clogging phenomena and indicated that both sites are not susceptible to major clogging risks.

INTRODUCTION

Ground-source heat pumps have demonstrated their ability to reduce the environmental footprint of building energy consumption. As has been demonstrated, owing to their original design, standing column wells (SCW) incur lower costs and have a higher thermal efficiency than traditional closed-loop configurations (O'Neill et al., 2006; Pasquier et al., 2016). The SCW is a coaxial uncased well in which groundwater constitutes the heat-carrier fluid. A major portion of the groundwater is recycled inside the SCW. Occasionally, some of the groundwater can be discharged outside the main well to force a converging flow towards the SCW (Pasquier et al., 2016). As with other open-loop systems, SCW can be affected by clogging processes if detrimental conditions are locally present. Although relatively rare in practice and with varying degrees of severity, this issue is well known to hydrogeologists. The main problem with clogging is that it is still difficult to anticipate, even though it has been reported that specific factors influence these processes, such as substratum mineralogy, groundwater quality, design, and geothermal operation. The main operations that favor scaling are the cooling period and the presence of CO₂ degasification (Eppner et al., 2017). The bleeding operation is beneficial to chemical stability as it allows the minimization of the impact of temperature modification (Eppner et al., 2017).

A promising strategy for anticipating clogging is to perform a laboratory column experiment to reproduce these factors. In open-loop systems, clogging can be observed in underground and aboveground equipment (Gjengedal et al., 2019). Kim et al. (2017) identified biological clogging in the underground equipment of an SCW, and Cercllet et al. (2020) observed minor calcite scaling on the aboveground equipment. A strategy to understand clogging processes involves carrying out column experiments. This method has multiple advantages, as demonstrated by the following two studies. For instance, Griffioen and Appelo (1993) performed a column experiment at a fixed temperature of 90 °C and identified calcite precipitation. In addition, this experiment highlighted the necessity of using native sediments and

Léo Cercllet (leo.cercllet@polymtl.ca) is a PhD student, Department of Civil, Geological and Mining Engineering, Polytechnique Montréal
Benoît Courcelles (benoit.courcelles@polymtl.ca) is a professor of civil engineering at Polytechnique Montréal
Philippe Pasquier (philippe.pasquier@polymtl.ca) is a professor of geological engineering at Polytechnique Montréal.

groundwater to anticipate the kinetic precipitation of natural systems. Rinck-Pfeiffer et al. (2000) demonstrated that column experiments have the advantage of identifying the interrelationships between the physical, biological, and chemical clogging processes. To help anticipate clogging at the design stage of an SCW system, we propose the use of a column experiment along with coupons made of copper and stainless steel to consider both temperature changes and the material of aboveground equipment.

COLUMN EXPERIMENTS

Column experiments were designed to identify clogging processes linked to SCW operation. As clogging can occur on underground and aboveground equipment, the experiment is composed of two parts, described below. Two sites were investigated in this study. Groundwater and drill cuttings from each site were collected and used to construct a column.

Column Construction

A schematic representation of the column experiment is shown in Figure 1. The large rectangle in Figure 1 (a) and photograph in Figure 1 (c) represent the underground SCW. It is composed of a column filled with drill cuttings and saturated with groundwater sampled from the SCWs. The relative density and soil distribution were measured to characterize drill cutting. Groundwater was injected at the bottom of the column at an initial flow rate of 0.012 L/min. A low flow was selected to maximize contact between the groundwater and drill cuttings. The internal column was 20.0 cm in diameter and 51.8 cm in height. Three pressure sensors were placed 22.25, 32.25, and 39.45 cm from the bottom. The maximum pressure in a real SCW corresponds typically to the water column height. This high pressure could not be reproduced using column experiment equipment. Note that the maximum pressure recorded by the sensors was 5.99 kPa and 6.05 kPa, respectively in Columns A and B. To avoid vacuum pressure in the column, the top was opened to the atmosphere allowing the gases dissolved to be equilibrated with the atmosphere. Consequently, the gases dissolved in groundwater can be equilibrated with the atmosphere. This situation is the worst for the scaling process (Eppner et al., 2017). A multiparameter probe for pH, ORP, temperature, and specific conductivity was placed at the exit from where the samples were collected. The equipment was calibrated every week. The cooling period is the most damaging for geothermal equipment (Eppner et al., 2017). Thus, a heating period of 4 °C was imposed as a conditioning period, followed by two cooling periods of 25 and 35 °C. The temperature was initially maintained for 14 days. The batch tests (not shown) concluded that it was sufficient to reach equilibrium with a lower surface-to-volume ratio. However, a period of seven days at a temperature of 20 °C was added to minimize the impact of a power breakdown that was initially planned in the building but did not occur. Subsequently, the same protocol was applied to both columns. Four different temperature conditions (4, 20, 25, and 35 °C) were imposed on the 25-liter groundwater reservoir, column, and multiparameter cell. The groundwater reservoir was immersed in a temperature-controlled cooling and heating bath. A cooling/heating circuit was wound around the column, and a multiparameter cell was used to prevent heat loss or gain. In addition, the column and multiparameters were insulated with a mineral wool layer and an aluminum layer. The tubes coming from or leaving the controller were also insulated.

The outlet groundwater was sent to a cell containing two coupons. This cell represents the aboveground part of a geothermal system. The coupons were composed of standard microscope slides made of copper and stainless steel. These materials were chosen because they are locally used in HVAC applications. At the end of the tests, coupon surfaces were analyzed using scanning electron microscopy (SEM) to identify any deposits. Finally, groundwater was collected in a thermoregulated reservoir and reinjected into the column. This experiment could reproduce a standing column that operates well under full recirculation mode.

Column Experiments

For each column, the experiment was performed for 50 and 52 d, and 36 and 38 samples were collected and filtered, respectively for Columns A and B. The major anions and cations were analyzed by ion chromatography. Alkalinity was measured using an automatic titrator from Hanna. These results were used to calculate the saturation index (SI) of each sample. The saturation index was calculated using the following equation:

$$SI = \log \left(\frac{IAP}{K_{sp}} \right) \quad (1)$$

where IAP is the ion activity product and K_{sp} is the solubility product.

The SI value indicates the saturation state of each mineral. If $SI > 0$, it is supersaturated, leading to precipitation. In contrast, if $SI < 0$, it is undersaturated, which leads to dissolution. This calculation was performed using the PHREEQC software on the database, wateq4f (Parkhurst and Appelo, 2013). At each site, drill cuttings and groundwater were collected to fill the columns. Groundwater was collected 48 h before the start of the experiment, was not filtered and was cooled during the 1- or 2-hour transport. The samples were stored in a cold chamber at 6 °C. Even if the reservoir was closed, degassing of the groundwater could have occurred before the column experiment started.

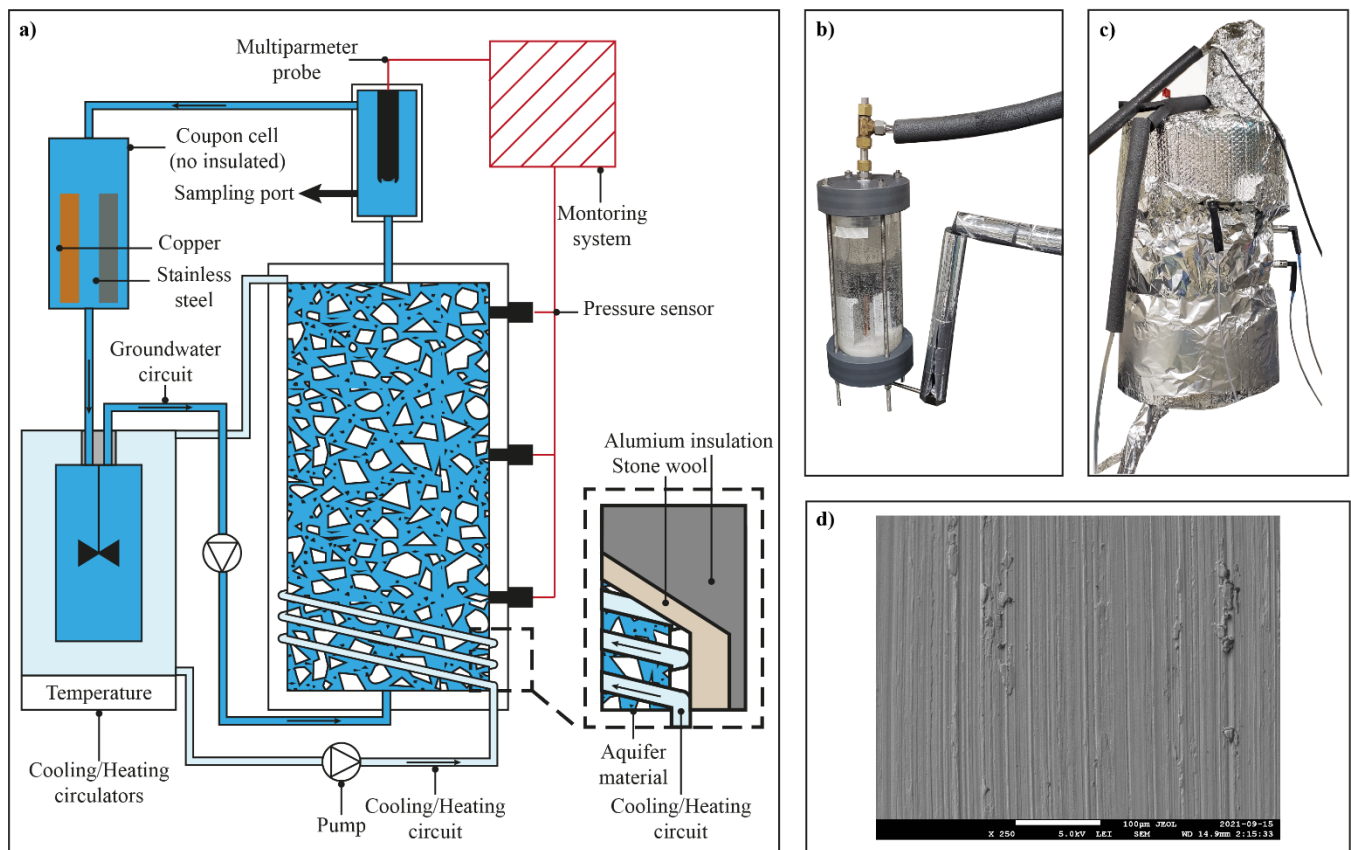


Figure 1 a) Schematic representation of the column experiments, the inset shows the spiral coil and two layers of insulation, b) coupon cell, c) experimental column and the multiparameter cell d) the microscope results for stainless steel before the experiment at a large focus x250.

Site A corresponded to the site presented by Robert et al. (2022). The bedrock is mainly composed of dolomite and quartz arenite. The main dimensions are 133.2 m in depth and 0.159 m in diameter. The initial groundwater temperature was 8.7 °C. The SCWs at Site A have only recently been commissioned. Site B corresponded to the site presented by

Beaudry et al. (2019). The bedrock is mostly composed of gray mudstone, siltstone, sandstone, and limestone. The main dimensions are a depth of 215 m and a diameter of 0.165 m. The initial groundwater temperature was 11.0 °C. This site has the advantage of being operated intermittently and has been studied since 2016. The chemical characteristics of the bedrock are presented in Table 1. The bedrock of Site A has more calcium and magnesium than that of Site B. Conversely, the bedrock of Site B has a greater concentration of sulfate and iron than Site A. As Site A has a loss on ignition (LOI) equal to its CO₂ content, all carbon seems to be in this form.

RESULTS AND DISCUSSION

This section presents the chemical analysis performed on Columns A and B, which are representative of Sites A and B, respectively. These analyses were performed using the results from the SEM of coupons to evaluate their impact on the aboveground equipment. The pressure records did not show significant pressure modifications during the 50- or 52-day column experiments. The hydraulic conductivity of Column A remained constant, whereas the hydraulic conductivity of Column B increased from $7.3 \cdot 10^{-7}$ m/s to $8.1 \cdot 10^{-7}$ m/s. An explanation for this slight change could be that the 25-liter reservoir did not bring enough contamination to clog columns A and B with porosities of 0.21 and 0.32. Nevertheless, this volume was chosen to achieve equilibrium between the rock and water in a short period of time. Indeed, the ratios of the rock surface to the water volume are 144 and 119 times higher than those of their real SCW, respectively, for Columns A and B. The ratio is an approximation that considers the cuttings as spherical and the SCW borehole as a smooth cylinder. This column test with recirculation is still representative of an SCW that is operated without bleeding. During this operation, a significant volume of water was recirculated inside the uncased well. The hypothesis was that equilibrium between the borehole and groundwater was achieved. Note that for temperatures of 4 °C and 35 °C, the insulation was not sufficient to keep the temperature constant across the bottom and the top of the column. The temperatures of the outlets were maintained at 8 °C and 32 °C.

Table 1. Geochemical and hydraulic characteristics of column experiment.

	Site A	Site B
Chemical formula (%)		
<i>Al₂O₃</i>	3.42	14.02
<i>CaO</i>	12.97	7.79
<i>MgO</i>	8.76	3.02
<i>Fe₂O₃</i>	1.20	6.62
<i>Na₂O</i>	0.06	1.05
<i>K₂O</i>	1.90	2.79
<i>MnO</i>	0.11	0.06
<i>SO₃</i>	1.40	2.63
<i>CO₂</i>	20.51	7.11
<i>LOI</i>	20.43	10.99
<i>Carbon (total)</i>	5.64	2.94
Hydraulics		
Porosity	0.21	0.32
Drill cutting mass (kg)	33.95	28.18
Relative density	2.76	2.71

Piper Diagram

The Piper diagram represents the concentration percentages of the major anions and cations. Figure 2 shows results of the samples collected in Columns A (36 samples) and B (38 samples). Note that 11 analyses for Column A have an electric balance of 5–10 %. All other analyses had electric balances of less than 5 %, indicating good chemical analyses. The two columns have different chemical compositions: The chemical composition of Column A has a repartition of approximately 30 % calcium / 70 % magnesium, whereas that of Column B corresponds to sulfated groundwater. However, the relative changes were not significant. Site A has been more exposed to calcium or magnesium carbonate

precipitation because of its chemistry. Site B has groundwater that mainly contains sulfates and bedrock with organic carbon and iron. Thus, this site has been more exposed to biochemical clogging. Indeed, calcite precipitation is generally slower than biological clogging for the range of temperatures tested. Therefore, Site B could be impacted in a shorter time frame than Site A. Because the chemical behaviors of these two sites were different, they were analyzed separately.

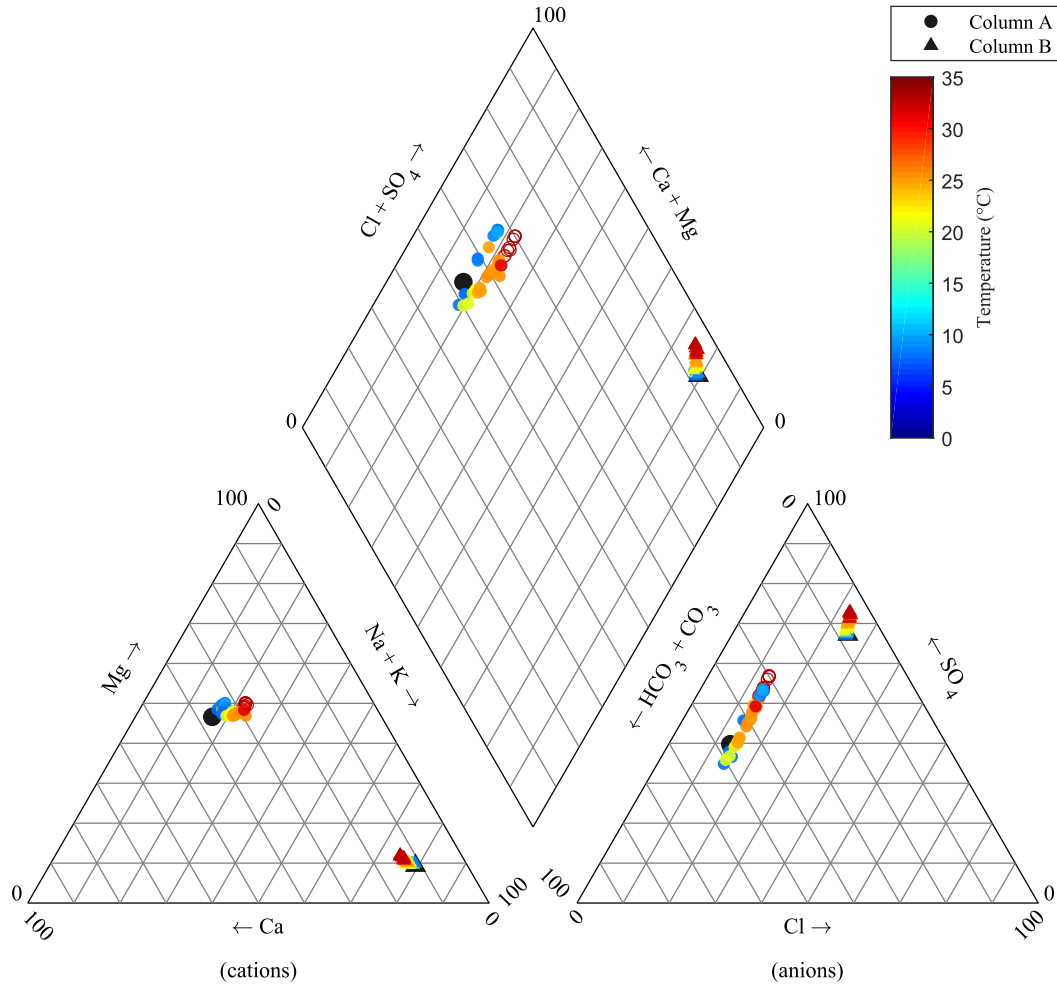


Figure 2 Piper diagram presenting the results for both column experiments. Empty bullet point corresponds to the analyses with electric balances greater than 5 %; the large black marker corresponds to the initial state.

Column A

Figure 3 shows the evolution of calcium, magnesium, and bicarbonate concentrations as a function temperature, and time. This figure shows a decrease in magnesium, calcium, and bicarbonate concentrations with increasing temperature and duration. This decrease is attributed to precipitation of calcite (CaCO_3) or dolomite ($\text{CaMg}(\text{CO}_3)_2$), as their saturation indexes (SI) remain greater than zero. The magnesite (MgCO_3) SI remained below zero, and the mineral remained dissolved. Owing to the decrease in magnesium concentration, dolomite precipitation is dominant in comparison to magnesite dissolution.

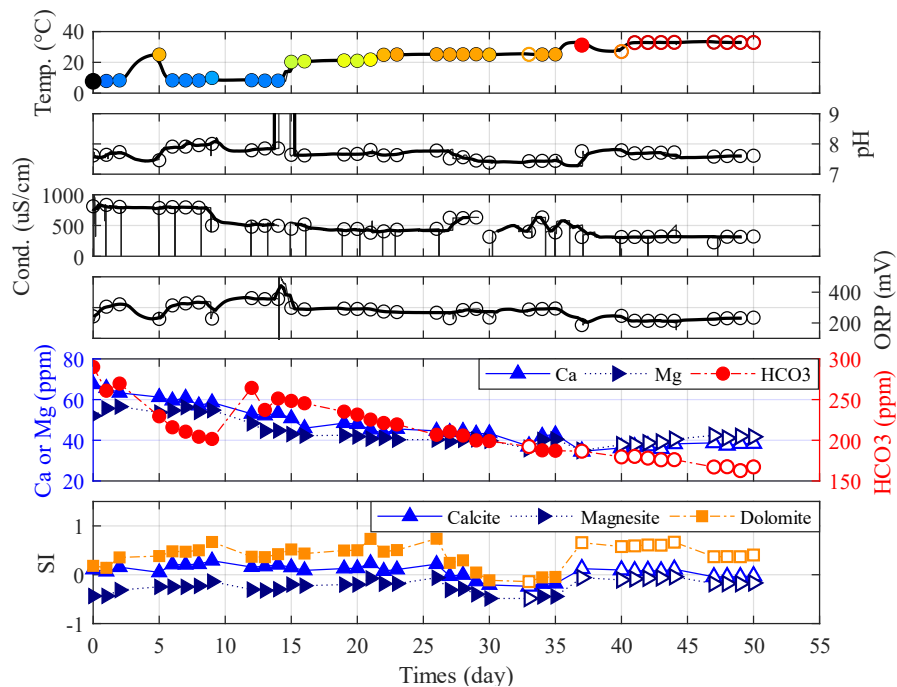


Figure 3 Physicochemical parameters and the carbonate precipitation for Column A as a function of time; empty marker corresponds to the sample with an electric balance of above 5 %.

Figure 4 shows the microscopic analysis of the stainless-steel coupons of Column A. The microscopic analysis in Figure 4 (a) shows minor roughness. In fact, some depositions were observed only with a close focus. The deposition of the stainless-steel coupons was analyzed using SEM, as shown in Figure 4 (b). SEM analysis corresponds to the observations in Figure 3 and is representative of a dolomite ($\text{CaMg}(\text{CO}_3)_2$) or magnesium-calcite (CaMgCO_3) deposit. Note that microscopic analysis of the copper coupon is not presented because the deposition was superficial and resulted mainly in oxidation. In conclusion, the column experiment at this site allowed for the identification of the principal cause of potential clogging, which is carbonate precipitation. Nevertheless, the weak rate of deposition on the coupon and weak hydraulic conductivity evolution in the column allowed us to consider this site as not at risk for clogging in the recirculation mode. The reservoir volume could have limited the deposits.

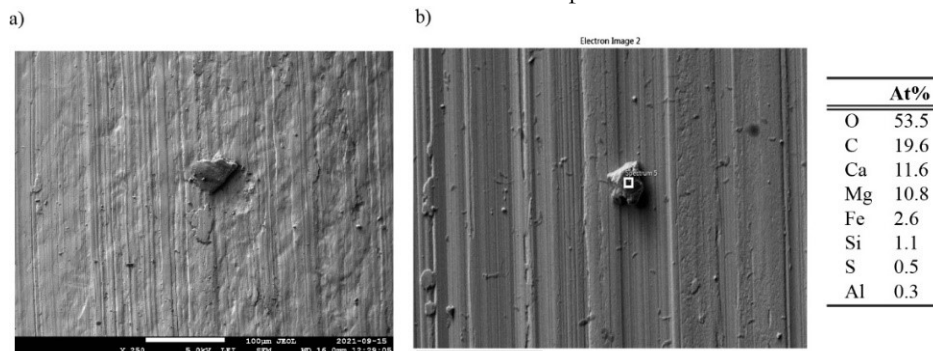


Figure 4 Microscope results for stainless steel in Column A. a) large focus at x250, b) close focus at x2500.

Column B

Figure 5 shows the evolution of magnesium, calcium, bicarbonate, and sulfate concentrations as a function of temperature, and time for Site B. The first observation is that the water surrounding Column B is more mineralized than that surrounding Column A. Thus, the site is naturally more exposed to clogging issues. The sulfate and calcium concentrations in Column B increased with temperature and time. The saturation indexes of gypsum ($\text{CaSO}_4 \cdot 2\text{H}_2\text{O}$) (not represented) and anhydrite (CaSO_4) remain below zero. Thus, the increase in calcium concentration seems to be related to the dissolution of gypsum or anhydrite. This concentration increase can eventually cause calcite (CaCO_3) precipitation, as shown in Figure 5. Calcite precipitation causes a decrease in bicarbonate concentration, which leads to the dissolution of dolomite or magnesite and an increase in magnesium concentration. Finally, the dissolution of gypsum can lead to dedolomitization (Appelo and Postma, 2004).

Note that iron concentrations were not analyzed in the groundwater. However, analyses indicated 6.62 % of iron oxides in the rock samples analyzed. The presence of pyrite (FeS_2) is then deemed likely in this geological context. The groundwater circuit is not isolated from the atmosphere. Therefore, groundwater recirculation can oxidize pyrite, which can lead to an increase in sulfate concentration and acidity. This acidity can neutralize alkalinity due to CO_3 and HCO_3 . In conclusion, the main geochemical process in the SCW is mineral dissolution, which can explain the small hydraulic conductivity change.

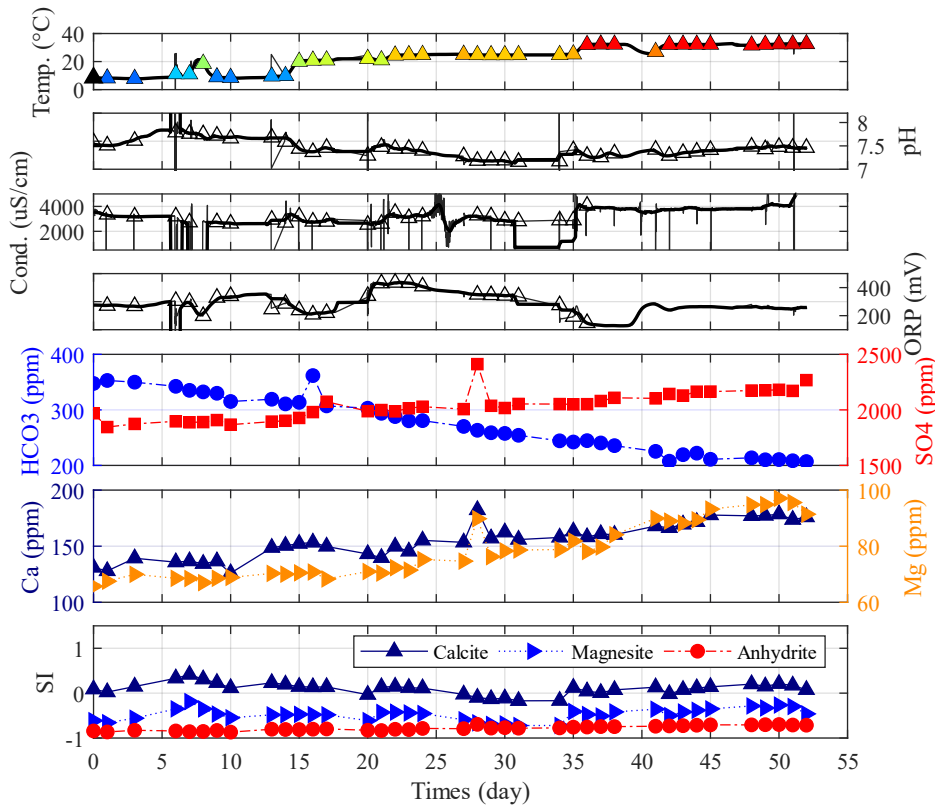


Figure 5 Physicochemical parameters and dissolution of anhydrite and diminution in carbonates for Column B as functions of time.

Another observation is that the deposition on coupons in Column B is more important than that in Column A, as shown in Figure 6 (a). This means that Site B is more exposed to clogging in the aboveground equipment. The deposits in Figure 6 (b) are likely to be organic matter composed of carbon, oxygen, iron, and sulfur (spectrum 3). Notably, iron concentration could be overestimated. Indeed, the analyses could have considered a part of the stainless-steel support

owing to the porosity of the organic matrix. The presence of an organic matrix is in accordance with the geochemistry of this site, which contains more organic carbon (Table 1). Inside the organic deposits, some salts, such as chloride or sodium, were identified (spectra 2 and 4). These results demonstrate the synergy between mineral precipitation and microbial growth. Note that calcium concentration could not be analyzed because of the proximity of carbon and oxygen peaks. This did not exclude the occurrence of calcite precipitation. As in Site A, the copper coupon had less deposition than the stainless-steel coupon. The main roughness observed was due to copper oxidation.

At Site B, the dissolution of the reactive bedrock with sulfur, iron, and carbon favors biochemical deposition in the aboveground equipment, and this deposition was only observed with a microscope. The column test did not reveal any significant clogging at this site. Indeed, the SCW has been operating at this site since 2016 and has not suffered from any major clogging. Minor depositions were observed twice using an optical flowmeter during routine verification. The first deposition was composed of calcite and was observed in January 2019 (Cercllet et al., 2020). The second deposition was observed in July 2019. These observations are illustrated in Figure 6. The deposits were mainly composed of carbon, sulfur, and iron. In conclusion, the column experiment identified two potential processes of deposition and their locations in the ground source heat pump system. These results, obtained in 52 days, correspond to the observations made at Site B after three years of operation. Thus, this column experiment had the ability to anticipate the scaling of aboveground equipment even though this site and the column did not suffer from any significant clogging.

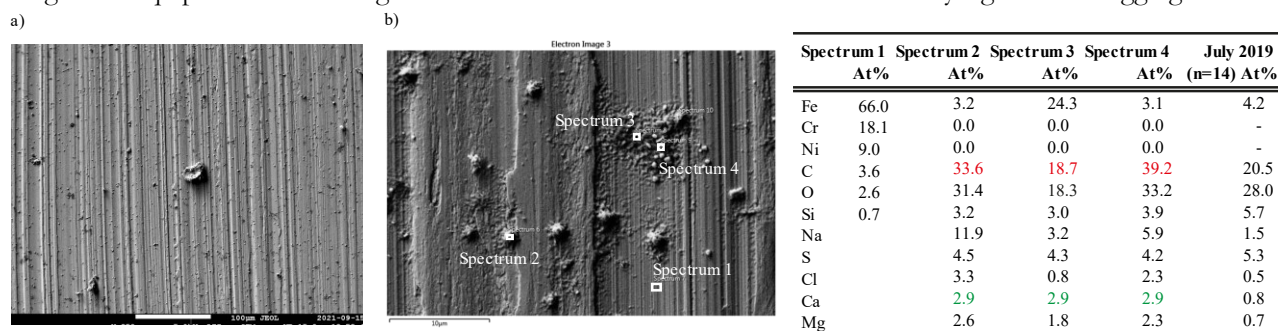


Figure 6 Microscope results for the stainless steel in Column B. a) large focus at x250. b) present scanning electron close focus at x2500 (red values are the highest imported concentration, green values are estimated). The column of July 2019 presents the mean results of the analysis performed on a deposit collected from Site A after 3 years of standing column well operation.

CONCLUSION

This study presented a protocol relying on a column experiment and coupons to predict clogging in SCW installations with temperature regulation and groundwater recirculation. The feedback from the operation of the two columns demonstrated that this experiment was appropriately designed to identify the main deposition processes. The small deposits observed in Column B after 52 days corresponds to the observation at Site B after three years of operation. In addition, these experiments highlighted the differences between the two sites under similar operating conditions. Experimental results indicate that Site B is more susceptible to biochemical clogging due to organic carbon and sulfates, whereas Site A is more sensitive to carbonate precipitation. However, the results and analyses indicate that neither site is prone to significant clogging risks. The limitations of our study were the possibility that the dissolved groundwater gases were modified before the column started. Further work is required to analyze a clogging site for evaluating underground equipment.

ACKNOWLEDGMENTS

The authors wish to acknowledge the support and funding provided by the Natural Sciences and Engineering Research Council of Canada (grant number RDCPJ 530945), Hydro-Québec, FTE drilling, Marmott Energies and Richelieu Hydrogeology.

REFERENCES

- Appelo, C.A.J., Postma, D., 2004. *Geochemistry, groundwater and pollution*. CRC press.
- Beaudry, G., Pasquier, P., Marcotte, D., 2019. *The impact of rock fracturing and pump intake location on the thermal recovery of a standing column well: model development, experimental validation, and numerical analysis*. Science and Technology for the Built Environment 25, 1052–1068. <https://doi.org/10.1080/23744731.2019.1648133>
- Cercllet, L., Courcelles, B., Pasquier, P., 2020. *Impact of Standing Column Well Operation on Carbonate Scaling*. Water 12, 2222. <https://doi.org/10.3390/w12082222>
- Eppner, F., Pasquier, P., Baudron, P., 2017. *A coupled thermo-hydro-geochemical model for standing column well subject to CO2 degassing and installed in fractured calcareous aquifers*. Geomechanics for Energy and the Environment 11, 14–27. <https://doi.org/10.1016/j.gete.2017.05.003>
- Gjengedal, S., Ramstad, R.K., Hilmo, B.O., Frengstad, B.S., 2019. *Fouling and clogging surveillance in open loop GSHP systems*.
- Kim, H., Mok, J.-K., Park, Y., Kaown, D., Lee, K.-K., 2017. *Composition of groundwater bacterial communities before and after air surging in a groundwater heat pump system according to a pyrosequencing assay*. Water 9, 891.
- O'Neill, Z.D., Spitler, J.D., Rees, S., 2006. *Performance analysis of standing column well ground heat exchanger systems*. ASHRAE
- Parkhurst, D.L., Appelo, C.A.J., 2013. *Description of input and examples for PHREEQC version 3: a computer program for speciation, batch-reaction, one-dimensional transport, and inverse geochemical calculations* (USGS Numbered Series No. 6-A43), Techniques and Methods. U.S. Geological Survey, Reston, VA.
- Pasquier, P., Nguyen, A., Eppner, F., Marcotte, D., Baudron, P., 2016. *Standing column wells. Advances in Ground-Source Heat Pump Systems* 269–294.
- Rinck-Pfeiffer, S., Ragusa, S., Sztajn bok, P., Vandeveld, T., 2000. *Interrelationships between biological, chemical, and physical processes as an analog to clogging in aquifer storage and recovery (ASR) wells*. Water Research 34, 2110–2118.
- Robert, S., Pasquier, P., Nguyen, A., 2022. *Impact of layered heterogeneity on thermal response test interpretation performed on a standing column well operated without bleed*. Geothermics 101, 102353. <https://doi.org/10.1016/j.geothermics.2022.102353>



Forecasting Hydraulic Head Changes in Injection Wells Using LSTM Network

Christopher Rose

Philippe Pasquier

Alain Nguyen

Gabrielle Beaudry

ABSTRACT

Monitoring of well's specific capacity is commonly used to plan maintenance of injection wells in open-loop GSHP and standing column well systems. However, this method does not consider the effect of temperature on hydraulic conductivity. A first step towards an alternative approach that does include the effect of temperature is proposed in this work. We present a long short-term memory network capable of predicting the water level in the injection well of an operating GSHP system. The methodology consists of building a training set using a numerical model. A total of 500 simulations were conducted to evaluate hydraulic head signals under various inlet temperatures and flow rates along with hydraulic and thermal parameters drawn from a uniform distribution. Predictive performance of the artificial neural network is tested on an operational data set. The resulting RMSE between the forecasted and operational data set is 14.8 cm.

INTRODUCTION

Open-loop ground source heat pump (GSHP) and standing column well (SCW) systems are often used with injection wells (IW). Indeed, reinjecting pumped groundwater back to the aquifer allows maintaining the well's sustainability along with limiting the impact on the piezometric surface caused by continuously extracting groundwater (Banks, 2012; Snijders and Drijver, 2016). In SCW systems, discharging a fraction of the pumped groundwater in IWs induces a drawdown in SCWs, thus increasing groundwater flow towards SCWs. This bleed amplifies advection, which in turn contributes in stabilizing groundwater temperature entering the GSHP and temporarily boosting the SCW's thermal efficiency (Pasquier *et al.*, 2016).

However, IWs are also subject to fouling, clogging and overflowing problems along with degradation of performance (Banks, 2012). Forcing water into an IW can lodge gas bubbles, particles or chemical precipitates in fractures or pore spaces, thus reducing the hydraulic conductivity of the surrounding aquifer (Banks, 2012). Water dynamic viscosity, being temperature-dependent, also plays a role in altering hydraulic conductivity. Since hydraulic conductivity is inversely proportional to dynamic viscosity, injection capacity during winter months can be twice as low as the one observed in summer (Bouwer, 2002). Even though many precautionary measures can be carried out to minimize fouling problems, such as injecting below the water table, maintaining overpressure and preventing entry of oxygen, early redevelopment of IWs remains important to extend their remaining use of life as severely clogged wells might be difficult to restore (Snijders and Drijver, 2016). Monitoring the well's specific capacity through regular water level measurements can help to plan preventive maintenance of IWs (Ballard, 2017; Snijders and Drijver, 2016). An alternative surveillance method

Christopher Rose (christopher.rose@polymtl.ca) is an M.A.Sc. candidate at Polytechnique Montréal, Canada.

Philippe Pasquier (philippe.pasquier@polymtl.ca) is a professor of geological engineering at Polytechnique Montréal, Canada.

Alain Nguyen (tuananhalain.nguyen@NRCan-RNCAn.gc.ca) is a research engineer at CanmetEnergy, Canada.

Gabrielle Beaudry (gabrielle.beaudry@polymtl.ca) is a research engineer at Polytechnique Montréal, Canada.

for open-loop GSHP is based on a step-drawdown test performed during normal system operation to determine potential fouling and clogging issues (Gjengedal *et al.*, 2019). Although monitoring systems in GSHP applications can be easily implemented, accumulation of large data sets and a lack of hydrogeology expertise for data interpretation are some of the reported issues with these surveillance methods (Gjengedal *et al.*, 2018, 2021). A new approach, based on residual analysis between predicted and measured water level in the well, has potential to detect gradual decreases in infiltration capacity. The key to this approach is to accurately predict the water level in an efficient manner, that is including the effect of temperature on hydraulic conductivity and without the burden of running a computationally heavy numerical model for every prediction task.

Artificial neural networks (ANN) can tackle various prediction tasks with large data sets as they are able to learn complex non-linear relationship between input and output variables. Artificial intelligence is a thriving field with increasing applications in GSHP. The use of ANN now concerns GSHP coefficient of performance prediction (Cho *et al.*, 2021; Esen and Inalli, 2009; Puttige *et al.*, 2021; Sun *et al.*, 2015), ideal control strategies for GSHP systems (Wang *et al.*, 2020) and for hybrid GSHP systems (Gang *et al.*, 2014), modeling of borehole heat exchanger (Puttige *et al.*, 2020), construction of g-functions (Dusseault and Pasquier, 2018, 2019; Pasquier *et al.*, 2018), inference of thermal parameters (Pasquier and Marcotte, 2020), prediction of disturbed ground temperature (Zhou *et al.*, 2021) and financial optimization of GSHP systems (Dusseault and Pasquier, 2021). The previously mentioned ANN applications mostly involved feedforward neural networks and multi-layer perceptrons. Long short-term memory (LSTM) network, a kind of neural network using only sequential data for prediction, have yet to be widely used in GSHP even though being broadly employed in time series forecasting due to their fast and accurate prediction. LSTM networks represent a promising tool for GSHP systems as one can learn long-term dependencies, such as seasonality, and daily patterns. The use of LSTM networks in GSHP has to this day only been applied to prediction of building's thermal load demand (Xie *et al.*, 2020; Zhang *et al.*, 2020), detecting anomaly energy consumption (Xu and Chen, 2020), and forecasting indoor temperature (Xu *et al.*, 2019).

Residuals between forecasted and measured hydraulic head can act as a surrogate to fouling problems in IWs. However, we first need to rigorously predict the aquifer's response under different operating controls. This paper addresses this issue by demonstrating the potential of LSTM networks to forecast negative drawdown in the IW of a GSHP system and by validating the results with an operational data set. The methodology relies on a simplified 2D-axisymmetric finite-element model (FEM) to generate training and validation data sets that consider the crucial effect of temperature on hydraulic conductivity. To the best knowledge of the authors, it is the first LSTM network used to predict water level variations of an operating IW using only a FEM at training and validation steps. Weights and biases of the different hidden layers are obtained by self-supervised learning. The ANN can predict variations of the water level in the operational IW within respectable errors in under a second when correctly trained on synthetic data. In the next sections, the principles behind LSTM network will be covered as well as the FEM used to construct the synthetic data set. The methodology proposed in this work is finally illustrated through an application on an operational data set.

LONG SHORT-TERM MEMORY NETWORK

LSTM network is a variety of recurrent neural network (RNN) and can be perceived as successive copies of the same ANN connected through time via hidden state variables (Olah, 2015). In other words, information at the current time step is connected to the next prediction task. Cells state is the main component in a LSTM cell as it stores relevant long-term dependencies rather than carrying it along over time steps like RNNs (Goodfellow *et al.*, 2016). LSTM cells also learn to decide when to self-reset their memory, based on the input sequence, thus making them adaptive even once trained (Gers *et al.*, 1999). As shown in Figure 1, a LSTM cell has four learned neural network layers (yellow boxes), consisting of three sigmoid layers and a hyperbolic tangent layer. The sigmoid layers act as regulation gates for the cell and hidden state as they filter the relevant (or irrelevant) information to be passed (or retained) to the next time step. Values are squeezed between 0 and 1 in a vector of length corresponding to the dimensionality of the cell state, where

more information is added (or removed) as values get closer to 1. The hyperbolic tangent layer, on the other hand, proposes new information to be added to the cell state via an output vector with values constrained in the range $[-1, 1]$.

The updated cell state (\mathbf{c}_t) results in a series of additions and/or subtractions on the cell state of the previous time step (\mathbf{c}_{t-1}). The forget gate (\mathbf{f}_t) determines what portion of the past cell state (\mathbf{c}_{t-1}) is irrelevant and should be deleted given the current variables (\mathbf{x}_t) and the past hidden state (\mathbf{h}_{t-1}). Writing new relevant information in the cell state is dictated by the input gate (\mathbf{i}_t) and the candidate values ($\tilde{\mathbf{c}}_t$). The updated hidden state (\mathbf{h}_t), which is also the output of the LSTM cell, is subsequently updated with a subset of the updated cell state that has been previously filtered by the output gate (\mathbf{o}_t) and passed through a hyperbolic tangent function, so that only relevant information is used for prediction at this time step. This process is then repeated for each time step in the sequence (Olah, 2015).

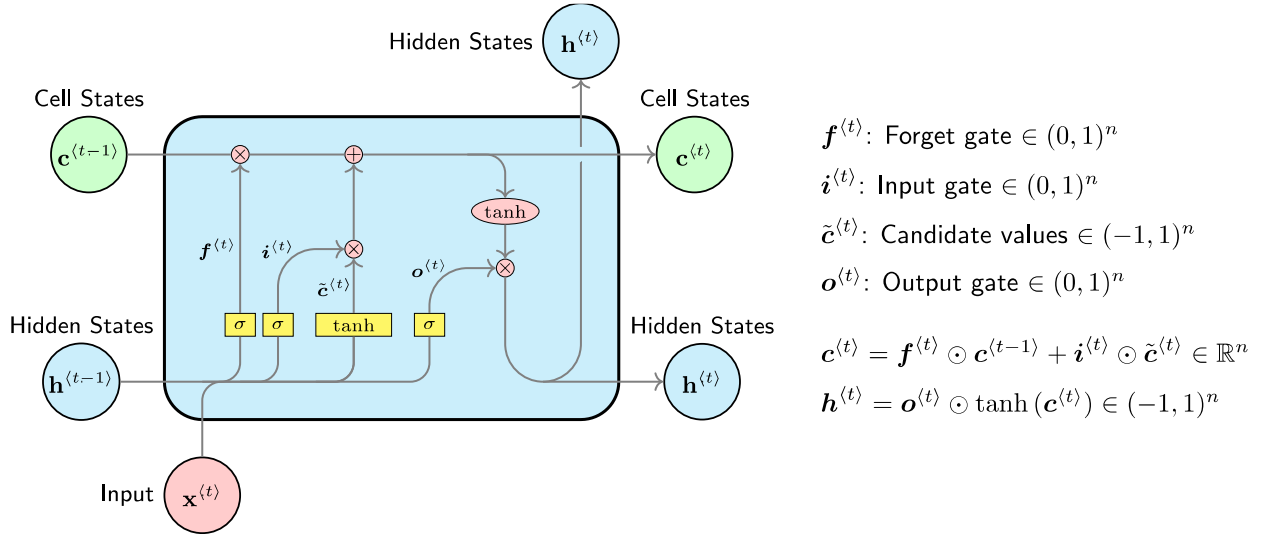


Figure 1 The structure of a typical LSTM cell where σ is a sigmoid layer, tanh (yellow) is a hyperbolic tangent layer, and where tanh (red) is the hyperbolic tangent function applied to a scalar. Note that \odot is the Hadamard product, n denotes the size of the cell and hidden state vectors.

CONSTRUCTION OF A TRAINING SET WITH A NUMERICAL MODEL

ANNs require large operational data sets to achieve acceptable prediction performance. Operational data being often difficult to obtain, one way to overcome this constraint is to build a training set using a FEM. Rigorously built FEMs can be quite computationally expensive and they most likely require field work to validate the model with experimental data. Since building a large synthetic data set can also be time consuming, the FEM used to train the network needs not to be as accurate as a numerical model used for prediction purposes. The LSTM network uses the FEM's inputs and output times series to learn non-linear and non-stationary physical processes.

Heat Transfer and Groundwater Flow Model

A simplified 2D-axisymmetric FEM in the COMSOL Multiphysics environment (COMSOL, 2021) is commonly used to couple groundwater flow and heat transfer to emulate a single SCW's operation and limit computation time (Beaudry *et al.*, 2018, 2019; Eppner *et al.*, 2017; Nguyen *et al.*, 2015). In this study, the validated model developed by Beaudry *et al.* (2019) to emulate an operational SCW connected to a geothermal laboratory has been modified to represent the geometry of the IW, that is also present on the study site (see Table 1). Note that the final depth of the reinjection pipe

corresponds to the mid-point of its perforated section. During the model’s development, care was taken to ensure that lateral boundary conditions were not significantly affecting the hydraulic heads and temperatures of the fluid returned to the IW. The domain is discretized into 5472 quadratic elements.

Table 1. Numerical Model’s Geometry

Parameters	Clayey Silt	Rock	Injection Well	Reinjection Pipe
Depth	3 m	152 m	152 m	130 m
Radius	30 m	30 m	83 mm	24.34 / 30.16 mm

Table 2 presents the properties of the four materials composing the IW and its surroundings. Water density and water dynamic viscosity were set as temperature-dependent variables in the model, which allows variations of hydraulic conductivity through time. One could refer to Beaudry *et al.* (2019) for a thorough description of the experimental site and numerical model. Note that hydraulic and thermal properties of the bedrock were drawn, for each simulation, from uniform distributions. This was done to illustrate the fact that even if local properties are quite uncertain, a well-trained LSTM network can reproduce accurately operational measurements.

Table 2. Numerical Model’s Parameters

Parameters	Unit	Clayey Silt	Rock	HDPE Pipe	Water
Porosity	-	0.2	0.01	0	-
Hydraulic Conductivity	ms ⁻¹	10 ⁻⁷	[3.5, 4.1]×10 ⁻⁷	10 ⁻⁹	-
Specific storage	m ⁻¹	10 ⁻³	[0.9, 1.1]×10 ⁻⁵	4×10 ⁻⁶	4×10 ⁻⁶
Volumetric heat capacity	MJm ⁻³ K ⁻¹	1.4	[1.8, 2.2]	2.17	4.18
Thermal conductivity	Wm ⁻¹ K ⁻¹	1.8	[2.5, 3.0]	0.42	0.59

Figure 2a illustrates the IW’s geometry and the model’s boundary conditions. One should note that an unspecified boundary condition indicates that a zero-flux boundary is set. The initial hydraulic head ($H_{t=0}$) of the model and the lateral boundary is fixed to 150 m relative to the model’s base. The inflow boundary ($v_{t,in}=V_{t,in}/A_{in}$) at the top of the IW is set as a time-varying stepwise function that includes the flow rate ($V_{t,in}$) and the cross-sectional area of the injection pipe (A_{in}). The initial temperature of the domain and the lateral boundary corresponds to a temperature profile (T_z) measured in the IW. The water temperature ($T_{t,in}$) and air temperature ($T_{t,air}$) are time-varying functions implemented in the model. Natural heat flux (q_{geo}) is fixed at the base of the model to 0.063 Wm⁻² and was obtained with the geothermal gradient and the thermal conductivity following the relation $q_{geo}=k \cdot dT/dz$.

Simulation Strategy

Once the FEM was built and operational, a total of 500 simulations were carried out to obtain the IW’s hydraulic response under different flow rate ($V_{t,in}$) and inlet temperature ($T_{t,in}$) time series. The FEM was simulated over a period of 36 days (864 hours) with a time step of 5 minutes. Hence, the length of every sequence forming the training set is 10369 steps. The 500 simulations were performed with thermal parameters (thermal conductivity and volumetric heat capacity) and hydraulic parameters (hydraulic conductivity and specific storage) drawn from the bounded uniform distributions shown in Table 2. A new time-varying function of inlet temperature ($T_{t,in}$) and flow rate ($V_{t,in}$) was used for each simulation. An example is shown in Figure 2b and 2c. The approach consisted of generating flow rate ($V_{t,in}$) and specific heat load (q) time series with values randomly sampled from 0, 6.67, 13.33 and 20 L/min and from 0, 25, 50 and 75 W/m. The length of the step intervals was also drawn following a uniform distribution from 2, 4, 6, 9, 12 and 18 days. The inlet temperature ($T_{t,in}$) was then derived from the infinite line-source model (Ingersoll *et al.*, 1954) using specific heat load (q) time series and corresponding thermal parameters. This approach allowed us to approximate the outlet temperature at the SCW, which was then used as the inlet temperature ($T_{t,in}$) at the IW while leaving the SCW out of the FEM and thus, speeding up simulation time. Assembling the complete training set required approximately 12.5 days on a quite busy server. An additional independent simulation was generated to assess the accuracy of the network.

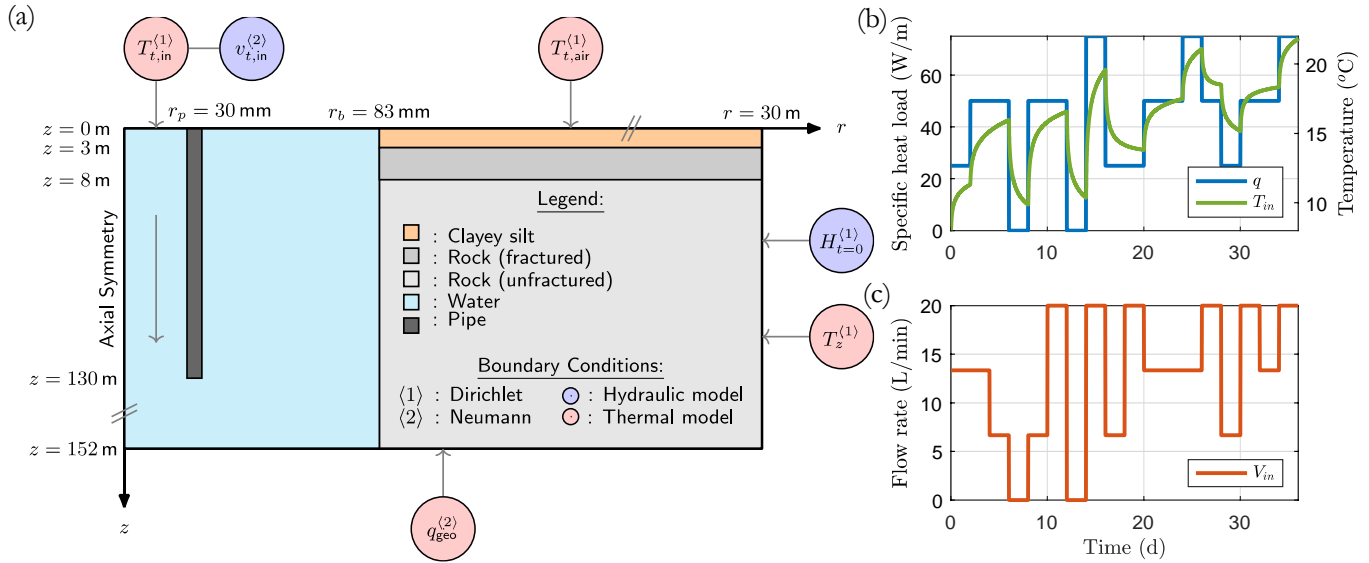


Figure 2 (a) Geometry and boundary conditions of the coupled numerical model used to generate the training data set. If unspecified, a zero-flux boundary is used (not to scale). (b) Generated specific heat load (q) stepwise function and corresponding injected water temperature (T_{in}) derived from the infinite line-source model used in the fifth simulation. (c) Flow rate (V_{in}) time series implemented in the fifth simulation.

PROPOSED LSTM NETWORK

In this study, the neural network was built using the Deep Learning Toolbox of MATLAB (MATLAB, 2021). Weights and biases of each layer in the network are modified at every iteration in the training phase to minimize an objective function (Goodfellow *et al.*, 2016). The optimal framework was identified as the one minimizing the mean squared error (MSE) and the root-mean-squared error (RMSE) on an independent synthetic validation set to prevent overfitting the data to the training set. LSTM networks with one to four layers combined with various activation layer (sigmoid, rectified linear unit and hyperbolic tangent) and regularization layer (dropout, layer normalization, batch normalization) were tested. Hyperparameters, such as the number of hidden units in each LSTM layer, initial learning rate and dropout probability were optimized using Bayesian optimization. Prior to training, inputs and outputs were rescaled to be in the range $[-1, 1]$. Such normalization is a standard practice as it accelerates the learning process with gradient-based algorithms (LeCun *et al.*, 2012). Flipping, a data augmentation technique, was used to improve performance prediction of the LSTM network (Wen *et al.*, 2021). Table 3 displays the parameters used to train the optimal LSTM network obtained from Bayesian optimization.

Table 3. Parameters for training the LSTM Network

Parameters	Value	Parameters	Value
Number of hidden layers	4	Epochs	10
Initial learning rate	0.0003	Mini-batch size	25
Learning rate drop factor	0.9	Loss function	MSE
Learning rate drop period	1	Optimizer	Adam
Dropout rate	0.2	Activation function	tanh

The optimal architecture, as illustrated in Figure 3, consists of an input layer, four hidden layers, that includes three LSTM layers, a fully connected layer, and an output layer. Layer normalization and dropout are the regularization techniques applied to the LSTM network. These layers prevent the neural network from overfitting, improve its

prediction performance and decrease training time (Ba *et al.*, 2016; Srivastava *et al.*, 2014). To ease the learning process, the network was trained to reconstruct $s_i/(V_{i,in}+1)$, that is the negative drawdown divided by the flow rate plus one. The output was then transformed back to s_i . This transformation prevented problems associated with fast-changing water levels and division by zero (zero flow rate). Training and validation sets were displaying a loss function (MSE) having an asymptotic behavior and a similar value at the end of the training phase, hence indicating good generalization from the trained network. The LSTM network allows negative drawdown prediction in the IW within an RMSE of 10.9 cm with respect to the synthetic validation time series.

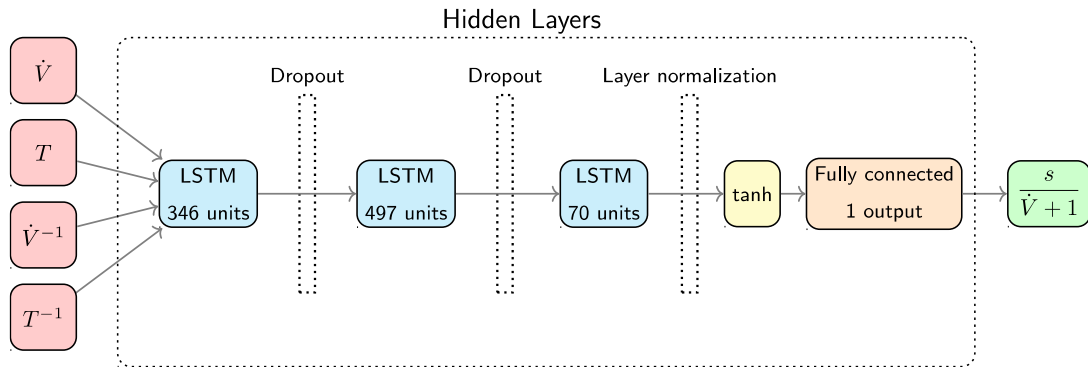


Figure 3 Architecture of the proposed LSTM network. Inputs are the flow rate and inlet temperature, as well as the inverse of their time series. The output is the negative drawdown divided by the flow rate plus one.

PERFORMANCE PREDICTION ON AN OPERATIONAL DATA SET

The operational data set used in this study was gathered by the geothermal laboratory of Polytechnique Montréal. The laboratory, now located in Varennes, Canada, is connected to a 215 m deep SCW and a 152 m deep IW located 10 m apart from each other in a moderately permeable bedrock (Beaudry *et al.*, 2018, 2019). Respectively, a variable speed submersible pump, an energy valve and a 24-kW water heater control the pumping rate, the bleed ratio, and the groundwater temperature. One should refer to Beaudry *et al.* (2018, 2019) for a comprehensive hydrogeothermal characterization and Cerlet *et al.* (2020) for details concerning equipment and sensors installed at the geothermal laboratory.

The predictive performance of the LSTM network was tested on a 36-day operation test conducted in summer 2019 at the geothermal laboratory. Figure 4a illustrates the monitored inlet and outlet temperature along with matching ground thermal loads during the experiment. Pumping rates in the SCW and discharge flow rates in the IW are also shown in Figure 4b. Multiple heating and recovery phases occurred during the experiment with heating power ranging from 0 to 24 kW (112 W/m). The operation was performed with two bleed periods where discharge flow rates were set at 7.5 L/min and 15 L/min (bleed ratio of 10%). Flow rates were recorded with a time step interval of 1 minute by an energy valve located inside the laboratory and having a 2 % accuracy. The water level in the IW was initially located at a depth of 1.8 m and was monitored in the annular space of the IW with a time step interval of 1 minute using a pressure sensor displaying an accuracy of 0.5 cmH₂O. The same probe contained a temperature sensor which recorded water temperatures with a 0.1 °C accuracy. A spline interpolation, for a time step of 5 minutes, and a low-pass filter were applied on the measurements to remove high-frequency noise.

The forecasted drawdown along with the operational measurements are illustrated in Figure 5. Results indicate a very good match during the first 18 days with an RMSE of 14.8 cm. Notice how the heads, and the underlying effect of

temperature, are well reproduced by the LSTM network between days 12 and 18 (RMSE of 7.3 cm). We will show below that the proposed neural network exhibits the expected predictive behavior regarding flow rate and inlet temperature. As one can notice, overflowing occurred in the IW between days 27 and 35 of the experiment when the discharge rate was set at 15 L/min. This is a clear example of a previously mentioned problem related to IW in GSHP system. Also, between the two bleeding periods, a positive drawdown is observed in the IW. Natural fluctuation of the water level from greater evapotranspiration and less recharge is a plausible explanation to this observation. Both wells being only 10 m apart, hydraulic interaction between the SCW and the IW might have contributed as well to the measured drawdown. The 2D-axisymmetric FEM used to train the LSTM network did not take into consideration natural factors affecting water levels nor the SCW, thus explaining the incapability of the ANN to accurately forecast this segment (RMSE of 30.4 cm). Nevertheless, for the first 18 days of the experiment, the predicted drawdown and the one observed during the experiment are in good agreement.

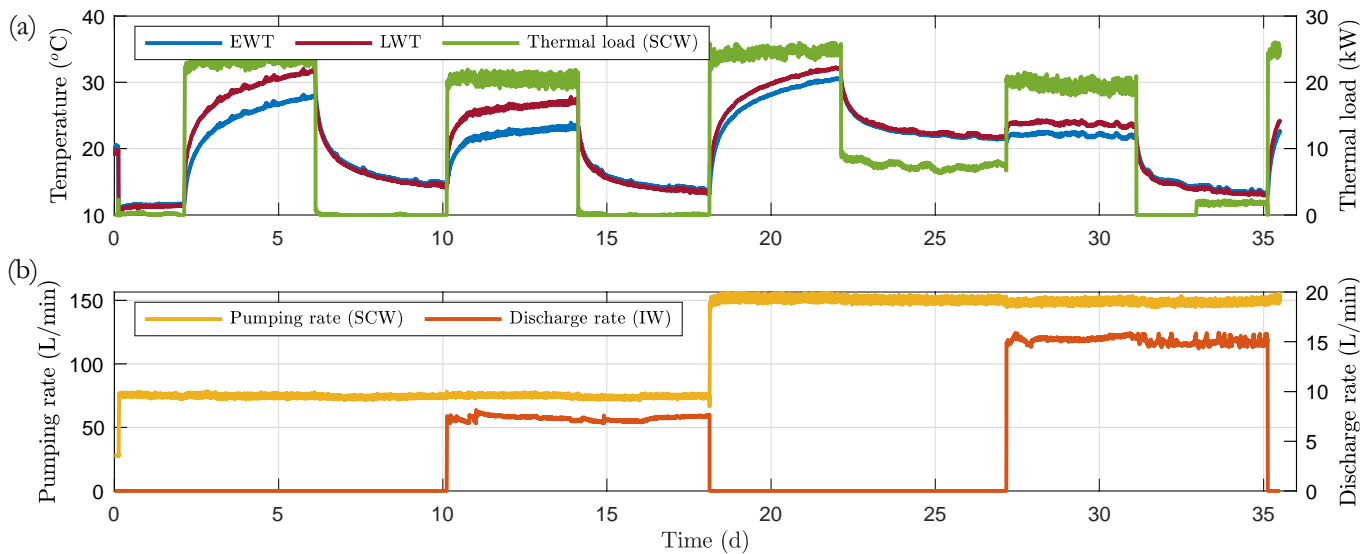


Figure 4 (a) Monitored entering water temperature (EWT), leaving water temperature (LWT) temperature and thermal load imposed to the 215-m SCW. (b) Recorded pumping rate in the SCW and discharge rate in the IW.

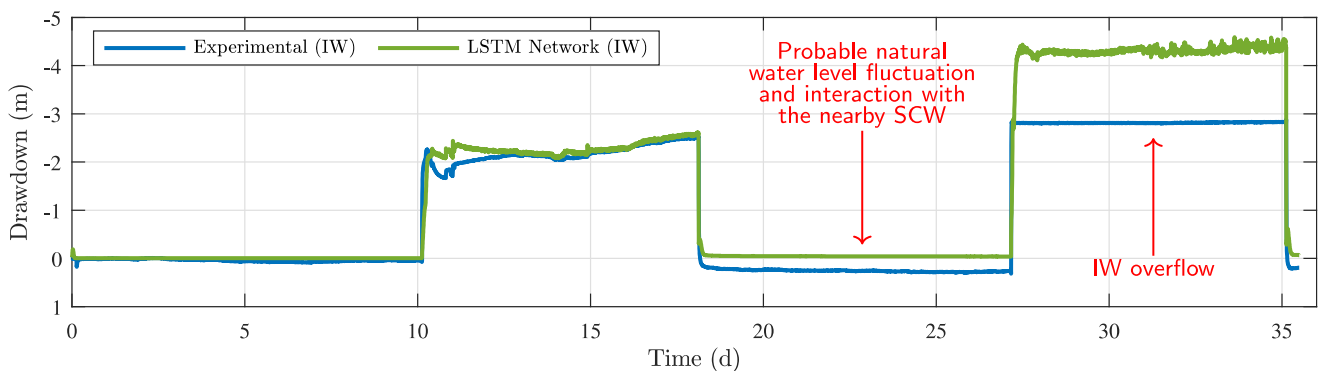


Figure 5 Operational measured drawdown in the IW and predicted drawdown by the LSTM network.

FURTHER RESULTS AND DISCUSSION

The impact of flow rate and inlet temperature on the forecasted drawdown has been studied to determine whether outputs displayed expected behaviors regarding water level variations and whether the proposed LSTM network could take into consideration the effect of temperature on hydraulic conductivity. To do so, different constant flow rates (2, 6, 10, 14 and 18 L/min) were fed to the LSTM network while using the same inlet temperature time series (see Figure 6a). The comparison is shown in Figure 6b.

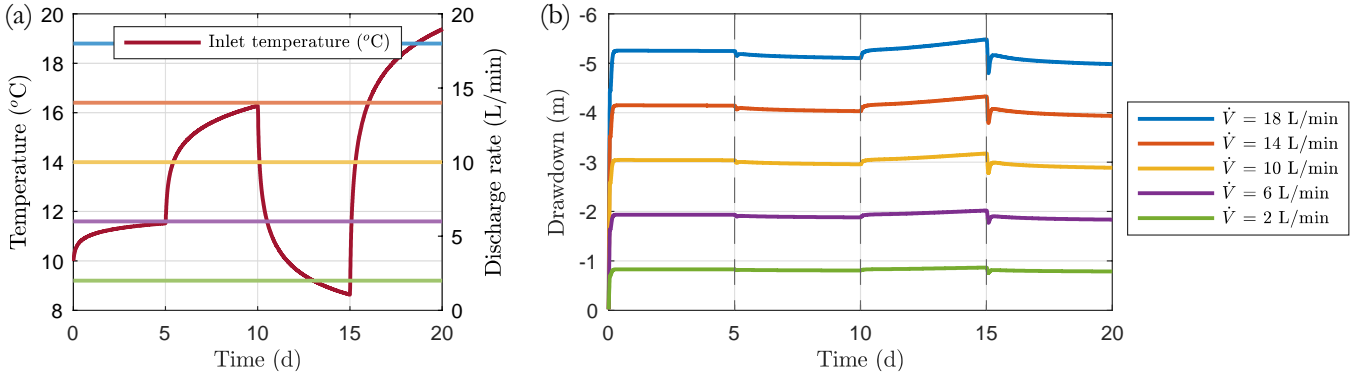


Figure 6 (a) Flow rates ($V_{i,m}$) and the inlet temperature ($T_{i,in}$) used to study their impact on drawdowns predicted by the LSTM network. (b) Drawdowns predicted by the LSTM network.

First and foremost, results show that forecasted negative drawdown in the IW increases proportionally with flow rates. Following Darcy's law for fluid flow in porous media (Darcy, 1856), analogous to Fourier's law of heat conduction (Fourier, 1878), drawdowns are supposed to vary proportionally with flow rates. Hence, predictions of the proposed LSTM network display the expected behavior with respect to flow rates. Furthermore, for an increasing inlet temperature, negative drawdown in the well should decrease as the hydraulic conductivity of the aquifer increases. Inversely, as the inlet temperature lessens, negative drawdown is supposed to increase. As seen in Figure 6b, this behavior is also respected for all flow rates, although appearing more preeminent with high flow rates due to the scaling effect of the figure. For example, between days 10 and 15, the inlet temperature dropped from 16.3 °C to 8.6 °C. This temperature variation resulted in an increase of the negative drawdown by 7.4 % with respect to the initial drawdowns at day 10 and that, for all flow rates. It is worth mentioning that the variation of the negative drawdown is similar for any given time intervals and flow rates. Thus, the impact of the inlet temperature on the network's response is similar for all flow rates and the LSTM network do consider the effect of temperature.

CONCLUSION

In this paper, a LSTM network was trained using 500 synthetic time series generated with a FEM coupling heat transfer and groundwater flow to predict negative drawdown in the IW of a GSHP system. The predictive performance of the ANN was tested on a 36-day operation at the geothermal laboratory of Polytechnique Montréal. The resulting RMSE between the forecasted and measured negative drawdown is 14.8 cm. As of now, this method, which considers the effect of temperature on hydraulic conductivity, has demonstrated its prediction performance on a short-time operational data set. The proposed LSTM network is specific to a particular site as it currently lacks generalization capabilities to be extended to different well geometries and other sites. Comparative studies with other ANN methods such as RNN, convolution neural network, transformer neural network and Bayesian neural network should be carried out to improve and compare forecasting performance.

ACKNOWLEDGMENTS

The authors acknowledge the support from partners of the Geothermal Research Chair on the Integration of SCWs in Institutional Buildings, namely Hydro-Québec, the Ministry of Higher Education of Québec, CSSMI, CSSDM, CSSS, Versa Profiles, Marmott Energy, CanmetEnergy and NSERC. Additionally, we thank the anonymous reviewers and colleagues (L. Jacques, L. Champagne-Péladeau) that provided constructive comments. This work was financed by the Natural Sciences and Engineering Research Council of Canada through grant number ALLRP 544477-19.

REFERENCES

- Ba, J. L., J. R. Kiros and G. E. Hinton. 2016. *Layer Normalization*. ArXiv:1607.06450.
- Ballard, T. 2017. *Using Specific Capacity to Monitor Well Performance*. Southeast Hydrogeology.
- Banks, D. 2012. *An introduction to thermogeology: Ground source heating and cooling (2nd ed)*. John Wiley & Sons, Ltd.
- Beaudry, G., P. Pasquier and D. Marcotte. 2018. *Hydrogeothermal characterization and modelling of a standing column well experimental installation*. Proceedings of the IGSHPA Research Track 2018.
- Beaudry, G., P. Pasquier and D. Marcotte. 2019. *The impact of rock fracturing and pump intake location on the thermal recovery of a standing column well: Model development, experimental validation, and numerical analysis*. Science and Technology for the Built Environment, 25(8), 1052–1068.
- Bouwer, H. 2002. *Artificial recharge of groundwater: Hydrogeology and engineering*. Hydrogeology Journal, 10(1), 121–142.
- Cercllet, L., B. Courcelles and P. Pasquier. 2020. *Impact of Standing Column Well Operation on Carbonate Scaling*. Water, 12.
- Cho, H. U., Y. Nam, E. J. Choi, Y.J. Choi, H. Kim, S. Bae and J. W. Moon. 2021. *Comparative analysis of the optimized ANN, SVM, and tree ensemble models using Bayesian optimization for predicting GSHP COP*. Journal of Building Engineering, 44.
- COMSOL. 2021. *COMSOL Multiphysics (6.0)* [Computer software]. COMSOL AB.
- Darcy, H. 1856. *Les fontaines publiques de la ville de Dijon: Exposition et application des principes à suivre et des formules à employer dans les questions de distribution d'eau : Ouvrage terminé par un appendice relatif aux fournitures d'eau de plusieurs villes, au filtrage des eaux et à la fabrication des tuyaux de fonte, de plomb, de tôle et de bitume*. V. Dalmont.
- Dusseault, B. and P. Pasquier. 2018. *Near-instant g-function construction with artificial neural networks*. Proceedings of the IGSHPA Research Track 2018.
- Dusseault, B. and P. Pasquier. 2019. *Efficient g-function approximation with artificial neural networks for a varying number of boreholes on a regular or irregular layout*. Science and Technology for the Built Environment, 25(8), 1023–1035.
- Dusseault, B. and P. Pasquier. 2021. *Usage of the net present value-at-risk to design ground-coupled heat pump systems under uncertain scenarios*. Renewable Energy, 173, 953–971.
- Eppner, F., P. Pasquier and P. Baudron. 2017. *A coupled thermo-hydro-geochemical model for standing column well subject to CO₂ degassing and installed in fractured calcareous aquifers*. Geomechanics for Energy and the Environment, 11, 14–27.
- Esen, H. and M. Inalli. 2009. *Modelling of a vertical ground coupled heat pump system by using artificial neural networks*. Expert Systems with Applications, 36(7), 10229–10238.
- Fourier, J. B. J. 1878. *The analytical theory of heat*. Cambridge : University Press.
- Gang, W., J. Wang and S. Wang. 2014. *Performance analysis of hybrid ground source heat pump systems based on ANN predictive control*. Applied Energy, 136, 1138–1144.
- Gers, F. A., J. Schmidhuber and F. Cummins. 1999. *Learning to forget: Continual prediction with LSTM*. 1999 Ninth International Conference on Artificial Neural Networks ICANN 99. (Conf. Publ. No. 470), 2, 850–855 vol.2.
- Gjengedal, S., R. Ramstad, B. Hilmo and B. Frengstad. 2019. *Fouling and clogging surveillance in open loop GSHP systems: A systematic procedure for fouling and clogging detection in the whole groundwater circuit*. Bulletin of Engineering Geology and the Environment, 79.
- Gjengedal, S., R. K. Ramstad, B. O. Hilmo and B. Frengstad. 2018. *Video inspection of wells in open loop ground source heat pump systems in Norway*. Proceedings of the IGSHPA Research Track 2018.
- Gjengedal, S., L.A. Stenvik, R. K. Ramstad, J. I. Ulfnes, B. O. Hilmo and B. S. Frengstad. 2021. *Online remote-controlled and cost-effective fouling and clogging surveillance of a groundwater heat pump system*. Bulletin of Engineering Geology and the Environment, 80(2), 1063–1072.
- Goodfellow, I., Y. Bengio and A. Courville. 2016. *Deep Learning*. The MIT Press.
- Ingersoll, L. R., O. J. Zobel and A. C. Ingersoll. 1954. *Heat conduction with engineering, geological and other applications*. Wisconsin U.P.

- LeCun, Y. A., L. Bottou, G. B. Orr and K.-R. Müller. 2012. *Efficient BackProp*. In Neural Networks: Tricks of the Trade (2nd ed.) (pp. 9–48). Springer.
- MATLAB. 2021. *MATLAB* (Version R2021b) [Computer software]. The MathWorks Inc.
- Nguyen, A., P. Pasquier and D. Marcotte. 2015. *Influence of groundwater flow in fractured aquifers on standing column wells performance*. *Geothermics*, 58, 39–48.
- Olah, C. 2015. *Understanding LSTM Networks*. Colah's Blog.
- Pasquier, P. and D. Marcotte. (2020). *Robust identification of volumetric heat capacity and analysis of thermal response tests by Bayesian inference with correlated residuals*. *Applied Energy*, 261.
- Pasquier, P., A. Nguyen, F. Eppner, D. Marcotte and P. Baudron. 2016. *Standing column wells*. In Advances in Ground-Source Heat Pump Systems (pp. 269–294). Woodhead Publishing.
- Pasquier, P., A. Zarrella. and R. Labib. 2018. *Application of artificial neural networks to near-instant construction of short-term g-functions*. *Applied Thermal Engineering*, 143, 910–921.
- Puttige, A. R., S. Andersson, R. Östin and T. Olofsson. 2020. *A Novel Analytical-ANN Hybrid Model for Borehole Heat Exchanger*. *Energies*, 13(23).
- Puttige, A. R., S. Andersson, R. Östin and T. Olofsson. 2021. *Application of Regression and ANN Models for Heat Pumps with Field Measurements*. *Energies*, 14(6).
- Snijders, A. L. and B. C. Drijver. 2016. *Open-loop heat pump and thermal energy storage systems*. In Advances in Ground-Source Heat Pump Systems (pp. 247–268). Woodhead Publishing.
- Srivastava, N., G. Hinton, A. Krizhevsky, I. Sutskever and R. Salakhutdinov. 2014. *Dropout: A Simple Way to Prevent Neural Networks from Overfitting*. *Journal of Machine Learning Research*, 15(56), 1929–1958.
- Sun, W., P. Hu, F. Lei, N. Zhu and Z. Jiang. 2015. *Case study of performance evaluation of ground source heat pump system based on ANN and ANFIS models*. *Applied Thermal Engineering*, C(87), 586–594.
- Wang, G., H. Wang, Z. Kang and G. Feng. 2020. *Data-Driven Optimization for Capacity Control of Multiple Ground Source Heat Pump System in Heating Mode*. *Energies*, 13(14).
- Wen, Q., L. Sun, F. Yang, X. Song, J. Gao, X. Wang and H. Xu. 2021. *Time Series Data Augmentation for Deep Learning: A Survey*. *Proceedings of the Thirtieth International Joint Conference on Artificial Intelligence*, 4653–4660.
- Xie, Y., P. Hu, N. Zhu, F. Lei, L. Xing, L. Xu. and Q. Sun. 2020. *A hybrid short-term load forecasting model and its application in ground source heat pump with cooling storage system*. *Renewable Energy*, 161, 1244–1259.
- Xu, C. and H. Chen. 2020. *Abnormal energy consumption detection for GSHP system based on ensemble deep learning and statistical modeling method*. *International Journal of Refrigeration*, 114, 106–117.
- Xu, C., H. Chen, J. Wang, Y. Guo and Y. Yuan. 2019. *Improving prediction performance for indoor temperature in public buildings based on a novel deep learning method*. *Building and Environment*, 148, 128–135.
- Zhang, C., J. Li, Y. Zhao, T. Li, Q. Chen and X. Zhang. 2020. *A hybrid deep learning-based method for short-term building energy load prediction combined with an interpretation process*. *Energy and Buildings*, 225.
- Zhou, S., J. Li, Y. Zhang, X. Liu and W. Zhang. 2021. *Prediction of the ground temperature variations caused by the operation of GSHP system with ANN*. *Geothermics*, 95.

A Case Study on High-Resolution Monitoring Network of Groundwater Heat Pump System

Ji-Young Baek

**Hae-Rim Oh
Seong-Sun Lee**

**Seung-Wook Ha
Kang-Kun Lee**

ABSTRACT

With the increasing installation of shallow geothermal energy, the importance of thermal impact prediction also increases in the system design stage. In nature, it is general that heterogeneity exists and it can affect the groundwater flow as well as the transport along to the flow. When predicting heat transport under the groundwater heat pump (GWHP) operation, however, impacts of heterogeneity have rarely been considered. In this study, to detect the hydraulic and thermal feedback to the two months of GWHP operation, a dense monitoring network was constructed with 12 monitoring wells at Eumseong-gun, Republic of Korea. The temperature was monitored in high resolution via fiber-optic distributed temperature sensing. During the GWHP operation, a very dynamic flow condition was generated with the hydraulic gradient between 0.005 and 0.07. The maximum temperature change at the nearest monitoring well was 2 °C. Observed hydraulic and thermal responses showed spatially heterogeneous results. While the heterogeneous responses of hydraulic change were stronger near the geothermal wells, those of temperature change were higher near the center of the thermal plume.

INTRODUCTION

In general, since nature is not homogeneous, the aquifer properties are shown spatial variability that can affect both groundwater flow and transport (Wu et al., 2005). The impacts of hydraulic heterogeneity on groundwater flow have been investigated by the systematic hydraulic tests in laboratory and field scales, or by the numerical model (Schwede et al., 2014; Somogyvari et al., 2017). The heterogeneity of aquifer also can affect heat transport occurring along with the groundwater flow and its impacts on transport results were studied through the tracer experiments and numerical model (Hamidi et al., 2019; Hoffmann et al., 2019). As several studies highlighted, the local heterogeneity can significantly affect hydraulic conditions near the injection and extraction points. Especially, under the GWHP operation, more complex flow is generated due to the dynamic injection environment. Although those complex flows can affect the flow and heat transport, the dense monitoring to consider the impacts of heterogeneity on thermal plume propagation during the dynamic injection environment has rarely been constructed and interpreted for the real scale experiments.

In this study, the GWHP system was installed at Eumseong-gun, Republic of Korea, and dense monitoring network was constructed with 12 monitoring wells. Especially, for temperature monitoring, fiber optic distributed temperature sensing was applied to obtain high-resolution spatial temperature data. Through the monitoring network, the hydraulic and thermal responses to the operation of the GWHP system were observed. Based on the observed temperature time-series data, the thermal front velocities were estimated for different four depths to figure out the impacts of inherent heterogeneity on flow and heat transport.

Kang-Kun Lee (kklee@snu.ac.kr) is a professor of school of earth and environmental sciences and Ji-Young Baek, Hae-Rim Oh, Seung-Wook Ha are PhD students and Seong-Sun Lee is a senior researcher at Seoul National University.

METHODS AND MATERIALS

Site description

The study area is located in Eumseong-gun, Republic of Korea. According to the watershed divides, it is contained in the Upper Miho Stream watershed, the north-center of the Geum River watershed. The geological composition of the study site is mainly explained by Jurassic Daebo granites (Kee et al., 2020). The sample core data of the borehole and the seismic refraction survey results showed the weathered soil covered a weathered rock layer which appears about 43 m in depth. The weathered rock consists of weathered biotite granite, and the main mineral composition of highly weathered biotite granite is quartz, albite, anorthite, and microcline with a small amount of hornblende, illite, and chlorite (Ju et al., 2022).

Two geothermal wells and 12 monitoring wells were fully screened for 40 m in depth. The ET of 76 m in depth consists of a polyethylene pipe and grouting material (bentonite for this site) to conduct the thermal response test. A background groundwater flow was locally generated from east to west in this site with a hydraulic gradient of 0.006 ± 0.0004 . The overall water level distribution was in the range of 76.24 m (a.s.l.) and 76.40 m (a.s.l.). For background groundwater temperatures within a site, there were few temperature differences in a horizontal direction with a small standard deviation of 0.05 °C, lower than the sensor accuracy (Figure 1). The mean background groundwater temperature on all monitoring wells was 13.7 °C. The hydraulic conductivity was determined as 1.97–2.98 m/d, using AQTESOLV (HydroSOLVE, Inc., USA) software to analyze the pumping test carried out at EM6 for 10.7 h by 16.6 m³/d.

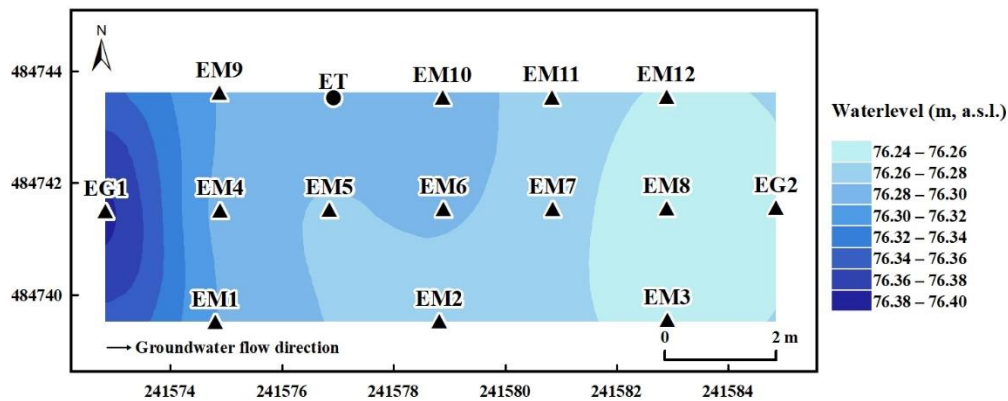


Figure 1 Background hydraulic head distribution. The ET is the borehole heat exchanger to conduct the thermal response test, EG wells are geothermal wells, and EM wells are monitoring wells.

GWHP system operation and monitoring network

A groundwater heat pump (GWHP) system was installed at the study site with two geothermal wells (EG1 and EG2 in Figure 1) and a monitoring network was densely constructed with 12 monitoring wells (EM1–12 in Figure 1) to catch the environmental change within groundwater able to reflect inherent local heterogeneity. To extract groundwater for heat exchange, a 1 HP submersible pump (ST-1808, Stairspumps, Republic of Korea) was installed at the 30 m depth of EG2 (pumping well). The pump was connected to the circulation pipeline which enable an indirect exchange of its

heat through the heat exchanger (Daesungheatenersys, Republic of Korea). Groundwater that temperature had been changed after the heat exchange was re-injected into EG1 (injection well). The GWHP system operated in a cooling mode from June 2, 2021, to July 31, 2021 (58 days).

For the real-time recording of the system operation status, a developed software was used to automatically control the GWHP system by regulating the power supply to the heat exchanger. The software recorded the operation state, load and source temperatures, and flow rate in the one-minute interval. Environmental changes due to the GWHP system were monitored by data loggers in terms of water level, temperature, and EC. TD-Diver (Schlumberger, The Netherlands) was selected to detect the water level as well as temperature and was installed at the 20 m depth of all monitoring wells. For the groundwater temperature and EC monitoring, CTD-Diver (Schlumberger, The Netherlands), and Levelogger LTC (Solinst, Canada) were installed at the 30 m depth of all monitoring wells. For the hydraulic head data, water level changes logged by TD-Diver were corrected via barometric pressure changes detected by Barologger (Solinst, Canada) installed at the 15 m depth of EM6. All loggers recorded the data in ten-minute intervals during and after the operation. In addition, a fiber-optic distributed temperature sensing (FO-DTS) system (Woori-system, Republic of Korea) was employed for temperature monitoring to obtain the temperature profile of each well. A 1600 m long two-core FO cable (SUS ARMORED, Woori-system, Republic of Korea) was installed at entire wells except for EG2 and it was connected to a DTS device (DTSX3000, Yokogawa, Japan) to detect the temperature changes. The applied FO-DTS system measured the temperature in less than one-second intervals with an accuracy of 0.5 °C and a spatial resolution of 1 m. For the temperature data measured by FO-DTS, pre-processing was performed by moving averaging to reduce the data noise. Detailed information on the constructed monitoring network is organized in Table 1.

Table 1. Detailed information on the monitoring system

Device (Manufacturer)	Installed well ID	Installed depth (m, b.g.s.)	Interval	Monitoring factors	Accuracy
TD-Diver (Schlumberger)	EG1, EM1–12	20 m	10 min	Water level	1 cmH ₂ O
				Temperature	0.1 °C
CTD-Diver (Schlumberger)	EM1–3, 8–10, 12	30 m	10 min	Water level	2.5 cmH ₂ O
				Temperature	0.1 °C
Levelogger LTC (Solinst)	EM4–7	30 m	10 min	EC	1 % of reading
				Water level	5 cmH ₂ O
FO-DTS (Woori-system)	EM1–12, EG1	Spatial resolution: 1 m	< 1 s	Temperature	0.05 °C
				EC	0.1 μS/cm

Thermal front velocity estimation

According to Levec and Carbonell (1985), when the thermal velocity in the fluid is the same as in the solid, the thermal front velocity can be expressed by the seepage velocity and volumetric heat capacity ratio as follows:

$$v^t = v^s/R \quad (1)$$

where the R is defined by (Bodvarsson, 1972)

$$R = \rho c/n_e \rho_f c_f \quad (2)$$

The seepage velocity can be written using Darcy's law as (Fetter, 2001)

$$v^s = q/n_e = Ki/n_e \quad (3)$$

With Eqs. (2) and (3), Eq. (1) can be rewritten as

$$v^t = v^s/R = Ki\rho_f c_f/\rho c \quad (4)$$

Thermal front velocity can be additionally estimated by the cross-correlation analysis of obtained temperature time-series. For time-series x_t and y_t , the cross-correlation coefficient at d is given by (Lo Russo et al., 2018)

$$r_{xy}(d) = C_{xy}(d)/\sigma_x\sigma_y \quad (5)$$

where

$$C_{xy}(d) = \frac{1}{N} \sum_{t=1}^{N-d} (x_t - \bar{x})(y_{t+d} - \bar{y}) \quad (6)$$

Thermal front velocity calculated by temperature time-series is defined as (Lo Russo et al., 2018)

$$v^t = D/L \quad (7)$$

where D [d] is the lag at the maximum r_{xy} .

RESULTS

Environmental changes during GWHP system operation

Water level change during the GWHP system operation. In the GWHP system, the injection and extraction occur repeatedly, but irregularly according to the heating or cooling demands. Due to that characteristic, complex hydraulic conditions can be generated during the operation. In this study, we monitored the environmental changes to investigate the flow and heat transport during the GWHP system considering the complex hydraulic conditions. The water level was monitored at 12 monitoring wells and the injection well at time intervals of ten minutes. In the results, while the background hydraulic gradient from EM4 to EM8 was relatively constant at 0.006 on average, during the GWHP operation, it showed a dynamic change up to 0.2 following the operation state.

Fig. 2 shows the observed hydraulic head data which was corrected by barometric pressure changes and elevation. In this study, the data were spatially divided into three parts: near the injection well (EM1, EM4, and EM9), the middle part (EM2, EM6, and EM10), and near the extraction well (EM3, EM8, and EM12). Near the injection well and the extraction well, the observed water levels showed a dynamic variation along with the complex cycle of system operation. The hydraulic head changes due to the injection and extraction were similar at monitoring wells that had the same distance to the injection and extraction wells. For example, water level changes at EM4 (2 m from the injection well) and EM8 (2 m from the extraction well) were 0.71 m and 0.75 m. However, the change patterns were different for the injection and extraction (Fig. 2a and Fig. 2c). In the middle part, where the distance to the injection well or the extraction well was the same (EM2, EM6, and EM10), the hydraulic head change was not noticeable due to the superposition effect of injection and extraction (Fig. 2b). Comparing the upper and lower parts, the hydraulic head change showed a spatial difference as it was larger in the upper part (EM9, and EM12) than in the lower part (EM1, and EM3) except for the EM2, and EM10.

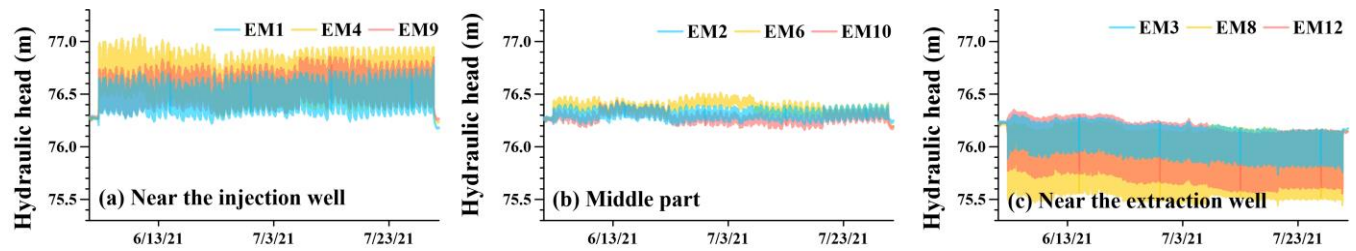


Figure 2 Observed hydraulic head at monitoring wells during the operation of the GWHP system (a) near the injection well, (b) at the middle part, and (c) near the extraction well.

Groundwater temperature changes during the GWHP system operation. During the GWHP system, the temperature change was monitored at the depth of 20 and 30 m by the temperature loggers as explained in Table 1. Also, in this study, we applied the FO-DTS method, which can record the temperature every 1 m depth at 12 monitoring wells and the injection well in real time, to obtain high-resolution temperature data in terms of spatial distribution. It was anticipated that the high-resolution data would enable an investigation of the impacts of heterogeneity on thermal plume propagation both in horizontal and vertical directions. The two temperature data, measured by temperature loggers and FO cable, showed good agreement with the averaged RMSE of 0.1 °C which is not exceeding the accuracy of the FO-DTS (0.5 °C) and temperature logger (0.1 °C). Especially for the wells that showed a temperature change of more than 0.9 °C (EM1–2, EM4–6, EM9–10, and EG1), the R-squared value was larger than 0.943. These results could ensure the applicability of FO-DTS in the detection of groundwater temperature changes during the GWHP system operation.

Figure 3 showed the spatial difference between the measured temperatures at the depths of 20 m and 30 m. The difference between the two temperature data was in the range of -0.2 °C to 0.8 °C and it increased along with the plume migration. The temperature difference between the two depths showed temporal and spatial variance, which can be evidence of the heterogeneity. For example, if the ground was homogeneous since injected hot water was transported along the groundwater flow direction, the temperature difference at the monitoring well cannot exceed that at the injection well. However, the experimental results showed that the maximum temperature difference at EM5 (monitoring well) was larger than that at EG1 (injection well). In other words, the thermal plume propagated faster at 20 m depth compared to at 30 m depth.

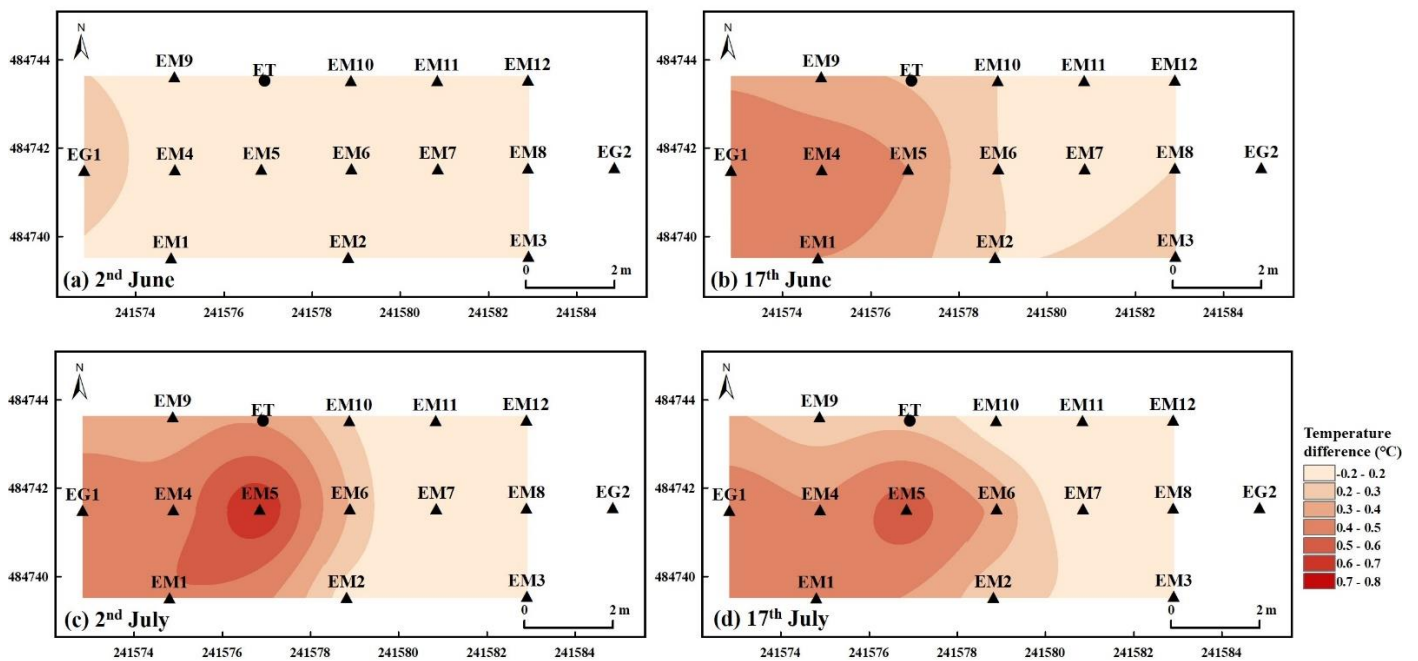


Figure 3 Spatial distribution of temperature difference between the depths of 20 m and 30m.

Estimated thermal front velocity

In this study, thermal front velocities were estimated by two different methods. That is the *theoretical* v^t (Eq. 4), calculated by the physical properties of the aquifer, and the *experimental* v^t (Eq. 7), estimated by the time delay of temperature time-series between two different wells. The *theoretical* v^t was calculated using the maximum and minimum values of hydraulic gradients and hydraulic conductivity. In this study, calculated *theoretical* v^t ranged from 0.10 m/d to 0.72 m/d (Fig. 4).

For the analysis of *experimental* v^t , the monitoring wells along the groundwater flow equations were used (EM1–EM2, EM4–EM7, and EM9–EM11) except EM3, EM8, and EM12 where the maximum temperature difference was lower than the sensing accuracy of FO-DTS (0.5 °C). The analysis was carried out using temperature data obtained from FO-DTS at four different depths of 20 m, 25 m, 30 m, and 35 m. In the cross-correlation analysis, the maximum cross-correlation coefficient of each case was larger than 0.62. The maximum cross-correlation coefficients were decreased with the increase of the well distance, which can indicate the correlation between the two time-series data was diminished according to the propagation of the thermal plume. In four cases, however, the cross-correlation was the highest from the very first time so the determined lag was minimal (e.g., $d = 1$ min) that was not reliable for representing the thermal velocity between the wells. Except for four cases, the resulted *experimental* v^t was in the range of 0.32 m/d to 1.21 m/d which was in a comparable range to the *theoretical* v^t (Fig. 4). Based on these results, it could be confirmed that the *experimental* v^t was reasonably estimated.

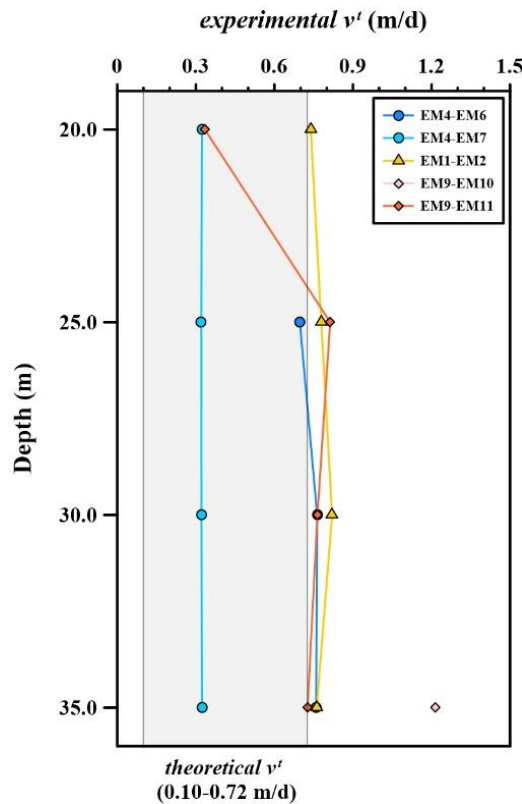


Figure 4 Calculated *theoretical* v^t for the study area and *experimental* v^t estimated at the specific depths (20, 25, 30, and 35 m).

CONCLUSION

In this study, the hydraulic and thermal changes were observed by a densely constructed monitoring network during the operation of the GWHP system installed in Eumseong-gun, Republic of Korea. To obtain high-resolution spatial temperature data, fiber optic distributed temperature sensing was applied. In the results, depth-averaged hydraulic responses to the GWHP system operation were different in monitoring wells that have the same distance to the geothermal wells, and those heterogeneous responses appeared stronger near the injection and extraction wells. Heterogeneity of thermal response appeared both vertical and horizontal. The vertical difference was the highest where the center of the thermal plume migrated. The estimated thermal front velocity supported the temperature monitoring results as it was different not only to the well intervals but also to the depths. As a further analysis, an inverse modeling will be performed using a numerical simulation to figure out the spatial distribution of effective hydraulic parameters. Based on that result, heat transport reflecting the hydraulic heterogeneity will be modeled to find out the possible impacts of heterogeneity on thermal plume propagation a short and long period of GWHP system operation.

ACKNOWLEDGMENTS

This work was supported by the National Research Foundation of Korea (NRF) grant funded by the Korea government (MSIP) (No. 2022R1A2C1006696).

NOMENCLATURE

v'	=	Thermal front velocity (m/d)
v^s	=	Seepage velocity (m/d)
R	=	Retardation factor (-)
n_e	=	Effective porosity (-)
ρc	=	Volumetric heat capacity (J/m ³ /K)
q	=	Specific discharge (m/d)
K	=	Hydraulic conductivity (m/d)
i	=	Hydraulic gradient (-)
d	=	Lag (d)
N	=	Length of data (-)
σ	=	Standard deviation of the time series (°C)
L	=	Distance between two points (m)

Subscripts

f	=	fluid
-----	---	-------

REFERENCES

- Bodvarsson, G. 1972. *Thermal problems in the siting of reinjection wells*. Geothermics 1(2): 63-66.
- Fetter, C.W. 2001. *Applied Hydrogeology*. Upper Saddle River, NJ: Prentice-Hall Inc.
- Hamidi, S., Heinze, T., Galvan, B., and Miller, S. 2019. *Critical review of the local thermal equilibrium assumption in heterogeneous porous media: Dependence on permeability and porosity contrasts*. Applied Thermal Engineering 147: 962-971.
- Hoffmann, R., Dassargues, A., Goderniaux, P., and Hermans, T. 2019. *Heterogeneity and prior uncertainty investigation using a joint heat and solute tracer experiment in alluvial sediments*. Frontiers in Earth Science 7, 108.
- Kee, W. S., Kim, S. W., Hong, P. S., Lee, B. C., Cho, D. R., Byun, U. H., ... and Lee, H. J. 2020. *1: 1,000,000 Geological map of Korea*. Korea Institute of Geoscience and Mineral Resources.

- Ju, Y., Györe, D., Gilfillan, S. M., Lee, S. S., Cho, I., Ha, S. W., ... and Lee, K. K. 2022. *Constraining the effectiveness of inherent tracers of captured CO₂ for tracing CO₂ leakage: Demonstration in a controlled release site*. Science of the Total Environment, 824, 153835.
- Levec, J. and Carbonell, R. G. 1985. *Longitudinal and lateral thermal dispersion in packed beds. Part I: Theory*. AIChE journal 31(4): 581-590.
- Lo Russo, S., Taddia, G., Dabove, P., Cerino Abdin, E., and Manzano, A. M. 2018. *Effectiveness of time-series analysis for thermal plume propagation assessment in an open-loop groundwater heat pump plant*. Environmental Earth Sciences 77(18): 1-11.
- Schwede, R. L., Li, W., Leven, C., and Cirpka, O. A. 2014. *Three-dimensional geostatistical inversion of synthetic tomographic pumping and heat-tracer tests in a nested-cell setup*. Advances in water resources 63: 77-90.
- Somogyvári, M. and Bayer, P. 2017. *Field validation of thermal tracer tomography for reconstruction of aquifer heterogeneity*. Water Resources Research 53(6): 5070-5084.
- Wu, J., Hu, B. X., and He, C. 2004. *A numerical method of moments for solute transport in a porous medium with multiscale physical and chemical heterogeneity*. Water resources research 40(1).



Modeling and performance evaluation of fractured thermal energy storage (FTES)

Max Hesselbrandt

José Acuña

ABSTRACT

Fractured thermal energy storage (FTES) is an open-loop type system that uses hydraulically propagated horizontal fracture planes for storage and extraction of heat in low-permeability hard rock formations. Groundwater circulation through the fracture system is accomplished by pumping and injection via a set of vertical peripheral wells symmetrically positioned around a central well. In this paper, a numerical approach for modeling of FTES systems based on the finite element method is presented. The modeling approach that is established can be used to investigate various storage design configurations and operation conditions. To demonstrate the application of the approach, an illustrative long-term simulation using a 3D model of a FTES system is performed, and the thermal performance of the modeled storage is evaluated in terms of energy and exergy efficiency indicators.

INTRODUCTION

Fractured thermal energy storage (FTES) systems involve the use of natural or artificially induced fractures in low-permeability rock for storage and extraction of thermal energy in the shallow ground. This type of open-loop storage system consists of multiple stacked sub-horizontal fractures that are interconnected by a number of vertically drilled boreholes. Typically, the boreholes are drilled in a symmetrical arrangement including a central well and peripheral wells spaced therefrom. In charging mode, heated groundwater is injected through the central well into the fractures, where the heat exchange with the rock matrix takes place. Once cooled, the water is extracted through the peripheral wells back to the heat exchanger where the cycle continues. During discharging, the water is circulated through the system in opposite direction.

The method of creating artificial fractures for promoting fluid flow and heat transport in hard rock, referred as the Hydrock concept in earlier publications, was introduced and tested already in the 1980's (Larson, Fridh, and Haag 1983; Larson 1984). Since then, the FTES technology has not received interest compared to other underground heat storage methods, such as borehole thermal energy storage (BTES) and aquifer thermal energy storage (ATES). However, FTES does not require the presence of a pre-existing permeable aquifer formation and could thus be, like BTES systems, more universally applicable than ATES systems. Also, being of open-loop type like ATES systems, FTES typically requires considerably fewer boreholes compared to a BTES system with comparable storage capacity (Hellström and Larson 2001). Hence, FTES could potentially combine some of the benefits associated with these conventional geothermal storage technologies.

Previous research on FTES systems has mainly focused on the rock fracturing processes employed to construct the

Max Hesselbrandt (max.hesselbrandt@bengt Dahlgren.se) is an energy consultant at Bengt Dahlgren AB. José Acuña (jose.acuna@bengt Dahlgren.se) is a PhD and researcher at the Royal Institute of Technology (KTH) as well as a manager at Bengt Dahlgren AB.

storage plant as well as hydraulic aspects of operation of the system, while less effort has been devoted to study the thermal processes involved. In the early experimental studies described by Larson (1984), the results from field tests performed in Bohus granite at Rixö, Sweden, demonstrated that fluid-driven crack propagation could effectively be controlled to produce approximately horizontal, parallel stacked fractures. Subsequent in situ studies investigated the effect of using propping agents for fracture stimulation (Eliasson, Sundquist, and Wallroth 1988). A research project aiming to develop equipment and methodology for utilization of shallow geothermal energy based on the Hydrock concept was initiated in the late 1990's in Norway. Within the project an extensive field test programme was conducted at two pilot plants (Bryn and EAB) located in the Oslo area, including hydraulic fracturing with water-only and with sand as propping agent as well as pumping tests and geophysical logging of the boreholes at the test sites (Ramstad 2004). Recently, Janiszewski et al. (2019) developed a numerical coupled hydro-mechanical model to study the interaction between natural fractures and hydraulically propagated fractures created for the construction of FTES plants. However, to the authors' best knowledge, there are only two studies in the literature that have focused on the thermal analysis of FTES systems. Hellström and Larson (2001) developed a coupled conduction-convection heat transport model of a FTES system using the explicit finite difference method (FDM) and performed a parameter study considering various geometrical parameters (e.g., spacing between fracture planes, number of peripheral wells, and storage diameter), operation conditions and fracture hydraulic properties. In the work by Ramstad (2004), results from the hydro-thermal finite element modelling of the Bryn and EAB pilot plants are presented. According to these studies, some important design considerations for FTES systems involve, for example, the spacing, number and aperture of fractures, the spacing between central and peripheral wells, and the heat conduction capability of the rock material within the storage.

Within the design process, the use of simulation models is critical for proper characterization and evaluation of FTES systems, yet the complex nature of coupled hydro-thermal processes in fractured rock imply serious challenges to the accurate analysis of the flow and transport problem under consideration. Therefore, adequate modeling techniques applicable to FTES need to be further explored. This paper presents a numerical approach for modeling of FTES systems based on the finite element code FEFLOW. In the model, wells and fractures are discretely represented by one- and two-dimensional finite elements embedded in a three-dimensional triangular mesh which represents the low-permeability rock matrix. Variations in inlet temperature and flow direction when shifting between charging and discharging mode of operation are considered. An illustrative simulation model is used to demonstrate the modeling approach presented in the paper, and the thermal performance of the modeled storage is evaluated in terms of energy and exergy efficiency.

FRACTURED THERMAL ENERGY STORAGE

A schematic sketch of a FTES system is given in Figure 1. The storage consists of the following main components:

1. Rock matrix – the solid part of the the rock mass, i.e., the storage medium.
2. Fracture planes – ideally horizontal or subhorizontal transmissive planar conduits that constitute the flow paths for the heat carrier as well as heat exchange surfaces between the heat carrier and the rock matrix.
3. Central and peripheral wells – vertical wells with packers installed at the sections of the boreholes that intersect the fracture planes.

The peripheral wells are symmetrically arranged around the central well. Fluid flow within the fracture planes is driven by a hydraulic gradient between the central wells and the peripheral wells, where sections with borehole-fracture intersections are packed-off from the remaining intervals of the well. During charging the flow is directed from the central well to the peripheral wells, and in the opposite direction during discharging. This operation strategy serves the purpose of creating thermal stratification within the storage to improve temperature retention during the course of

storage cycle. A similar design and operation approach can be employed for high temperature BTES systems, where the borehole heat exchangers are joined together in parallel strings containing series-connected loops ordered from the center to the peripheral region of the storage.

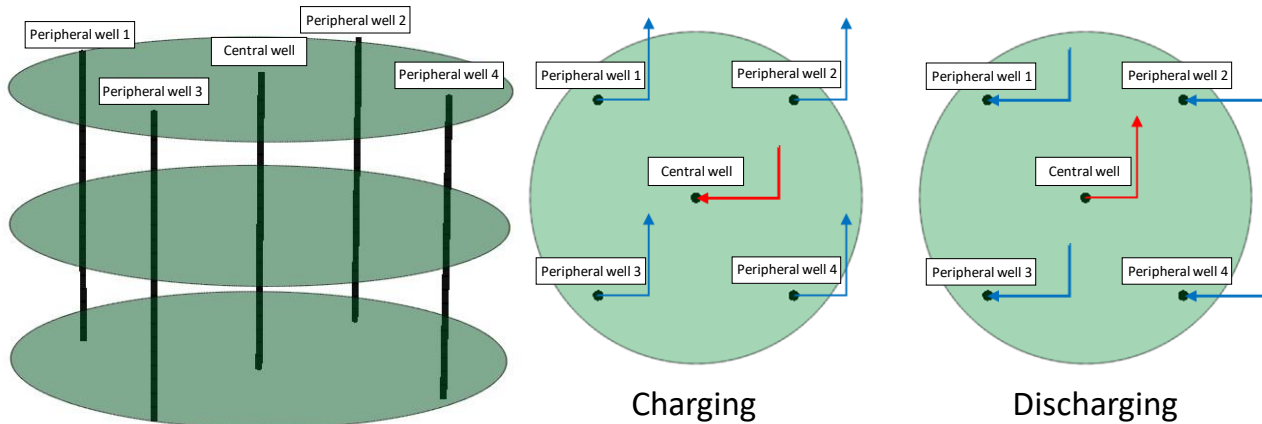


Figure 1 Principle sketch of a FTES system.

METHODOLOGY

Modeling of FTES systems involves solving the coupled problems of fluid flow and heat transport within fractures and the rock matrix. Since fluid flow in the rock mass is concentrated on preferential flow paths due to the presence of distinct fractures, the common assumption of the ground as a single continuum may not be suitable to adequately describe the processes occurring within the fractured medium (Berre, Doster, and Keilegavlen 2019). Instead, hybrid discrete-continuum models or approaches where fracture geometries are represented fully explicitly may be better suited.

In this work, the commercial finite element code FEFLOW 7.4 is selected for modeling of groundwater flow and heat transport within the FTES system (Diersch 2014). Application of the so-called discrete feature approach available in FEFLOW allows for modeling of flow and transport in fractures and other features that can be described by geometric representations of a lower dimension than the porous host medium structure. Considering a three-dimensional problem, 1D line or 2D areal elements representing e.g., wells and fractures can be embedded in and combined with the 3D discretization that represents the host rock matrix. The lower-dimensional elements are placed along the edges and faces of the 3D mesh. Flow and transport related properties (e.g. type of law of flow motion, hydraulic aperture) are assigned to each discrete feature. As thoroughly described by Diersch (2009), FEFLOW solves the coupled system of flow and transport balance equations governing in the discrete feature domains and the 3D finite element domain.

In the following sections, the general modeling approach applied in this work is described. Conceptually, the model features are divided into three groups i.e., solid rock matrix features, fractures, and wells. For simplification purposes, only saturated flow is considered, and the rock matrix is modeled as a homogeneous, isotropic and impermeable material. Fracture properties are assumed to be uniform and homogeneous within each fracture plane, and all fractures are assumed to be identical. All fractures and wells are assumed to extend only in horizontal and vertical directions, respectively.

Model development

Figure 2 shows an example of discretization of a FTES system model consisting of 5 pumping wells and 11 fracture planes. The discretization of the octagonal-shaped model domain is accomplished by first constructing a horizontal 2D unstructured mesh. The 2D mesh is refined locally in the region occupied by fracture planes, including the interspace between the well locations. Specifically, the mesh around the wells is refined in such that an ideal spacing between the well nodes and surrounding nodes is applied to achieve highest numerical accuracy (Diersch et al. 2011). The 2D mesh plane is extruded along the depth axis to create a 3D vertically structured mesh structure. The grid is partitioned into plane layers of triangular prismatic elements. As shown in Figure 2 b), the vertical grid is locally refined along the depth interval containing (packed-off) well sections and fracture features.

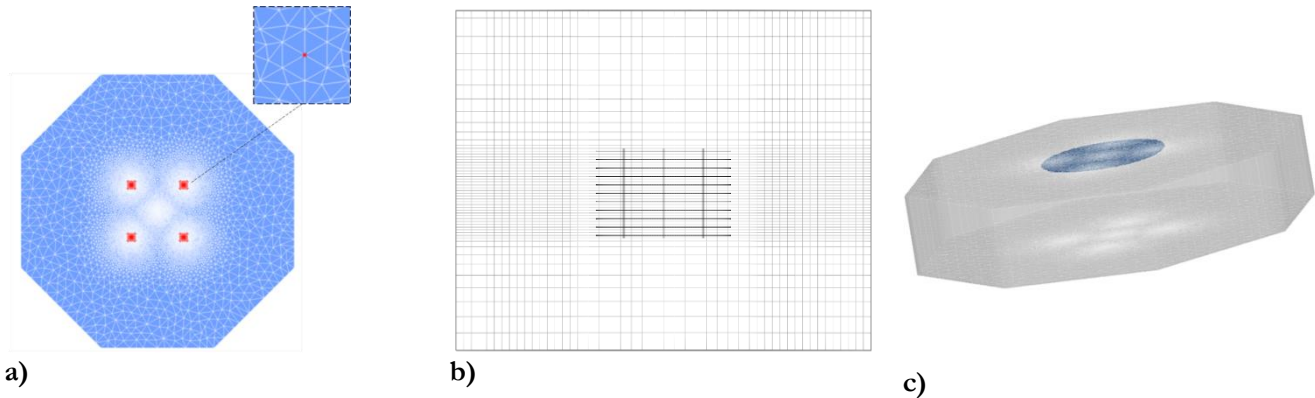


Figure 2 Overview of the model discretization. a) Horizontal 2D unstructured mesh. b) Vertical structured mesh including positions of fractures planes and wells. c) Two-dimensional fracture features (highlighted in blue) assigned to the model along the horizontal faces of the 3D finite elements.

As mentioned previously, FEFLOW allows inclusion of fractures using 2D discrete features that can be added onto the faces of the 3D elements representing the rock matrix. In this work, fracture planes (approximately disc-shaped) are added to the model by assigning discrete features along horizontal element faces located at the interface between the layers of the discretization grid (see Figure 2 c)). Fluid flow along discrete features can be determined using either the Darcy, Hagen-Poiseuille or Manning-Strickler laws of flow. In this study the Hagen-Poiseuille law is used for fracture flows, which assumes the fluid flow to be laminar between two smooth, parallel plates. It uses the hydraulic aperture as frictional input parameter to characterize the hydraulic conductivity of the fracture, and is closely related to the well-known cubic law that states that the fracture transmissivity is proportional to the cube of its aperture (Diersch 2009).

Due to the assumption of the rock matrix being impermeable, fluid flow within the model will exclusively occur along the fractures and the well sections that connect the fracture planes. In FEFLOW, well features (or more precisely the packed-off sections of the wells in the present case) can be modeled using the special “multilayer well” boundary condition (BC). Multilayer wells are assigned along vertical edges of the discretization and are thus represented by 1D elements. This kind of BC is technically a combination of a point sink/source BC assigned at the lowermost node of the well and a highly conductive linear discrete feature along the well section. The multilayer wells intersect with all fractures, thus allowing the flow to be distributed within the model and between the injection and extraction wells (Figure 3). The injection and extraction of heat into and from the model domain is modelled using a fixed inlet temperature condition by imposing a Dirichlet type BC on the lowermost node of the multilayer wells that are operating as injection wells. The calculation of the heat outflow from the model domain is handled internally by the solver, by imposing a heat sink BC on the lowermost nodes of the extraction wells.

The specified boundary conditions for flow and heat transport can be set to vary during transient simulation according to a predefined time series. During charging the central well is set as injection well and the peripheral wells are set as extraction wells, and vice-versa during discharging operation. The BCs at the well locations can also be turned off during simulation to simulate operation inactivity periods.

Undisturbed hydraulic and thermal conditions are assumed to be uniform throughout the model domain. A steady state-solution is run to established initial conditions for the transient simulation, assuming hydraulic and thermal Dirichlet BCs on the lateral surfaces of the model while no-flux conditions are assumed and imposed on the top and bottom boundaries.

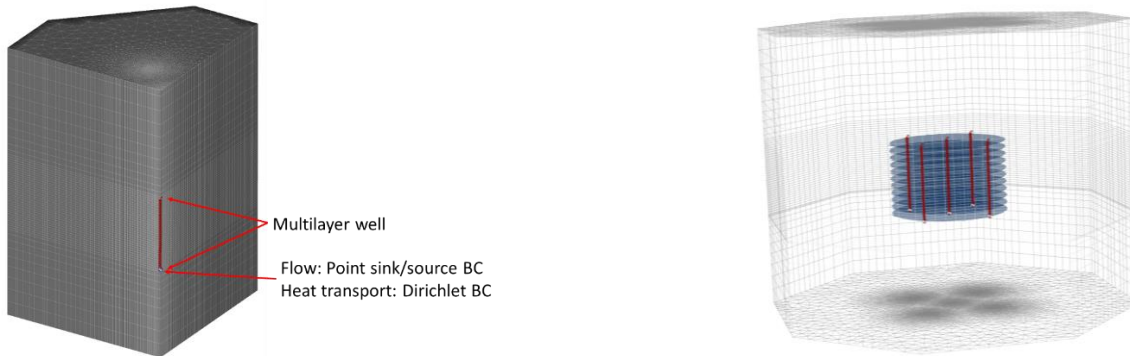


Figure 3 Assignment of multilayer well and heat transport BC for modeling injection and extraction of heat and water.

Model application

An illustrative simulation case is developed to demonstrate the modeling approach presented in the previous section. Table 1 summarizes the key design, material and operation parameters and their values.

Table 1. Storage design and operation parameters.

Design and material parameters	Value	Operation parameters	Value
Storage radius (well spacing)	31.0 m	Total fluid flow rate	4 l/s
Well diameter	0.165 m	Charging inlet temperature	90 °C
No. of central/peripheral wells	1/4	Discharging inlet temperature	45 °C
No. of fracture planes	22	Charging period	180 days
Fracture spacing	3.73 m	Inactivity after charging	30 days
Fracture radius	37.2 m	Discharging period	110 days
Fracture hydraulic aperture	800 μm	Inactivity after discharging	45 days
Rock vol. heat capacity	2.16 MJ/m ³ /K	Total length of storage cycle	365 days
Rock thermal conductivity	3.0 W/mK		
Rock hydraulic conductivity	1e-17 m/s		

The storage design consists of 4 peripheral wells spaced 31 m apart from a single central well. The fracture system consists of 22 horizontal, circular planes evenly distributed along the packed-off sections of the wells that extend from 49 m to 129 m below the top of the model domain. The hydraulic conductivity of the rock matrix is assumed to be very low (1e-17 m/s), meaning that the fluid exchange between fractures and matrix is practically negligible. Considering also that the undisturbed hydraulic head is assumed to be uniform throughout the model, any effect of heat losses due to natural groundwater movements is neglected. For all other material properties, default values have been adopted (FEFLOW 7.4 n.d.). As initial conditions, an undisturbed ground temperature of 7 °C and an hydraulic

head of 0 m are assumed throughout the model. The FTES system is simulated for 16 annual cycles according to the operation scheme shown in Table 1. The octagonal-shaped model domain is discretized into a mesh of 1 465 426 finite elements portioned into 75 layers. Within the storage region the vertical discretization is 1.87 m. The total height and width of the model domain are 213.6 m and 147.8 m, respectively.

Thermal performance evaluation

The performance of the FTES system is evaluated based on the approach proposed by Lazzarotto et al. (2020) for the analysis of seasonal system energy and exergy efficiency of thermal storages. The seasonal system energy efficiency (η) is defined by the ratio of extracted and injected thermal energy per storage cycle (Eq. 1).

$$\eta = \frac{Q_d}{Q_c} = \frac{\int_{\tau_c}^{\tau_c+\tau_d} \dot{m}(t)c_p [T_r(t) - T_f(t)] dt}{\int_0^{\tau_c} \dot{m}(t)c_p [T_f(t) - T_r(t)] dt} \quad (1)$$

In Eq. 1, T_r and T_f are the return and forward temperatures of the circulating water, \dot{m} is the mass flow, and τ_c and τ_d are the time duration of charging and discharging periods, respectively. The seasonal system exergy (ψ) efficiency is expressed as

$$\psi = \frac{Ex_d}{Ex_c} = \frac{\int_{\tau_c}^{\tau_c+\tau_d} \dot{m}(t)c_p \left\{ [T_r(t) - T_f(t)] - T_0 \ln \frac{T_r(t)}{T_f(t)} \right\} dt}{\int_0^{\tau_c} \dot{m}(t)c_p \left\{ [T_f(t) - T_r(t)] - T_0 \ln \frac{T_f(t)}{T_r(t)} \right\} dt} \quad (2)$$

where T_0 is a reference temperature that is equal to the undisturbed temperature of the ground (280.15 K). All temperatures in Eq. 2 are expressed in Kelvin.

RESULTS AND DISCUSSION

The simulation model of the FTES system described in the previous sections is used to determine the return temperature of the circulating water under the scenario conditions specified in Table 1, and the amount of injected and extracted thermal energy and exergy as well as seasonal system performance indicators are evaluated according to Eq. 1 and Eq. 2. The simulation results obtained for 16 storage cycles of operation are summarized in Figure 4. After a few years of temperature build-up within the storage, the amount of extracted thermal energy and exergy stabilizes at around 1 400 MWh/year and 222 MWh/year, respectively, which corresponds to a seasonal system energy efficiency of ~50% and a seasonal system exergy efficiency of ~45%. During the 16th storage cycle, the discharge power varies between 700 kW and 390 kW. Under the conditions considered for the simulation, this range corresponds to return temperatures varying between 87 °C and 68 °C during the final discharging period.

Considering a forward temperature of 90 °C used during charging, these results imply that the FTES system performs relatively well regarding its temperature retention ability (i.e. its exergy efficiency). Achieving a high discharge return temperature, perhaps at the cost of a somewhat lower energy efficiency, may be of crucial significance in high-temperature storage applications as part of the stored heat in the optimal case could be recovered without the use of heat pumps. Due to the open-loop nature of the system, FTES technology possesses a promising potential in minimizing temperature losses and achieving a high exergy performance, for example in comparison with closed-loop BTES systems that also rely on conduction-based heat transfer within the storage medium. It should, however, be emphasized that the fracture system and other ground conditions considered in this study are idealized, hence possible sources of heat losses should be investigated in future work.

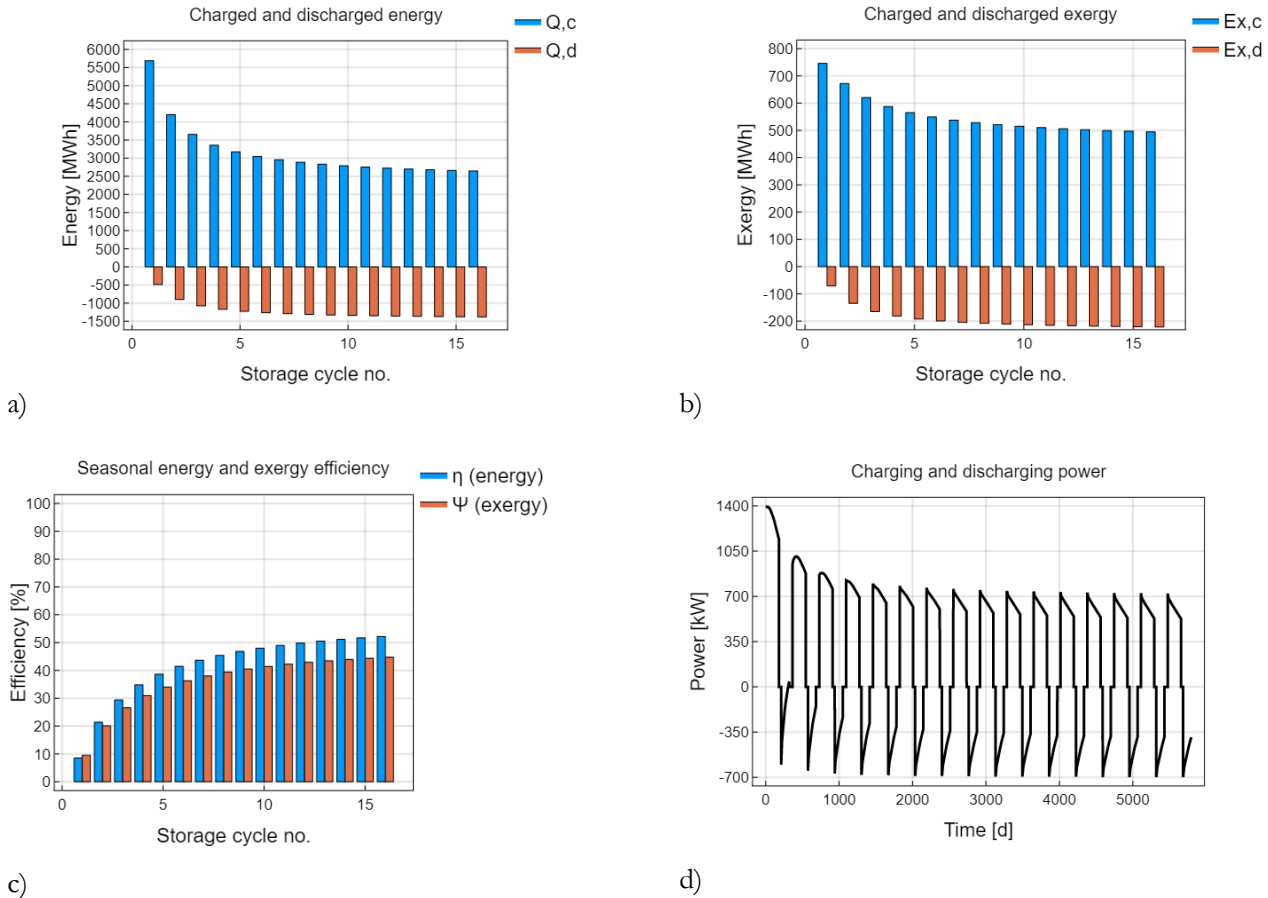


Figure 4 a) Charged/discharged thermal energy per storage cycle. b) Charged/discharged thermal exergy per storage cycle. c) Seasonal system energy and exergy efficiencies. d) Charging/discharging power rates.

CONCLUSIONS

This work presents an approach for the modeling of fractured thermal energy storage systems based on the finite element code FEFLOW. Although coupled flow and heat transfer problems in fractured rock is highly complex in nature, the discrete feature approach available in FEFLOW for modeling of fracture flow and transport provides a relatively simple and computationally efficient means of simulating the hydraulic and thermal processes occurring within a FTES system. The numerical model that is established can be utilized to study the design and operation conditions of FTES systems, including, for example, well and storage dimensions, different fracture system configurations as well as various heat loading conditions. As demonstrated, long-term simulations can be performed to evaluate the performance of the storage system over its life time. The energy and exergy efficiency indicators employed in this study can usefully be included in the design process for optimization purposes as well as for comparisons with other heat storage technologies. Future work is addressed to investigate the importance of key parameters in FTES design, and to study FTES system performance under more realistic, non-idealized conditions.

ACKNOWLEDGMENTS

The authors acknowledge that this work was funded by Hydroc Energy Storage AB.

NOMENCLATURE

η	=	energy efficiency (-)
ψ	=	exergy efficiency (-)
τ	=	time duration
c_p	=	specific heat capacity (J kg ⁻¹ K ⁻¹)
Ex	=	exergy (J)
T	=	temperature (K)
T_0	=	reference temperature (K)
Q	=	energy (J)

Subscripts

c	=	charging
d	=	discharging
f	=	forward
r	=	return

REFERENCES

- Berre, I., F. Doster and E. Keilegavlen. 2019. "Flow in Fractured Porous Media: A Review of Conceptual Models and Discretization Approaches." *Transport in Porous Media* 130 (1): 215–36. <https://doi.org/10.1007/s11242-018-1171-6>.
- Diersch, H.J.G . 2009. "Discrete Feature Modeling of Flow, Mass and Heat Transport Processes by Using FEFLOW." In *DHI-WASY Software FEFLOW: White Papers, Vol. 1, Finite Element Subsurface Flow & Transport Simulation System*, 151–98. Berlin: DHI-WASY GmbH.
- Diersch, H.J.G . 2014. *FEFLOW Finite Element Modeling of Flow, Mass and Heat Transport in Porous and Fractured Media*. Berlin, Heidelberg: Springer Berlin Heidelberg.
- Diersch, H.J.G., D. Bauer, W. Heidemann, W. Rühaak, and P. Schätzl . 2011. "Finite Element Modeling of Borehole Heat Exchanger Systems: Part 2. Numerical Simulation." *Computers & Geosciences* 37 (8): 1136–47. <https://doi.org/10.1016/j.cageo.2010.08.002>.
- Eliasson, T., U. Sundquist and T. Wallroth . 1988. "Stimulation Experiments with Water and Viscous Fluid at the HDR Geothermal Research Site in the Bohus Granite, SW Sweden." Publ. Fj-6. HDR Geothermal Energy Project. Göteborg: Department of Geology, Chalmers University of Technology and University of Göteborg.
- "FEFLOW 7.4 Documentation - Default Values." n.d. Accessed July 8, 2021. http://www.feflow.info/html/help74/feflow/14_References/default_values.html.
- Hellström, G. and S.Å. Larson . 2001. "Seasonal Thermal Energy Storage – the HYDROCK Concept." *Bulletin of Engineering Geology and the Environment* 60 (2): 145–56. <https://doi.org/10.1007/s100640100101>.
- Janiszewski, M., B. Shen and M. Rinne . 2019. "Simulation of the Interactions between Hydraulic and Natural Fractures Using a Fracture Mechanics Approach." *Journal of Rock Mechanics and Geotechnical Engineering* 11 (6): 1138–50. <https://doi.org/10.1016/j.jrmge.2019.07.004>.
- Larson, S.Å . 1984. "Hydraulic Fracturing in the Bohus Granite, SW-Sweden. Test for Heat Storage and Heat Extraction." *Geothermal Resources Council Transactions* 8: 447–49.
- Larson, S.Å, B. Fridh and Ö. Haag. 1983. "Hydrock - Värmelager i Berg. Anläggning Av Värmeväxlarytor Med Hjälp Av Hydraulisk Uppspräckning; HYDROCK - Metoden." Publ. B222. Göteborg, Sweden: Chalmers University of Technology/University of Göteborg.
- Lazzarotto, A., W. Mazzotti Pallard, M. Abuasbeh and J. Acuña . 2020. "Performance Evaluation of Borehole Thermal Energy Storage Systems Through Energy and Exergy Analysis." In . Reykjavik.
- Ramstad, R. K . 2004. "Ground Source Energy in Crystalline Bedrock - Increased Energy Extraction by Using Hydraulic Fracturing in Boreholes." 185. Doctoral thesis, Department of Geology and Mineral Resources Engineering, Faculty of Engineering Science and Technology, Norwegian University of Science and Technology. <https://ntnuopen.ntnu.no/ntnu-xmlui/handle/11250/235847>.



Economic Optimization and Parametric Analysis of Large Hybrid Ground Source Heat Pump Systems: A Case Study

Alain Nguyen
Martin Kegel

Parham Eslami-Nejad

Justin Tamasauskas

ABSTRACT

Hybrid ground source heat pump systems offer a solution to reduce initial costs and make systems more economically viable. Their design is however complex and their financial profitability difficult to establish. The design of hybrid system is usually determined by following rough rules and is neither mathematically rigorous nor optimized. In this paper, a methodology recently introduced by the same authors for economic optimization of hybrid ground source heat pump systems is used to carry out a parametric analysis and assess the impact of uncertainty on the optimal design solution. The results show that all the parameters have significant impact on the optimization, and the ground heat exchanger construction costs and ground source heat pump COP had the most impact on the net present value. However trends are difficult to observe because of the non-linear nature of the problem, and thus there is a need for more robust optimization of hybrid GSHP systems under uncertainty.

INTRODUCTION

Ground source heat pump (GSHP) systems are considered as a solution for efficient heating and cooling in buildings (Qi et al. 2004). In order to reduce project costs, they are often integrated with auxiliary heating/cooling systems to cover peak demands of buildings (Soni et al. 2016). However, demonstrating the financial viability of these so-called hybrid GSHP systems is a challenge due to the varying technical and economic conditions at each site and in each city.

There exist many studies on economic analysis of hybrid GSHPs, from simple techno-economical analysis (Seo et al. 2018, Yousefi et al. 2018) to more complex financial optimization approaches (Retkowski et al. 2014, Henault et al. 2016, Nguyen et al. 2016, Ikeda et al. 2017, Kayaci et al. 2018, Beckers et al. 2018, Aditya et al. 2020, Dusseault and Pasquier. 2021). Finding the optimal design of a hybrid GSHP system that minimizes the expected long-term cost while providing significant energy savings remains a complicated and computationally tedious task. In general, the difficulty of optimizing GSHP systems can be mainly associated with three tasks. First, it calls for the repetitive construction of the transfer functions of the borefield. Second, it involves constrained nonlinear programming for multi-year hourly simulations. Third, it requires finding the global optimal solution of a multidimensional multimodal cost function. Recently, Nguyen et al. (2022) developed a new simulation-based method that efficiently performs these three tasks for

Alain Nguyen (tuananhalain.nguyen@NRCan-RNCan.gc.ca) is a research scientist at CanmetEnergy, Canada.
Parham Eslami-Nejad (parham.eslaminejad@NRCan-RNCan.gc.ca) is a research scientist at CanmetEnergy, Canada.
Justin Tamasauskas (justin.tamasauskas@NRCan-RNCan.gc.ca) is a research engineer at CanmetEnergy, Canada.
Martin Kegel (martin.kegel@NRCan-RNCan.gc.ca) is a research engineer at CanmetEnergy, Canada.

rapid economic optimization of large hybrid geothermal heat pump systems. The objective of this article is to use this new algorithm to carry out a parametric analysis and assess the impact of uncertainty on the proposed optimal design.

METHODOLOGY

For large commercial buildings, hybrid GSHP systems can be a reliable alternative to conventional boiler and chiller systems. For a simple illustration, Fig. 1 shows a two-pipe system with terminal air handling (AH) units, but can be extended to four-pipe systems or water loop heat pump systems for simultaneous multi-zone cooling and heating. In such system, the GSHP serves as the primary system while the gas boilers and air-cooled chillers are used as back-up auxiliary systems during peak hours, hence the term "hybrid".

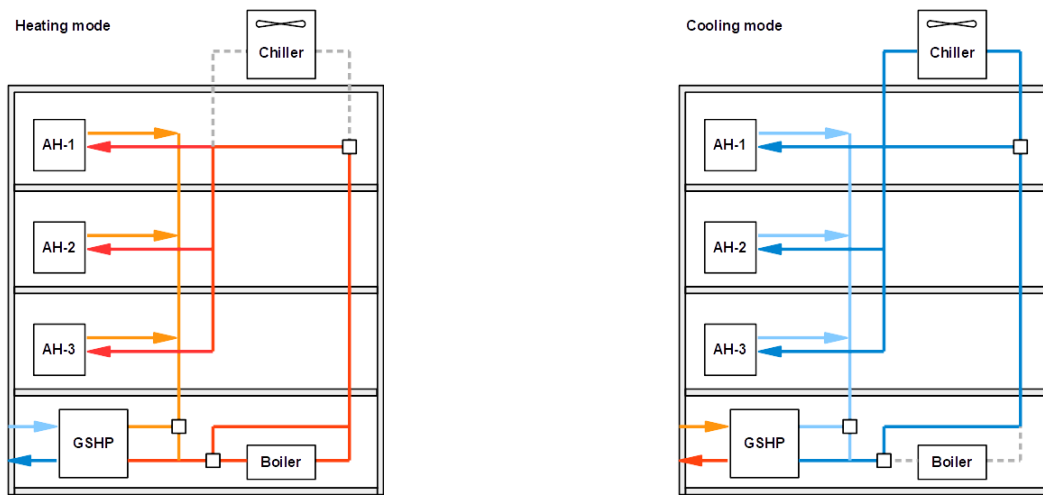


Figure 1. A hybrid ground source heat pump in a two-pipe system with terminal air handling (AH) units. Left: Heating mode. Right: Cooling mode.

On the source side of the GSHPs, we consider conventional vertical grouted ground heat exchangers (GHE) sized to maintain fluid temperature within design temperature limits so that the GSHPs can operate continuously as the system's first stage, even during peak periods. In off-peak periods, the auxiliary systems are bypassed with appropriate controls and valves, thereby maximizing system energy efficiency. We assume that the GSHPs are equipped with variable frequency drives to minimize cycling and maximize efficiency during part load periods.

Based on these assumptions, the energy saving provided by a given hybrid GSHP design is evaluated by means of dynamic hourly energy simulations. In this study, the methodology outlined in Nguyen et al. (2022) is used as a base for all simulation, optimization and parametric analysis. The general methodology aims to numerically model the hybrid GSHP system to assess its long-term cost and identify, through optimization algorithms, the design parameters that maximize its economic performance. The procedure in determining the optimal design outlined in Nguyen et al. (2022) is as follows:

1. Construct the objective function described in terms of the net present value (NPV) as a function of three design parameters: 1) the borefield geometry, 2) the minimum fluid temperature limit, and 3) the maximum fluid temperature limit;
2. Optimize the objective function to provide the design that maximize the NPV.

Objective function

Naturally, the design of hybrid GSHP systems is a complex task involving many technical and financial parameters. For example, increasing the capacity of the heat pump leads to more energy savings, but also requires more drilling and therefore higher construction costs. Hence, the design's Net Present Value, expressed as the difference between the Net Present Cost of the reference boiler/chiller system and the hybrid GSHP system, is adopted as the sole indicator of the objective function. The NPV over a 20-year period expressed as in terms of three design parameter:

$$NPV = fun_{obj}(F, T_{min}, T_{max})$$

where F is the distance between the boreholes in a circular layout, T_{min} is the minimum fluid temperature limit and T_{max} is the maximum fluid temperature limit. The first parameter F is used generate the position vectors of the boreholes by means of Delaunay triangulation (Fig. 2), and ultimately, to generate the g -function of the borefield (Nguyen 2021).

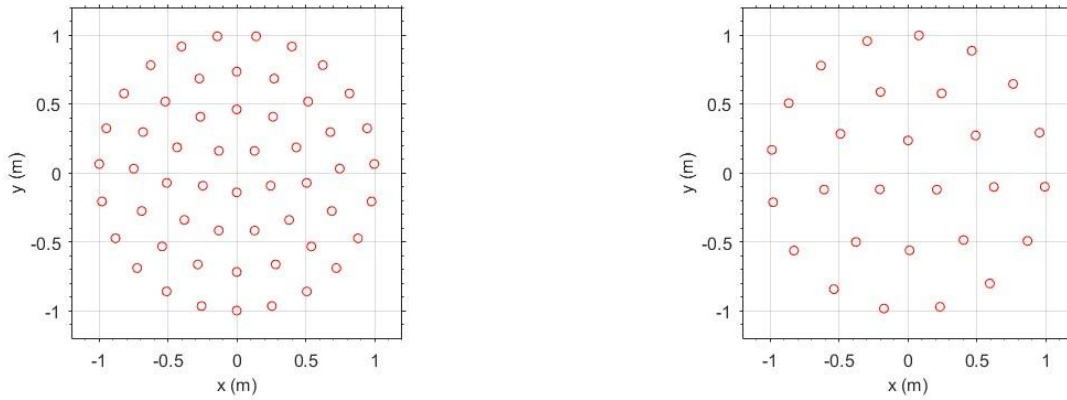


Figure 2. A borefield layout in a unit circle generated by Delaunay triangulation. Left: $F = 0.25$. Right: $F = 0.35$.

The second and third parameter are used to control the GSHP capacity. Simply put, increasing design temperature limits (i.e. lowering T_{min} and increasing T_{max} allows the GSHP system to operate at higher capacity, but at the cost of a lower COP (Nguyen, 2021). Ultimately, the three design parameters are used for standard calculation of the heat pump source inlet fluid temperature, which allows for the evaluation of the energy cost. The energy cost of the hybrid GSHP system is estimated based on local electricity and gas tariffs from 2018 (Table 1). Electricity tariffs include a tiered tariff for monthly consumption and a tariff for maximum power demand monthly, while gas tariffs include only a staggered tariff for monthly consumption. Note that in this study, natural gas prices are comparable with electricity prices. We remind the reader that these prices are specific to the GSHP market in Canada and that the relevant costs should be used for studies in other regions of the world.

Here we consider Hybrid GSHP systems as capital assets. To take into account their depreciation and their eventual replacement, the depreciation costs are calculated on an annual basis according to the linear method without salvage value. The lifetime of a GHE and GSHP is assumed to be 75 years and 25 years, while the lifetime of a gas boiler and chiller is assumed to be 20 years and 15 years, respectively. In sum, the NPV over a 20-year period considers the cost of boreholes, GSHPs, boilers and chillers, their depreciation cost, the operation cost and the debt repayment.

Table 1. Energy tariffs.

Source	Criteria	Rates	Unit
Electricity	≤ 210 MWh/mo.	4.99	¢/kWh
	≥ 210 MWh/mo.	3.70	¢/kWh
	any kW	14.46	\$/kW
	CO2 emissions	1.3	gCO2e/kWh
Gas	≤ 341 MWh/yr.	4.71	¢/kWh
	$\leq 1,023$ MWh/yr.	4.45	¢/kWh
	$\leq 3,413$ MWh/yr.	4.02	¢/kWh
	CO2 emissions	214	gCO2e/kWh

A positive NPV indicates that the proposed hybrid GSHP project will be profitable relative to the reference system, while a negative NPV will result in a net loss. In this methodology, we assume similar maintenance and design costs for the hybrid and reference systems, so that neither of them affects the NPV. Finally, a representative energy model of a large office building in Montreal, Canada is used as a base for all analysis. The corresponding load profile is shown in Fig. 3. The peak heating load and cooling load are 836 kW, 696 kW respectively, while the total annual energy demand for heating and cooling are 915 MWh and 385 MWh, respectively. For more details, one could refer to Nguyen et al. (2022) for a thorough description of the ground thermal parameters, heat pump COP curves, economic parameters, as well as costs.

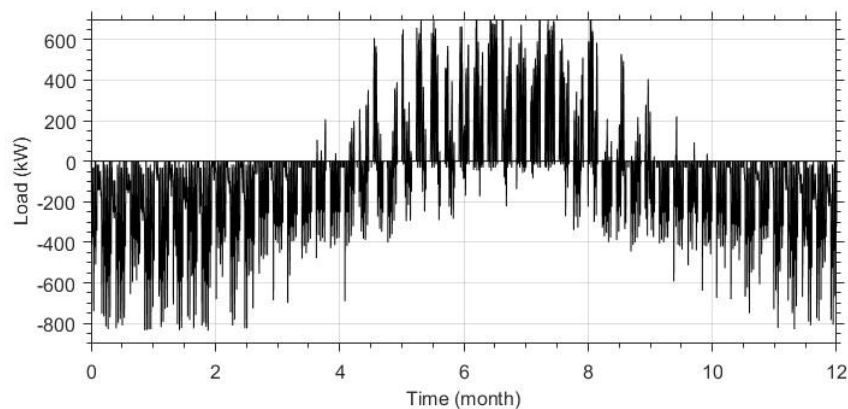


Figure 3. A hybrid ground source heat pump in a two-pipe system with terminal air handling (AH) units Left: Heating mode. Right: Cooling mode.

Parametric analysis

In this article, a parametric study was performed to evaluate the effect of uncertainty on the optimal solution found by the algorithm. We focus on four parameters to generate a set of eight alternative cases, where the value of each parameter is set to 80% or 120% of the base value. The four parameters are: 1) the building load, 2) the construction cost of the GHE, 3) the ground thermal conductivity and 4) the heat pump COP. Building load uncertainty could be related to weather conditions, building occupancy and/or retrofitting, while COP uncertainty could be related to load fluid temperature, part load and/or control strategy.

The parametric analysis is divided into two parts. In the first part, the base optimal design is used with new parameters

to evaluate the effect of each parameter on the economic performance of the base design. This will be quantified using the NPV value of each case. In other words, it is shown how the uncertainty of some design parameters affects the economic performance of the project if the design is not adapted accordingly. In the other part, it is shown that for each case a specific optimal design exists that could increase both the NPV and the energy performance of the project.

Table 2. Parametric analysis

Heading Number One	Q _b	Cost	K _s	COP
Base	1.0	1.0	1.0	1.0
Case 1	0.8	1.0	1.0	1.0
Case 2	1.2	1.0	1.0	1.0
Case 3	1.0	0.8	1.0	1.0
Case 4	1.0	1.2	1.0	1.0
Case 5	1.0	1.0	0.8	1.0
Case 6	1.0	1.0	1.2	1.0
Case 7	1.0	1.0	1.0	0.8
Case 8	1.0	1.0	1.0	1.2

RESULTS AND DISCUSSION

First, the base case optimal design obtained with the optimization is the following: 29 boreholes with [T_{min},T_{max}] = [-3.30,32.00]). Table 3 then presents the heat pump heating and cooling load coverages and the NPV of different cases including the base case if the optimal base design is kept for all other cases. To calculate the results listed in Table 3, all cases use base optimal design. As shown in Table 3, the base case covers 35% and 52% of the building heating and cooling peak demands respectively however it can cover more than 80% of the total heating and cooling demands of the building with the overall COP of 3.8. In this case, the optimal NPV is \$1.45e+05. It is obvious that if the building load is lower by 20% (Case 1) with the same base design, both building heating and cooling load coverages will increase. However, it is interesting to mention that the NPV drops significantly by 61%. To put it very simply, this is due to spending the same GHE construction costs for less energy savings. It is also shown that the COP improves slightly (from 3.8 to 3.94) due to the lower design temperature limit. On the other hand, a 20% building load increase results in less building heating and cooling load coverages and a 15% increase in the NPV. As shown for cases 3 and 4, the change in the construction cost does not change the building load coverage as 29 boreholes are always used. However, a ±20% change in the GHE construction cost would cause a ±46% change in the NPV.

Table 3. Performance and NPV of base optimal design.

Heading Number One	COP	HEAT(%peak/%tot)	COOL(%peak/%tot)	Base Optim Design NPV (\$)
Base	3.80	35.4/82.8	52.4/80.2	1.45e+05
Case 1	3.94	49.0/92.1	66.4/91.2	5.69e+04
Case 2	3.75	27.6/73.1	43.0/70.5	1.67e+05
Case 3	3.80	35.4/82.8	52.4/80.2	2.11e+05
Case 4	3.80	35.4/82.8	52.4/80.2	7.87e+04
Case 5	3.78	28.9/74.9	44.3/72.1	8.73e+04
Case 6	3.86	41.8/88.2	59.5/86.4	1.75e+05
Case 7	3.19	43.3/89.1	52.1/79.9	7.15e+04
Case 8	4.37	31.4/78.4	52.5/80.3	1.27e+05

If the ground thermal conductivity is 20% lower in reality than the value used for the design, the heat pump works with lower COP and covers less building load which means consuming more energy, and therefore the NPV decreases (here by 40%). On the contrary, a 20% higher K_s improves the performance of the heat pump and covers more building load which means reducing the energy consumption of the system and therefore contributes to a 21% higher NPV. Table 3 shows that K_s and the building load heating and cooling coverages are directly correlated. This means that the increase in the K_s would increase the building load coverages and vice versa. However, the change in the COP did not present any obvious trend for both the load coverages and the NPV. Both lower and higher COPs (Cases 7 and 8) result in lower NPV of 51% and 12% respectively. This is explained by the higher total energy consumption of the system in both cases. In Case 7, the increase in the total building heating load coverage is not enough to compensate for the energy consumption increase associated with lower COP. It is worth mentioning that if the COP is higher by 20%, the ground load is also higher and the building heating load coverage drops because the GSHP capacity modulates to avoid reaching the cutoff, and therefore the auxiliary heat is used more. Building cooling load coverage does not vary significantly by the $\pm 20\%$ change in the COP. It is very important to realize that higher COP does not necessarily result in higher NPV if the optimal base design is used. In other words, to benefit economically from an improved COP the design has to be optimized accordingly for higher COP values. Interestingly, note that the mean NPV is lower than base case NPV (\$1.22e+05 vs \$1.45e+05).

Case-specific optimal design:

Table 4 presents the optimum number of GHEs and the design temperature limit (T_{min} and T_{max}) of each case while Table 5 summarizes the results in terms of performance and NPV of each case-specific optimal design. Note that the NPV column is always higher than the one in Table 3. This means that if the uncertainty of parameters is accounted for carefully before the design phase, a specific design would exist that maximizes the NPV of the project. For instance in Case 1, where the building load is lower by 20% compared to the base case, the optimized solution includes a higher design temperature limit (i.e. higher $T_{min} = -0.52^\circ\text{C}$ and lower $T_{max} = 31.95^\circ\text{C}$) with 38% more GHEs compared to the base optimal design (40 in Case 1 instead of 29 in the base case). This allows the heat pump to operate at higher COP.

Table 4. Optimal design parameters

Heading Number One	N borehole	T_{min}	T_{max}
Base	29	-3.30	32.00
Case 1	40	-0.52	31.94
Case 2	34	-3.78	32.00
Case 3	50	-1.03	31.81
Case 4	26	-3.23	32.00
Case 5	33	-3.60	32.00
Case 6	45	-0.73	31.98
Case 7	25	-1.95	32.00
Case 8	49	-2.74	32.00

Among the cases, a 20% decrease in the heat pump COP (Case 7) and a 20% increase in the GHE construction cost (Case 4) result in using fewer GHEs for their specific optimal designs. For instance, in Case 7, the optimization algorithm reduces the number of boreholes and therefore the construction costs to compensate for the increase in the operation costs caused by the lower COP. However, in Case 4, the optimization algorithm decreases the number of boreholes to

directly compensate for the increase in the construction costs of the boreholes. On the other hand, lower GHE construction costs and higher COP of the heat pump allow using significantly more boreholes for achieving an economically optimum design (72% more boreholes for lower GHE construction costs and 69% more boreholes for higher heat pump COP). A 20% reduction in the ground thermal conductivity results in a slight change in the number of boreholes (only by 14% from 29 to 33). In general, trends are difficult to observe because of the non-linear nature of the problem. It is thus also worth investigating the effect of the parameters on the optimization routine.

Table 5. Performance and NPV of case-specific optimal design.

Heading Number One	COP	HEAT(%peak/%tot)	COOL(%peak/%tot)	Case Optim Design NPV (\$)
Base	3.80	35.4/82.8	52.4/80.2	1.45e+05
Case 1	4.37	46.8/91.4	100/100	9.59e+04
Case 2	3.71	34.4/82.0	52.0/80.0	1.87e+05
Case 3	4.31	45.3/90.7	100/100	2.44e+05
Case 4	3.77	31.0/77.8	46.2/74.0	7.94e+04
Case 5	3.76	34.4/81.7	51.6/79.7	9.39e+04
Case 6	4.34	46.2/91.2	100/100	1.86e+05
Case 7	3.31	30.5/77.2	43.8/71.2	1.30e+05
Case 8	4.70	48.2/92.0	100/100	1.75e+05

Building load

For Case 1, the optimization routine found an optimal NPV of \$9.59e+04 which is lower than the Base case. As mentioned before this optimized solution consists of 40 boreholes connected to GSHPs that allow the system to cover 47% of the peak heating load (91.4% of the total requirement) and 100% of the cooling demand, throughout the 20 years. Based on the results of the optimal design for Case 1, using a chiller to generate auxiliary cooling cannot be justified economically and therefore the entire cooling is fulfilled using the GSHP. It is also noteworthy that the NPV of this case is improved by 69% compared to the NPV of Case 1 in Table 3 when the optimization is not used. If an optimization routine is used for Case 2 where the building load is 20% more than the base case, the NPV is improved by 30% compared to Case 2 listed in Table 3. For Case 2, the optimized solution consists of 17% more boreholes (34 boreholes) than the Base case allowing the GSHPs to provide relatively similar building heating/cooling load coverage despite the increase in the building load. It could also imply that using GSHP for bigger building load results in better economic performance and potentially shorter discounted payback.

GHE construction costs

If the GHE construction costs are lower by 20% (Case 3), results indicate that it makes a better economic sense to cover the whole building cooling load with the GSHPs and therefore eliminate the chiller as the costs are not any more justified. Furthermore, the load coverage by the GSHPs during the heating season increases, and therefore smaller boiler capacity is required. Case 3 appears to demonstrate the biggest impact on the project NPV by 68% improvement compared to the Base case. This is because the GHE construction costs are a significant portion (more than 50%) of the project investment and therefore a 20% reduction would generate a significant impact on the project NPV. It is also worth mentioning that the improvement in the NPV was reported 45% without performing the optimization and optimization can maximize the NPV improvement to 68% compared to the Base case. On the other hand, the increase in the GHE construction costs drops the NPV more than any other parameter by 45%. This again highlights the importance of the GHE construction cost certitude to design an economically optimum system for the project.

Ground thermal conductivity

In Case 5 where K_s is lower than the expected value by 20%, the building load coverage in both heating and cooling is not significantly influenced. Therefore, the optimized solution uses 4 more boreholes than the Base case to compensate for the GSHP capacity decline due to the lower K_s . However, the NPV is still reduced by 35% because the GSHP works at lower COP due to the lower design temperature limit. If K_s is 20% higher than the expected value (Case 6), both the COP and the building load coverage increase significantly. This allows eliminating the chiller unit and using a smaller boiler. The optimized solution improves the NPV of Case 6 further to 28% compared to the Base case from the 21% improvement reported in Table 4.

GSHP COP

If COP is lower by 20%, the optimized solution recommends using 4 boreholes less than the Base case to lower the construction costs and therefore compensate for the increase in the operation costs. Despite decreasing the number of boreholes, the NPV was still reduced by 10%. However, this is significantly better than using the base optimal design in which the NPV is reduced by 50% in Case 7 (Table 3). As shown in Table 5, in this case, both the building load coverage and the annual COP drop significantly. In Case 8, the optimized solution embraces the potential of higher COP by using 49 boreholes that allow increasing the building load coverage and eliminating the chiller unit in this case. The specific optimal design for Case 8 improves the NPV by 21% compared to the base optimal design whereas using the Base case with higher COP decreases the NPV by 12% (Case 8 in Table 3).

CONCLUSION

In this paper, the optimization routine developed by Nguyen et al. (2022) used to carry out a parametric analysis and assess the impact of uncertainty on the proposed optimal design. The effect of four parameters were studied: 1) the building load, 2) the construction cost of the GHE, 3) the ground thermal conductivity and 4) the heat pump COP. The results show that all the parameters have significant impact on the optimization, but trends are difficult to observe due to the non-linear nature of the problem. It was shown that the GHE construction costs and GSHP COP had the most impact on the NPV, hence they would be key parameters for an optimal design that has to be evaluated carefully in advance. This work opens doors for more robust and stochastic optimization of hybrid GSHP systems under uncertainty.

ACKNOWLEDGMENTS

The authors would like to acknowledge the funding received by the Office of Energy Research and Development (OERD) of Canada through the Energy Innovation Program (EIP) to undertake this research.

NOMENCLATURE

COP	=	<i>Coefficient of performance (-)</i>
fun_{obj}	=	<i>Objective function (-)</i>
Q_b	=	<i>Building load (kW)</i>
NPV	=	<i>Net present value (\$)</i>
F	=	<i>Relative distance (-)</i>
T_{min}	=	<i>Minimum fluid temperature ($^{\circ}C$)</i>
T_{max}	=	<i>Maximum fluid temperature ($^{\circ}C$)</i>
K_s	=	<i>Ground thermal conductivity ($W/m^{\circ}C$)</i>

REFERENCES

- Aditya G.R, Mikhaylova O, Narsilio G.A, Johnston I.W. 2020. Comparative costs of ground source heat pump systems against other forms of heating and cooling for different climatic conditions. *Sustainable Energy Technologies and Assessments* 42:100824.
- Beckers K.F, Aguirre G.A, Tester J.W. 2018. Hybrid ground-source heat pump systems for cooling-dominated applications: Experimental and numerical case-study of cooling for cellular tower shelters. *Energy and Buildings* 177:341--350.
- Dusseault B, Pasquier P. 2021. Usage of the Net Present Value-at-Risk to Design Ground-Coupled Heat Pump Systems Under Uncertain Scenarios. *Renewable Energy* 173:953--971.
- Hénault B, Pasquier P and Kummert M. Financial Optimization and Design of Hybrid Ground-Coupled Heat Pump Systems. *Applied Thermal Engineering* 2016;93:72--82.
- Ikeda S, Choi W, Ooka R. 2017. Optimization method for multiple heat source operation including ground source heat pump considering dynamic variation in ground temperature. *Applied Energy* 193:466--478.
- Kayaci N, Demir H. 2018. Long time performance analysis of ground source heat pump for space heating and cooling applications based on thermo-economic optimization criteria. *Energy and Buildings* 163:121--139.
- Qi Z, Gao Q, Liu Y, Yan Y.Y, Spitler J.D. 2014. Status and development of hybrid energy systems from hybrid ground source heat pump in China and other countries. *Renewable and Sustainable Energy Reviews* 29:37--51.
- Retkowski W, Thöming J. 2014. Thermoeconomic optimization of vertical ground-source heat pump systems through nonlinear integer programming. *Applied energy* 114:492--503.
- Soni S.K, Pandey M, Bartaria V.N. 2016. Hybrid ground coupled heat exchanger systems for space heating/cooling applications: A review. *Renewable and Sustainable Energy Reviews* 60:724--738.
- Seo Y, Seo UJ, Kim JH. 2018. Economic feasibility of ground source heat pump system deployed in expressway service area. *Geothermics* 76:220--230.
- Nguyen H.V, Law Y.L, Zhou X, Walsh P.R, Leong W.H, Dworkin S.B. 2016. A techno-economic analysis of heat-pump entering fluid temperatures, and CO₂ emissions for hybrid ground-source heat pump systems. *Geothermics* 61:24--34.
- Nguyen A, Pasquier P. 2021. A successive flux estimation method for rapid g-function construction of small to large-scale ground heat exchanger. *Renewable Energy* 165:359-68.
- Nguyen A. 2021. Determination of the ground source heat pump system capacity that ensures the longevity of a specified ground heat exchanger field. *Renewable Energy* 169:799-808.
- Nguyen A, Tamasauskas J, Kegel M. 2022. A method for fast economic optimization of large hybrid ground source heat pump systems. *Geothermics* 104:102473.
- Yousefi H, Ármannsson H, Roumi S, Tabasi S, Mansoori H, Hosseinzadeh M. 2018. Feasibility study and economical evaluations of geothermal heat pumps in Iran. *Geothermics* 72:64--73.



Ground heat exchangers with large diameter pipes: What are the benefits?

Jasmin Raymond

Jean-Sébastien Gosselin

Jean-François Lavoie

ABSTRACT

The geothermal industry has recently been opting for large high-density polyethylene pipes to design vertical ground heat exchangers of ground-coupled heat pump system. Thus, we hypothesized that large diameter pipes can help improve heat exchange rate with the subsurface and made this study with the objective of quantifying the benefits gained with U-loop configurations. The finite line source equation and the multipole model were used to evaluate the maximum heat exchange rate that can be achieved with increasing pipe diameter. Sizing calculations were then performed for a school building in Boston. Ground heat exchangers with a single U-pipe having a nominal diameter of 1.25, 1.5 and 2 inches, as well as a double U-pipe, having a nominal diameter of 1.5 inches, were considered. Results highlighted that the double loop is by far the most efficient configuration, followed by the single loop with a 2 inches pipe diameter, respectively providing heat exchange rates that were 16% and 6% greater and total borehole length that were 22 and 9% smaller when compared to single loop with a 1.25 inches diameter. The use of large diameter pipes was shown without a doubt to benefit ground heat exchanger performances.

INTRODUCTION

Designing ground-coupled heat pump (GCHP) systems requires to minimize the borehole thermal resistance of closed-loop ground heat exchangers (GHE) to maximize heat transfer with the subsurface and ultimately decrease the total borehole length required to fulfill the building energy requirements. Boreholes are an expensive component of GCHP systems (Hénault et al., 2016; Robert and Gosselin, 2014), which can be made financially attractive by increasing the thermal performances of GHE. Various options are available to increase the performance of GHE, which commonly includes (1) adjusting the borehole diameter (Luo et al., 2013), (2) increasing the thermal conductivity (TC) of the grout mixture (Desmedt et al., 2012; Lee et al., 2012, 2011) and (3) selecting proper pipe configuration and material (Raymond et al., 2015). Besides, previous research specifically has been done to increase the TC of pipes by mixing high-density polyethylene (HDPE) with additives such as carbon-based nanoparticles (Gosselin et al., 2017). Moreover, coaxial pipe configurations have been extensively studied as it showed elevated GHE performances due to its large surface area and volume of water (Acuña et al., 2011; Acuña and Palm, 2013; Holmberg et al., 2016; Tago et al., 2005; Zanchini et al., 2010). GHE with a double U-pipe was additionally shown to outperform single U-pipe GHE (Florides et al., 2013; Sivasakthivel et al., 2017). Although significant developments in GHE design occurred over the last decade, improvements have not always readily been implemented in the field by practitioners who are dealing with complex installation procedures and requirements. However, one tendency that has been observed in the geothermal heat pump industry is to design GHE with large diameter pipes. For example, the sales of geothermal pipes at Versaprofiles having a 1.5 inches diameter have doubled from 2020 to 2021 and 2 inches diameter pipes have recently become available. This illustrates market-driven changes but what are the benefits of this practice?

Discussing with practitioners looking for innovations that do not add excessive installation complexity, we hypothesized that increasing the pipe diameter can improve thermal performances of GHE. Thus, this study was made with the objective of comparing the performance of different GHE configurations having regular and large diameter pipes. Our scientific hypothesis was verified with computations made in two methodological steps. Initially, maximal heat extraction (heating) and injection (cooling) rates were analytically calculated for GHE configurations with different pipe diameters. Then, sizing calculations for a typical high school building located in a climate corresponding to that of




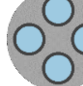
Jasmin Raymond (jasmin.raymond@inrs.ca) is a professor of hydrogeology and geothermal energy at the Institut national de la recherche scientifique, Jean-Sebastien Gosselin (jsgosselin@geostack.ca) is a geoscientist at Geostack and Jean-François Lavoie (jf.lavoie@versaprofiles.com) is an operation manager at Versaprofiles.

Boston, USA, were made considering the same GHE configurations. In each part of this study, calculations were carried out to highlight the effect of the GHE pipe diameter.

MATERIALS AND METHOD

The study allowed to evaluate the performance of single U-pipe GHE made of HDPE and having a nominal pipe diameter of 1.25, 1.5 and 2 inches, as well as a double U-pipe GHE made of HDPE and having a nominal pipe diameter of 1.5 inches. A surface dimension ratio (SDR) of 11 was considered for all pipe cases. The dimensions of the pipes for each configuration were determined according to the D3035-14a standard (ASTM, 2014). Thus, four different GHE configurations were compared in this study (Table 1). Characteristics of the GHE other than the size and configuration of the pipes were chosen to represent common field conditions. The distance between the center of the pipes (shank spacing) represents an intermediate case between pipes pressed against the wall of the borehole (with clips) and pipes stuck together. The diameter of each borehole was defined based on discussions with practitioners to make sure the pipes can be easily installed into the boreholes. The pipe TC was assumed to be 0.4 W/m/°C for all configurations, which is characteristic of HDPE, and the borehole was assumed to be filled with a thermally enhanced grout having a TC of 1.70 W/m/°C. The heat carrier fluid was assumed to be composed of a mixture of water and propylene glycol with a concentration of 30%.

Table 1 – Characteristics of the ground heat exchangers compared in this study.

Feature	Unit	Single loop 1.25	Single loop 1.5	Single loop 2	Double loop 1.5
Scale drawing	-				
Borehole diam.	mm (in)	114.3 (4.5)	127.0 (5.0)	139.7 (5.5)	152.4 (6.0)
Shank spacing	mm (in)	57.15 (2.25)	63.5 (2.50)	69.85 (2.75)	86.106 (3.39)
Pipes inner diam.	mm (in)	34.036 (1.34)	38.862 (1.53)	48.768 (1.92)	38.862 (1.53)
Pipes outer diam.	mm (in)	42.164 (1.66)	48.260 (1.90)	60.452 (2.38)	48.260 (1.90)
Pipe TC	W/m/°C	0.4	0.4	0.4	0.4
Grout TC	W/m/°C	1.70	1.70	1.70	1.70

The calculations in study were carried out using an analytical solution describing heat transfer between the GHE and the ground:

$$T_f - T_0 = -\frac{q'_b}{k_g} \cdot G(FO) - q'_b \cdot R_b^* \quad (1)$$

where T_f and T_0 (°C) are the temperature of the heat carrier fluid and the ground at initial condition, respectively, q'_b (W/m) is the heat transfer rate per unit length between the borehole and the ground, k_g (W/m/°C) is the ground TC, G is the thermal response G-function calculated with the finite line source equation (Lamarche and Beauchamp 2007) expressed as a function of the Fourier number FO , and R_b^* (°C·m/W) is the effective fluid-to-ground thermal resistance of the borehole calculated with the multipole method (Claesson and Hellström 2011).

In the first part of this study, the maximum heat injection and extraction rate that can be achieved with each of the four configurations were calculated by rearranging equation 1 as:

$$q'_b = -\frac{T_f - T_0}{R_b^* + \frac{G(FO)}{k_g}} \quad (2)$$

and by using the following heat budget equation for the borehole:

$$q'_b = \frac{\dot{m} \cdot C \cdot (T_{fo} - T_{fi})}{L_b} \quad (3)$$

Moreover, the average temperature of the fluid in the borehole (T_f) and the initial temperature of the ground (T_0) were calculated with:

$$T_f = (T_{fo} + T_{fi})/2 \quad (4)$$

$$T_0 = q''_g \frac{(0.5L_b - 4)}{k_g} + T_{g4m} \quad (5)$$

where T_{fo} and T_{fi} (°C) are the temperature of the fluid leaving and entering the GHE, \dot{m} (kg/s) is the mass flow rate of the heat carrier fluid, C (J/kg/°C) is the specific heat of the fluid, L_b (m) is the length of the borehole, q''_g (W/m²) is the terrestrial heat flow, and T_{g4m} is the average undisturbed ground temperature at a depth of 4 m below the ground surface.

The calculations were carried out using a volumetric flow rate of 1.07 L/s for all GHE configurations in both heating and cooling mode. This value was selected to ensure turbulent flow in all pipe sizes (Reynold number above 2500). The use of an identical volumetric flow rate was necessary to make the comparison of results meaningful. The entering water temperature in the borehole T_{fi} was set to a value of -0.5°C in heating mode and to a value of 27.5°C in cooling mode. A mean ground temperature at a depth of 4 m equal 10.5°C was used, which is characteristic for the city of Boston, USA (Wilcox and Marion 2008), and a terrestrial heat flow of 0.064 W/m² was considered to calculate the geothermal gradient, which is typical for North-East America (Blackwell and Richards 2004). The idea was to account for the increase of ground temperature that is expected with boreholes of different lengths.

Equations 2 and 3 constitute a system with two equations and two unknowns that can thus be solved to find the values of q'_b and T_{fo} for a given borehole configuration and set of fluid and ground conditions. The calculations were performed with a Python script and a time of 30 days was considered. Scoping calculations of heat extraction and injection rates between the borehole and the ground for time-varying between 1 and 300 days showed that the heat exchange rate stabilizes after approximately 30 days, both in heating and cooling mode for all the borehole configurations.

Using this problem-solving strategy, maximum heat extraction and injection rates in the ground were first calculated for 152.4 m (500 ft) long boreholes and a ground TC of 2.5 W/m/°C. Then, the impact of the borehole length on the GHE performance was assessed by calculating additional heat extraction and injection rates for boreholes of 205.7 m (675 ft) and 259.1 m (850 ft), while keeping the ground TC at a value of 2.5 W/m/°C. Finally, the impact of the ground TC on the performance of the heat exchangers was assessed by carrying out the calculations for 152.4 m (500 ft) long boreholes using a ground TC of 1.6 W/m/°C (typical of moist clay) and 3.4 W/m/°C (typical of granite), in addition to the calculations that were carried out previously with a TC of 2.5 W/m/°C (typical of saturated sandstone). The values of ground TC were chosen to represent ranges commonly associated to geological materials (Clauser 2014).

In this second part, the VersaGLD software (Gosselin and Lamarche 2018) was used to do sizing calculations considering our four GHE configurations (Table 1) in order to evaluate borehole length reduction that can be achieved with a larger pipe diameter. The thermal load profile of a typical high-school building in the climate conditions of Boston

was selected for the sizing calculations (National Renewable Energy Laboratory, 2014). Peak heating loads were clipped out to balance the average yearly heating and cooling loads assuming that 75% of the heating requirements would be covered by the geothermal system and the remaining 25% would be covered by an auxiliary heating system.

The mean yearly, maximum monthly, and peak hourly heating and cooling loads calculated from the clipped hourly building loads are presented in Table 2. The loads were entered in VersaGLD to calculate the required length of GHE with the three-pulse approach proposed in the ASHRAE handbook (ASHRAE 2015). Similar to part 1, the finite line source equation (Lamarche and Beauchamp 2007) was used for the thermal response function and the multipole model (Claesson and Hellström 2011) for the borehole thermal resistance. A period of 10 years was used for the mean yearly load, of 30.44 days for the monthly load and of 6 hours for the peak hourly load. A ground TC of 2.5 W/m/°C was selected for all sizing calculations to represent average ground conditions. The strategy used for the sizing calculations was to add boreholes to the borehole field until the length of the individual borehole was close to 152.4 m (500 ft), which is the target drilling length. Borehole horizontal spacing was assumed to be 6 m and boreholes were placed in a rectangular or square grid.

Table 2 – Mean yearly, maximum monthly, and peak hourly loads of a typical high-school building considered for sizing calculation.

Load	Units	Cooling	Heating
Mean yearly load	kW	-98.36	182.49
Max. monthly load	kW	-307.02	412.06
Peak hourly load	kW	-810.93	959.58

The initial ground temperature was again calculated with equation 5 and was 12.40°C for a borehole length of 152.4 m (500 ft). Based on this value, the entering water temperature at the heat pump inlet was set to -1°C in heating mode and 28°C in cooling mode, which is in agreement with the recommendations in ASHRAE (2015). The calculated borehole length requirements were obviously longer in heating mode for this heating dominated building and were thus compared below.

A first comparative analysis was conducted by fixing the conditions on the heat pump side. More specifically, the total flow rate of the heat carrier fluid and the COP were set to the same values for the four different GHE configurations. The total flow rate of the heat carrier fluid was set to 76.70 L/s, a value that ensured turbulent flow in both heating and cooling mode for all pipe sizes. The COP in heating and cooling mode were set to a value of 3.1 and 4.7, respectively, based on the energy efficiency requirement for geothermal heat pump of the Energy Star program. A second comparative analysis was conducted by using variable conditions on the heat pump side. The COP values in heating and cooling were calculated in VersaGLD from performance data of a high efficiency and high capacity commercial water-to-water heat pump (model TMW840; ClimateMaster, 2016). The total flow rate of the heat carrier fluid was optimized in order to minimize the total length of each GHE, while respecting the minimum and maximum flow requirements of the heat pump. Although this case can be more realistic, the results are difficult to compare with each other because multiple factors are then causing changes in total borehole length. It is then difficult to highlight the impact of the pipe diameter on the global results.

RESULTS

Complete results for this study are presented in a report prepared by Gosselin et al. (2021) that is freely available at INRS library while most interesting results are summarized in the four tables below.

Under a constant borehole length (152.4 m; 500 ft), an average ground TC (2.5 W/m. /°C) and the use of HDPE SDR-11 pipes, the double loop 1.5 is by far the most efficient configuration, with heat extraction and injection rates per unit length that are 15.7% and 16.5% larger than those calculated for the single loop 1.25 and 9.8% and 10.1% larger than those calculated for the single loop 2 (Tables 3 and 4). This is explained by the fact that the double loop 1.5 configuration

offers a heat exchange pipe surface that is 2.28 greater than that of the single loop 1.25 and 1.6 greater than that of the single loop 2. Analytical calculations also showed that using larger single U-pipe allowed performance gains, with heat extraction and injection rates per unit length that are 5.4% and 5.8% greater for the single loop 2 than those calculated for the single loop 1.25. Results were similar when comparing the performance of GHE with a longer borehole. For the three lengths considered (152.4 m – 500 ft, 205.7 m – 675 ft and 259.1 m – 850 ft), the double loop 1.5 is always the most efficient configuration. However, the difference between the heat extraction and injection rates per unit length calculated between each configuration become less important as the length of the borehole increase. For example, the difference between the heat extraction rates per unit length calculated for the double loop 1.5 and the single loop 1.25 configuration is 15.7% for 152.4 m (500 ft) long boreholes, 15.1% for 205.7 m (675 ft) long boreholes, and 14.4% for 259.1 m (850 ft) long boreholes. Again, results were similar when comparing the performance of GHE under different ground TC. However, the relative performance increase of the double loop 1.5 compared to the other configurations becomes larger when the ground TC increases. For example, the difference between the heat extraction rates per unit length calculated for the double loop 1.5 and single loop 1.25 configuration is 14.4% when the ground thermal conductivity is 1.6 W/m/°C, 15.7% when it is 2.5 W/m/°C, and 16.8% when it is 3.4 W/m/°C.

Table 3 – Ground heat extraction rates (heating) calculated with a ground thermal conductivity of 2.5 W/m /°C and 152.4 m (500 ft) long boreholes.




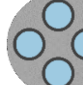




Parameter	Units	Single loop 1.25	Single loop 1.5	Single loop 2	Double loop 1.5
Scale drawing	-				
R_b^*	m.°C /W	0.094	0.094	0.089	0.064
q_b'	W/m	36.61	37.35	38.57	42.36
$\Delta q_b'$	%	0	2.0	5.4	15.7

Table 4 – Ground heat injection rates (cooling) calculated with a ground thermal conductivity of 2.5 W/m/°C and 152.4 m (500 ft) long boreholes.

Parameter	Units	Single loop 1.25	Single loop 1.5	Single loop 2	Double loop 1.5
Scale drawing	-				
R_b^*	m.°C /W	0.092	0.091	0.085	0.060
q_b'	W/m	-43.15	-44.07	-45.65	-50.26
$\Delta q_b'$	%	0	2.1	5.8	16.5

Results for sizing calculations of the typical school building in Boston indicated that under average ground conditions and a fixed flow rate entering the heat pump, the double loop 1.5 remains by far the most efficient configuration with a total borehole length that is 22.3% lower than that calculated for the single loop 1.25 (Table 5). Sizing calculations additionally showed the performance gained by using larger pipes with a total borehole length for the single loop 2, which is 9% lower than that calculated for the single loop 1.25 and 5.5% lower than that calculated for the single loop 1.5. Results obtained for the comparative analysis with variable heat pump conditions remain similar, with the double loop 1.5 being the most efficient configuration and larger pipes for single loop configurations offered a reduction of total borehole length (Table 6). The difference between the total borehole lengths calculated in Table 5 and

Table 6 can be attributed to two main factors. First, larger COP values were obtained in the second case compared to the first (between 4.35 and 4.46 in heating and 5.25 and 5.79 in cooling for the second analysis). A more efficient heat pump resulted in longer boreholes for such a heating dominated building. Second, the optimization of the flow rates in

the second analysis resulted in substantially lower volumetric flow rates in the single loop 1.25 (50.47 L/s) and single loop 1.5 (56.78 L/s) compared to the single loop 2 (69.40 L/s) and the double loop 1.5 (100.94 L/s) configurations. Larger flow rates result in a heat pump that is again more efficient. For example, the heating COP for the double loop 1.5 and the single loop 2 was 4.46 and 4.40. On the other hand, the COP of heating for the single loop 1.5 and the single loop 1.25 was 4.35 and 4.34. Moreover, larger flow translates into a smaller temperature difference between the fluid entering and leaving the heat pump. However, this can be compensated by increasing the length of the GHE to decrease the total number of boreholes, but that was not done in the second analysis to keep comparison simple.

Table 5 – Borehole length with fixed conditions on the heat pump size.









Parameter	Units	Single loop 1.25	Single loop 1.5	Single loop 2	Double loop 1.5
Scale drawing	-				
R_b^*	m·°C/W	0.091	0.090	0.084	0.058
N_b	-	85	82	77	67
L_b	m	152.2	151.9	152.8	149.9
L_{total}	m	12937	12459	11768	10046
ΔL_{total}	%	0	-3.7	-9	-22.3

Table 6 – Borehole length with variable conditions on the heat pump size.

Parameter	Units	Single loop 1.25	Single loop 1.5	Single loop 2	Double loop 1.5
Scale drawing	-				
R_b^*	m·°C/W	0.100	0.098	0.092	0.062
N_b	-	98	97	96	88
L_b	m	153.3	152.3	152.4	152.8
L_{total}	m	15022	14771	14635	13444
ΔL_{total}	%	0	-1.7	-2.6	-10.5

DISCUSSION AND CONCLUSIONS

Increasing the GHE pipe diameter and/or using a double U-pipe configuration appear to be readily applicable improvements that are simple to implement, especially when compared to modifying the pipe material (Gosselin et al. 2017) or opting for a coaxial GHE configuration requiring numerous pipe fusions in the field (Raymond et al., 2015). GCHP system installers often prefer the ease of single and double loop installations that are compatible with a large pipe diameter and where pipes are rapidly lowered in boreholes for which there is no pipe fusion except for the bottom U-bend and the connection at surface. Considering the results obtained in this study, opting for large diameter pipes can provide increased thermal performances of GHE, especially when choosing a double U-loop configuration. Adjustments maybe be needed when designing the ground loop that would require large valves and pump sizes.

In fact, the performance of four different GHE configurations was compared in this study under various conditions to highlight gains associated with large diameter pipes. Those are single loop GHE made of HDPE and having a nominal pipe diameter of 1.25, 1.5 and 2 inches as well as double loop GHE made of HDPE and having a nominal pipe diameter of 1.5 inches. Increasing the pipe diameter in all configurations reduced the borehole thermal resistance that is multiplied to the peak ground load when performing sizing calculations, which resulted in borehole length savings attributed to the ground power coverage. Sizing calculations were made over a period of ten years, but results are expected similar if the duration of the yearly ground load is increase. Overall, the double loop 1.5 GHE is by far the most efficient solution

for all situations. For the single loop configurations, the use of larger pipe size always resulted in better performances, which confirmed our original working hypothesis, but the gain is not as important as when using a double versus single loop configuration. This study further demonstrated the importance of borehole length, ground TC and heat pump conditions on the calculated GHE performances. In all cases, the conclusions remained similar. Even with deep boreholes, high ground TC or favorable flow conditions for the heat pump, the double loop 1.5 configuration is the one that best performed. Whether this thermal performance gain can translate into financial savings to reduce the installation cost of a GCHP is the next question to tackle and for which practitioners may have an opinion to share during this IGSHPA conference.

ACKNOWLEDGMENTS

This work was made by Geostack and INRS in collaboration to Versaprofiles that fully funded the research.

NOMENCLATURE

C	=	specific heat capacity (J/kg/°C)
$ Fo $	=	Fourier number (-)
$ G $	=	Thermal response function (-)
$ k $	=	thermal conductivity (W/m/°C)
$ L $	=	length (m)
$ \dot{m} $	=	mass flow rate (kg/s)
$ N $	=	number of (-)
$ q' $	=	heat exchange rate per unit length (W/m)
$ q'' $	=	Earth heat flux (W/m ²)
$ R^* $	=	effective fluid-to-ground thermal resistance (°C·m/W)
$ T $	=	temperature (°C)

Subscripts

$ b $	=	borehole
$ f $	=	fluid
$ g $	=	ground
$ i $	=	entering
$ o $	=	leaving
$ 0 $	=	initial condition
$ 4m $	=	4 m depth

REFERENCES

- Acuña, J., P. Mogensen, and B. Palm. 2011. *Distributed Thermal Response Tests on a Multi-Pipe Coaxial Borehole Heat Exchanger*. HVAC&R Research 17 (6): 1012–29. <https://doi.org/10.1080/10789669.2011.625304>.
- Acuña, J., and B. Palm. 2013. *Distributed Thermal Response Tests on Pipe-in-Pipe Borehole Heat Exchangers*. Applied Energy 109 (0): 312–20. <https://doi.org/10.1016/j.apenergy.2013.01.024>.
- ASHRAE. 2015. Geothermal Energy. In *ASHRAE Handbook - HVAC Applications*, edited by ASHRAE, 34.1-34.34. Atlanta: American Society of Heating, Refrigerating and Air-Conditioning Engineers.
- ASTM. 2014. ASTM Standard D3035. Standard Specification for Polyethylene (PE) Plastic Pipe (DR-PR) Based on Controlled Out-Side Diameter. West Conshohocken: ASTM International.
- Blackwell, D.D., and M. Richards. 2004. *Geothermal Map of North America*. American Association of Petroleum Geologist, <http://smu.edu/geothermal/2004NAMap/2004NAMap.htm>.
- Claesson, J., and G. Hellström. 2011. *Multipole Method to Calculate Borehole Thermal Resistances in a Borehole Heat Exchanger*. HVAC&R Research 17 (6): 895–911. <https://doi.org/10.1080/10789669.2011.609927>.
- Clauser, C. 2014. Thermal Storage and Transport Properties of Rocks, II: Thermal Conductivity and Diffusivity. In *Encyclopedia of Solid Earth Geophysics*, edited by HarshK. Gupta, 1431–48. Encyclopedia of Earth Sciences Series. Springer Netherlands. http://dx.doi.org/10.1007/978-90-481-8702-7_67.
- ClimateMaster. 2016. Submittal Data - Tranquility Large Water-To-Water (TMW) Series. LC975. Oklahoma City: ClimateMaster. <http://www.climatemaster.com>.
- Desmedt, J., J. Van Bael, H. Hoes, and N. Robeyn. 2012. Experimental Performance of Borehole Heat Exchangers and Grouting Materials for Ground Source Heat Pumps. International Journal of Energy Research 36 (13): 1238–46. <https://doi.org/10.1002/er.1898>.

- Florides, G., E. Theofanous, I. Iosif-Stylianou, S. Tassou, P. Christodoulides, Z. Zomeni, E. Tsiolakis, et al. 2013. *Modeling and Assessment of the Efficiency of Horizontal and Vertical Ground Heat Exchangers*. Energy 58 (September): 655–63. <https://doi.org/10.1016/j.energy.2013.05.053>.
- Gosselin, J.-S., and L. Lamarche. 2018. *VersaGLD: A Cross-Platform Software for Doing Quick Comparison Analysis of Ground Coupled Heat Pump (GCHP) Exchanger System (version 0.3.13)*. <https://github.com/cgq-qgc/versagld/releases/tag/v0.3.13>.
- Gosselin, J.-S., J. Raymond, S. Gonthier, M. Brousseau, and J.-F. Lavoie. 2017. *Nanocomposite Materials Used for Ground Heat Exchanger Pipes*. Proceedings of IGHSPA Technical/Research Conference and Expo, 373–83. Denver. <https://doi.org/10.22488/okstate.17.000530>.
- Gosselin, J.-S., J. Raymond, and M. Blouin. 2021. *Comparative Analysis of the Performance of Typical Geothermal Heat Exchangers*. Report R2071. Quebec City: Institut national de la recherche scientifique - Centre Eau Terre Environnement.
- Hénault, B., P. Pasquier, and M. Kummert. 2016. *Financial Optimization and Design of Hybrid Ground-Coupled Heat Pump Systems*. Applied Thermal Engineering 93 (January): 72–82. <https://doi.org/10.1016/j.applthermaleng.2015.09.088>.
- Holmberg, H., J. Acuña, E. Næss, and O.K. Sønju. 2016. *Thermal Evaluation of Coaxial Deep Borehole Heat Exchangers*. Renewable Energy 97: 65–76. <https://doi.org/10.1016/j.renene.2016.05.048>.
- Lamarche, L., and B. Beauchamp. 2007. *A New Contribution to the Finite Line-Source Model for Geothermal Boreholes*. Energy and Buildings 39 (2): 188–98. <https://doi.org/10.1016/j.enbuild.2006.06.003>.
- Lee, C., M. Park, S. Min, S.-H. Kang, et al. 2011. *Comparison of Effective Thermal Conductivity in Closed-Loop Vertical Ground Heat Exchangers*. SET2010 Special Issue 31(17): 3669–76. <https://doi.org/10.1016/j.applthermaleng.2011.01.016>.
- Lee, C., M. Park, T.-B. Nguyen, B. Sohn, et al. 2012. *Performance Evaluation of Closed-Loop Vertical Ground Heat Exchangers by Conducting in-Situ Thermal Response Tests*. International Symposium on Low Carbon and Renewable Energy Technology 2010 (ISLCT 2010) 42 (June): 77–83. <https://doi.org/10.1016/j.renene.2011.09.013>.
- Luo, J., J. Rohn, M. Bayer, and A. Priess. 2013. *Thermal Efficiency Comparison of Borehole Heat Exchangers with Different Drillhole Diameters*. Energies 6 (8). <https://doi.org/10.3390/en6084187>.
- National Renewable Energy Laboratory. 2014. *Commercial and Residential Hourly Load Profiles for All TMY3 Locations in the United States [Data Set]*. <https://dx.doi.org/10.25984/1788456>.
- Raymond, J., S. Mercier, and L. Nguyen. 2015. *Designing Coaxial Ground Heat Exchangers with a Thermally Enhanced Outer Pipe*. Geothermal Energy 3 (7): 14. <https://doi.org/10.1186/s40517-015-0027-3>.
- Robert, F., and L. Gosselin. 2014. *New Methodology to Design Ground Coupled Heat Pump Systems Based on Total Cost Minimization*. Applied Thermal Engineering 62 (2): 481–91. <https://doi.org/10.1016/j.applthermaleng.2013.08.003>.
- Sivasakthivel, T., M. Philippe, K. Murugesan, V. Verma, and P. Hu. 2017. *Experimental Thermal Performance Analysis of Ground Heat Exchangers for Space Heating and Cooling Applications*. Renewable Energy 113 (December): 1168–81. <https://doi.org/10.1016/j.renene.2017.06.098>.
- Tago, M., K. Morita, M. Sugawara, and T. Fujita. 2005. *Heat Extraction Characteristics by Coaxial Heat Exchanger*. Heat Transfer—Asian Research 34 (7): 496–513. <https://doi.org/10.1002/htj.20083>.
- Wilcox, S, and W Marion. 2008. *Users Manual for TMY3 Data Sets*. Technical Report 58. Battelle: Office of Energy Efficiency and Renewable Energy. <https://www.nrel.gov/docs/fy08osti/43156.pdf>
- Zanchini, E., S. Lazzari, and A. Priarone. 2010. *Improving the Thermal Performance of Coaxial Borehole Heat Exchangers*. Energy 35 (2): 657–66. <https://doi.org/10.1016/j.energy.2009.10.038>.

Ground heat exchanger performance with variable speed ground-source heat pumps

Geoffrey Viviescas

Michel Bernier

ABSTRACT

The objective of this paper is to compare the required length and performance of ground heat exchangers as well as heat pump energy consumption for fixed and variable speed ground-source heat pumps. In the first part of the paper, a physics-based model of a water-to-water heat pump is briefly presented. This model is incorporated in TRNSYS simulations using a performance map where variable speed operation is handled through a linear relationship linking the COP to the percentage of the full capacity being used. The ground heat exchanger is modeled using a thermal resistance and capacitance approach to account for borehole thermal capacity. Simulations are performed on a typical residential building located in a cold climate (Montréal, Canada) and equipped with either a fixed or variable speed ground-source heat pump. Results are obtained for eight cases with: variable or fixed speed operation (VSC or FSC), with or without consideration of borehole thermal capacity (TC or NTC), and with annual heating needs covered at 90% or 100% by the heat pump. The differences in the required borehole length between the TC and NTC cases are relatively small. The smallest required borehole length is for the FSC-90%-TC case (180 m) and the longest is for the VSC-100%-TC case (250 m). The VSC-100% case has the largest seasonal Performance factor (SPF) at 4.14 and the FSC-90% case has the lowest at 3.11.

INTRODUCTION

Ground-source heat pumps equipped with variable speed compressors (VSGSHP) offer the possibility of matching the building heating and cooling loads by modulating the compressor speed. This is accomplished by tuning the inlet frequency (typically down to 20-30 Hz and up to 90-120 Hz) to the electric motor of the compressor. Thus, contrary to fixed speed ground-source heat pumps (FSGSHP) which operate in on/off mode, VSGSHP operates continuously except for low load conditions. Furthermore, VSGSHP can meet a greater portion of the heating loads without requiring auxiliary heat. Thus, the ground heat exchanger (GHE) of a VSGSHP will experience loads that are different than the ones of an FSGSHP. In turn, this affects the required length and thermal performance of the GHE.

Bouheret and Bernier (2018) have reviewed the literature on variable capacity water-to-air ground-source heat pumps. They proposed an approach to model a commercially available product (ClimateMaster, 2022) that can provide heating, cooling, and domestic hot water (DHW). They showed that the annual SPF (i.e. ratio of the annual energy requirement for heating, cooling, and DHW over the annual electricity consumption) can reach 3.64. However, their analysis did not examine the impact of the variable speed operation on the GHE itself.

A residential-size ground-source integrated heat pump (GSIHP) system was developed by Rice et al. (2013). Experimental test results were used to calibrate a model in TRNSYS which was used to predict annual energy savings for five US locations. Results indicate that the GSIHP offered average savings of 55% when compared to a typical air source heat pump (ASHP). The required length of the GHE for the GSIHP was 25% higher than a ground-source heat pump equipped with a desuperheater for DHW. Except for this last article, very few studies have examined in detail the impact of the operation of a VSGSHP on the performance of GHE.

Thus, the objective of this paper is to compare the required length and performance of ground heat exchangers (GHE) as well as heat pump energy consumption for fixed and variable speed ground-source heat pumps. The paper starts with a brief description of the system being investigated. Then, the heat pump model used in the simulations is presented.

Geoffrey Viviescas (geoffrey.viviescas@polymtl.ca) is a Ph.D. candidate and Michel Bernier (michel.bernier@polymtl.ca) is a professor of mechanical engineering at Polytechnique Montreal.

This is followed by a presentation of the results and concluding remarks.

SYSTEM UNDER INVESTIGATION

The system under investigation is shown in Figure 1 and the characteristics of the main components are given in Table 1 along with the model (Type) used in the TRNSYS simulations. It consists of a residence located in Montréal and heated by a water-to-water heat pump coupled to a vertical GHE. Space cooling is not considered in this study and the same configuration is used for FSGSHP and VSGSHP. A thermostat activates a circulation pump that feeds a series of radiators with hot water from a buffer tank to maintain the house at 21 °C. The buffer tank provides a means to decouple the heat pump operation from the distribution loop in the building. Buffer tanks are commonly used for fixed-speed heat pumps to avoid excessive cycling. It is also possible to link a VSGSHP directly to a distribution loop given the ability to provide varying load side temperatures. However, it was decided to keep the buffer tank for the VSGSHP system considering that comparisons were to be made with FSGSHP.

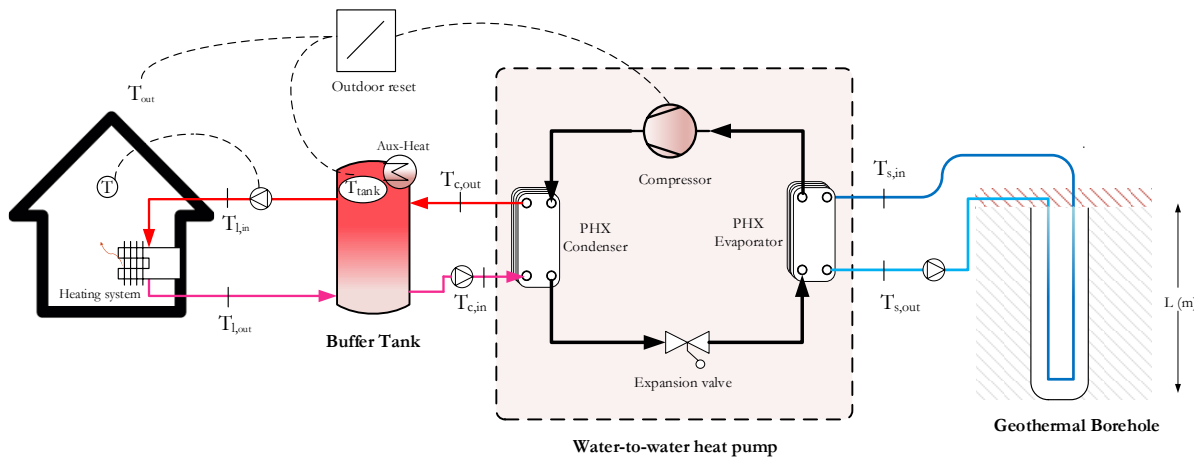


Figure 1 Schematic representation of the system under investigation

Table 1 Main components used in simulations

Component	TRNSYS TYPE	Principal characteristic	Value
Building	88	Overall building loss coefficient, UA [kW/K]	0.225
		Building mass, MC _p [kJ/K]	50000
Buffer tank	158	Volume [m ³]	0.5
		Height [m]	2
		Auxiliary heaters [kW]	2 x 2.5
FSGSHP	927	Performance given in Figure 4 for a fixed frequency of 60 Hz	
VSGSHP	Slightly modified version of Type 1323_v2a	Performance given in Figure 4	
Borehole	243 (in-house model developed to model borehole thermal capacity- See Godefroy et al. (2016)	Borehole radius [m]	0.075
		Ground thermal conductivity [W/m-K]	2.22
		Ground thermal capacitance [kJ/m ³ /K]	2000
		Grout thermal conductivity [W/m-K]	0.833
		Grout thermal capacitance [kJ/m ³ /K]	0 or 3900
		Pipe thermal conductivity [W/m-K]	0.416
		Borehole thermal resistance [m-K/W]	0.178

The top tank temperature is regulated by an aquastat which sends a signal to the heat pump to operate. In the case of the FSGSHP, an on/off signal is sent to the heat pump. For the VSGSHP, the compressor speed is regulated to achieve the desired outlet temperature (i.e. the top tank temperature). The top tank set point temperature, T_{set} , is adjusted using a simple outdoor reset control based on the ambient temperature, T_{out} , ($T_{set} = -0.556 \times T_{out} + 33.3$) leading to maximum and minimum tank set point temperatures of 50 °C and 25 °C, respectively.

This enables lowering the tank temperature in mild weather to increase heat pump COP and reduce energy consumption. If the heat pump is unable to meet the tank set point temperature, two auxiliary heaters (2.5 kW each) are activated in stages when the tank temperature is 2 °C and 3 °C below T_{set} . On the source side, the heat pump is connected to a ground heat exchanger (GHE) and two constant flow circulating pumps are activated whenever the heat pump is operating.

VARIABLE SPEED GROUND-SOURCE HEAT PUMP MODEL

A VSGSHP model was developed for this study and integrated in TRNSYS using a performance map. This model is part of a broader study aimed at developing a detailed physics-based and experimentally validated model of a water-to-water heat pump. Initial steps towards this goal were documented recently (Viviescas et al., 2021) and more details on this model will be presented in the near future. The following paragraphs contain only the salient features of the model that are pertinent to the present study.

The VSGSHP modeled here is equipped with two plate heat exchangers (evaporator and condenser), a variable speed compressor, and an expansion valve as shown in Figure 1. Each of these four components is modeled individually and linked together via the refrigeration cycle. Steady-state operation is assumed at each time step and pressure drops in both heat exchangers are assumed to be negligible. R-410A is used as the refrigerant. Detailed heat transfer models are used for both heat exchangers. This enables the prediction of the number of degrees of superheating and subcooling for a given refrigeration flow rate (Viviescas et al., 2021). A constant enthalpy process is assumed in the expansion valve. The compressor requires special treatment and the next paragraphs describe the approach used here.

Researchers have proposed various approaches to model variable speed compressors. For example, Shao et al. (2004) proposed a model built on second-order correlations based on condensation and evaporation temperature for the basic frequency. These correlations are then corrected with a second-order frequency correlation for other frequencies. In this work, the compressor is modeled using an extension of the approach suggested in standard CAN/ANSI/AHRI 540-2020 (AHRI, 2020). This standard proposes to fit fixed-speed experimental data into a third-order polynomial equation with 10 coefficients as shown in Equation 1 :

$$X = C_1 + C_2T_s + C_3T_D + C_4T_s^2 + C_5T_DT_s + C_6T_D^2 + C_7T_s^3 + C_8T_DT_s^2 + C_9T_sT_D^2 + C_{10}T_D^3 \quad (1)$$

where C_1 to C_{10} are the regression coefficients, T_D is the discharge dew point temperature in °C, (i.e. condensing temperature corresponding to saturation at $x=1$), T_s is suction dew point temperature in °C, (i.e. evaporating temperature corresponding to saturation at $x=1$), and X is either the power input (in W), cooling capacity (in W), or refrigerant mass flow (kg h⁻¹).

This approach has been adapted here to include variable speed compressors by introducing frequency as a parameter. This variable is related to the speed of rotation of the compressor and therefore the mass flow rate and the power of the compressor depending on the frequency. Preliminary statistical analysis indicates that using a third order polynomial with 20 coefficients correlates both the mass flow rate and power of a variable speed compressor with good accuracy:

$$X = C_1 + C_2T_s + C_3T_D + C_4f_{Hz} + C_5T_s^2 + C_6T_D^2 + C_7f_{Hz}^2 + C_8T_s f_{Hz} + C_9T_D f_{Hz} + C_{10}T_sT_D + C_{11}T_sT_D f_{Hz} + C_{12}T_s^2T_D + C_{13}T_D^2T_s + C_{14}T_s^2 f_{Hz} + C_{15}f_{Hz}^2T_s + C_{16}T_D^2 f_{Hz} + C_{17}f_{Hz}^2T_D + C_{18}T_s^3 + C_{19}T_D^3 + C_{20}f_{Hz}^3 \quad (2)$$

where f_{Hz} is the frequency in Hz.

The compressor power and refrigerant mass flow rate given by equation 2 were coupled to the rest of the components of the model resulting in a set of nonlinear equations. The solution of this set of equations gives the heating capacity (at the condenser) and the COP which is simply the ratio between the capacity and the power given by Equation 2. A commercially available scroll compressor (Danfoss VSH088-G) was chosen for this study. The estimation of the coefficients was carried out using the STATISTICA® software using multiple linear regression. The resulting coefficients are presented in Table 2.

The values of these coefficients are specific to this compressor. Modeling of other compressors that differ in size and design is planned in a further study.

Figure 2 shows a comparison between the experimental results and the 20-coefficient equation for the power input. It can be seen that the agreement between the 20-coefficient equation and experimental results is very good. The mean and maximum differences are 0.8 % and 3.5 % over the full range of conditions (similar results were obtained for the mass flow rate). It should be noted that the resulting degrees of superheating or subcooling did not always correspond exactly to the values associated with Equation 2. In these cases, the equation contained in Appendix D of the standard (AHRI, 2020) was used to adjust mass flow rates for various degrees of superheat by using the change in refrigerant density at the suction of the compressor.

The original plan was to develop a TRNSYS type with its own internal solver that could perform such calculations at each time step in a simulation. However, this proved to be difficult due to convergence issues associated with the correct choice of guess values to solve the set of nonlinear equations. Instead, individual component models were implemented and linked together in the Engineering Equation Solver (EES, 2022) software tool where guess values could be changed more easily. The integrated models were solved by changing the frequency (from 30 to 90 Hz in increments of 10 Hz) and the inlet temperatures of both secondary fluids (from -2 to 10 °C in increments of 2 °C for the source side and from 30 to 50 °C in increments of 5 °C on the load side). For this study, the flow rates of the secondary fluids were kept constant (at 0.5 kg/s) to limit the number of independent variables.

Table 2 Input coefficients to equation 2

	Power [W]	Mass-flow [kg/h]		Power [W]	Mass-flow [kg/h]
C1	-2200.6	-12.80	C11	0.0067	0.00029
C2	-55.6	-0.4251	C12	0.0275	-0.00036
C3	151.6	-0.2964	C13	-0.0175	-0.00043
C4	79.8	8.4103	C14	0.0059	0.00354
C5	-1.612	0.0189	C15	0.0006	0.00002
C6	-3.923	-0.01016	C16	-0.0058	-0.00026
C7	-0.4734	-0.00058	C17	0.01828	-0.00014
C8	0.2950	0.28141	C18	-0.0067	0.00154
C9	0.5560	0.03704	C19	0.0451	-0.00001
C10	1.5683	0.01319	C20	-0.00032	-0.00001

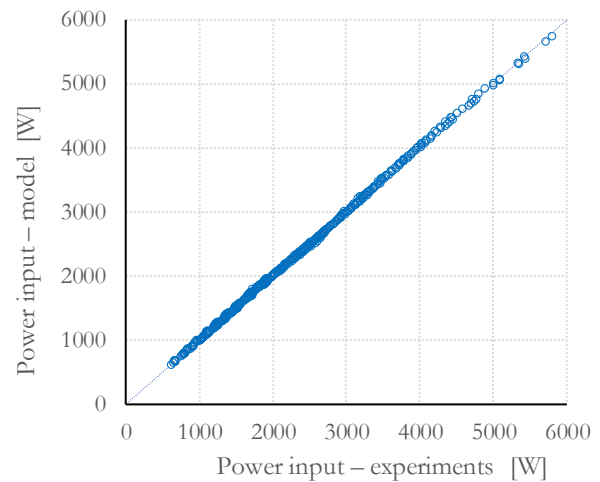


Figure 2 Comparison of the 20-coefficient model with manufacturer data.

It is interesting to examine the performance of the VSGSHP for several conditions. Figure 3 shows the normalized heating capacity for three combinations of $T_{s,in}/T_{c,in}$ and seven frequencies. As expected, the COP increases as the temperature difference between the source and load temperatures decreases. For a given $T_{s,in}/T_{c,in}$ combination the COP reaches a peak value at different frequencies. For example, for the 5°C /35°C combination, the COP is maximum at 50 Hz and it decreases when the frequency is either increased or decreased. As expected, the heating capacity increases with frequency as the refrigerant flow rate increases.

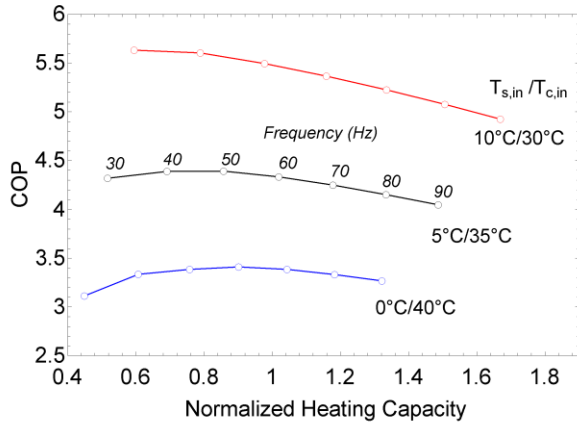


Figure 3 Normalized heating capacity for the VSGSHP

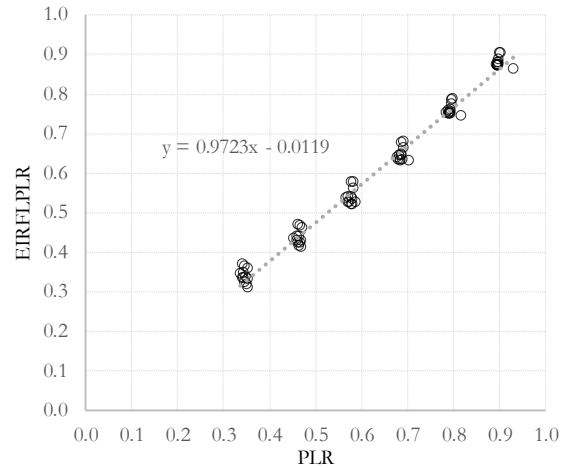


Figure 4 Part load performance of the VSGSHP

The full set of data was split in two: Data at full load (90 Hz) and data at partial load (from 30 to 80 Hz). Figure 5 shows the first few lines of the performance map at full load. Data were normalized at 5°C on the source side and 35°C on the load side.

30	35	40	45	50	!Entering Load Temperatures (C)		
-2	0	2	4	6	8	10	!Entering Source Temperatures (C)
0.855	0.896				!Normalized Heat Capacity, normalized power at 90Hz, 30[°C], -2[°C]		
0.898	0.902				!Normalized Heat Capacity, normalized power at 90Hz, 30[°C], 0[°C]		
0.944	0.908				!Normalized Heat Capacity, normalized power at 90Hz, 30[°C], 2[°C]		

Figure 5 Excerpt of the performance map of the VSGSHP at full load (90 Hz)

To account for operation at other frequencies (i.e. at part load), the approach implemented in TRNSYS Type 1323_v2a (variable speed heat pump model) is used. The energy input ratio as a function of temperature (EIRFPLR) is calculated as a function of the ratio of the actual capacity to the full load capacity (also known as the Part Load Ratio, PLR) for the same source and load inlet temperatures. Using the second set of data it was then possible to establish a correlation between EIRFPLR and PLR. As shown in Figure 4 a linear relationship was found to fit the data with relatively good accuracy. Also, since compressor operation below 30 Hz is not recommended, the curve stops at a PLR \sim 0.35. Thus, whenever a PLR of 0.35 is reached, the VSGSHP stops and cycles to meet the set point temperature. The original TRNSYS Type 1323_v2a was modified to account for cycling operation below 30 Hz.

The FSGSHP was modeled in TRNSYS using Type 927 which also uses a performance map. To make a fair comparison between the VSGSHP and the FSGSHP, the same compressor was used for the FSGSHP but with a fixed operating frequency of 60 Hz.

Heat pump cycling losses for either the FSGSHP or the VSGSHP (below 30 Hz) are handled using the approach proposed by Fuentes et al. (2016) which is based on an experimental study carried out to characterize the behavior of water-to-water heat pumps that operate under partial load. Start-up (C_d) and degradation (C_c) coefficients equal to 0.22 and 0.998 are used.

RESULTS AND DISCUSSION

Simulations are performed over 10 years with a 6-minute time step. The required borehole length is determined on a trial and error basis, where the length is varied until the minimum inlet temperature to the heat pump reaches a value of 0 °C. Of interest are the required length of the borehole, the annual energy consumption, the coefficient of performance COP, and the seasonal performance factor (SPF).

Various scenarios are explored to cover the following three effects: Variable or fixed speed operation (VSC or FSC),

with or without (TC or NTC) consideration of borehole thermal capacity, and the proportion of the annual heating needs (90% or 100%) covered by the heat pump. The cases are identified with an acronym such as VSC-100%-TC. A total of eight cases are presented to cover the various combinations. In terms of the proportion of the annual heating needs being covered by the heat pump, it was decided to examine two cases where 90% and 100% of the annual heating needs are covered by the heat pump. In other words, in the first case, auxiliary heat provides 10% of the annual heating load (typically at peak load conditions) while in the second case auxiliary heat is not required.

Global annual results are shown in Table 3 for the eight cases while Table 4 presents the peak load on the borehole, q_h , as well as the monthly (q_m) and yearly (q_y) average loads, values which are typically used in borehole sizing (Philippe et al. 2010). The peak borehole load is particularly important and might be responsible for up to 50 to 80% of the required length. As shown in Table 3, the rated heating capacity is substantially higher when 100% of the annual needs are covered. For example, for the VSC-TC cases, the rated heating capacities are 9.51 kW and 5.69 kW for the 100% and 90% cases, respectively. This has a substantial impact on the peak borehole load. As shown in Table 4 for the same two cases, the peak hourly loads are 6.36 kW and 4.54 kW, respectively. The monthly ground loads during the peak month are also quite different (4.80 vs 4.17 kW) as well as the yearly ground load (2.29 vs 2.15 kW).

Table 3. Rated heating capacity and power as well as various annual energy values

Parameter	Units	VCS-100% TC	VCS-100% NTC	VSC-90% TC	VSC-90% NTC	FSC-100% TC	FSC-100% NTC	FSC-90% TC	FSC-90% NTC
Rated Heating Capacity	[kW]	9.51	9.51	5.69	5.69	9.87	9.87	5.56	5.56
Rated Heating Power	[kW]	2.36	2.36	1.41	1.41	2.36	2.36	1.33	1.33
Heating needs by HP	[kWh/y]	26354	26353	23879	23870	26317	26317	23757	23706
Bore energy extracted	[kWh/y]	20129	20125	18195	18186	20021	20021	18073	18015
Compressor energy	[kWh/y]	6225	6229	5684	5685	6297	6297	5684	5690
Auxiliary Energy	[kWh/y]	33	35	2324	2330	0	0	2310	2316
% Auxiliary heating	%	0.12	0.13	9.73	9.76	0.00	0.00	9.72	9.77

Table 4. Hourly, monthly and annual max loads on the borehole for the 8 cases

Parameter		VCS-100% TC	VCS-100% NTC	VSC-90% TC	VSC-90% NTC	FSC-100% TC	FSC-100% NTC	FSC-90% TC	FSC-90% NTC
Peak hourly mean ground load [kW]	q_h	6.36	6.53	4.54	4.81	6.53	6.65	4.15	4.36
Monthly mean ground load [kW]	q_m	4.80	4.84	4.17	4.20	4.87	4.89	3.94	3.96
Yearly mean ground load [kW]	q_y	2.29	2.29	2.15	2.15	2.29	2.28	2.06	2.06

The required borehole length for each case is shown in Figure 6. The first point to note is that there is not a large difference in the required borehole length when borehole thermal capacity is included in the borehole model. One would have expected the FSC cases to show greater differences between the TC and NTC cases since cycling should enable the borehole thermal capacity to dampen the peak loads (Gagné-Boisvert and Bernier, 2016). However, peak conditions for the FSC cases last for several hours which eliminates the beneficial effect of borehole thermal capacity. For the VSC cases, the heat pump capacity is adjusted at every time step and the borehole load changes accordingly, and these changes are dampened by borehole thermal capacity. This can be seen in Figure 7 where the borehole load and outlet temperature variations at peak conditions are shown for one week in the middle of January. The borehole load variation is smoother when borehole thermal capacity is included. As shown in Figure 7, this leads to a slightly lower required borehole length when TC is included. Since the differences in results between TC and NTC cases are small, only TC results will now be compared. As shown in Figure 6, the minimum required length is for the FSC-90% cases at 180 m while the maximum length is for the FSC-100% cases at 255 m, a difference of about 40%. This difference is simply because values of q_h , q_m , and q_y are all higher for the FSC-100% case as shown in Table 4. The same reasoning applies when the VSC-100% and the VSC-90% cases are compared.

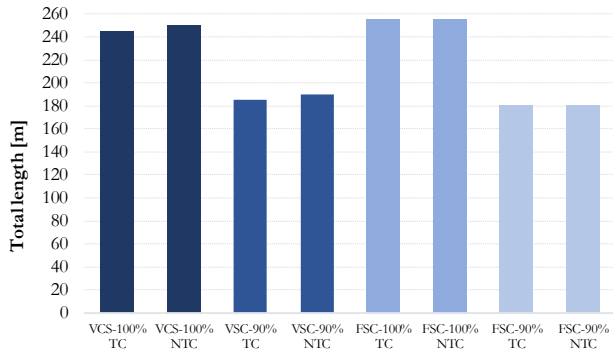


Figure 6 Required borehole length for the eight cases

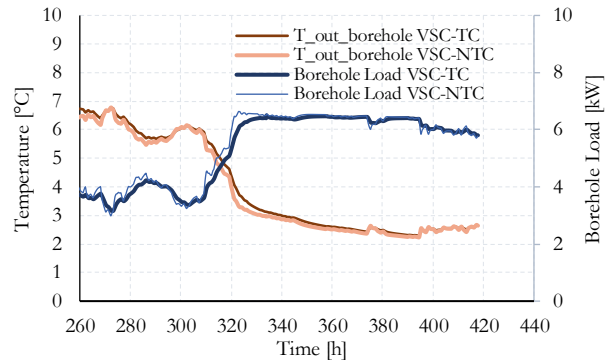


Figure 7 VSC-100% (TC-NTC) cases during peak conditions

When the annual heating load is met entirely by the heat pump including at peak conditions (FSC-100%-TC and VSC-100%-TC) it is interesting to note that the VSC has a lower required borehole length (245 m) when compared to the FSC case (255 m), a difference of 4%. This difference is explained by different values of q_h , q_m , and q_v as shown in Table 4. The higher value of q_h is because at peak load (approximately represented by the 0°C/40°C curve in Figure 3) the COP is higher at 60 Hz (for the FSGSHP) than at 90 Hz (for the VSGSHP operating at the maximum frequency). A higher COP implies that the borehole load is higher for the same load. Figure 8a shows the variation of the top tank temperature, outlet borehole temperature, and borehole load around the peak conditions. For $t < 320$ h, the cycling of the FSC can be seen. For $320 < t < 400$ h, at peak conditions, the FSC operates continuously. After $t > 400$ h cyclic operation is also shown. In contrast, the VSC shows much smoother variations of the top tank temperature, outlet borehole temperature, and borehole load throughout this time interval.

The situation is reversed when 90% of the annual heating load is met by the heat pump: the VSC has a higher required length (185 m) than the FSC (180 m), a 3 % difference. Here the difference is attributable to the heat pump capacity at peak conditions. Even though care was taken to obtain the same amount of auxiliary energy on an annual basis (10%), results in Table 4 reveal that the annual amount of auxiliary heat is 9.73 and 9.76 % for the VSC and FSC, respectively. Thus, the VSC requires slightly more heat from the borehole. Furthermore, the VSC and FSC have different COP (Figure 3). These two factors lead to different values of q_h at peak conditions, 4.54 kW for the VSC case and 4.15 kW for the FSC case, which explains the difference in the borehole length.

Figure 8b shows a comparison between the VSC-100% and FSC-90% cases around peak conditions. As was observed in Figure 8a, the cycling nature of the FSC can be seen. In addition, the operation of the two auxiliary heaters is shown with the first stage at 2.5 kW and the two stages at 5 kW. The borehole load at the peak conditions is a little below 4 kW for the FSC case while it is slightly above 6 kW for the VSC case.

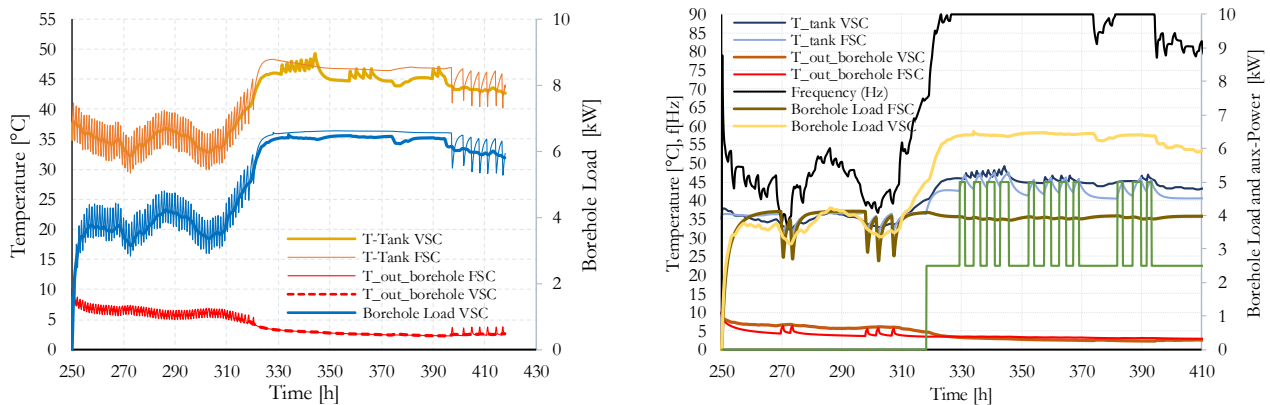


Figure 8 System behaviour a) VSC100% vs FSC100%; b) VSC-100% vs FSC90%

The black line in figure 8b shows the compressor frequency during the period of highest thermal load. For $t < 320$ h, the VSC works at reduced speeds operating at frequencies between 30-90 Hz. For $320 < t < 370$ h, at peak conditions, the VSC operates continuously at full capacity (90Hz).

Another metric for comparison is the seasonal performance factor (SPF) which is defined here using:

$$SPF = \frac{\sum_{j=1}^n Q_{Load,j}}{\sum_{j=1}^n (W_{net,j} + W_{aux,j})} \quad (3)$$

where n is the number of times steps during the heating season, $Q_{load,j}$ is the amount of energy required to heat the building, $W_{net,j}$ is the amount of energy required by the compressor and $W_{aux,j}$ is the amount of auxiliary heating plus the amount of energy associated with cyclic losses. SPF values for four cases are shown in Figure 9.

The VSC-100% case has a higher SPF (4.14) than the FSC-100% case (4.01). Since there is no auxiliary heating, in either case, the difference is due to a combination of higher COP for the VSC-100% case and higher cycling losses for the FSC-100% case. The VSC-90% case has also a higher SPF than the FSC-90% case (3.25 vs 3.11). Aside from the higher cycling losses associated with the FSC case, two other reasons explain this difference. First, the nominal capacity of the VSC is slightly higher than that of the FSC (see Table 3), reducing the use of auxiliary heating (9.73% compared to 9.76% for the FSC). Secondly, the temperature difference between the source and the load (borehole and tank) oscillates less in the VSC leading to less oscillation in the value of the temperatures and better COPs.

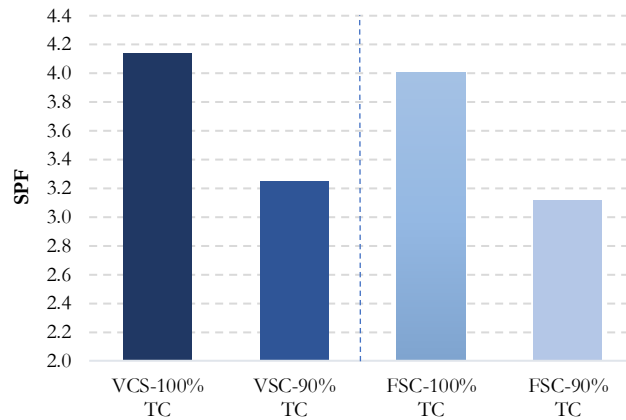


Figure 9 Seasonal performance factor (SPF) for four cases

CONCLUSION

The required length and thermal performance of ground heat exchangers, as well the heat pump energy consumption for fixed and variable speed ground-source heat pumps, are investigated in this study. In the first part of the paper, the fixed and variable speed ground-source heat pump models are described. The compressors are modeled using third-order correlations with 20 coefficients obtained by adapting the standardized procedure of the AHRI 540-2020 standard. The global model is assembled in the EES software tool to solve the system of nonlinear equations. This information is used to develop a performance map along with a modified version of TRNSYS Type1323_v2a used to model variable speed water-to-water heat pumps. Ten-year simulations of a residence located in Montréal are performed with a six-minute time step.

In the results section, various scenarios are explored to cover the following three effects: Variable or fixed speed operation (VSC or FSC), with or without (TC or NTC) consideration of borehole thermal capacity, and with annual heating needs covered at 90% or 100% by the heat pump. The differences in the required borehole length between the

TC and NTC cases are relatively small in the present case probably because the residential building has a long and almost constant peak period which reduces the beneficial effect of borehole thermal capacity. The smallest required length is for the FSC-90%-TC case (180 m) and the longest is for the VSC-100%-TC case (250 m). This represents a 40% difference. The VSC-100% case has the largest SPF at 4.14 and the FSC-90% case has the lowest SPF at 3.11. This is due to the negligible use of auxiliary heating and the reduction in heat pump cycling losses for the VSC-100% case. A comparison between the VSC-100% and the FSC-100% cases, thus with no auxiliary heating, indicates that variable speed operation leads to a better SPF (4.14 vs 4.01) and to a 3.2% reduction in annual energy consumption.

Cooling-dominated or balanced systems were not considered in this study. For cooling-dominated systems, the higher COP of the VSC would most likely lead to shorter boreholes. As for balanced systems, it is difficult to predict whether the FSC or the VSC would lead to shorter boreholes without doing further studies. Furthermore, pumping energy on both the source and load sides should also be considered. The conclusions obtained here are specific to the present case. Different climates, buildings, and types of compressors need to be examined to generalize the conclusions.

NOMENCLATURE

T_{out} =	room temperature (°C)		
T_{set} =	tank temperature set point (°C)		Subscripts
$T_{s,in}$ =	temperature out from the borehole (°C)	c =	condenser
$T_{c,in}$ =	temperature out tank to heat pump (°C)	s =	source

REFERENCES

- AHRI. 2020. National standard CAN/ANSI/AHRI 540-2020 Performance Rating of Positive Displacement Refrigerant Compressors.
- ASHRAE. 2015. Chapter 34 Geothermal energy. ASHRAE Handbook, HVAC applications, Atlanta, GA:.
- Bouheret, S. and M. Bernier. 2018. *Modelling of a water-to-air variable capacity ground-source heat pump*. Journal of Building Performance Simulation, 11(3), 283-293.
- Climatemaster. 2022, Trilogy-45. [Online] Available at: <https://www.climatemaster.com/homeowner/news/climatemaster/climatemaster/trilogy-45> [Accessed 21 March 2022].
- Danfoss, 2022. VSH088 model. [Online] Available at: <https://www.manualslib.com/manual/1966573/Danfoss-Vsh088.html?page=12#manual>
- Engineering Equation Solver (EES). 2022. F-chart software, Madison, Wiscosin, v11.365.
- Enertech, 2018. WV models water-to-water heat pumps – Installation & Operations Manual. [Online] Available at: <https://geocomfort.com/residential-products/item/guide-wv> [Accessed 11 May 2022].
- Fuentes, E., D.A. Waddicor and J. Salom. (2016). *Improvements in the characterization of the efficiency degradation of water-to-water heat pumps under cyclic conditions*, Applied Energy, 179: 778-89.
- Gagné-Boisvert L. and M. Bernier. 2016. *Accounting for borehole thermal capacity when designing vertical geothermal heat exchangers*. ASHRAE summer conference, St-Louis, Missouri, June 2016. Paper ST-16-C027.
- Godefroy, V., C. Lecomte, M. Bernier, M. Douglas and M. Armstrong. 2016. *Experimental validation of a thermal resistance and capacity model for geothermal boreholes*. ASHRAE winter conference, Orlando, Florida, January 2016. Paper OR-16-C047.
- Philippe, M., M. Bernier and D. Marchio. 2010. *Sizing Calculation Spreadsheet: Vertical Geothermal Borefields*. ASHRAE Journal, 52(7), 20-28.
- Rice, K., V. Baxter, S. Hern, T. McDonwell, J. Munk and B. Shen. 2013. *Development of a residential ground-source integrated heat pump*. ASHRAE Transactions, 119(1).
- Shao, S., S. Wenxing, X. Li and H. Chen. 2004. *Performance representation of variable-speed compressor for inverter air conditioners based on experimental data*. International Journal of Refrigeration, 27(8): 805-815.
- Viviescas, G., S. Houaida, M. Bernier and M. Kummert. 2021. *Energy performance advantages of using multiple compressors in a heat pump operating in heating mode*. IBPSA-Canada, eSim 2021 Conference. [Online] Available at: http://www.ibpsa.org/proceedings/eSimPapers/2021/Contribution_1211_final_a.pdf [Accessed 11 May 2022].



Impacts of Prospective LEED Building's Energy Loads on a Borehole Heat Exchanger: A Case Study in Central Illinois

Zilong Zhao
Xinlei Wang

Andrew Stumpf

Yu-Feng Lin

ABSTRACT

Assessing the thermal behavior in the subsurface surroundings of a borehole heat exchanger (BHE) is necessary for evaluating the performance of GSHP systems. In this study we undertook a preliminary thermal analysis on a constructed GSHP system that is coupled to a LEED-certified building, the Campus Instructional Facility (CIF), at the University of Illinois at Urbana-Champaign. The building is designed to utilize multiple energy-saving technologies that achieve a building performance of LEED-Gold certification. Energy modeling of the entire building was performed in DesignBuilder software by considering all of the high efficiency thermal-insulated features, and the building energy load was obtained and used in the iterations of the ground thermal response model. An analytical model (Erol & François 2018) was applied to evaluate the thermal response from a single BHE within a multilayer geology considering the annual energy extraction/rejection from the building. A parallel scenario was considered for comparison when the GSHP was coupled to a building with a typical heating-dominated load profile in central Illinois. The difference in the development of isotherms around the BHE are simulated to demonstrate the benefits of coupling green buildings and GSHP. This research may facilitate the wider implementations of GSHP systems with energy-efficient buildings.

INTRODUCTION

Ground source heat pumps (GSHPs) have been widely adopted to exchange thermal energy between buildings and the underground. However, the high-upfront cost and system degradation over their lifespan has prohibited their further penetration in the current heating and cooling marketplace. System degradation and lower efficiencies may result from the lack of knowledge of the local ground thermal properties, the mismatch between building heating and cooling loads, the over-conservative design in the borefields, etc. (Zanchini et al., 2012; Zhao et al., 2021). Recent research has revealed that a multilayered geology and the presence of groundwater have significant impacts on the performance of GSHP (Stylianou et al., 2019; Zhao et al., 2022). When it comes to simulating GSHP long-term operations (At least for 1 year, including all the seasonal effects), the observed ground thermal behaviors may provide strategies to optimize their design and operation.

Across the globe, buildings energy systems account for approximately 40% of their total energy consumptions and 36% of their carbon emissions (Al Shargabi et al., 2022). LEED (Leadership in Energy and Environmental Design) developed a rating systems for confirming the sustainability of buildings (U.S. Green Building Council, 2022). Compared to other buildings with traditional heating and cooling systems, a LEED-certified building provides substantial benefits from a multitude of aspects, among which the low heating-cooling loads are a requirement that reduce the electricity usage for air conditioning. Therefore, these measures allow GSHP systems to be implemented with a lower temperature heat extraction/rejection when connected to the ground avoiding long-term overheating. However, significantly increase in the installation of GSHP was not observed in green buildings. The high upfront cost of GSHP prohibits the designers from including the shallow geothermal into system integration during the budgeting process. Yet, it was still found that in many cases, the long-term energy cost constitutes a significant weight of the life cycle budget for green buildings

Xinlei Wang (xwang2@illinois.edu) is a professor of agricultural and biological engineering and Zilong Zhao is a research assistant at University of Illinois at Urbana-Champaign. Andrew Stumpf and Yu-Feng Lin are principal research scientists at Prairie Research Institute.

(Dwaikat et al., 2018; Filippini et al., 2022). Therefore, this paper presents the preliminary results of a case study in central Illinois, where a LEED-certified instructional facility was conditioned by GSHP, to evaluate the feasibility and economics of GSHP on green buildings. The in-situ information of the building and the energy modeling were first introduced, then followed by the explanation of the analytical thermal response model, and finally the results of the simulation were delivered.

IN-SITU BUILDING INFORMATION AND MODELING

Campus Instructional Facility (CIF) is a four-story building dedicated to academic and classroom use, located on the campus of The University of Illinois at Urbana-Champaign (UIUC). At the southeastern side of the building, a 40-well geothermal borefield of 137.5-m depth is completed and expected to cover 65% of the entire heating-cooling demand of the building. Besides a GSHP system, the building is innovatively designed by incorporating multiple sustainable elements, such as daylighting, radiant panels, and air ventilation, etc. which makes it a unique case study associated with GSHP implementation. To model the energy consumption of the building, a 3D building model was established and simulated using a commercial software, DesignBuilder. The simulation engine of DesignBuilder is the EnergyPlus software, which was developed by the American Energy Association in 2011 (See et al., 2011). To obtain the dynamic seasonal load of CIF, the thermal properties of the building envelopes, the personnel and lighting loads, and the indoor temperature settings within different zones, etc. were applied as inputs. Table 1 lists the input parameters in the building energy model. Figure 1 shows the location of the building and its exterior appearance in both in-situ view and model view. Figure 1 d) presents the simulation results in DesignBuilder, where the variation of annual ambient temperature profile for the entire building was provided. Since the aim of this study is to show the thermal response of the ground around a single borehole, the borehole load is simply computed as the total load divided by the number of boreholes. To compare the performance between the studied building (CIF) and the conventional one (Control), a parallel set of thermal properties was applied to external wall, roof and fenestrations, as indicated by the bracket values in Table 1, and the daily load for a single borehole was plotted in Figure 1 e). As observed, the heating and cooling loads in the CIF are generally lower compared to the “control”. To be more specific, the average heating loads in the worst month (Jan) are 17.33 kW (Control) and 7.27 kW (CIF), respectively. In summer, the applied high-performance insulation technologies and the intense educational activities in CIF increase its cooling demand, thus making it a slightly cooling-dominated profile (490.7 kW for cooling and 418.4 kW for heating as total building loads). In contrast, the cooling load in the “control” profile is lower than heating load (578.3 kW for cooling and 737.3 kW for heating as total building loads). To simplify the model, the impacts of COP’s annual variations on the discrepancy of borehole loads and building loads were neglected. Instead, the COP was considered as a constant value (4) in both cases. Thus, the building loads (For a single borehole) were then simply ratioed by COP to be converted as borehole loads and the direct inputs in the ground thermal response model, as shown in Figure 1 e).

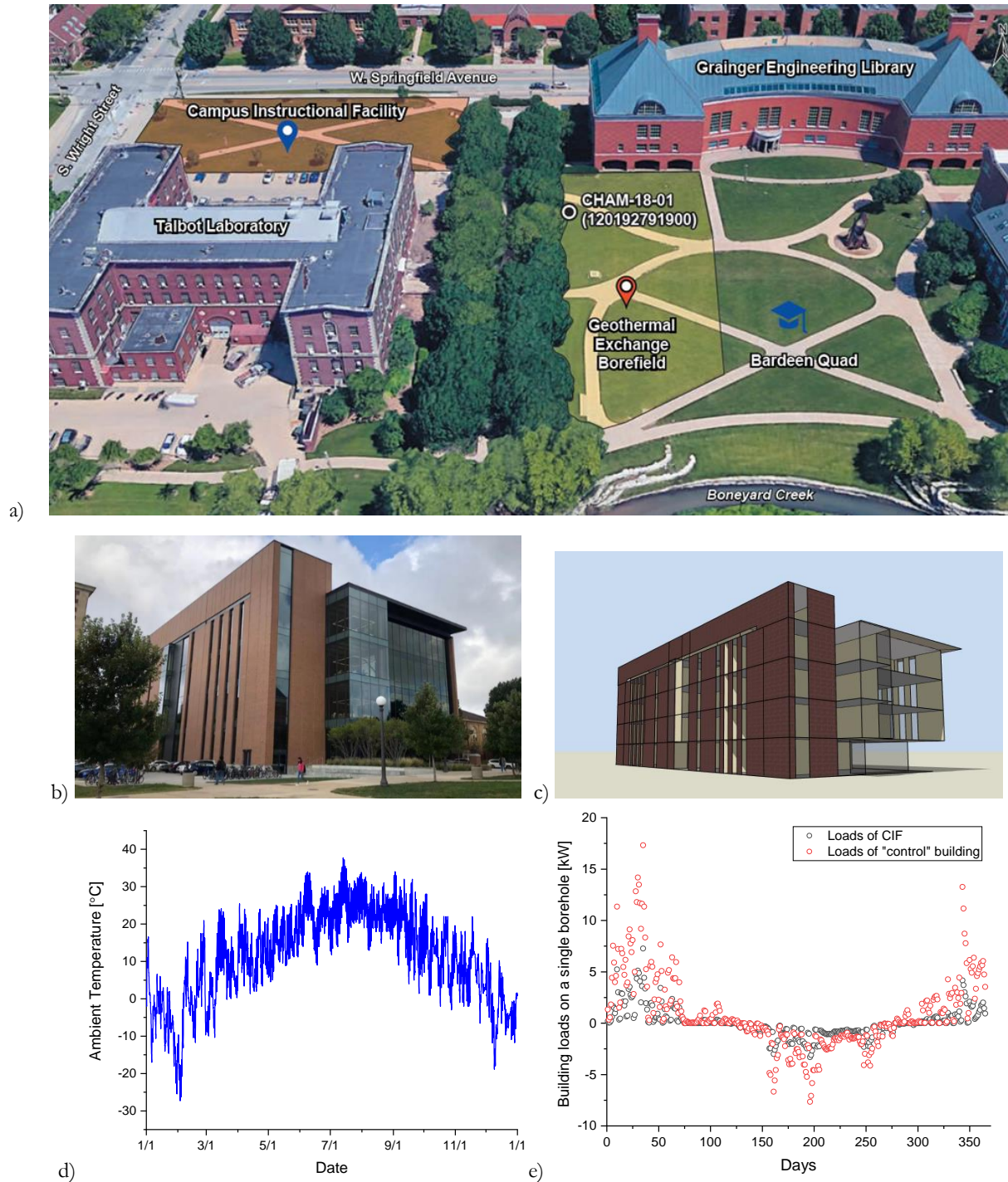


Figure 1 Modeling of Campus Instructional Facility (CIF). (a) Location of the CIF viewed in Google Earth with 3D buildings layer (Google Earth, 2022; Stumpf et al., 2021). (b) In-situ view. (c) Model view in DesignBuilder. (d) Variations of annual ambient temperature. (e) Variations of annual building thermal loads on a single borehole. Negative and positive values denote the cooling and heating loads respectively.

Table 1 Model input parameters in DesignBuilder for the LEED building and the “control” building

Item	Value/Description
U-value of external wall	0.055 (0.35) W/m ² -K
U-value of roof	0.03 (0.25) W/m ² -K
U-value of fenestration	0.35 (2.76) W/m ² -K
Window-to-wall ratio	38%
Fenestration SC	0.44 (0.135)
Fenestration transmittance	0.78 (0.73)
Lighting	4.62 W/m ²
Personnel	40 W/person
Temperature settings	Heating: 21.1 °C 35% RH Cooling: 23.9 °C 50% RH
Outdoor design conditions	Summer: 35 °C Winter: -24.4 °C
Weather file	University of Illinois, Willard

ANALYTICAL MODEL FOR MULTILAYER GROUND THERMAL RESPONSE

To evaluate the transient temperature variation surrounding the borehole, an analytical model was implemented in this study to integrate the building energy load profiles measurements. Erol and François (2018) developed a multilayer model for effectively calculating the temperature change from any observation point. The model mainly consists of two segments—the thermal response in the specified layer (denoted by subscript “1”), and the thermal response from adjacent layers (denoted by subscript “2...n”). In their original study, the heterogeneity of the subsurface physical properties within the same geologic layer was even considered, with assigning different values to the longitudinal and transversal changes in thermal diffusivity and conductivity. Nevertheless, the current field study on campus of UIUC did not consider differences in material properties in 3 dimensions. The analytical model has thus been simplified from the computations represented by the following equations, where x , y , z denote the spatial coordinates, r is the radial distance, and t time. Further, q denotes the heat flux per unit length of borehole; v and α denote the thermal transport velocity and thermal diffusivity, respectively.

$$\Delta T(x, y, z, t) = \Delta T_1 + \Delta T_2 + \dots + \Delta T_n \quad (1)$$

$$\Delta T_1(x, y, z, t) = \frac{q}{2\pi k_1} \exp\left(\frac{xv_1}{2\alpha_1}\right) \left\{ \int_0^{z_1} f_1(x, y, z, t) dz' - \int_{-z_1}^0 f_1(x, y, z, t) dz' \right\} \quad (2)$$

$$\Delta T_n(x, y, z, t) = \frac{q}{2\pi k_n} \exp\left(\frac{xv_n}{2\alpha_n}\right) \left\{ \int_{z_{n-1}}^{z_n} f_n(x, y, z, t) dz' - \int_{-z_n}^{-z_{n-1}} f_n(x, y, z, t) dz' \right\} \quad (3)$$

$$f_n(x, y, z, t) = \frac{1}{4r} \left[\exp\left(\frac{-rv_n}{2\alpha_n}\right) \operatorname{erfc}\left(\frac{r-v_nt}{2\sqrt{\alpha_n t}}\right) + \exp\left(\frac{rv_n}{2\alpha_n}\right) \operatorname{erfc}\left(\frac{r+v_nt}{2\sqrt{\alpha_n t}}\right) \right] \quad (4)$$

To analyze the seasonal effects on the extent and migration of thermal plumes, one-year and three-year building load profiles were integrated into the model, and the iteration code was run in MATLAB. The initial ground temperature was set as 11°C as the in-situ thermal response tests indicated. To include the effects of adjacent geologic layers, the subsurface environment beneath CIF was divided into three lithologies with different hydrological and thermal properties measured by Burch et al (1999) and Stumpf et al. (2021), respectively, as shown in Table 2. The main groundwater flow exists in the second layer, while an extremely low velocity was assigned to the other two layers. The temperature of groundwater was set to be the same as initial ground temperature, 11°C.

Table 2 Geological layered properties

Lithologies	Depth range (m bgs)	Thermal diffusivity (mm ² /s)	Groundwater velocity (m/s)
Till	0~22.4	1.01	1×10 ⁻⁸
Sand and gravel	22.4~85.5	1.47	2.07×10 ⁻⁷
Clay and bedrocks	85.5~137	1.20	1×10 ⁻⁸

RESULTS AND DISCUSSION

The graphs by the end of December obtained from the one-year and three-year simulation results are shown in this section, where both vertical and horizontal temperature profiles are presented. The horizontal domain (X-Y) was divided into 41 × 41 grids and the length of each grid was set as 0.5 m to better visualize the far field temperature. The vertical domain (X-Z) was divided into 81 × 41 grids and the length of grid in radial direction was set as 9.375 × 10⁻³ m to show the temperature gradient near the borehole. The sectional X-Y planes were selected at the depths of 55 m and 110 m below ground surface (bgs), which are the lithologies with the maximum and minimum groundwater flow velocities. The groundwater was set to flow towards the increasing values of direction-X. As observed in Figure 2, at the depth of 110 m, within the deepest lithology, the isotherms are dispersed symmetrically from the center of BHE. While for the sand and gravel where the groundwater flow is 2.07 × 10⁻⁷ m/s, the rejected heat in summer slightly migrates along the downstream of groundwater. The modeling results indicated very minor temperature change in the surroundings of the BHE, as the temperature at the majority of the grids fell into the range of 10.3 °C ~ 11.2 °C. Also, negligible difference was observed between the temperature contours by the end of first year and third year, indicating the thermal steady state was reached early in the first year. Furthermore, the migration of heat plume was not significant, partially because groundwater flow is relatively slow. It also indicates that the rejected heat from CIF was sufficiently mild to be offset by the surrounding environment before it further developed in the x direction.

The simulation results for BHE coupled to a building with a traditional heating and cooling system, referred as the “control”, are presented in Figure 3, where a heating-dominated profile is observed. In the lowest lithology, the minimum temperature simulated near the wall of borehole (x = 0.5 m) reached 7.89 °C and 7.76 °C by the end of first and third year, respectively. With the presence of groundwater flow, the overcooling was slightly mitigated. As the cold center migrates in the x direction, the heat extraction near BHE becomes effective. At the same radial distance (x = 0.5 m), the temperature decreased from 8.64 °C to 8.57 °C as time marched from one year to three years. The severeness of overcooling in the scenario of “control” and CIF was further visualized in Figure 4. As one can observe, as it approaches from far field to the borehole wall, the difference between the magnitudes of temperature drops in “control” and CIF increases. Also, the presence of groundwater may narrow this gap in the upstream as it may refresh the local ground temperature.

The comparison between the vertical temperature profiles of the CIF and control is shown in Figure 5. To better visualize the temperature difference between the different lithologies and scenarios, a depth of 40-137 m was chosen to generate the isotherms. As demonstrated, much milder temperature drop was found in the CIF scenario when compared to the “control”. In the “control” scenario, the maximum temperature decrease at the borehole wall was 10.55 °C, while when it comes to CIF, it was 2.73 °C, which reduced 74.1% of the thermal anomaly. Furthermore, the presence of groundwater may reduce the effects of either heating or cooling, introducing benefits to the performance of BHE.

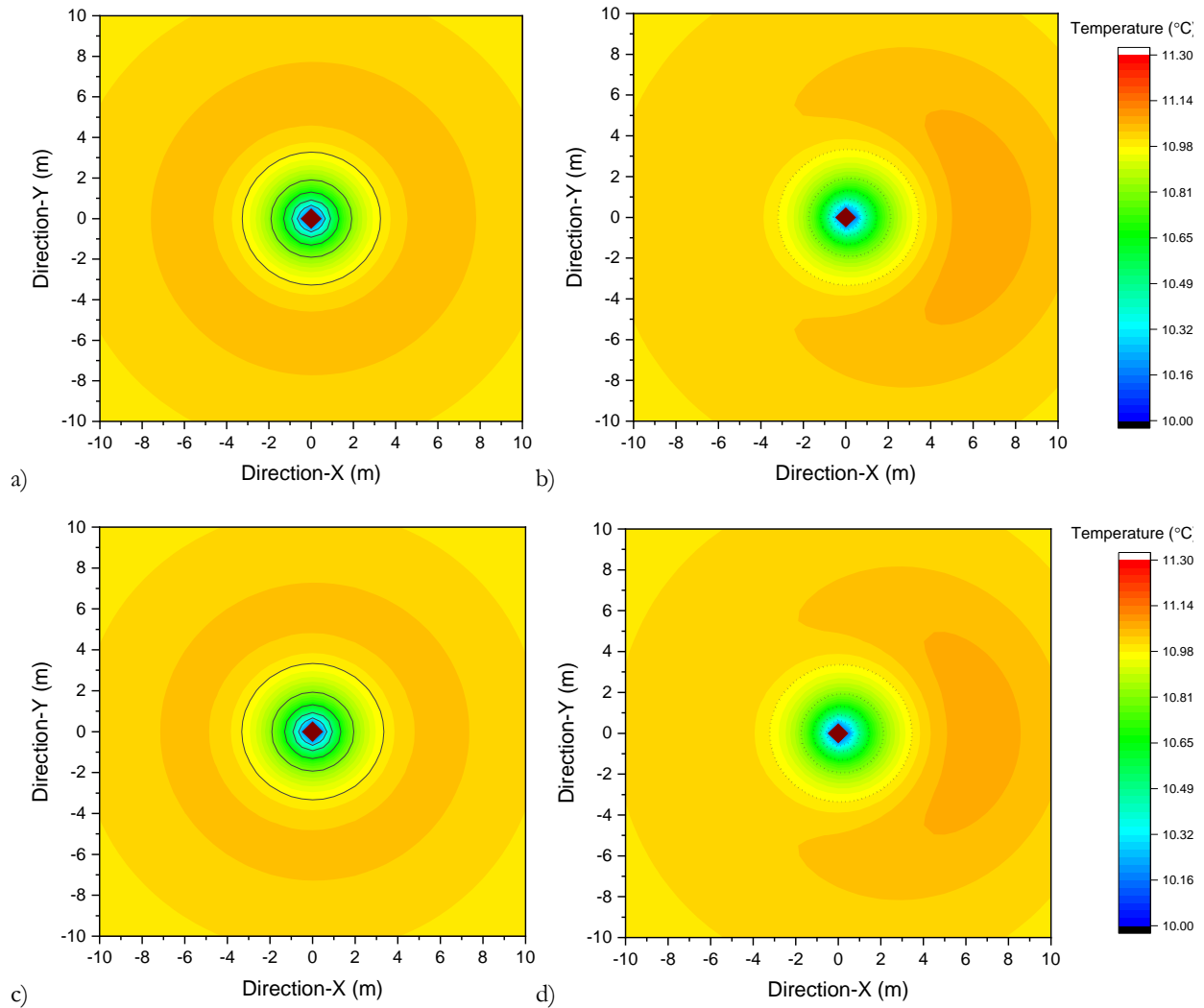
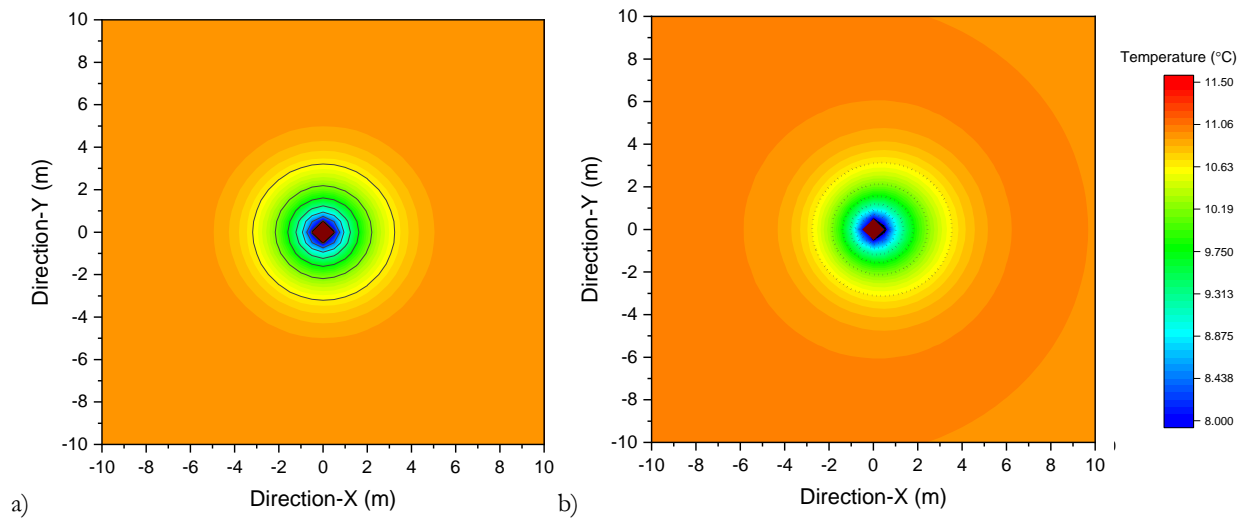


Figure 2 Isotherms around the BHE coupled at the CIF by the end of first year (Dec 31st) at a) depth of 110 m (with minimum groundwater flow). b) depth of 55 m (with 2.07×10^{-7} m/s groundwater flow). Temperatures at the end of third year (Dec 31st) in the lithologies at c) depth of 110 m and d) depth of 55 m.



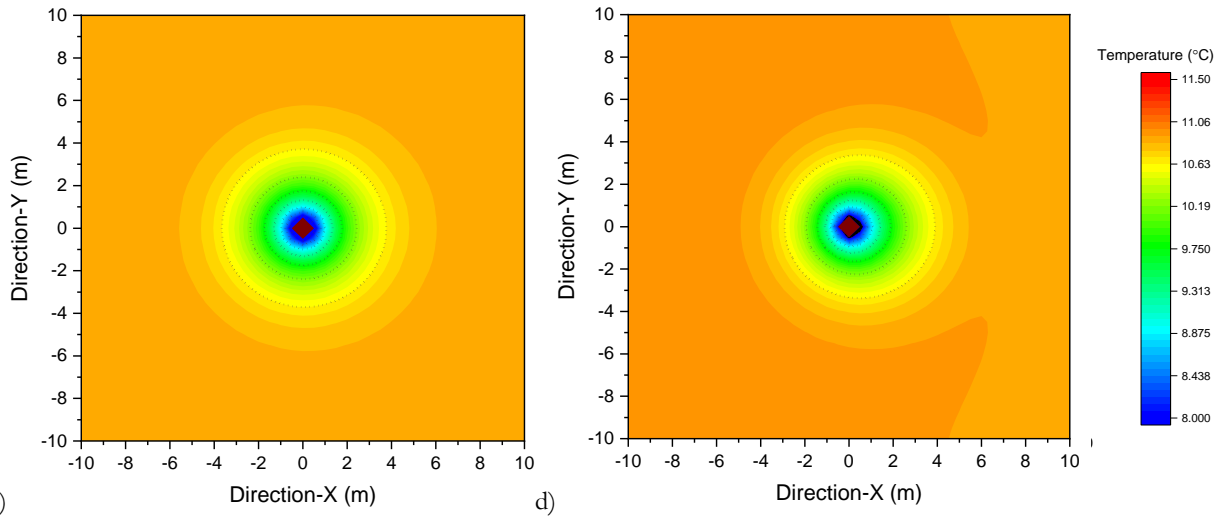


Figure 3 Isotherms around the BHE coupled with the “control” building at the end of first year (Dec 31st) at depths of a) 110 m (with near-zero groundwater flow) and b) 55 m (with 2.07×10^{-7} m/s groundwater flow). By the end of third year (Dec 31st), the temperature decrease, and isotherms are shown at depths of c) 110 m and d) 55 m.

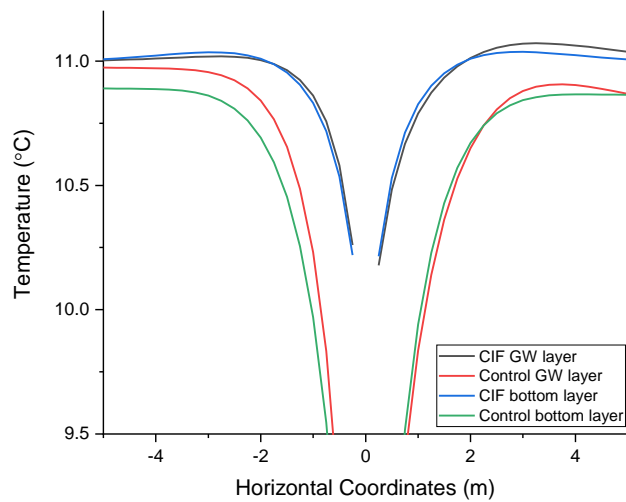


Figure 4 The one-dimensional temperature profiles along the direction-X at horizontal sectional planes with/without groundwater abundance in the scenario of CIF and “control” by the end of third year (Dec 31st). GW denotes the layer with highest groundwater velocity.

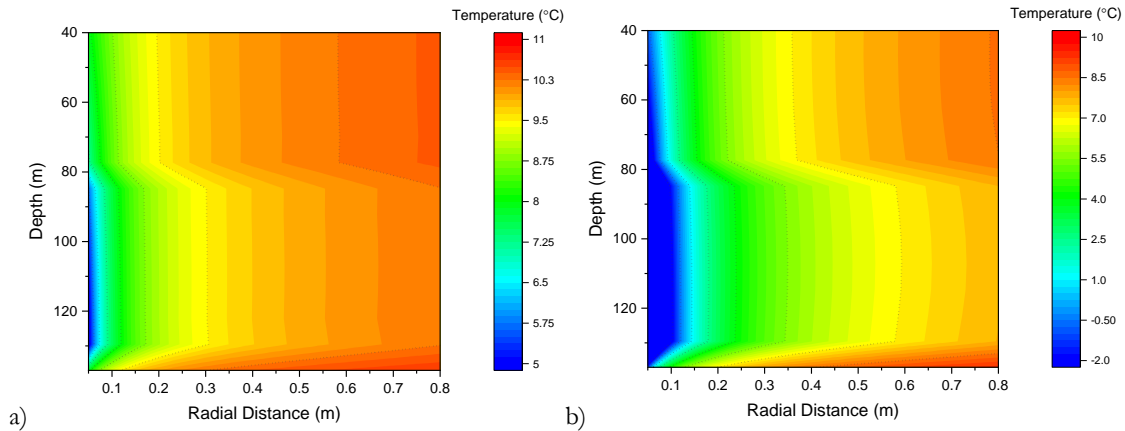


Figure 5 The vertical temperature profile along the BHE between 40-137 m bgs by the end of the third year (Dec 31st) for a) BHE coupled with CIF. b) BHE coupled with “control” building.

CONCLUSION

This study investigated the ground thermal response from a single BHE for two buildings with different energy loads—the CIF building which is seeking LEED certification and the “control” with a traditional energy system. As the two buildings were simulated with the same borehole length, the results showed that the prospective LEED building may significantly reduce the possibility of overheating and overcooling the ground. By the end of the third year of operation, the simulation for the BHE coupled with the CIF suggests there would be a 74.1% lower temperature drop at the borehole wall compared to the “control” building in central Illinois. The groundwater flow in this lithology was observed to be very slow, though flowing groundwater had beneficial impacts on dissipating thermal anomalies. This study provide evidence on the necessity of climate-adaptive building envelopes when a GSHP is implemented. Nevertheless, the LEED buildings require higher constructional cost compared with others. Therefore, future efforts should be put on the life-span economic analysis of GSHP to evaluate its financial feasibility in practice.

ACKNOWLEDGMENTS

We acknowledge the financial support from the National Institute of Food and Agriculture, U.S Department of Agriculture (Hatch project No. ILLU-741-359) and the Student Sustainability Committee at the University of Illinois at Urbana-Champaign. We would also like to acknowledge the computing support from the Illinois Water Resources Center.

NOMENCLATURE

- α = Thermal diffusivity (m²/s)
- β = Thermal expansion coefficient (1/K)
- q = Specific heat load (W/m)
- r = Radial distance from the line source (m)
- ν = Kinematic viscosity (m²/s)
- t = Time (s)
- x, y, z = Spatial coordinates (m)
- ξ' = Integrating factor (-)

T = Temperature of the ground (°C)

Subscripts

n = Number of ground layers

Special

Control = The building with envelopes using traditional thermal properties

REFERENCES

- Al-Shargabi, A, A. Almhafdy, D. M. Ibrahim, M. Alghieth, F. Chiclana. 2022. *Buildings' energy consumption prediction models based on buildings' characteristics: Research trends, taxonomy, and performance measures*. Journal of Building Engineering. 54: 104-577.
- Burch, S.L., R.D. Olson, and A.P. Visocky. 1999. *Ground-water investigation for the University of Illinois: Champaign, Illinois*, Illinois State Water Survey, Contract Report 636, 47 p.
- Dwaikat, L.N., Ali, K.N. 2018. *Green buildings life cycle cost analysis and life cycle budget development: Practical applications*, Journal of Building Engineering. 18: 303-311.
- Erol, S and B. François. 2018. *Multilayer analytical model for vertical ground heat exchanger with groundwater flow*. Geothermics 71: 294-305.
- Filippini, M., Obrist, A. 2022. *Are households living in green certified buildings consuming less energy? Evidence from Switzerland*, Energy Policy. 161: 112-724.
- Google Earth 9.163.0.0 2022. *University of Illinois at Urbana-Champaign campus (40.112456 °N; 88.228289 °W)*. Online. Available through: ibit.ly/bcxW. Accessed May 29, 2022.
- International Energy Conservation Code. 2018. *IECC Compliance Guide for homes in Illinois*.
- International Passive House Association. 2022. *Passive House certification criteria*.
- See, R, P. Haves, P. Sreekanthan, J. O'Donnell, M. Basarkar, K. Settlemyre. 2011. *Development of a user interface for the energyplus whole building energy simulation program*, Proceedings of the 12th International IBPSA Conference, Sydney, Australia.
- Stumpf, A, Y. Lin, T. D. Stark. 2021. *Subsurface Characterization, Monitoring, and Modeling of a Geothermal Exchange Borefield for the Campus Instructional Facility at the University of Illinois at Urbana-Champaign*. Illinois State Geological Survey. Circular 606, 35p.
- Stylianou, I. I, S. Tassou, P. Christodoulides, L. Aresti, G. Florides. 2019. *Modeling of vertical ground heat exchangers in the presence of groundwater flow and underground temperature gradient*. Energy and Buildings. 192: 15–30.
- U.S. Green Building Council. 2022. *LEED rating system*.
- Zanchini, E, S. Lazzari, A. Priarone. 2012. *Long-term performance of large borehole heat exchanger fields with unbalanced seasonal loads and groundwater flow*. Energy 38: 66-77.
- Zhao Z. Y. Xu, Y. Lin, X. Wang, P. Wang, 2021. *Probabilistic modeling and reliability-based design optimization of a ground source heat pump system*. Applied Thermal Engineering. 197: 117-341.
- Zhao Z. Y. Lin, A. Stumpf, X. Wang, 2022. *Assessing impacts of groundwater on geothermal heat exchangers: A review of methodology and modeling*. Renewable Energy. 190: 121-147.

Transient heat transfer in ground heat exchangers under groundwater flow

Carlos Prieto

Massimo Cimmino

ABSTRACT

An analytical solution for the transient heat transfer under groundwater flow for ground heat exchangers (GHEs) is presented. The method is an extension of the transient multipole expansion that describes the transient heat transfer as a pure conduction phenomenon inside and around a GHE including arbitrarily positioned pipes in the grout, coupling an irrotational and incompressible potential field in the ground with constant far-field velocity. The method does not rely on the supposition that groundwater flows through the GHE but instead moves around it. The method is validated against a finite element analysis model comparing the borehole wall temperature for two cases considering different single U-tube pipes position. It is shown that the thermal resistances inside the GHE do not respect the general symmetry condition ($R_{ij} \neq R_{ji}$ and $R_{ii} \neq R_{jj}$) as opposed to the pure conduction problem.

INTRODUCTION

One of the main components of ground source heat pump (GSHP) systems are ground heat exchangers (GHEs) which allow heat transfer between the building and the ground. In many applications the heat transfer between the GHE and the ground can be treated as pure heat conduction due to diffusion in the ground. However, there are cases where the impact of groundwater flow on the heat transfer process is significant. When groundwater is present, the heat transfer process is given by three effects: conduction in the ground, conduction in the groundwater and advection by groundwater. Current analytical models consider that the fluid within the ground moves unidirectionally through the GHE and not around it. This allows the classical heat conduction models such as infinite/finite line sources (ILS/FLS) (Ingersoll et al., 1948; Eskilson, 1987) and cylindrical heat source (CHS) (Carslaw and Jaeger, 1947) to be extended to their analogs when groundwater is present resulting in the moving infinite/finite line sources (MILS/MFLS) (Diao et al., 2004; Molina-Giraldo et al., 2011) and moving cylindrical heat source (MCHS) (Al-Khoury et al., 2020). These models have been used to study the response between the ground and the periphery of the GHE due to the presence of groundwater, finding that when the groundwater velocity increases, the average borehole wall temperature decreases and thus the average temperature of the circulating fluid decreases (in cooling mode) (Sutton et al., 2003; Cai et al., 2020; Wagner et al., 2013). However, how diffusion-advection of groundwater flow moving around GHE affects the heat transfer between the circulating fluid in the pipes and the borehole wall due to grout diffusion has not been studied, as well as whether the position of the pipes plays an important role in the overall heat transfer.

This paper presents a new analytical solution for the heat transfer problem that relates the groundwater flowing around the GHE by extending the transient multipole expansion for pure conduction presented by Prieto and Cimmino (2021a) in which any number of pipes could be placed inside the GHE. The groundwater model is reduced from diffusion-

Carlos Prieto (carlos.prieto@polymtl.ca) is a Ph.D. candidate and Massimo Cimmino (massimo.cimmino@polymtl.ca) is a professor of mechanical engineering at Polytechnique Montréal.

advection to a diffusion-reaction model using a special change of variable and coefficient simplification for the reaction term. The average borehole wall temperature for two different pipe positions of a single U-tube is calculated and compared with a finite element analysis (FEA) model to validate the present solution. Thermal resistances are calculated to understand how the pipes position impacts the overall thermal response of the GHE.

MATHEMATICAL MODEL

Figure 1 shows a top view of a GHE containing two pipes ($\partial\Omega_i, \partial\Omega_j$) arbitrarily positioned (O_i, O_j) within the grout (Ω_1) and bounded by the borehole wall ($\partial\Omega_b$) with respect to the ground (Ω_2). The heat-carrier fluid inside the pipes has a constant temperature (T_{fi}) at each pipe i . The geometrical parameters of the GHE are the borehole wall radius (r_b) and the outer pipe radius (r_i) at each pipe i . The thermal properties of the grout and the ground are considered isotropic, constant, and homogeneous. k_b, k_s are the thermal conductivities of grout and ground, and α_b, α_s are the thermal diffusivities of the grout and ground, respectively. The ground has a constant porosity (ϵ) that allows groundwater to pass through with constant volumetric heat capacity $(\rho c_p)_f$ and thermal conductivity (k_f) through the whole ground domain. The ground is considered as a semi-infinite domain and extends to $r_e \rightarrow \infty$.

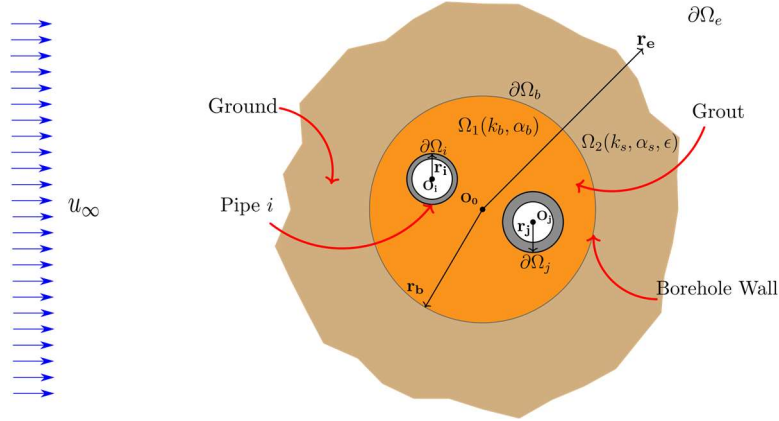


Figure 1 Domain geometry around a GHE

The transient multipole expansion of Prieto and Cimmino (2021a) is extended to describe the heat transfer phenomenon inside and outside the GHE considering groundwater flow. The original transient multipole expansion describes the heat conduction inside the periphery of the GHE for pipes arbitrarily positioned in the grout. As opposed to several existing models in the literature, the groundwater flow does not pass over the GHE but flows around it. It is assumed that the flow is incompressible and irrotational with constant far-field velocity (u_∞), resulting in a potential field.

Diffusion-advection model

The partial differential equation known as the advection-diffusion equation is used to describe the phenomenon of heat transfer in and out of the GHE for polar coordinates (ρ, ϕ) and time (t) :

$$\frac{\partial T_i}{\partial t} + \frac{(\rho c_p)_f}{(\rho c_p)_i} H(\rho - r_b) \vec{u} \cdot \nabla T_i = \alpha_i \nabla^2 T_i \quad (1)$$

where $H(\rho - r_b)$ is the Heaviside function which is defined as 0 if $\rho < r_b$ and 1 otherwise, T_i is the temperature field for domain Ω_i , $\alpha_i (= k_i / (\rho c_p)_i)$ is the thermal diffusivity for each Ω_i ($\alpha_b = \alpha_1$ and $\alpha_{s,eff} = \alpha_2$). The ground has an

effective thermal conductivity and capacity given by volume average properties defined as $k_{s,eff} = k_f \epsilon + (1 - \epsilon)k_s$ and $(\rho c_p)_{s,eff} = (\rho c_p)_f \epsilon + (1 - \epsilon)(\rho c_p)_s$, respectively. The velocity vector field, \vec{u} , is derived considering the continuity equation in the ground for a fluid moving with a density ρ_f :

$$\frac{\partial \rho}{\partial t} + \nabla \cdot (\rho_f \vec{u}) = 0 \quad (2)$$

For an incompressible and irrotational flow, Equation 2 is then a potential field $\nabla^2 \psi = 0$ which means $\vec{u} = \nabla \psi$. For a non-slip boundary condition at $\partial \Omega_b$ ($\vec{n}|_{r_b} \cdot \vec{u} = 0$), the velocity field with constant far-field velocity is then:

$$\vec{u} = u_\infty \left(1 - \frac{r_b^2}{\rho^2}\right) \cos \phi \hat{e}_\rho - u_\infty \left(1 + \frac{r_b^2}{\rho^2}\right) \sin \phi \hat{e}_\phi = u_\rho \hat{e}_\rho + u_\phi \hat{e}_\phi \quad (3)$$

where \hat{e}_ρ and \hat{e}_ϕ are unitary vectors in the radial and tangential directions, respectively. The potential field is then $\psi = u_\infty \left(1 + \frac{r_b^2}{\rho^2}\right) \rho \cos \phi$.

The boundary and initial conditions of the advection-diffusion equation (Equation 1) are given by:

$$-\beta_k r_k \frac{\partial T_1}{\partial \rho} \Big|_{r_k} + T_1|_{r_k} = T_{fk} \text{ on } \partial \Omega_k \quad (4.1)$$

$$T_1|_{r_b} = T_2|_{r_b} \text{ on } \partial \Omega_b \quad (4.2)$$

$$-k_b \frac{\partial T_1}{\partial \rho} \Big|_{r_b} = -k_{s,eff} \frac{\partial T_2}{\partial \rho} \Big|_{r_b} + [(\rho c_p)_f u_r T_2]|_{r_b} \text{ on } \partial \Omega_b \quad (4.3)$$

$$T_2|_{r_e \rightarrow \infty} = T^0 \text{ on } \partial \Omega_e \quad (4.4)$$

$$T_i(\rho, \phi, 0) = T^0 \text{ in } \Omega_1 \cup \Omega_2 \quad (4.5)$$

Equation 4.1 corresponds to a Robin boundary condition for each pipe k with constant fluid temperature T_{fk} , where $\beta_k = 2\pi k_b R_k$ is the dimensionless fluid-to-outer wall pipe thermal resistance and R_k the fluid-to-outer wall pipe thermal resistance. Equations 4.2 and 4.3 describe the continuity conditions for temperature and heat flux, respectively. Here, it is important to mention that Equation 4.3 is different from the ones encountered in the literature since the dissipation term, $[(\rho c_p)_f u_r T_2]|_{r_b}$, is included. In this case, this term is equal to zero since the radial velocity at the borehole wall is 0 due to non-slip condition. Equations 4.4 and 4.5 are the far-field temperature and initial temperature, which are both equal to the undisturbed ground temperature T^0 .

Groundwater transient multipole expansion

The resolution of the problem defined by Equations 1 and 4 is based on the methodology proposed in Prieto and Cimmino (2021a), which separates the heat transfer model as the sum of two subproblems, in this case: a) transient advection-diffusion equation with homogeneous boundary conditions ($T_{i,h}$), and b) steady-state advection-diffusion equation with non-homogenous boundary conditions ($T_{i,ss}$). The following change of variable is introduced to relate the potential field ψ with the temperature field:

$$T_{i,h} = \Gamma_{i,h} e^{\frac{1}{2\alpha_{s,eff}} \left(\frac{(\rho c_p)_f}{(\rho c_p)_{s,eff}} \right) H(\rho - r_b) \psi} = \Gamma_{i,h} e^{f(\rho, \phi)} \quad (5.1)$$

$$T_{i,ss} - T^0 = \Gamma_{i,ss} e^{\frac{1}{2\alpha_{s,eff}} \left(\frac{(\rho c_p)_f}{(\rho c_p)_{s,eff}} \right) H(\rho - r_b) \psi} = \Gamma_{i,ss} e^{f(\rho, \phi)} \quad (5.2)$$

The mathematical model for $T_{i,h}$ is reduced to a diffusion-reaction model and defined as:

$$\frac{\partial \Gamma_{i,h}}{\partial t} + H(\rho - r_b) \left(\frac{(\rho c_p)_f}{(\rho c_p)_{s,eff}} \right)^2 \left(\frac{u_\rho^2 + u_\phi^2}{4\alpha_i} \right) \Gamma_{i,h} = \alpha_i \nabla^2 \Gamma_{i,h} \quad (6.1)$$

$$-\beta_k r_k \frac{\partial \Gamma_{1,h}}{\partial \rho} \Big|_{r_k} + \Gamma_{1,h} |_{r_k} = 0 \quad \text{on } \partial \Omega_k \quad (6.2)$$

$$\Gamma_{1,h} |_{r_b} = \Gamma_{2,h} |_{r_b} e^{f(r_b, \theta)} \quad \text{on } \partial \Omega_b \quad (6.3)$$

$$-k_b \frac{\partial \Gamma_{1,h}}{\partial \rho} \Big|_{r_b} = -k_{s,eff} \frac{\partial \Gamma_{2,h}}{\partial \rho} \Big|_{r_b} e^{f(r_b, \theta)} \quad \text{on } \partial \Omega_b \quad (6.4)$$

$$\Gamma_{2,h} |_{r_e \rightarrow \infty} = 0 \quad \text{on } \partial \Omega_e \quad (6.5)$$

$$\Gamma_{i,h}(\rho, \phi, 0) = (T^0 - T_{i,ss}) / e^{f(\rho, \phi)} \quad \text{in } \Omega_1 \cup \Omega_2 \quad (6.6)$$

For $T_{i,ss}$, the problem is described as:

$$H(\rho - r_b) \left(\frac{(\rho c_p)_f}{(\rho c_p)_{s,eff}} \right)^2 \left(\frac{u_\rho^2 + u_\phi^2}{4\alpha_i} \right) \Gamma_{i,ss} = \alpha_i \nabla^2 \Gamma_{i,ss} \quad (7.1)$$

$$-\beta_k r_k \frac{\partial \Gamma_{1,ss}}{\partial \rho} \Big|_{r_k} + \Gamma_{1,ss} |_{r_k} = T_{fk} - T^0 \quad \text{on } \partial \Omega_k \quad (7.2)$$

$$\Gamma_{1,ss} |_{r_b} = \Gamma_{2,ss} |_{r_b} e^{f(r_b, \phi)} \quad \text{on } \partial \Omega_b \quad (7.3)$$

$$-k_b \frac{\partial \Gamma_{1,ss}}{\partial \rho} \Big|_{r_b} = -k_{s,eff} \frac{\partial \Gamma_{2,ss}}{\partial \rho} \Big|_{r_b} e^{f(r_b, \phi)} \quad \text{on } \partial \Omega_b \quad (7.4)$$

$$\Gamma_{2,ss} |_{r_e \rightarrow \infty} = 0 \quad \text{on } \partial \Omega_e \quad (7.5)$$

An approximation of the reaction coefficient $u_\rho^2 + u_\phi^2 = u_\infty^2 \left(1 - \frac{2r_b^2}{\rho^2} \cos 2\phi + \frac{r_b^4}{\rho^4} \right) \approx K_{gw} u_\infty^2$ is proposed to simplify the model presented in Equations 6.1 and 7.1. This approximation is valid since $u_\rho^2 + u_\phi^2$ has a maximum value of $4u_\infty^2$ for $\rho = r_b, \phi = (2n + 1)\pi$ for $n \in \mathbb{Z}$ and a minimum value of 0 for $\rho = r_b, \phi = n\pi$. Moreover, when ρ is sufficiently large when compared with r_b , the value is u_∞^2 . It was found that $K_{gw} = 1.6$ produces a good approximation.

Equation 6.1 has a similar structure to those expressed in Prieto and Cimmino (2021a). Thus, assuming that $\Gamma_{i,h}$ is spatiotemporally separable as $\Gamma_{i,h} = X_i(\rho, \phi) \tau(t)$ results in a Sturm-Liouville problem with $\tau(t) = \exp\left(-(\lambda_i^j)^2 \alpha_i t\right)$ for unique j eigenvalues for each domain i denoted as λ_i^j . The continuity condition requires that $\alpha_1 (\lambda_1^j)^2 = \alpha_2 (\lambda_2^j)^2$ must hold for all time t . Therefore, the problem $X_i(\rho, \phi)$, defined as the Helmholtz equation for the interior of the GHE (i.e. X_1), has the same formulation as that of the transient multipole expansion for a point \mathbf{x} with coordinates related to a particular pipe center \mathcal{O}_k given by $\mathbf{x}_k = (\rho_k, \phi_k)$ and for the GHE center $\mathbf{x}_0 = (\rho_0, \phi_0)$:

$$X_1(\mathbf{x}; \lambda_1^j) = \sum_{l=-M}^M \gamma_l^0 J_l(\lambda_1^j \rho_0) e^{il\phi_0} + \sum_{k=1}^N \sum_{l=-M}^M \gamma_{l,j}^k H_l^{(1)}(\lambda_1^j \rho_k) e^{il\phi_k} \quad (8)$$

For the ground domain, the expansion for X_2 is slightly different:

$$X_2(\mathbf{x}; \lambda_2^j) = \sum_{l=-M}^M \delta_l^0 H_l^{(1)}(\sigma_j \rho_0) e^{il\phi_0} \quad (9)$$

where $\sigma_j^2 = (\lambda_2^j)^2 - u_\infty^2 \left(\frac{K_{gw}}{4\alpha_2^2} \right) \left(\frac{(\rho c_p)_f}{(\rho c_p)_{s,eff}} \right)^2$, and J and $H^{(1)}$ are the first kind Bessel and Hankel functions,

respectively. The calculation of the eigenvalues is done by means of singular value decomposition (SVD), as done by Prieto and Cimmino (2021a). The coefficients $\gamma^0, \gamma^k, \delta^0$ are the coefficients that match the boundaries and calculated for each eigenvalue.

The full solution for $T_{i,h}$ is given by a Fourier-Bessel expansion:

$$T_{i,h}(x, t) = \sum_{j=1}^{\infty} C_j X_i(x; \lambda_i^j) e^{-(\lambda_i^j)^2 \alpha_1 t + f(\rho, \phi)} \quad (10)$$

where C_j are in this case:

$$C_j = \frac{\frac{k_b}{\alpha_b} \int_{\Omega_1} (T^0 - T_{2,ss}) \bar{X}_1 d\Omega_1 + \frac{k_{s,eff}}{\alpha_{s,eff}} \int_{\Omega_2} (T^0 - T_{2,ss}) \bar{X}_2 e^{2f(r_b, \phi) - f(\rho, \phi)} d\Omega_2}{\frac{k_b}{\alpha_b} \int_{\Omega_1} X_1 \bar{X}_1 d\Omega_1 + \frac{k_{s,eff}}{\alpha_{s,eff}} \int_{\Omega_2} X_2 \bar{X}_2 e^{2f(r_b, \phi)} d\Omega_2} \quad (11)$$

The coefficients expressed in Equation 11 are obtained by means of the quasi-orthogonal conditions of the Sturm-Liouville problem and using Green's second identity.

Similarly, for Equation 7.1, the same procedure is done. For the grout, the same multipole expansion presented in Prieto and Cimmino (2021a) is used:

$$\Gamma_{1,ss} = \alpha_0 + \sum_{m=1}^h \left[\alpha_m \left(\frac{\rho_0}{r_{max}} \right) \cos(m\phi_0) + \beta_m \left(\frac{\rho_0}{r_{max}} \right) \sin(m\phi_0) \right] + \sum_{k=1}^N \left\{ \gamma_0^k \ln \rho_k + \sum_{m=1}^h \left[\gamma_m^k \left(\frac{\rho_k}{r_{min}} \right) \cos(m\phi_k) + \delta_m^k \left(\frac{\rho_k}{r_{min}} \right) \sin(m\phi_k) \right] \right\} \quad (12)$$

For the ground, the multipole expansion is given by:

$$\Gamma_{2,ss} = \sum_{l=-h}^h \delta_l^0 K_l \left(u_{\infty} \left(\frac{\sqrt{Kgw}}{2\alpha_2} \right) \left(\frac{(\rho c_p)_f}{(\rho c_p)_{s,eff}} \right) \rho_0 \right) e^{il\phi_0} \quad (13)$$

where K is the modified Bessel function of the second kind of order l and $\alpha, \beta, \gamma, \delta$ are the coefficients that match the boundaries which are different from the homogenous problem.

RESULTS

The average borehole wall temperature (T_b) is evaluated using the present method and FEA for 4 different far field velocities: $u_{\infty} = 0, 10^{-6}, 10^{-5}, 10^{-4} \text{ m/s}$. Two cases are studied, with the same thermal properties and geometrical parameters shown in Table 1 but with different positioning of the pipes: (I) the pipes are positioned at $O_1(-0.05, 0)$, $O_2(0.05, 0)$, and (II) $O_1(0, 0.05)$, $O_2(0, -0.05)$. The FEA model for both cases is composed of 5504 nodes and 9906 triangular elements (second order Lagrange elements) with $r_e = 55 \text{ m}$. The parameters for the multipole expansion are set to $M = 14$ and $h = 30$, doubling those shown in Prieto and Cimmino (2021a) due to the exponential term in the continuity conditions (Equations 6.3-6.4 and 7.3-7.4), and the first 100 eigenvalues are used.

TABLE 1. GHE PARAMETERS

Parameter	Value	Parameter	Value
Grout thermal conductivity	$k_b = 0.81 \text{ W/(mK)}$	Borehole radius	$r_b = 0.075 \text{ m}$
Grout thermal diffusivity	$\alpha_b = 2.13 \times 10^{-7} \text{ m}^2/\text{s}$	U-tube pipe outer radius	$r_k = 0.021082 \text{ m}$
Ground thermal conductivity	$k_s = 2.4 \text{ W/(mK)}$	Dimensionless fluid-to-pipe thermal resistance	$\beta_k = 0.480281$
Ground thermal diffusivity	$\alpha_s = 1.2 \times 10^{-6} \text{ m}^2/\text{s}$	Undisturbed ground temperature	$T^0 = 10 \text{ }^\circ\text{C}$
Groundwater thermal conductivity	$k_f = 0.48 \text{ W/(mK)}$	Porosity	$\epsilon = 0.2$
Groundwater thermal capacity	$(\rho c_p)_f = 4.2 \times 10^6 \text{ J/(m}^3\text{K)}$	Shank spacing	$e = 0.1 \text{ m}$

Figure 2 shows the average borehole wall temperature calculated by the present method (dotted line) and the FEA

method (solid line) for cases I and II for a period of 60000 s with a time-step equal to 60s considering the four different far-field velocities with fluid temperatures equal to $T_{f1} = T_{f2} = 20$ °C for both cases. Figure 2 also shows temperature contours for the final simulation time with $u_\infty = 10^{-5}$ m/s. As expected, when the far-field velocity increases the average borehole wall temperature decreases and reaches the quasi-steady-state condition earlier. The maximum absolute differences between the proposed method and the FEA appear at approximately 180 h (10740 s) with values of 0.105, 0.115, 0.117, 0.061°C for case I and 0.090, 0.103, 0.106, 0.024°C for Case II, for each far-field velocity $u_\infty = 0, 10^{-6}, 10^{-5}, 10^{-4}$ m/s, respectively. At the final simulation time, the maximum difference between the proposed method and the FEA is 0.010°C for case I with $u_\infty = 10^{-6}$ m/s. The main reason for this discrepancy is the simplification in Equations 6.1 and 7.1 for the reaction coefficient. The relatively small errors show that the coefficient K_{gw} can be used to successfully simplify the problem without significant loss of accuracy. Figure 2 also shows that the borehole wall temperatures are different in cases I and II for the same far-field velocity when $u_\infty \geq 10^{-5}$ m/s. This implies that, under groundwater flow, the orientation of the U-tube influences the internal thermal resistances.

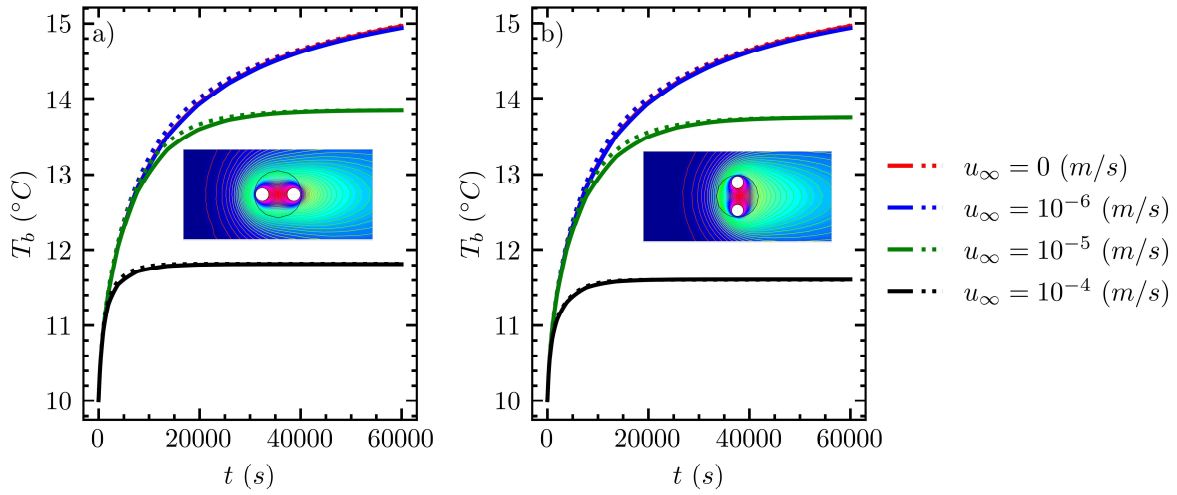


Figure 2 Average borehole wall temperature comparison between FEA (continuous line) and present method (discontinuous line) for 4 different far-field velocities: a) Case I and b) Case II

The internal thermal resistances are defined by:

$$T_{f1} - T_b = R_{11}q_1 + R_{12}q_2 \quad (14.1)$$

$$T_{f2} - T_b = R_{21}q_1 + R_{22}q_2 \quad (14.2)$$

where $q_k = (T_{fk} - \overline{T_1|_{r_k}})/R_k$ is the heat flow at each pipe k , with $\overline{T_1|_{r_k}}$ the average outer-wall pipe temperature. Internal thermal resistances are generally symmetrical ($R_{11} = R_{22}$ and $R_{12} = R_{21}$) in the absence of groundwater flow when symmetrical positioned pipes are considered. To estimate the thermal resistances, two pairs of arbitrary constant fluid temperatures for both pipes are used to solve the system of equations defined by Equations 14. Figures 3 and 4 show the thermal resistances defined in Equation 14 for the two cases, with Figures 3a and 4a corresponding to $u_\infty = 0$ m/s. The internal thermal resistances are symmetrical for this velocity. The thermal resistances calculated with the multipole method developed by Claesson and Hellström (2011) for the quasi-steady-state condition (conduction problem) are $R_{11} = R_{22} = 0.291$ mK/W and $R_{12} = R_{21} = -0.029$ mK/W for both cases. Comparing these

resistances with the final simulation time shown in Figure 3a and Figure 4a, the thermal resistances are $R_{11} = R_{22} = 0.285 \text{ mK/W}$ and $R_{12} = R_{21} = -0.027 \text{ mK/W}$. As expected, thermal resistances are symmetrical and are in good agreement with the classical multipole method. There are small differences between the multipole method and the transient multipole expansion since the transient multipole has not reached steady state. When $t \rightarrow \infty$, the thermal resistances approach to those calculated by Claesson and Hellström (2011).

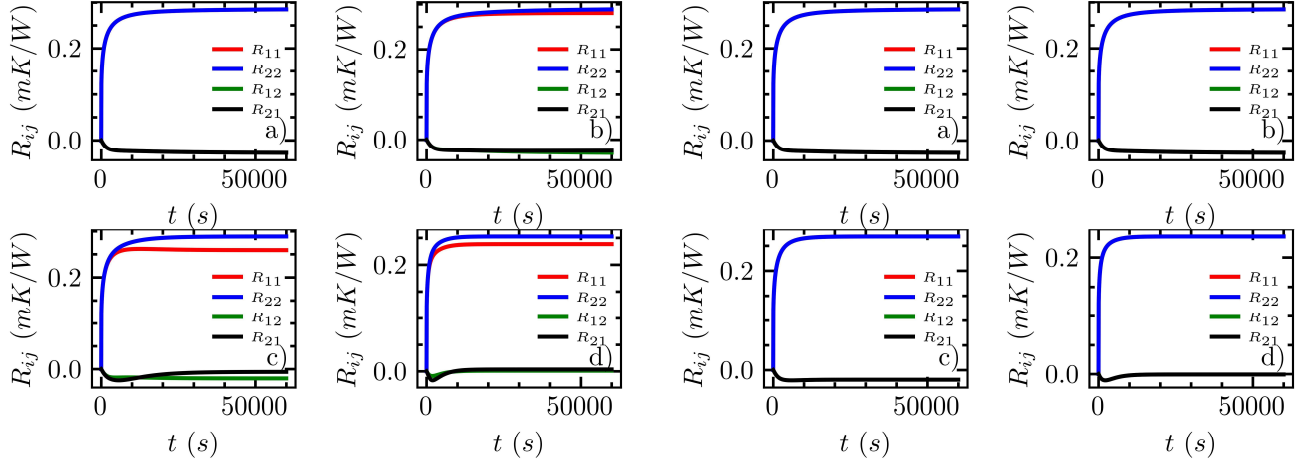


Figure 3 Internal thermal resistances for case I with different far-field velocities: a) $u_\infty = 0 \text{ m/s}$, b) $u_\infty = 10^{-6} \text{ m/s}$, c) $u_\infty = 10^{-5} \text{ m/s}$ and d) $u_\infty = 10^{-4} \text{ m/s}$

Figure 4 Internal thermal resistances for case II with different far-field velocities: a) $u_\infty = 0 \text{ m/s}$, b) $u_\infty = 10^{-6} \text{ m/s}$, c) $u_\infty = 10^{-5} \text{ m/s}$ and d) $u_\infty = 10^{-4} \text{ m/s}$

As shown on Figures 3b-d for case I, the thermal resistances decrease when the far-field velocity increases, and the symmetry tends to break down at higher far-field velocities. This is not the case on Figures 4b-d for case II where the symmetry holds at all far-field velocities. At the final time, the values of the thermal resistances are $R_{11} = 0.281, 0.259, 0.239, R_{22} = 0.289, 0.289, 0.253, R_{12} = -0.029, 0.020, 0.0, R_{21} = -0.024, -0.006, 0.003$ for case I, and $R_{11} = R_{22} = 0.285, 0.267, 0.234, R_{21} = R_{21} = -0.027, -0.02, -0.001$ for case II, respectively, for each far-field velocity $u_\infty = 10^{-6}, 10^{-5}, 10^{-4} \text{ m/s}$.

On Figures 3c-d and 4c-d, it is observed that the resistances R_{11} and R_{22} are not equal for case I, however they are equal for case II. This interesting result shows that even though the pipes are symmetrically distributed within the GHE, the symmetry condition does not hold in general. The fact that case II does present symmetry is because the far-field velocity is perpendicular to the spacing between the pipes. This allows using Green's identities to show that for this case the symmetry condition holds. It is also interesting to observe the behavior of resistances R_{12} and R_{21} for both cases I and II. Figures 3d and 4d show that these resistances tend to 0 as the velocity increases. In both cases, this behaviour on thermal resistances is explained in that the heat transfer is due to heat exchange between each pipe and the borehole wall rather than the pipes transferring heat to each other, therefore the groundwater is dissipating heat from the pipes.

CONCLUSION

A new analytical method for the study of conduction-advection heat transfer inside and around of a GHE was presented. The method allows including a potential field in the ground flowing around the GHE, in this case incompressible and irrotational. No simplification inside the GHE is made, allowing to place different pipe positions. Also, when posing

the complete mathematical model, a new boundary condition is considered in Equation 4.3 which takes into account the energy dissipation by means of the groundwater advection.

As a first validation, the method was compared with a high-fidelity FEA simulation, which showed that the present method possesses good agreement despite making an approximation in the reduction of the diffusion-reaction problem by introducing a K_{gw} coefficient. With this new analytical method, it was shown that the position of the pipes slightly changes the temperature around the GHE. The observation of the temperature around the borehole wall showed that the thermal resistances coming from the linear conduction problem inside the GHE are not symmetric ($R_{ii} \neq R_{jj}$ and $R_{ij} \neq R_{ji}$). It was found that when the groundwater velocity is sufficiently large, the heat transfer problem is one-dimensional, meaning that to calculate the heat flux of each pipe it is sufficient to know the temperature of each pipe and the average borehole temperature as $R_{ij} \rightarrow 0$ for $i \neq j$.

With these results, the use of methods such as thermal resistance capacitance (TRC) methods should be revisited when including groundwater flow, as the delta-circuit is not always valid. Extending the method from 2D to 3D including thermal interactions between boreholes and time-dependent fluid temperatures could be done using a segmented MFLS solution (Cimmino and Baliga, 2019) and a modified equivalent borehole method (Prieto and Cimmino, 2021b) with a coefficient updating scheme as done in Prieto and Cimmino (2021a, 2022).

ACKNOWLEDGMENTS

This study is funded by the Natural Sciences and Engineering Research Council of Canada (NSERC) [grant number: RGPIN-2018-04471].

REFERENCES

- Al-Khoury, R., N. Bnilam, M. Arzanfudi and S. Saeid. 2020. *A spectral model for a moving cylindrical heat source in a conductive-convective domain*. International Journal of Heat and Mass Transfer 163: 120517.
- Cai, S., X. Li, M. Zhang, J. Fallon, K. Li and T. Cui. 2020. *An analytical full-scale model to predict thermal response in boreholes with groundwater advection*. Applied Thermal Engineering 168: 114828
- Carslaw, H. S. and J. C. Jaeger. 1947. *Conduction of heat in solid*. Oxford: Clarendon Press.
- Cimmino, M. and B. R. Baliga. 2019. *A hybrid numerical-semi-analytical method for computer simulations of groundwater flow and heat transfer in geothermal borehole fields*. International Journal of Thermal Sciences 142: 366–378.
- Claesson, J. and G. Hellström. 2011. *Multipole method to calculate borehole thermal resistances in a borehole heat exchanger*. HVAC&R Research 17(6): 895-911.
- Diao, N., Q. Li and Z. Fang. 2004. *Heat transfer in ground heat exchangers with groundwater advection*. International Journal of Thermal Sciences 43 (12):1203-1211.
- Eskilson, P. 1987. *Thermal analysis of heat extraction boreholes*. Ph.D. Thesis. Lund university, Lund, Sweden.
- Ingersoll, L. R., O. J. Zobel and A. C. Ingersoll. 1948. *Heat conduction with engineering and geological applications*. Heat Conduction with Engineering and Geological Applications:278.
- Molina-Giraldo, N., P. Blum, K. Zhu, P. Bayer and Z. Fang. 2011. *A moving finite line source model to simulate borehole heat exchangers with groundwater advection*. International Journal of Thermal Sciences 50(12): 2506-2513
- Prieto, C. and M. Cimmino. 2021a. *Transient multipole expansion for heat transfer in ground heat exchangers*. Science and Technology for the Built Environment 27(3): 253-270
- Prieto, C. and M. Cimmino. 2021b. *Thermal interactions in large irregular fields of geothermal boreholes: the method of equivalent boreholes*. Journal of Building Performance Simulation 14(4): 446-460.
- Prieto, C. and M. Cimmino. 2022. *Semi-Analytical Method for 3D Transient Heat Transfer in Thermally Interacting Fields of Ground Heat Exchangers*. Thermo 2(3): 171-199.
- Sutton, M. G., D. W. Nutter and R. J. Couvillion. 2003. *A ground resistance for vertical bore heat exchangers with groundwater flow*. Journal of Energy Resources Technology 125(3): 183-189.
- Wagner, V., P. Blum, M. Kübert and P. Bayer. 2013. *Analytical approach to groundwater-influenced thermal response tests of grouted borehole heat exchangers*. Geothermics 46:22-31.



Dynamic simulation of ground source heat pump systems with non-stationary convolutions

Gabrielle Beaudry

Philippe Pasquier

ABSTRACT

Advective processes related to groundwater motion and flow rates have a significant impact on the thermal performance of ground source heat pump systems. Including these elements during the design phase, however, remains a challenging task, as few computationally efficient modeling tools allow for their adequate and accurate representation. The present work addresses this issue by presenting the experimental validation of non-stationary convolutions for predicting the thermal response of a ground heat exchanger to both transient heat loads and advection. First, the method is outlined along with a simple demonstration case emulating the time-variation of groundwater velocity. Then, it is validated against experimental data retrieved from a 35-day multi-flow rate thermal response test conducted on a real standing column well. The results show a mean absolute error of 0.28 °C between the experimental and simulated results, which represents good accuracy considering the complexity of the thermo-hydro-processes at work. The high computing efficiency of the proposed technique is also demonstrated and suggests its potential for future implementation in common-use design tools.

INTRODUCTION

Advective processes bear a significant impact on the thermal performance of ground source heat pump systems. Groundwater motion has notably been associated with a better thermal efficiency (Fan et al. 2007, Zanchini et al. 2012, Nguyen et al. 2017), reductions of the total borehole length and lower installation costs (Capozza et al. 2013, Samson et al. 2018). Flow rate control has also shown to provide energy gains and operating costs savings in closed-loop and standing column well (SCW) systems (Zarella et al. 2018, Beaudry et al. 2022). However, these elements are seldom considered during the design phase, partly due to modeling challenges.

Currently, the analytical solution of the moving infinite line source (MILS) allows predicting the effect of constant and steady-state groundwater flow on the temperature increment induced by a line source of heat (Sutton et al. 2003, Diao et al. 2004, Pasquier and Lamarche 2022). Consideration of more complex processes, such as transient or groundwater source heat pumps operations, usually requires using advanced and computationally intensive numerical models. Such models can be simplified through the evaluation of a transfer function representing their normalized thermal behavior, following the well-known temporal superposition theory (Claesson and Dunand 1983, Spitler and Bernier 2016). A stationary convolution product then commonly allows rapidly assessing the response to transient and dynamic heat loads, on the condition that the hydraulic conditions remain constant. This technique was recently extended to the simulation of various dynamic advective processes in ground source heat pump operations (Beaudry et al. 2021). Namely, the authors were able to reproduce the results of various simulations emulating the time-variation of circulation flow rate and groundwater velocity in a closed-loop ground heat exchanger (GHE), and the time-variation of the

Gabrielle Beaudry (gabrielle.beaudry@polymtl.ca) is a research associate and Philippe Pasquier is a professor of geological engineering at Polytechnique Montréal.

pumping and discharge flow rates in a SCW, while reducing the computing time of several orders of magnitude compared with a reference numerical model.

The present work intends to illustrate the potential of the non-stationary convolution (NSC) technique. First, the theory behind the method is recapped along with a simple demonstration case emulating the time-variation of groundwater velocity. Then, it is for the first time validated against experimental data retrieved from a 35-day multi-flow rate thermal response test (MF-TRT) conducted on a real SCW.

NON-STATIONARY CONVOLUTIONS FOR EFFICIENT DYNAMIC SIMULATIONS

The present section summarizes an efficient simulation strategy aimed at predicting the thermal behavior of GHEs subject to dynamic heat loads as well as time-varying hydraulic conditions. The proposed strategy relies on non-stationary convolutions, a method developed in Beaudry et al. (2021) that is an extension of the well-known superposition principle to non-stationary cases. The following text details the theoretical development of the method along with a simple synthetic demonstration case and a numerical verification of the results.

Theoretical development

The temporal superposition is commonly used to evaluate the evolution of a GHE's temperature increment $\Delta T(t)$ in response to a dynamic heat load function. It is expressed as a convolution product in Eq. 1:

$$\Delta T(t) = (f * g)(t) = \sum_{j=1}^t f(t_j) \cdot g(t - t_{j-1}) \quad \text{with} \quad f(t_i) = q(t_i) - q(t_{i-1}) \quad (1)$$

where $f(t)$ is the incremental heat load function and $g(t)$ is the response model's transfer function. The latter represents the temperature response of a given simulation model to a normalized constant input heat load (e.g., $q(t)=1$ W/m). Eq. 1 is valid for stationary conditions, which means that all hydraulic conditions, such as groundwater velocities and circulation flow rates, must remain constant.

It has been demonstrated in recent works that the time-variation of hydraulic conditions can be considered through non-stationary convolutions (Beaudry et al. 2021, 2022). First, this method implies that the problem be defined over a simulation period using m constant time steps $t_{i=1,2,\dots,m}$. It must also be divided into $s=1,2,\dots, n$ segments, each corresponding to one individual set of constant hydraulic states and represented by a different transfer function $g_{s=1,2,\dots,n}$. Note that the time indexes defining the transitions between segments are represented with $\mu_{s=1,2,\dots,n-1}$.

As a second step, the n stationary convolution products of each transfer function with the incremental heat load function $\Delta T_s(t) = (f * g_s)(t)$ are computed and combined so that the resulting function $\Delta T_{comb}(t)$ achieves the concatenation of each segment's results over their respective periods of application, such as:

$$\Delta T_{comb}(t_i) = (f * g_{s,i})(t) \quad (2)$$

where $g_{s,i}(t)$ is the transfer function relevant during segment s at time t_i . Note that this operation achieves a discontinuous transition from one convolution product to another at transition times t_{μ_s} . To represent the actual behavior of the signal following a change in hydraulic state, it is proposed to enforce a gradual transition through the evaluation and application of a scaled correction function $\lambda(t)$:

$$\lambda(t_i) = k_{s,i} \cdot \Delta T_{comb,\lambda}(t_i) \quad \text{with} \quad \Delta T_{comb,\lambda}(t_i) = (f_\lambda * g_{s,i})(t) \quad (3)$$

where $f_\lambda(t)$ is the correction incremental input function calculated from function $q(t)$ with $q(t \geq t_{\mu_s})=0$ and $k_{s,i}$ are scaling factors aimed at preserving the signal continuity over the transitions. These factors are defined for segment s at time t_i such as $k_{s,i}=0$ if $t_i < t_{\mu_s}$, or else $k_{s,i} = (\Delta T_{NSC}(t_{\mu_s}) - \Delta T_s(t_{\mu_s})) / \lambda(t_{\mu_s})$. Lastly, the resulting correction function can then be added to obtain the final solution $\Delta T_{NSC}(t)$:

$$\Delta T_{NSC}(t) = \Delta T_{comb}(t) + \lambda(t) \quad (4)$$

Step-by-step demonstration

This section aims at demonstrating one possible application of the proposed NSC method to a simple synthetic case. The demonstration case that was selected emulates heat injection in a single borehole that would be affected by transient aquifer flow. Note that this scenario would be likely to occur during a thermal response test on a GHE located near a pumping station.

Problem definition. First, the problem is defined over a period of 7 d with $m=10080$ constant time steps of 1 min. The problem is also divided into $n=2$ segments, with the groundwater velocity set at $v=1e-7$ m/s during segment $s=1$, and at $v=1.5e-6$ m/s during segment $s=2$, the latter starting at $t_{\mu_1=2880}=2$ d. The dynamic heat load function $q(t)$ as well as the groundwater velocity function $v(t)$ are illustrated in Fig. 1 a) and b).

Prior to solving this dynamic problem with the NSC, an essential step is the evaluation of the transfer functions representing the system's response to a constant heat load. In the present case, the analytical expression of the MILS recently proposed by Pasquier and Lamarche (2022) was used. More precisely, the transfer functions obtained with the MILS represent the mean temperature $\Delta\bar{T}(t)$ along the borehole wall when a constant heat impulsion of $q=1$ W/m is applied. Note that a constant groundwater velocity of $v=1e-7$ m/s was considered in the case of transfer function $g_1(t)$, and $v=1.5e-6$ m/s in the case of $g_2(t)$. Eq. 5 presents the MILS solution of Pasquier and Lamarche (2022). The parametric definition of the problem is detailed in Table 1 while the resulting transfer functions are shown in Fig. 1 c). Note that to simplify the demonstration, the equivalent borehole resistance is neglected.

$$\Delta\bar{T}(t) = \frac{qI_0(2\sqrt{b})}{4\pi k_g} \left(2K_0(2\sqrt{b}) - E_1(b\tau)I_0(2\sqrt{b}) - e^{-b\tau} \sum_{m=1}^{\infty} \sum_{n=0}^{\infty} \frac{b^n(m-1)!}{(-\tau)^m(m+n)!2} \right) \text{ with } b = \left(\frac{r_b v_D c_w}{4k_g} \right)^2 \text{ and } \tau = \frac{4\alpha t}{r_b^2} \quad (5)$$

Table 1. Parameters used for the evaluation of the transfer functions

Parameter	Symbol	Unit	$g_1(t)$	$g_2(t)$
Borehole radius	r_b	m	0.1	0.1
Water volumetric heat capacity	C_w	MJ/(m ³ K)	4.20	4.20
Ground thermal conductivity	k_g	W/(mK)	2.4	2.4
Darcy velocity	v_D	m/s	1e-7	1.5e-6
Specific heat load	q	W/m	1	1
Ground volumetric heat capacity	C_g	MJ/(m ³ K)	1.92	1.92

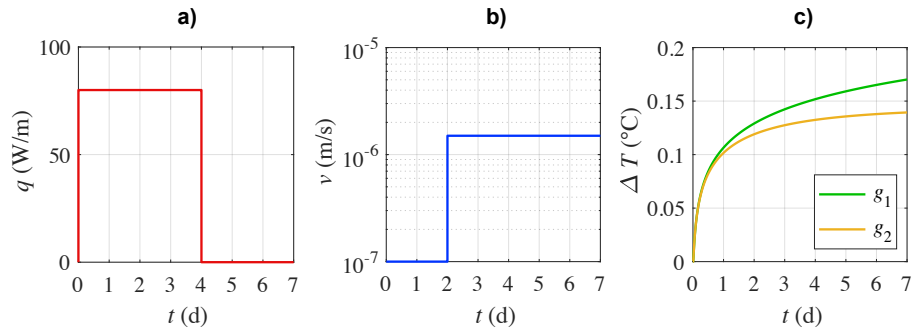


Figure 1 Definition of the demonstration case's problem representing heat injection in a single borehole with transient aquifer flow. a) heat load function, (b) groundwater velocity function, and c) corresponding transfer functions (see Table 1 for parametric description).

Solution. The steps of the NSC leading to the fast computation of the temperature response at the borehole wall following the dynamic conditions presented in Fig. 1 are illustrated in Fig. 2 below. The first step consists of a) computing the incremental heat load function $f(t)$. Then, b) the convolution products of this function with transfer functions $g_1(t)$ and $g_2(t)$, as well as their combination $\Delta T_{comb}(t)$, are evaluated. Note that the combination function achieves an abrupt transition between both convolution products at transition time $t_{2880}=2$ d.

To achieve a smooth transition between convolution products, the scaled correction function $\lambda(t)$ must be calculated and added to the combination results. This implies that c) the correction incremental input function $f_\lambda(t)$ is evaluated. Note that this can be done using Eq. 1, where all values following transition time $t_{2880}=2$ d in function $q(t)$ are replaced with zeros. Then, d) the convolution products of $f_\lambda(t)$ with both transfer functions $g_1(t)$ and $g_2(t)$, as well as their combination $\Delta T_{comb,\lambda}(t)$, are calculated. Finally, the scaling factors aiming at preserving the signal continuity are obtained, such as $k_{1,i}=0$ for $t_i < t_{2880}$ and $k_{2,i}=0.08$ for the following times, then allowing the evaluation of the correction function $\lambda(t)$.

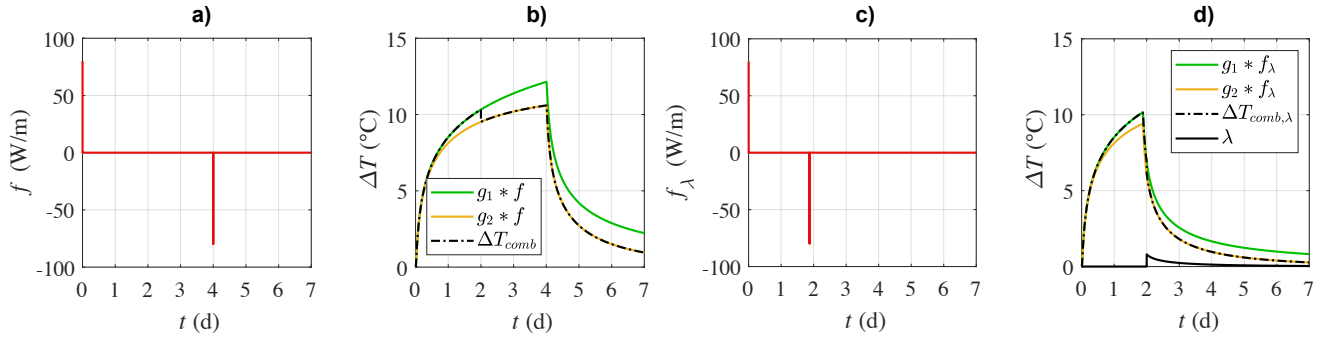


Figure 2 Step-by-step resolution of the NSC. a) incremental input function b) combination of convolution products, c) correction incremental input function, and d) combination and scaling of the correction function.

Results and numerical verification. The final solution $\Delta T_{NSC}(t)$ is presented in Fig. 3 along with convolution products $\Delta T_1(t)$ and $\Delta T_2(t)$, which represent alternative solutions that would have been obtained if the groundwater velocity stayed constant at $v(t)=1e-7$ m/s and $1.5e-6$ m/s, respectively. One can appreciate the difference between the NSC solution and the constant ones, a fact that illustrates the potential impact of groundwater flow on GHEs' operations.

Fig. 3 also displays the solution of the same problem obtained with a finite-element model developed in COMSOL Multiphysics (Comsol 2022). As one can see, both signals are well superposed, which allows verifying the accuracy of the proposed NSC technique to evaluate the solution to dynamic simulations involving the time-variation of groundwater velocity. The numerical model's meshing and final solution at $t=7$ d are shown in Fig. 3 for the benefit of the reader. Note that the NSC calculations were achieved in 0.028 s, compared to 38 min for the numerical simulation using the same 1-min time step.

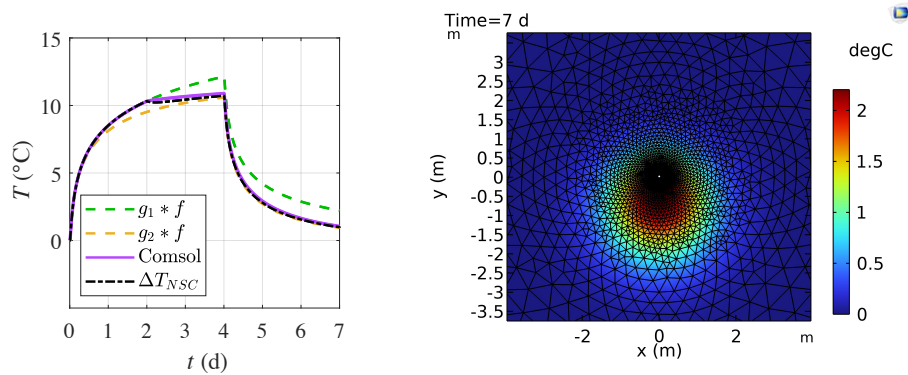


Figure 3 Numerical verification of the solution provided by the NSC for the synthetic test case emulating heat injection in a single borehole with transient aquifer flow. Comparison of the NSC and numerical final solutions (left), and close-up of the numerical model emulating a line-source of heat at $t = 7$ d (right).

EXPERIMENTAL VALIDATION

In the previous section, the NSC method was applied to a simple case emulating the temperature response of a GHE to time-varying heat loads and groundwater flow. It should be noted that the NSC allows considering various other dynamic advective heat transfer processes, namely fluid circulation flow rates in closed-loop systems, and pumping and discharge flow rates in SCWs (Beaudry et al. 2021).

To demonstrate the accuracy as well as the large application range of the NSC, the following section presents an experimental validation of this method that relies on data acquired during a MF-TRT performed on a real SCW in 2019.

Data acquisition

Description of the experimental setup. The experimental site is located near Montreal, Canada. A 215-m-deep SCW (\varnothing 165 mm) is connected to a mobile geothermal laboratory assembled in a 12.2-m marine container and equipped with, among other equipment, a 24-kW water heater and a comprehensive data control and acquisition system (see Fig. 4). See Beaudry et al. (2019), Nguyen et al. (2020), and Cerlet et al. (2020) for further details about this installation.

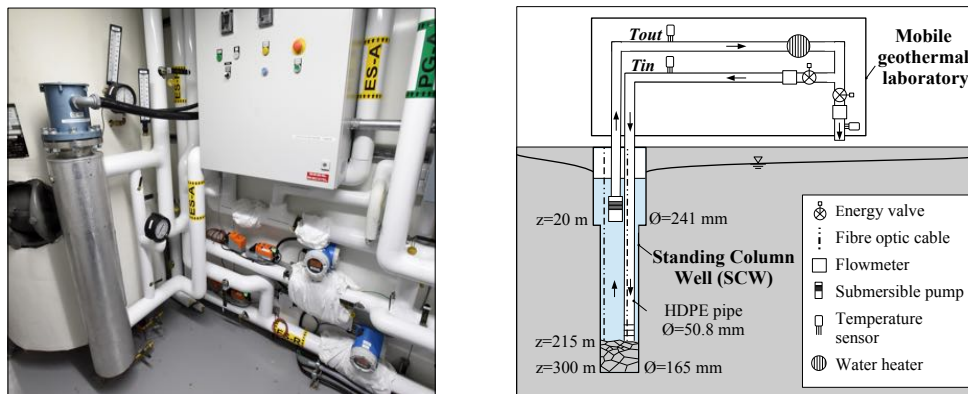


Figure 4 Simplified experimental apparatus used for the MF-TRT. Photo of the water heater and flowmeters inside the geothermal laboratory (left) and schematic view of the SCW and mechanical equipment (right).

Multi-flow rate thermal response test. Between June 3rd and July 9th, 2019, a 35-day MF-TRT was conducted on the experimental SCW to evaluate the influence of pumping and discharge flow rates on the thermal behavior of the system. Prior to the test, a temperature profile was measured in the SCW using a downhole temperature sensing system (see Fig. 5 a). Following a 2-day recirculation phase, four subsequent heating-restitution cycles were then achieved using the 24-kW water heater. The heat load (Q) imposed to the SCW was verified with the energy balance equation and is presented in Fig. 5 b). Note that the power consumption of the submersible pump (1.4 kW) and the high air temperature during the test (around 20 °C outside and 30 °C inside the laboratory) were considered as heat contamination sources. The pumping (\dot{V}) and discharge (\dot{B}) flow rates were also monitored during the test and are presented in Fig. 5 c) and d).

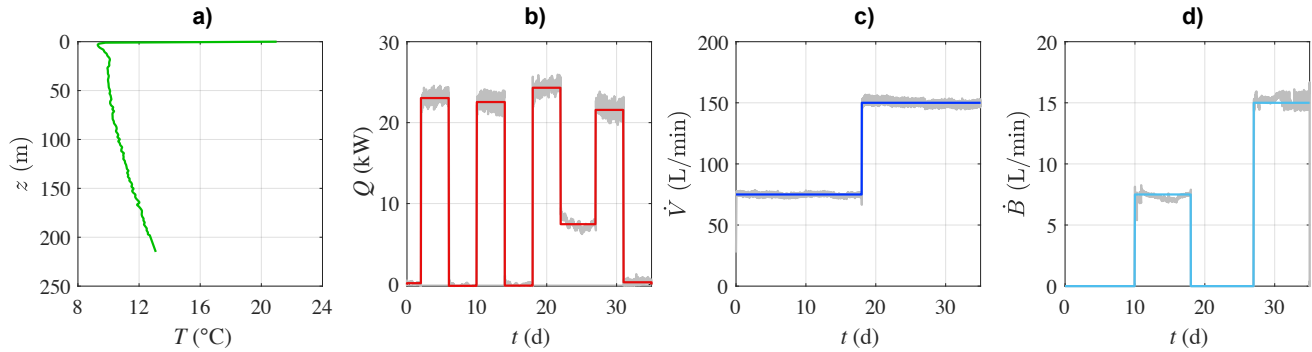


Figure 5 Experimental data acquired during the MF-TRT. a) temperature profile measured in the annular space of the SCW prior to the test, b) heating load applied to the groundwater loop, c) pumping flow rate, and d) discharge flow rate during the test. The minutely data is presented in grey, and the average step-value is colored.

Modeling particularities

The NSC method was used to predict the evolution of the temperature at the outlet of the well $T_{out}(t)$ in response to the heat load and flow rate functions shown in Fig. 5. The methodology is the same that was presented earlier, except for the nature of the response model used in the evaluation of the transfer functions, and for the consideration of the non-uniform temperature profile.

Numerical transfer functions. The thermal behavior of SCWs is highly influenced by the coupled processes of heat transfer and groundwater flow, both in the aquifer and inside the well. Thus, a high-precision finite-element model coupling heat transfer to Darcian groundwater flow was employed as a response model. Note that the model was built to emulate the experimental SCW system and was validated against experimental data in Beaudry et al. (2019). The numerical model was first used to evaluate the transfer functions g_s representing the normalized response of the SCW to a constant heat load of 1 kW (see Fig. 6), a method that was used and described in previous works (Pasquier and Marcotte 2014, Nguyen et al. 2017, Beaudry et al. 2021). To this end, the model was solved four times, that is one time for each different set of constant flow rates corresponding to the MF-TRT.

Non-uniform thermal boundary condition. The mean ground temperature along borehole depth T_0 is often added to the temperature increment calculated in the convolution process to obtain the final solution. To account for the combined effect of the non-uniform hydraulic conductivity and temperature profile, a second set of transfer functions h_s was rather evaluated in the present case (see Fig. 6), as proposed for stationary cases in Nguyen et al. (2017). The NSC was then performed using these transfer functions and a unitary input to obtain a time-varying function $T_0(t)$.

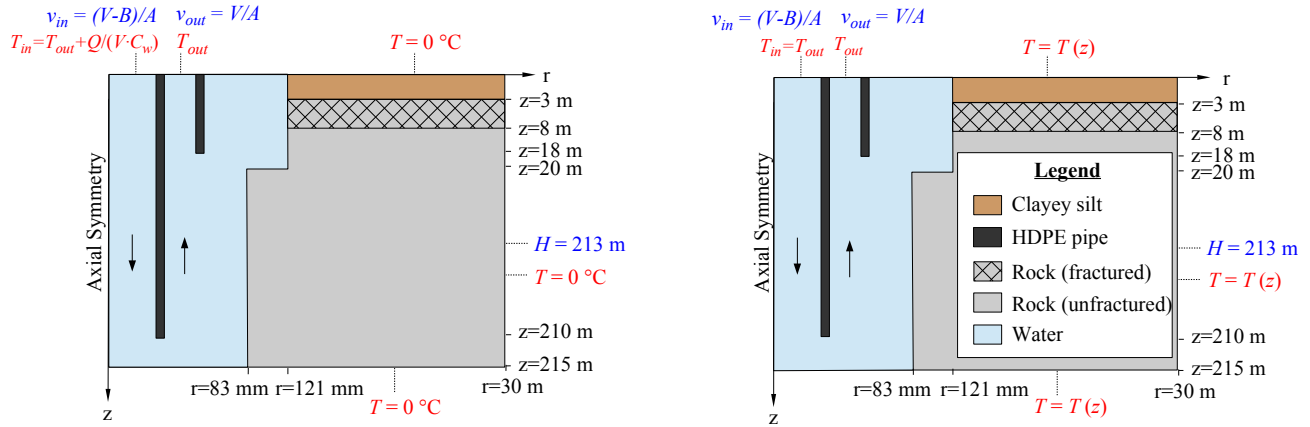


Figure 6 Geometry, hydraulic (blue) and thermal (red) boundary conditions of the numerical model coupling heat transfer to Darcian groundwater flow. Definition for the evaluation of transfer functions g_s with uniform thermal boundary conditions (left) and h_s with non-uniform thermal boundary conditions (right). Adapted from Beaudry et al. (2019).

Results

The results of the experimental validation are presented in Fig. 7. Fig. 7 a) first displays the temperature increment of the groundwater at the outlet of the well in response to the heating loads and operating flow rates that was calculated with the NSC. In Fig. 7 b), the response of the system to the non-uniform temperature profile and operating flow rates is shown. At last, Fig. 7 c) illustrates the superposition of the NSC final solution with the experimental results. Both signals display the same behavior, and a mean absolute error (MAE) of 0.28 °C is calculated, which demonstrates the accuracy of the NSC method for predicting the temperature response of a GHE to time-varying heat loads and operating flow rates. Note that Figure 7 c) also compares the outlet fluid temperature that would have been obtained using a stationary convolution with a constant circulation flow rate of $\dot{V}=75$ L/min, a constant discharge flow rate of $\dot{B}=0$ L/min and a uniform initial ground temperature of 11 °C. From Figure 7 c), it is clear that the NSC can not only accurately reproduce the experimental measurements but can also take into account the dynamic operation of the GHE, a feature that stationary convolution can visibly not integrate accurately over a long simulation period of 35 days.

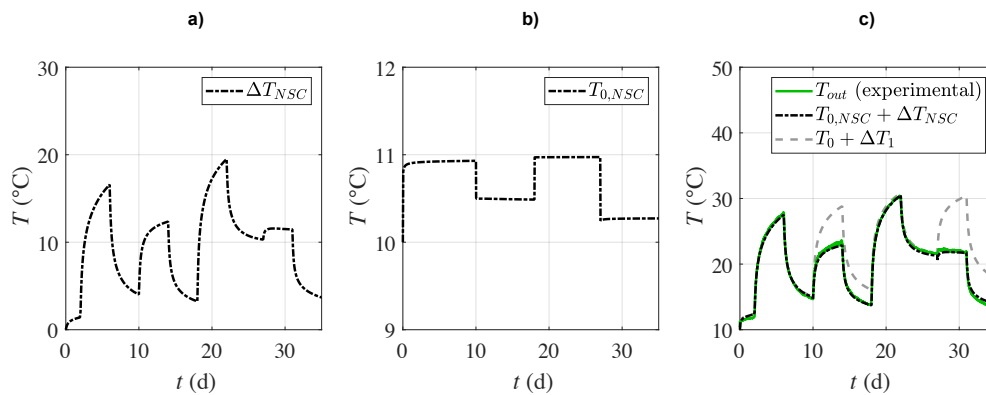


Figure 7 Experimental validation of the NSC against a multi-flow rate thermal response test. a) temperature increment at the borehole's outlet calculated with the NSC, b) temperature at the borehole's outlet considering the non-uniform temperature profile and c) superposition of the NSC with the experimental results (MAE=0.28 °C), and comparison with a stationary solution.

Finally, note that the whole convolution process took 9.5 s while the simulation time required to obtain the four transfer functions is around 80 min. By comparison, a fully dynamic numerical simulation with the finite-element method using the same 1-min time step lasted for approximately 26 h. For the moment, the main limitation to the use of NSC is the effort required to obtain numerically the various transfer functions. Additional works based on the use of artificial neural networks to obtain instantly the transfer function of closed-loop GHEs (Pasquier et al. 2018, Dusseault and Pasquier 2019) or of SCWs (Jacques and Pasquier 2022a, 2022b) are already undergoing and should ease this constraint.

CONCLUSIONS

Previous numerical verifications have shown the robustness and accuracy of non-stationary convolutions for dynamic simulation, including for transient circulation flow rates in closed-loop GHEs, and for transient circulation and discharge flow rates in SCWs. In this work, the potential of non-stationary convolutions has been illustrated with a simple analytical problem as well as with a real thermal response test lasting 35 days. The results show the ability of non-stationary convolutions to reproduce analytical and experimental temperature responses. The high computational efficiency of the proposed technique is also demonstrated and suggests its potential for future use in mainstream design tools.

ACKNOWLEDGMENTS

The authors acknowledge the support from partners of the Geothermal Research Chair on the Integration of SCWs in Institutional Buildings, namely Hydro-Québec, the Ministry of Higher Education of Québec, CSSMI, CSSDM, CSSS, Versa Profiles, Marmott Energy, CanmetEnergy and NSERC. This work was financed by the Natural Sciences and Engineering Research Council of Canada through grant number ALLRP 544477-19.

NOMENCLATURE

α	=	Thermal diffusivity (m ² /s)
A	=	Area (m ²)
\dot{B}	=	Discharge flow rate (m ³ /s)
C	=	Volumetric heat capacity (J/m ³ ·K)
κ	=	Thermal conductivity (W/m·K)
q	=	Specific heat load (W/m)
Q	=	Heat load (W)
r	=	Radial distance from the line source (m)
t	=	Time (s)
T	=	Temperature (°C)
\dot{V}	=	Pumping flow rate (m ³ /s)
v_D	=	Darcy velocity (m/s)

Subscripts

b	=	borehole
w	=	water
g	=	ground
o	=	initial

REFERENCES

- Beaudry, G., Pasquier, P., Marcotte, D., 2021. A fast convolution-based method to simulate time-varying flow rates in closed-loop and standing column well ground heat exchangers. *Renewable Energy* 174, 55–72.
- Beaudry, G., Pasquier, P., Marcotte, D., 2019. The impact of rock fracturing and pump intake location on the thermal recovery of a standing column well: model development, experimental validation, and numerical analysis. *Science and Technology for the Built Environment* 25, 1052–1068.
- Beaudry, G., Pasquier, P., Marcotte, D., Zarrella, A., 2022. Flow rate control in standing column wells: A flexible solution for reducing the energy use and peak power demand of the built environment. *Applied Energy* 313, 118774.
- Capozza, A., De Carli, M., Zarrella, A., 2013. Investigations on the influence of aquifers on the ground temperature in ground-source heat pump operation. *Applied Energy* 107, 350–363.
- Cercllet, L., Courcelles, B., Pasquier, P., 2020. Impact of standing column well operation on carbonate scaling. *Water* 12.
- Claesson, J., Dunand, A., 1983. Heat extraction from ground by horizontal pipes. Swedish Council of building Research, Swedish Council for Building Research. ed. Stockholm.
- Comsol Multiphysics, 2022. COMSOL, Version 5.5. Burlington, MA, USA.
- Diao, N., Li, Q., Fang, Z., 2004. Heat transfer in ground heat exchangers with groundwater advection. *International Journal of Thermal Sciences* 43, 1203–1211.
- Dusseault, B., Pasquier, P., 2019. Efficient g-function approximation with artificial neural networks for a varying number of boreholes on a regular or irregular layout. *Science and Technology for the Built Environment* 25, 1023–1035.
- Fan, R., Jiang, Y., Yao, Y., Shiming, D., Ma, Z., 2007. A study on the performance of a geothermal heat exchanger under coupled heat conduction and groundwater advection. *Energy* 32, 2199–2209.
- Jacques, L., Pasquier, P., 2022a. Interpretation of a thermal response test in a Bayesian framework to infer the hydraulic properties surrounding a standing column well. Presented at the EGU General Assembly 2022, Vienna, Austria.
- Jacques, L., Pasquier, P., 2022b. Uncertainty assessment of the hydraulic properties surrounding a standing column well with a thermal response test. IGSHPA Research Track 2022, Las Vegas., United States. Currently under review.
- Nguyen, A., Beaudry, G., Pasquier, P., 2020. Experimental assessment of a standing column well performance in cold climates. *Energy and Buildings* 226, 110391.
- Nguyen, A., Pasquier, P., Marcotte, D., 2017. Borehole thermal energy storage systems under the influence of groundwater flow and time-varying surface temperature. *Geothermics* 66, 110–118.
- Pasquier, P., Lamarche, L., 2022. Analytic expressions for the moving infinite line source model. *Geothermics* 103, 102413.
- Pasquier, P., Zarrella, A., Labib, R., 2018. Application of artificial neural networks to near-instant construction of short-term g-functions. *Applied Thermal Engineering* 143, 910–921.
- Pasquier, P., Marcotte, D., 2014. Joint use of quasi-3D response model and spectral method to simulate borehole heat exchanger. *Geothermics* 51, 281–299.
- Samson, M., 2018. Influence of groundwater flow on cost minimization of ground coupled heat pump systems. *Geothermics* 73, 100–110.
- Spitler, J.D., Bernier, M., 2016. Vertical borehole ground heat exchanger design methods, in: *Advances in Ground-Source Heat Pump Systems*. Elsevier, pp. 29–61.
- Sutton, M.G., Nutter, D.W., Couvillion, R.J., 2003. A ground resistance for vertical bore heat exchangers with groundwater flow. *Journal of Energy Resources Technology* 125, 183–189.
- Zanchini, E., 2012. Long-term performance of large borehole heat exchanger fields with unbalanced seasonal loads and groundwater flow. *Energy* 38, 66–77.
- Zarrella, A., Emmi, G., De Carli, M., 2017. A simulation-based analysis of variable flow pumping in ground source heat pump systems with different types of borehole heat exchangers: A case study. *Energy Conversion and Management* 131, 135–150.

A technical and economic evaluation of a ground source heat pump with thermal and battery energy storage systems for residential dwellings in Quebec

Saeed Kimiaei

Sina Kazemi-Ranjbar

Parham Eslami-Nejad

ABSTRACT

Ground source heat pump (GSHP) systems have been identified as promising solutions to help buildings achieve future carbon neutral targets. However, two main barriers decelerate the wide adoption of this technology in every location. One barrier is the high initial cost, which is sometimes justified by high local energy prices. The other potential barrier that always imposes a major bottleneck on a transition to electrification by using GSHP systems is the impact on the electrical grid at peak demand times. In this study, a solution has been proposed to address both issues by integrating thermal and battery energy storage systems into a conventional GSHP system. Numerical simulations are performed to evaluate the technical and economic feasibility of the proposed configuration. In addition, a comparative analysis is performed with other commonly recognized GSHP configurations with and without thermal energy storage. Results show that the new configuration requires a 22% shorter borehole by using the thermal energy storage, and reduces the annual peak electricity demand by almost 500kW cumulatively by using the battery energy storage. These benefits contribute to improving the net present value of the new configuration by 23% compared to the conventional GSHP configuration.

INTRODUCTION

The transition toward a sustainable society will be accelerated with greener and more energy-efficient technologies that emit lower amounts of greenhouse gas emissions (Shi et al. 2021). The heating and cooling energy use of buildings account for 22% of the total electricity produced (Schwartz et al. 2017). In this regard, ground-sourced heat pump systems (GSHP) offer an attractive solution in terms of energy efficiency and sustainability. But one of the major issues for their development is their high initial cost, which has resulted in a payback period of more than 14 years (Nguyen et al. 2016; Lu et al. 2017; Eslami Nejad et al. 2017). Because of this, in cold climate countries such as Canada, their most expensive components (boreholes and heat pumps) are usually designed undersized and topped up with a less efficient auxiliary heating system. The undersized system jeopardizes the superior energy efficiency of the GSHP systems. The addition of a less efficient auxiliary heating system, such as electric resistance heating in Quebec, Canada, not only increases the cost of the electricity bill for the user but also puts more pressure on the grid during peak hours. Therefore, several solutions have been proposed to further improve the efficiency of hybrid GSHP systems and address their high peak electricity demands.

To diminish the pressure on the grid, one possibility is the integration of thermal, electricity storage, or both systems into the GSHP system. By using thermal energy storage (TES), the excess heat produced during off-peak periods by the heat pump is stored in the storage medium and used during peak hours to meet the building's energy demand. Eslami Nejad et al. (2017) proposed a self-assisted GSHP system that is linked to a double U-tube borehole with two

Saeed Kimiaei is a researcher at Sharif University of Technology, Sina Kazemi-Ranjbar is a researcher at Sharif University of Technology, and Parham Eslami-Nejad (parham.eslaminejad@NRCan-RNCAN.gc.ca) is a research scientist at CanmetENERGY in Varennes.

independent circuits. In this system, the ground plays the role of TES so that the excess heat produced by the heat pump during off-peak hours is injected into the ground through one of the U-tubes inside the borehole. The proposed self-assisted system can decrease the peak power demand by 47%. However, the proposed system increases the total power consumption by 4.1%. Shi et al. (2021) combined an underground hybrid water and phase-change-material (PCM) storage system with a GSHP system and showed that the electricity consumption during peak hours is reduced by 40%. However, they reported a 4.5% increase in total electricity consumption. In general, coupling the TES system with the GSHP system reduces the systems' peak power consumption significantly, as high as much as 50%, although the total power consumption increases by up to 8% (Shi et al. 2021;Hirmiz et al. 2019;Eslami Nejad et al. 2017). Lv et al. (2016) performed a thermal and economic analysis of a GSHP system integrated with a TES system for a typical building in Tianjin through a TRNSYS simulation. It was shown that coupling the TES system with the GSHP system could save 35.2% and 18.3% of the operation costs during the heating and cooling seasons, respectively.

Few studies have been conducted on building electricity storage using batteries to reduce or eliminate the electricity consumption of GSHP systems during peak hours. Kamazani et al. (2022) recently performed a techno-economic analysis of a combined GSHP, PCM, and photovoltaic thermal collector (PVT) system. Using multi-objective optimization, they concluded that the combined system can achieve both economic and energy efficiency targets. The results demonstrated that the annual necessary energy use of the GSHP system can be reduced by 6.5% using integrated PVT and batteries.

In this study, to address the peak electricity demand and the initial cost issues of GSHP systems, a TES system is integrated with a GSHP system; furthermore, a relatively small battery energy storage (BES) system is used to reduce the peak electricity demand during time periods identified by the local utility (Hydro-Québec). It is to take economic advantage of the existing rebate program offered by Hydro-Québec for reducing electricity consumption during peak hours. All this is conceptualized through a new GSHP configuration in which TES and BES are both integrated with a GSHP system. Comprehensive thermal and economic analyses are performed to investigate the merits of the proposed system in comparison with other cases.

2. Systems descriptions and case studies

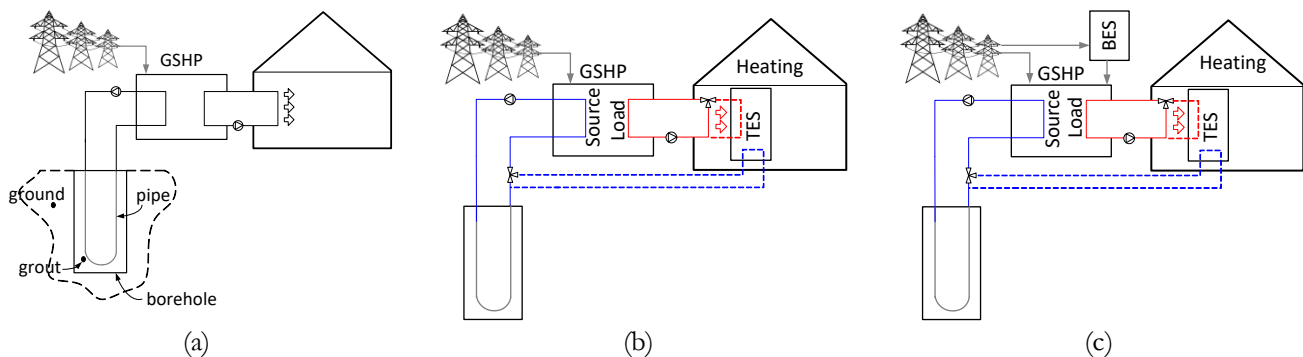


Figure 1. Schematic presentation of the system configurations used for (a) Case 1, (b) Case 2, and (c) Case 3

In this section, a new GSHP configuration integrated with thermal and battery storage systems along with two other conventional GSHP configurations and a reference case with baseboard electric heating is described in detail.

2.1 Case R

This case refers to a conventional system used for the heating and cooling of residential dwellings in the province of Quebec, Canada. In Case R, an air conditioning system and an electric resistance baseboard system are used to provide the cooling and heating loads of a building, respectively. This case is used as a reference case, and its results are compared against other cases considered in this project.

2.2 Case 1

The subject of this case is a simple GSHP system, in which the heat pump is connected to a single U-tube vertical borehole. The heat pump capacity and the borehole size are such that 100% of the building's heating and cooling loads are fulfilled, and, therefore, there is no need for auxiliary heating/cooling in this case (Figure 1a).

2.2 Case 2

This case concerns a self-assisted GSHP system linked to a single U-tube borehole (Figure 1b). For this case, during the heating season, a TES tank (water and phase change material) is charged during off-peak hours using the extra heat produced by the heat pump. During peak hours, the stored energy is used to increase the GSHP's entering fluid temperature (EFT). The storage temperature is 25°C, and the tank is charged when the temperature is below 25°C. The control strategy is optimized to avoid unnecessary heat pump power consumption for charging the storage tank. The tank is used when the EFT falls below -6°C to prevent the HP from turning off. The heat pump capacity is the same as in Case 1, and the borehole is sized to ensure that the EFT does not reach the cutoff temperature (-6°C).

2.3 Case 3

Case 3 refers to the proposed new configuration where both TES and BES systems are used to store thermal energy and electricity respectively, during off-peak hours (Figure 1c). The BES system is used to supply heat pump power during high peak electricity consumption events announced in advance by Hydro-Québec (Quebec's public utility). The conditions for charging and discharging the TES tank are the same as in Case 2. For charging the BES system, the power consumption of the GSHP should be less than the GSHP's peak power consumption (in this case, 4.90 kW). During cooling seasons, Case 1, Case 2, and Case 3 operate identically (Figure 1a). In Case 3, the heat pump capacity and the borehole size are both the same as that in Case 2. Similar to cases 1 and 2, the heat pump in Case 3 never stops due to going beyond the cutoff temperature.

3. Methodology

3.1 Single U-tube borehole

The numerical model used for the single U-tube borehole is based on the work of Pasquier et al. (2012) with slight modifications to account for axial heat conduction inside the borehole. This model is a 3-D transient model that uses the thermal resistance and capacitance approach to simulate heat transfer inside the borehole and the ground. In this model, the thermal capacities of the grout and fluid are also taken into account. For the ground model, the transient heat conduction equations are discretized by using the finite volume method. The resulted system of linear equations is solved by using the Gauss-Seidel method

3.2. Thermal and battery energy storage

For the thermal storage tank containing phase change material (PCM) and water, a stratified model is used similar to the one used by Hirmiz et al. (2018). The PCM is considered to be encapsulated in 2 cm thick horizontal rectangular slabs. In this model, the heat transfer inside the tank is assumed to be one-dimensional and the PCM is considered to

melt consistently in one direction. The parameters used for the simulation of the borehole and TES are all given in Table 1.

The BES system is modeled relatively simply without considering any efficiency or performance degradation. It is assumed that it takes one hour to charge the BES system (5kWh capacity) from 0% to 100%. Also, the battery size is selected to provide the entire required power of the heat pump during one hour.

Hourly simulations over a thirty-year period are performed for cases 1, 2, and 3; however, it is assumed that the results of Case R do not change over time, and therefore, in Case R, the hourly simulation results for the first year are applied to each year.

3.3 Building load

All the cases are used to provide heating and cooling loads of a 210 m² building . The building is a typical 1980's single-family detached home without ventilation located in Montréal, Canada (Kegel et al. 2012). An hourly load profile of this building is simulated using TRNSYS v.17 (Klein et al. 2010). The building's peak heating and cooling loads are 14.18 kW and 4.21 kW, respectively; furthermore, the building's annual space heating and cooling demands are 29,023 kWh and 1,510 kWh, respectively. Montréal's building load profile and ambient air temperature can be found in Eslami Nejad et al. (2017).

Table 1. Parameters used for case simulation

	Parameters	Value	Unit	Parameters	Value	Unit
Borehole	Diameter	15	cm	Shank	3.6	cm
	Material	Sand+Bentonite+Water		Thermal capacity	983	J/(kg.K)
Grout	Density	1984	kg/m ³	Thermal conductivity	1.4	W/(m.K)
	Material	HDPE		Conductivity	0.48	W/(m.K)
Pipe	Wall thickness	0.4	cm	Density	1350	kg/m ³
	Outer diameter	4.2	cm	Thermal capacity	900	J/(kg.K)
Ground	Thermal conductivity	2	W/(m.K)	Undisturbed temp.	10	°C
	Thermal diffusivity	0.075	m ² /day	Initial temp.	10	°C
Working fluid	Type	Water-Ethylene Glycol (38%)		Flow rate	0.44	kg/s
	Density	1045	kg/m ³	Specific heat	3720	J/(kg.K)
	Viscosity	1.254×10 ⁻²	Pa.s	Thermal conductivity	0.4	W/(m.K)
TES tank	Type	Water+PCM (Calcium Chloride Hexahydrate)		Latent heat capacity	195	kJ/kg
	Melting temperature	25	°C	Sensible heat capacity	2.2	kJ/(kg.K)
	Volume	0.355	m ³	Surface heat loss coefficient	0.9	W/(m ² .K)
	PCMDensity	1530	kg/m ³			

3.4 Heat Pump

For cases 1, 2, and 3, the same heat pump is used to provide the building's heating and cooling loads. The heat pump's COP and nominal heating capacity as a function of the EFT are demonstrated in figures 2a and 2b, respectively. The air conditioning system in Case R uses the same cooling COP and capacity curves as those shown in figures 2a and 2b to satisfy the building cooling load; however, the EFT is equivalent to the ambient air temperature in Case R. It is important to mention that to simulate the charging of the TES system and the heating of the building, the data from the 15.56°C and 43.33°C curves are used, respectively.

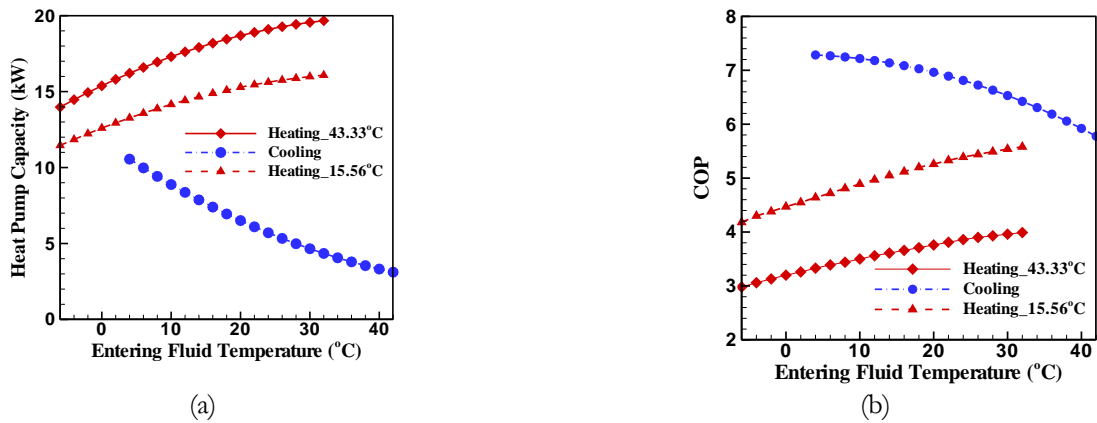


Figure 2. (a) Heat pump capacity and (b) COP curves

3.3 Cost analysis

The initial costs of the systems are presented in tables 2 and 3 for Case R and cases 1-3 respectively. GSHP costs include the heat pump, borehole installation, and piping costs. The data presented by Hakkaki-Fard et al. (2015) are used with a price increase factor to account for inflation during these years. The initial cost of the TES is calculated based on material costs listed in Hirschey et al., 2018. The BES initial cost is considered 600\$/kWh based on the average price of the existing battery manufacturer for houses.

Table 2. Total construction costs for Case R

	Mode	Type	Nominal Capacity (kW)	Cost (CAD)	Total Cost (CAD)
Case R	Cooling	Air conditioning system	5.42	1,390	3,030
	Heating	Baseboard	17	1,640	

Table 3. Total construction costs for cases 1, 2 and 3

	Heat pump Nominal Capacity at 20°C EFT (kW)	GSHP cost (CAD)	TES with PCM costs (CAD)	BES costs (CAD)	Total costs (CAD)
Case 1	19.36	22,120	0	0	22,120
Case 2	19.36	18,120	1,500	0	19,620
Case 3	19.36	18,120	1,500	3,000	22,620

The operating cost includes electricity consumption costs. Quebec’s electricity rates for residential dwellings, which are 6.319¢/kWh for the first 40 kWh/day and 9.749¢/kWh for the remaining energy consumed, are used. Also, the rebate program in Quebec for the reduction of electricity use in residential homes during peak demand times is accounted for in the cash flow calculation for Case 3. In the rebate program, for a maximum of 100 hours during winter, if customers reduce their power consumption during the peak demand times by more than 2 kW, they enjoy a rebate of 51.967¢/kW on their electricity bill. Furthermore, it is assumed that the systems in cases 1, 2, and 3 are being financed through a bank loan in exchange for a cash down payment, future payments of the remaining principal amount, and the annual interest. The annual payment (loan repayment) is calculated based on the equations presented by Nguyen et al. (2022) as follows:

$$M_y = IC \times (1-d) \times \frac{f}{1-(1+f)^{-s}} \quad (1)$$

where, IC , d , f , s , and y are initial cost, rate of cash down payment, fixed loan term, loan term and year number, respectively. The other economic parameters include C_y , NPC , and NPV , which are cash flow at year y , net present cost, and net present value, respectively, and are calculated as follows:

$$C_y = M_y + (O_y - R_y) \times (1+i)^y \quad (2)$$

$$NPC = IC \times d + \sum_{y=1}^{30} \frac{C_y}{(1+r)^y} \quad (3)$$

$$NPV = NPC_{Case R} - NPC_{Case j} \quad \text{where } j = 1, 2 \text{ or } 3 \quad (4)$$

In the above equations, O_y and R_y are the operating costs and the rebate at year number y , respectively; in addition, i and r are the inflation and discount rates, respectively. The amounts of the discount rate, inflation rate, fixed loan term, and rate of cash down payment are 7%, 3.4%, 3%, and 20%, respectively. Also, the amount of the loan term (s) is assumed to be 5 years.

RESULTS AND DISCUSSION

This section consists of two parts. In the first part, the results of the thermal performance evaluation of all the cases are presented using the total energy use (EU_{total}), the peak electric power consumption (peak demand), the overall system coefficient of performance (COP), and other related parameters such as the thermal energy added to the fluid entering the heat pump from the TES system (Q_{st}) as well as the heat loss from the TES system (Q_{loss}). In the second part, the results of the economic evaluation of all the cases are quantified using the net present value (NPV) and the discounted payback.

As shown in Table 4, the reference case consumes the highest amount of electricity, three times more than Case 1 on an annual basis. As mentioned before, the issue of Case 1 might be the costs associated with the borehole installation. Results showed that the required borehole length can be reduced significantly if a TES tank (water+PCM) is integrated into Case 1. The borehole length is calculated so that the GSHP system never reaches the cutoff temperature (-6°C) while operating during peak hours.

As shown in Table 4, the borehole length is reduced by 22% in Case 2 compared to Case 1 (from 182 m in Case 1 to 142 m in Case 2) by integrating a 355-liter tank. Case 2 consumes 4% more electricity than Case 1 due to the heat loss from the TES tank and the fact that the GSHP system with a shorter borehole works at lower temperatures in the heating mode. In Case 2, 527 kWh is stored annually in the TES system to increase the EFT to above -6°C when required. The average annual heat loss from the TES system is also reported, at 77 kWh. The peak electric power consumption is nearly the same in cases 1, 2, and 3 (4.82 kW in Case 1 and 4.9 kW in cases 2 and 3) and it is significantly reduced (more than 60%) compared to Case R. The system installed in Case 3 is the same as the one installed in Case 2 except for a relatively small BES system (5 kWh), which is added to take advantage of Quebec's rebate program for reducing the electricity consumption at peak times. The BES system is used to supply the electricity to the GSHP system during 100 events (100 hours) announced in advance by Hydro-Québec. As presented in Table 4, using the BES system does not have any effect on the system's energy performance, and, therefore, the results for Case 3 are the same as those reported for Case 2.

Table 4. Results of 30-year simulations (annual average values)

	Borehole Length (m)	Thermal Storage Tank Volume (m ³)	Battery Capacity (kWh)	EU _{total} (kWh)	Peak Demand (kW)	COP	Q _{ST} (kWh)	Q _{loss} (kWh)
Case R	NA	0	0	29233	14.18	1.04	NA	NA
Case 1	182	0	0	9299	4.82	3.28	NA	NA
Case 2	142	0.355	0	9725	4.90	3.14	527	77
Case 3	142	0.355	5	9725	4.90	3.14	527	77

In the second part, the results of the economic analysis are discussed. As mentioned in the cost analysis section, for cases 1, 2, and 3, 20% of the construction costs are paid upfront (initial costs) and the rest is paid in equal yearly payments over 5 years (loan term equals 5 years). As shown in Table 5, Case R has the highest net present cost (NPC), which is \$46,227. It is worth mentioning that 93% of the NPC of Case R is its electricity costs (\$43,197). The net present value (NPV) of the other cases is calculated based on Case R (Equation 4). As shown in Table 5, Case 3 has the highest NPV (\$18,733). Quebec's rebate program for the reduction of consumption at peak times contributes to this case's NPV increase of \$4,493 over 30 years. It is worth mentioning that Case 2 can reduce the peak of Case R significantly; however, it cannot reduce the peak power demand of Case 1 since it has a shorter borehole. In order to use the rebate, peak reduction is calculated and compared against similar systems, Case 1, 2, and 3. Although the electricity consumption of Case R is 300% greater than that of cases 3 and 2, its electricity cost is 383% greater. This is due to Hydro-Québec's different electricity rates for under and over 40kWh daily consumption. Cases 1, 2, and 3 rarely consume more than 40kWh of electricity per day. Among cases 1, 2, and 3, Case 1 has the lowest NPV due to the higher borehole construction costs. However, this case has the lowest electricity cost, which is four times less than the electricity cost of the reference case (Case R) but only 4% less than the electricity costs of cases 2 and 3. Using Case 3 instead of Case 1 improves the NPV by 23% over 30 years.

Table 5. Results of the economic analysis

	Initial Costs (CAD)	Loan Repayment (CAD)	Electricity Costs (CAD)	Rebates (CAD)	NPC (CAD)	NPV (CAD)	Discounted Payback (Years)
Case R	3,030	0	43,197	0	46,227	0	----
Case 1	4,424	15,843	10,786	0	31,053	15,174	12.1
Case 2	3,924	14,053	11,262	0	29,238	16,989	10.4
Case 3	4,524	16,201	11,262	4,493	27,494	18,733	10.9

For Case 1, the discounted payback is calculated slightly over 12 years based on the costs of the reference case; however, it is calculated at 10.4 and 10.9 years for Case 2 and Case 3 respectively. Although the increase in the NPV is noticeable if Case 3 is used, the discounted payback might not encourage the building owners to invest in the technology. It is worth mentioning that the loan term (5 years) has a significant impact on the discounted payback of cases 1, 2, and 3. For instance, the loan term of 20 years with an upfront payment of 20% of the system costs, potentially drops the discounted payback of both cases 2 and 3 below 2 years which will be very attractive for building owners. This means that if the borehole installations are at least considered as part of the building infrastructure, the long-term loan can be used to significantly reduce the technology's discounted payback. In terms of the discounted payback, Case 2 shows a slightly earlier return of investment compared to Case 3; however, Case 3 presents the highest NPV among all cases considered in this study.

CONCLUSION

In this paper, a new GSHP configuration integrated with both thermal and battery energy storage systems is investigated to quantify its economic and thermal performance. This configuration is compared against conventional GSHP configurations and the commonly used electric resistance baseboard and air conditioning system in Quebec, Canada. It is shown that using the rebate program for reducing electricity consumption at specific peak times, the new configuration integrated with TES and BES systems presents the highest NPV over a 30-year operation period. Furthermore, the annual electricity consumption and the peak power consumption of all the GSHP cases (cases 1-3) are significantly reduced, by more than 60%. Due to the different electricity rates for different daily electricity consumption levels, the electricity price can be reduced by as much as 75% compared to the base case with electric resistance baseboard heaters.

Future works on this topic would include accounting for depreciation costs of system components such as the heat pump, the battery, the air conditioning system, and the baseboard electric heater. Furthermore, the model of the battery can be improved to account for the performance and capacity degradation over years. Parametric analysis of the effect of electricity costs, borehole installation costs, and battery costs on the NPV of the cases would also be beneficial for making the right choices.

ACKNOWLEDGMENTS

The authors would like to acknowledge the funding received by the Office of Energy Research and Development (OERD) of Canada through the Energy Innovation Program (EIP) to undertake this research.

NOMENCLATURE

C_y	= Cash flow
d	= Rate of cash down payment
f	= Fixed loan term
i	= Inflation rate
IC	= Initial cost
M_y	= Loan repayment
NPC	= Net present cost
NPV	= Net present value
O_y	= Operating cost
r	= Discount rate
R_y	= Rebate cost
s	= <i>Loan term</i>

Acronyms

BES	= Battery energy storage
EFT	= Entering fluid temperature
GSHP	= Ground source heat pump
PCM	= Phase change material
TES	= Thermal energy storage

REFERENCES

- Eslami Nejad, P., et al. (2017). "Heat pump capacity effects on peak electricity consumption and total length of self-and solar-assisted shallow ground heat exchanger networks." Proceedings of the IGSHPA Technical/Research Conference and Expo.
- Hakkaki-Fard, A., et al. (2015). "A techno-economic comparison of a direct expansion ground-source and an air-source heat pump system in Canadian cold climates." *Energy* **87**: 49-59.
- Hirmiz, R., et al. (2018). "Performance enhancement of solar absorption cooling systems using thermal energy storage with phase change materials." *Applied Energy* **223**: 11-29.
- Hirmiz, R., et al. (2019). "Performance of heat pump integrated phase change material thermal storage for electric load shifting in building demand side management." *Energy and Buildings* **190**: 103-118.
- Kamazani, M. A. and C. Aghanajafi (2022). "Multi-objective optimization and exergoeconomic evaluation of a hybrid geothermal-PVT system integrated with PCM." *Energy* **240**: 122806.
- Kegel, M., et al. (2012). "Life cycle cost comparison and optimisation of different heat pump systems in the Canadian climate." *Proceedings of eSim*: 492-505.
- Lu, Q., et al. (2017). "Economic analysis of vertical ground source heat pump systems in Melbourne." *Energy* **125**: 107-117.
- Lv, J., et al. (2016). "Running and economy performance analysis of ground source heat pump with thermal energy storage devices." *Energy and Buildings* **127**: 1108-1116.
- Nguyen, A., et al. (2022). "A method for fast economic optimization of large hybrid ground source heat pump systems." *Geothermics* **104**: 102473.
- Nguyen, H. V., et al. (2016). "A techno-economic analysis of heat-pump entering fluid temperatures, and CO2 emissions for hybrid ground-source heat pump systems." *Geothermics* **61**: 24-34.
- Pasquier, P. and D. Marcotte (2012). "Short-term simulation of ground heat exchanger with an improved TRCM." *Renewable Energy* **46**: 92-99.
- Schwartz, L., et al. (2017). "Electricity end uses, energy efficiency, and distributed energy resources baseline." Report by Lawrence Berkeley National Laboratory, LBNL-1006983. <https://cmp.lbl.gov/publications/electricity-end-uses-energy>
- Shi, L., et al. (2020). "A novel geothermal heat pump system integrated with underground thermal storage for shifting building electric demands." 13th IEA Heat Pump Conference, May 11-14, 2020 Jeju, Korea.



Investigation of Design and Control Strategies for Combining Photovoltaic Thermal (PVT) Solar Modules with Ground-Source Heat Pump Systems: Case Example for Net Zero Building in a Moderately Cold Climate

Sulaiman Almoatham
Mariana Moreno-Pena
Steve Hamstra

Andrew Chiasson
Cy Yavuzturk
Micah Zender

Rydge Mulford
Roshan Revankar
Steve Melink

ABSTRACT

A synergistic coupling of a ground source heat pump (GSHP) system with photovoltaic thermal (PVT) modules for a cooling dominated net-zero building in a moderately cold climate is presented in this study. As individual systems, GSHP and PVT systems have experienced sluggish market penetration; GSHP systems have relatively high capital cost compared to conventional heating and cooling systems, while PVT systems have niche applications mainly limited to swimming pool heating in moderate to cold climates. Coupled together, the design of the holistic system is non-unique; the ground heat exchanger (GHX) could be designed to optimize efficiency of the PV cells, or the PVT array could be designed for thermal management of annual ground thermal load imbalances on the ground heat exchanger (GHX), or some combination of these design approaches. Given the non-unique design approach for these coupled systems, this study examined various design, control, and operating strategies through hourly simulation software (TRNSYS) for a 20-year life cycle of the system of an actual zero-energy building in a moderately cold climate, which is quite cooling-dominated owing to its superior envelope design. The PVT design and control strategies were aimed at reducing the size of the GHX versus improving the electrical production of the PV. The investigated control strategies found that it is possible to reduce the size of the GHX by 40%, and increase PV electrical energy production by 5%. The control strategy of using nocturnal cooling by the PVT to unload stored thermal energy from the GHX achieved the lowest life-cycle cost. The nocturnal monthly cooling energy unloaded varied between 30 and 140 kWh/m² for summer and winter months over the 20 years of simulation period.

INTRODUCTION

Widespread electrification of the built environment is a key societal component toward achieving carbon neutrality. However, space heating and cooling energy is responsible for 55% of the residential and commercial buildings energy consumption, and the building sector accounts for one third of the global energy use and greenhouse gas emissions (IEA (2020)). Heat pumps offer a solution toward efficiently electrifying space heating needs, but moving toward a fully electric grid utility system increases peak electricity supply requirements. Use of photovoltaic (PV) systems

Sulaiman Almoatham (almoathams1@udayton.edu) is a Doctoral Candidate at the University of Dayton and a lecturer in the Department of Mechanical Engineering, Prince Sattam bin Abdulaziz University. Andrew Chiasson is an Associate Professor, Rydge Mulford is an Assistant Professor, and Mariana Moreno-Pena is undergrad student in the Department of Mechanical & Aerospace Engineering, University of Dayton. Cy Yavuzturk is a Professor of Mechanical, Aerospace, and Acoustical Engineering, University of Hartford. Roshan Revankar is a Project Engineer, Steve Hamstra is Senior Vice President of Engineering, Micah Zender is Product Development Manager, and Steve Melink is President of Melink Zero.

is an obvious choice for on-site electricity production in buildings, but energy production is low in northern winter months. Ground-source heat pump (GSHP) systems, as one of the most energy-efficient heating and cooling technologies currently available, are viable to support building decarbonization by mitigating the overall costs and impacts of space heating, but larger scale market uptake remains hindered by their high capital costs and long payback periods, particularly in buildings with unbalanced annual loads that require prohibitively large ground heat exchangers.

Many energy-efficient buildings may combine PV systems with GSHP systems, but using a photovoltaic-thermal (PVT) system for thermal management of a GSHP system is far less common. Coupled to a building with a superior envelope, PVT-GSHP systems have potential to cost-affordably achieve net-zero energy in the built environment. The challenge in the design of these systems lies in optimizing the size of the PVT and ground heat exchanger (GHX); a GHX size could be optimized to cool PVT modules, thus increasing PV production, or the PVT size could be optimized to heat or cool the GHX, thus minimizing the GHX size and cost. Alternately, both subsystems could be optimized to achieve lowest life-cycle cost.

The following is a review of the current state of the literature regarding GSHP thermal imbalance issues and hybrid GSHP systems, and the use of the PVT array.

Ground-source heat pump (GSHP) systems have gained acceptance as clean, efficient, and life-cycle cost-effective technology used for space heating and cooling. GSHP systems use the relatively stable temperature of the Earth as a heat source and/or sink, which results in significant energy savings compared to conventional HVAC systems. However, when thermal loads on the GHX are not balanced over the annual cycle, the underground temperature tends to increase (in cooling-dominated applications) or decrease (in heating-dominated applications) over the life cycle of the system, which results in the necessity to design large, cost-prohibitive GHX (Georgiev et al. 2020; Yavuzturk and Spitler 2000). Alternatively, hybrid GSHP systems utilize a supplemental heat rejection/generation component to offset some portion of the thermal load on the ground, thereby reducing the size and capital cost of the GHX. Many supplemental components have been studied in the literature, such as cooling towers, boilers, and solar collectors (Chiasson 2016).

Hybrid GSHP system design for cooling-dominated buildings utilizing cooling towers is the subject of much of the scientific literature. For example, several hourly simulation studies were developed to determine the lowest life cycle cost of various operation and control strategies for hybrid GSHPs with cooling towers (Yavuzturk and Spitler 2000; Yi et al. 2008; Hackel et al. 2009; Hackel, S., Pertzborn 2011).

Hybrid solar GSHP systems have been intensely studied for heating-dominated buildings. For example, Chiasson and Yavuzturk (2003) studied the performance of solar thermal collectors coupled with GSHP for a heating-dominant school in the northern US. The solar collectors were used to recharge the ground which resulted in GHX reduction between 4.5 m per m² and 7.7 m per m² of solar collectors. In experimental work, Georgiev et al. (2020) examined hybrid solar-GSHP for a small house in Bulgaria. They found that solar charging of the boreholes resulted in a 1-2°C increase in the temperature of the borehole, which prevented ground temperature depletion and offset the ground temperature decrease due to the GSHP heating operation.

Hybrid solar GSHP systems for cooling-dominated applications have been rarely investigated, but some published studies do exist. For example, Lhendup et al.(2012) tested the performance of an inter-seasonal cool storage system consisting of two solar collectors and two GHXs, where one GHX was used for high-temperature thermal energy storage and the other for cool temperature thermal energy storage. Heat was rejected through the longwave thermal radiation exchange between the unglazed collector and the sky at night. Their experiment resulted in 0.5°C ground temperature reduction and 120 W/m² of cooling by the solar collectors during 80 days of the experiment.

The potential of nocturnal cooling of typical PVT panels has been tested by Hu et al. (2020). Their experiment suggested that it is possible to cool the PVT plate temperature by up to 9°C below the ambient temperature (Hu et al. 2020). Furthermore, Eicker and Dalibard (2011) have tested the nocturnal cooling of PVT modules in a residential zero energy

building in Madrid, Spain. Their system was able to achieve 60 – 65 W/m² of cooling when the PVT collector was used to cool a warm storage tank, and 40 – 45 W/m² of cooling when the thermal energy was directly used to cool a ceiling.

This article aims toward evaluating the optimal design and operating strategy of GSHP systems integrated with solar PVT array in a net-zero cooling-dominated building in a cold climate.

The objectives of this research are to: (1) examine the effect of various control strategies of the hybrid system on the GHX size and the PVT performance; (2) optimize the GHX size using the nocturnal cooling effect of the PVT array as the objective function; and (3) evaluate the economic viability of the hybrid system with a 20-year life-cycle cost analysis.

METHODOLOGY

The following sections describe a potential hybrid GSHP-PVT system connected to an existing net-zero building in Cincinnati, Ohio. Models to predict the performance of the standalone GSHP, PV systems, and hybrid GSHP-PVT system were developed in the TRNSYS modeling environment for hourly simulation. The simulation was used to study the effect of four different control strategies of the hybrid system on the size and the performance of the GSHP and PVT, allowing an economic analysis to be conducted.

System description and control strategies

GSHP systems reject heat to the ground in cooling mode or extract heat from the ground in heating mode. Owing to the large time constant of the Earth, the heat pump entering fluid temperature (EFT) increases or decreases over time. For this simulation, the GHX was sized to maintain the maximum and minimum EFT at 35°C and 0°C within the simulation period (20 years). A representative schematic of the system built in the TRNSYS modeling environment is shown in Figure 1.

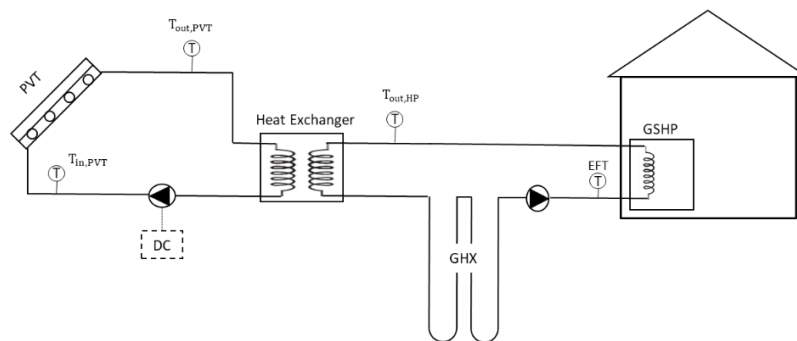


Figure 1. Schematic diagram of the hybrid system.

Four possible system control strategies are listed in Table 1. The control strategies are designed to either extract or reject heat to reduce the size of the GHX or to increase the efficiency of the photovoltaic panels. The first control strategy reduces the GHX size by using radiative losses from the PVT panels to cool the GSHP loop during non-sun hours, rejecting excess heat from the ground. The second control strategy improves the PV efficiency by cooling the PVT loop with the heat pump exiting fluid using the GHX as a heat sink. However, cooling the PV loop doesn't necessarily increase the efficiency at all the times, compared to reference PV, due to the high heat pump exiting temperature, especially during summer. Thus, the third control strategy will ensure an efficiency improvement by allowing the fluid to run through the PVT only if it is less than the PV cell operating temperature. The last control strategy combines both improving the PV efficiency and reducing the GHX size by cooling the PV array during the day and cooling the GHX during the night, thereby running the system pump continuously. The control strategies were simulated using a differential controller (TRNSYS Type 911). The controller monitors the PVT outlet temperature ($T_{out,PVT}$), heat pump

exiting fluid temperature ($T_{out,HP}$), PVT inlet temperature ($T_{in,PVT}$), and PV cell temperature ($T_{cell,PVT}$). The differential control temperature selected was 3°C.

Table 1. System control strategies

CS*	Objective	Control
CS#1	Reduce number of boreholes	Run the PVT loop pump if $(T_{out,HP} - T_{out,PVT}) > 3^{\circ}\text{C}$
CS#2	Increase PV efficiency	Run the PVT loop pump if $(T_{out,PVT} - T_{out,HP}) > 3^{\circ}\text{C}$
CS#3	Increase PV efficiency	Run the PVT loop pump if $(T_{cell,PVT} - T_{in,PVT}) > 3^{\circ}\text{C}$
CS#4	Cool the PV array during day Cool the GHX during night	Run the PVT loop pump continuously

* Hybrid GSHP-PVT Control Strategy

Sub-systems

Building loads and description

The building used for this study is an existing two-story, small office building located in southwestern Ohio, USA, and was designed for net-zero energy use. The building has 2,790 m² of conditioned floor space with a super-insulated envelope comprised of R30 (RSI 5.3) walls (insulated with spray foam), and R50 (RSI 8.8) roof (constructed of multi-layered foam board). High-performance window and door systems are included in the design for maximum daylighting, minimum heat gain in the summer and heat loss in the winter. Electrical loads are minimized through the use of smart LED lighting with occupancy sensors and dimming control. Additionally, the building utilizes innovative hydronic heating and cooling with heat pumps, auxiliary heat sinks/sources, and a thermal battery to minimize electric demand during both summer and winter conditions. A solar PV system is used as a parking lot canopy to produce clean energy for the building and electric cars connected to the system. EV chargers were included in 80% of the parking spaces. Although the building is located in a mixed-humid/cold climate (2700 heating degree day (18°C base)), the high-performance building envelope results in an annual cooling to heating load ratio to be around 6, which is a load profile more common to a much warmer climate zone. The thermal peak cooling and heating loads of the building are 129 and 96 kW, respectively. The building’s total annual energy cooling and heating are 142,159 and 23,849, respectively. The building loads profile is shown in Figure 2. The annual, maximum, and minimum air temperature of location are 12 °C, 41 °C, and -27 °C. The annual average relative humidity is 78%.

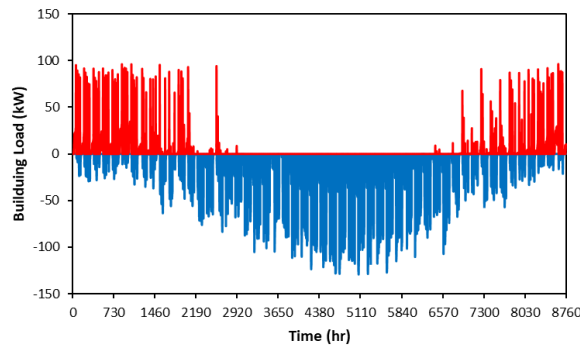


Figure 2. Hourly heating loads (positive) and cooling loads (negative) for the example building.

Photovoltaic Thermal (PVT), Ground Heat Exchanger (GHX), and Heat pump (HP)

A PVT component model was developed and added to the TRNSYS library for this work. The thermal collector efficiency is determined using Equation 1 (Burch et al. 2004):

$$\eta = F_R(\tau\alpha) - F_R U_L \times \frac{T_i - T_{amb}}{G_{net}} \quad (1)$$

Where the terms F_r , U_L , T_i , T_{amb} are the heat removal factor, heat loss coefficient, fluid inlet temperature, and ambient temperature, respectively. The net incident radiation, G_{net} , includes both the total solar radiation, G_{sun} , and the infrared radiation from the PVT plate to the sky, G_{sky} , as given in Equation 2 and 3.

$$G_{net} = G_{sun} - \left(\frac{\varepsilon}{\alpha} G_{sky}\right) \quad (2)$$

$$G_{sky} = \sigma \left(T_{cell}^4 - T_{sky}^4\right) \quad (3)$$

where σ is Stefan-Boltzman constant, T_{cell} is the PV cell temperature, and T_{sky} is the effective sky temperature given as a function of dew point temperature, cloud cover, atmospheric pressure, and time of the day. The effective sky temperature is calculated using the Martin and Berdahl (1984) correlation. The PVT modules used in this simulation have an area of 1.45 m², electrical efficiency of 13.6%, heat removal factor ($F_R \tau\alpha$) of 0.6, and heat loss slope ($F_R U_L$) of 15 (W·m⁻²·K⁻¹). Each collector has flow rate of 108 (kg·h⁻¹). The derating factor which includes shading, dust accumulation, wiring losses was assumed to be 85%. Also, the power degradation was assumed to be 0.5% per year.

Simulation of the GHX performance is accomplished with TRNSYS component Type 557. The ground and grout thermal conductivity was assumed to be 2.1 and 2.4 (W·m⁻¹·K⁻¹), respectively. Each borehole has a radius of 0.127 m and a borehole spacing of 7 m. The peak design volumetric flow rate is 2.5 L/min per kW of peak building load.

A component model describing the performance of water-to-air geothermal heat pumps has been developed for hourly GSHP system simulations. Inputs to the heat pump model include the thermal loads, entering fluid temperatures, and fluid mass flow rates. Dynamic modeling of the heat pump load side involves imposing the building loads on the heat pumps, and thus zone temperatures were not explicitly modeled. Linear curve-fit equations to manufacturer's heat pump catalog data are employed to compute the heat rejection in cooling mode, heat absorption in heating mode, and the heat pump energy consumption as a function of the heat pump source entering fluid temperature. Outputs provided by the models include exiting fluid temperature, energy consumption, fluid mass flow rate, and heat pump COP. For this work, the heat pump heating COP was modeled to vary linearly from 4.0 to 5.0 at entering source temperatures ranging from 0°C to 20°C, respectively. The heat pump cooling COP was modeled to vary linearly from 7.0 to 4.5 at entering source temperatures ranging from 10°C to 32°C, respectively.

Economic analysis

The economic performance of the standalone GSHP and the hybrid system was compared using the total cost of ownership (TCO) which is the net present value of the capital cost, operation cost, and operation saving over the 20 years simulation period. The operation cost includes the heat pump electricity consumption and the PVT pump electricity consumption, and the operation saving includes the PV electricity generation. TCO's were calculated assuming an 8% discount rate, \$50/m drilling cost (which includes all underground work), \$0.12/kWh electricity price, \$2.7/W PV cost, and \$4/W PVT cost (BRE National Solar Centre and Delta-ee 2016).

RESULTS AND DISCUSSION

Performance of standalone GSHP and PV reference systems

The standalone GSHP system required 2800 m (28 x 100 m) of borehole length to meet the heat pump entering fluid (EFT) design over the 20-year simulation period. Moreover, standalone PV system analysis was performed as a reference for comparison with the electrical production of the PVT in the hybrid system. This simulation used 13.8 kW (100 m²) of PV for all the analyses. The PV system size was not designed to cover the building electricity load but was determined where the maximum GHX length reduction is possible. The PV resulted in an average of 15,567 kWh per year of energy

production.

Performance of the hybrid system with the control strategies

The first control strategy reduced the required boreholes field by 40% by extracting the thermal load from the GHX. This strategy did not improve the PV production since it runs mostly during the night. On the contrary, the second and third control strategies improved the annual PV production by 4.56% and 3.84%, respectively, while increasing the GHX length by 7% and 4.6%, respectively. The best PV performance improvement was by the last control strategy where the PVT loop is running continuously to charge and recharge the ground alternately. It improved the annual PV production by 5.26% while decreasing the borehole length by 35%. The heat pump consumption was within 4% for all cases. Table 2 summarizes the hybrid system performance under different control approach. The presented values are then averaged over the 20 years simulation period.

Table 2. hybrid system performance under different control strategies

System	Borehole length	HP consumption (kWh/year)	PVT electrical production (kWh/year)	PV production difference	PVT pump consumption (kWh/year)
Standalone GSHP	28 x 100 (2800 m)	32,553	-	-	-
Standalone PV	-	-	15,567	-	-
Hybrid GSHP-PVT CS#1	17 x 100 (1700 m)	31,220	15,569	0.01%	5,882
Hybrid GSHP-PVT CS#2	30 x 100 (3000 m)	32,732	16,277	4.56%	2,129
Hybrid GSHP-PVT CS#3	29 x 101 (2929 m)	32,729	16,165	3.84%	1,170
Hybrid GSHP-PVT CS#4	19 x 96 (1824 m)	31,678	16,386	5.26%	9,636

Nocturnal cooling effect on the GHX

The first control strategy was aimed at reducing the length of the boreholes by rejecting heat during the night using the PVT. The nighttime cooling was effective in offsetting some of the ground loads and reducing the GHX length. Through iterative optimization of the system, it was possible to reduce the length of the total borehole by 40% with 100 m² of PVT. The borehole length reduction was maximized with PVT solar collector array size of 100 m² (13.8 kW).

Figure 3a shows the monthly cooling energy of the PVT collectors for the 1st and 20th year of the simulation. Figure 3b also shows a monthly breakdown of the convective and radiative losses. The cooling energy increased over the years due to the gradually increasing GHX temperature. The average annual cooling energy of the PVT was 64 and 119 kWh/m² for the 1st and 20th year, respectively, with a variation between 30 and 140 kWh/m² for the summer and winter months. Furthermore, the convective losses dominated the losses due to the cold climate of the location. It is interesting to note that the net radiation losses are negatives in summer because it included both the short and the longwave radiation as described by Equation 2.

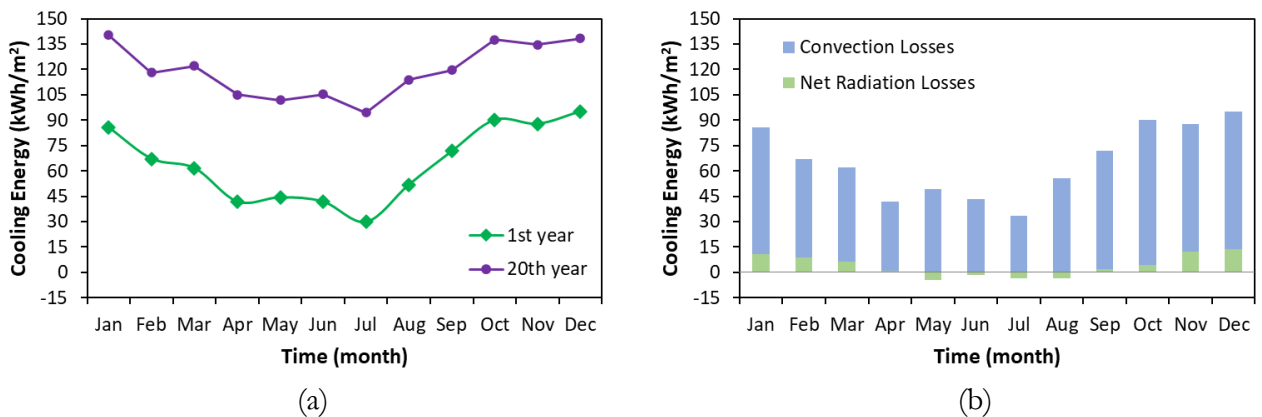


Figure 3. (a) 1st and 20th year's monthly cooling energy (b) monthly breakdown of the convective and radiative losses.

The fitted curve of the PVT modules cooling power with a temperature difference between inlet fluid and ambient air temperature is shown in Figure 4a. The cooling power increases nearly linearly with the increase of the temperature difference. The fitted curve relation of the cooling power with temperature difference is expressed as: $16 \times (T_{in} - T_{amb}) + 22$. Conversely, the PVT modules cooling power decreased with the increase of the relative humidity as shown in Figure 6b. The fitted curve relation of the cooling power with relative humidity is expressed as: $-0.13 \times (RH) + 184$.

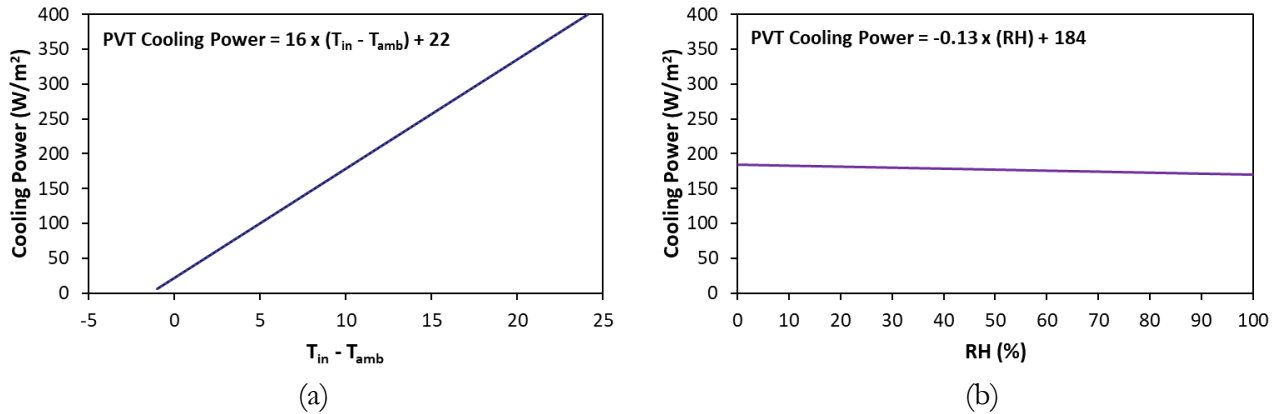


Figure 4. Fitted curve of PVT cooling power with: (a) inlet and ambient temperature difference (b) relative humidity.

Economic analysis

An economic analysis was performed to evaluate the hybrid system with each of the control strategies, and results are summarized in Table 3. The total capital cost of hybrid GSHP-PVT system control strategies 1 and 4 are close to the cost of the standalone GSHP with the additional benefit of PV electrical production. The systems with control strategies 2 and 3 produce electricity but increase the cost by approximately 45% compared to the standalone GSHP and 15% compared to the standalone GSHP with PV system. Thus, the total cost of ownership over 20-years is the lowest for a hybrid system with control strategy 1. It is followed by the hybrid system with control strategy 4 and the standalone GSHP. In addition, compared to the standalone GSHP, the hybrid system control strategies 1 and 4 reduced the TCO by 7.17% and 1.45%, respectively, while the hybrid system control strategies 2 and 3, and the standalone GSHP with PV system increased the TCO by 27.33%, 24.78%, 10.61%, respectively.

Table 3. Summary of the economic analysis.

System	GSHP		PV/T			Total		
	Capital Cost (\$)	Annual HP Energy Consumption (\$/year)	Capital Cost (\$)	Annual PV Production (\$/year)	Annual Pump Energy Consumption (\$/year)	Capital Cost (\$)	Cost of Ownership (\$)	TCO Difference (%)
Standalone GSHP	140,000	3,906	-	-	-	140,000	178,354	-
Standalone GSHP + PV	140,000	3,906	37,260	1,868	-	177,260	197,273	10.61%
Hybrid system CS#1	85,000	3,746	55,200	1,868	706	140,200	165,570	-7.17%
Hybrid system CS#2	150,000	3,928	55,200	1,953	255	205,200	227,095	27.33%
Hybrid system CS#3	146,450	3,927	55,200	1,940	140	201,650	222,544	24.78%
Hybrid system CS#4	91,200	3,801	55,200	1,966	1,156	146,400	175,770	-1.45%

CONCLUSION

Various operational strategies of the hybrid GSHP system coupled with PVT collectors are proposed in this study as an attempt to reduce the GHX size and increase the PV efficiency for a net-zero building in a moderately cold climate. The main findings were:

- Nocturnal cooling using the PVT built into the hybrid system was capable of reducing GHX size by up to 40% compared to the standalone GSHP system.
- Using the ground to cool the PV panels increased the PV production by between 3.86%- 5.86% depending on the control strategy. However, it also increased the size of the GHX.
- Using the PVT loop to extract heat from the GHX features the lowest TCO followed by operating the PVT loop continuously throughout night and day. The TCO of the system is mostly driven by the upfront cost of the GHX boreholes.
- The average annual cooling energy provided by the PVT is 64 and 119 kWh/m² for the 1st and 20th year, respectively.
- The monthly cooling energy varied between 30 and 140 kWh/m² for the summer and winter months over the 20 years of the simulation period.

REFERENCES

- BRE National Solar Centre, and Delta-ee. 2016. "Evidence Gathering – Low Carbon Heating Technologies, Hybrid Solar Photovoltaic Thermal Panels."
- Burch, Jay, Craig Christensen, Jim Salasovich, and Jeff Thornton. 2004. "Simulation of an Unglazed Collector System for Domestic Hot Water and Space Heating and Cooling." *Solar Energy* 77 (4 SPEC. ISS.): 399–406. <https://doi.org/10.1016/j.solener.2003.12.014>.
- Chiasson, Andrew D. 2016. *Geothermal Heat Pump and Heat Engine Systems: Theory and Practice*. John Wiley & Sons.
- Chiasson, Andrew D., and Cenk Yavuzturk. 2003. "Assessment of the Viability of Hybrid Geothermal Heat Pump Systems with Solar Thermal Collectors." *ASHRAE Transactions* 109 PART 2: 487–500.
- Eicker, Ursula, and Antoine Dalibard. 2011. "Photovoltaic-Thermal Collectors for Night Radiative Cooling of Buildings." *Solar Energy* 85 (7): 1322–35. <https://doi.org/10.1016/j.solener.2011.03.015>.
- Georgiev, Aleksandar, Rumen Popov, and Emil Toshkov. 2020. "Investigation of a Hybrid System with Ground Source Heat Pump and Solar Collectors: Charging of Thermal Storages and Space Heating." *Renewable Energy* 147: 2774–90. <https://doi.org/10.1016/j.renene.2018.12.087>.
- Hackel, S., Pertzborn, A. 2011. "Effective Design and Operation of Hybrid Ground-Source Heat Pumps: Three Case Studies." *Energy and Buildings* 43: 3497–3504.
- Hackel, Scott, Gregory Nellis, and Sanford Klein. 2009. "Optimization of Cooling-Dominated Hybrid Ground-Coupled Heat Pump Systems." *ASHRAE Transactions* 115 PART 1: 565–80.
- Hu, Mingke, Bin Zhao, Xianze Ao, Suhendri, Jingyu Cao, Qiliang Wang, Saffa Riffat, Yuehong Su, and Gang Pei. 2020. "An Analytical Study of the Nocturnal Radiative Cooling Potential of Typical Photovoltaic/Thermal Module." *Applied Energy* 277 (April): 115625. <https://doi.org/10.1016/j.apenergy.2020.115625>.
- IEA (2020). n.d. "Energy Efficiency Indicators." Paris. <https://www.iea.org/reports/energy-efficiency-indicators>.
- Lhendup, Tshewang, Lu Aye, and Robert James Fuller. 2012. "Experimental Study of Coolth Charging of an Inter-Seasonal Underground Thermal Storage System." In *Proceedings of the 50th Annual Conference, Australian Solar Energy Society.—Melbourne*. <https://www.researchgate.net/publication/239731286>.
- Martin, Marlo, and Paul Berdahl. 1984. "Characteristics of Infrared Sky Radiation in the United States." *Solar Energy* 33 (3): 321–36. [https://doi.org/https://doi.org/10.1016/0038-092X\(84\)90162-2](https://doi.org/https://doi.org/10.1016/0038-092X(84)90162-2).
- Yavuzturk, Cenk, and Jeffrey D. Spitler. 2000. "Comparative Study of Operating and Control Strategies for Hybrid Ground-Source Heat Pump Systems Using a Short Time Step Simulation Model." *ASHRAE Transactions* 106.
- Yi, Man, Yang Hongxing, and Fang Zhaohong. 2008. "Study on Hybrid Ground-Coupled Heat Pump Systems." *Energy and Buildings* 40 (11): 2028–36. <https://doi.org/10.1016/j.enbuild.2008.05.010>.



The Characterization of Helical Steel Pile Performance Under Varying Soil Conditions

Krystal J. Henry-Mathieu, Sylvie Antoun and Seth B. Dworkin

ABSTRACT

Ground-Source Heat Pumps (GSHPs) are a clean alternative to traditional space heating and cooling technologies. GSHPs take advantage of relatively constant ground temperatures as a medium for heat exchange, in contrast to the use of highly variable air temperatures. Conventional systems use a heat pump paired with a borehole heat exchanger to exchange heat with the ground. Widespread use of these systems has been impeded by high initial costs and low short-term return on investment. Helical steel piles (HSP) are structural elements that are drilled into the soil to provide support to buildings. With only minor modifications, these structures have shown promise as a viable alternative to the use of the conventional borehole heat exchanger. At present, there is little understanding of the functionality and the optimal design of HSPs as heat exchangers under different soil properties such as heterogeneity, porosity and saturation content. Therefore, the focus of this paper is to investigate the performance of HSPs under different heterogeneous soil conditions using numerical analysis. This paper presents the results of a numerical study of HSP performance under varying moisture contents.

INTRODUCTION

With calls to reduce greenhouse gas emissions across the globe, there is a significant need for innovative solutions to produce reliable energy with a reduced environmental impact. In Canada, space heating accounts for approximately 80% of energy consumption residentially and 63% of energy consumption globally [1]. Most sustainable energy options are either unreliable in terms of energy production, too expensive or negatively impactful on other components of the environment.

Geothermal energy is considered a viable option for meeting the heating and cooling demands in many climates (including Canada, where this research is being conducted), as opposed to the standard heating and cooling technologies that rely heavily on fossil fuels. This energy source uses a ground source heat pump (GSHP) to supply heating/cooling to buildings. GSHPs work in conjunction with a heat exchanger which carries a working fluid to be the agent for heat exchange in the subsurface. Conventional heat exchangers use a horizontally oriented system or a vertically oriented system. Horizontal ground heat exchangers are buried at shallow depths (~2-3 meters) beneath the surface leaving the system more susceptible to changing soil temperatures. In contrast, vertical heat exchangers use borehole loops with polyethylene (PEX plastic) piping that is drilled to depths of up to 250 m beneath the surface, making use of much more constant soil temperatures [1]. However, as a result of the extensive drilling, geothermal energy has very high installation costs which along with the system's low initial return on investment and long payback periods, has hindered its ability to be implemented widely.

Helical Steel Piles (HSPs), typically between 6 meters and 20 meters in length, are structural elements that are drilled into the ground for the support of buildings. In addition to their structural benefits, HSPs have shown promise as an innovative alternative to the conventional borehole heat exchanger (BHE). However, HSPs require a simpler installation procedure (using threaded or welded connections), and in many cases could further reduce overall costs by serving a dual purpose of structural support and exchanging usable heat to be used for building climate control. HSPs utilize a helix welded to the bottom of the pile which allows the HSP to be screwed into the soil without the need for

a pre-drilled borehole [2]. The thermal properties of the HSP, soil and working fluid allow for reliable heat transfer throughout the year. During the cooling season (spring/summer months), the warm fluid exchanges heat with the soil to return cooler fluid for the cooling of the building. In the warming season (fall/winter months), the cool fluid extracts heat from the soil to return to the warmer fluid for the heating of buildings. While the shorter nature of HSPs relative to conventional ground heat exchange options is a part of the benefits of the design, this leaves the system more susceptible to the conditions of the soil surface and thus soil properties may play an important role in their performance. The use of steel piles as a heat exchanger has been featured in numerous studies such as those conducted by Jalaluddin et al. [3] and Lyu et al. [8] which focus on evaluating the performance of pile heat exchangers with a variation of pile designs. As a result of impactful research, many pile systems have also been installed across the globe in the past decade. While pile heat exchange as a whole is not a new concept, the structural configuration suggested by Nicholson et al. [1] is unique. The proposed pile design uses tubular steel piles fit with PEX plastic piping for fluid flow into the pile. The fluid can then circulate through the volume of the steel pile casing to exchange heat with the surrounding soil. This design also implores a laminar flow regime rather than turbulent flow, the commonly used flow regime in ground heat exchange systems.

Past computational work has focused on optimizing the performance of the piles for the application in a real-world system. A model of a single HSP was created by Nicholson et al. [1] and validated using experimental data of a heat exchange system from Jalaluddin, et al. [3] and Jalaluddin, et al. [4], that closely represented the proposed HSPs. This model was also used to optimize the performance of the HSP based on its geometry (length and overall geometry). While the implications of various thermal properties on heat transfer are generally well defined, understanding the extent to which these properties impact heat exchange using a helical steel pile is critical in understanding the system's overall performance. To better understand the functionality of HSPs as heat exchangers, a numerical analysis was conducted to further evaluate the HSP's energy performance under varying soil conditions. The main objective of this paper is to validate the thermodynamics and heat exchange behaviour of an HSP by comparing the numerical predictions of the previously built CFD model with experimental data, as well as to further evaluate the HSP's energy performance under varying soil conditions using the validated model.

METHODOLOGY

Model development

To investigate the performance of the helical piles as heat exchangers in different soil conditions, a combination of numerical modelling and experimental testing was needed. In this study, a numerical modelling approach was followed. The original numerical model was developed using the COMSOL Multiphysics® software [7] and solved the governing equations using coupled (laminar flow) fluid dynamics and heat transfer.

Model Validation

The present research seeks to build on the results of an ongoing experimental/modelling research campaign being conducted by the co-authors. Previous modelling and optimization work focused on the initial design and characterization of the heat transfer performance of a novel helical steel pile as an in-ground heat exchanger [1].

An experimental site with eight piles has been installed at the Eby Rush Transformer Station in Waterloo, Canada. The pilot project focused on the design, installation, and commissioning of an eight-geo-pile GSHP test site. The Eby Rush experiments have yielded operational data from the summer cooling season (August 2021) to the fall/winter heating season (November 2021), which were analyzed and used for model validation in the present work. More details of the experimental setup can be found in [2].

The numerical models were developed using the COMSOL Multiphysics® software [7] and solved for the governing equations using coupled (laminar flow) fluid dynamics and heat transfer. The HSP modelled in this work has a length of 20 m with an outer diameter of 13.97 cm (5.5 inches). The numerical outlet temperature results were compared

with the experimentally measured results given the same inlet water temperature and flow rate values obtained from the tests conducted at the Eby Rush site. A diagram of the HSP can be seen in Figure 1.

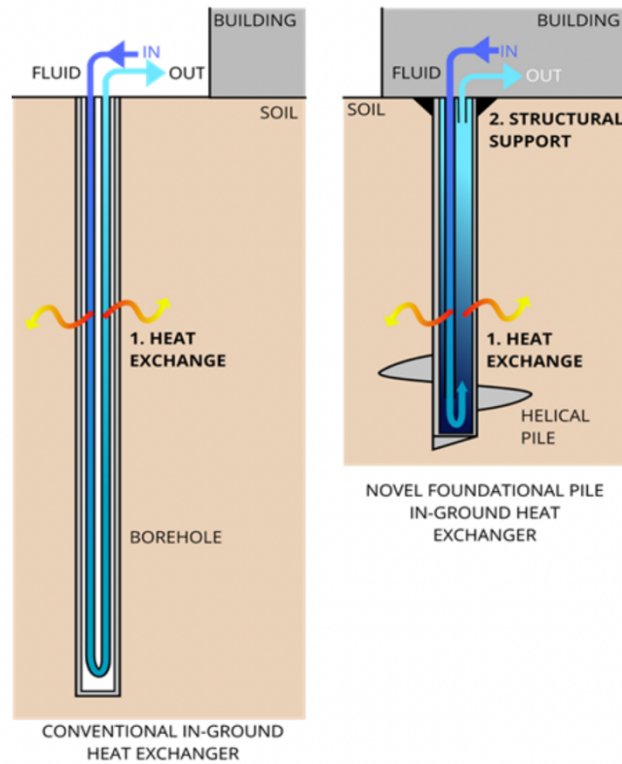


Figure 1: Comparison between a conventional u-tube in-ground heat exchanger (left) and the novel pile design (right) proposed by Nicholson et al. [1]

The far-field ground temperature in the model was kept constant at 12°C throughout the depth of the soil column during both the heating and cooling seasons to reduce simulation costs (time constraints). This was due to a lack of soil temperature data for the location, varying with time and depth. The physical and thermal material properties of the HSP and interior piping can be further found in [2]. The fluid (water) and solid material properties of the pipe are calculated as functions of temperature.

The boundary and initial conditions applied for heat transfer and laminar flow used in this work are:

- Both the pile and soil domain are initially at rest, maintaining an initial temperature of 12°C
- The inlet flow is defined by a time-dependent boundary temperature with a 1-minute time step, which varies across the test period.
- A constant flow rate of 2.6 L/min was applied as a normal inflow at the inlet pipe boundary. The value was kept constant for all the tests based on the experimental data.
- The outlet pipe boundary is defined as an outflow/outlet.
- No heat flux was applied at the topsoil surface boundary (adiabatic).
- The far-field soil was kept at a constant temperature of 12°C.

Model Modification

The original single pile model was modified to consider different soil properties within the physics of heat transfer. The focus of this study is to assess the performance of an HSP as a heat exchanger under different moisture contents. To complete this analysis, data retrieved from the literature [5] was used to alter the thermophysical properties of the soil (soil thermal conductivity, porosity, particle density and texture). One location (Ontario, Canada) was chosen from the dataset for two unique soil types (sandy soil and loamy soil).

The particle densities from the respective Ontario soils were used to calculate the dry bulk densities of the soil using formula 1.

$$\rho_b = (1-\eta) * \rho_s \quad (1)$$

Where ρ_s is the particle density of the soil, ρ_b is the bulk density of the soil and η is the soil porosity of the soil.

Soil heat capacity (C_p) was also taken from the literature [6]. Due to a lack of relevant soil data, the heat capacities of both sandy and loamy soils were considered to be between 830-1483 J/kg*K and 1140-2090 J/kg*K respectively, ranging from low to high moisture content in the soil. This was done as generally; soil heat capacity and soil moisture content are positively correlated. In a second simulation, soil heterogeneity was also created manually by adhering to general soil principles with depth, specifically ensuring that high porosity soils remained closer to the surface. This was done to simulate what is often seen in soils with multiple layers as soils deeper beneath the surface often have lower porosities due to soil compaction. Soil compaction is also related to higher bulk density and this concept was adhered to while creating heterogeneity in the soil. The soil data used in each of the simulations (thermal conductivity and heat capacity) can be found in Table 1.

TABLE 1

Soil Type/ Soil ID	λ_{dry}	$\lambda_{0.25}$	$\lambda_{0.50}$	$\lambda_{0.75}$	λ_{sat}	$C_{p,dry}$	$C_{p,0.25}$	$C_{p,0.50}$	$C_{p,0.75}$	$C_{p,sat}$
ON-04, Sandy Soil	0.261	1.12	1.438	1.49	1.67	830	997	1165	1324	1483
ON-03, Loamy Soil	0.21	0.983	1.15	1.35	1.52	1140	1377	1615	1852	2090

λ = Soil Thermal Conductivity in W/m*K

C_p = Soil Heat Capacity in J/kg*K

Model Mesh and Solver

A finite element mesh was used to simulate heat transfer using the single HSP. The mesh included the fluid within the pile, the pile walls as well as the surrounding soil. A free tetrahedral shape mesh was used across the larger surfaces in the model with the entire model domain containing 280,029 total mesh elements (Figure 2).

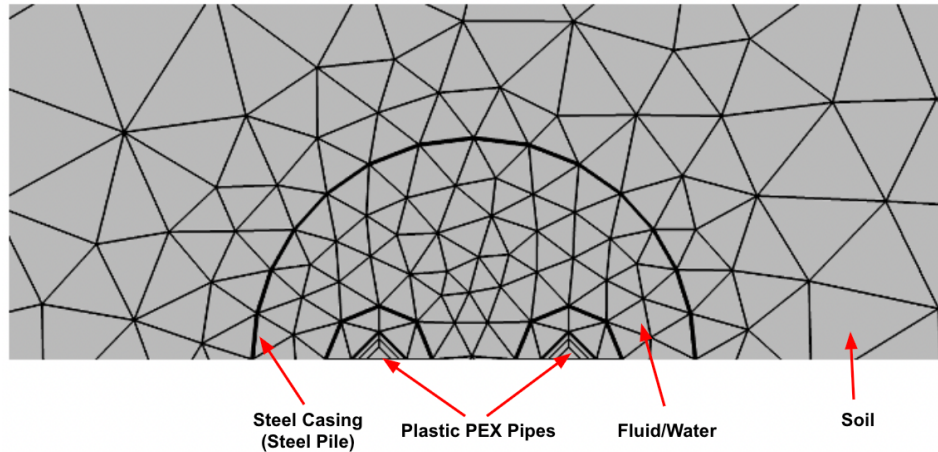


Figure 2: Single helical steel pile COMSOL model mesh components

Calculating Heat Exchange

Based on the results of the simulations for both soil types, the magnitude of heat exchange at each time interval was calculated using formula 2.

$$HE = Q * \rho * C_p * (T_{in} - T_{out}) \quad (2)$$

Where HE is the heat exchange across a single HSP, T_{in} is the inlet water temperature to the HSP, T_{out} is the outlet temperature coming out of the HSP, Q is the flow rate of the water into the pile, ρ is the density of water and C_p is the specific heat capacity of water. The heat exchange values for each testing date, soil type, and saturation level were averaged and used for an analysis of the system's performance under varying soil moisture contents.

RESULTS AND DISCUSSION

It is well understood that heat transfer as a whole is susceptible to the changing thermal properties within soil throughout seasons and across climate regions. An experimental study done by Hu et al. [9] investigated the importance of soil moisture content and soil thermal conductivity as they relate to heat exchange. The results of this study showed the critical nature of these soil properties for both a geothermal system's performance as well as the recovery of the soil following intermittent use. It is unclear however the extent to which soil thermal properties such as thermal conductivity and heat capacity would impact a helical steel pile's ability for heat exchange. The main objective of this study is to characterize the soil's impact and generate information that is needed in the consideration of the industrial implementation of HSPs.

The modified CFD model was used in this study to evaluate the impact of soil thermal properties on its performance based on simulated heat exchange values. The CFD model was validated and compared to experimental data. To validate the model, it was assumed that the soil temperature remained at an undisturbed 12 °C during each test and that the soil volume is considered a non-porous, homogeneous solid medium. Following model validation, data from each of the Ontario soil simulations were post-processed and used to calculate the average heat exchange between the soil and the piles for each soil type in both heating and cooling seasons. The following sections outline the result of each simulation.

A. Model Validation Results

Model validation results were analyzed using absolute error which is defined as the difference between the observed value and the true value. The model validation used inlet temperature data collected from tests done at the pilot project site. Figure 3 shows the results of two different days in summer, requiring the pile to return cooler water temperatures to the outlet of the pipe that would be used for the cooling of the building. The results of the August 22nd and August 24th cooling validation simulations yielded an absolute error of 1.22 K and 1.26 K respectively. This level of error could be reduced by using data closer to the soil properties of the test site. The results of both the simulations and the experimental tests resulted in a difference in temperature (ΔT) of 10°C between the inlet and the outlet of the pile. The large difference in temperature can be attributed to both the structural design of the steel piles as well as the flow regime used for fluid flow (Figure 1). The laminar flow regime allows the water to have a longer residence time as it circulates throughout the interior volume of the steel pile. In effect, greater heat exchange can take place.

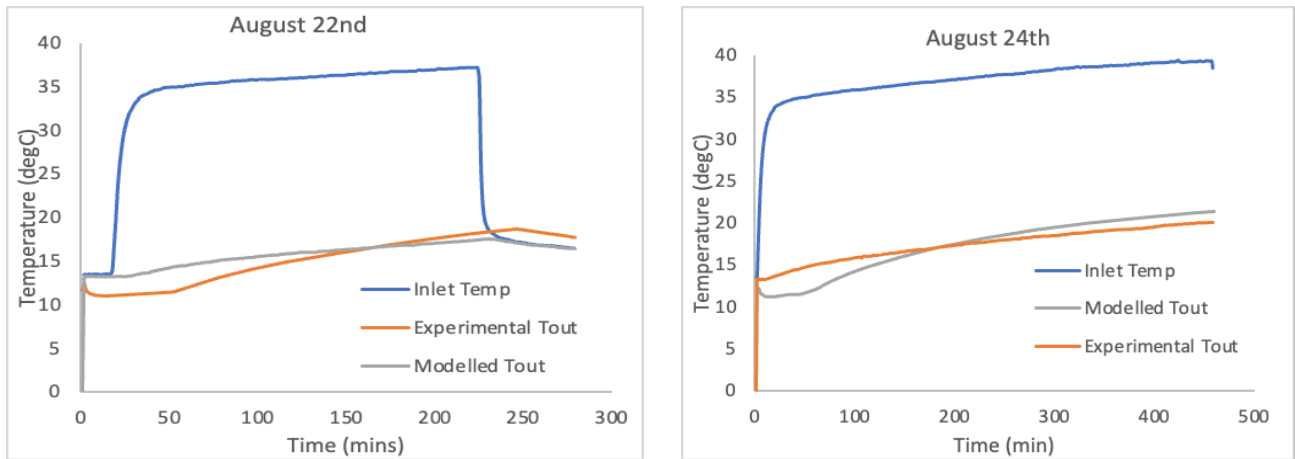


Figure 3: Model validation results for August 22nd and August 24th (cooling season)

Figure 4 shows the results of a cooling test taking place late in the cooling season (early autumn). The experimental outlet temperatures and the modelled outlet temperatures both remained relatively constant throughout the entirety of the test, likely due to the low-temperature difference between soil and air at this point in the season. The October 4th and October 6th simulations yielded an absolute error of 0.49 K and 0.85 K respectively.

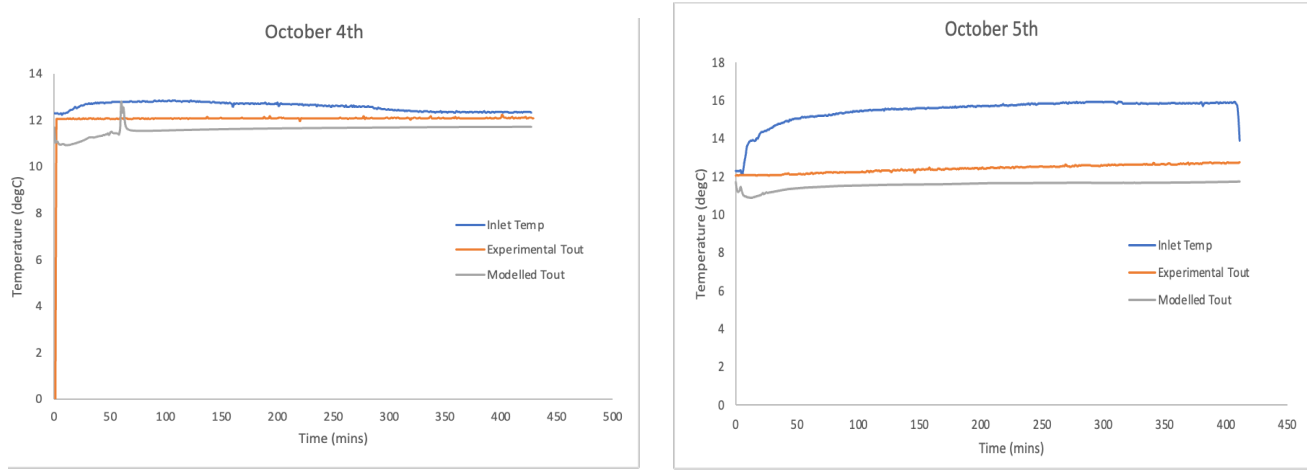


Figure 4: Model validation results for October 4th and October 5th (heating season)

Finally, Figure 5 shows the results of two heating simulations using inlet temperatures from November. The simulations for November 23rd and 24th yielded much higher absolute and relative error, 1.96 K and 2.39 K respectively. This result was expected due to the assumption that the soil temperature would remain at a constant 12 °C. This assumption is not realistic to the seasonal behaviour of the soil.

Reducing the soil temperature to between 6°C and 8 °C would potentially have yielded closer results to the experimental data.

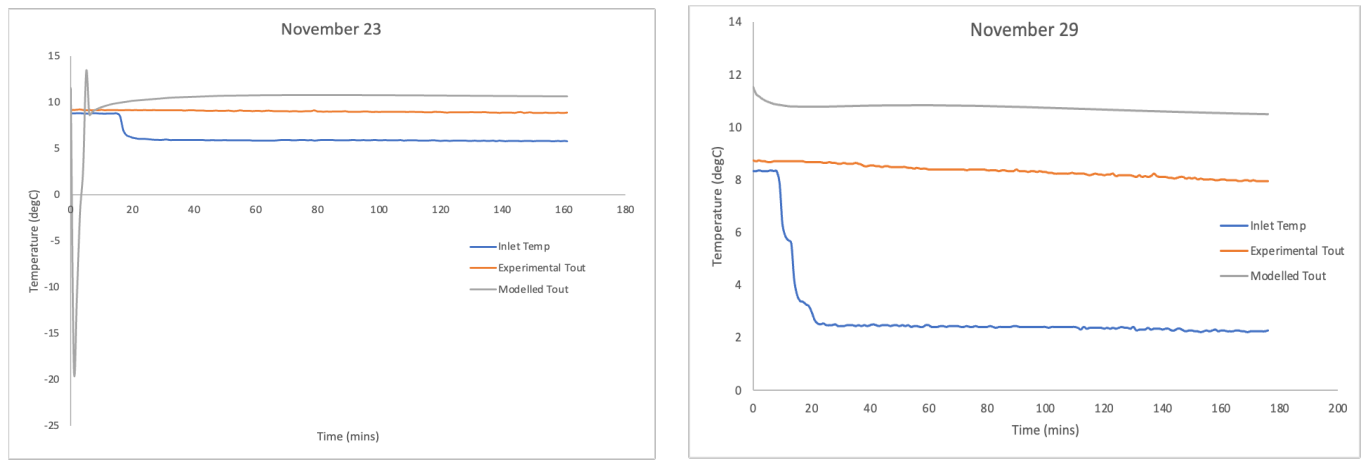


Figure 5: Model validation results for November 23rd and November 29th (cooling season)

B. Sandy Soil Simulations

Ontario soil data (ON-04) from literature [5] was used to simulate a homogeneous sandy soil under different soil saturation contents. Due to both software limitations and time constraints, it was assumed that the soil was solid, however, varying thermal properties were used to simulate the behaviour of soil and heat transfer under the chosen saturation conditions. Table 2 below shows the results of each simulation.

TABLE 2

Thermal Load	HE _{Dry}	HE _{0.25}	HE _{0.50}	HE _{0.75}	HE _{Sat}
Cooling	3094.15 W	3456.6 W	3581 W	3581 W	3641.2 W
Heating	791 W	793 W	793 W	793 W	795 W

The results of the cooling simulation for sandy soil showed that while there is a significant amount of heat exchange when the soil is dry, heat exchange increases with saturation content. The simulation for fully saturated soil amounted to 3641.2 W of average heat exchange by the single pile in, a nearly 600 W difference in heat exchange from the dry soil. This is likely due to the thermal properties of water which significantly improve the thermal capabilities of soil, showing the importance of soil moisture content to heat exchange, particularly under a cooling thermal load (Figure 6). These values can also be attributed to high inlet temperatures during the experimental tests (as high as 35°C). The presence of a heat exchanger between the HSPs and the heat pump at the pilot site in conjunction with the design of the HSPs allow for the observed inlet temperatures. Similar inlet temperatures were used to test energy piles using a different structural configuration by You et al. [10] which yielded comparable heat exchange results (inlet temperature of 35°C yielding a total heat exchange rate of 2100W), further confirming the heat exchange capacity of energy piles as a whole. However, inlet temperatures at such high values would not typically be seen in a fully operational system due to the system specifications of the heat pump and thus is a limitation of this study. Further simulations are needed to simulate the HSPs performance without the use of the heat exchanger however, this is beyond the scope of this study.

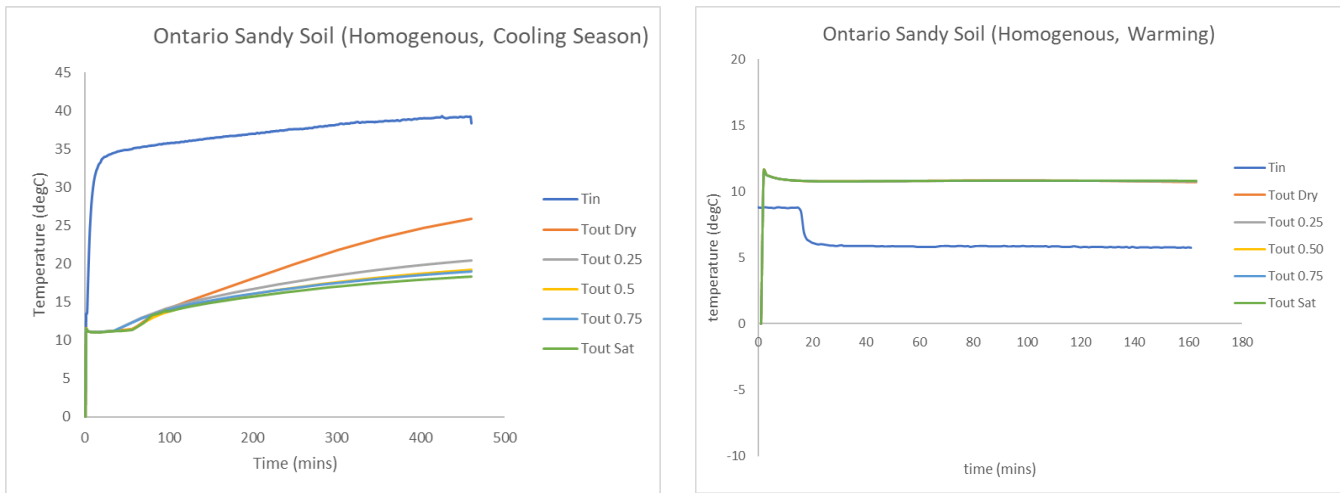


Figure 6: Homogeneous sandy soil model results using saturation levels from dry to fully saturated in increments of 0.25

The heating test for sandy soil presented significantly different results. Overall, the difference in heat exchange with varying water content can be considered negligible during the heating tests (November data). Simulations at each of the saturation levels during the heating season resulted in an average heat exchange of 794 W, a drastic difference from the cooling season results. It is possible that having inlet temperatures that are so close to the soil temperatures resulted in little variation in heat exchange. As seen in the validation data for November 23rd in figure 5, the ΔT of the experimental inlet and outlet temperatures is only 2.82°C. Greater average heat exchange may have been seen with the use of inlet temperature data from a colder time of the year (January or February). Another possibility for the general reduction in heat exchange is that the density of water is slightly greater at lower temperatures which impacts

thermal conductivity. This may cause an innate reduction in heat exchange during the colder seasons for saturated soils.

C. Loamy Soil Simulations

Ontario soil data (ON-03) from literature [5] was used to simulate a homogeneous loamy soil under different soil saturation contents. The same assumptions made for the simulation of an HSP in sandy soil were made for the loamy soil simulation and thus it yielded similar results. Heat transfer between the soil and fluid domains was the greatest under fully saturated conditions during the cooling season, with an average heat exchange of 3668.5 W. For the heating season, the loamy soil also had relatively low heat exchange rates with an average of 793 W of heat exchanged at each saturation level. Table 3 shows the complete heat exchange results for each test.

TABLE 3

Thermal Load	HE _{Dry}	HE _{0.25}	HE _{0.50}	HE _{0.75}	HE _{Sat}
Cooling	3150W	3523.2W	3569.4W	3625.8W	3668.5W
Heating	793W	793W	793W	793W	793W

Overall, the results of the loamy soil simulations were very similar to that of the sandy soil. The cooling season yielded high heat exchange values whereas the heating simulations for each saturation content had negligible differences in the magnitude of heat exchange (Figure 7).

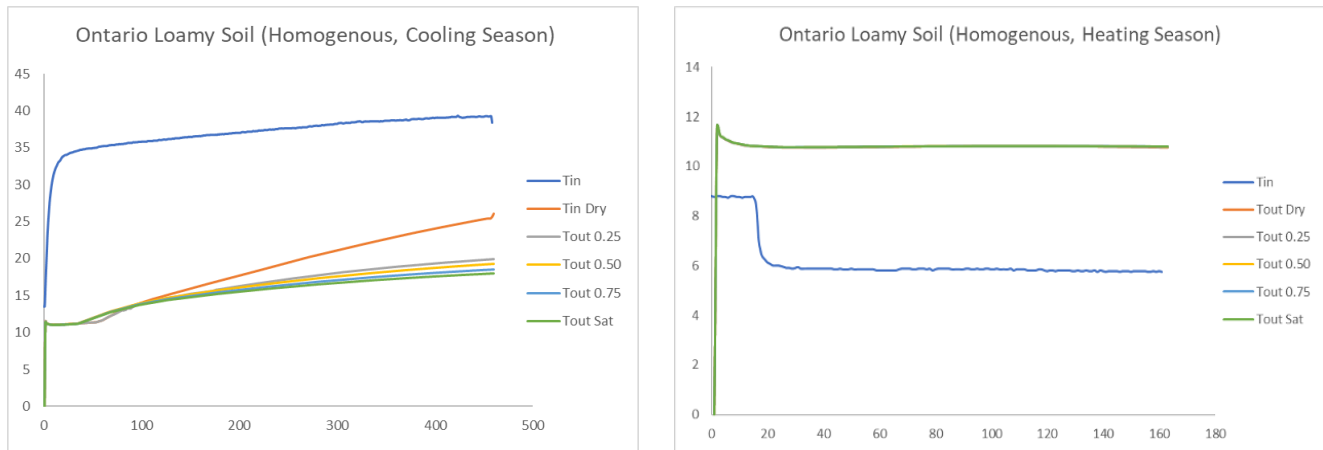


Figure 7: Homogeneous loamy soil model results using saturation levels from dry to fully saturated in increments of 0.25

D. Heterogeneous Soil Simulation

Soil data in Canada is sparse and incomplete which poses a barrier for soil-related research. As a result, a heterogeneous soil was created manually using three Ontario soil datasets (ON-04, ON-05 and ON-06) from the literature [5] and creating soil layers beneath the soil surface. As the soil layers were created manually, certain soil principles were followed to mimic what would more likely be seen in nature. The results of this simulation would not reproduce the exact heat exchange magnitude of an HSP in these conditions but rather speak to the general behaviour of the pile. Inlet temperatures from the cooling season were used in this test due to the negligible

fluctuations in heat transfer seen in the homogenous tests during the heating season. As seen in Table 4 the difference in heat exchange between dry soil and the fully saturated soil was approximately 366 W, which is 121 W less than the heat exchange seen under homogeneous sandy soil conditions. This small difference is due to the weighted average of thermal conductivities used to create the heterogeneous soil. While the weighted average of the heterogeneous saturated thermal conductivity is the same as that of the homogenous sand, the dry thermal conductivity of the heterogeneous soil is slightly lower than the sandy soil under the same thermal load (figure 8). This would have caused a slight reduction in heat exchange under fully saturated soil conditions.

TABLE 4

Thermal Load	HE _{Dry}	HE _{0.25}	HE _{0.50}	HE _{0.75}	HE _{Sat}
Cooling	3254.8W	3502.7W	3547.2W	3588.2W	3620.7W

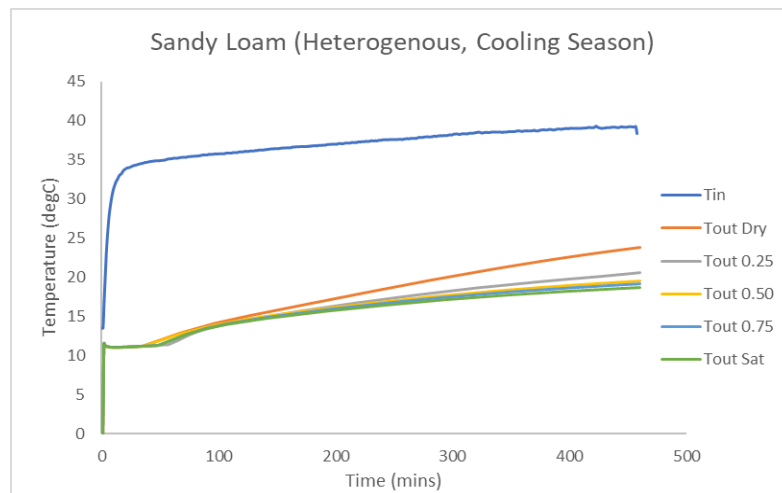


Figure 8: Simulation results for the heterogeneous soil (Sandy Loam) created under a cooling load

E. Limitations

As aforementioned, to reduce simulation times, the soil domain was considered a solid with varying soil physical and thermal properties based on the outlined simulation purposes. This assumption does not fully take into account the convective heating that takes place within the pores of the soils when filled with water. As such, this particular model could only allude to the HSP's general heat exchange behaviour and may not produce exact values. In addition, due to a lack of usable Canadian soil data, many assumptions were made regarding soil thermal properties, namely the specific ranges of heat capacity used for each soil type. Using these ranges assumes that heat capacity and water content have a directly linear relationship; this may not be necessarily the case depending on the other soil properties involved and the changes in soil thermal properties with temperature. In addition, the tests used in this study were short in duration and thus do not represent the steady state operation of the system. As such, longer tests are both necessary and planned as part of our future work.

SUMMARY AND CONCLUSIONS

Due to high costs, low initial return on investment and long payback periods, conventional geothermal systems have not seen widespread implantation across the globe. Helical steel piles have the potential to operate as a dual-purpose system, providing structural support to buildings while also acting as a heat exchanger for ground source heat pumps. This aspect of helical steel piles would reduce the associated costs of geothermal installations, addressing a key barrier. By modifying an existing COMSOL model of a single HSP that was validated with experimental data from a pilot project installed at our partner facility, the system's performance was simulated under varying soil conditions. The soil conditions were varied based on saturation content and heterogeneity using sand and loam soil data from two Ontario, Canada soils.

The results of the sandy soil model indicated that during the cooling season the greatest heat exchange can be seen under full soil saturation, yielding a change in temperature of 3641.2 W. During the heating tests for the same soil, however, heat exchange values were very small with an average of 793 W across all saturation types, likely due to the inlet temperatures being very close to the ground temperatures at the time that the inlet temperature data was taken (November). These trends were also seen in the simulation for the loamy soil. Under a cooling thermal load, the highest heat exchange was 3668.5 W under fully saturated conditions in the loamy soil. Under a heating load, the loam soil simulation also only predicted a temperature difference of 793 W. Heterogeneous soil was created using three Ontario, Canada soils and simulated under a cooling load for varying saturation contents. Overall, the results of the simulation were similar to both the sand and loam in terms of the HSP's heat exchange behaviour, however, the difference in heat exchange between dry heterogeneous soil and saturated heterogeneous soil was less than that of the homogenous soils. This was due to a lower weighted average of soil thermal conductivities under saturated conditions in the heterogeneous soil. Overall, soil moisture does play an important role as it pertains to ground heat exchange in the warmer months. However, the results of the heating season simulations did not indicate as strong of a dependence. To confirm this connection, it would be beneficial to improve the heating season simulations using data from colder months in the winter season. Future work will aim to focus on applying different physics to the COMSOL model to take into account the convective heat transfer within the pores of the soil as well as the impact of groundwater flow on heat transfer.

ACKNOWLEDGMENTS

The authors thank Innovia Geo Corp. for providing expertise, resources, and funding for the experimental site. The authors acknowledge the Canada Research Chairs program, the Natural Sciences and Engineering Research Council of Canada (NSERC), and the Independent Electricity System Operator Grid Innovation Fund for financial support.

REFERENCES

- [1] Nicholson, S. R. (2021). Characterization of a novel in-ground heat exchanger for applications in sustainable building energy and maintaining permafrost. <https://doi.org/10.32920/19852672.v1>
- [2] Nicholson, S.R., Mwesigye, A., Dworkin, S.B., 2019. Modelling and optimization of helical steel piles as in-ground heat exchangers for Ground-Source Heat Pumps. IOP Conf. Ser.: Mater. Sci. Eng. 609, 052026. <https://doi.org/10.1088/1757-899X/609/5/052026>
- [3] Jalaluddin, A. Miyara, K. Tsubaki, S. Inoue, and K. Yoshida, “Experimental study of several types of ground heat exchanger using a steel pile foundation,” *Renewable Energy*, vol. 36, no. 2, pp. 764–771, 2011.
- [4] Jalaluddin, Jalaluddin & Miyara, Akio. (2012). Thermal performance investigation of several types of vertical ground heat exchangers with different operation mode. *Applied Thermal Engineering*. s 33–34. 167–174. [10.1016/j.applthermaleng.2011.09.030](https://doi.org/10.1016/j.applthermaleng.2011.09.030).
- [5] Tarnawski, V. R., Momose, T., McCombie, M. L., & Leong, W. H. (2014). Canadian field soils thermal-conductivity data and modeling. *International Journal of Thermophysics*, 36(1), 119–156. <https://doi.org/10.1007/s10765-014-1793-z>
- [6] Alnefaie, K. A., & Abu-Hamdeh, N. H. (2020). Specific heat and volumetric heat capacity of some Saudian soils as affected by moisture and density. *International Journal of Materials*, 7. <https://doi.org/10.46300/91018.2020.7.8>
- [7] COMSOL Multiphysics (R) v. 5.3 (Stockholm: COMSOL AB)
- [8] Lyu, W., Pu, H., & Chen, J. (N. (2020). Thermal performance of an energy pile group with a deeply penetrating U-shaped heat exchanger. *Energies*, 13(21), 5822. <https://doi.org/10.3390/en13215822>
- [9] Hu, Z., Zhu, M., He, W., Meng, X., Yang, C., & Xu, Z. (2022). Experimental study and performance evaluation of a ground heat exchanger with different intermittent ratios and soil thermal properties. *Geothermics*, 102, 102402. <https://doi.org/10.1016/j.geothermics.2022.102402>
- [10] You, S., Cheng, X., Guo, H., & Yao, Z. (2014). In-situ experimental study of heat exchange capacity of CFG pile geothermal exchangers. *Energy and Buildings*, 79, 23–31. <https://doi.org/10.1016/j.enbuild.2014.04.021>



Experimental Performance Analysis of a Dual-Source Heat Pump Integrated with Thermal Energy Storage

Lingshi Wang

Xiaobing Liu
Anthony Gehl

Bo Shen
Liang Shi

Xiaoli Liu
Ming Qu

ABSTRACT

To mitigate disturbances to the electric grid resulting from the growing penetration of intermittent and decentralized renewable generation, a dual-source (air source and ground source) heat pump (DSHP) integrated with thermal energy storage (TES) was developed. The DSHP can use either ambient air or the shallow subsurface of the ground to provide space heating or space cooling to the building as the conventional heat pump and produce hot/cold water for charging TES. Using dual sources (air and ground) can reduce the required size of the expensive ground heat exchangers while retaining high energy efficiency. During the off-peak period, the DSHP cools/heats the TES with low-cost electricity or overproduced renewable power. The stored cooling/heating energy in the TES is released during peak hours of the electric grid to meet the thermal demands of the building without consuming electricity to run the DSHP. A 2-ton (7 kW) prototype DSHP was developed and integrated with a 50-gallon (189 L) TES tank filled with a phase change material. Field tests were conducted to characterize the performance of the integrated system operating in various operation modes.

INTRODUCTION

Renewable power generated with wind, solar, and geothermal energy can replace part of the fossil fuel consumption for electricity generation and thus reduce greenhouse gas emissions. However, the mismatch between the intermittent renewable power supply and the fluctuating electric demand limits the high penetration of renewable energy (MIT, 2011; King et al., 2011). Thermal energy storage (TES) has attracted increasing attention to addressing this challenge (Calderon et al., 2020; Guelpa and Verda, 2019; Wang et al., 2020, 2022).

Buildings in the United States consume 75% of all US electricity and are responsible for 80% of peak electric demand (EIA, 2018). Among all power consumption in buildings, 40%–70% is for thermal loads, including space heating and cooling (Wang et al., 2020). Because heat pumps can provide space cooling, space heating, and water heating, integrating TES systems with heat pumps could shift or level the behind-the-meter electric demand of buildings. When integrating

Lingshi Wang is an R&D Associate Staff, Xiaobing Liu (liux2@ornl.gov), Bo Shen and Anthony C. Gehl are Senior R&D Staff, and Xiaoli Liu is a postdoc at Oak Ridge National Laboratory. Liang Shi is a Ph.D. candidate and Ming Qu is a Professor at Purdue University. This manuscript has been authored by UT-Battelle, LLC, under contract DE-AC05-00OR22725 with the US Department of Energy (DOE). The US government retains and the publisher, by accepting the article for publication, acknowledges that the US government retains a nonexclusive, paid-up, irrevocable, worldwide license to publish or reproduce the published form of this manuscript or allow others to do so, for US government purposes. DOE will provide public access to these results of federally sponsored research in accordance with the DOE Public Access Plan (<http://energy.gov/downloads/doe-public-access-plan>).

TES with a heat pump, the TES can be charged using low-cost electricity to store cooling or heating energy during the off-peak period. The stored energy can be discharged during peak hours to meet the thermal demands of the building without consuming electricity to run the heat pump.

To prove the feasibility of integrating TES into the heat pump system for demand response, this study developed a 2-ton (7 kW) prototype dual-source (air source and ground source) heat pump (DSHP) integrated with a 50-gallon (189 L) TES tank filled with phase change materials (PCMs) for residential applications (i.e., single-family houses). This integrated system not only provides heating and cooling to a building but also produces hot/cold water for charging the TES. The addition of an air source allows the heat pump to extract heat from or reject heat to the ambient when the ambient air is at favorable temperatures for highly efficient operation. At other times, the heat pump will use the ground as its heat sink/source to retain high efficiency. Because the thermal load of the ground heat exchanger is reduced, the required size of the expensive ground heat exchangers can also be reduced. Thus, the system can be more economically competitive than conventional ground source heat pump systems while retaining high energy efficiency. Field tests were conducted to evaluate the performance of the DSHP operating in various operation modes. This paper presents the charging and discharging performance of the integrated TES and DSHP for cooling operation.

SYSTEM CONFIGURATION AND TEST FACILITY

A prototype DSHP was designed and built at the US Department of Energy's Oak Ridge National Laboratory (ORNL). As shown in Figure 1, the DSHP circulates the refrigerant through either of the two parallel source-side heat exchangers: a ground source tube-in-tube heat exchanger or an air source microchannel heat exchanger. On the load side, the DSHP also has two parallel heat exchangers: an indoor direct expansion (DX) coil for producing hot or cold air, and a brazed plate heat exchanger to produce hot or chilled water for storing energy in the TES. A four-way valve switches between cooling and heating operation modes. Two thermo-expansion valves control the exit superheat degrees of the air source and the ground source heat exchanger, respectively, when they are working as evaporators. An electronic expansion valve controls the superheat degree out of the brazed heat exchanger when producing chilled water to charge the TES. A liquid receiver and a suction line accumulator were installed at the liquid line and before the suction port of the compressor to buffer the refrigerant charge among multiple operation modes, including space cooling and heating, as well as cooling and heating energy storage, using ground or air source. Five motorized ball valves isolate unused heat exchangers and manage charging migration during mode transitions. Figure 1a shows the cooling mode operation of the DSHP system, and Figure 1b shows an integrated DSHP and TES system for a residential application.

Integrating a DSHP with a TES tank enables shifting electric demand for space heating/cooling from on-peak hours to off-peak hours of the electric grid. During the off-peak period, the DSHP can simultaneously or alternatively provide space heating/cooling and supplies heating/cooling energy to the TES. During the on-peak hours, the stored energy is discharged from the TES through a fan coil to heat or cool the building without consuming electricity to operate the DSHP. The integrated DSHP and TES can be operated in 14 different modes, as listed in Table 1.

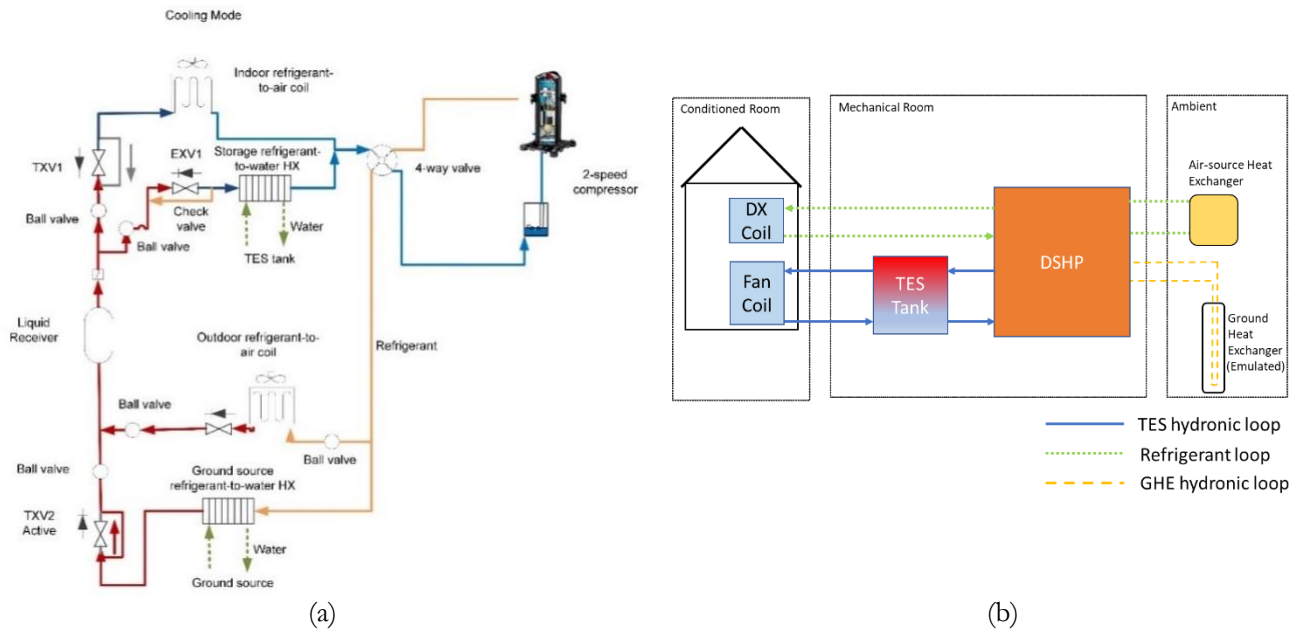


Figure 1 (a) Schematic of a DSHP in cooling mode, and (b) integration of a DSHP and TES in a residential application. EXV: electronic expansion valve; HX: heat exchanger; TXV: thermo-expansion valve

Table 1: Operating modes of the integrated DSHP and TES system

Mode	Source	Load	Performance
Heating	Ground	Space heating	Function tested
		Charging TES	Function tested
		Space heating and TES discharging	Function tested
	Air	Space heating	Function tested
		Charging TES	Function tested
		Space heating and TES discharging	Function tested
Cooling	Ground	Space cooling	Function tested
		Charging TES	Function tested (presented in this paper)
		Space cooling and TES discharging	Function tested
	Air	Space cooling	Function tested
		Charging TES	Function tested (presented in this paper)
		Space cooling and TES discharging	Function tested
TES discharge	Off	Space heating through fan coil unit	Function tested
		Space cooling through fan coil unit	Function tested (presented in this paper)

An experimental 2-ton (7 kW) DSHP integrated with a 50-gallon (189 L) TES tank filled with PCM was installed at ORNL's two-story Flexible Research Platform (FRP-2) at ORNL, as shown in Figure 2. ORNL's FRP-2 is a 3,200 ft² (297 m²) 2-story building with 10 zones and a 12-ton (42 kW) distributed ground source heat pump system, which comprises 4 extended range water source heat pump (WSHP) units and a common water loop that connects the source side of the WSHP units. The FRP hosts a ground source emulator, which is a mechanical system that can maintain the supply water temperature of the common water loop at a user-specified temperature within the range of 45°F to 95°F (7°C to 35°C). A pump circulates water flow through all the WSHP units. One of the WSHP units was modified to be a DSHP with a 2-ton (7 kW) cooling capacity. An outdoor unit containing a microchannel heat exchanger and an axial

fan is connected to the WSHP to enable air-source operation. There are more than 500 various sensors installed in the FRP-2 to measure the temperature, pressure, and flow rates of air, water, and refrigerants of the heat pumps and other HVAC systems in the building. The specifications of the measurement instrumentations for the integrated DSHP and TES system are provided in Table 2.

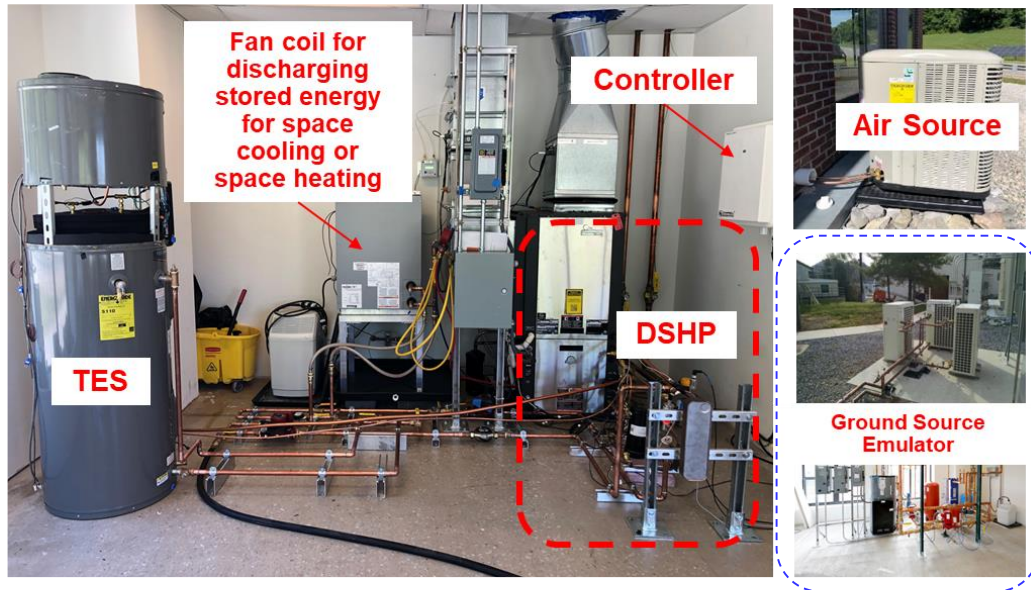


Figure 2 On-site photo of the developed DSHP and TES system

Table 2: Specifications of the measurement instrumentations

Measured property	Instrument	Range	Uncertainty
Water temperature	T-type thermocouple probes (Omega)	-270°C to 370°C	±0.5°C
Water flow rate	FTB4607 Long-Life Pulse Output Water Meters	0.22–20 GPM (0.83-75.7 LPM)	±1.5% of rate
Power	WNB-3Y-208-P Watt Node Pulse Electric Power Meter	0.375 Wh per pulse	±0.5% of reading
Air flow rate	Veltron DPT 2500-plus Differential Pressure and Flow Transmitter	0–1,760 CFM (0-2990 m ³ /h)	±0.25% of the full scale
Air humidity and temperature	HMT330 Humidity and Temperature Transmitters	0%–100% relative humidity (RH), -40°C to 180°C	±(1.5 + 0.015 × reading) %RH, ±0.2°C

RESULTS AND DISCUSSIONS

A series of tests were conducted to verify the function of each of the 14 operation modes listed in Table 1. Key performance metrics were evaluated based on the measured data, including heating and cooling capacity, coefficient of

performance (COP), and supply air and water temperature. The charging and discharging performances for cooling with a 70°F (21.1°C) heat sink temperature (from an air source or ground source) are presented in this paper. In the tests presented here, water/ice was used as the PCM given its low cost and high thermal conductivity, as described in Table 3. Water was sealed in 48 aluminum tubes, which are 36 in. (91 cm) tall with a 2 in. (5 cm) diameter. These tubes were filled into the TES tank and occupied 52% of the tank volume. Antifreeze solution (30% propylene glycol in volume) was used to fill the remaining volume of the TES tank and transfer heat between the DSHP and the water in the tubes. The shortcoming of using water as a PCM is that its melting/freezing temperature is fixed at 32°F (0°C), so its solid-liquid phase change is only for storing cooling energy. This TES tank can also be used for sensible heat storage. Other PCMs can be used to store cooling or heating energy at a higher phase-changing temperature. Performance tests of the TES using other PCMs are reported by Wang et al. (2022).

Table 3: Physical properties of the PCM than can be added to the TES tank

PCM type	Composition	Latent heat	Freezing temperature	Melting temperature	Thermal conductivity (20°C)	Specific heat capacity	Density	Volumetric latent heat
		J/g	°C	°C	W/(m·°C)	kJ/(kg·°C)	g/cm ³	J/cm ³
Organic	Methyl laurate	176	3	5	0.15 (liquid), 0.23 (solid)	1.7	0.87	153
Inorganic	Water	334	0	0	0.6 (liquid), 2.2 (solid)	4.2	1	307

The COP of the DSHP was calculated with Eq. (1):

$$COP = \frac{\dot{Q}_{hydr} + \dot{Q}_{DX}}{W} \quad (1)$$

where \dot{Q}_{hydr} is the cooling or heating energy from the plate heat exchanger for charging the TES, \dot{Q}_{DX} is the cooling or heating energy provided by the DX coil, and W is the compressor power draw.

\dot{Q}_{hydr} and \dot{Q}_{DX} were calculated with Eqs. (2) and (3), respectively.

$$\dot{Q}_{hydr} = \dot{m}_w c_{p,w} \Delta T_{hydr} \quad (2)$$

$$\dot{Q}_{DX} = \dot{m}_a \Delta h_a \quad (3)$$

where \dot{m}_w is the measured flow rate, $c_{p,w}$ is the specific heat (constant), and ΔT_{hydr} is the measured temperature difference between the inlet and outlet water at the plate heat exchanger; \dot{m}_a is the measured flow rate, and Δh_a is the enthalpy difference between the supply air and return air at the DX coil. Enthalpy was calculated based on the measured temperature and humidity of the air.

The accumulated energy charged in/discharged from the TES (E_{TES}) was calculated with Eq. (4).

$$E_{TES} = \int \dot{Q}_{TES} dt \quad (4)$$

where t is time and \dot{Q}_{TES} is the cooling or heating energy charged in/discharged from the TES, which was calculated with Eq. (5).

$$\dot{Q}_{TES} = \dot{m}_w c_{p,w} \Delta T_{tank} \quad (5)$$

where ΔT_{tank} is the temperature difference between the inlet and outlet of the tank, which are located at the top and bottom of the tank.

The state of charge (SOC) of the TES is defined as the ratio of the cumulative thermal energy charged into the TES to

the maximum thermal storage capacity of the TES, as expressed in Eq. (6),

$$SOC = \frac{E_{TES}}{Q_{TES,max}} \times 100\% \quad (6)$$

where $Q_{TES,max}$ is the maximum thermal storage capacity of the TES for cooling.

The state of discharge (SOD) is computed from Eq. (7).

$$SOD = 100\% - SOC \quad (7)$$

Figure 3 displays the charging performance of the TES tank in the DSHP system for cooling. As the charge of the TES tank started, the chilled antifreeze solution was supplied to the tank inlet at the bottom of the tank to store cooling energy inside the tank. Figure 3a shows that the tank inlet temperature first decreased from 51.6°F (10.9°C) to 21.3°F (-5.9°C) almost linearly. This process (from 11:59 to 12:11) was sensible cooling with a heat flow rate that varied from 5.17 to 1.46 kW (Figure 3b). The cooling COP dropped from 6 to 2.3 (Figure 3d) with the decrease in the tank inlet temperature. Since 12:11, the tank inlet temperature was maintained within a narrow range from 20.4°F to 21.7°F (-6.4°C to -5.8°C) with a cooling rate of 1.36–1.63 kW. This process was dominated by latent cooling with a cooling COP of approximately 2.13–2.44. Figure 3c shows that the antifreeze flow rate dropped in the same pattern as its temperature because of the increased viscosity of the antifreeze solution at lower temperatures. The state of charge in Figure 3b indicated that the TES tank took less than 4 h to be charged to 81% of its full capacity by the DSHP. The total cooling energy charged to the TES tank is 7.4 kWh, and the maximum storage capacity of the tank was 9 kWh when water was used as a PCM. For comparison, when only sensible cooling was stored in the 50-gallon (189 L) tank by cooling water from 51.6°F (10.9°C) to 32°F (0°C), 2.2 kWh of cooling energy can be stored. Thus, adding latent cooling of ice increases the cooling storage capacity by more than four times.

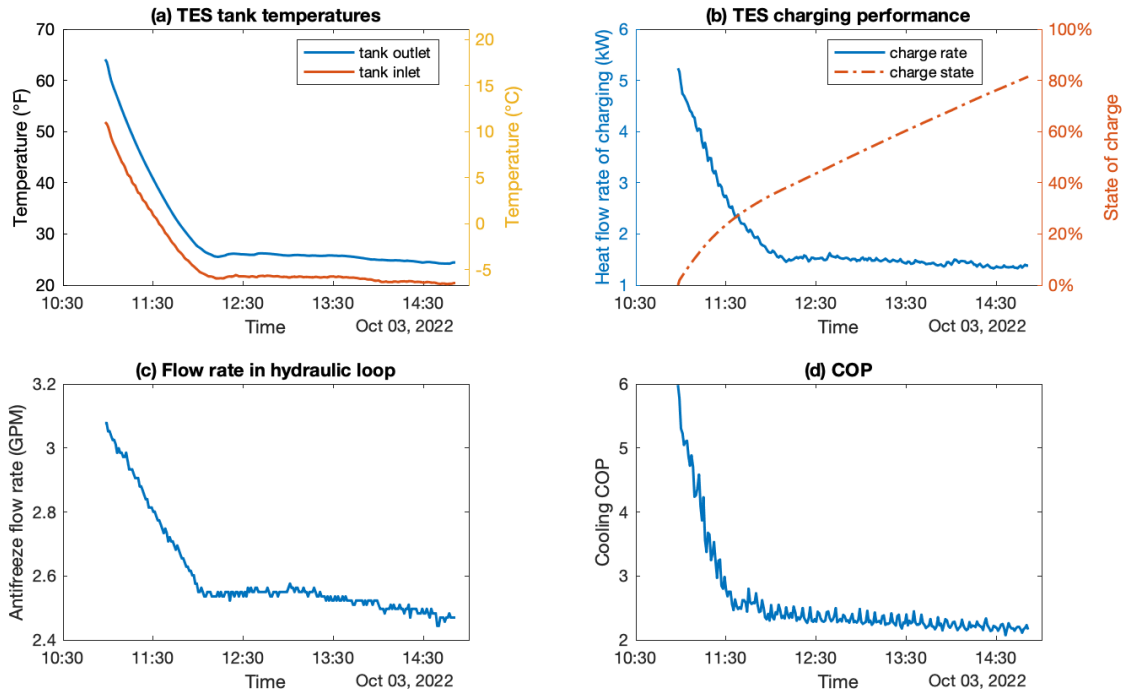


Figure 3 Cooling charge performance of the integrated DSHP and TES system running with an air source: (a) tank temperatures, (b) heat flow rate and state of charge, (c) flow rate of antifreeze, and (d) cooling COP.

Figure 4 presents the discharging performance of the TES tank for space cooling. As shown in Figure 4a, the TES tank provided chilled fluid at the outlet (at the bottom of the tank) with a temperature lower than 55°F (12.8°C) for approximately 2 h. The room temperature was maintained at the 75°F (23.9°C) set point with a fluctuation of around $\pm 0.5^\circ\text{F}$ ($\pm 0.3^\circ\text{C}$). During the process of (0) – (1) in the figure, from 15:38 to 16:12, the discharging rate (Figure 4b) dropped from 8.86 to 4.40 kW with an antifreeze flow rate of approximately 2.6 GPM (9.8 LPM) (Figure 4c). When the room temperature reached the set point, the TES discharging was suspended. The slope of the tank outlet (supply) temperature change was relatively small during this period, primarily because of the latent cooling capacity of the TES system. After the room temperature exceeded the upper limit of the temperature set point at 16:24, the TES tank discharged chilled water again until it reached a state of discharge of 81.2% at 17:49. The slope of the tank outlet temperature rise changed around 17:20 when most latent cooling was depleted (i.e., ice was melted in the tubes inside the tank). The higher slope at the process (2) – (3) in the figure indicates sensible cooling during this period. During a 2.2 h operation, the total cooling energy discharged from the tank was 7.98 kWh. The total discharged cooling was slightly higher than the total stored cooling because of the following two factors: (1) the tank temperature at the end of the discharge process was 3.45°F (1.9°C) higher than the starting temperature of the charging process, so more sensible cooling was released in the discharge process; and (2) the ice/frost cumulated on the surface of the plate heat exchanger and the hydronic piping during the charging process melted during the discharging process, which increased the cooling energy output. Overall, the roundtrip efficiency of the TES was nearly 1 with little heat loss.

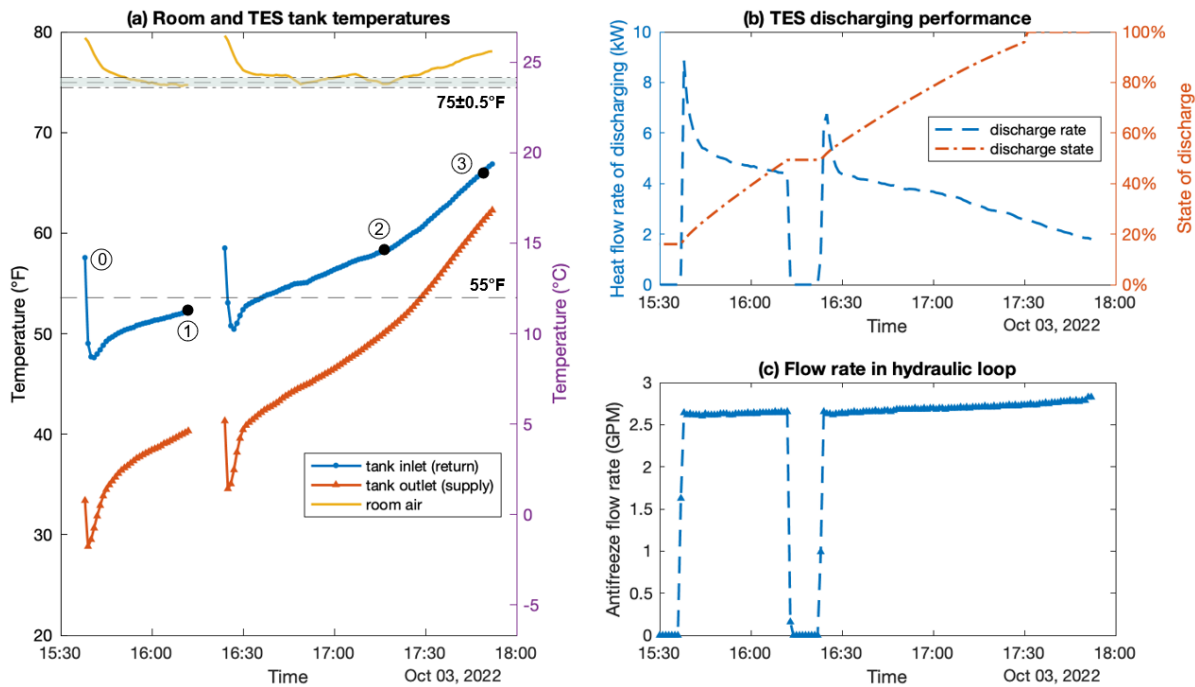


Figure 4 Discharging performance of a TES tank in the DSHP system: (a) room and tank temperatures, (b) heat flow rate and state of discharge, and (c) flow rate of antifreeze.

CONCLUSIONS AND FUTURE WORK

A 2-ton (7 kW) DSHP integrated with a TES that has 9 kWh thermal storage capacity was developed to condition room air and produce hot/cold water for charging TES either alternatively or simultaneously. The DSHP can use an air source

or a ground source (or both) depending on weather conditions. Field tests were conducted with the DSHP and TES system to evaluate its performance in various operation modes. The results presented in this paper indicate that the DSHP can cool the TES below the freezing point of water and make ice to store cooling energy. With the latent cooling of ice, the maximum storage capacity of the TES tank is 9.1 kWh, which is four times that of storing only sensible cooling in the 50-gallon (189 L) tank by cooling water from 51.55°F (10.9°C) to 32°F (0°C). It took 4 h for the DSHP to charge the TES to 81% of its full capacity using ambient air (ranging from 70°F (21.1°C) to 75°F (23.9°C)) as a heat source. During the ice-making process, the tank inlet temperature was maintained between 20.42°F and 21.65°F (-6.4°C and -5.8°C) with a heat transfer rate ranging from 1.36 to 1.63 kW and a cooling COP of approximately 2.13–2.44. The 7.4 kWh cooling energy stored in the TES tank was released in 2.2 h before the supply water temperature from the TES tank reached 55°F (12.8°C). Overall, the roundtrip efficiency of the TES was nearly 1 with little heat loss.

In future studies, the integrated DSHP and TES will be operated with automated control, either rule-based or model-predictive, to demonstrate the load-shifting performance of the system under real weather conditions in ORNL's FRP-2. Future studies will also include replacing the water in the aluminum tubes with an organic PCM, methyl laurate, which can be frozen at 37.4°F (3°C) and melted at 41°F (5°C). The higher freezing and melting temperature of methyl laurate may allow the heat pump to operate at a higher evaporating temperature and subsequently with a higher COP. However, methyl laurate has a much lower thermal conductivity than ice. Carbon fiber inserts will be added to the methyl laurate to increase heat transfer from the tube surface to and within the methyl laurate.

ACKNOWLEDGMENTS

This study was funded by the US Department of Energy (DOE) Office of Energy Efficiency and Renewable Energy, Geothermal Technologies Office. This manuscript has been authored by UT-Battelle, LLC, under contract DE-AC05-00OR22725 with the US Department of Energy (DOE). The US Government retains and the publisher, by accepting the article for publication, acknowledges that the US government retains a nonexclusive, paid-up, irrevocable, worldwide license to publish or reproduce the published form of this manuscript or allow others to do so, for the US government purposes. DOE will provide public access to these results of federally sponsored research in accordance with the DOE Public Access Plan (<http://energy.gov/downloads/doe-public-access-plan>).

REFERENCES

- Calderón, A., C. Barreneche, K. Hernández-Valle, E. Galindo, M. Segarra, and A. I. Fernández. 2020. *Where is Thermal Energy Storage (TES) research going? – A bibliometric analysis*. *Solar Energy* 200: 37–50.
- Guelpa, E. and V. Verda. 2019). *Thermal energy storage in district heating and cooling systems: A review*. *Applied Energy*, 252: 113474.
- King, J., T. Mousseau, and R. Zavadil. (2011). Eastern Wind Integration and Transmission Study. National Renewable Energy Laboratory, Golden, CO.
- MIT (2011). The Future of the Electric Grid. Massachusetts Institute of Technology, Cambridge, MA.
- U.S. Energy Information Administration (2018). Annual Energy Outlook 2018. Washington, DC. <https://www.eia.gov/outlooks/aeo/2>
- Wang, L., Xiaobing Liu, Zhiyao Yang, Kyle R. Gluesenkamp. (2020). *Experimental study on a novel three-phase absorption thermal battery with high energy density applied to buildings*. *Energy*, 208:118311.
- Wang, L., X. Liu, M. Qu, L. Shi, and X. Zhou. (2022). “*Experimental Evaluation of Thermal Storage Performance of a Dual-Purpose Underground Thermal Battery*.” Proceedings of 2022 GRC Conference, August 28-30, Reno, Nevada

Long-term sustainable operation of hybrid geothermal systems through optimal control

Iago Cupeiro Figueroa

Lieve Helsen

ABSTRACT

Hybrid geothermal systems such as hybrid GEOTABS typically comprise a geothermal heat pump that supplies the main building thermal energy needs, complemented by a fast-reacting supplementary production and/or emission system for the peak building thermal loads. Optimal predictive controllers such as Model Predictive Control (MPC) are desired for these complex systems due to their optimized and automated energy savings potential (while providing the same or better thermal comfort) thanks to system integration and their anticipative action. However, the predictions of these controllers are typically limited to a few days. Consequently, the controller is unaware whether abusive energy injection/extraction into/from the soil will deplete the source over the years. This paper investigates in which cases the long-term dynamics of the borefield ought to be included in the MPC formulation. A simulation model of a hybrid GEOTABS system is constructed. Different borefield sizes, ground imbalance loads, and electricity/gas ratios are evaluated. The model control inputs are optimized to minimize the energy use in 5 years through (i) a reference Optimal Control Problem (OCP) for the 5 years, solved in hourly time-steps and (ii) an MPC control with a prediction horizon of 1 week. The obtained results reveal that MPC can be up to 20% far from the true optimal, especially in the cases where the borefield is undersized and there is a large cost gap between the different energy systems.

INTRODUCTION

Optimal control of buildings relies on predicting their behaviour using techniques such as mathematical modelling, data science or a combination of both (Arroyo, (2022)). One common feature of these approaches is that they optimize towards future system behaviour, typically for a few days. However, the time constant of the ground dynamics in ground source heat pump systems is too large to be captured by these prediction windows. Consequently, the controller is unaware of whether (i) is achieving an optimal solution and (ii) will deplete the ground-source in the long term, thereby hampering the sustainable use of the ground.

The borefield long-term dynamics can be well predicted using its characteristic thermal response function or g-function (Eskilson (1987)). Thus, this article follows a physics-based Model Predictive Control (MPC) approach, eliminating the need for large training datasets. MPC uses a mathematical model of the building envelope and the energy system along with forecasted disturbances (weather and occupancy) to predict the building dynamic behavior and the energy system efficiencies over a prediction horizon of typically a few days. An optimization problem finds the optimal control input sequence that minimizes an objective function (energy use, CO₂ emissions, operational costs...) while a set of thermal comfort and technical constraints is enforced. Only the first inputs of the sequence are applied as the optimization problem is recursively solved at each control time step.

Few authors have proposed formulations to incorporate the borefield long-term dynamics. Verhelst (2012) and Jorissen (2018) introduced a penalty cost to the dominant ground load in the objective function to reduce the borefield yearly

Iago Cupeiro Figueroa (iagocupeiro@protonmail.com) is a former researcher (now building control expert at DeltaQ NV/SA) and Lieve Helsen is professor at the Mechanical Engineering Department in KU Leuven.

imbalances. However, the determination of such a penalty relies on trial-and-error. Antonov (2014) imposed yearly cyclic conditions on the ground temperatures in an optimal control problem (OCP) of one year. Still, the approach can be sub-optimal because (i) a yearly thermal imbalance can be allowed depending on the borefield size and (ii) the freedom of MPC to take decisions is more limited due to the ground temperatures constraints. Cupeiro Figueroa et al. (2020) extended the MPC objective function with a shadow cost that estimates the overall yearly objective. The performance of the approach depends on a set of long-term predictions of the building heating and cooling loads. The contribution of this paper is to take a step back and investigate in which cases the long-term dynamics of the borefield ought to be included in the MPC formulation.

METHODOLOGY

To that end, we construct a model of a building equipped with a hybrid geothermal system using verified high-fidelity models from the Integrated District Energy Assessment Simulations (IDEAS) Modelica library (Jorissen et al. 2018). The model equations are then reformulated into a non-linear optimization problem using Toolchain for Automated Control and Optimization (TACO) (Jorissen et al. 2019). The optimization problem aims at finding the control inputs that minimize a target function while keeping thermal comfort in the building. This optimization problem is solved in hourly time-steps over a 5-year period (i) once covering the whole 5-year period (OCP) and (ii) recursively each hour for the upcoming week (receding horizon, MPC). Two target functions are evaluated: minimization of the energy costs and minimization of the operational costs. In addition, the optimization is solved for different borefield sizes and different levels of borefield imbalance. The results of both approaches are then compared for each specific case.

Case study

The building is modelled as a hybrid GEOTABS (Himpe et al. (2018)) represented in Figure 1, i.e. it comprises a geothermal heat pump (GEO) that supplies low temperature heating and uses passive cooling for high temperature cooling through a thermally activated building structure (TABS). The hybrid character lies in the extension with a fast-reacting auxiliary production and/or emission system for the peak periods. In this case, an additional gas boiler for heat production and an active chiller for cold production are installed. The building can also choose between thermally activating the building structure (TABS) through embedded pipes and air conditioning as the slow and fast-reacting emission systems. Thus, the building case study is hybrid both at the production and emission sides. However, the gas boiler and the chiller can only supply energy to the fast-reacting emission system whereas the TABS are only fed by the ground source heat pump (GSHP) or passive cooling heat exchanger.

The control input variables include the control of the production systems: u_1 for the GSHP, u_2 for the gas boiler, and u_3 for the chiller; the valve openings that control the mass flow rates (and in consequence the heat/cold supply) to the different emission systems u_4 , u_5 , u_6 and u_7 and the 3-way valve that determines the TABS mode u_8 . Since non-linear optimization problems do not accept binary inputs, this 3-way mixing valve needs to be considered as modulating in the simulation study. However, in practice, this valve is expected to be on/off to choose between heating or cooling mode in TABS. All pumps and fans work at a constant pressure head.

Table 1 lists the equations of the components presented in Figure 1. The HVAC equipment is sized to supply the design heat and cold loads, computed according to the standard ISO 12831-1:2017. For specific details on the design nominal values and the used fit coefficients, we refer to the work of Cupeiro Figueroa (2021). The building is modelled as a single space of 1200 m² using the IDEAS library *RectangularZone* component, which assumes a perfectly mixed air volume within a rectangular construction geometry subjected to dynamic heat transfer relations. The outer walls, roof/floor and glazing U-values are 0.21, 0.18 and 1.3 W/(m²K) respectively. Internal walls are also included to account for the internal

thermal mass of the building. The building is assumed to be located in Brussels, Belgium, and as such a typical meteorological year weather file is used. Equation 1 shows the GSHP correlations which assume a linear COP and condenser power, where A_i are the fit coefficients, and $T_{eva,in}$ and $T_{con,in}$ are the inlet working fluid temperatures of the evaporator and condenser and $T_{eva,nom}$ and $T_{con,nom}$ are the nominal temperatures of the evaporator and condenser, respectively. The gas boiler (Equation 2) and the chiller (Equation 3) are assumed to supply/extract heat in linear relation to their modulation signal. While the gas boiler is assumed to have a 100% efficiency, the chiller performance is dependent on the outdoor temperature T_{out} , with B_i being the fit coefficients. Although in this case all pumps are considered to work at a constant pressure head, the pressure drops that some of them need to overcome can vary as a function of the valves opening $u_4, u_5, u_6,$ and u_7 . For the hydraulic schematic in Figure 1, it is trivial that only the passive cooling pump power $\dot{W}_{pum,pc}$ and the heat pump condenser pump power $\dot{W}_{pum,hp}$ are affected by these valve openings. The 3-way valve opening u_8 affects the TABS heating and cooling pumps, but their sum remains constant. The heat exchanger is based on the NTU-epsilon method for counter-flow heat exchangers as formulated in Equation 5, where \dot{C}_{min} and \dot{C}_{max} are the minimum and maximum heat capacity rates, \dot{C}_r is the heat capacity ratio, NTU is the number of transfer units, ϵ is the effectiveness of the heat exchanger and $T_{hex,bot,in}$ and $T_{hex,cold,in}$ are the inlet temperatures in the heat exchanger at the hot and the cold side, respectively. The circulation pump model corresponds to a slightly modified version of the IBPSA library model based on similarity laws (Wetter (2013)). A flow coefficient k correlates the pump pressure head Δp and the corresponding mass flow rate \dot{m} (Equation 6a). The pump electric power \dot{W}_{pum} cubically increases with the mass flow rate, with \dot{m}_{nom} being the nominal mass flow rate of the pump and $\dot{W}_{pum,nom}$ the corresponding nominal power (Equation 6b). The borefield model corresponds to the analytical long-term model used by Cupeiro Figueroa et al. (2020), which is based on a radial resistance-capacitance network to model the borehole short-term heat transfer and the temporal superposition of the g-function and a continuous load-shifting algorithm formulation to model the ground long-term heat transfer.

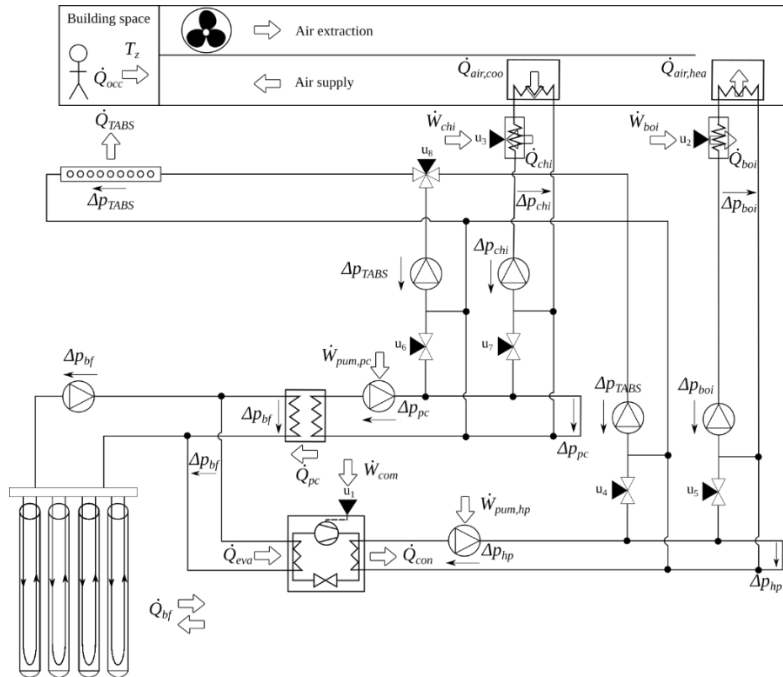


Figure 1 Schematic presentation of the considered hybrid GEOTABS case, main energy flows, and fluid network pressure drops.

Table 1. Model equations of HVAC components presented in Figure 1. Specific design details can be found in Cupeiro Figueroa (2021)

Component	Equations
Zone	IDEAS <i>Zone</i> model. See description by Jorissen et al. (2018)
Ground source heat pump	$\dot{Q}_{con} = u_1 \dot{Q}_{con,nom}$ (1a)
	$COP = A_1 + A_2 (T_{eva,in} - T_{eva,nom}) + A_3 (T_{con,out} - T_{con,nom})$ (1b)
	$\dot{W}_{com} = \dot{Q}_{con} / COP$ (1c)
	$\dot{Q}_{eva} = \dot{Q}_{con} - \dot{W}_{com}$ (1d)
Gas boiler	$\dot{Q}_{boi} = u_2 \dot{Q}_{boi,nom}$ (2a)
	$\dot{W}_{boi} = \dot{Q}_{boi}$ (2b)
Chiller	$\dot{Q}_{chi} = u_3 \dot{Q}_{chi,nom}$ (3a)
	$EER = B_1 + B_2 T_{out}$ (3b)
	$\dot{W}_{chi} = -\dot{Q}_{chi} / EER$ (3c)
Valves	$\dot{m}_i = u_i \dot{m}_{nom}$ (4a)
	$\dot{m}_i = u_i \dot{m}_{nom,1} + (1 - u_i) \dot{m}_{nom,2}$ (4b)
Heat exchanger	$\dot{C}_r = \dot{C}_{min} / \dot{C}_{max}$ (5a)
	$NTU = UA / \dot{C}_{min}$ (5b)
	$\varepsilon = \frac{1 - e^{-NTU(1-\dot{C}_r)}}{1 - \dot{C}_r e^{-NTU(1-\dot{C}_r)}}$ (5c)
	$\dot{Q}_{hex} = \varepsilon \dot{C}_{min} (T_{hex,hot,in} - T_{hex,cold,in})$ (5d)
Pump/fan	$\Delta p = (\dot{m} / k)^2$ (6a)
	$\dot{W}_{pum} = (\dot{m} / \dot{m}_{nom})^3 \dot{W}_{pum,nom}$ (6b)
Borefield	Borefield analytical model. See description by Cupeiro Figueroa et al. (2020)

Considered cases

The methodology is applied for three different ground loads representing a different level of building and borefield imbalance, manipulated by varying the occupancy internal gains \dot{Q}_{occ} of the building: an extraction-dominated case (ED), an injection-dominated case (ID) and a balanced case (B) are considered. The borefields (with H_b the borehole length) are sized using the modified ASHRAE equation (Ahmadfard and Bernier (2018)) to keep the average fluid temperature between 2 °C and 18 °C using ground loads computed from a previous dynamic simulation with MPC in the building but assuming a perfect source (i.e., infinite energy can be extracted from the field) as the borefield. Size 1 uses the three load pulses, corresponding to an oversized borefield that can cover all ground loads. Size 2 applies the monthly load pulse of the dominant side, corresponding to a slightly undersized borefield. Size 3 only considers the monthly load pulse of the non-dominant side, corresponding to an extremely undersized borefield. For the balanced case, only two sizes are considered since the difference between monthly loads is negligible. The borefield is a 2x2 squared borefield with a relative distance between boreholes of 6 m, an undisturbed ground temperature T_s of 10 °C, a ground thermal conductivity k_g of 2 W/(mK), a ground thermal diffusivity a_g of 9.26E-7 m²/s and a borehole thermal resistance R_b of 0.1 mK/W. The considered cases and the ground loads resulting from the MPC dynamic simulation are summarized in Table 2. For a detailed description of the other borefield parameters (which are kept constant), we refer to Cupeiro Figueroa (2021).

Table 2. Summary of the considered borefield cases and used ground loads in the ASHRAE equation.

	Extraction-dominated (ED)	Injection-dominated (ID)	Balanced (B)			
\dot{Q}_{occ} [kW]	0	7.5	3.8			
Size 1 – H_b [m]	122.0	169.8	114.3			
Size 2 – H_b [m]	57.2	59.0	37.5			
Size 3 – H_b [m]	12.9	18.0	N/A			
	Extraction	Injection	Extraction	Injection	Extraction	Injection
q_b [kW]	-13.5	11.9	-13.1	21.2	-13.2	17.5
q_m [kW]	-6.3	1.5	-2.0	6.5	-4.2	4.1
q_y [kW]	-2.0	0.0	0.0	2.1	0.0	0.0

OPTIMIZATION SPECIFICATIONS

A closed-loop non-linear optimization problem is set up using the same building model equations, i.e. there does not exist model mismatch, and state updates are not necessary. In addition, perfect weather predictions are considered, eliminating uncertainties of any kind. The initial conditions set the building states at 20 °C, the borefield states at the undisturbed ground temperature, and the weather conditions at the beginning of the heating season. The optimization problem is subjected to the model equations and the target function can be formulated as:

$$\min_{u_k} J = \min_{u_k} \sum_{k=1}^N [c_{el} \dot{W}_{com,k} + c_g \dot{W}_{boi,k} + c_{el} \dot{W}_{chi,k} + c_{el} \dot{W}_{pum,pc,k} + c_{el} \dot{W}_{pum,hp,k} + \sum_{j=1}^{n_s} \sigma_{j,k} s_{j,k}] \Delta t_k \quad (7)$$

where the terms c_{el} and c_g represent the electricity and gas price respectively. For the minimization of the energy use case, these terms are set to 1, whereas for the minimization of the operational costs the considered electricity/gas price ratio is 5:1. Instead of hard constraints, a set of n_s quadratic penalization costs $s_{j,k}$ is introduced to ensure feasibility, and weighted with a scaling factor $\sigma_{j,k}$ to speed up the optimization, including:

1. The violation of the lower comfort bound, set at 21 °C and with a –5 °C setback during night.
2. The violation of the upper comfort bound, set at 25 °C and with a +5 °C setback during night.
3. The GSHP lower temperature safety constraint, set at 0 °C.
4. The GSHP upper temperature safety constraint, set at 40 °C.
5. A dew point temperature protection for TABS imposed on the water temperature to avoid condensation of air humidity on the surfaces.
6. A constraint to avoid the use of the passive cooling heat exchanger for heating the building.

The number of steps N depends on whether an OCP or MPC is formulated. The former solves the optimization problem in one shot for a number of steps $N=43800$ (5 years in hourly steps), whereas the latter recursively solves the optimization problem at each hourly step for a number of steps $N=14$ using an increasing time-step Δt_k that covers a period of one week.

RESULTS AND DISCUSSION

Target: minimizing energy use

Since we consider the OCP to be the best obtainable result, an MPC efficiency is defined as the ratio between the total energy use of the MPC and the total energy use of the OCP. Table 3 compares these efficiencies for each borefield size and imbalance load using the energy use minimization formulation. As expected, the cases where the borefield is oversized present almost 100% efficiency since there is no risk of depleting the ground source. The small loss of optimality is caused due to the accumulation of minor errors caused by not considering the full horizon. For the extraction-dominated and balanced cases, there is a substantial drop in the MPC efficiency for the undersized borefields. Surprisingly, the efficiency losses in the injection-dominated cases are not as considerable as in the other two cases and especially given the energy use difference between the passive cooling pump and the active chiller. This effect is later explained.

Table 3. MPC efficiency for each considered case when minimizing the energy use.

	Extraction-dominated (ED)	Injection-dominated (ID)	Balanced (B)
Size 1	99.1%	98.02%	98.9%
Size 2	81.0%	96.7%	79.4%
Size 3	83.2%	93.4%	N/A

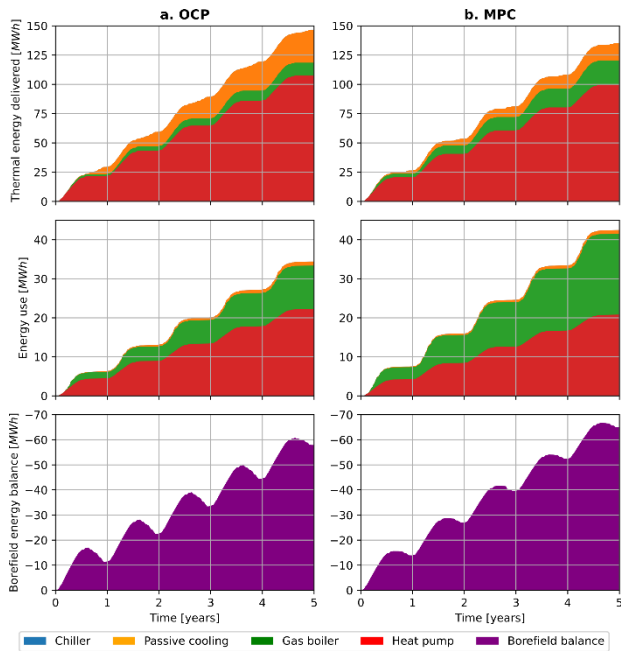


Figure 2 Thermal energy delivered, energy use, and borefield energy balance for Case ED – Size 2.

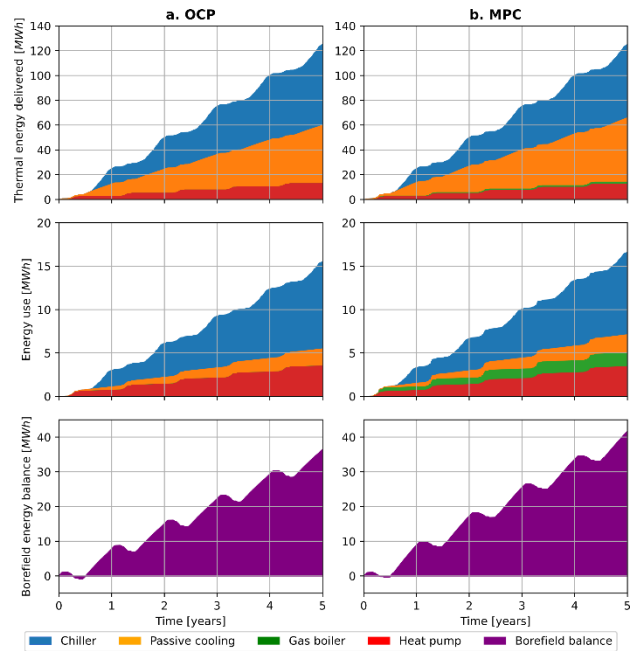


Figure 3 Thermal energy delivered, energy use, and borefield energy balance for Case ID – Size 3.

All cases where the MPC efficiency is lower than 95% are further analyzed in Table 4. Figure 2 shows the evolution of the building's main energy flows over the 5 years for Size 2 in the extraction-dominated case. Since the borefield is undersized, both optimizations deliberately recirculate heat from the building (from the GSHP and external gains) to

the source-side circuit to keep using the GSHP over the gas boiler. This behavior is optimal since the energy use of the gas boiler is in the order of 5 times higher due to the GSHP COP, thus covering all heating needs by the gas boiler would imply an increase in energy use. The heat re-circulation is achieved using the 3-way mixing valve that regulates the amount of heat/cold that is supplied to the TABS, and which connects the heating and cooling circuits. This behavior is largely magnified in Size 3. However, the OCP limits this behavior and shifts the thermal regeneration of the ground in summer by working at the lower comfort limit as shown in Figure 4, therefore minimizing further the use of the gas boiler.

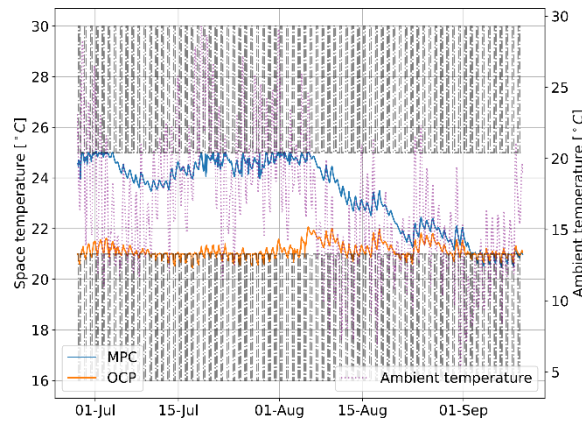


Figure 4 Temperature evolution of the building space at the end of the cooling season for Case ED – Size 2. Black dashed lines represent the comfort boundaries.

Table 4. Performance results for the cases with MPC efficiency < 95%.

		ED – Size 2		ED – Size 3		ID – Size 3		B – Size 2	
[MWh]		OCP	MPC	OCP	MPC	OCP	MPC	OCP	MPC
Heat pump (w/ pump)	\dot{Q}	107.3	99.7	117.0	117.6	13.2	12.8	52.0	48.9
	\dot{W}	22.3	20.8	24.5	23.5	3.55	3.47	11.2	10.6
Gas boiler	\dot{Q}	11.1	20.7	60.0	78.1	0.01	1.56	1.01	5.37
	\dot{W}	11.1	20.7	60.0	78.1	0.01	1.56	1.01	5.37
Passive cooling pump	\dot{Q}	28.2	15.0	82.4	87.0	47.1	51.9	55.8	51.0
	\dot{W}	1.06	1.00	1.18	1.18	1.97	2.13	1.62	1.55
Active chiller	\dot{Q}	0.00	0.00	0.00	0.47	65.4	59.3	1.33	0.89
	\dot{W}	0.00	0.00	0.00	0.08	10.1	9.52	0.23	0.16
Recirculated heat	\dot{Q}	3.34	6.53	65.9	74.1	0.98	2.78	2.30	4.31
Total energy use	\dot{W}	34.5	42.5	85.7	102.9	15.6	16.7	14.1	17.7

For the injection-dominated case, the OCP energy use of passive cooling is lower than MPC, but due to a higher heat recirculation by the latter one as shown in Figure 3. This heat recirculation eventually decreases the passive cooling capacity for summer, and in turn, the same temperature behaviors as shown in Figure 4 are observed. This also causes a marginal increase in the energy use of the chiller. Nevertheless, the main source of energy use savings comes from eliminating the need for the gas boiler. Size 3 is undersized for both heating and cooling and the OCP gives preference to the heating side due to the larger differences in energy use between the GSHP and the gas boiler compared to passive

cooling and the chiller. In addition, the cost of regenerating the soil to have more cooling capacity for the next season using the GSHP is much higher than the cost of regenerating the soil to have more heating using the passive cooling pump. Due to these energy use differences, the balanced undersized case also shows similar behavior to the extraction-dominated cases, giving more priority to use the gas boiler as little as possible.

Target: minimizing operational costs

Table 5 compares the MPC efficiencies for each borefield size and imbalance load using the operational costs minimization formulation. All MPC efficiencies are above 95%. The energy use differences between the GSHP and the gas boiler are offset by the electricity/gas price ratio considered. This highlights that the design of the building energy system must go hand in hand with these ratios. The concept of “undersized” borefield is correlated to these factors.

Table 5. MPC efficiency for each considered case when minimizing the operational costs.

	Extraction-dominated (ED)	Injection-dominated (ID)	Balanced (B)
Size 1	98.5%	99.2%	98.6%
Size 2	98.9%	95.9%	98.1%
Size 3	97.1%	96.6%	N/A

CONCLUSION

This paper presents an MPC benchmarking study against its reference OCP in a modular hybrid GEOTABS building case. Results show that the performance of MPC is close to the optimal solution in the cases where the borefield is sized to cover all building’s loads. However, for undersized borefields that aim at exploiting the hybrid characteristics of the building, there is a substantial loss of performance by the MPC since it does not account for the long-term effects. When a high electricity/gas price ratio is included in the optimization, the MPC efficiency increases in all cases. This is logical since all borefields were designed based on the ground energy loads and not the cost of energy. Next steps towards a performance analysis for different electricity/gas and COP ratios as well as design criteria are discussed in Cupeiro Figueroa (2021) and left for future work.

In general, due to the low cost of passive cooling, it is beneficial to provide extra cooling in summer to regenerate the ground source and avoid the use of the less efficient gas boiler in winter. On the other hand, providing extra heating through the GSHP does not seem to be a cost-effective way of regenerating the ground in the long-term due to its similar costs compared to the active chiller and the ground losses. A cheap regeneration solution (from the operational perspective) such as solar collectors or sewer water recovery may be of consideration for future study. Long-term MPC formulations can increase the MPC efficiency (Cupeiro Figueroa and Helsen (2022)) and should be further explored when these seasonal energy systems are installed.

NOMENCLATURE

α	=	Thermal diffusivity (m ² /s)	MPC	=	Model Predictive Control
Δ	=	Associated unit increase or difference (-)	OCP	=	Optimal Control Problem
ϵ	=	Effectiveness (-)	p	=	Pressure (Pa)
\dot{C}	=	Heat capacity flow (W/K)	\dot{Q}	=	Heat flow rate (W)

COP	=	Coefficient of performance (-)	R	=	Thermal resistance (K/(mW))
EER	=	Energy efficiency ratio (-)	T	=	Temperature (°C or K)
GSHP	=	Ground source heat pump	TABS	=	Thermally activated building structure
IDEAS	=	Integrated District Energy Assessment Simulations	TACO	=	Toolchain for Automated Control and Optimization
k	=	Thermal conductivity (W/(mK)) or flow coefficient (-)	u	=	System input (-)
\dot{m}	=	Mass flow rate (kg/s)	\dot{W}	=	Energy use (-)

Subscripts

b	=	Borehole	hex	=	Heat exchanger
bf	=	Borefield	hp	=	Heat pump
boi	=	(Gas) boiler	max	=	Maximum
chi	=	Chiller	min	=	Minimum
con	=	Condenser	nom	=	Nominal
com	=	Compressor	occ	=	Occupancy
eva	=	Evaporator	pc	=	Passive cooling

REFERENCES

- Ahmadfard, M. and Bernier, M., 2018. *Modifications to ASHRAE's sizing method for vertical ground heat exchangers*. Science and Technology for the Built Environment, 24(7), pp.803-817.
- Antonov, S. 2014. *Should the optimization horizon in optimal control of ground-coupled heat pump systems cover the inter-seasonal time scale?* ASHRAE Transactions 120, 346
- Arroyo, J. 2022. *Synergy Between Control Theory and Machine Learning for Building Energy Management*. Ph.D (Doctoral dissertation, Thesis). Department of Mechanical Engineering, KU Leuven, Leuven, Belgium (2022)
- Cupeiro Figueroa, I., Cimmino, M. and Helsen L., 2020. *A methodology for long-term model predictive control of hybrid geothermal systems: The shadow-cost formulation*. Energies 13 (23). Special Issue: Advances in Ground Heat Exchangers and Ground-Coupled Heat Pumps.
- Cupeiro Figueroa, I., 2021. *Short- and long-term optimal control of hybrid GEOTABS buildings*. Ph.D (Doctoral dissertation, Thesis). Department of Mechanical Engineering, KU Leuven, Leuven, Belgium (2021)
- Cupeiro Figueroa, I. and Helsen L. 2022. *Long-term optimal control of hybrid ground source heat pump systems. How far are we from the optimum?* Heat Pumping Technologies Magazine, Issue 2, 2022. <https://doi.org/10.23697/qfda-5j66>
- Eskilson, P., 1987. *Thermal analysis of heat extraction boreholes*. Ph.D (Doctoral dissertation, Thesis). Department of Mathematical Physics, University of Lund Lund, Sweden (1987).
- Himpe, E., Vercautere, M., Boydens, W., Helsen, L. and Laverge, J., 2018. *GEOTABS concept and design: state-of-the-art, challenges and solutions*. In REHVA Annual Meeting Conference Low Carbon Technologies in HVAC. Brussels, Belgium.
- Jorissen, F., 2018. *Toolchain for Optimal Control and Design of Energy Systems in Buildings*. Ph.D (Doctoral dissertation, Thesis). Department of Mechanical Engineering, KU Leuven, Leuven, Belgium (2018)
- Jorissen, F., Reynders, G., Baetens, R., Picard, D., Saelens, D. and Helsen, L., 2018. *Implementation and verification of the IDEAS building energy simulation library*. Journal of Building Performance Simulation, 11(6), pp.669-688.

- Jorissen, F., Boydens, W. and Helsen, L., 2019. *TACO, an automated toolchain for model predictive control of building systems: implementation and verification*. Journal of building performance simulation, 12(2), pp.180-192.
- Verhelst, C., 2012. *Model predictive control of ground coupled heat pump systems for office buildings*. Ph.D (Doctoral dissertation, Thesis). Department of Mechanical Engineering, KU Leuven, Leuven, Belgium (2012)
- Wetter, M., 2013. *Fan and pump model that has a unique solution for any pressure boundary condition and control signal*. In Proc. of the 13-th IBPSA Conference (pp. 3505-3512). Chambéry, France.



A control strategy evaluation framework for Ground Source Heat Pumps using Standing Column Wells

Giulio Tonellato
Gabrielle Beaudry

Michaël Kummert
Philippe Pasquier

José A. Candanedo

ABSTRACT

Standing column wells (SCWs) are efficient ground heat exchangers (GHEs) that have a significant cost saving potential. Recent developments have shown that they can also adapt successfully to cold climates despite previous concerns about operating near the freezing point. Therefore, new research frontiers are now being explored as the integration of this type of GHE to a real case study building model has hardly been analyzed until now. An institutional building has been selected for a SCW demonstration project in Mirabel, Canada. This paper includes in one single model the building the Heating Ventilation and Air Conditioning (HVAC) system and the SCWs. The objective is to develop a software framework to analyze the impact of building operation strategies on the entire system during winter. Peak loads revealed to be the most critical points to control as the groundwater can freeze if the heat extraction is too high. Night indoor air temperature setbacks can bring significantly high peak loads whenever the building is heated to be occupied during the day. This paper shows that, using a bleed ratio above 20 %, a night setback can be successfully operated ramping up the temperature in around 3 hours.

INTRODUCTION

Worldwide efforts to fight global warming have resulted in stricter energy efficiency standards and regulations, particularly in the building sector (UNFCCC, 2015). Ground Source Heat Pumps (GSHP) have been identified as a technology with great energy savings potential and worldwide application potential (Sarbu and Sebarchievici, 2014). However, high drilling costs for conventional closed-loop Ground Heat Exchangers (GHE) are slowing down mass adoption of the GSHP technology (Alshehri et al., 2019). For this reason, different GHEs, have been studied over the years such as open-loop systems, that use groundwater as a heat carrier fluid for the heat pump, being therefore able to operate closer to the undisturbed ground temperature, with thermodynamic efficiency advantages (Snijders and Drijver, 2016). These systems need shallower or fewer boreholes than closed-loop GHE, thus significantly reducing the investment costs (Snijders and Drijver, 2016). However, the design of pumping and injection wells often requires heavy and expensive field investigations to ensure that the site has suitable hydrogeological conditions and that the aquifer is productive enough to sustain the operation of GSHPs (Pasquier et al., 2016).

Standing column wells (SCW) offer an interesting alternative to both systems: they draw water from the ground as open-loop systems, but the pumped groundwater is for the most part reintroduced in the same boreholes (Pasquier et al., 2016). For this reason, field investigations are not as extensive as for fully open wells. Moreover, a portion of the groundwater can also be reinjected in a separate well if required by the local jurisdiction. This process (called “bleed”

Giulio Tonellato (giulio.tonellato@polymtl.ca) is a Ph.D. student, Michaël Kummert (michael.kummert@polymtl.ca) is professor of mechanical engineering, Gabrielle Beaudry (gabrielle.beaudry@polymtl.ca) is a research associate and Philippe Pasquier (philippe.pasquier@polymtl.ca) is professor of geological engineering, all at Polytechnique Montréal, Canada.

José Candanedo Ibarra (jose.candanedoibarra@nrccan-mcan.gc.ca) is research scientist at CanmetENERGY Varennes, Canada.

or “bleeding”) makes water extracted by the well closer to the undisturbed ground temperature, leading to a better coefficient of performance (COP) of the heat pump. These characteristics make SCWs more economical and more suitable for high density urban areas. However, there are still some obstacles in their widespread application because of the lack of user-friendly and easily accessible tools for their design and operation.

This paper’s objective is to tackle the operation phase of SCWs during winter peak demands developing a simulation framework that can assess the impact of different control strategies on the entire system. An optimal control can reduce ground heat extraction peaks, reducing the risk of groundwater freezing and leading to capital cost savings as fewer or shorter boreholes would be required. To show the potential of this tool, some preliminary results will be presented analyzing the impact of variations in the indoor temperature setpoint, such as night setback strategies.

The case study building is a primary school, located in Mirabel (Québec, Canada), selected as a demonstration project for the application of SCWs in Québec. As heating is the main energy consumption driver in this location, this work is focused on the heating season.

Standing column wells in cold climates

The most recent convincing experimental demonstration of the benefits of SCWs in cold climates was published by Nguyen et al. (2020). The study was conducted in a geothermal laboratory located in Varennes, Québec, Canada. Results show that the heat extraction from the ground (between 120 W/m and 160 W/m) is around 2.5 times higher than for conventional closed-loop GHE system (in the range of 50-55 W/m (Michopoulos et al., 2013; Pahud and Matthey, 2001; Wang et al., 2013), while keeping the groundwater temperature above 0 °C during peak heating periods. Thus, it shows that previous concerns (Minea, 2013) about operating these GHEs in winter, can be addressed by proper design and control of SCWs and HVAC system. Noticeably, promising results were obtained despite the following issues:

- Bleed was operated in this experiment only for 30 % of the time to ensure that the outlet groundwater could stay over 7 °C. When bleeding was operated, for the 80 % of the time the bleed rate was limited to 10 %.
- The geological environment was not favorable: the hydraulic conductivity of the aquifer ($K = 5.7 \cdot 10^{-7} \text{ m/s}$) in Varennes is low as well as the thermal conductivity ($k = 2.74 \text{ W m}^{-1} \text{ K}^{-1}$) (Beaudry et al., 2019). Furthermore, the groundwater composition promoted carbonate scaling (Cercllet et al., 2020).

In a recent study, Beaudry et al. (2022) used detailed heat transfer models to analyze the performance of cold-climate SCWs in more favorable geological conditions. The results show that the heat extraction can reach 197–246 W/m, meaning that SCWs require around 4-5 times fewer or shorter boreholes compared to closed-loop GSHPs systems.

In the literature both experimental (Beaudry et al., 2019; Cho et al., 2016; Lee et al., 2019; Lim and Lee, 2021; Minea, 2013; Nguyen et al., 2020; Orio et al., 2005; Pasquier et al., 2016) and simulation studies (Beaudry et al., 2022, 2021; Nguyen et al., 2013) addressed the performance of GSHP systems using SCWs, some of which also explored different groundwater bleeding strategies (Beaudry et al., 2022; Nguyen et al., 2020, 2013).

Few studies address the combined operation of the building HVAC system and the SCWs. Beurcq (2019) modeled a typical office building with a water loop exchanging heat with an SCW and distributed on-off water-to-air heat pumps. The simulation used a Thermal Resistance Capacitance Model (TRCM) to model the ground; this approach resulted in a long simulation time. The results show that both the bleeding control strategy and the building setpoints must be controlled in an integrated manner to optimize the system performance during cold periods.

In this paper, we use a detailed building model of a primary school with hot and cold water loops served by a central variable-speed water-to-water heat pump and an auxiliary electric heater. The water-to-water heat pump source side is connected to a heat exchanger with the SCW. The ground model relies on a fast convolution method (Dusseault et al., 2018) based on transfer functions generated in Beaudry et al. (2022) for this case study building..

A demonstration project for SCWs

The case study building is the “*Clé-des-champs*” primary school, a 2780 m² (net floor area) building with two floors located in Mirabel, about 40 km outside Montréal. The installation of the GSHP system has been deployed between 2021 and 2022. Robert et al. (2022) conducted experiments to assess the thermal response of the ground without bleeding and Beaudry et al. (2022), modeled the ground response of the 5 SCWs simulating different bleed strategies.

The ground-source heat pump system with 5 SCWs and one reinjection well replaces a system with fuel oil and electric boilers. The ventilation system was also retrofitted with a new Air handling Unit (AHU) and a heat recovery unit.

METHODOLOGY

To assess the impact of the building operation on the HVAC system and on the ground, all the components must be included in the same model. The methodology of this work is summarized in the following steps:

- Development and calibration of the building’s thermal loads model in TRNSYS (Klein, 2017)
- Creation of a HVAC model in TRNSYS representing the mechanical plans of the renovation project
- Integration of boreholes’ ground response through a co-simulation with MATLAB (Mathworks Inc., 2020) using fast convolution-based methods to calculate the groundwater temperatures (Dusseault et al., 2018)
- Adjustments on the controls to replicate the control sequence plans of the building
- Evaluation of different indoor air set temperature strategies

Building energy model

The Space Heating (SH) demand of the school has been estimated with a dynamic energy model developed in TRNSYS, a transient system simulation tool (Klein, 2017). Geometrical dimensions of walls, windows, roof and all the related layers’ composition were retrieved from the building plans. The building has been modeled in 3D with SketchUp 2019 (Trimble Inc., 2019) using the TRNSYS SketchUp plugin (Figure 1).

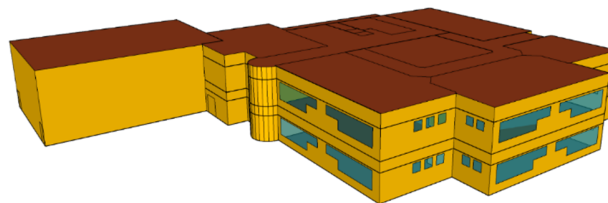


Figure 1 3D model of Cle-des-champs school built on SketchUp 2019

The thermal properties of the structures’ layers were retrieved from Quebec’s building certification standard (Novoclimat, 2020) and from ASHRAE Handbook 2017 (ASHRAE Inc, 2017). Transmittivity of structures (U values) and thermal capacities are listed in Table 1 for the main elements of the building envelope.

Table 1. Thermal properties of the building envelope

Structure	Thermal Capacity [kJ/(m ² K)]	U value [W/(m ² K)]
Roof	20.4	0.39
Suspended Ceiling	0.25	3.51
Floor (1 st floor)	123.2	1.27
Internal Wall	172.5	1
External Wall	348.6	0.31
Ground Floor	1039.2	1.90

Schedules and densities for all internal gains are retrieved from school timetables. Their values have been estimated according to the Canadian National Energy Code for Buildings (NECB) (National Research Council of Canada, 2017), and to the ASHRAE 90.1 standard (ASHRAE Inc, 2019). They are reported in Table 2 together with ventilation rates and other HVAC parameters.

The weather data files used for the model validation (years 2015-2018) are retrieved from CWEEDS (Environment Canada, 2020) and from Whitebox Technologies Inc (WBT) (White Box Technologies, 2022) for the airport of Mirabel (Québec) which is located near the school.

Table 2. Internal Gains and HVAC parameters

Parameter	Value	Unit	Source/Notes
Occupancy heat gains	73.3	W/person	ASHRAE 90.1
Lights heat gains	8.7	W/m ²	CNEB 2017
Equipment heat gains	5	W/m ²	CNEB 2017
Ventilators heat gains	7	W/m ²	CNEB 2017
Ventilation air flow rate	≈ 6	ACH (h ⁻¹)	Mechanical plans, zone dependent
Sensible ventilation heat recovery	89	%	Mechanical plans (not considered for validation)
Temperature setpoint for validation	20-21	°C	Building Management System, zone dependent
Thermal power distribution limit	195.3	kW	Baseboard heaters + air handling unit

In TRNSYS, the ground's floor temperature is simulated with a 3D ground coupling model based on a finite difference approach available with Type 1244, which uses Kasuda's correlation (Kasuda and Archenbach, 1965). Also, as infiltration rates heavily influence energy calculations, a detailed infiltration model recently developed by NIST has been used (Ng et al., 2018). This model considers the impacts of wind velocity and of stack effect.

Previous electric and fuel oil bills were used for model validation. The model's energy demand predictions for 2016, 2017 and 2018 were respectively -4.32 %, -6.55 % and -0.7 % compared to the bills for those years. Since the bills also account for system losses like the fuel oil boiler's heat release (inside the building), the TRNSYS demand was considered consistent with the bills.

Ground response modelling

The objective of the ground response model is to predict the borehole outlet temperature as a function of inlet temperature, mass flow rate and ground temperature.

The fastest methods known in literature to simulate GHEs with varying heating power profile are based on the principle of superposition. For closed-loop systems, temporal and spatial superposition are used together to estimate the thermal interference between the boreholes (Spitler and Bernier, 2016) through transfer functions called "g-functions". A convolution combines these g-functions with an incremental load vector to give the thermal response. The transfer functions are usually generated beforehand using analytical solutions such as the Finite Line Source (FLS) (Cimmino and Bernier, 2014) and they depend exclusively on the geometry of the borehole's field and on time.

The same principle can be applied to SCWs with the exception of the transfer functions' generation (Beaudry et al., 2021). Analytical solutions such as the FLS are exclusively accounting for heat conduction, whereas for SCWs heat advection has a major role as most of the heat transfer is mostly made through the transfer of mass (Pasquier et al., 2016; Robert et al., 2022). Thus, the transfer functions for SCWs must be generated numerically. As some g-functions were already elaborated for the this case study by Beaudry et al. (2022) through a 3D finite difference model, they are also used in this work.

Regarding the type of existing efficient convolution methods, solutions in Laplace domain (Lamarche, 2009), spectral domain (Marcotte and Pasquier, 2008; Pasquier and Marcotte, 2013) or with matrix product (Dusseault et al., 2018) have

shown to be much faster than time domain's non-recurrent summations. For this work, a matrix product has been used as it has been proved to be remarkably faster (stable at ≈ 4.7 ms) than time domain and spectral domain convolution's algorithms (linearly growing to 0.5 s after ≈ 5500 hours of simulation) when integrated to a timestep-by-timestep approach such as the one of TRNSYS. The matrix product uses different g -functions depending on the selected combination of pumping and bleeding flow rates.

It is worth mentioning that all convolution methods rely on linearity and stationarity of the model's response, which therefore requires a constant circulation and bleed flow rates. Only recently, Beaudry et al. (2021) developed a non-stationary convolution method to simulate GHEs using closed-loop or SCWs. However, this non-stationary convolution method has not yet been integrated into TRNSYS through matrix products, which would allow an acceptable simulation speed for this study. Therefore, at this stage only constant flow rates and bleeding rates are considered and non-stationary conditions will be implemented in future work.

The groundwater flow rate is a key parameter for the system's performance: the higher the flow rate, the smaller the temperature difference at the heat exchanger, thus reducing the risk of freezing. Precedent studies which analyzed bleeding strategies (Beaudry et al., 2022; Beurcq, 2019; Nguyen et al., 2020) used higher flow rates with higher energy demands. Since this work focuses on peak loads, the pumping rate is kept at its maximum (568 L/min).

To validate the ground response model integrated in TRNSYS, a simple setup has been created to replicate the results of Beaudry et al. (2022) when using constant flow rate conditions, in particular with the g -function produced with 408 L/min of pumping flow rate and 82 L/min of discharging flow rate. The model is validated over the EWT (outlet borehole temperature) and the LWT (inlet borehole temperature). For the LWT the RMSE results is 0.251 °C and the R2 score 97.6 %, for the EWT the RMSE is 0.122 °C and the R2 score is 97.7 %.

HVAC model

The HVAC system TRNSYS model is shown in Figure 2. The control of the 70 tons water to water heat pump consists in a 4 °C dead band control with a 48 °C setpoint on the return temperature.

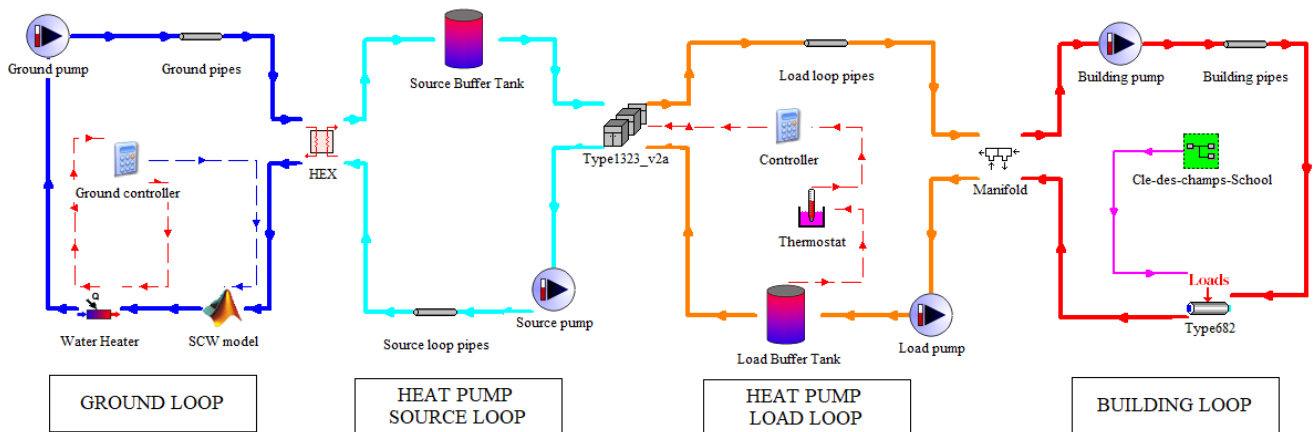


Figure 2 HVAC model in TRNSYS

The TRNSYS model is organized in 4 loops: (1) the ground loop, (2) the Heat Pump's (HP) source loop, (3) the HP's load loop and (4) the building loop.

- 1. Ground loop.** To simulate the ground response, MATLAB is used through a co-simulation process. MATLAB stores the ground heat loads and the outlet flow rate temperatures in vectors, which are used to perform the convolutions with a matrix product. To prevent freezing in the heat exchanger, an electric heater is placed after the

boreholes as safety measure. This solution, inspired by previous studies (Beaudry et al., 2022; Nguyen et al., 2020), is a first attempt to deal with freezing issues without using solely the electric boiler to heat the building. This heater adds to, but does not replace, ground heat extraction, keeping the overall COP above 1. However, more efficient solutions will be evaluated in future work. As the heater is applied to the HP entering water temperature (EWT), it will be called “EWT heater” for the rest of the paper.

2. **HP source loop.** As the focus is on heating, the cold manifold is not modeled and the fluid (a solution of water and 30 %vol of propylene glycol) is directly pumped to the heat pump’s evaporator. A plate heat exchanger is put between the evaporator and the ground loop to prevent the heat pump’s evaporator to be in contact with the groundwater. The flow rate is kept constant at 9.46 L/s.
3. **HP load loop.** The flow rate is kept constant at 4.8 L/s to ensure stable operation of the heat pump. The connection to the load loop is operated with a manifold model which provides a thermal exchange depending on the flow rate ratio.
4. **Building loop.** As the HVAC system is complex some simplifying assumptions are taken into the TRNSYS model. For instance, the heating distribution system is all considered in one single load loop through a simple thermal load block which reads directly the total thermal load of the school. The flow rate in the load loop is controlled so that the temperature difference in the distribution system does not exceed 10 °C. Most of the time, however, the temperature difference is lower, as the flow rate in the load loop is set to a minimum of 2 L/s. The limitation of this approach is that the TRNSYS building model elaborates ideal loads based on an ideal internal temperature control that reaches exactly the setpoint required, and then imposes the calculated loads on the water loop. More realistic controllers can be implemented in TRNSYS but this has not been done at this stage.

RESULTS AND DISCUSSION

The objective of the paper was to develop a tool capable of assessing the impact of different control strategies on a HVAC system using SCWs. Some preliminary results will be presented here to show its potential.

Three indoor set temperature setback scenarios will be compared for the 2nd and 3rd days of February 2015, which contains the major load peaks of the year, an outside temperature varying between -14 °C and -26 °C and the wind speed that reaches peaks of around 4 m/s. The first one ramps up from a setback of 2 °C in about one hour and the other two recover the ramp more gradually in around 3 hours before the building is occupied (i.e. 8 AM).

Since the groundwater flow rate has to be kept constant due to the stationary convection, a bleed of 20 % of the total groundwater flow rate is analyzed for the first two scenarios and a 30 % bleed ratio for the third one. The latter is analyzed to understand its potential advantages during demand peaks. Table 3 summarizes the three scenarios that have been tested.

Table 3. Simulated Scenarios

Characteristics	Scenario 1	Scenario 2	Scenario 3
Duration of setback	1 h	3 h	3 h
Bleed ratio	20 %	20 %	30 %
Power cap	No	Yes	Yes
HP’s compressor energy use (kWh)	1062.5	1066.3	1054.1
EWT heater energy use (kWh)	31.6	0	0
Maximum total power (kW)	68.7	37.9	37.5

The results of three scenarios are shown in Figure 3 for the total power consumed (on the middle) and boreholes' temperatures (on the bottom) in relation to the indoor air temperature (on the top).

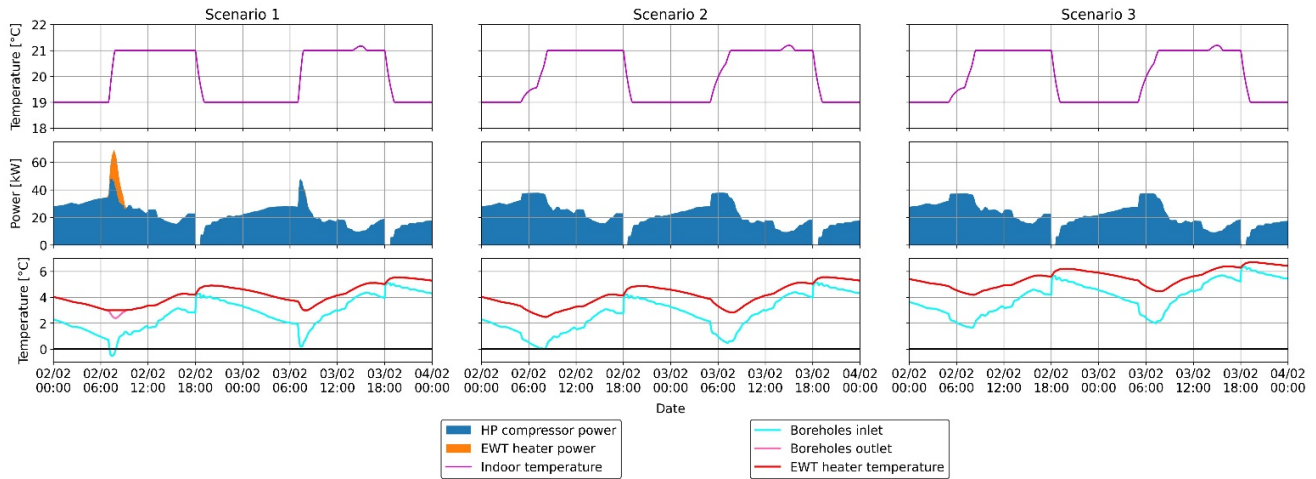


Figure 3 Results for the 3 Scenarios. On the top the indoor air temperature of the building. In the middle the power consumed by the HP compressor and the EWT heater. On the bottom the groundwater temperature at the inlet of the SCWs, on the outlet (visible in pink only in Scenario 1) and after the EWT heater.

Scenario 1. In the first day represented (2nd of February) the EWT heater is used to try to avoid groundwater freezing, but keeping the outlet temperature at 3 °C is not sufficient and the temperature after the heat exchanger drops below 0 °C. The power consumed by the water heater is above 20 kW bringing the total power spike to over 72 kW.

Scenario 2. The indoor temperature setback is ramped in about 3 hours through a power cap that limits the distribution of thermal power to the building. The power is capped using a linear interpolation method which takes the external temperature as independent variable. With this power limitation, the total power peak spikes at around 38 kW. Thanks to this power limitation, the water heater is never required with 20 % bleed to avoid water freezing as the minimum borehole's inlet temperature is 0.01 °C. As this temperature is dangerously close to 0 °C, to avoid the freezing risk, either the bleed could be risen to 30 % during the temperature setpoint variations or the EWT heater could be switched on to keep at least 2.5 °C at the boreholes' outlet. As shown with Scenario 3, if the bleed ratio is kept at 30 %, the inlet temperature stays above 1.6 °C. A non-stationary convolution model would allow to simulate this bleed variation only near heat demand peaks, keeping a lower bleed rate for the rest of the time.

Scenario 3. Using a 30 % bleed ratio keeps the groundwater temperature after the heat exchanger safely above 1.6 °C. The total power peak is 37.5 kW. Just 0.5 kW less than with 20 % bleed (Scenario 2). In terms of performance, the difference with Scenario 2 stands in the groundwater temperature, showing that a 20 % bleed rate is already sufficient to have a high COP and a higher bleed is only required to avoid groundwater freezing during demand peak events.

Discussion. A fast conventional setback (Scenario 1), as expected, is not a viable option as the groundwater freezes even with a large use of the EWT heater. Using a more gradual setback to ramp up the temperature (Scenario 2) in 3 hours instead seems to be a more feasible solution even if the groundwater arrives near the freezing point. Operating 30 % bleed ratio (Scenario 3) near demand peaks could be useful to avoid groundwater freezing risks while it is reducing the power peaks only of a small amount. It should be noted that using a constant temperature setpoint could avoid these power peaks, but it would consume about 13 % more energy to keep a higher setpoint when the building is not occupied. These are preliminary results, which are shown to present the potential of this control strategy framework. Further work will be addressed to produce more complete results.

Limitations. The objective of this first stage of the project was to draft a first simplified control framework of a SCW system. The ideal indoor temperature control does not take into consideration fluctuations of a real thermostatic control which could alter the demand peaks. Constant groundwater flow rates limit the flexibility potential of the system but as shown in this article it is still possible to evaluate the behaviour of the system during demand peaks and how these can be addressed with preheating strategies. The highest possible groundwater flow rate was used specifically to analyse the peak demands and pumping energy was neglected at this stage. Finally, the heat pump on/off control is still a simple deadband, which limits the potential of the heat pump to operate more efficiently.

CONCLUSIONS

In this paper, a control strategy evaluation framework for buildings using GSHPs with SCWs has been developed. An HVAC system with SCWs is modeled together with a real case study building, located in Mirabel, Québec, Canada. In recent years most of previous concerns over the use of SCWs have been solved and a recent experimental application proved that SCWs can be used in cold climates despite not favorable ground conditions. The installation of SCWs in an institutional building in Québec allows to better explore their performance when interacting with a building. The impact of different indoor air set temperature strategies on the entire system is analyzed under maximum groundwater flow conditions, as most of control and water freezing problems are caused during peak loads. Simulations suggest that ramping the setback over 3 hours allow to operate the system without the use of the fluid heater with just a 20 % bleed, although a 30 % bleed would be recommended near peak loads as a safety factor. Future work with the model will focus on overcoming some current limitations and will explore more advanced control strategies, such as Model Predictive Control (MPC), with the objective of further reducing power peaks.

ACKNOWLEDGMENTS

The authors acknowledge the support from partners of the Geothermal Research Chair on the Integration of SCWs in Institutional Buildings, namely Hydro-Québec, the Ministry of higher education of Québec, our partner school centers (CSSMI, CSSDM, CSSS), Versa Profiles, Marmott Energy, CanmetEnergy (Natural Resources Canada) and NSERC. Additionally, we thank the anonymous reviewers and colleagues (G. Dion and D. Hernandez) that provided constructive comments. This work was financed by the Natural Sciences and Engineering Research Council of Canada through grant number ALLRP 544477-19.

REFERENCES

- Alshehri, F., Beck, S., Ingham, D., Ma, L., Pourkashanian, M., 2019. Techno-economic analysis of ground and air source heat pumps in hot dry climates. *Journal of Building Engineering* 26, 100825. <https://doi.org/10.1016/j.job.2019.100825>
- ASHRAE Inc, 2019. ASHRAE Standard 90.1-2019 - Energy Standard for Buildings Except Low-Rise Residential Buildings.
- ASHRAE Inc, 2017. ASHRAE Handbook 2017 - Fundamentals.
- Beaudry, G., Pasquier, P., Marcotte, D., 2021. A fast convolution-based method to simulate time-varying flow rates in closed-loop and standing column well ground heat exchangers. *Renewable Energy* 174, 55–72. <https://doi.org/10.1016/j.renene.2021.04.045>
- Beaudry, G., Pasquier, P., Marcotte, D., 2019. The impact of rock fracturing and pump intake location on the thermal recovery of a standing column well: model development, experimental validation, and numerical analysis. *Sci Technol Built En* 25, 1052–1068. <https://doi.org/10.1080/23744731.2019.1648133>
- Beaudry, G., Pasquier, P., Marcotte, D., Zarrella, A., 2022. Flow rate control in standing column wells: A flexible solution for reducing the energy use and peak power demand of the built environment. *Applied Energy* 313, 118774. <https://doi.org/10.1016/j.apenergy.2022.118774>
- Beurcq, C., 2019. Control Strategies for Standing Column Wells in a Cold Climate (M. Eng. Thesis). Ecole Polytechnique, Montreal (Canada).
- Cercllet, L., Courcelles, B., Pasquier, P., 2020. Impact of standing column well operation on carbonate scaling. *Water* (Switzerland). <https://doi.org/10.3390/w12082222>

- Cho, J.-H., Nam, Y., Kim, H.-C., 2016. Performance and Feasibility Study of a Standing Column Well (SCW) System Using a Deep Geothermal Well. *Energies* 9. <https://doi.org/10.3390/en9020108>
- Cimmino, M., Bernier, M., 2014. A semi-analytical method to generate g-functions for geothermal bore fields. *International Journal of Heat and Mass Transfer* 70, 641–650. <https://doi.org/10.1016/j.ijheatmasstransfer.2013.11.037>
- Dusseault, B., Pasquier, P., Marcotte, D., 2018. A block matrix formulation for efficient g-function construction. *Renewable Energy* 121, 249–260. <https://doi.org/10.1016/j.renene.2017.12.092>
- Environment Canada, 2020. Canadian Weather Energy and Engineering Data Sets (CWEEDS files) and Canadian Weather for Energy Calculations (CWEC files) [WWW Document]. URL https://climate.weather.gc.ca/prods_servs/engineering_e.html
- Kasuda, T., Archenbach, P.R., 1965. Earth Temperature and Thermal Diffusivity at Selected Stations in the United States. *ASHRAE Transactions* 71.
- Klein, S.A., 2017. TRNSYS 18 : A Transient System Simulation Program.
- Lamarche, L., 2009. A fast algorithm for the hourly simulations of ground-source heat pumps using arbitrary response factors. *Renewable Energy* 34, 2252–2258. <https://doi.org/10.1016/j.renene.2009.02.010>
- Lee, D.Y., Seo, B.M., Hong, S.H., Choi, J.M., Lee, K.H., 2019. Part load ratio characteristics and energy saving performance of standing column well geothermal heat pump system assisted with storage tank in an apartment. *Energy* 174, 1060–1078. <https://doi.org/10.1016/j.energy.2019.03.029>
- Lim, K., Lee, C., 2021. Coefficient of performance and heating and cooling thermal performance characteristics using a standing column well and cross-mixing balancing well heat exchanger methods. *Energy Reports* 7, 1444–1459. <https://doi.org/10.1016/j.egy.2021.03.001>
- Marcotte, D., Pasquier, P., 2008. Fast fluid and ground temperature computation for geothermal ground-loop heat exchanger systems. *Geothermics* 37, 651–665. <https://doi.org/10.1016/j.geothermics.2008.08.003>
- Mathworks Inc., 2020. MATLAB 2020b.
- Michopoulos, A., Zachariadis, T., Kyriakis, N., 2013. Operation characteristics and experience of a ground source heat pump system with a vertical ground heat exchanger. *Energy* 51, 349–357. <https://doi.org/10.1016/j.energy.2012.11.042>
- Minea, V., 2013. Experimental investigation of the reliability of residential standing column heat pump systems without bleed in cold climates. *Appl Therm Eng* 52, 230–243. <https://doi.org/10.1016/j.applthermaleng.2012.11.031>
- National Research Council of Canada, 2017. National energy code of Canada for buildings 2017.
- Ng, L.C., Ojeda Quiles, N., Dols, W.S., Emmerich, S.J., 2018. Weather correlations to calculate infiltration rates for U. S. commercial building energy models. *Build Environ* 127, 47–57. <https://doi.org/10.1016/j.buildenv.2017.10.029>
- Nguyen, A., Beaudry, G., Pasquier, P., 2020. Experimental assessment of a standing column well performance in cold climates. *Energy Buildings*. <https://doi.org/10.1016/j.enbuild.2020.110391>
- Nguyen, A., Pasquier, P., Marcotte, D., 2013. Development of an ODE model featuring a three level bleed control and an off-loading sequence for standing column wells. *Proceedings of BS2013, Chambéry, France* 26–28.
- Novoclimat, 2020. Exigences techniques Novoclimat – Maison et Petit bâtiment multilogement. Québec énergie et ressources naturelles.
- Orio, C.D., Chiasson, A., Johnson, C.N., Deng, Z., Rees, S.J., Spitler, J.D., 2005. A survey of standing column well installations in North America. *ASHRAE Transactions* 111 Part 2.
- Pahud, D., Matthey, B., 2001. Comparison of the thermal performance of double U-pipe borehole heat exchangers measured in situ. *Energy and Buildings* 33, 503–507. [https://doi.org/10.1016/S0378-7788\(00\)00106-7](https://doi.org/10.1016/S0378-7788(00)00106-7)
- Pasquier, P., Marcotte, D., 2013. Efficient computation of heat flux signals to ensure the reproduction of prescribed temperatures at several interacting heat sources. *Applied Thermal Engineering* 59, 515–526. <https://doi.org/10.1016/j.applthermaleng.2013.06.018>
- Pasquier, P., Nguyen, A., Eppner, F., Marcotte, D., Baudron, P., 2016. Standing column wells. *Advances in Ground-Source Heat Pump Systems Chapter 10*, 269–294. <http://dx.doi.org/10.1016/B978-0-08-100311-4.00010-8>
- Robert, S., Pasquier, P., Nguyen, A., 2022. Impact of layered heterogeneity on thermal response test interpretation performed on a standing column well operated without bleed. *Geothermics* 101, 102353. <https://doi.org/10.1016/j.geothermics.2022.102353>
- Sarbu, I., Sebarchievici, C., 2014. General review of ground-source heat pump systems for heating and cooling of buildings. *Energy and Buildings* 70, 441–454. <https://doi.org/10.1016/j.enbuild.2013.11.068>
- Snijders, A.L., Drijver, B.C., 2016. Open-loop heat pump and thermal energy storage systems, in: Rees, S.J. (Ed.), *Advances in Ground-Source Heat Pump Systems*. Woodhead Publishing, pp. 247–268. <https://doi.org/10.1016/B978-0-08-100311-4.00009-1>

- Spitler, J.D., Bernier, M., 2016. Vertical borehole ground heat exchanger design methods, in: Rees, S.J. (Ed.), *Advances in Ground-Source Heat Pump Systems*. Woodhead Publishing, pp. 29–61. <https://doi.org/10.1016/B978-0-08-100311-4.00002-9>
- Trimble Inc., 2019. SketchUp 2019.
- UNFCCC, 2015. COP 21 Agenda : Updated compilation of information on mitigation benefits of actions, initiatives and options to enhance mitigation ambition.
- Wang, H., Zhao, Q., Wu, J., Yang, B., Chen, Z., 2013. Experimental investigation on the operation performance of a direct expansion ground source heat pump system for space heating. *Energy and Buildings* 61, 349–355. <https://doi.org/10.1016/j.enbuild.2013.02.042>
- White Box Technologies, 2022. Weather Data for Energy Calculations [WWW Document]. URL <http://weather.whiteboxtechnologies.com/> (accessed 4.16.22).

Machine-learning-based models for predicting the performance of Ground-source heat pumps using experimental data from a residential Smart Home in California.

Antash Najib

Abbas Hussain

Sreenidhi Krishnamoorthy

ABSTRACT

Ground-source heat pumps (GSHP) reject (extract) heat to a lower (higher) temperature sink (source) as compared with air-source heat pumps which allows them to operate more efficiently. With the rapid development in the field of artificial intelligence, data-driven based Machine-Learning (ML) models are playing an important role in simulating various building energy systems including GSHP. In this paper, ML models have been applied to predict the performance of a water-water GSHP. The models presented in this paper, require climate data (which is readily available or easily measurable) and the power consumed in the previous time-step for predicting the power consumption for the current time-step. The models were rigorously trained using measured data from a residential technological demonstration home located in Davis, California. Data spanning from October 2018 to April 2019, i.e. heating mode, was used in the study. Eight linear and non-linear ML models were employed and the results show that the linear models namely, multiple linear regression (MLR), elastic net (ELN) and support vector regression (SVR) can predict the power consumption with a very high level of accuracy. Within the linear models, the coefficient of variation of the root mean squared error (CV-RMSE) for the MLR was 4.04062 which was 0.19% and 0.05% less than the ELN and SVR model respectively. Within the five non-linear models, gradient boosting decision tree (GBDT) exhibited the lowest CV-RMSE i.e. 4.26141 (which is 5.46% higher than the MLR model). The CV-RMSE for extreme gradient boosting trees (XGBT) was the highest (i.e. 45.42% higher than the MLR model). Thus MLR model can be used to accurately predict the power consumption of the GSHP system.

INTRODUCTION

Buildings account for around 40% of the total world energy use (Shukla et al., 2022) and Heating Ventilation and Air-Conditioning (HVAC) systems in buildings account for the majority of this energy (Kumar et al., 2018). Thus reducing the energy consumption in buildings is essential in the effort to reduce GHG emissions.

One effective method of reducing the energy consumption of buildings is accurate prediction of the HVAC load profile and performance which allows an effective energy management & control plan to be formulated in advance (Fan et al., 2019). There are two methods for predicting HVAC profile and performance, 1) physical simulation models and 2) Soft computational data-driven models. The latter is rapidly gaining popularity with the development of artificial intelligence and Internet of Things (IoT) (L. Zhang et al., 2021). In this paper, several data driven based Machine Learning (ML) models have been applied for predicting the performance of a high-efficiency GSHP installed in a design house at Davis, California.

Antash Najib (anajib@ucdavis; antash.najib@pnec.nust.edu.pk) and Abbas Husain are assistant professors in the Mechanical Engineering Department at National University of Science & Technology, Islamabad, Pakistan and Sreenidhi Krishnamoorthy is an Engineer scientist in the Energy Utilization division of Electric Power Research Institute, Palo Alto, CA USA.

LITERATURE REVIEW

In order to design, optimize and control complex HVAC systems, several ML based models have been presented in the past. Park et al. (2018) presented an hourly GSHP system performance prediction model based on a multiple linear regression (MLR) and an artificial neural network (ANN). Entering source-side temperature, both entering and leaving load-side temperatures, ambient air temperature along with the heating load data was used to predict the system overall Coefficient of Performance (COP). Sun et al. (2015) developed an artificial neural network (ANN) model and an adaptive neuro-fuzzy inference system (ANFIS) model to predict the COP of the heat pump using both entering and leaving source-side and load-side temperatures. Lu et al. (2019) used an ensemble approach using random forest (RF) for hourly performance predictions for GSHP coupled to one hundred vertical type GHEs. In addition to parameters used by previous researchers, models by Lu et al. (2019) also required both load-side and source-side flowrates and pressures along with the cooling to heating load ratio. Although the accuracies of some of these studies is reasonably high, these models can only be used if the load-side and source-side fluid temperatures (and in some cases even the heating loads) are known which is generally not the case. In contrast, the models presented in this paper, after they have been trained, only need climate data (Ambient air temperature, relative humidity, solar insolation and previous time-step power for predicting the power for next time-step).

RESEARCH METHODOLOGY

The overall research architecture of the GSHP performance (power prediction) is shown in Figure 1. The process can be divided into two stages. The first stage is data preprocessing in which data cleaning and feature selection is done to get meaningful dataset. In the next stage training, testing and comparison of various ML model is carried out. Outliers are eliminated from the original data by using the rule of interquartile range i.e. the values outside the specified range are regarded as abnormal data and imputed.

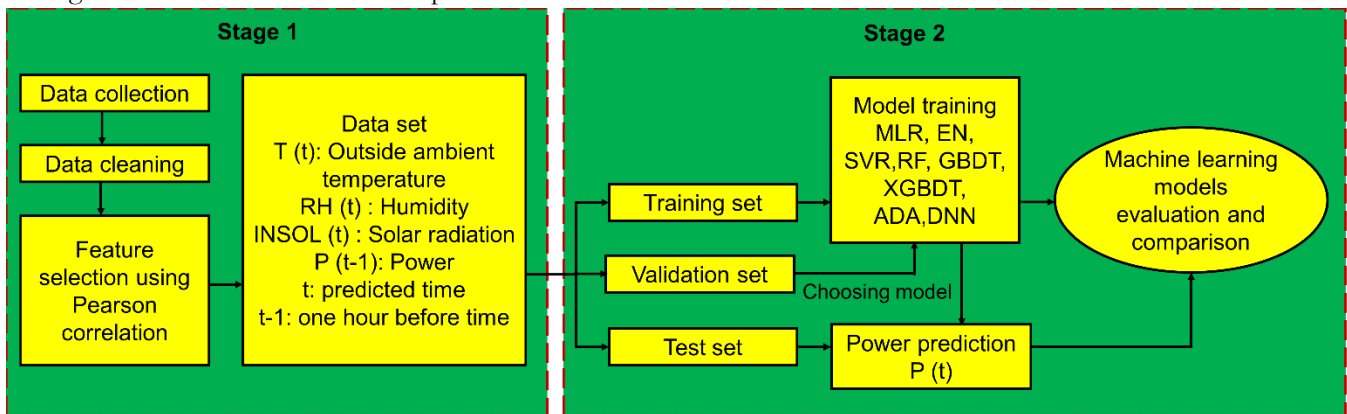


Figure 1 Research Architecture

Selection of model inputs is one of the most important tasks in machine learning. Feature selection is the process of reducing the number of input variables when developing a predictive model. If the number of input variable in model is too high, information redundancy and interference will occur. Therefore, feature selection is effective in reducing the dimensionality, removing irrelevant and redundant feature and thereby, reducing the computational cost. There are several feature selection methods available in the literature (L. Zhang & Wen, 2019), out of which statistical based method (Pearson correlation) is used in this research. Eight prediction algorithms are employed in this study, including multiple linear regression (MLR), elastic net (ELN), support vector regression (SVR), random forests (RF), gradient

boosting decision tree (GBDT), extreme gradient boosting trees (XGBT), Adaboost (ADA) and deep neural network (DNN). These prediction techniques are selected due to their popularity in previous studies (L. Zhang et al., 2021). Details of each ML model is widely available in the literature (Ahmad et al., 2014; Lu et al., 2019; L. Zhang & Wen, 2019) and therefore is not repeated here. The entire data-set is randomly divided into training data (50%), testing data (30%) and validation data (20%). The Scikit-learn library in Python is utilized to implement these prediction techniques and the grid search method is used to optimize the parameters. Normalization of the input feature is achieved via z-score normalization.

Case Study

Data measured from Honda Smart Home was used in this study which is a net-zero energy demonstration house located in Davis, California and serves as a pilot home or “living laboratory” for various advance building energy technologies. The building employs eight large diameter shallow-bore vertical helical GHEs connected in parallel and are coupled to a water-to-water heat pump. Space conditioning to the house using radiant floor delivery on the first floor and by using radiant ceiling panels on the second floor by the heat pump only (i.e. no auxiliary systems for peak hours). Table 1 reports various design the characteristics of this site (Davis Energy Group, 2013). Further details have been provided by Najib et al. (2019). The site has an extensive monitoring scheme under which measurements are obtained every minute by in-situ sensors. All climate parameters, temperature and flow-rates at numerous locations for the source-side (ground loop), load-side (hydronic building loop), indoor air etc. Power consumed is also measured for each application. The subsequent section discusses the subset of measured parameters that were used for the ML models.

Table 1. Design parameters at the case study site

Parameters	Values
Building parameters	
-Total conditioned floor area	189.5 m ² (2040 ft)
-No. of stories	2
Ground Heat Exchanger	
-Helix pitch & diameter	0.1524 m (6 in.) & 0.5588 m (22 in.)
-GHE center to center distance	4.572 m (15 ft)
-Depth of helical pipe top	0.914 m (3 ft)
-Helical pipe height	5.1816 m (17 ft)
-Nominal pipe diameter	½ in. (nominal size)
-Tube material	High Density Polyethylene (HDPE)
-Backfill	Native soil
-Heat transfer fluid/ heat pump type	Water/ water-water
-Heat Pump nominal capacity	Heating: 6.27 kW (21380 Btu/h) Cooling: 7.33 kW (25000 Btu/h)

Feature Selection and Hyperparameter Optimization

In this study, average hourly data from 1st October, 2018 to 30th April, 2019 is utilized. Although summer and winter season data can be analyzed using similar techniques, only results for winter data are presented for the sake of brevity. In total, the dataset contains 5089 observations. As mentioned in the literature review section, the aim of this paper is to be able to predict the heat pump power consumption using climate data. Therefore, the input feature space was restricted to only climate parameters (Ambient temperature, relative humidity, solar insolation, rainfall, wind direction and wind speed) and power for previous temperatures. Pearson correlation between each feature and the power was calculated which is shown Table 2. The result shows that previous time-step power has the strongest correlation with

the predicted time-step power. Solar radiation has a weak correlation, but it is taken as an input feature as it affects both the load side (reduced solar heat gain by the building leads to a higher demand for heating from the heat pump) and the source side (higher solar radiation incident on the ground, allows higher temperatures at the source side). Thus solar radiation is related to various other parameters, which is why it was included in the analysis for completeness. Features such as wind speed, wind direction and rainfall have a very weak correlation and were thus excluded from the analysis.

Table 2. Results for correlation analysis

	T °C (°F)	RH (%)	INSOL Wm ⁻² (BTU ft ⁻² h ⁻¹)	Rainfall mm (in.)	Wind speed ms ⁻¹ (mph)	Wind direction °	P (t-1) kW (BTU h ⁻¹)
Correlation	-0.16	0.18	-0.09	-0.009	-0.039	-0.037	0.98

Table 3 presents the summary of numeric variables in the dataset. Figure 2 shows the power profile in the data set. As it is seen from the figure that power load distribution has different pattern, on some intervals it has significantly larger values, therefore it is important to select the prediction model which has ability to identify the pattern distribution efficiently. The hyperparameter tuning is done by using grid search method with 3 cross fold validation. The optimized parameters are shown in Table 2. In this study the number of neurons at each hidden layer in DNN model is 6 and Mini-Batch training strategy is utilized in the training process to improve the data utilization.

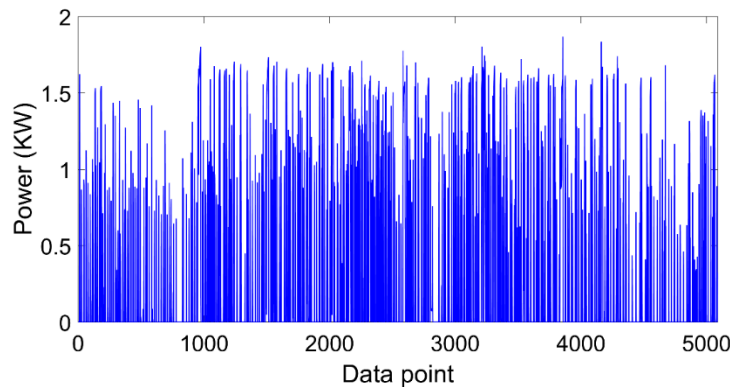


Figure 2 Power data profile in the dataset

Table 3. Summary of numeric variable in the dataset

Variable	Min	Mean	Max
T	-0.74°C (30.67°F)	12.74°C (54.94°F)	26.81°C (80.25°F)
RH (%)	7.06	60.54	88.10
INSOL	0	150.34 Wm ⁻² (47.91 BTU ft ⁻² h ⁻¹)	641.57 Wm ⁻² (204.46BTU ft ⁻² h ⁻¹)
P (kW)	0	0.25 kW (853 BTU h ⁻¹)	1.86 kW (6346 BTU h ⁻¹)

Table 4. Hyperparameter optimization

S.no	Model	Parameters	Start	Stop	Step	Optimized parameter
1	SVR	C	1	10	1	9
		epsilon	0.001	0.2	0.00995	0.001
2	ELN	L1_ratio	0	1	0.01	0.99
		alpha	1.00E-05	1.00E-01	0.019998	0.0001
3	RF	Max depth	3	11	1	6

		n_estimator	50	200	10	189
4	GBDT	Learning rate	0.01	0.2	0.01	0.0699
		Max depth	3	11	1	3
		n_estimator	50	200	10	150
5	ADA	Learning rate	0.01	0.2	0.01	0.0699
		Max depth	3	11	1	6
		n_estimator	50	200	10	70
6	XGBT	Learning rate	0.01	0.2	0.01	0.19
		Max depth	3	11	1	3
		n_estimator	50	200	10	60
7	DNN	learning_rate_init	0.001	0.01	0.0009	0.009999
		max_iter	100	200	10	100
		hidden layer size	2	6	1	6

RESULT AND DISCUSSION

The prediction performance is evaluated by three metrics, i.e., the squared correlation coefficient (R^2), mean absolute error (MAE), and coefficient of variation of the root mean squared error (CV-RMSE).

$$MAE = \frac{\sum_{i=1}^n |\hat{y}_i - y_i|}{n} \quad (1)$$

$$CV - RMSE = \frac{\sqrt{\frac{1}{n} \sum_{i=1}^n (\hat{y}_i - y_i)^2}}{\frac{\sum_{i=1}^n \hat{y}_i}{n}} \quad (2)$$

$$R^2 = 1 - \frac{\sum_{i=1}^n (y_i - \hat{y}_i)^2}{\sum_{i=1}^n (y_i - \bar{y})^2} \quad (3)$$

Where n represents the total number power values (data points), y_i represents the actual power value, \hat{y}_i represents the predicted value of power from the model, and \bar{y} represents the average values of the actual power. CV-RMSE is considered a reasonable statistical evaluation index and if its value is less than 10% then the model is sufficiently close to the physical reality (W. Zhang et al., 2021). The closer the value of R^2 is to 1, the better the prediction accuracy of the model. Table 4 summarizes the resulting RMSE, CV-RMSE, R^2 and MAE. It is shown from the table that the resulting CV-RMSE value of all models are under 10% which shows that all models can be used for the prediction of power.

The prediction performance of ensemble machine learning algorithms i.e. (RF, GBDT, XGBDT, ADA) and DNN which are non-linear models are less than the linear machine learning models i.e., (MLR, ELN, and SVR). This is expected as the output i.e. predicted power consumption of current time-step is highly correlated with the previous time-step power. Out of these eight ML models, XGBDT has the lowest performance and the resulting CV-RMSE value is 5.876, MAE is 0.00450 and R^2 is 0.99916. Comparison within the non-linear ML models (i.e. ensemble and DNN) shows that GBDT has the highest accuracy with CV-RMSE value of 4.261, MAE of 0.00415 and R^2 of 0.99956. Within the linear ML models (MLR, ELN and SVR), MLR has the highest accuracy with CV-RMSE value of 4.04062, MAE is 0.00389 and R^2 is 0.99960.

Table 5. Prediction performance on testing data

Method	MAE	RMSE	R^2	CV-RMSE
MLR	0.00389	0.00992	0.99960	4.04062
ELN	0.00361	0.00994	0.99960	4.04849
SVR	0.00398	0.00993	0.99960	4.04268
RF	0.00425	0.01078	0.99953	4.38983
GBDT	0.00415	0.01046	0.99956	4.26141

ADA	0.00450	0.01085	0.99952	4.42004
XGBT	0.00783	0.01441	0.99916	5.87600
DNN	0.00537	0.01083	0.99952	4.41048

Figure 3 and Figure 4 show the actual power and the error (actual-predicted power) for all the ML models for the entire testing data. Figure 3 depicts the performance of the linear ML models. It can be seen that the power predicted by all three models is very close and the power predicted by MLR and ELN are indistinguishable in the figure. The errors lie within the range of 0.05 kW to -0.05 kW. The lower figure shows the same parameters over a magnified time scale (Jan 1st, midnight to Jan 5th, midnight i.e. 4-day period). It should be noted that only the training data is shown in the figures and the missing points are those that were randomly selected as training data. As expected, most errors are encountered when the models are used to predict non-zero power consumption values.

Figure 4 illustrates the performance of the non-linear ML models. It can be seen that the error band for the non-linear ML models is larger (0.11 kW to -0.09 kW) than that for the linear models. The trend shows that XGBDT and DNN models generally have lower accuracies while the remaining three models shown overall better accuracy.

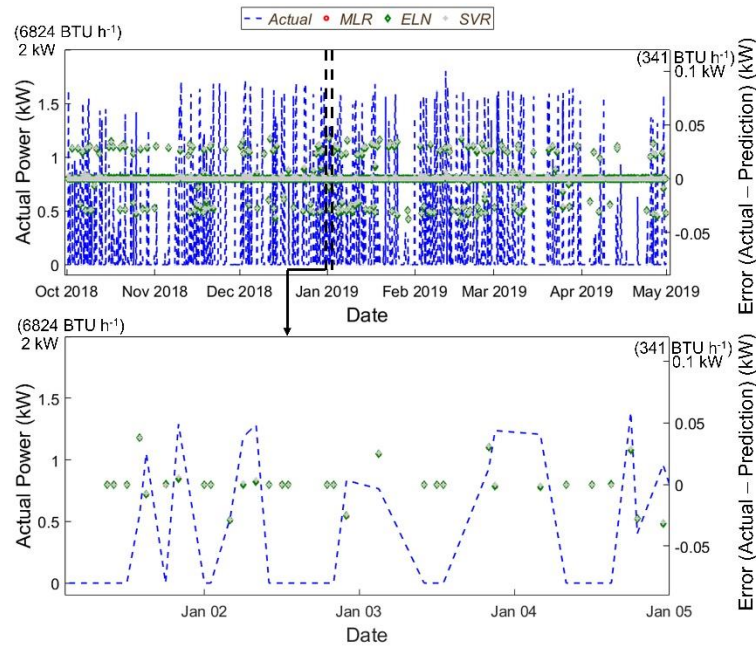


Figure 3 Upper figure shows the actual power consumption (left y-axis) and the error (actual – predicted power) (right y-axis) for each linear ML model for the entire testing data. Lower figure shows the same parameters over a magnified time scale (Jan 1st, midnight to Jan 5th, midnight i.e. 4-day period).

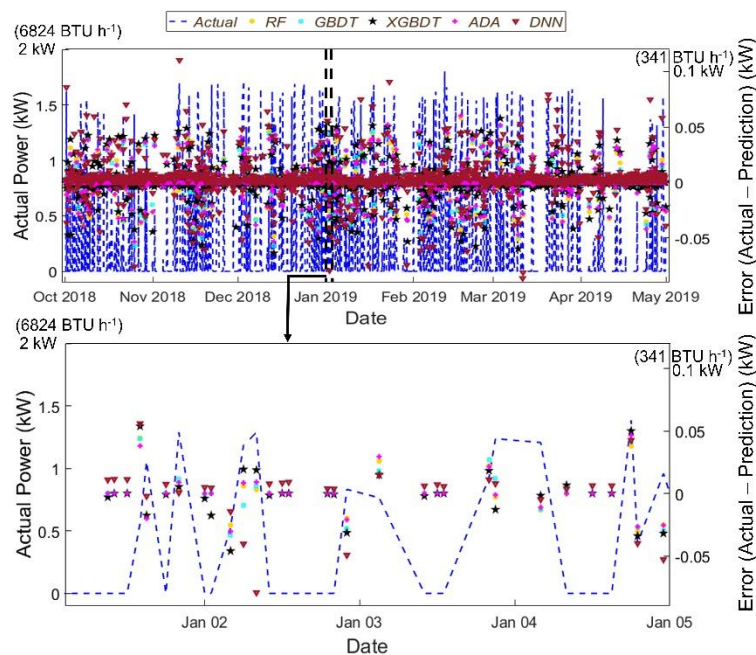


Figure 4 Upper figure shows the actual power consumption (left y-axis) and the error (actual – predicted power) (right y-axis) for each non-linear ML model for the entire testing data. Lower figure shows the same parameters over a magnified time scale (Jan 1st, midnight to Jan 5th, midnight i.e. 4-day period).

CONCLUSION

The results indicate that using only climate data (which is readily available or easily measurable) and the power consumed in the previous time-step, the linear ML models can predict the power consumption to a very high level of accuracy. Within the linear models, the coefficient of variation of the root mean squared error (CV-RMSE) for the MLR was 4.04062 which was 0.19% and 0.05% less than the ELN and SVR model respectively. Within the five non-linear models, gradient boosting decision tree (GBDT) exhibited the lowest CV-RMSE i.e. 4.26141 (which is 5.46% higher than the MLR model). In conclusion, MLR model can be used to accurately predict the power consumption of the GSHP system. Further work on applying these models to cooling data is also underway.

ACKNOWLEDGMENTS

The authors are thankful to Michael Koenig of Honda Smart Home, Davis, USA for his assistance with HSH datasets.

REFERENCES

- Ahmad, A. S., M. Y. Hassan, M. P. Abdullah, H. A. Rahman, F. Hussin, H. Abdullah and R. Saidur. 2014. *A review on applications of ANN and SVM for building electrical energy consumption forecasting*. Renewable and Sustainable Energy Reviews, 33: 102-109. <https://doi.org/10.1016/j.rser.2014.01.069>
- Davis Energy Group. 2013. Honda Smart Home Mechanical Plans. https://cdn.powerequipment.honda.com/tumblr/Mechanical_and_Plumbing.zip
- Fan, C., Y. Liao and Y. Ding. 2019. Development of a cooling load prediction model for air-conditioning system control of office buildings. International Journal of Low-Carbon Technologies, 14(1): 70-75. <https://doi.org/10.1093/ijlct/cty057>

- Kumar, S., S. K. Pal, and R. P. Singh. 2018. *A novel method based on extreme learning machine to predict heating and cooling load through design and structural attributes*. Energy and Buildings, 176: 275-286. <https://doi.org/10.1016/j.enbuild.2018.06.056>
- Lu, S., Q. Li, L. Bai and R. Wang. 2019. *Performance predictions of ground source heat pump system based on random forest and back propagation neural network models*. Energy Conversion and Management, 197: 111864. <https://doi.org/10.1016/j.enconman.2019.111864>
- Najib, A., A. Zarrella, V. Narayanan, P. Grant and C. Harrington. 2019. *A revised capacitance resistance model for large diameter shallow bore ground heat exchanger*. Applied Thermal Engineering, 162: 114305. <https://doi.org/10.1016/j.applthermaleng.2019.114305>
- Park, S. K., H. J. Moon, K. C. Min, C. Hwang and S. Kim. 2018. *Application of a multiple linear regression and an artificial neural network model for the heating performance analysis and hourly prediction of a large-scale ground source heat pump system*. Energy and Buildings, 165: 206-215. <https://doi.org/10.1016/j.enbuild.2018.01.029>
- Shukla, P. R., J. Skea, A. Slade, A. Al Khourdajie, R. van Diemen, and J. Malley. 2022. *In IPCC, 2022: Climate Change 2022: Mitigation of Climate Change*. Contribution of Working Group III to the Sixth Assessment Report of the Intergovernmental Panel on Climate Change. Cambridge University Press. https://report.ipcc.ch/ar6wg3/pdf/IPCC_AR6_WGIII_FinalDraft_Chapter09.pdf
- Sun, W., P. Hu, and F. Lei, N. Zhu and Z. Jiang. 2015. *Case study of performance evaluation of ground source heat pump system based on ANN and ANFIS models*. Applied Thermal Engineering, 87: 586-594. <https://doi.org/10.1016/j.applthermaleng.2015.04.082>
- Zhang, L., and J. Wen. 2019. *A systematic feature selection procedure for short-term data-driven building energy forecasting model development*. Energy and Buildings, 183: 428-442. <https://doi.org/10.1016/j.enbuild.2018.11.010>
- Zhang, L., J. Wen, Y. Li, J. Chen, Y. Ye, Y. Fu and W. Livingood. 2021. *A review of machine learning in building load prediction*. Applied Energy, 285, 116452. <https://doi.org/10.1016/j.apenergy.2021.116452>
- Zhang, W., J. Yu, A. Zhao and X. Zhou. 2021. *Predictive model of cooling load for ice storage air-conditioning system by using GBDT*. Energy Reports, 7: 1588-1597. <https://doi.org/10.1016/j.egy.2021.03.017>



An open library of g-functions for 34,321 configurations

Jeffrey D. Spitler

Timothy West

Xiaobing Liu

Ishraque Borshon

ABSTRACT

Thermal response functions, known as g-functions, are commonly used in ground heat exchanger design tools and whole building energy simulation programs to simulate the ground heat exchanger performance. Calculation of g-functions can be quite computationally time-consuming, particularly as the number of boreholes gets large. However, once the g-function is computed, the actual simulation time can be quite short, particularly if a hybrid time-step (Cullin and Spitler 2011) approach is used. Because of this, pre-computed g-function libraries are commonly used in design tools and building simulation tools. This paper describes development of a new, publicly available library containing g-functions for 34,321 borehole field configurations; for each configuration, g-functions are provided for 5 depths to allow interpolation between different borehole-to-height ratios. The available configurations include configurations in standard shapes: lines, rectangles, open rectangles, L-shapes, and U-shapes. It also includes new configurations: C-shapes, lopsided-U-shapes, and zoned rectangles, which are rectangular configurations with different interior and perimeter spacing of the boreholes

INTRODUCTION

Thermal response functions, known as g-functions, are commonly used in ground heat exchanger design tools and whole building energy simulation programs to simulate the ground heat exchanger performance. G-functions were originally developed by Prof. Johan Claesson and his graduate students at the University of Lund in Sweden (Claesson and Eskilson 1988, Eskilson 1987, Hellström 1991). g-Functions are unique to a specific borehole field configuration (geometry, e.g., 5 rows of 10 boreholes spaced 5m apart) and borehole depth.

Calculation of g-functions can be quite computationally time-consuming, particularly as the number of boreholes gets large. However, once the g-function is computed, the actual simulation time can be quite short, particularly if a hybrid time-step (Cullin and Spitler 2011) approach is used. Because of this, pre-computed g-function libraries are commonly used in design tools and building simulation tools. In practice, the g-functions are pre-calculated for specific configurations; for each configuration, multiple depths are pre-computed for interpolation purposes. Then, a design tool can iteratively try different configurations and adjust the depth to find the correctly sized ground heat exchanger. Furthermore, the g-functions scale with several non-dimensional parameters that allow wider application than the specific horizontal spacing and depths used in the pre-calculation.

Currently available libraries, implemented in eQUEST (Liu and Hellström 2006), GLHEPRO (Spitler 2000), and EED (BLOCON 2015) have less than 1000 possible configurations and are proprietary. This paper describes development of a new, publicly available library containing g-functions for 34,321 configurations; for each configuration, g-functions

Jeffrey D. Spitler (spitler@okstate.edu) is a professor, Timothy West and Ishraque Borshon are research assistants, at Oklahoma State University. Xiaobing Liu is senior research staff at Oak Ridge National Laboratory.

are provided for 5 depths. Calculation of the library was made possible by a new tool, *cpgfunction* (Cook and Spitler 2021) and thousands of computing hours on the Oklahoma State University High Performance Computing Center (OSUHPCC) cluster. The available configurations include configurations in standard shapes: lines, rectangles, open rectangles, L-shapes, and U-shapes. It also includes new configurations: C-shapes, lopsided-U-shapes, and zoned rectangles, which are rectangular configurations with different interior and perimeter spacing of the boreholes. An example showing the advantage of the zoned rectangular configuration is presented below.

With recent developments in calculation of g-functions (Prieto and Cimmino 2021) that allow calculation of g-functions in a few seconds, even for fields that have hundreds of boreholes, it might be argued that libraries are not needed. Yet, there are applications in automated design and large parametric studies with multiple buildings and numerous locations where the difference between a few seconds and milliseconds is quite important. Furthermore, the Prieto and Cimmino (2021) equivalent borehole model is implemented in Python with extensive use of libraries and is not readily reducible to a DLL¹ that could be used with a compiled program that is readily installable by practicing engineers.

The library is available at the US DOE Geothermal Data Repository: <https://doi.org/10.15121/1811518>. Fuller explanation of how to use the library is given in the report by Spitler et al. (2021), available at the same link.

METHODOLOGY

This section briefly describes the procedure used to calculate the g-functions. The g-functions are calculated with a tool that is called “*cpgfunction*” (Cook and Spitler 2021). It is based on the finite line source methodology developed by Cimmino (2018a, 2018b) for an open-source tool written in Python, called *pygfunction*. *Cpgfunction* is written in C++. *Cpgfunction* was developed to reduce memory consumption, which can be quite high for large numbers of boreholes, exceeding 96 GB in many cases. For calculating large numbers of g-functions, as was done here, the memory requirements can become critical when running on a cluster. Keeping the memory requirements below 96 GB allowed full use of the most common compute nodes on the Oklahoma State University High Performance Computing Cluster (OSUHPCC 2020). The time requirement is also improved for most cases, but for large numbers of regularly spaced boreholes, the computation times are similar. For further information on *cpgfunction*, see Cook and Spitler (2021).

The g-functions are calculated with the “Uniform borehole wall temperature” (UBHWT) boundary condition. That is, the heat input at each segment is adjusted to give uniform (but time-varying) temperatures at the borehole walls. This is the method commonly used to develop other g-function libraries and has been used to size ground heat exchangers for commercial systems for the last 30 years. A burial depth of 2 m is chosen to be representative of US practice.

Arguably, the “Uniform inlet fluid temperature” (UIFT) conditions are more physically realistic, since the boreholes of ground heat exchangers are generally plumbed in parallel, and all receive approximately the same inlet fluid temperature at any time. However, the g-functions calculated with the UIFT condition will be slightly different than those calculated with the UBHWT condition, and they have a dependence on the local borehole thermal resistance and the mass flow rate of the fluid. The g-functions also depend on the number of segments used – like most numerical analyses, increasing the number of cells or volumes increases the accuracy, with diminishing returns. A grid-independency analysis using typical values of borehole thermal resistance and mass flow rate was performed using the UIFT boundary condition. Results for the UBHWT boundary condition were compared to those obtained with the UIFT boundary condition and it was found that a smaller number of segments with the UBHWT boundary condition could closely approximate the g-functions calculated with the UIFT boundary condition, using typical borehole thermal resistances and mass flow rates. This investigation yielded the number of segments summarized in Table 1. These values were used to calculate the library g-functions and this method is referred to as the “adaptive discretization scheme.”

¹ The lead author would be happy to be proved wrong on this point. A publicly available open-source but compiled to DLL g-function calculation tool would be quite useful to bridge the gap between research and practice.

Table 1. Adaptive discretization scheme (NBH= Number of boreholes; BH=borehole)

Depth (m)	Range (NBH)	Segment Length (m)	Number of segments/BH
24	All	8	3
48	All	12	4
96	All	12	8
192	NBH < 120 BH	16	12
192	NBH ≥ 120 BH	12	16
384	NBH < 220 BH	16	24
384	NBH ≥ 220 BH	12	32

The library presented here represents weeks of computation time on the OSU High Performance Computing Cluster (OSU HPCC), and it would not have been feasible to develop such a library without access to this or a similar resource. Additionally, the memory consumed for computing converged UIFT g-functions would not have been feasible, even with access to the OSU HPCC. The 8-9x memory reduction of Cpgfunction (Cook and Spitler 2021) combined with the adaptive discretization scheme resulted in a near 80x memory reduction. This resulted in an ability to run a significant majority of the calculations on nodes that contained less memory, of which there are nearly 14x as many nodes available on the OSU HPCC.

RESULTS – THE LIBRARY

The library contains configurations previously available – rectangles, open rectangles, L-shapes, and U-shapes - though these configurations are considerably expanded from previously available libraries with larger numbers of boreholes, and, in some cases, up to 3 perimeter rows. The line cases and single borehole case are contained within the rectangle cases. Several of these cases are shown in Figure 1.

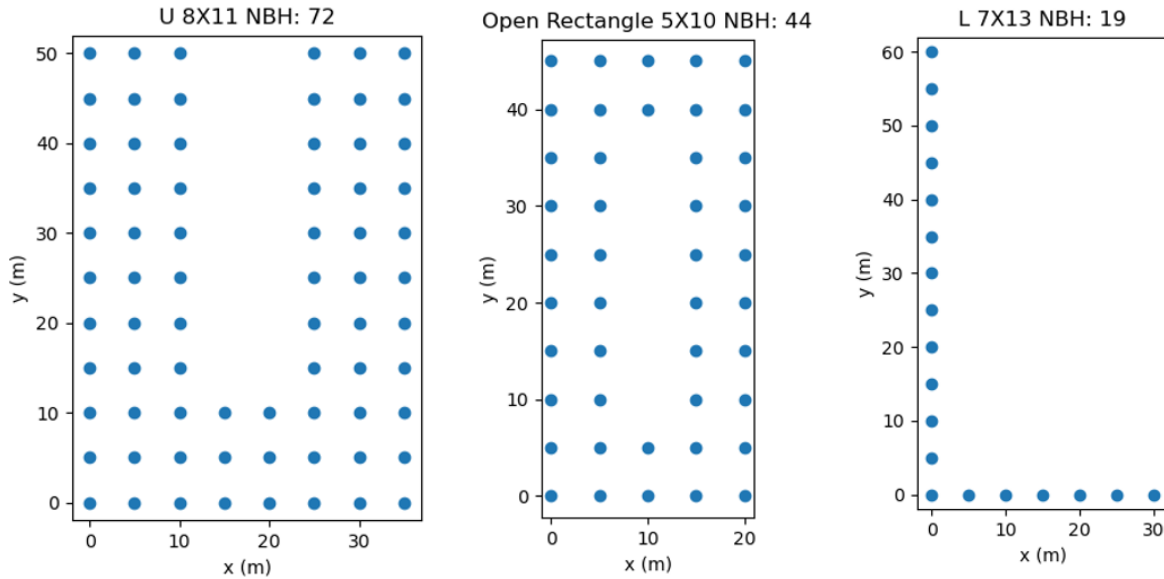


Figure 1 Configurations with 3,2,1 perimeter borehole rows

The new library provides several new configurations. The zoned rectangle configuration (Spitler, et al. 2020) was inspired by the fact that, for large rectangular borehole fields coupled to systems with significant heat imbalance, the

perimeter boreholes are more effective in either dissipating heat or extracting heat than the interior boreholes, which can become thermally saturated with time. Spitler et al. (2020) illustrate this for a case with 9x16 boreholes, dominated by heat rejection. The zoned rectangles have a perimeter zone and an interior zone, with the perimeter zone having smaller borehole spacing than the interior zone. In all cases calculated for the library, the perimeter zone contains a single perimeter row of boreholes, and the interior zone contains all interior boreholes.

In addition to the zoned rectangles, two additional shapes, the C-shape and Lopsided U (LopU) shapes, are new library configurations intended to support automated searching for an optimal borehole configuration within a rectangularly-constrained land area. The C-shape is equivalent to an open rectangle, but with some perimeter boreholes removed from one side of the rectangle. The LopU-shape is equivalent to a U, but with some perimeter boreholes removed. The new configurations are illustrated in Figure 2.

The C-shape and LopU-shape support the automated design search by helping to provide a continuous unimodal domain, where moving from one configuration to the next with increased number of boreholes will always reduce the amount by which the design temperatures are exceeded. Within a design tool, where the building may take any size, having a continuous unimodal domain that goes from, say, a 32x32 rectangle down to a single borehole allows for a working design to be identified in any case. So, for example, starting with the maximum number of boreholes, the domain might be something like 32x32 rectangle \rightarrow a zoned rectangle with 124 perimeter boreholes and 870 interior boreholes $\rightarrow \dots^2 \rightarrow$ zoned rectangle with 124 perimeter boreholes and 1 interior borehole \rightarrow open rectangle with 124 boreholes \rightarrow C-shape with 123 boreholes $\rightarrow \dots \rightarrow$ C-shape with 95 boreholes \rightarrow U-shape with 94 boreholes \rightarrow LopU with 93 boreholes $\rightarrow \dots \rightarrow$ LopU with 63 boreholes \rightarrow L-shape with 62 boreholes $\rightarrow \dots \rightarrow$ L-shape with 31 boreholes \rightarrow line with 30 boreholes $\rightarrow \dots \rightarrow$ single borehole. Table 2 lists all the borehole field configurations currently available in the expanded g-function library (Spitler et al. 2021).

Each g-function is represented by 27 pairs of $\ln(t/t_s), g$ values, with $3.003 \geq \ln\left(\frac{t}{t_s}\right) \geq -8.5$. The thermal properties and depth affect the value of the time scale, t_s , but generally this would cover times between 12 hours and a day at the low end, and hundreds of years at the high end. At the low end, short time-step g-functions (Xu and Spitler 2006) would generally be added in order to use the g-function for simulations.

Accessing the library g-functions is described in the library guide (Spitler, et al. 2021) and an example Python source code is included. For general design use, the g-functions for specific configurations are calculated with set spacings between boreholes and five different borehole depths. Non-dimensional scaling parameters are used to interpolate between the g-functions for the same configuration but with different depths, as described in the library guide.

VALIDATION

The tool used to calculate the library g-functions, cpfunction, was shown (Cook and Spitler 2021) to give nearly an exact match to pyfunction (Cimmino 2018) with g-functions having less than 0.1% RMSE difference. Results from either tool depend on the boundary scheme, the number of segments, and matching the geometry of the borehole field. For purposes of comparison, design depths were computed for three prototypical buildings (hotel, office, and school) in three locations (Atlanta, Chicago, Minneapolis) using GHEDT (Cook 2021) with the new library g-functions and with g-functions calculated with the equivalent borehole method (EBM) (Prieto and Cimmino 2021). The EBM g-functions were calculated with eight non-uniform segments as described by Cook (2021). The resulting design depths

² Here, the ellipsis represents a systematic reduction in rows and columns in such a way that at each step either an interior row or column would be eliminated, and then the row or column spacing is adjusted to have uniform interior spacing in each direction, though the spacing between rows and columns may vary slightly. The decision to eliminate a row or column is decided in favor of whichever elimination will maintain the most equal row spacing and column spacing. In general, this systematic reduction tends to alternately eliminate rows or columns.

for the two different g-function calculation procedures, as shown in Fig. 3, have a maximum difference of 1.8% for the nine cases. These differences are considerably less than other uncertainties in the design, such as the future building loads and should therefore be adequate for design purposes.

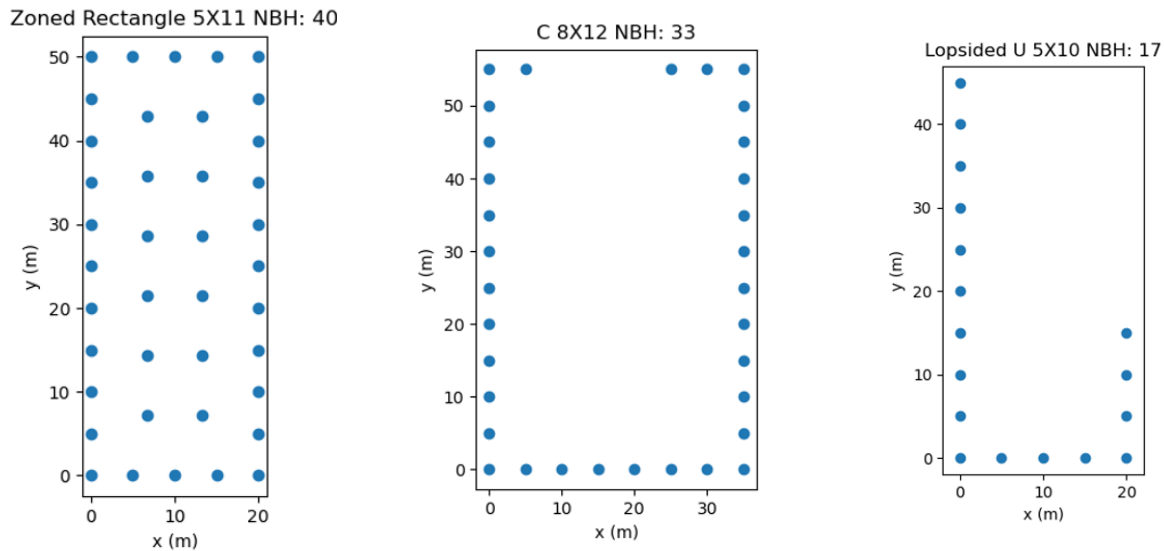


Figure 2 New configurations

Table 2. Library contents overview

Configuration Name	Number of configurations	Notes
Rectangle	1,651	Up to 1024 boreholes
Zoned Rectangle	12,615	
Open Rectangle	2,332	Up to 3 perimeter rows
C-shape	4,525	
L-shape	495	
U-shape	3,248	
Lopsided U-shape (LopU)	9,455	

EXAMPLE – ZONED RECTANGLE

As an example, a GSHP system serving a 5-story hospital building in Atlanta (Fig. 4) is considered. The 241,310 ft² (22,428 m²) building is simulated with a DOE prototype (USDOE 2022) hospital building model, with the original HVAC system replaced by a distributed GSHP system. As shown in Fig. 4, the hospital requires cooling and heat rejection year-round and therefore represents an extreme case for ground heat exchanger design. An early version of the GHEDT design tool (Cook 2021) was used to select specific configurations and determine the required borehole depth for two configuration types: (1) conventional rectangular array with fixed uniform bore spacing, termed the “square or near square” design routine in Spitler and Cook (2020); (2) constrained within a given land area that matches the “square or near square” land area, but with smaller bore spacing in the perimeter and larger bore spacing in the center zone of the borehole field (“Zoned rectangle” design) (Spitler and Cook 2021). In addition to the borehole field layout, various maximum bore depths are also investigated. Details of the GHE design are given by Spitler et al. (2021).

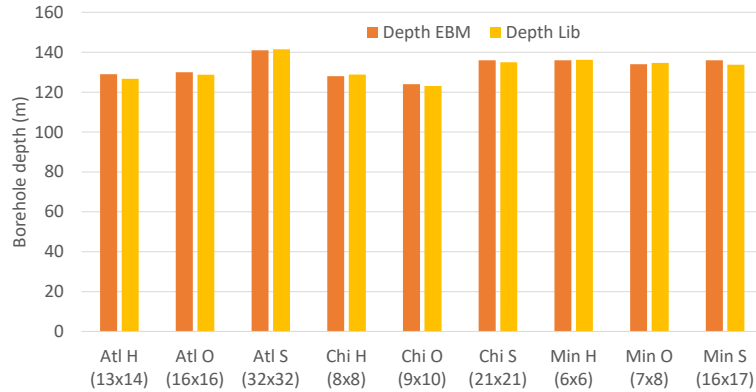


Figure 3 Comparison of borehole depths sized with GHEDT using g-functions from the library and g-functions computed with the EBM for three buildings (H=hospital; O=office; S=school) at three locations

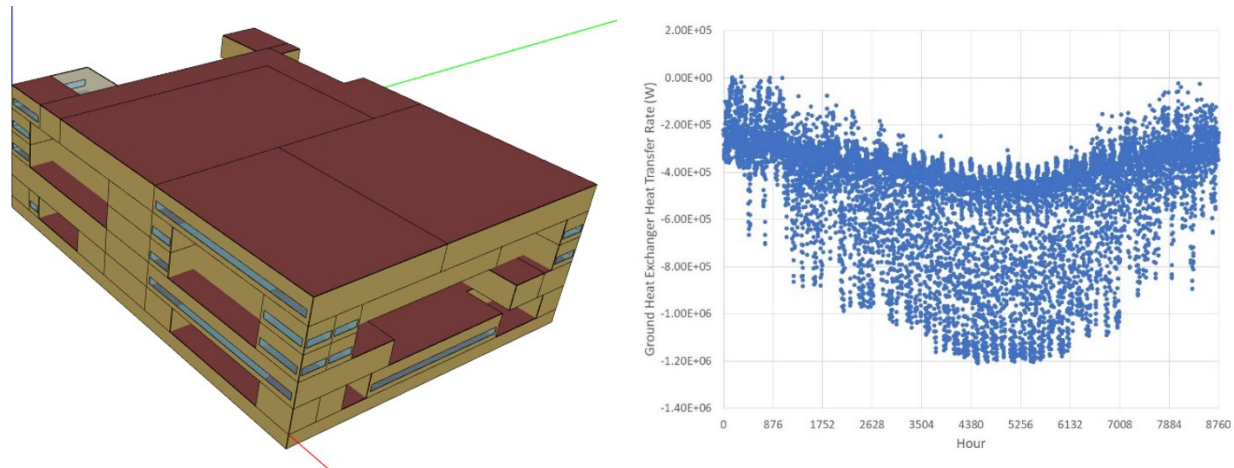


Figure 4 Hospital building (left) with hourly thermal loads imposed on the GHE (right)

Ground heat exchanger designs resulting from the different configuration types are listed in Table 3 and the total bore length of each design is graphically presented in Figure 5. For the same land area (42,630 m²) needed for a conventional rectangular design, using the “Zoned rectangle configuration” and 119 m individual bore depth, the total bore length is reduced by 37% compared with the conventional rectangular design. The two design configurations are shown in Figure 6. With the conventional borehole field configuration, the total bore length is only reduced by 3% if the maximum bore depth is increased from 90 m to 95 m without changing bore spacing. However, with the “Zoned rectangle configuration” and a 95 m maximum bore depth (MBD), the total bore length is reduced by 21% compared with the baseline. The zoned rectangle configuration takes advantage of the fact that in a large configuration with significant heat imbalance, the perimeter boreholes are more effective in dissipating heat than the boreholes in the center zone (Spitler et al. 2020).

Table 3. Example results

Configuration type and depth constraint	NBH	Spacing	Depth (m)	Configuration	Total bore length (m)	Change (%)
---	-----	---------	-----------	---------------	-----------------------	------------

Square or near-square w/ 90 m max. depth	930	7	87.2	Rec 31X30	81,096	-
Square or near-square w/ 95 m max. depth	841	7	94	Rec 29X29	79,054	-3%
Zoned w/ 95 m max. depth	678		94.9	Zoned 27X26 (576 interior BH)	64,342	-21%
Zoned w/ 100 m max. depth	608		98.9	Zoned 27X26 (506 interior BH)	60,131	-26%
Zoned w/ 120 m max. depth	426		119.3	Zoned 27X26 (324 interior BH)	50,822	-37%

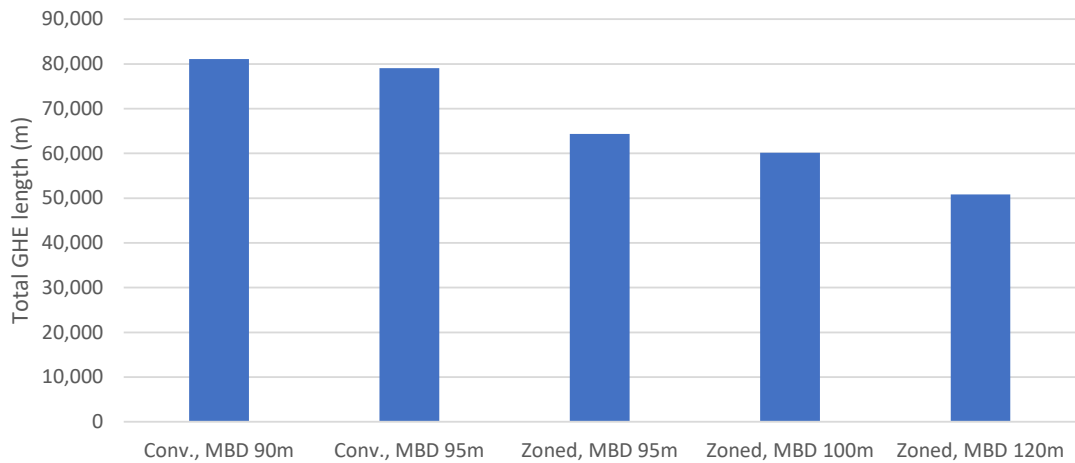


Figure 5 Total borehole length for two configuration types and different maximum borehole depths (MBD)

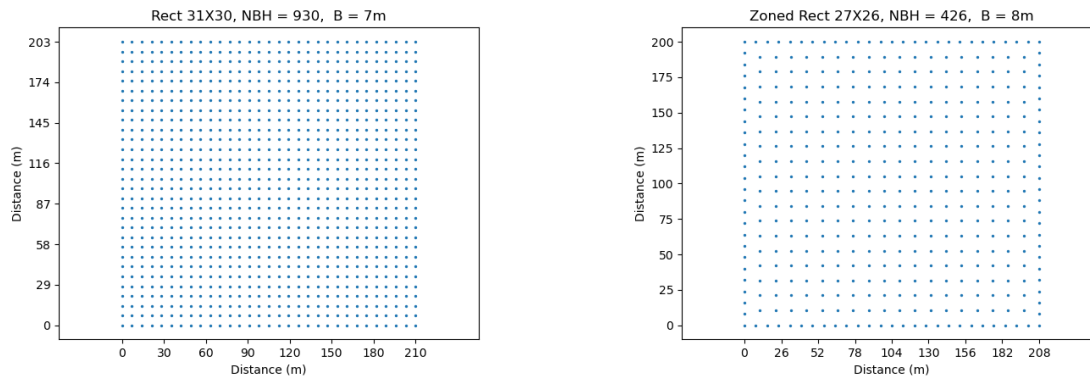


Figure 6 Base case (left) and zoned rectangle with 37% less total borehole length

CONCLUSIONS

This paper has presented a new publicly available library of g-functions for use in design of ground heat exchangers and energy analysis of ground-source heat pump systems. Despite recent developments in fast calculation of g-functions, there are still several applications where library look-up of g-functions will be preferred over on-the-fly calculations. The library contains new configurations not previously available, and, in total, about 35 times as many configurations as previously available proprietary libraries. The availability of this new library will aid in design of efficient ground-

source heat pump systems. One of the new configurations, the zoned rectangle, with smaller perimeter borehole spacing than interior spacing, was shown to be advantageous for a cooling-dominated Atlanta hospital, allowing significantly less drilling while using the same land area.

ACKNOWLEDGMENTS

Development of this library was funded through Department of Energy contract DE-AC05-00OR22725 via a subcontract from Oak Ridge National Laboratory. Computation of the library g-functions was made possible by the Oklahoma State University High Performance Computing Center. The g-function calculation tool, cpfunction, and scripts for running the library cases were developed by Mr. Jack Cook who was supported by Oklahoma State University via the OG&E Energy Technology Chair and by the Center for Integrated Building Systems.

REFERENCES

- BLOCON. 2015. "Earth Energy Designer (EED) Version 3.2 Manual." <https://buildingphysics.com/eed-2/>.
- Cimmino, M. 2018. pygfunction: an open-source toolbox for the evaluation of thermal. eSim 2018, Montréal, IBPSA Canada. 492-501.
- Clæsson, J and P. Eskilson. 1988. Conductive heat extraction to a deep borehole: Thermal analyses and dimensioning rules. Energy (Oxford), 13(6), 509–527. [https://doi.org/10.1016/0360-5442\(88\)90005-9](https://doi.org/10.1016/0360-5442(88)90005-9)
- Cui, P., X. Li, Y. Man and Z. Fang. 2011. *Heat transfer analysis of pile geothermal heat exchangers with spiral coils*. Applied Energy 88(11): 4113-4119.
- Cook, J. C. and J. D. Spitler 2021. Faster computation of g-functions used for modeling of ground heat exchangers with reduced memory consumption. Building Simulation 2021. Bruges, Belgium, IBPSA.
- Cullin, J. R. and J. D. Spitler. 2011). "A computationally efficient hybrid time step methodology for simulation of ground heat exchangers." Geothermics 40(2): 144-156.
- Eskilson, P. 1987. Thermal Analysis of Heat Extraction Boreholes. Ph.D. thesis. University of Lund.
- Hellström, G. 1991. Ground heat storage: thermal analyses of duct storage systems. Ph.D. thesis. University of Lund.
- Liu, X. and G. Hellström 2006. Enhancements of an Integrated Simulation Tool for Ground-Source Heat Pump System Design and Energy Analysis. Ecostock 2006. Stockton State College, Pomona, NJ.
- Prieto, C. and M. Cimmino. 2021. Thermal interactions in large irregular fields of geothermal boreholes: the method of equivalent boreholes. Journal of Building Performance Simulation 14(4): 446-460.
- Spitler, J. D., J. C. Cook and X. Liu 2020. A Preliminary Investigation on the Cost Reduction Potential of Optimizing Bore Fields for Commercial Ground Source Heat Pump Systems. Proceedings, 45th Workshop on Geothermal Reservoir Engineering, Stanford, California, Stanford University.
- Spitler, J.D. 2000. GLHEPRO -- A Design Tool For Commercial Building Ground Loop Heat Exchangers. Proceedings of the Fourth International Heat Pumps in Cold Climates Conference, Aylmer, Québec. August 17-18, 2000.
- Spitler, J. D., J. Cook, T. West and X. Liu 2021. G-Function Library for Modeling Vertical Bore Ground Heat Exchanger, Oak Ridge National Laboratory. <https://doi.org/10.15121/1811518>
- Spitler, J.D. and J.C. Cook 2020. "Sizing Ground Heat Exchangers with Rectangular Constraints." Oklahoma State University. Milestone Report Submitted to ORNL on 12/31/2020.
- Spitler, J.D. and J.C. Cook 2021. "Sizing Ground Heat Exchangers with Rectangular Constraints." Oklahoma State University. Milestone Report Submitted to ORNL on 02/26/2021.
- USDOE 2022. Prototype Building Models. <https://www.energycodes.gov/prototype-building-models> accessed May 7, 2022
- Xu, X. and J. D. Spitler. 2006. *Modelling of Vertical Ground Loop Heat Exchangers with Variable Convective Resistance and Thermal Mass of the Fluid*. 10th International Conference on Thermal Energy Storage - Ecostock 2006, Pomona, NJ. 8.

“Novel tool and guidelines for ground source heat pumps in densely populated areas”: a Swedish project.

Maria Letizia Fasci, Linus Eriksson

ABSTRACT

With one system installed for every twenty inhabitants, Sweden is by far the country with the highest penetration of Ground Source Heat Pumps (GSHPs). Unsurprisingly, it has initiated a project to support designers and decision makers working with GSHPs in densely populated areas. The project includes the development of a software implementing state-of-the-art ground heat transfer models, the study of possible scientific-based guidelines for the release of drilling permits, and the analysis of ground temperature data from densely populated areas.

We believe that Sweden being a forerunner in this field, the lessons learned during this project will be useful for other countries. Therefore, in this article, we discuss the progress of our project: we present the developed software and examples of its applications; summarize the discussion on the possible guidelines; and describe the process to retrieve data about densely populated areas.

INTRODUCTION

With 20-25% of its two million single-family houses heated through Ground Source Heat Pumps (GSHPs), Sweden has the highest penetration of GSHPs in the world (Rees, 2016). In certain areas, the penetration of GSHPs is even significantly higher than the national average (SGU, 2022). When installed in small residential buildings, GSHPs are typically used for heating purposes only; therefore, the continuous heat extraction of several neighbouring systems can lead to their thermal interference and performance degradation. Therefore, in Sweden, it is recommended – and in Stockholm it is mandated - to maintain a distance of at least 20 m between boreholes belonging to different properties (SGU, 2016). However, a software to allow shorter distances by increasing the depth of the energy wells has been proposed already in 2005 (Stockholms stad, 2005).

Since 2005, new mathematical methods for GSHPs in densely populated areas (Rivera et al., 2017; Fasci et al., 2021; Fasci et al., 2022a) and the increased computational speed allows more accurate simulations. Moreover, recommending a minimum distance between the boreholes is relatively arbitrary as it may be unnecessary in areas with a few systems and too permitting in areas with many systems. Therefore, a new Swedish project was started in 2021 to:

1. Create a new software implementing the state-of-the-art models to calculate the temperature influence between neighbouring boreholes
2. Propose and analyse new possible guidelines
3. Collect data from densely populated areas to study the real influence between neighbouring systems

Maria Letizia Fasci (mlfasci@kth.se) is a PhD student and Linus Eriksson is a Master student at the Department of Energy Technology, KTH – Royal Institute of Technology, Stockholm (Sweden).

In this article, we describe the progress on our three working packages, with a focus on the first one.

WORK PACKAGE 1: GSHPsDESIGNER (THE SOFTWARE)

Models implemented

GSHPsDesigner can simulate the annual-average wall temperature of all the boreholes of an area by using two different models: the Finite Line Source (FLS) (Li et al., 2016) and the Stacked Finite Line Source (SFLS) (Fasci et al., 2021) models. The software refers to these models respectively as FLS_I and FLS_{IV}. These models are suited for grounds characterized by heat conduction as the dominating heat transfer phenomenon - as it is for most of Sweden - and provide the upper and lower boundaries of the range within which the ground temperature is expected to fall (Cimmino, 2015). Both FLS_I and FLS_{IV} could also take into account the thermal influence of the built environment (Rivera et al., 2017; Fasci et al., 2022a); however, this possibility is currently not implemented. The models allow to account for the heat extraction from all the boreholes in an area. They can consider the exact year when the different boreholes started operating and account for the exact positions of each borehole, i.e., they can model irregular borehole configurations. However, they assume vertical borehole heat exchangers, while in reality borehole heat exchangers may also be inclined.

So far, we have not focused on the computational speed of the models. While FLS_I typically provides results in seconds, FLS_{IV} requires tens of minutes for areas with hundreds of boreholes. Possible acceleration techniques exist for FLS_{IV}, e.g., assuming a piece-wise linear borehole load (Lamarche, 2017), but have not been implemented yet.

GSHPsDesigner can also simulate the hourly temperature of the carrier fluid of one specific borehole in the area. A constant borehole resistance that connects the borehole wall temperature to the fluid return temperature is used for this purpose (Javed and Spitler, 2016). Calculating the fluid temperature with hourly resolution for several years would be computationally expensive using a standard convolution product for the temporal superposition. Therefore, a load aggregation scheme is used for this calculation (Claesson and Javed, 2012).

Comparison with other software

Other software for the design of GSHPs exist, e.g., BHEDesigner8 (Università di Genova, 2022), EED (Hellström and Sanner, 1994), GLHEPRO (Spitler, 2000). The fundamental difference between GSHPsDesigner and most existing software is its scope. GSHPsDesigner is dedicated to small residential systems, it was born out of the need to account for the thermal influence between neighbouring independent systems, as this influence may be relevant (Fasci, 2022b). On the contrary, most other software focus on the design of commercial installations, and do not include the possibility to account for the influence of neighbouring systems. This difference in their scope is reflected in the models implemented to compute the borehole wall temperature: the existing software use the g-functions (Eskilson, 1987), a method for hydraulically connected boreholes; GSHPsDesigner uses the FLS (Li et al., 2016) and SFLS (Fasci et al., 2021) models, in their versions suitable for hydraulically independent boreholes.

Another difference is the user for which the software are designed: existing software are mostly meant for designers, GSHPsDesigner is also suited for decision makers, thus it also provides functions to check the satisfaction of given requirements, e.g., temperature in the underground. In this, it is a follow up on *Temperatursänkning3000* (Stockholms stad, 2005), another software dedicated to Swedish residential areas. However, *Temperatursänkning3000* is limited to the possibility of accounting for maximum 16 neighbouring boreholes while GSHPsDesigner is not limited in the number of boreholes it can account for. Moreover, *Temperatursänkning3000* limits its scope to the suggestion of an increased borehole length to compensate for the neighbouring boreholes while GSHPsDesigner includes more functions, e.g., providing information about the ground temperature evolution and the carrier fluid temperature. Finally, GSHPsDesigner is also thought for researchers with access to the source code and the possibility to modify it. In this respect, it is inspired by *pygfunction*, the python library dedicated to the calculations of g-functions (Cimmino, 2018).

The input data

The main functionality of GSHPsDesigner is to simulate the ground temperature evolution in presence of GSHP

installations. Several inputs are necessary for this scope. These can be divided into two main categories:

- Ground properties
- Boreholes characteristics

The ground properties include the thermal conductivity and diffusivity, and the undisturbed ground temperature. The ground properties vary locally; therefore, for the design of relatively large systems, they are typically measured by means of thermal response tests (TRTs) (Gehlin, 2002). However, such measurements are relatively expensive, and their cost is unjustified for single-family houses. Typical properties for the geographical location of the installations are usually assumed instead. These properties can typically be extrapolated from the geology of the place and the literature on soil and rock types. However, to accelerate the calculation of the ground properties, we recommend the creation of a database containing the necessary ground information as a function of the geographical location considered. Moreover, we suggest including the information from the TRTs performed for the bigger installations in the database.

Concerning the borehole characteristics, the boreholes positions, lengths and years of installation must be known. For Sweden, this data is available on the SGU website (SGU, 2022). However, this information cannot be retrieved automatically but needs to be retrieved manually for each system, making the process time-consuming and sensitive to errors. The net annual heat loads are another necessary input. At the moment, the boreholes heat loads cannot be retrieved from Swedish public sources. Moreover, this information might not be retrievable at all, since typically, in small installations, boreholes heat loads are not measured. However, recent installations are equipped with sensors that make an estimation possible. Therefore, we believe that, for new installations, the information on the boreholes heat load should be available. Finally, the borehole load is estimated during the design phase of a GSHP system. These estimations may be used as a reference when no measurements are available. Other types of estimations may be possible considering the electricity bills or the building types. However, we expect that accessing and using this information may be more complicated than accessing the information on the systems design.

Given the uncertainty on the input data, the possibility to run Monte Carlo simulations or sensitivity analysis has been considered. However, nothing has been implemented in this respect yet.

Needs of decision makers and designers

Decision makers. Once the guideline to determine the sustainability of a GSHP is decided, our software will help the decision makers in determining whether the guideline is respected or suggest how to make that possible. For being useful for the Swedish decision makers, the software needs to:

1. Be easy to install and use by administrators without a scientific or engineering background
2. Provide the results in a few minutes
3. Determine whether a request should be accepted or rejected, but also suggest modifications to make a rejected proposal acceptable, e.g., proposing a longer borehole
4. Offer default input for information that might not otherwise be retrievable, e.g., borehole heat loads

In order to satisfy the needs of the decision makers, the software has the following characteristics:

1. The software consists of a Julia package (Bezanson et al., 2017). People with no programming experience likely need guidance for its installation. Detailed instructions are available for this reason. Microsoft Excel (Microsoft Corporation, 2018) can be used as an interface to input the data and obtain the results, simplifying the use of the software. The possibility to create a “standard software”, typically easier to use, is also under discussion
2. Two different models to evaluate the ground temperature evolution have been implemented, a conservative and an optimistic – more accurate - model. When analysing areas of hundreds of boreholes, the more accurate model may give results in tens of minutes. However, the conservative model always gives results in less than a few minutes. This allows the decision makers to take preliminary decisions in the desirable time.

3. The software is able to suggest an increased borehole length to prevent an unwanted ground temperature change; proposing to recharge the borehole during summer will also be considered
4. Default values for the ground characteristics and borehole heat extractions are used unless otherwise specified. The default values for the ground are typical for granite, most common rock in Sweden. The default values for the borehole heat extraction refer to a linear heat extraction of 15 W/m as a yearly average

Designers. Designers need to establish the techno-economic performance of a GSHP system. This requires the simulation of the system operation. This is a function of the ground-loop fluid temperatures that our software can simulate. However, our software is not currently able to simulate the whole GSHP operation. Moreover, the heat pump (HP) manufacturers have shown a higher interest in implementing our algorithms in their own rather than adopting a new software. Therefore, we are thoroughly commenting the source code of the software so that programmers can translate it to a different programming language if needed. In addition, the Excel interface may be used to connect GSHPsDesigner to another software. Finally, the possibility of implementing the necessary functions for the techno-economic analysis is planned for the future, but no effort has been initiated in this direction yet.

Examples of application

Borehole wall temperature evolution. GSHPsDesigner can simulate the borehole wall temperatures in an area with a high density of independent boreholes. To show this function, we have selected a recent installation in an area characterized by diversified systems in terms of size and installation period, with the oldest installation dating back to 1998. The area considered is shown in Figure 1. The installation of interest is represented by the blue square, the neighbouring installations taken into account in the simulation are the squares within the orange area, corresponding to the 50 closest boreholes. This number was chosen because it had already been calculated that accounting for the 50 closest boreholes or the 450 closest boreholes resulted in less than 0.2 K difference for this scenario (Eriksson, 2022). The file containing the input for the simulations is available online (Fascì, 2022a).



Figure 1 Map of the energy boreholes in Södra Ängby (Stockholm, Sweden). In orange the area containing the boreholes accounted for in the simulation; in blue the borehole under study.

The software calculates the temperature evolution both assuming that there are no neighbouring installations and accounting for the neighbouring installations given as an input by the user. As for now, it is up to the user to decide how many boreholes to consider in the simulation. However, it was shown that considering boreholes beyond a certain distance becomes insignificant (Fascì et al., 2019). A future version of the software will suggest the size of the area the user should consider in their simulation. As already mentioned, the software uses two different models for the computation of the temperature evolution: a more conservative, less accurate and faster to run model, referred to as FLS_I; and a more optimistic, more accurate and slower to run model, referred to as FLS_{IV} (Fascì et al., 2021). For our case study, the computational time of FLS_I was 0.7 s; the computational time of FLS_{IV} was 246 s. The results obtained with the two models are shown in Figure 2. For thorough details of how to use GSHPsDesigner through the excel interface and information on other functionalities of GSHPsDesigner we refer to Fascì et al. (2022b).

Figure 2 shows that the temperature on the borehole wall of the new system was, according to the simulations, 2 K lower than it would have been if undisturbed already after 1 year of operation. This is attributable to the several neighbouring systems that have been operating for already a decade or more. After 25 years, the temperature is forecasted to be 5 K lower. These results, related to a real case study, show the importance of accounting for the neighbouring systems to correctly size a new installation, and the importance of the availability of tools like GSHPsDesigner for this scope. The difference between the two models implemented in the software - FLS_I and FLS_{IV} – is always lower than 0.5 K, confirming that FLS_I can be a valid solution for a fast evaluation of a neighbourhood.

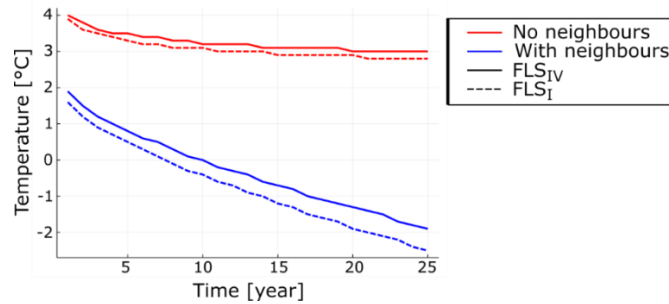


Figure 2 Annual average temperature evolution of the borehole under study (blue borehole in Figure 1).

Minimum required length to respect a temperature threshold. Another feature of GSHPsDesigner is checking whether new installations may cause the underground temperature to vary more than a desired magnitude, and if it is the case proposing the adoption of longer boreholes. We showcase this feature on the same area as in Figure 1. We have assumed that all the buildings currently without a GSHP install an identical borehole; the new fictitious boreholes are installed together with the real newest installation (blue square in Figure 1) and are identical to it, i.e., 170 m deep. This corresponds to eleven new fictitious installations along with the one real new installation. The data about the new installations are available in Fasci (2022a). We have then calculated if the suggested borehole length allows the satisfaction of the temperature requirement or how much longer the borehole length should be. We have conducted a sensitivity study on the temperature change allowed: this varies between 13 – 15 K; 13 K is a threshold already overcome with the current installations, 15 K is a threshold that would not be overcome with the initial borehole length proposed.

We have considered different scenarios:

- Base scenario: the fifty existing installations are equal to the real existing installations
- Scenario(s) 5%, 8% and 10%: the existing boreholes are 5%, 8% and 10% longer than the real existing installations; the total extraction from the boreholes is unchanged compared to the real scenarios. This results in a lower heat extraction per borehole length

The results are shown in Figure 3.

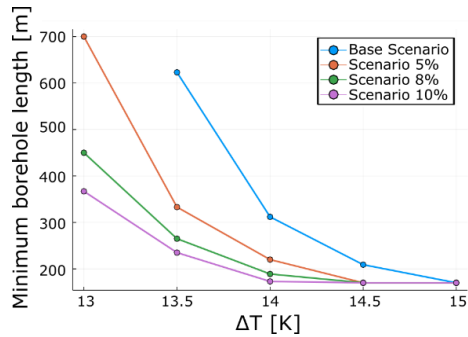


Figure 3 Minimum borehole length as a function of the maximum temperature change allowed. Results assuming the actual borehole length for the existing boreholes (Base Scenarios) or deeper boreholes (Scenarios 5%, 8%, 10%).

Figure 3 shows that the minimum borehole length allowed may be very sensitive to the temperature change allowed. For example, in the Base Scenario, the proposed borehole length of 170 m would be acceptable if a temperature change of 15 K were allowed ; however, the borehole length should be increased to 209 m, 312 m and 623 m if the temperature change allowed were respectively 14.5, 14.0 and 13.5 K. The new boreholes could not be installed at all if the maximum temperature change allowed were 13 K since this threshold would be already exceeded with the existing installations. This shows the importance – for a country that decides to limit the underground temperature change – of carefully selecting the temperature threshold, since being excessively conservative may result in the need of unnecessarily expensive installations thus limiting the access to this technology. Moreover, such a high sensitivity of the borehole length on the underground temperature change allowed, on top of the uncertainty on the input data and the model itself, suggests that sensitivity and Monte Carlo analysis should be preferred to deterministic approaches.

Figure 3 also shows that if the new installations alone were responsible for respecting a given temperature threshold while the old boreholes were designed without taking into account future installations, this could result in the need of extremely long boreholes for the new owners, possibly completely precluding the new installations. However, if a neighbourhood is designed since the beginning so that all the boreholes share the responsibility of limiting the underground temperature change, this may be possible with an increase of a few meters by every borehole. For example, if the existing fifty boreholes had been 5% longer, i.e., 3-10 m longer, the new boreholes would need to be 50 m - rather than 142 m- longer than the initial design to respect a temperature change limit of 14 K; if the existing boreholes had been 8% longer the new boreholes would need to be 19 m longer than the initial design; if the existing boreholes had been 10% longer the new boreholes would need to be only 3 m longer.

WORK PACKAGE 2: GUIDELINES

Another goal of this project is to suggest new possible guidelines to guarantee a sustainable penetration of GSHPs. At the moment, different countries have different rules/recommendations (Hähnlein et al., 2013). The recommendations are heterogeneous even within Sweden, where, for example, in Stockholm one must obtain a drilling permit to install a GSHP, but in other areas the permit is not required (Rydel, 2013). As we write this article, the investigation of the guidelines has not started yet; however, a few possibilities have been suggested.

A possible guideline may concern a threshold on the maximum ground temperature change for environmental reasons; in fact, changes in the ground temperature affect the microbiological activity in the ground and may affect the bacterial and faunal community as well (Hähnlein et al., 2013). Another possible guideline would involve the prescription of a minimum heat carrier fluid temperature; in fact, in Sweden, residential GSHPs typically shut down if the return temperature from the ground is lower than -12/-7 °C to prevent damages to the compressor (Wurtz, 2022). Frequent such shut downs would undermine the energy savings and techno-economic profitability of these systems, and should therefore be avoided. Other guidelines such as imposing a maximum temperature change on property borders for a fair access to geothermal energy, and making the new owners pay for the unexpected economic loss of the previous owners

have been proposed. These four possible guidelines will soon be investigated.

WORK PACKAGE 3: DATA

In order to evaluate the accuracy of the software against real measurements and monitor the state of the underground temperature we want to gather data about the heat extractions and return temperatures from boreholes in densely populated areas. Retrieving this data is the biggest challenge of this project. Data collection from older installations is practically impossible due to the absence of sensors, while data collection from recent installations is hindered by privacy regulations and sometimes lack of communication between the sensors in the system and the heat pump manufacturers (Wurtz, 2022). To obtain data from an installation, the most straight forward procedure for us is to:

1. Check, for each property, who the HP manufacturer is (this information is openly available from the drilling permits for Stockholm (Stockholms stad, 2022))
2. Ask the HP manufacturer if they have data from that installation
3. If the data exists, ask the HP owner if their data can be shared

This procedure cannot be automatised and is very time consuming. As a matter of fact, as for now, we have only obtained data from two installations belonging to employees of our project partners.

We believe that relying on GSHPs without monitoring the evolution of the underground temperature around the installations can lead to under- or overexploiting the shallow geothermal heat, comparable to using wood oblivious of the size of the forest. Therefore, we believe that basic information like the borehole heat loads and the supply and return temperatures from the boreholes should be measured and easily available as it currently is for the boreholes positions and years of installations. For this scope, we suggest that this data is made available in a database.

CONCLUSION

We have presented an ongoing Swedish project to promote the sustainable penetration of GSHPs. We have focused on describing GSHPsDesigner, the open-source software under development implementing state-of-the art research and designed so that designers and decision makers can use it. We have shown that the software can analyse a relatively big area in a few seconds or minutes, depending on the accuracy wanted. We have studied a real area in Stockholm and discovered mathematically that existing installations should already be significantly affected by their neighbours, making the use of such software paramount for optimal design. We have also summarized possible guidelines that we will investigate to ease the sustainable penetration of GSHPs. One of our simulations has pointed out the importance of carefully analysing the possible guidelines to avoid unnecessarily hindering the installation of new systems. Finally, we have described the inefficient process that we currently have to undergo to obtain data from real installations hoping that countries that have recently started installing these systems plan since the beginning methods to collect data and make them easily accessible.

ACKNOWLEDGMENTS

This project is supported by the Swedish Energy Agency under grant P43647-3. It is supervised by Alberto Lazzarotto and Joachim Claesson and in partnership with Bengt Dahlgren Geoenergi, Borrföretagen i Sverige, Neoenergy Sweden, Nibe, Nowab, Stockholms stad, Svenskt Geoenergicentrum, Thermia and Täby kommun. The partnering bodies are respectively represented by José Acuña and Max Hesselbrandt, Pär Malmborg, Göran Hellström, Daniel Hagberg and Martin Forsén, Jan-Erik Nowacki, Amanda Salguero Engström, Signhild Gehlin, Albrecht Wurtz and Sandra Alfredsson, Lars Lindqvist. We are grateful to the project partners for the interesting discussions leading to the development of GSHPsDesigner and the writing of this paper. We also thank Patrick Meisner for proofreading.

REFERENCES

Bezanson, J., A. Edelman, S. Karpinski and V.B. Shah. 2017. *Julia: A fresh approach to numerical computing*. SIAM Review, 59(1): 65-98.

- Cimmino, M. 2015. *The effects of borehole thermal resistances and fluid flow rate on the g-functions of geothermal bore fields*. International Journal of Heat and Mass Transfer 91: 1119–1127.
- Cimmino, M. 2018. *pygfunction: an open-source toolbox for the evaluation of thermal response factors for geothermal borehole fields*. In Proceedings of eSim 2018, the 10th conference of IBPSA-Canada (pp. 492-501). IBPSA. ISBN 978-2-921145-88-6.
- Claesson, J. and S. Javed. 2012. *A load-aggregation method to calculate extraction temperatures of borehole heat exchangers*. ASHRAE Transactions 118: 530–539.
- Eriksson, L. 2022. *Performance of ground source heat pumps in densely populated areas*. Bachelor Thesis. Department of Energy Technology, KTH - Royal Institute of Technology, Stockholm, Sweden.
- Eskilson, P. 1987. *Thermal Analysis of Heat Extraction Boreholes*. Ph.D. Thesis. Department of Mathematical Physics, Lund Institute of Technology, Lund, Sweden.
- Fasci, M. L., A. Lazzarotto, J. Acuña and J. Claesson. 2019. *Analysis of the thermal interference between ground source heat pump systems in dense neighborhoods*. Science and Technology for the Built Environment, 25: 1069-1080.
- Fasci, M. L., A. Lazzarotto, J. Acuña, and J. Claesson. 2021. *Simulation of thermal influence between independent geothermal boreholes in densely populated areas*. Applied Thermal Engineering, 196: 117241.
- Fasci, M. L., W. Mazzotti, A. Lazzarotto, and J. Claesson. 2022a. *Temperature of Energy Boreholes Accounting for Climate Change and the Built Environment - a New Model for its Estimation*. SSRN preprint 4113861.
- Fasci, M. L. 2022a. *GSHPsDesigner*. Retrieved from: <https://gitlab.com/mlfasci/GSHPsDesigner/-/tree/master/Projects>
- Fasci, M. L., A. Lazzarotto, and J. Claesson. 2022b. *GSHPsDesigner: an open access tool for ground-source heat pumps designer and decision makers*. European Geothermal Congress 2022, Berlin, Germany.
- Fasci, M. L. 2022b. *Air-, ground- and dual-source heat pumps a comparison between energy-efficient systems for a Swedish dwelling*. BuildSim Nordic 2022, Copenhagen, Denmark.
- Gehlin, S. 2002. *Thermal response test: method development and evaluation*. PhD thesis. Luleå University of Technology, Luleå, Sweden.
- Hähnlein, S., P. Bayer, G. Ferguson and P. Blum. 2013. *Sustainability and policy for the thermal use of shallow geothermal energy*. Energy Policy, 59: 914-925.
- Hellström, G., and B. Sanner. 1994. *Software for dimensioning of deep boreholes for heat extraction*. Proc. Calorstock, 94, 195-202.
- Javed, S. and J. D. Spitler. 2016. *Calculation of borehole thermal resistance*. In S. J. Rees, Advances in Ground-Source Heat Pump Systems. Woodhead Publishing.
- Lamarche, L. 2017. *g-function generation using a piecewise-linear profile applied to ground heat exchangers*. International Journal of Heat and Mass Transfer, 115: 354-360.
- Li, M., K. Zhu and Z. Fang. 2016. *Analytical methods for thermal analysis of vertical ground heat exchangers*. In S. J. Rees, Advances in Ground-Source Heat Pump Systems. Woodhead Publishing.
- Microsoft Corporation. 2018. *Microsoft Excel*. Retrieved from <https://office.microsoft.com/excel>.
- Rees, S. J. 2016. *An introduction to ground-source heat pump technology*. In S. J. Rees, Advances in Ground-Source Heat Pump Systems. Woodhead Publishing.
- Rivera, J. A., P. Blum and P. Bayer. 2017. *Increased ground temperatures in urban areas: estimation of the technical geothermal potential*. Renewable Energy, 103: 388-400.
- Rydel, D. A. 2013. *Geoenergi borrhål som avviker och hamnar under en grannes fastighet - Gör de intrång i grannens äganderätt?* Master Thesis. Stockholm University, Stockholm, Sweden.
- SGU, Sverige Geologiska Undersökning. 2016. *Vägledning för att borra brunn*. Retrieved from: <https://resource.sgu.se/produkter/broschyrer/vagledning-normbrunn-16.pdf>.
- Spitler, J.D. 2000. *GLHEPRO -- A Design Tool For Commercial Building Ground Loop Heat Exchangers*. Proceedings of the Fourth International Heat Pumps in Cold Climates Conference, Aylmer, Québec. August 17-18, 2000.
- SGU, Sverige Geologiska Undersökning. 2022. *Wells*. Retrieved from <https://apps.sgu.se/kartvisare/kartvisare-brunnar.html>.
- Stockholms stad. 2005. *Beräkningsprogram för dimensionering av energibrunnar*. Retrieved from <https://boende.stockholm/siteassets/mitt-boende/blanketter/miljoforvaltningen/varmepumpar/om-berakningsprogram-for-dimensionering-av-energibrunnar.pdf>.
- Stockholms stad. 2022. *e-arkiv Stockholm*. Retrieved from <https://etjanst.stockholm.se/earkivet/>.
- Università di Genova. 2022. *GeoSensingDesign.org*. Retrieved from <https://en.geosensingdesign.org/>.
- Wurtz, A. 2022. *Personal communication*. Designer and software developer at Thermia.



Development of a Web-based Screening Tool for Ground Source Heat Pump Applications

Xiaobing Liu

**Jason DeGraw
Mark Adams
Niraj Kunwar**

**Mini Malhotra
Gina Accawi
Joshua New**

**Wes Forman
Brett Brass
Jean Guo**

ABSTRACT

Ground source heat pump (GSHP) technology has great potential to help the nation meet its energy and decarbonization goals, but several barriers hinder the wide application of GSHP. Important barriers include the lack of a coherent toolset for analyzing the technical feasibility and economic viability of the GSHP application. The current design and analysis methods are ineffective and require significant expertise to apply. Although building energy modeling is increasingly important in designing buildings, the tools for GSHP modeling and simulation are lacking. A web-based free-to-use tool is being developed for quick techno-economic analysis of GSHP applications in nearly any building in the United States. This tool is enabled by improvements in the calculation methodology to allow rapid sizing of borehole configurations that provide significant cost savings. The screening tool currently uses US Department of Energy (DOE) prototype building models and an extended g-function library to size ground heat exchangers and simulate the performance of GSHP systems. The team is integrating with DOE's Oak Ridge National Laboratory's AutoBEM program to automatically create a building model based on user inputs. This paper introduces the structure, components, features, and results of the web-based screening tool for GSHP applications. Future directions for further developing the tool are also discussed.

INTRODUCTION

Ground-source heat pumps (GSHPs) can efficiently keep residential and commercial buildings thermally comfortable year-round. However, the application of GSHPs is hindered by their high initial cost, mostly because of the cost of drilling boreholes in the ground to install ground heat exchangers (GHEs) (Liu et al. 2019). This factor plays an important role in decision making. A public-facing tool that can accurately analyze the costs and benefits of investing in GSHPs will help identify GSHP projects with favorable economics.

However, such a tool does not yet exist. Most existing tools are dedicated to sizing the GHE, which is the most unique and critical component of a GSHP system (GLHEPro 2016, Gaia Geothermal LLC 2016, BLOCON 2017).

Xiaobing Liu (liux2@ornl.gov), Jason DeGraw, Mini Malhotra, Wes Forman, Mark Adams, Gina Accawi, Brett Brass, Niraj Kunwar, and Joshua New are R&D Staff at Oak Ridge National Laboratory.

This manuscript has been authored by UT-Battelle, LLC, under contract DE-AC05-00OR22725 with the US Department of Energy (DOE). The US government retains and the publisher, by accepting the article for publication, acknowledges that the US government retains a nonexclusive, paid-up, irrevocable, worldwide license to publish or reproduce the published form of this manuscript, or allow others to do so, for US government purposes. DOE will provide public access to these results of federally sponsored research in accordance with the DOE Public Access Plan (<http://energy.gov/downloads/doe-public-access-plan>).

These GHE sizing tools rely on inputs of the thermal loads of the GHE, which must be estimated or calculated with other methods or programs. Also, these dedicated GHE sizing tools do not predict the performance of a GSHP system. The feasibility of installing a GSHP system for a specific project is usually assessed based on heating and cooling degree days to estimate the building thermal loads and required equipment capacity, and size of the GHE (NRC 2005). This rough estimation often results in a GSHP system that does not meet economic expectations or a GSHP system that does not perform as efficiently as it could.

The size and cost of a GHE are sensitive to the amount of energy rejected to the ground when cooling compared with the amount of energy extracted when heating. Given the large thermal mass of the ground, the heat transfer process of a GHE is almost completely transient, and thus both the peak and the total thermal loads of a GHE need to be accounted for when sizing a GHE. The thermal loads are affected by the design and operation of the building and its mechanical system. As buildings become more complex owing to the increasing diversity in functions and efforts to reduce the environmental footprint of buildings, building energy simulation (BES) is more commonly used to predict the thermal loads of a building. Integrating BES with the GHE design tool not only provides a seamless transition between the building's thermal loads and the GHE sizing but also, more importantly, allows the user to assess the effects on the GHE size and the GSHP system performance resulting from variations in the design and operation of the building and its mechanical system (Liu and Hellström 2006). With a side-by-side comparison between a GSHP system and a conventional HVAC system that serves the same building, the energy savings and carbon emission reductions resulting from using the GSHP system can be evaluated. Furthermore, an integrated tool enables a simulation-based holistic design approach for lowering the overall cost and energy consumption of the building by improving the design and controls of the building and the GSHP system.

The bottleneck of the simulation-based design approach is creating a detailed and accurate BES model to predict thermal loads. This work is time-consuming and requires many inputs. Having access to a software package that can estimate hourly thermal loads with minimal user input will be beneficial. Additionally, GHE sizing tools should be improved to allow highly customizable designs of the GHE so that the GHE performance can be optimized based on the given thermal loads and the constraints of the available land area for installing the GHE.

The goal of this project was to develop a web-based and user-friendly techno-economic analysis tool for quickly assessing the viability of applying a GSHP for a given residential or commercial building. This tool, the GSHP Screening Tool, is based on EnergyPlus and OpenStudio (NREL 2020), the US Department of Energy's (DOE's) flagship program in BES, and the latest development in GHE modeling, which can quickly simulate the performance of highly customized GHE designs with satisfactory accuracy (Spitler et al. 2020, 2021a). The project initially considered systems in which the GHE is expected to meet most of the thermal load; a hybrid configuration that uses a combination of GHE and conventional heat rejection/addition equipment may be included in the future.

This paper reviews the implementation of the web-based GSHP Screening Tool, including an automated process for creating GSHP system simulation and sizing GHEs within a given rectangular land area; the interfaces of the web-based screening tool; and examples of the screening results of GSHP applications in 16 prototype commercial buildings in 15 climate zones in the United States.

METHODOLOGY

The three components of the GSHP Screening Tool are (1) an auto-sizing tool for vertical bore GHE (VBGHE), which allows highly customized borehole field patterns; (2) a seamless approach to integrating the state-of-the-art BES programs, EnergyPlus and OpenStudio, with the advanced VBGHE sizing tool; and (3) a user-friendly interface to accept user inputs, display key simulation results, and perform economic analysis based on the cost data of HVAC equipment and energy prices.

The auto-sizing tool of the VBGHE was developed and integrated with an OpenStudio Workflow to establish a

fully automated process for replacing an existing HVAC system sub-model in a BES model with a GSHP system, sizing each component of the GSHP system, including the VBGHE, and simulating the performance of the GSHP system. A web interface was also developed to take user inputs and display screening results from an automated design and economic analysis process. The structure and data flow of the automated process is shown in Figure 1.

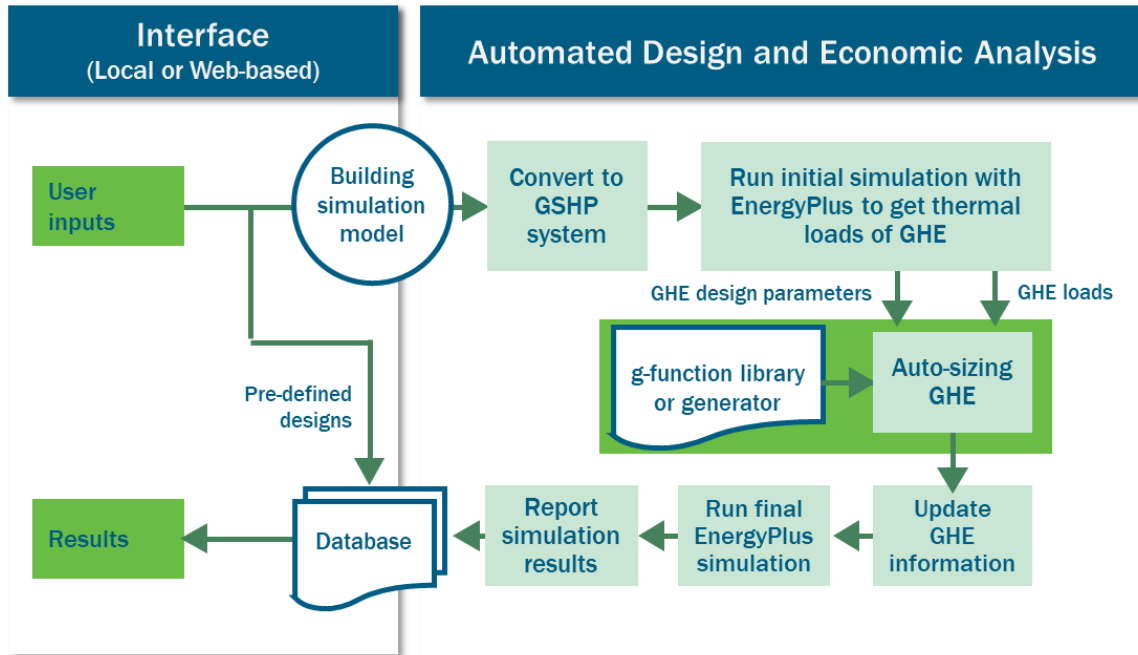


Figure 1 Flowchart of the GSHP Screening Tool.

The automated design and economic analyses start from a BES model, which can be an existing BES model (created with the OpenStudio program) or a simplified BES model created with AutoBEM, developed by DOE’s Oak Ridge National Laboratory (ORNL) (New et al. 2018), for almost any existing building that can be specified through a satellite view of the United States. The design and economic analyses include the following subsequential steps:

1. Replace the existing HVAC system in the BES model with a GSHP system using an OpenStudio measure.
2. Simulate the initial design of the GSHP system to obtain the thermal loads of the VBGHE. In this initial simulation, the borehole number is estimated based on the floor space of the building. Default values are used for borehole depth (200 ft [61 m]), response factors of VBGHE (i.e., the g-functions), and borehole design parameters. The program can calculate the undisturbed ground temperature based on a user-specified location of the building. Users can specify ground thermal properties or take default values.
3. Size the VBGHE with a new design tool to determine the borehole field arrangement and the depth of each borehole, as well as the associated g-functions.
4. Update the input of the BES model with the described sizing results of the VBGHE.
5. Perform a simulation of the updated GSHP system to predict its performance and perform a simulation with the original HVAC system to establish a baseline for comparison.
6. Report key performance metrics of the simulated GSHP system and pass them to the interface and a database.

The GSHP system was designed and simulated based on the following criteria. Default values of VBGHE design

parameters are listed in Table 1.

- Existing HVAC systems in a building are replaced with a new distributed GSHP system, which provides independent climate control in each thermal zone of a building without using any supplemental heating or cooling system.
- The rated heating and cooling coefficients of performance of the GSHP unit are 4.0 and 6.5, respectively. EnergyPlus auto-sizes and simulates water-to-air heat pumps of distributed GSHP systems. The entering water temperature of the heat pump is from the supply water temperature of the GHE, so the effect of GHE supply temperature on the heat pump efficiency is modeled in annual simulations.
- A VBGHE with boreholes laid out in a square of a near-square field with 6.1 m bore spacing is sized to maintain the leaving fluid temperature of the VBGHE between 1°C and 35°C year-round.
- Outdoor air is provided with a dedicated ventilation system in parallel with the distributed GSHP system.
- Energy savings are not only from the higher operational efficiency of the GSHP system but also the avoided simultaneous heating and cooling, which is common in the conventional variable air volume systems, as well as the improved fan control and fan efficiency.

Table 1. Default values of VBGHE design parameters

Parameter	Default value	Parameter	Default value
Borehole radius (m)	0.0762	Grout heat capacity (kJ/m ³ -K)	3,901
U-tube pipe thickness (m)	0.002	Ground conductivity (W/m-k)	1.29*
U-tube pipe outer diameter (m)	0.027	Ground heat capacity (kJ/m ³ -K)	2,347
U-tube leg spacing (m)	0.025	Undisturbed ground temperature (°C)	Site-specific. Calculated with the method by Xing and Spitler (2015)
Pipe conductivity (W/m-K)	0.39	Bore spacing (m)	6.1
Pipe heat capacity (kJ/m ³ -K)	1,542	Maximum GHE supply temp. (°C)	35
Grout conductivity (W/m-k)	1.29	Minimum GHE supply temp. (°C)	1

* The screening tool allows users to change the ground thermal conductivity value through the interface.

Simulations of DOE prototype models for 16 types of commercial buildings (DOE 2022) in 15 US climate zones (ASHRAE 2021) were performed with an existing conventional HVAC system and a new GSHP system, separately. The simulation results are stored and managed through a database. These precalculated results can quickly indicate the techno-economic viability of a GSHP application.

NEW DESIGN TOOL FOR VBGHE

The state-of-the-art design method for VBGHEs, which are the most used type of GHE (especially for commercial buildings), is based on thermal response functions known as g-functions (Eskilson and Claesson 1988). A new g-function generator was developed that overcomes the limitations of previous efforts. This generator can calculate g-functions on the fly during the iterative configuration selection and sizing process for VBGHEs (Cook and Spitler 2021a). In addition, an extended g-function library for more than 34,000 borehole field configurations was generated and published to provide more options for designing VBGHEs (Spitler et al. 2021b). The new g-function generator and the extended g-function library were leveraged to develop a new design tool, named GHEDesigner, that can automatically select and size VBGHEs with flexible configurations. Intermodal validation indicates GHEDesigner provides results that differ by less than 4% for the same burial depth and load representation as constrained to GLHEPro (2016), a widely accepted design tool for VBGHEs. Furthermore, GHEDesigner enables many alternative designs that are not possible with existing design tools, such as various spacing among boreholes, boreholes with inclined angles, and boreholes with nonuniform depths in a bore field. It can find the near-optimal

borehole field arrangement within the user-specified available regular or irregular land area (Spitler et al. 2022a). Case studies have shown that the required drilling can be reduced by using a near-optimal borehole field arrangement (in some cases, by greater than 40%) while meeting the thermal loads (Spitler et al. 2020, 2022a, 2022b). The reduced drilling requirement can help lower the cost and enable the wider adoption of GSHP systems.

EXAMPLE OF PRECALCULATED RESULTS

Simulations with various combinations of the following design parameters were conducted and the key simulation results were stored in a database. The following pre-calculated results can provide quick information for GSHP screening.

- Sixteen DOE commercial prototype buildings, which are designed based on the 2007 version of ASHRAE Standard 90.1 (ASHRAE 2011) to represent existing buildings that are near the time to retrofit their existing HVAC systems
- Fifteen climate zones in the United States
- Two HVAC systems: (1) an existing HVAC system in the prototype building and (2) a distributed GSHP system
- Four variations in windows
 - Minimum code-compliant windows (used in the original prototype models)
 - High-performance windows
 - A 20% larger window-to-wall (WWR) ratio than that used in the prototype models
 - High-performance windows and a 20% larger WWR
- Two levels of ground thermal conductivities: low and high

Table 2 lists key screening results of the GSHP retrofit for 16 types of commercial buildings in 15 climate zones in the United States (indicated in the header using 1A–8A), which includes the percentage of annual energy cost savings, GHE length per system capacity, simple payback period, and annual return on investment (ROI). As noted, the current analysis does not include hybrid systems. The following observations can be made:

- The percentage of energy cost savings from a GSHP system is generally higher in very hot or cold climates (note darker green columns for climate zones 1A, 2A, 2B, and 8A in the first part of the table). However, the required length of GHE per ton of GSHP system capacity is also very high in these climates (note the red columns in the second part of the table). This resulted in higher payback periods and lower or negative annual ROI for most building types in those climates (note red cells in the third and fourth tables).
- Small hotels, outpatient hospitals, and high-rise apartments are among a few building types that have a higher-energy cost savings percentage from a GSHP system installation in most climate zones (note rows with darker green cells in the first table). Even though these building types have the moderately high required length of GHE per ton of GSHP system capacity (note corresponding rows having lighter green cells in the second part of the table) requiring higher capital cost, installing a GSHP system is generally cost-effective for these buildings in most moderately hot or cold climate zones with a lower payback period and a higher annual ROI (note green cells in the third and fourth parts of the table).

Table 2. Examples of key screening results of GSHP applications¹

Energy Cost Savings (%)	1A (Very Hot Humid)	2A (Hot Humid)	2B (Hot Dry)	3A (Warm Humid)	3B (Warm Dry)	3C (Warm Marine)	4A (Mixed Humid)	4B (Mixed Dry)	4C (Mixed Marine)	5A (Cool Humid)	5B (Cool Dry)	6A (Cold Humid)	6B (Cold Dry)	7A (Very Cold)	8A (Subarctic /Arctic)
High-rise Apartment	38.7	36.5	37.1	32.1	30.1	21.1	32.5	29.8	27.8	33.3	31.2	34.2	31.4	33.6	36.0
Mid-rise Apartment	24.4	22.7	24.3	20.2	19.4	14.6	20.4	19.9	19.1	19.4	20.9	23.5	19.7	17.5	18.1
Hospital	21.1	30.6	28.0	30.3	27.5	20.1	31.3	28.6	25.0	30.0	29.8	30.9	30.1	30.8	35.2
Outpatient Healthcare	38.2	39.9	38.8	38.4	36.7	35.2	40.0	37.7	38.0	39.9	39.8	40.1	39.4	42.1	46.7
Large Hotel	35.8	34.3	31.7	29.5	25.8	19.8	28.0	22.1	22.6	27.8	23.1	27.1	22.7	26.3	28.0
Small Hotel	43.9	44.1	45.3	41.6	40.2	36.1	41.2	42.4	39.1	42.1	43.9	42.2	42.3	43.2	45.5
Large Office	20.8	20.5	14.8	19.0	12.8	4.1	19.0	10.6	7.0	13.5	10.9	13.6	10.9	12.2	13.6
Medium Office	19.0	20.6	19.0	18.1	14.6	10.5	20.0	12.7	17.2	21.1	16.1	24.0	18.1	24.2	29.1
Small Office	15.6	15.5	16.5	13.6	13.0	8.9	13.8	13.7	11.1	13.8	14.2	14.5	14.6	14.3	15.0
Full Service Restaurant	23.3	24.2	25.9	22.4	22.9	9.8	23.8	21.2	19.5	23.6	22.8	26.2	24.2	27.1	29.3
Quick Service Restaurant	17.4	19.5	22.3	18.3	19.4	11.6	20.0	17.3	16.9	19.7	18.0	22.0	20.3	23.2	27.7
Strip Mall	25.0	26.7	30.1	23.7	24.8	15.5	23.8	22.2	20.3	23.0	23.4	23.9	23.4	24.2	26.8
Stand-alone Retail	30.0	29.6	30.2	28.7	28.4	23.0	29.5	26.8	24.3	30.4	29.5	31.8	30.9	32.2	35.8
Primary School	23.9	22.3	22.0	18.4	16.9	12.1	19.4	14.6	14.5	19.2	15.7	20.1	16.4	20.5	23.9
Secondary School	35.4	33.5	30.3	28.4	23.8	12.7	28.8	19.2	17.8	27.0	21.2	27.6	22.5	27.5	29.8
Warehouse	22.0	12.3	23.8	11.1	17.1	3.3	10.0	9.0	4.6	10.0	8.6	11.2	7.6	12.4	8.2

GHE Length per System Capacity (ft/ton)	1A (Very Hot Humid)	2A (Hot Humid)	2B (Hot Dry)	3A (Warm Humid)	3B (Warm Dry)	3C (Warm Marine)	4A (Mixed Humid)	4B (Mixed Dry)	4C (Mixed Marine)	5A (Cool Humid)	5B (Cool Dry)	6A (Cold Humid)	6B (Cold Dry)	7A (Very Cold)	8A (Subarctic /Arctic)
High-rise Apartment	432	352	485	261	381	148	207	219	138	215	156	289	188	430	1,055
Mid-rise Apartment	378	310	443	214	337	136	175	185	118	186	129	255	180	390	982
Hospital	483	398	541	308	383	231	251	253	203	228	199	189	171	153	163
Outpatient Healthcare	463	368	508	283	362	221	230	244	192	210	190	177	164	143	340
Large Hotel	398	305	450	227	316	148	182	186	136	168	138	143	117	136	400
Small Hotel	295	234	349	172	254	147	143	156	125	128	115	117	103	105	286
Large Office	416	339	463	259	343	194	208	218	169	190	167	161	145	125	142
Medium Office	342	286	430	213	297	154	178	186	143	165	138	136	119	188	610
Small Office	317	260	379	206	275	114	165	167	129	156	123	209	152	298	74,286
Full Service Restaurant	373	290	409	203	281	90	149	153	98	145	109	125	92	130	584
Quick Service Restaurant	402	302	437	197	299	86	146	164	87	145	105	129	107	195	674
Strip Mall	310	259	369	172	258	107	142	152	96	140	101	170	163	246	687
Stand-alone Retail	262	239	362	163	227	86	124	137	98	103	95	131	84	192	600
Primary School	439	342	453	250	315	193	207	216	150	202	162	179	126	277	802
Secondary School	408	310	410	240	286	167	192	191	127	182	144	161	124	242	691
Warehouse	244	168	332	144	202	86	207	146	204	281	218	383	318	570	1,567

Simple Payback (year)	1A (Very Hot Humid)	2A (Hot Humid)	2B (Hot Dry)	3A (Warm Humid)	3B (Warm Dry)	3C (Warm Marine)	4A (Mixed Humid)	4B (Mixed Dry)	4C (Mixed Marine)	5A (Cool Humid)	5B (Cool Dry)	6A (Cold Humid)	6B (Cold Dry)	7A (Very Cold)	8A (Subarctic /Arctic)
High-rise Apartment	12	11	16	9	13	8	7	8	6	7	6	8	7	13	26
Mid-rise Apartment	18	16	22	12	17	8	10	10	7	11	7	10	10	24	53
Hospital	16	8	13	6	9	8	5	6	6	5	5	4	4	3	3
Outpatient Healthcare	9	7	10	5	7	4	4	5	4	4	4	3	3	2	5
Large Hotel	10	8	14	8	13	8	7	10	8	7	7	6	6	6	16
Small Hotel	9	7	10	6	8	5	5	5	4	4	3	4	3	3	7
Large Office	18	15	32	13	27	50	11	23	28	15	18	13	15	11	12
Medium Office	28	22	39	19	34	25	15	27	15	13	17	9	12	12	31
Small Office	33	28	43	25	34	19	19	21	20	18	15	22	17	31	2,324
Full Service Restaurant	19	15	18	12	14	11	8	8	6	7	6	5	4	5	18
Quick Service Restaurant	30	21	23	15	16	8	9	10	6	8	6	6	5	8	18
Strip Mall	26	21	24	17	19	13	13	13	10	13	9	15	13	24	59
Stand-alone Retail	18	18	25	14	18	9	11	12	11	9	8	11	7	16	46
Primary School	19	17	25	15	21	19	13	20	14	13	14	11	10	15	35
Secondary School	14	12	20	12	18	23	10	18	14	11	13	9	10	14	33
Warehouse	24	25	25	24	18	28	33	26	49	50	44	55	75	78	310

Annual ROI (%)	1A (Very Hot Humid)	2A (Hot Humid)	2B (Hot Dry)	3A (Warm Humid)	3B (Warm Dry)	3C (Warm Marine)	4A (Mixed Humid)	4B (Mixed Dry)	4C (Mixed Marine)	5A (Cool Humid)	5B (Cool Dry)	6A (Cold Humid)	6B (Cold Dry)	7A (Very Cold)	8A (Subarctic /Arctic)
High-rise Apartment	0.88	1.59	(0.37)	2.33	0.60	3.27	3.49	2.84	4.33	3.60	4.51	2.97	3.88	0.66	(2.82)
Mid-rise Apartment	(1.12)	(0.36)	(2.00)	1.02	(0.74)	2.84	2.06	1.99	3.93	1.47	3.82	1.92	2.01	(2.03)	(5.78)
Hospital	(0.42)	2.92	0.64	4.17	2.47	3.03	5.37	4.41	4.73	5.50	5.80	6.72	6.81	7.86	8.54
Outpatient Healthcare	2.53	4.00	1.98	5.08	3.72	6.06	6.38	5.70	6.92	6.75	7.23	7.85	8.01	9.33	5.74
Large Hotel	2.12	2.90	0.09	3.28	0.81	3.00	3.82	2.09	3.52	4.17	3.55	4.88	4.44	4.90	(0.24)
Small Hotel	2.57	3.75	1.98	4.90	3.22	5.46	5.82	5.84	6.47	6.50	7.51	7.33	8.02	7.86	3.67
Large Office	(0.96)	(0.27)	(3.93)	0.65	(2.97)	(5.99)	1.60	(2.21)	(3.19)	(0.07)	(1.03)	0.86	(0.21)	1.48	1.39
Medium Office	(3.22)	(2.18)	(4.90)	(1.43)	(4.14)	(2.79)	(0.07)	(3.16)	(0.29)	0.61	(0.68)	2.40	0.92	0.87	(3.67)
Small Office	(4.00)	(3.32)	(5.30)	(2.69)	(4.25)	(1.43)	(1.44)	(1.93)	(1.62)	(1.01)	(3.62)	(1.90)	(0.80)	(3.62)	(22.11)
Full Service Restaurant	(1.47)	(0.08)	(1.07)	1.14	0.33	1.27	3.29	2.89	4.47	3.69	4.91	5.47	6.68	5.63	(0.67)
Quick Service Restaurant	(3.60)	(1.69)	(2.24)	(0.05)	(0.57)	3.26	2.42	2.13	4.77	2.98	4.56	4.86	5.82	3.28	(0.58)
Strip Mall	(2.86)	(1.74)	(2.41)	(0.67)	(1.27)	0.70	0.58	0.45	2.12	0.65	2.49	0.24	0.59	(2.22)	(6.34)
Stand-alone Retail	(1.01)	(1.11)	(2.74)	0.17	(1.16)	2.24	1.60	0.78	1.48	2.39	2.84	1.51	3.45	(0.31)	(5.39)
Primary School	(1.41)	(0.73)	(2.63)	(0.23)	(1.90)	(1.19)	0.70	(1.41)	0.19	0.79	0.14	1.80	1.88	0.06	(3.93)
Secondary School	0.04	0.79	(1.61)	0.86	(1.05)	(2.18)	1.87	(0.97)	0.44	1.70	0.78	2.58	2.02	0.60	(3.59)
Warehouse	(2.51)	(2.72)	(2.65)	(2.31)	(1.15)	(2.55)	(3.39)	(2.52)	(5.03)	(5.20)	(4.82)	(5.46)	(7.18)	(7.02)	(12.73)

¹ Based on heating and cooling degree-days, ASHRAE (2021) defines climate zones 1 through 8 as very hot, hot, warm, mixed, cool, cold, very cold, and subarctic/arctic; and subclimate zones A, B, and C as moist, dry, and marine, respectively.

REAL-TIME SIMULATION WITH AUTOMATED MODEL CREATION AND SIMULATION

To evaluate GSHP applications in other buildings that were not precalculated, a fully automated process was implemented to create a BEM and perform the screening analysis, as depicted in Figure 2. AutoBEM was used to automatically create a BEM. The BEM was created based on a few characteristics of a building, including the footprint, height, principal function, and age (New et al. 2018). AutoBEM has a database covering 98% of the 125,714,640 existing buildings detected in the United States, and it adopts other building properties, such as occupancy, equipment, and insulation, from the DOE prototype buildings to complete the BEM. With this fully automated process, users can specify an existing building from a satellite view of a map and all the needed calculations will be performed automatically to determine the cost and benefits of retrofitting the existing conventional HVAC system with a new GSHP system.

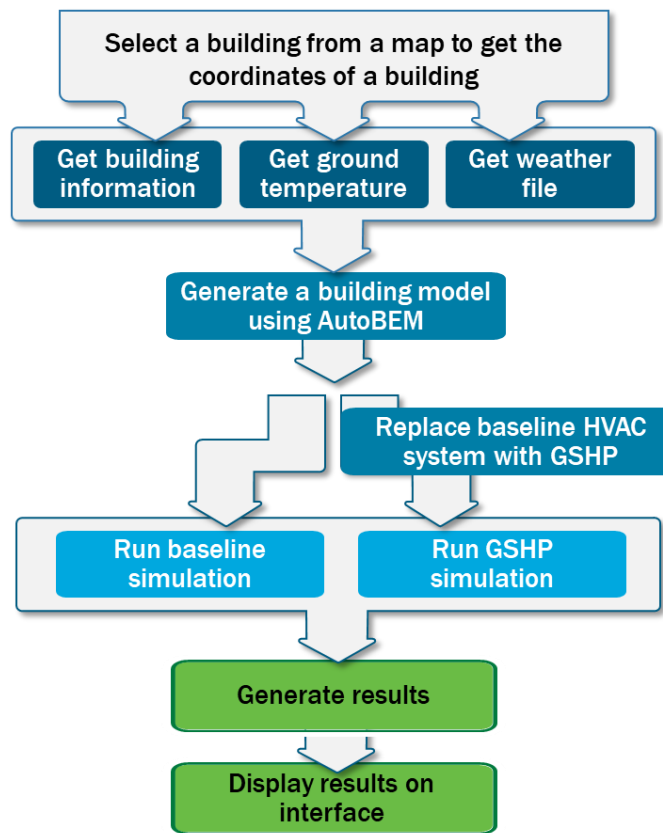


Figure 2 Flowchart of an automated real-time simulation for a user-selected existing building.

WEB INTERFACE

The web interface was built using the JHipster framework stack, which comprises Java EE (a programming language) with MySQL (a relational database) and an Angular/HTML front end. The web application has three web pages. The first page (Figure 3) collects user input for the climate zone, building type, and vintage of the target building through dropdown menus. Also, a map feature allows users to select the location of any existing building shown on the satellite view of the map. The map feature will determine the climate zone of the location. Other fields on this page display more information about the target building, including the existing heating and cooling system (or the default HVAC system if it is new construction), total floor area, and number of floors.

BETA RELEASE

Please select the type of simulation you would like to view

Pre-configured building

Real time simulation

Basic Building Information

Fill out the form that best represents your building information.

[Click here for help](#)

Climate Zone * 5A (Cool Humid)

Building Type * Secondary School

Existing or New building Existing

Heating Type Gas furnace and gas boiler

Cooling Type Packaged air conditioner and air-cooled chiller

Total Floor Area 210,900 sqft

Number of Floors 2

Inputs with * mean they are required.

Next

Figure 3 The first page of the web-based GSHP Screening Tool for selecting a target building.

The second page (Figure 4) allows users to select some design parameters of the building and the GHE. These parameters include the ventilation rate, WWR, window type, and ground thermal conductivity. Fields are initially set to default values, but users can change the fields to select different values. Users can select the “Simulate” button at the right-bottom of this webpage to display precalculated results or run real-time automated design and analysis.

BETA RELEASE

Building Design Parameters

Ventilation * Standard

Window to Wall Ratio * Default

Window Type * Default

GHE Design Parameters

Type of GHE Vertical

Ground Conductivity * Low

Back Simulate

Figure 4 The second page of the web-based GSHP Screening Tool for selecting design parameters.

The results are displayed on the third page (Figure 5), including the total borehole length and the total capacity of the GSHP system, benefits, and the economics of the GSHP system compared with the conventional HVAC system commonly used for the simulated building. The displayed results include annual savings in electricity, natural gas, site

energy, and source energy, as well as the reduction in annual carbon emissions, annual peak electricity demand, and annual water usage. In addition, the cost premium of the GSHP system,² simple payback period, and annual ROI are displayed. These economic results can be updated in real-time based on user inputs of the prices of natural gas, electricity, water, and GHE.

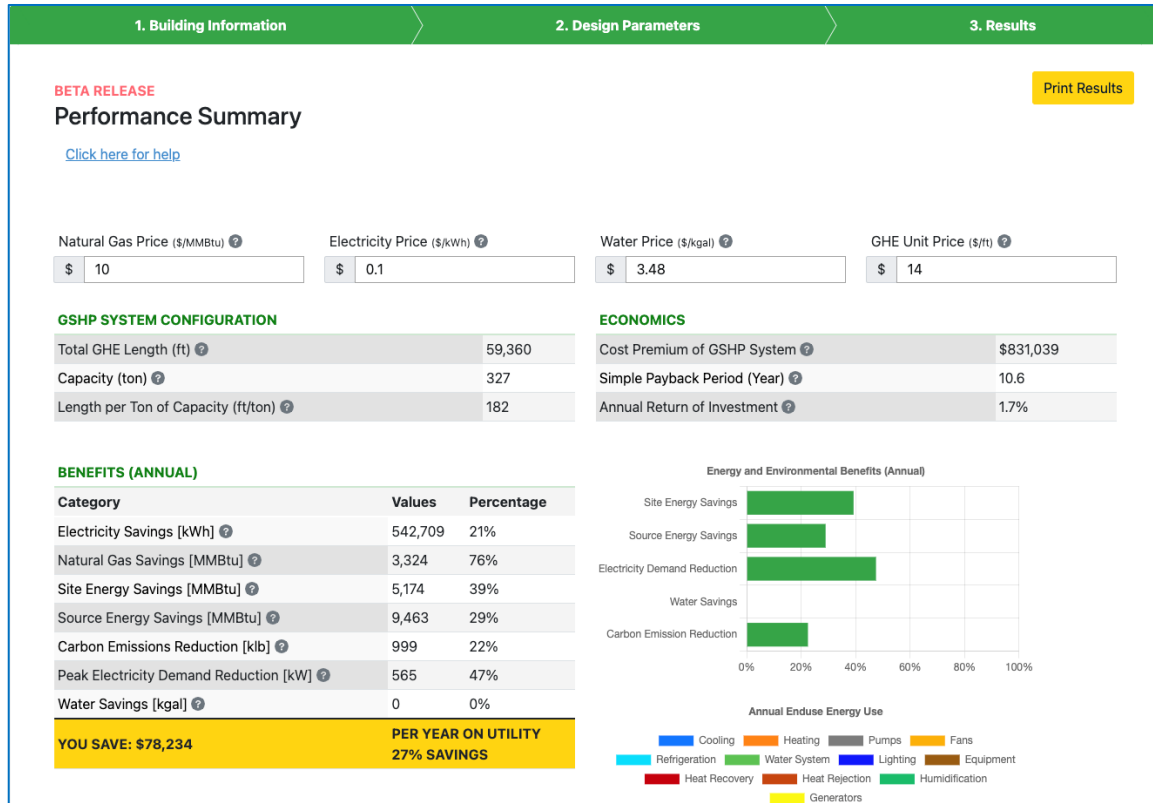


Figure 5 The third page of the web-based GSHP Screening Tool for displaying results.

CONCLUSIONS AND FURTHER DEVELOPMENT

A web-based tool to quickly evaluate the techno-economic feasibility of GSHP applications was developed to enable wider consideration and adoption of GHP technologies. A beta version of the tool (<https://gshp.ornl.gov/>) is now available online. The GSHP Screening Tool includes precalculated screening results with DOE prototype building models in 15 climate zones in the United States. It also enables real-time simulation of almost any existing building in the United States by integrating with ORNL’s AutoBEM to automatically create a building model based on simple inputs of footprint, height, function, and age of the building. The results of this tool include the design, benefits, and economics of the GSHP system compared with the conventional HVAC system commonly used for the simulated building. The economic results can be updated in real-time based on user inputs of the prices of natural gas, electricity, water, and GHE.

Further development is planned to improve flexibility, convenience, and accuracy of the screening, including

- Adding a function to obtain utility rates from utility companies serving the region where the building is located;

² In the alpha release, the cost premium of the GSHP system is approximated as the cost of the GHE.

- Allowing users to perform hypothetical analyses to evaluate alternative designs of the building and the GSHP system, including hybrid systems in which part of the load is met through other systems (e.g., a GSHP combined with a cooling tower or boiler), user inputs for the desired supply temperature range of the GHE, and proper models of the phase change of water in the ground surrounding the borehole when the GHE is allowed to run at a below-freezing temperatures;
- Compiling and integrating a database of available ground thermal conductivities in the United States; and
- Compiling and integrating a database of the costs of conventional HVAC and GSHP systems in the United States

ACKNOWLEDGMENTS

The development of this library was funded through the US Department of Energy contract DE-AC05-00OR22725 with Oak Ridge National Laboratory. This project used the resources of Oak Ridge National Laboratory's Building Technologies Research and Integration Center. The US government retains and the publisher, by accepting the article for publication, acknowledges that the US government retains a nonexclusive, paid-up, irrevocable, worldwide license to publish or reproduce the published form of this manuscript or allow others to do so, for the US government purposes.

REFERENCES

- ASHRAE. 2011. *90.1-2010 User's Manual: ANSI/ASHRAE/IES Standard 90.1—Energy Standard for Buildings except Low-Rise Residential Buildings*. Atlanta, Georgia.
- ASHRAE. 2021. *ANSI/ASHRAE Standard 169-2021—Climatic Data for Building Design Standards*. Atlanta, Georgia.
- BLOCON. 2017. "Earth Energy Designer (EED) Version 4 Update Manual." Retrieved February 13, 2019, from <https://buildingphysics.com/eed-2/>.
- Cook, J. C. and J. D. Spitler. 2021. "Faster computation of g-functions used for modeling of ground heat exchangers with reduced memory consumption." *Building Simulation 2021*. Bruges, Belgium, IBPSA.
- DOE (US Department of Energy). 2022. Prototype Building Models. [Online] Available at <https://www.energycodes.gov/prototype-building-models> (accessed May 7, 2022).
- Eskilson, P. and J. Claesson. 1988. "Simulation Model for Thermally Interacting Heat Extraction Boreholes." *Numerical Heat Transfer* 13(2): 149–165.
- Gaia Geothermal LLC. 2016. *Ground Loop Design: Geothermal Design Studio 2016 Edition User's Manual*.
- GLHEPro. 2016. *GLHEPro 5.0 For Windows User's Guide*. Oklahoma State University. Distributed by IGSHA.
- Liu, X and G. Hellström. 2006. "Enhancements of an Integrated Simulation Tool for Ground-Source Heat Pump System Design and Energy Analysis." In *Proceedings of the 10th International Conference on Thermal Energy Storage*, Richard Stockton College of New Jersey, May 31–June 2, 2006.
- Liu, X., P. Hughes, K. McCabe, J. Spitler, and L. Southard. 2019. *GeoVision Analysis Supporting Task Force Report: Thermal Applications—Geothermal Heat Pumps*. ORNL/TM-2019/502, Oak Ridge National Laboratory, Oak Ridge, Tennessee.
- New, J. R., M. Adams, P. Im, H. Yang, J. Hambrick, W. Copeland, L. Bruce, and J. A. Ingraham. 2018. "Automatic Building Energy Model Creation (AutoBEM) for Urban-Scale Energy Modeling and Assessment of Value Propositions for Electric Utilities." In *Proceedings of the International Conference on Energy Engineering and Smart Grids (ESG)*, Fitzwilliam College, University of Cambridge, Cambridge, United Kingdom, June 25–26, 2018.
- NRC (Natural Resources Canada). 2005. "Ground-Source Heat Pump Project Analysis." In *Natural Resources Canada's Renewable and Electrical Energy Division*. <https://publications.gc.ca/collections/Collection/M39-111-2005E.pdf>.
- NREL (National Renewable Energy Laboratory). 2020. "OpenStudio – Current Features." http://nrel.github.io/OpenStudio-user-documentation/getting_started/features/.

- Spitler, J. D., J. C. Cook, and X. Liu. 2020. "A Preliminary Investigation on the Cost Reduction Potential of Optimizing Bore Fields for Commercial Ground Source Heat Pump Systems." In *Proceedings of the 45th Workshop on Geothermal Reservoir Engineering*. Stanford, California, Stanford University.
- Spitler, J. D. and J. C. Cook. 2021a. "Sizing Ground Heat Exchangers with Rectangular Constraints." Oklahoma State University. Milestone Report Submitted to ORNL on 02/26/2021.
- Spitler, J. D., J. Cook, T. West, and X. Liu. 2021b. *G-Function Library for Modeling Vertical Bore Ground Heat Exchanger*. Oak Ridge National Laboratory, Oak Ridge, Tennessee. <https://doi.org/10.15121/1811518>.
- Spitler, J. D., T. Timothy, and X. Liu. 2022a. "Ground Heat Exchanger Design Tool with RowWise Placement of Boreholes." Submitted to the 2022 IGSHPA annual conference, December 6-8, Las Vegas, Nevada.
- Spitler, J. D., T. Timothy, X. Liu, and I. Borshon. 2022b. "An open library of g-functions for 34,321 configurations." Submitted to the 2022 IGSHPA annual conference, December 6-8, Las Vegas, Nevada.
- Xing, L. 2014. *Estimation of Undisturbed Ground Temperatures using Numerical and Analytical Modeling*. Ph.D. Thesis. Oklahoma State University.